ASD-TDR-63-324

SYMPOSIUM ON THE ROLE OF SUBSTRUCTURE IN THE MECHANICAL BEHAVIOR OF METALS

TECHNICAL DOCUMENTARY REPORT NO. ASD-TDR-63-324

April 1963

406 794

Directorate of Materials and Processes
Aeronautical Systems Division
Air Force Systems Command
Wright-Patterson Air Force Base, Ohio

FOREWORD

[illegible] contains papers presented at a symposium sponsored by [illegible] Metallurgy Branch, Metals and Ceramics Laboratory, Directorate [illegible] and Processes. The symposium was held at the Air Force [illegible] site at Orlando AFB, Florida on 5,6, and 7 December 1962.

With the increased demand upon the capabilities of metals, it is necessary to increase our understanding of the fundamental properties which influence their mechanical behavior. The existence of substructure in crystalline materials has been recognized for many years and has been shown to have important effects on their properties.

Through the development of new research tools, such as transmission electron microscopy and advanced x-ray diffraction, great progress in defining the role of substructure has been made in recent years and it was felt that the time was appropriate for a symposium. Papers were invited to cover both the state-of-the-art and current research in progress and were divided into the following four sessions: (1) Experimental Techniques for Observing and Measuring Substructure; (2) Development of Substructure by Deformation, Recovery, and Recrystallization; (3) The Role of Substructure in Yielding, Twinning, and Fracture; and (4) The Role of Substructure in Transformation and Precipitation. A fifth session consisted of a panel discussion which summarized the main contributions of the conference and highlighted the critical problems which remain to be solved.

The Physical Metallurgy Branch wishes to express appreciation for the excellent support provided by the session chairmen who not only acted in this capacity, but also planned the material to be covered and invited the papers. They were Professor S. Weissmann, Professor C. S. Barrett, Professor W. S. Owen, Dr. L. S. Darken, and Professor M. Cohen who chaired the respective sessions mentioned above.

ABSTRACT

The papers contained in this technical documentary report were presented at a symposium which dealt with the subject of substructure and its effect on the mechanical properties of metals. The symposium was held in Orlando, Florida on 5-7 December 1962. Both review papers and reports of current research are included. The following general subject areas are covered: experimental techniques for observing and measuring substructure; development of substructure by deformation, recovery, and recrystallization; the role of substructure in yielding, twinning, and fracture; and the role of substructure in transformation and precipitation.

This technical documentary report has been reviewed and is approved.

I. PERLMUTTER
Chief, Physical Metallurgy Branch
Metals and Ceramics Laboratory
Directorate of Materials and Processes

TABLE OF CONTENTS

Internal Friction Studies of Substructure*

A. V. Granato
University of Illinois, Urbana, Illinois

Abstract

A review is given of the type of information concerning mechanical properties of crystals obtainable from internal friction measurements. The methods of measurement, together with their advantages, disadvantages and limitations are outlined. Results are described within a framework in which defect interactions are considered from the "particle" point of view. A selection of results found by internal friction techniques which are often difficult to obtain by other methods is described. These include recent measurements which have contributed to the understanding of dislocation interactions with point defects and phonons, as well as dislocation distributions in deformed materials.

I. Introduction

A. Concerning the Definition of Substructure. If by substructure, one means structure having to do with small angle boundaries, then it must be admitted at the outset that internal friction methods have so far provided us with very little information about this aspect of mechanical behavior. On the other hand, if the definition of substructure is broadened to include other defects, as has been suggested, then we find that internal friction methods supply us with much information of a type which is often difficult to acquire by other methods. For the purposes of the present article, we shall regard grain boundaries as the primary structure, and all other defects including single dislocations, dislocations in interaction with other dislocations to form small angle boundaries, point defects, etc., as composing the substructure.

B. Mobility of Dislocations. The extent to which internal friction techniques can be used to study dislocations the extent to which the dislocations are mobile. In a solid containing no defects, ultrasonic plane waves should propagate without attenuation. A plane wave traveling in a solid containing dislocations is attenuated, and the attenuation depends sensitively upon the mobility

*Manuscript released by authors March 1963 for publication as an ASD Technical Documentary Report.

of the dislocations. The mobility, in turn, depends upon the interactions of dislocations with point defects, phonons and other dislocations. Thus, measurements of internal friction, or ultrasonic wave propagation in crystals, are uniquely suited for the study of dislocation interactions with other defects. On the other hand, if the dislocation interactions are such as to render the dislocations immobile, then no internal friction is obtained. Thus the technique is limited to the study of mobile dislocations.

C. Some General Features of Internal Friction Measurements. Advantages of internal friction measurements derive from (1) the sensitivity of the method, (2) the selectivity of the measurements, (3) the fact that the results can be made quantitative, and (4) the fact that the measurements are non-destructive. For example, defect concentrations of the order of 10^{11} cm^{-3} can have an important effect on the internal friction. Also, the internal friction is sensitive only to those point defects which arrive at dislocations, in contrast to properties such as resistivity, which are sensitive to all the defects in the lattice. The method is especially suited to the study of defect interactions, since it is only by these interactions that changes in the ultrasonic wave propagation characteristics are induced. A large amount of detail can be found because of the large number of variables which can be controlled (frequency, strain amplitude, temperature, point defect concentration, ultrasonic mode orientation, purity, deformation, and others). As a disadvantage, a detailed theory or model of dislocation interactions is required to interpret the results. The latter difficulty is one which has held up progress in the use of this technique until quite recently.

Measurements of internal friction tend to complement, and not to compete with measurements made by direct observations and also with other indirect observations. Internal friction measurements differ from other indirect observations in sensitivity and in the linearity of the effects with defect concentrations. For example, properties such as resistivity, lattice parameter, density and stored energy are usually linear in the defect concentration, and this fact leads to simplicity in interpretation of results. However, it is normally necessary to have defect concentrations considerably in excess of parts per million to obtain measurable effects. On the other hand, internal friction measurements require more interpretation (the internal friction depends on the fourth power of the pinning point density in common cases), but fewer defects are required for measurable effects and more detail is obtained in the measurements.

D. Methods of Measurement. A great deal of work so far has been done in the kilocycle and megacyle range, although some work has also been carried out at lower frequencies. The techniques used have been well described in many places.[1] We shall only mention here some of those features of importance in work on the study of defects in crystals. In the 10-40 kilocycle range the technique usually used is to set up a standing wave in a long thin specimen. A typical size of specimen might be about a quarter inch in diameter and two inches in length. Harmonics of the fundamental vibration may also be used but there are difficulties here because different parts of the specimen are excited for different harmonics. The specimen may be driven into resonance by an eddy current drive or by a quartz rod attached to the specimen. The advantage of the former method of coupling is that measurements as a function of temperature are easily made. Even in the latter case, the quartz may be bonded to the specimen at a strain node so that deformation arising from differential expansion at the specimen-quartz interface during temperature changes does not disturb the measurement greatly. The strain amplitude may be varied from below 10^{-8} to above 10^{-5}, depending upon the specimen damping.

Measurements in the 3-300 mc/sec range are made using the pulse technique. Specimens are often in the shape of flat cylindrical disks with typical dimensions of half inch in thickness and one inch in diameter. A thin quartz transducer disk, of diameter half inch or less, is attached by means of an extremely thin bonding layer. The transducer is used both as a transmitter and receiver of ultrasonic pulses. After each round trip in the specimen the pulse is detected and all the echoes are displayed on an oscilloscope, from which the attenuation is measured. Measurements as a function of temperature offer difficulties here, since the differential expansion at the specimen-quartz interface introduces deformation in soft crystals. However, frequency measurements are easier to make here than in the kilocycle region. All odd harmonics of the fundamental driving frequency of the quartz can be used until the attenuation becomes too large to measure. Also several modes of propagation (longitudinal and shear) can usually be used, permitting a study of orientation effects. Normally the strain amplitudes available are low, of the order of 10^{-7} or less. The major difficulty in specimen preparation here is in the requirement that the two reflecting faces be accurately parallel. For measurements above about 50 mc/sec, optical tolerances are often required. It is possible to mount the transducer on the end face of a tensile specimen, so that measurements of attenuation and velocity can be made during deformation.[2] In

summary, measurements as a function of temperature and strain amplitude are easy in the kilocycle region and difficult in the megacycle region, but measurements as a function of deformation, frequency and orientation are easy in the megacycle region and difficult in the kilocycle region.

In what follows, we give first a discussion of the model used in interpreting internal friction effects, then a framework in terms of defect interactions in which the experiments are to be discussed, and finally, a discussion of a limited selection of experiments as examples of the type of information concerning mechanical properties obtainable from internal friction experiments.

II. The Model

A. Types of Effects. There are a number of ways in which dislocations can contribute to internal friction. A dislocation segment oscillating between two pinning points (vibrating string model) gives one characteristic type of damping. Dislocations which break away from pinning points under stress lead to another type. Dislocations which move by overcoming Peierls barriers are supposed to give rise to the low temperature Bordoni peaks. There are also other mechanisms, models for which have not yet been developed. In particular, there is not as yet a suitable model for the highly deformed state. However, the single dislocation segment model which neglects interactions between dislocations seems to work surprisingly well for moderate deformation (up to about 4%). In what follows we discuss only the vibrating string model since its predictions are definite and many experimental checks of these predictions are now available. We are interested in answering first basic questions such as "What is the physical source of the damping?" and "What is a pinning point?". Then having settled this, we look to see how internal friction measurements can be applied to the study of mechanical properties of crystals.

B. Dislocation Contribution to the Total Strain. The basis for internal friction effects lies in the fact that dislocation motion contributes to the total strain developed in a specimen under stress. For a given applied stress, a solid containing dislocations has a larger strain than a perfect crystal, so that the elastic modulus appears to be lower. Under the action of an alternating stress, the dislocation component of the strain may lag behind the applied stress. This leads then not only to a reduction in modulus but also to a damping of the applied stress. Simple estimates of the magnitude of

the expected effect for typical dislocation densities lead to much larger values than the observed effects if it is assumed that the dislocations are perfectly mobile with no restrictions on their motion. It may therefore be concluded that there must be impediments to the motion of dislocations. Generally speaking, the same types of obstacles have been assumed as those assumed in yield stress theories, where a similar problem is faced. These are, for example: atomic pinning points, network points, jogs, other dislocations, etc. But even with such restrictions, one must explain why the dislocation motion lags behind the applied stress. For smooth dislocation motions, one may imagine that the dislocation is viscously damped as it moves through the electron or phonon gas. Also impediments which lead to a jerky motion of the dislocation will lead to a phase lag. Examples of the latter type of effect are provided by motion over Peierls barriers at low stresses, and catastrophic unpinning of dislocations at high stresses.

C. Vibrating String Model. A model, proposed by Koehler,[3] and developed further by Granato and Lücke,[4] using an analogy between a vibrating string in a viscous medium and dislocation oscillations has been proven to be correct in most of its particulars. In this model, advantage is taken of the fact that a dislocation has an effective mass per unit length and an effective tension. Thus an equation of motion for small oscillations of a dislocation may be written as

$$A\,Y_{tt} + B\,Y_{t} - C\,Y_{xx} = b\sigma \qquad (1)$$

where A is the effective mass for unit length, Y is the dislocation displacement measured from the equilibrium position as indicated in Fig. 1, B is the viscous damping constant, C is the tension, b the Burgers vector, σ the applied stress, t the time, x a coordinate along the dislocation, and subscripts denote differention. The solution of Eq. (1) together with the boundary conditions $Y(o)$ and $Y(\ell) = 0$, where pinning points are placed at $x = 0$ and ℓ gives the dislocation displacement Y as a function of the frequency ω of the applied stress $\sigma(\omega)$. Using this the dislocation strain and then the effective modulus (or ultrasonic wave velocity) and decrement (or ultrasonic wave attenuation) is easily found. The resulting decrement has a typical resonance type frequency behavior, which depends, however, on the magnitude of the viscous damping constant B. Theoretical estimates of the damping constant to be expected for dislocation interactions with phonons[5] and electrons[6] have been made by Leibfried and Eshelby. From these one expects

(1) that the phonon interaction is much larger than the electron interaction, and (2) that the phonon interaction is so large that the dislocation resonance is overdamped. This has the effect of broadening out the resonance and moving it to lower frequencies. Also when account is taken of the fact that not all dislocations have the same length, the expected maximum is broadened out further. For typical expected dislocation segments of length of order 1 micron, the expected resonance frequency is at about 10^9 cycles/sec. However, because of the large damping (we may picture the dislocation as a string moving in heavy molasses), the maximum may be brought down to frequencies as low as 100 kc/sec. At the same frequencies where the decrement goes through a maximum, dispersion in the elastic constant is expected. As is indicated schematically in Fig. 1, the displacement of the dislocation is a function of frequency. (The dislocation strain, and thus the modulus reduction is proportional to the area swept out by the dislocation.) At low frequencies, the velocity of the dislocation is small so that the viscous force is small. The displacement is then limited by the tension forces and is parabolic in shape. At high enough frequencies, however, the viscous forces become dominant, and the displacement of the dislocation cannot achieve its full value. In this case the dislocation moves more like a rigid rod over most of its length, coming down to zero displacement only near the pinning points. Thus we expect the effect of pinning points to be large at low frequencies and negligible at high frequencies.

The dispersion effect is illustrated in Fig. 2 in which the velocity of compressional waves was measured by Granato, de Klerk, and Truell[7] in a sodium chloride crystal as a function of frequency before and after a slight deformation. Before deformation there is only a small dispersion of 0.5% centered at about 75 mc/sec. After the deformation, the magnitude of the dispersion has increased to about 4% and has moved to a lower frequency (35 mc/sec). At room temperature, the dispersion was observed to gradually recover towards the initial condition, presumably as a result of dislocation pinning by deformation induced defects. The interpretation of the effect according to the vibrating string model is as follows. At low frequencies, the dislocations are in phase with the ultrasonic stress. When the stress is applied, the apparent elastic constant (and therefore the ultrasonic velocity) is reduced because the dislocation motion makes the specimen less rigid. However, at high frequencies the dislocations can no longer follow the rapidly changing stress, so that the modulus approaches the true elastic value.

The frequency dependence of the decrement arising from dislocation motion is illustrated in Fig. 3. These are measurements by Stern and Granato[8] showing the effect of cobalt gamma irradiation on the decrement of high purity copper. Before irradiation, the decrement has a maximum at a few megacycles. The gamma rays produce electrons which are energetic enough to displace lattice atoms, giving interstitials which can be effective as pinning points. After 50 hours of irradiation in a 6000 c cobalt source, the height of the maximum decreased and the location increased to about 100 mc/sec. The decrement at low frequencies is much more sensitive to the increased number of pinning points than that at high frequencies, as we expected from our previous discussion of Fig. 1.

According to the theory, the height of the maximum should be proportional to ΛL^2 and the location of the maximum proportional to $1/BL^2$ where Λ is the total dislocation density, and L is the average loop length. At frequencies much lower than that at which the maximum occurs, the decrement should be proportional to $\Lambda L^4 B\omega$ and the modulus to ΛL^2. The predicted dependence on loop length has been confirmed by Thompson and Holmes.[9] Thus measurements of the height and location of the decrement in the megacycle range give the same information as measurements of the decrement and modulus in the kilocycle range. Actually, the two quantities which can be determined from the measurements are the ratios Λ/B and $L/\Gamma c$.[8] Before dislocation densities and loop lengths can be determined, the damping constant B and tension c must be known. We shall discuss means by which the damping constant can be determined in a later section.

III. A Formal Framework In Terms of Defect Interactions.

Because the internal friction effects depend entirely upon the interactions of dislocations with other defects, we shall find it convenient to classify the effects in terms of defect interactions using the "particle" point of view introduced by Seitz.[10] The defects to be considered are dislocations, point defects and phonons. This omits but two of the six primary defects in crystals: electrons and excitons. (Foreign atoms have been lumped into the point defect category together with vacancies and interstitials.) We consider first dislocation interactions between pairs of defects.

A. Dislocation-phonon Interations.

We first note that phonons interact with dislocations in essentially two ways. Just as in the case of Brownian motion of a particle in an external field, a dislocation moving through a phonon gas under the action of an external applied stress is subject to both a

viscous drag and to fluctuations in displacement. The latter effect is thought to give rise to the Bordoni peak, but will not be discussed here.

B. Dislocation-point Defect Interaction. The best known interaction of this type is that first discussed by Cottrell.[11] Because an oversized (or undersized) impurity can relieve the strain energy of the lattice by moving to the dilated (or compressed) region near a dislocation, the dislocation will be bound to the impurity. The binding strength will be small, at most of the order of a few tenths of an electron volt, so that a sufficiently large stress can pull the dislocation away from immobile point defects. Interstitial atoms and vacancies can also act as pinning points. Other possibilities are jogs, dislocation nodes, intersections and places where a dislocation may move out of the slip plane.

C. Dislocation-dislocation Interactions. Dislocations may interact with other dislocations at a distance through their long range stress fields, and also (more strongly) at points of contact. Presumably these effects should become important in deformed materials where the dislocation density is high. The difficulty here is that the predictions of any theory for these effects depend sensitively on the model assumed, but so far no simple model has been established as being representative. Presumably small angle boundaries and pile-ups which are mobile should lead to internal friction with certain special characteristics. Calculations for these configurations have not yet been attempted. Perhaps as a result of the direct observations reported at this conference, we shall learn which of the possible arrangements should be taken most seriously as models for damping in heavily deformed materials. Generally speaking, the measurements show that for high enough deformation, the damping decreases. This shows that the effect of dislocation interactions in inhibiting dislocation mobility more than compensates for the increased dislocation density.

D. Point Defect-Phonon Interactions. By using dislocations as an intermediary defect, diffusion effects can be studied. For example, by measuring the rate at which dislocations are pinned as a function of temperature, the activation energy of migration of defects can be measured.

E. Dislocation-phonon-point Defect Interactions. The combined effect of triple interactions between these basic defects shows up in a striking way in measurements of the effect of thermal fluctuations on dislocation breakaway from pinning points at high strain amplitudes. This is an area which has not yet been exploited.

IV. Some Selected Experiments of Interest in the Study of Mechanical Behavior of Crystals.

A. Dislocation--Phonon interactions. Recently the properties of the internal friction of copper at megacycle frequencies have been studied by Alers and Thompson[12] and also by Stern and Granato.[8] These experiments are complementary since Alers and Thompson studied the attenuation and velocity in a copper crystal before and after neutron irradiation as a function of temperature and orientation, while Stern and Granato studied the attenuation changes during gamma irradiation as a function of irradiation time and frequency. The results will be discussed together. As already noted earlier, and as is easily seen from Fig. 3, at high frequencies, the attenuation depends only on the dislocation density and the damping constant, and not on the loop length or dislocation line tension. By making an independent count of the dislocation density, the magnitude of the damping constant could be determined. Furthermore, the damping constant was found to be linear in temperature. The latter fact is in accord with what is to be expected if scattering by phonons is the source of the damping, since the damping constant should then be proportional to the phonon density according to Leibfried or linear in temperature (at not too low temperatures). The magnitude of the damping constant found was somewhat in excess (about a factor of 4) of that given by Leibfried's estimate. A similar discrepancy is found in the ratio of the observed to the calculated thermal resistance at low temperatures caused by dislocations. Both Alers and Thompson and Stern and Granato concluded that the physical source of the damping at megacycle frequencies was the scattering of phonons by the moving dislocations and that the vibrating string model is applicable. In addition, by extrapolation of megacycle results into the kilocycle range, and vice versa, Granato and Stern[13] were able to show that the same mechanism accounts for the part of the damping observed in the kilocycle range which can be removed by irradiation pinning. Thus it seems safe to say that the question as to the source of the damping is now understood.

An interesting side result here is that from these results, a question that arose early in dislocation theory can now be answered. The question is: "Can relativistic velocities of dislocations be achieved at stresses near the yield stress?" The answer is no. From the value of the magnitude of the dislocation-phonon interaction strength deduced ultrasonically, one finds that in copper at room temperature the relation between velocity and stress[8] is

$$v/c = \sigma/(75G) \qquad (2)$$

where c is the shear wave velocity and G is the shear modulus. Since the theoretical yield stress of a perfect crystal is of order G/30, stresses of the order of the yield stress of perfect crystals would be required for relativistic velocities.

The question which remains is: "What is the mechanism of the scattering of phonons by dislocations?" It has not yet been determined whether this is due to scattering by the strain field (which changes the elastic constants in the vicinity of the dislocation) or whether the scattering is due to a reradiation of sound waves by the dislocation under the influence of the incident phonons.

It has been pointed out by Mason[14] that the same mechanism limits the velocity of dislocations at high stresses as found by Johnston and Gilman[15] in direct observations of the motion of etch pits. From these direct observations, the damping constant for LiFl is found from the relation

$$b\sigma = Bv \qquad (3)$$

to be 7.0×10^{-4} (c.g.s. units). This is the same value found for copper ultrasonically. An ultrasonic experiment in LiF is now in progress at Illinois which should check these independent methods. If the ultrasonic determination agrees with that found from the Johnston-Gilman technique, then it should be possible to determine the dislocation-phonon interaction strength for other materials by the (simpler) ultrasonic method.

B. Dislocation-pinning point interactions. Recently, a significant step forward was taken in this area by Bauer and Gordon,[16] who showed that it is possible, by combining ultrasonic and optical measurements, to identify the atomic configuration which is effective in pinning a dislocation in NaCl. Bauer and Gordon found that dislocation pinning in x-irradiated NaCl proceeded at the same rate at low temperatures as it did at room temperature. From this they concluded that diffusion of point defects is not involved in the pinning process and that the pinning points must be produced at the dislocation core. Further, they discovered that dislocations pinned by irradiation at low temperatures can be unpinned by light. This effect is shown in Fig. 4. Bauer and Gordon note that a model used to explain dislocation pinning must satisfy many conditions to be in agreement with their observations. First, defects must be created at, or in the immediate vicinity of, free dislocation segments; in addition, these defects must act as strong pinning points. Furthermore, the pinning defect

must possess a characteristic optical absorption band and must be simple enough to be "dissolved" when it is ionized or excited. In the case of rock salt it is found, for example, that unpinning is produced only by light with wavelengths within a fairly narrow band centered about 6300Å. Finally, the defect must occur generally in the alkali halides (with the possible exception of LiF). The model must also be capable of explaining how dislocation pinning can be reversed at low temperatures but converted to a permanent type of pinning if the crystal is warmed to room temperature, and how unpinning illumination is capable of unpinning dislocations at low temperatures while F illumination can cause additional pinning at all temperatures. The model put forward by Bauer and Gordon which fits all these experimental facts is one in which the pinning point is identified as a complex consisting of a jog on a dislocation formed by a Cl-ion and a F-center located one atom distance away and below the slip plane. Because this F-center is in a region where the crystal structure is dilated its absorption band is shifted toward the red, i.e., from 4500Å to 6300Å, an amount which is in agreement with the shift calculated from the strain field about a dislocation in rock salt. Ionization of the F-center by 6300Å light results in electrostatic attraction between the negative-ion vacancy so formed and the Cl-ion forming the jog on the dislocation; recombination of this Cl-ion and its neighboring vacancy causes the pinning point to "dissolve". The model predicts that if a crystal irradiated at low temperature is warmed up in the dark to a temperature where F-centers can diffuse and then cooled down again, it should no longer be possible to remove the pinning points by illumination, as is observed.

Another experiment by Baker[17] establishes the result that the velocities observed by Johnston and Gilman are not the velocities of the dislocations at a given stress level, but only the velocities of the pinning points. Baker observes periodic dislocation motion of amplitude 1000b at stress levels an order of magnitude below the macroscopic yield stress. The velocity of the dislocations is then of order 1cm/sec ($v \sim dw$, where d is the amplitude of motion and w is the frequency of oscillation). This result demonstrates that the Peierls force is not effective in limiting dislocation motion. The dislocations oscillate at high speeds between pinning points. The overall motion of the dislocations is limited by the speed of the pinning points. This result is a good example of ways by which internal friction measurements can help to distinguish between various postulated deformation mechanisms.

The fact that the dislocations in NaCl are not Peierls stress limited can also be seen from the low temperature elastic modulus measurements of Bauer and Gordon[16] shown in Fig. 5. The fact that the modulus of unirradiated NaCl is lower than that in the irradiated state shows that the dislocations are mobile even at helium temperatures.

As a final example of the study of dislocation-pinning point interactions we may note the interesting observation made by Hikata and Tutumi[18] shown in Fig. 6. They find a striking similarity in the curves of creep rate and ultrasonic attenuation in aluminum at room temperature. In this case the pinning points must be carried along with the dislocations as they move through the lattice. This suggests that jogs may be the effective pinning points in these measurements. The similarity in the shape of the curves may be understood if both depend primarily on the distance between pinning points and this distance is assumed to decrease with time at constant load. This is so because both attenuation and creep rate depend sensitively upon the distance L between pinning points. The former depends upon the 4th power of L, whereas the latter should depend exponentially upon L. Presumably, L decreases because of jog formation in dislocation intersections. Measurements of both attenuation and velocity should permit one to compute the creep rate curve completely from ultrasonic data.

C. Point defect-phonon interactions. An example of the way in which point defect diffusion migration activation energies can be determined is given by the analysis by Granato, Hikata and Lücke[19] of the recovery data of A.D.N. Smith.[20] Smith deformed copper specimens by 1 percent and measured the recovery of the modulus as a function of temperature and recovery time. By assuming that the recovery mechanism is the pinning of dislocations by deformation induced defects, an activation energy of 1 eV was found, which was assumed to be that for vacancy migration energy. At the time of this assignment, all other assignments for this quantity were either near 0.8 eV or less or 1.2 eV or more. In the meantime, the migration energy has been determined by Simmons and Balluffi,[21] and the ultrasonic value is the only previous assignment in agreement with their value. This suggests that the ultrasonic method may be a useful one for such studies.

A second example of the way in which ultrasonic effects can be used in the study of point defect motion is provided by the measurements of Thompson, Blewitt and Holmes,[22] shown in Fig. 7. In this experiment the modulus (or frequency) of a copper specimen was measured as a function of temperature after a neutron bombardment. The modulus at first decreases

with temperature in the normal way, but at about 40°K, this process is interrupted. Interstitials are known to move at this temperature, and presumably the normal decrease of modulus is being compensated by dislocation pinning by interstitials. After the pinning is complete, the modulus continues to decrease in the normal fashion. When the specimen is recooled, no anomalous effects occur, indicating that the dislocations are now fully pinned and no longer contribute to the modulus. This measurement provides a good example of the selectivity property of ultrasonic measurements. Only those interstitials which migrate to dislocations are detected. Electrical resistance measurements show that annealing occurs at temperatures below 40°K, but these defects do not travel to dislocations.

D. Dislocation-dislocation interactions. It may be expected that, with increasing deformation, dislocation-dislocation interactions should become important. A maximum in the damping as a function of deformation is often observed.[2,23] However, for deformations of less than a few percent, the observed results seem to be understandable on the basis of the vibrating string model, neglecting dislocation interactions. Some interesting results concerning the distribution of dislocations on various slip systems have recently been obtained by Hikata, Chick, Elbaum and Truell.[24] In these experiments, ultrasonic attenuation and velocity as well as stress were measured continuously as a function of strain. The aluminum specimen was oriented for single slip, and ultrasonic waves of two different orientations were used. The results are shown in Figs. 8 and 9. In Fig. 8, results are given for the case where the ultrasonic wave had no shear stress component in the primary glide system. After an initial rise, the stress-strain curve clearly indicates the existence of easy glide for approximately 0.2 percent tensile strain. The corresponding attenuation change is very similar to the stress-strain curve, with little increase of attenuation during the easy glide region even though the dislocation density is increasing greatly as can be seen from the results of Fig. 9. The behavior of longitudinal waves, which have shear stress components in the primary glide system, is quite different. As seen in Fig. 9, the attenuation increases quite rapidly with increasing strain, from the beginning of the deformation, and does not exhibit any special characteristics associated with easy glide. These results show clearly the sensitivity of the ultrasonic measurements to the distribution of dislocations. With further development of the technique, we may look forward to the possibility of having continuous plots of dislocation density and loop lengths as a function of strain in various slip systems.

A second point of much interest in these measurements concerns the interesting variations in the ultrasonic velocity. This is of great usefulness in checking certain fine details in the predictions of the theory,[25] but will not be discussed here.

V. Conclusions.

It is clear that ultrasonic measurements provide us with much useful information concerning defect interactions of importance in understanding the mechanical behavior of crystals. In this review we have discussed qualitative features of a few selected results, but it should be emphasized that results in quantitative form are obtained. Some of the conclusions which have been noted are:

1. The physical source of the sound damping is the dislocation-phonon interaction. Relativistic dislocation velocities cannot be achieved in copper and LiF at room temperature at the yield stress.

2. The vibrating string model is confirmed by the measurements. This model appears to apply even for moderate (up to a few percent) deformation.

3. The atomic configuration making up a pinning point has been identified in NaCl.

4. Deformation in common alkali halides is determined by the motion of pinning points. The dislocation is free to move between such points. Similar considerations seem to apply for creep in aluminum.

5. The migration activation energies of point defects in small concentrations can be determined ultrasonically.

6. A detailed description of dislocation densities and loop lengths in various slip systems may be obtained ultrasonically.

Work currently in progress on the effect of thermal fluctuations on dislocation unpinning promises to provide us with useful information concerning the temperature dependence of the yield stress. There is a need for models suitable for describing the internal friction of heavily deformed materials.

REFERENCES

* Work supported in part by U. S. Atomic Energy Commission

1. W. P. Mason, "Physical Acoustics and the Properties of Solids", D. Van Nostrand, Princeton, New Jersey (1958).

2. A. Hikata, R. Truell, A. Granato, B. Chick and K. Lücke, J. Appl. Phys. 27, 396 (1956).

3. J. S. Koehler, "Imperfections in Nearly Perfect Crystals" (Ed. by W. Shockley, J. H. Hollomon, R. Maurer and F. Seitz) Wiley, New York (1952) Ch. 7.

4. A. Granato and K. Lücke, J. Appl. Phys. 27, 583, 789 (1956).

5. G. Leibfried, Z. Phys. 127, 344 (1950).

6. J. D. Eshelby, Proc. Roy. Soc. (London) A197, 396 (1949).

7. A. Granato, J. de Klerk and R. Truell, Phys. Rev. 108, 895 (1957).

8. R. Stern and A. Granato, Acta Met. 10, 358 (1962).

9. D. O. Thompson and D. K. Holmes, J. Appl. Phys. 27, 713 (1956).

10. F. Seitz, "Imperfections in Nearly Perfect Crystals", (Ed. by W. Shockley, J. H. Hollomon, R. Maurer and F. Seitz) Wiley, New York (1952) Ch. 1.

11. A. H. Cottrell, "Report of a Conference on the Strength of Solids" (University of Bristol, England, Physical Society, London, 1948) p. 30.

12. G. A. Alers and D. O. Thompson, J. Appl. Phys. 32, 283 (1961).

13. A. Granato and R. Stern, J. Appl. Phys. 33, 2880 (1962).

14. W. P. Mason, J. Acoust. Soc. Amer. 32, 458 (1960).

15. W. G. Johnston and J. J. Gilman, J. Appl. Phys. 30, 129, (1959).

16. C. L. Bauer and R. B. Gordon, J. Appl. Phys. 33, 672 (1962).

17. G. S. Baker, Acta Met. 10, 448 (1962).

18. A. Hikata and M. Tutumi, J. Phys. Soc. Japan 14, 687 (1959).

19. A. Granato, A. Hikata and K. Lücke, Acata Met. 6, 470 (1958).

20. A. D. N. Smith, Phil. Mag. 44, 453 (1953).

21. R. O. Simmons and R. W. Balluffi, To be published.

22. D. O. Thompson, T. H. Blewitt and D. K. Holmes, J. Appl. Phys. 28, 742 (1957).

23. J. Weertman and J. S. Koehler, J. Appl. Phys. 24, 624 (1953).

24. A. Hikata, B. Chick, C. Elbaum and R. Truell, Acta Met. 10, 423 (1962).

25. R. Truell and A. Granato, To be published in Proceedings of the 1962 Tokyo Conference on Defects.

REFERENCES

* Work supported in part by U. S. Atomic Energy Commission

1. W. P. Mason, "Physical Acoustics and the Properties of Solids", D. Van Nostrand, Princeton, New Jersey (1958).

2. A. Hikata, R. Truell, A. Granato, B. Chick and K. Lücke, J. Appl. Phys. 27, 396 (1956).

3. J. S. Koehler, "Imperfections in Nearly Perfect Crystals" (Ed. by W. Shockley, J. H. Hollomon, R. Maurer and F. Seitz) Wiley, New York (1952) Ch. 7.

4. A. Granato and K. Lücke, J. Appl. Phys. 27, 583, 789 (1956).

5. G. Leibfried, Z. Phys. 127, 344 (1950).

6. J. D. Eshelby, Proc. Roy. Soc. (London) A197, 396 (1949).

7. A. Granato, J. de Klerk and R. Truell, Phys. Rev. 108, 895 (1957).

8. R. Stern and A. Granato, Acta Met. 10, 358 (1962).

9. D. O. Thompson and D. K. Holmes, J. Appl. Phys. 27, 713 (1956).

10. F. Seitz, "Imperfections in Nearly Perfect Crystals", (Ed. by W. Shockley, J. H. Hollomon, R. Maurer and F. Seitz) Wiley, New York (1952) Ch. 1.

11. A. H. Cottrell, "Report of a Conference on the Strength of Solids" (University of Bristol, England, Physical Society, London, 1948) p. 30.

12. G. A. Alers and D. O. Thompson, J. Appl. Phys. 32, 283 (1961).

13. A. Granato and R. Stern, J. Appl. Phys. 33, 2880 (1962).

14. W. P. Mason, J. Acoust. Soc. Amer. 32, 458 (1960).

15. W. G. Johnston and J. J. Gilman, J. Appl. Phys. 30, 129, (1959).

16. C. L. Bauer and R. B. Gordon, J. Appl. Phys. 33, 672 (1962).

17. G. S. Baker, Acta Met. 10, 448 (1962).

18. A. Hikata and M. Tutumi, J. Phys. Soc. Japan 14, 687 (1959).

19. A. Granato, A. Hikata and K. Lücke, Acata Met. 6, 470 (1958).

20. A. D. N. Smith, Phil. Mag. 44, 453 (1953).

21. R. O. Simmons and R. W. Balluffi, To be published.

22. D. O. Thompson, T. H. Blewitt and D. K. Holmes, J. Appl. Phys. 28, 742 (1957).

23. J. Weertman and J. S. Koehler, J. Appl. Phys. 24, 624 (1953).

24. A. Hikata, B. Chick, C. Elbaum and R. Truell, Acta Met. 10, 423 (1962).

25. R. Truell and A. Granato, To be published in Proceedings of the 1962 Tokyo Conference on Defects.

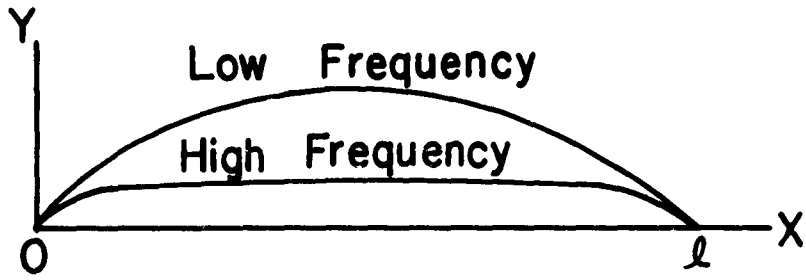

Fig. 1 Schematic dislocation displacement y(x) as a function of coordinate x for a) low frequencies and b) high frequencies. At low frequencies the displacement is limited by tens. n forces. At high frequencies, the displacement is limited by viscous forces.

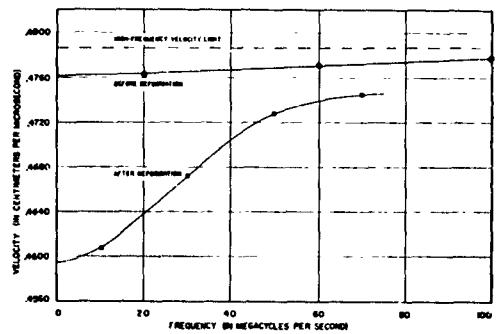

Fig. 2 Velocity dispersion for compressional elastic waves propagating in the (100) direction in NaCl. Deformation increases the magnitude of the dispersion from 0.5% to 4% and moves it to lower frequencies. (After Granato, de Klerk and Truell.)

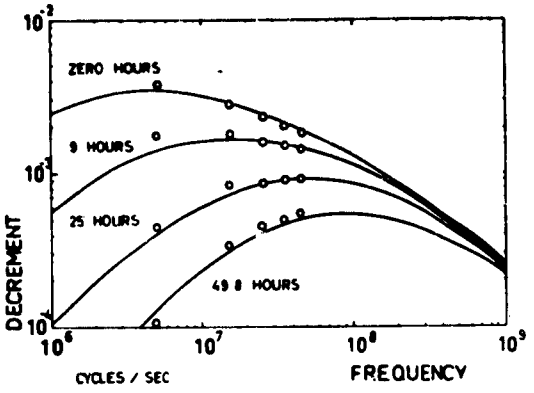

Fig. 3 The dislocation decrement as a function of frequency for several times during cobalt gamma irradiation in a 6000 curie source. The solid curves are theoretical. (After R. M. Stern and A. Granato.)

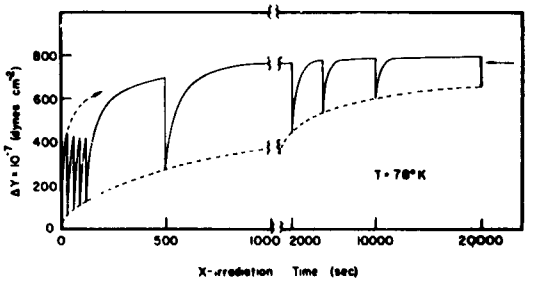

Fig. 4 Behavior of the modulus change of a deformed NaCl crystal, ΔY, during successive x-irradiations and exposure to visible illumination. (After Bauer and Gordon.)

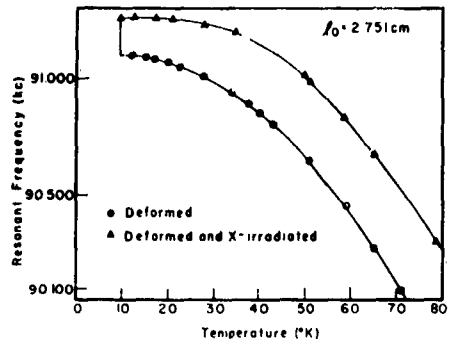

Fig. 5 Dependence of the resonant frequency of a deformed NaCl crystal, before and after x-irradiation, on temperatures between liquid-helium and liquid nitrogen temperature. l_o represents the room temperature specimen length. (After Bauer and Gordon.)

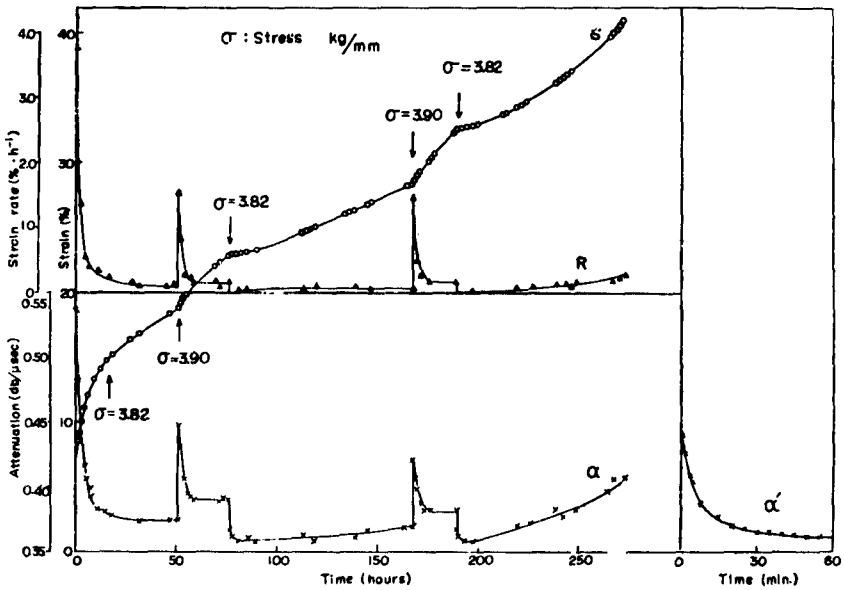

Fig. 6 Curve S: Creep strain-time relation.
Curve α: Attenuation-time relation.
Curve R: Creep rate-time relation.
Curve α': Recovery of attenuation.
(After Hikata and Tutumi.)

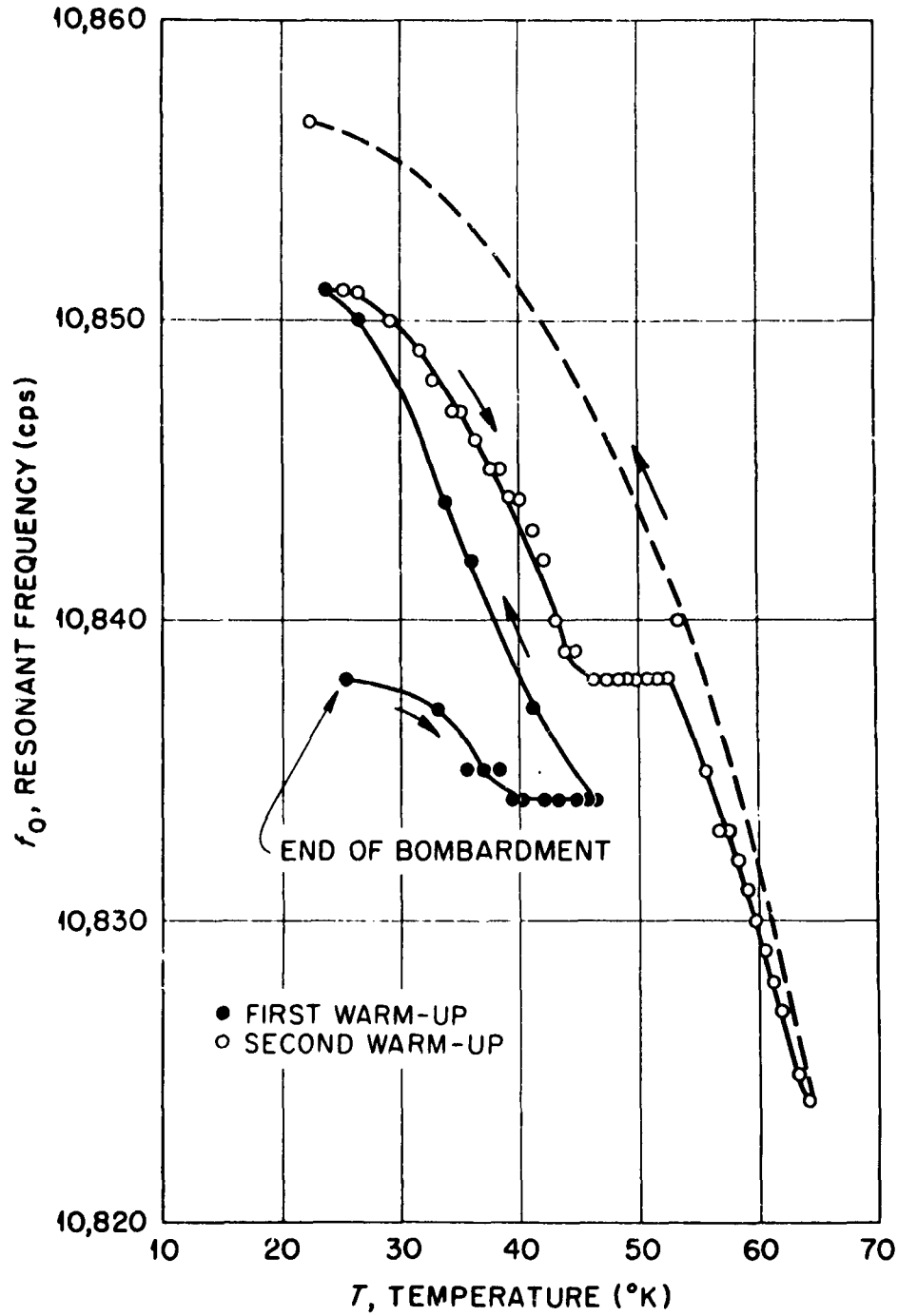

Fig. 7 The charge in resonant frequency with temperat upon warming up from fast neutron irradiation at 20°K. (After Thompson, Blewitt and Holmes.)

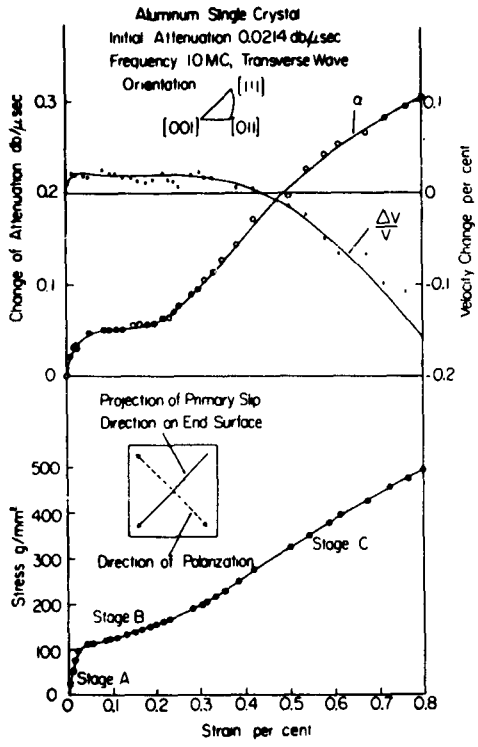

Fig. 8 Stress, shear wave attenuation and velocity change as a function of total strain for <0.5> orientation. The polarization direction of the shear wave is perpendicular to the projection of primary slip direction on end surface. (After Hikata, Chick, Elbaum and Truell.)

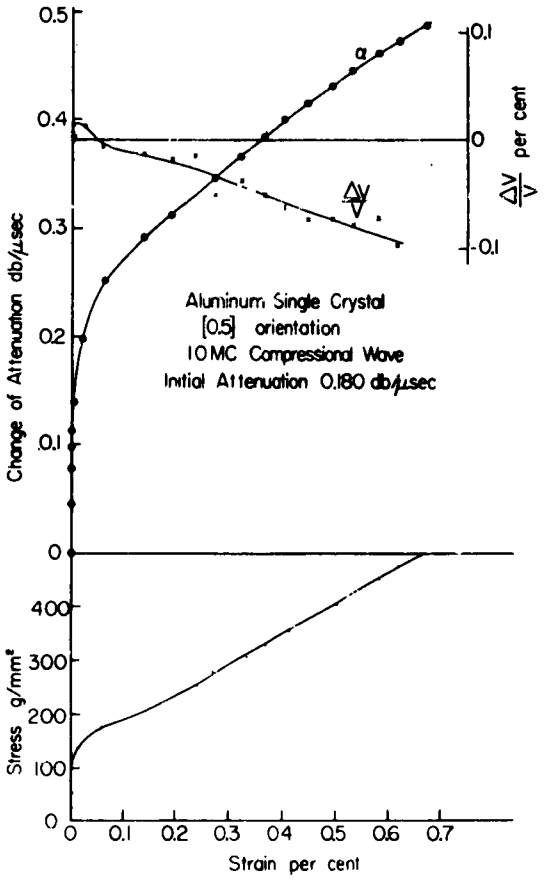

Fig. 9 **Stress, longitudinal wave attenuation and velocity change as a function of total strain for <0.5> orientation. (After Hikata, Chick, Elbaum and Truell.)**

STORED ENERGY AND SUBSTRUCTURE

Michael B. Bever
Department of Metallurgy
Massachusetts Institute of Technology

1. Introduction

1.1 Stored Energy and Substructure

The stored energy of cold work is the sum of the energy effects of the imperfections created by the deformation process and retained until the time of measuring. In view of the difficulty of differentiating between the effects of various structural elements, measurements of the stored energy may appear to hold little promise of contributing to the knowledge of substructure. Yet the stored energy of cold work not only has been interpreted in terms of variables of the deformation process and the deformed metal, but is becoming increasingly well understood in relation to structural factors. This paper will be concerned with the relation of the stored energy to the substructure on the basis of the pertinent literature.

1.2 Types of Substructure

In the broadest sense, the substructure comprises all imperfections present within the grain boundaries (large-angle boundaries) of a polycrystalline metal or present in a single crystal. This will be called here the "total substructure" without further differentiation. The subboundaries (low-angle boundaries), conventionally designated "substructure" are revealed at an intermediate level of resolution. They will be called "intermediate substructure". At the ultimate level, the substructure is composed of crystal imperfections such as dislocations, point defects, stacking faults, and twinning faults. Imperfections may occur individually or they may interact with other members of their own class or with members of one of the other classes. The imperfections will be classified here as "ultimate substructure".

In solid-solution alloys deformation may in addition to structural effects cause configurational effects, such as the destruction of short-range and long-range order and changes in the interaction of imperfections with solute atoms. These processes affect the stored energy, but the destruction of order is not normally considered as a change in substructure.

Metals in the as-solidified or annealed state contain some elements of substructure. A small part of this is an equilibrium feature, but most is due to non-equilibrium causes. However, the substructure present in as-solidified or annealed metals is of limited extent and its energy effects are so small that they can usually be ignored. Pronounced substructures are generated by cold work, irradiation, creep, cyclic loading, electrodeposition and thermal shock. This discussion will be limited to the substructure formed by cold work.

1.3 Measurement of the Stored Energy

The stored energy of cold work as a function of variables and its release during annealing have been subjects of extensive investigation. The energy expended in the deformation process and the ratio of the stored to the expended energy have attracted interest since the earliest investigations of the stored energy. More recently efforts have been made to relate stored energy measurements to changes during deformation and annealing in such properties, as hardness, electrical conductivity and density, and structural changes have been followed by light microscopy, electron microscopy and X-ray diffraction.

The methods of measuring the stored energy of cold work are of two types. Single-step methods determine the stored energy as the difference between the expended work and the heat evolved during deformation. The work is determined from stress-strain relations or by such means as a ballistic pendulum. The heat is determined from the adiabatic temperature rise of the specimen or by deformation inside a calorimeter. The single-step methods are unique in that they can supply information on the kinetics of heat evolution during and immediately after the deformation process.

In the two-step methods, the specimen is deformed and the stored energy is then measured calorimetrically. The calorimetric methods measure the heat effects of bringing the cold worked and a standard specimen to the same final state, such as the annealed state or solution in a solvent. Annealing methods also give information on the kinetics of energy release during the annealing of cold worked metals. Another two-step method involves metal solution calorimetry; for the required precision, special combinations of solutes and solvents have to be used, such as gold-silver alloys and a tin solvent.

In most methods, the enthalpy rather than the internal energy of cold work is measured. Their difference, however, is negligible.

2. The Total Stored Energy as a Function of Variables

The total stored energy, representing the total substructure, is a function of macroscopic variables which affect either the deformation process or the deformed metal. In the former category are the strain, the deformation temperature, the strain rate and the type of deformation. In the latter category are the nature and composition of the metal and its grain structure. The effects of these variables will be summarized in this section. A detailed account may be found in a review of the subject of the stored energy (Titchener and Bever, 1958)*.

2.1 Strain

The stored energy increases with strain at small and moderate strains. The results of several investigations of copper are plotted in Fig. 1 (Clarebrough

---

* The references are listed alphabetically at the end of this paper.

Hargreaves and West, 1955; Clarebrough, Hargreaves and Loretto, 1958; Gordon, 1955; figure after Titchener, 1961). The decrease in the rate of energy absorption with increasing strain should be noted. The energy stored by a gold-silver alloy deformed at room temperature and 78°K is shown in Fig. 2 (Appleton and Bever, 1963; Titchener and Bever, 1959). At room temperature, the energy stored by this alloy approaches a saturation value both in torsion and wire drawing. No decrease in the rate of energy absorption was observed at 78°K.

2.2 Temperature

As the temperature of deformation decreases, the stored energy increases. This relation, which is shown in Fig. 2 and more explicitly in Fig. 3 (Appleton and Bever, 1963) can be expressed by stating that the stored energy increases with a decrease in the ratio of the temperature of deformation T_w to the melting point T_m and the ratio of the temperature of deformation to the recrystallization temperature T_r.

2.3 Strain Rate

The strain rate can have an effect on the amount of energy stored. While at low and intermediate rates the energy stored by a gold-silver alloy is independent of strain rate, with further increases in strain rate it first increases and then decreases (Titchener and Bever, 1959). A maximum in the stored energy has been found at 4°K (Appleton and Bever, 1963). The decrease in the energy probably can be attributed to a rise in temperature of the specimens.

2.4 Deformation Process

Although the values for torsion and wire drawing in Fig. 2 are nearly equal, different deformation processes, under otherwise identical conditions, can lead to saturation values of the stored energy which differ appreciably (Titchener and Bever, 1959). This difference is probably at least in part due to differences in the temperature rise caused by the deformation process, but differences in microplastic behavior may also play a role.

2.5 Nature of Metallic Element

Knowledge of the dependence of the stored energy on the metal is limited. Most measurements have been made on face centered cubic metals. Also, a comparison of different metals is complicated by the effect of impurities on the stored energy. However, in general, the stored energy increases with the melting point and recrystallization temperature of a metal. This generalization is consistent with the increase in the stored energy as the ratios of the temperature of deformation to the melting temperatures (T_w/T_m) and to the recrystallization temperature (T_w/T_r) decrease.

2.6 Composition

The stored energy, in general, increases with impurity content. White and Koyama, 1962, discussed their observations and observations by Clarebrough et al., 1955, according to which impurities may either increase or decrease the amount of energy stored.

Larger concentrations of solute tend to increase the stored energy; as shown in Fig. 4 for the gold-silver system (Greenfield and Bever, 1957). At most, only a fraction of this increase (a maximum of about 30 cal/g-atom at 50 at. pct) is due to the destruction of short-range order. The increase of the stored energy is related to the increase of the recrystallization temperature with increasing solute concentration.

2.7 Grain Structure

At low strains, fine-grained copper under otherwise identical conditions stores a measurably larger amount of energy than coarse-grained copper, as shown in Fig. 1 (Clarebrough et al., 1958). This effect has also been observed by Loretto and White, 1961; White, 1962; and Williams, 1962.

2.8 The Ratio of the Stored to the Expended Energy

The expended energy has a bearing on the mechanisms of energy storage and work hardening. Fig. 5 shows the ratio of the stored to the expended energy E_s/E_w as a function of strain at room temperature and 78°K for a gold-silver alloy deformed in torsion (Appleton and Bever, 1963).

3. The Release of the Stored Energy

3.1 General

A cold worked metal is unstable and under favorable kinetic conditions returns to the annealed state by recovery and recrystallization. The driving force for these restoration processes is the free energy of cold work. In general, it is nearly equal to the internal energy, that is, to the stored energy of cold work usually measured.

The stored energy is released during the restoration processes and the kinetics of this release are indicative of the kinetics of these processes. The release of stored energy often takes place in well defined temperature ranges or time intervals; in some cases, it is possible to assign peaks in the release curves to a specific mechanism, such as the annealing out of vacancies or recrystallization. The energy released during prerecrystallization stages and the energy released during recrystallization, expressed as fractions of the total stored energy, E_p/E_s and E_r/E_s, are significant in interpreting the substructure.

The energy release can be investigated by

(1) anisothermal annealing as a function of temperature during continuous heating

(2) isothermal annealing as a function of time at constant temperature

(3) isochronal annealing as a function of anrealing for fixed times at different temperatures

A special mechanism of energy release involves mechanical deformation (work softening).

The literature on the release of the stored energy will be summarized briefly in this section. It has been reviewed extensively in several publications (Bever, 1957; Titchener and Bever, 1958; Clarebrough, Hargreaves and Loretto, 1962a).

3.2 Anisothermal Annealing

Following earlier investigations of the stored energy by anisothermal annealing, such as those of Sato, 1931, and Quinney and Taylor, 1937, a series of papers by Clarebrough, Hargreaves and their collaborators has made great contributions to the knowledge of the release of stored energy and the kinetics of the restoration of cold worked metals. Typical examples of their results will be presented.

The energy release by pure copper during continuous heating is shown in Fig. 6 (Clarebrough, Hargreaves and West, 1955). The release is almost entirely due to recrystallization which is represented by the peak in the curve. This is preceded by a small recovery effect. The decreases in hardness and electrical resistivity during recrystallization should be noted.

The energy release by copper containing 0.35% arsenic and 0.05% phosphorus is shown in Fig. 7 (Clarebrough et al., 1955). A plateau in the release curve preceding the recrystallization peak indicates the occurrence of prerecrystallization phenomena. Similar prerecrystallization processes probably take place in pure copper at or near room temperature, but impurities restrain these processes, which then occur at higher temperatures where they can be observed during annealing experiments.

The energy release by commercial nickel is shown in Fig. 8 (Clarebrough et al., 1955). The prerecrystallization phenomena include a small well developed peak, which is attributed to the annealing out of vacancies. Clarebrough, Hargreaves, Loretto and West, 1960, found such a peak also in nickel of higher purity, but the plateau was absent. Part of the release curve for commercial nickel has been explained by calculations of Nicholas, 1955, who assumed that point defects anneal out at the boundaries of subgrains. The first decrease in the resistivity curve shown in Fig. 8, which is not accompanied by a change in hardness, also indicates the annealing out of vacancies.

Michell and coworkers have combined measurements by anisothermal calorimetry of the energy stored in nickel with structural investigations by X-ray diffraction (Michell and Haig, 1957; Michell and Lovegrove, 1960).

Anisothermal annealing can be adapted to operation below room temperature. In an investigation of copper, deformed at 88°K, Henderson and Koehler, 1956, found several distinct annealing stages and substages. Van den Beukel, 1961, qualitatively confirmed these findings for copper and also reported results for gold, silver, and nickel.

3.3 Isothermal Annealing

Measurements of the release of stored energy by isothermal annealing are of fundamental importance and have contributed much to the understanding of the kinetics of energy release. Borelius, Berglund and Sjöberg, 1952, applied isothermal calorimetry to measuring the energy stored by aluminum, copper and zinc and Gordon, 1955, using the same method, measured the energy stored in copper. Some of Gordon's results are shown in Fig. 9. Aström, 1955, annealed specimens of aluminum isothermally at progressively higher temperatures and followed changes in their substructure by metallography. Some of his results are shown in Fig. 10. Bailey and Hirsch, 1960, combined isothermal calorimetry of the stored energy in silver with electron transmission microscopy. The interpretation of their stored energy measurements in terms of the substructure observed by them has attracted particular attention.

3.4 Isochronal Annealing

The stored energy present in a gold-silver alloy after deformation at 78°K or room temperature and holding for various times at different temperatures is shown in Fig. 11 (Greenfield and Bever, 1956). After deformation at 78°K, two stages of release are indicated.

The curve in the lower part of Fig. 12 shows the energy release during isochronal annealing of filings of a gold-silver alloy (Averbach, Bever, Comerford and Leach, 1956). This curve is consistent with the corresponding curve in Fig. 11. The upper part of Fig. 12 shows results of a correlated X-ray investigation and hardness values, which will be discussed below.

3.5 Work Softening Effect

Observations of a work softening effect are shown in Fig. 13 (Titchener and Bever, 1960). A specimen cold worked at 78°K released energy when brought to room temperature as the thermally unstable imperfections annealed out. Additional deformation at room temperature caused a further decrease in the stored energy by the removal of mechanically unstable imperfections. This second decrease in stored energy was accompanied by a decrease in microhardness, which indicated that dislocations played a part in the process.

An appreciable decrease in the stored energy occurs when specimens of a gold-silver alloy deformed at 4°K are brought to 78°K (Appleton and Bever, 1963). No work softening was found to result from secondary deformation at 78°K after primary deformation at 4°K, but the strain levels as well as the temperatures were different from those of the earlier investigation.

4. Stored Energy and Total Substructure

Since the total stored energy represents the total substructure, the effects of variables on the stored energy are also indicative of their effects on the substructure. The conclusions which can be drawn on this basis will be summarized.

4.1 Strain

The increase in stored energy with increasing strain can be attributed to an increase in the number of imperfections and an intensification of their interaction as the deformation progresses. The increase in the energy also raises the question as to whether new types of imperfections are generated at higher strains. Under conditions where the stored energy attains saturation, the substructure reaches a steady state in the sense that as many imperfections are formed as are released by a work softening mechanism. In this connection, it is significant that measurements of the stored energy can be made after deformation to moderate and large strains at which the substructure is so highly developed and so complex that it cannot be observed directly in detail. Stored energy measurements because of their statistical or integrating nature, therefore, assume a particular usefulness at higher strains.

4.2 Temperature

The increase in stored energy with decreasing temperature suggests that the number of imperfections increases and that they may interact with each other more intensively. It is also known from other evidence that at low temperatures, additional types of imperfections are generated. The extent to which the increase in the energy is due to the suppression of thermally activated processes of energy release is not well known. The ratio of the stored to the expended energy may give some semi-quantitative information on this problem and some light may be shed on it by a suitable application of a single-step method of stored energy measurement.

4.3 Composition

The tendency of impurities and solute additions to increase the stored energy is connected with their tendency to cause the retention of imperfections.

4.4 Grain Structure

The increase in stored energy with decreasing grain size at small strains suggests that substructure forms more readily or is retained more completely in fine-grained metals. The elimination of this difference with increasing strain can be explained by the progressive accumulation of imperfections in the interiors of the grains regardless of their size.

Conrad and Christ, 1962, related the dependence of stored energy on grain size to the variation in dislocation density with the grain size of the deformed metal. They based their argument on the decrease in the average distance moved by a dislocation owing to the increase in the number of dislocation sources with increasing grain boundary area.

4.5 General

It has been shown in this section that four of the seven variables affecting the stored energy mentioned in Section 2 permit some conclusions to be reached concerning the substructure. Corresponding conclusions are also possible for the other variables. Further insight into the effects of variables can be gained from investigations of the stored energy in which simultaneous changes of other properties are investigated.

5. Stored Energy and Intermediate Substructure

The intermediate substructure, as defined in this paper, consists of the subboundaries. A correlation between the intermediate substructure and the stored energy, therefore, requires some coordinated knowledge of the subboundaries. Work involving both stored energy and substructure was carried out by Aström, 1955, who used light microscopy, and by Averbach et al., 1956, and Michell and coworkers, 1957 and 1960, who used X-ray diffraction methods.

Aström's values of the stored energy and hardness are shown in Fig. 10. He deduced from these data and his metallographic observations that (1) a recovery process (not involving detectable structural changes) occurred at about 80°C, (2) the substructure underwent a change between 180 and 250°C and (3) the metal recrystallized at 350°C. He did not definitely identify the process involving the substructure, but suggested that it was either subgrain growth or polygonization, or both.

Averbach et al., 1956, measured by calorimetry the energy stored in filings of a gold-silver alloy in the deformed state and after annealing at different temperatures between room temperature and 500°C (Fig. 12). They measured the elastic strain energy and the short-range order parameter. From the latter, they calculated by the quasi-chemical theory energy values after different annealing treatments. No stacking faults or twin faults were observed. Averbach et al. subtracted the energy effects due to strain and changes in short-range order from the stored energy measured calorimetrically and considered the remainder to be interfacial energy. They estimated the total interfacial area from the particle size measured by X-ray diffraction and from this derived a specific interfacial energy. The results, recalculated after some corrections, arising from a discussion by Michell, 1958, appear to be reasonable; in particular, they show an upward trend after annealing above 250°C (Averbach, Bever, Comerford and Leach, 1958).

In the cold worked specimens approximately two-thirds of the stored energy was accounted for by interfacial energy, only 5% by elastic strain and the balance by the destruction of short-range order. During recovery, the subgrain size increased slightly, a small amount of stored energy was released, presumably due to this subgrain growth, but the specific interfacial energy changed little. A partial relief of local strains occurred. During recrystallization, the subgrain size increased rapidly, the specific interfacial energy increased, presumably to a value of the random grain boundary energy, and the remaining local strains disappeared.

Michell and Haig, 1957, combined a structural investigation by X-ray diffraction of nickel grindings before and after annealing with measurements of the stored energy. The apparent particle sizes of the deformed powder extended over an appreciable range depending on the manner of analysis and the energies calculated from them showed a corresponding range. Also, the calculated values of the energy were lower than the measured value. The authors discussed this discrepancy in terms of the assumed distribution of strains. Two stages in the relief of strain were observed. The first, which did not involve a change in particle size, was attributed to recovery and the second occurred during recrystallization with an attendant increase in apparent particle size.

Michell and Lovegrove, 1960, reported a similar investigation of the annealing of bulk specimens of nickel. The stored energies derived from various methods of analysis of particle size were spread over a large range. Best agreement with the measured energy values was obtained by assuming a Gaussian distribution of the strain.

The importance of the interfacial energy of subparticles, which is brought out by the X-ray diffraction investigations, raises the question as to how changes in the stored energy resulting from changes in variables are related to the interfacial energy. As an example of this problem, it may be considered whether the change in the stored energy with composition is associated with a change in the interfacial energy and if so, whether this is due to a change in the total interfacial area or in the specific interfacial energy.

In concluding this section, a consequence of the method of finding interfacial energy of subboundaries by subtracting the energies of all other mechanisms from the total measured energy should be emphasized. This method tends to overstate the interfacial energy, which will be reduced as energies attributable to other mechanisms are considered. In general, however, these energies are likely to be small.

6. Stored Energy and Ultimate Substructure

6.1 Dislocations

Dislocations, in addition to making up the subboundaries, constitute other elements of substructure. They may occur in random arrangements or in regular networks and groups such as pile-ups, in which they interact with each other.

The simplest analysis of the stored energy in terms of dislocations assumes individual non-interacting dislocations. The measured stored energy, or that part of it which can be attributed to dislocations, is divided by the estimated value of the specific energy of a dislocation in order to find the dislocation density. Alternatively, if the dislocation density is known or can be estimated, the specific energy of a dislocation can be found.

Seitz and Read, 1941, Koehler, 1941, 1942, and Bragg, 1945, calculated a dislocation density of 10^{12} per cm^2 after cold work from values of the stored energy

reported by Taylor and Quinney, 1934, 1937. This high value of the density can be explained by the low specific energy values assumed by these authors.

In more recent investigations, dislocation densities derived from stored energy values have been compared with densities derived from changes in other properties measured on identical samples. Table 1 reports the results for copper of Clarebrough, Hargreaves and West, 1957. The dislocation densities obtained by them from changes in the hydrostatic density, $\Delta D/D$, are larger than those obtained from the stored energy, E_s; the incremental resistivity, $\Delta\rho$, gave even larger values. Clarebrough et al. discussed this discrepancy and Boas, 1957, commented on a similar discrepancy in nickel. Seeger, 1957, pointed out that the dislocation density based on hydrostatic density changes, recalculated on a different basis, agreed satisfactorily with the value derived from the stored energy. He also suggested that the dislocation density derived from the resistivity change might be reduced if stacking faults contributed to the resistivity change.

Clarebrough et al., 1962b, reported dislocation densities derived from stored energy and hydrostatic density changes for silver and gold, together with the values for copper based on the investigation by Clarebrough, Hargreaves and West, 1957 (see Table 2). The discrepancy had been reduced substantially by the use of a new figure for the effect of a dislocation on the density (Stehle and Seeger, 1956). Since the effects of dislocations on the resistivity of copper, silver and gold were almost identical, in spite of the difference in the stacking fault energies of these metals, the possibility that stacking faults make significant contributions to the resistivity of a dislocation seemed to be ruled out.

Bailey and Hirsch, 1960, from dislocation densities measured by electron microscopy and calorimetric values of the stored energy, obtained a specific energy of a dislocation of approximately 8 ev/atom plane in polycrystalline silver deformed in tension. Electron microscope observations showed a cellular structure. No change was observed in dislocation densities or distribution during recovery, but the energy remaining after recovery, E_r (released during subsequent recrystallization), was only about half the total stored energy, E_s, except at high strains. Pertinent data are given in Table 3.

Bailey and Hirsch calculated stored energies of dislocations occurring singly (E_1) and in groups of two, three, and four dislocations (E_2, E_3, and E_4). Table 4 lists these energies for different values of the radius, R, of the stress field. The agreement of the calculated values with the measured value is satisfactory, especially for the largest value of R and groups of three or four dislocations. The authors concluded that the interaction energy can be accounted for by groups of this size, the long range stresses of which do not cancel. They explained the decrease in stored energy during recovery by a small rearrangement of dislocations in the cell boundaries. They concluded that the stored energy values were compatible with the observed dislocation distribution and that the long-range stresses were at most accounted for by groups of three or four dislocations in the cell boundaries; also, after recovery, the dislocation energies were within a factor of 2 of the theoretical value of the self-energy. In particular, they believed that no pile-ups needed to be postulated and they also did not observe them by electron microscopy.

Bailey and Hirsch also calculated the stored energy from the flow stress assuming a pile-up model. The values are shown in Table 5. Since they were an order of magnitude larger than the experimental values, the authors concluded that the pile-up model did not account satisfactorily for the flow stress and stored energy. They found fairly close agreement between the experimental values and values calculated by the forest theory. They attributed the remaining discrepancy to some long-range stresses or a contribution of point defects to the stored energy. Since the dislocation arrangements observed in nickel, copper, gold, and aluminum were similar to those in silver, Bailey and Hirsch concluded that the same work hardening mechanism operated in these metals. However, since pile-ups had been observed in stainless steel and alpha brass, they admitted the possibility that long-range stresses might be important in them.

Clarebrough, Hargreaves, Head and Loretto, 1961, criticized the equation used by Bailey and Hirsch for the calculation of the energy from the flow stress. In particular, they stated that the outer cut-off radius should not appear in it. They derived an equation for the stored energy from an analysis due to Stroh, 1953. They calculated values for several metals; that for silver is included in Table 5. Clarebrough et al. concluded that the pile-up theories could not be dismissed on the basis of the measurements of the flow stress and the stored energy alone, but also emphasized that the agreement should not be taken as proof of their correctness.

Clarebrough et al. pointed out that earlier results for nickel (Clarebrough et al., 1955) which showed a large energy evolution during recovery ($E_p/E_s = 0.70$) was similar to the observations for silver by Bailey and Hirsch. They agreed in attributing a large part of this release to a rearrangement in the cell boundaries during recovery. They also mentioned the possibility of loss of dislocations during thinning in the preparation of electron microscope specimens.

Seeger and Kronmüller, 1962, stated that the equation used by Bailey and Hirsch for connecting the flow stress and the energy incorrectly assumed that a group of n dislocations can be treated as a superdislocation of dislocation strength (nb) and that this overestimates the energy stored in the stress fields between the dislocations. The stored energy connected with the overlap of the stress fields is only slightly larger than the stored energy due to stress fields of individual dislocations. They used a dislocation model developed for stage II of the stress-strain curve of face-centered metals and calculated the energy of pile-ups and the work expended in the deformation of a single crystal. From this they calculated a value of the ratio of the stored to the expended energy, E_s/E_w. They considered the agreement of the experimental values for copper, gold, and nickel with the calculated ratio as satisfactory. They also calculated stored energies for the specimens of silver deformed by Bailey and Hirsch, which are included in Table 5. Seeger and Kronmüller concluded that their theory accounted reasonably well for the experimental results, except at the highest strains, where work softening effects could be expected.

Faulkner and Ham, 1962, reported data for aluminum in which the dislocation density was determined by electron microscopy. The specific energies derived from the stored energy were surprisingly large. They concluded that the density of dislocations in thin films of aluminum differs systematically from the bulk values, probably owing to losses during thinning.

Li, 1960, analyzed the elastic properties of a dislocation wall and concluded that its strain energy is smaller than that of a set of dislocations of the same sign distributed within a circle, the diameter of which is approximately equal to the height of the wall. He called attention to the fact that local groupings of dislocations of the same sign generated by a deformation process such as bending interfere with the method of measuring the dislocation density by the amount of stored energy.

Li, 1961, showed that a release of an appreciable amount of energy may occur, as observed by Bailey and Hirsch during the recovery of polycrystalline silver, without an observable change in the dislocation distribution if low-angle twist boundaries are formed by a crossed grid of screw dislocations. This would cause a large energy difference with only a slight rearrangement of dislocations. Li suggested that the kinetics of this rearrangement probably require some thermal activation and that it, therefore, takes place during recovery. The large energy change with only minor visible rearrangement according to Li places the method of determining dislocation densities from stored energy in jeopardy. It should be recognized, however, that the occurrence of the grids has not been demonstrated. Also, the difficulties of evaluation would arise from difficulties of measuring the dislocation density rather than of the energy.

6.2 Point Defects

The estimated values of the energy of point defects and aggregates of point defects in face-centered cubic metals published in the literature appear to be satisfactory. It is, therefore, possible to arrive at estimates of the concentration of these defects, if the energies attributable to them are known from measured values of the stored energy. However, it is often difficult to separate the effects of point defects from those of other imperfections and to differentiate between the effects of different aggregates of point defects.

Point defects are particularly important at low temperatures. This lends interest to the work of Henderson and Koehler, 1956, van den Beukel, 1961, and Greenfield and Bever, 1956. In particular, Henderson and Koehler estimated a vacancy concentration of 1.6×10^{-4} from the stored energy release by a specimen compressed 65%.

The temperature range for the annealing out of point defects in nickel is higher than in the other face-centered cubic metals investigated to date. This permits the energy effect of point defects in cold worked nickel to be measured above room temperature. The results of an investigation by Clarebrough et al., 1960, summarized in Table 6, include concentrations of interstitials and vacancies, as well as the concentration of dislocations, which is derived from recrystallization.

A recent finding by Appleton and Bever, 1963, suggests that, at least in gold-silver alloys, point defects play less of a role at 78°K than has been assumed. They found that between room temperature and 78°K, the stored energy, E_s, increased, but the ratio E_s/E_w increased little more than the stored energy, E_s. This indicates that the expended energy also increased, which is in accord with the measured stress-strain curves at room temperature and 78°K. These observations can be explained by an increase in the density of dislocations and an

intensification of their interaction. Between 78° and 4°K, however, the stored energy and the ratio E_s/E_w increased appreciably, while the stress-strain curve changed much less. This suggested strongly an increase in the concentration of point defects generated during deformation at 4°K over that generated at 78°K.

6.3 Other Imperfections

The relation of other imperfections, such as stacking faults or twinning faults, to the stored energy seems to have received little consideration in the literature. However, data on their concentrations and specific energy are becoming available and this will make it possible to include them in the evaluation of stored energy measurements.

7. Conclusion

It has been shown that the stored energy of cold work can be related to the total substructure, the intermediate substructure and the ultimate substructure. The detailed interpretations possible for the various investigations differ considerably. The statistical nature of the stored energy has been shown to be advantageous in revealing certain features of the total substructure. On the other hand, under favorable conditions, it has been possible to differentiate between elements of substructure on the basis of stored energy values.

Additional investigations of the stored energy are needed. In particular, further investigations combining stored energy measurements with the measurement of changes in other properties should be made. Also, research should be extended to body-centered cubic and hexagonal close-packed metals. In this way, it will become possible to partition the stored energy, even in complex cases, by allocating specific energies to all operative mechanisms.

Acknowledgments

The author thanks Dr. Peter M. Robinson for very valuable help in the writing of this manuscript. He is also indebted to several investigators who communicated to him work in advance of publication.

References

A. S. Appleton and M. B. Bever, 1963 - Trans. Met. Soc. AIME (in press).

H. U. Åström, 1955 - Ark. Fysik, vol. 10, p. 197.

B. L. Averbach, M. B. Bever, M. F. Comerford, and J. S. Ll. Leach, 1956 - Acta Met., vol. 4, p. 477.

B. L. Averbach, M. B. Bever, M. F. Comerford and J. S. Ll. Leach, 1958 - Acta Met., vol. 6, p. 142.

J. E. Bailey and P. B. Hirsch, 1960 - Phil. Mag., vol. 5, p. 485.

M. B. Bever, 1957 - Creep and Recovery, Am. Society for Metals, Cleveland, p. 14.

W. Boas, 1957 - Dislocations and Mechanical Properties of Crystals, Conference held at Lake Placid, Sept. 1956, Wiley, New York, p. 333.

G. Borelius, S. Berglund, and S. Sjöberg, 1952 - Ark. Fysik, vol. 6, p. 143.

W. L. Bragg, 1945 - Trans. N. E. Coast Instn. Engrs. Shipb., vol. 62, p. 25.

H. Conrad and B. Christ, 1962 - AIME Symposium on Recovery and Recrystallization of Metals (to be published).

L. M. Clarebrough, M. E. Hargreaves, A. K. Head and M. H. Loretto, 1961 - Phil. Mag., vol. 6, p. 819.

L. M. Clarebrough, M. E. Hargreaves and M. H. Loretto, 1958 - Acta Met., vol. 6, p. 725.

L. M. Clarebrough, M. E. Hargreaves and M. H. Loretto, 1961 - Phil. Mag., vol. 6, p. 807.

L. M. Clarebrough, M. E. Hargreaves and M. H. Loretto, 1962a - AIME Symposium on Recovery and Recrystallization of Metals (to be published).

L. M. Clarebrough, M. E. Hargreaves and M. H. Loretto, 1962b - Phil. Mag., vol. 7, p. 115.

L. M. Clarebrough, M. E. Hargreaves, M. H. Loretto and G. W. West, 1960 - Acta Met., vol. 8, p. 797.

L. M. Clarebrough, M. E. Hargreaves and G. W. West, 1955 - Proc. Roy. Soc., vol. A 232, p. 252.

L. M. Clarebrough, M. E. Hargreaves and G. W. West, 1957 - Acta Met., vol. 5, p. 738.

E. A. Faulkner and R. K. Ham, 1962 - Phil. Mag., vol. 7, p. 279.

P. Gordon, 1955 - Trans. AIME, vol. 203, p. 1043.

P. Greenfield and M. B. Bever, 1956 - Acta Met., vol. 4, p. 433.

P. Greenfield and M. B. Bever, 1957 - Acta Met., vol. 5, p. 125.

J. W. Henderson and J. S. Koehler, 1956 - Phys. Rev., vol. 104, p. 626.

J. S. Koehler, 1941 - Phys. Rev., vol. 60, p. 397.

J. S. Koehler, 1942 - Amer. J. Phys., vol. 10, p. 275.

J. C. M. Li, 1960 - Acta Met., vol. 8, p. 563.

J. C. M. Li, 1961 - Jl. Appl. Phys., vol. 32, p. 1873.

M. H. Loretto and A. J. White, 1961 - Acta Met., vol. 9, p. 512.

D. Michell and F. D. Haig, 1957 - Phil. Mag., vol. 2, p. 15.

D. Michell, 1958 - Acta Met., vol. 6, p. 141.

D. Michell and E. Lovegrove, 1960 - Phil. Mag., vol. 5, p. 499.

J. F. Nicholas, 1955 - Phil. Mag., vol. 46, p. 87.

H. Quinney and G. I. Taylor, 1937 - Proc. Roy. Soc., vol. A 163, p. 157.

S. Sato, 1931 - Sci. Rep. Tohoku Univ., vol. 20, p. 140.

A. Seeger, 1957 - Dislocations and Mechanical Properties of Crystals, Conference held at Lake Placid, Sept. 1956, Wiley, New York, p. 347.

A. Seeger and H. Kronmüller, 1962 - Phil. Mag., vol. 7, p. 897.

A. Seeger and G. Schoeck, 1953 - Acta Met., vol. 1, p. 519.

F. Seitz and T. A. Read, 1941 - Jl. Appl. Phys., vol. 12, p. 100.

H. Stehle and A. Seeger, 1956 - Z. Phys., vol. 146, p. 217.

A. N. Stroh, 1953 - Proc. Roy. Soc., vol. A 218, p. 391.

G. I. Taylor and H. Quinney, 1934 - Proc. Roy. Soc., vol. A 143, p. 307.

A. L. Titchener and M. B. Bever, 1958 - Progress in Metal Physics, vol. 7, Pergamon Press, London, p. 247.

A. L. Titchener and M. B. Bever, 1959 - Trans. Met. Soc. AIME, vol. 215, p. 326.

A. L. Titchener and M. B. Bever, 1960 - Acta Met., vol. 8, p. 338.

A. L. Titchener, 1961 - Acta Met., vol. 9, p. 379.

A. van den Beukel, 1961 - Physica, vol. 27, p. 603.

J. L. White, 1962 - Discussion of Clarebrough et al. in AIME Symposium on Recovery and Recrystallization of Metals (to be published).

J. L. White and K. Koyama, 1962 - Personal communication.

R. O. Williams, 1962 - Personal communication.

Table 1

Deformation, % Compression	Density of Dislocations in Copper, N lines/cm^2		
	From E_s	From $\Delta D/D$	From $\Delta\rho$
30	8.5×10^{10}	4×10^{11}	5×10^{12}
55	1.1×10^{11}	6×10^{11}	7×10^{12}
70	1.3×10^{11}	8×10^{11}	9×10^{12}

Clarebrough, Hargreaves and West, 1957

Table 2

Metal	Deformation, % Compression	Density of Dislocations, N lines/cm^2		$\Delta\rho/N$, $\mu\Omega$cm/d.line/cm^2
		From E_s	From $\Delta D/D$	
Cu	70%	1.33×10^{11}	2.8×10^{11}	28×10^{-14}
Ag	75%	1.50×10^{11}	2.8×10^{11}	34×10^{-14}
Au	75%	0.74×10^{11}	1.4×10^{11}	35×10^{-14}
Ni	70%	1.06×10^{11}	—	94×10^{-14}
Al	75%	0.40×10^{11}	—	33×10^{-14}

Clarebrough, Hargreaves and Loretto, 1961 and 1962b

Table 3

Deformation %	Measured Dislocation Density N lines/cm^2	E_s, cal/g-a	E_r, cal/g-a	E_s/N, eV/at.pl.
11	2.2×10^{10}	2.70	1.25	9.1
21	5.2×10^{10}	5.10	2.83	7.3
32	6.8×10^{10}	7.75	4.9	8.4
43	—	7.27	6.03	—
			Avge.	8.3

Polycrystalline silver, deformed in tension
Bailey and Hirsch, 1960

Table 4

Stress Field R, A.U.	Calculated Stored Energy (eV/at. plane) E_1 (1)	E_1 (2)	E_2 (1)	E_3 (1)	E_4 (1)
200	2.66	1.90	—	—	—
1,000	3.38	2.61	4.1	4.62	5.16
10,000	4.4	3.63	6.16	7.7	9.3

(1) Bailey and Hirsch, 1960
(2) According to Schoeck and Seeger, 1953

Table 5

Deformation, %	Stored Energy, cal/g-a			
	Exptl.	Calculated from Flow Stress		
		(1)	(2)	(3)
11	2.7	21.2	—	3.0
21	5.1	37.0	—	5.6
32	7.8	54.0	—	8.2
43	7.3	64.0	9.6	9.71

Polycrystalline silver, deformed in tension

(1) Bailey and Hirsch, 1960

(2) Clarebrough et al., 1961

(3) Seeger and Kronmüller, 1962

Table 6

Annealing Stage	Energy Evolved E_s, cal/g-a	Defect Assumed	Concentration from E_s	Assumed Specific Energy
→ 200°C	2.58	Interstitials	2.2×10^{-3} at.%	5 eV
200–350°C	3.28	Vacancies	9.5×10^{-3} at.%	1.5 eV
Recrystallization	11.78	Dislocations	1.06×10^{11} cm/cm^3	4.4×10^{8} eV/cm

Nickel (99.85%) compressed 70% and annealed

Clarebrough et al., 1960

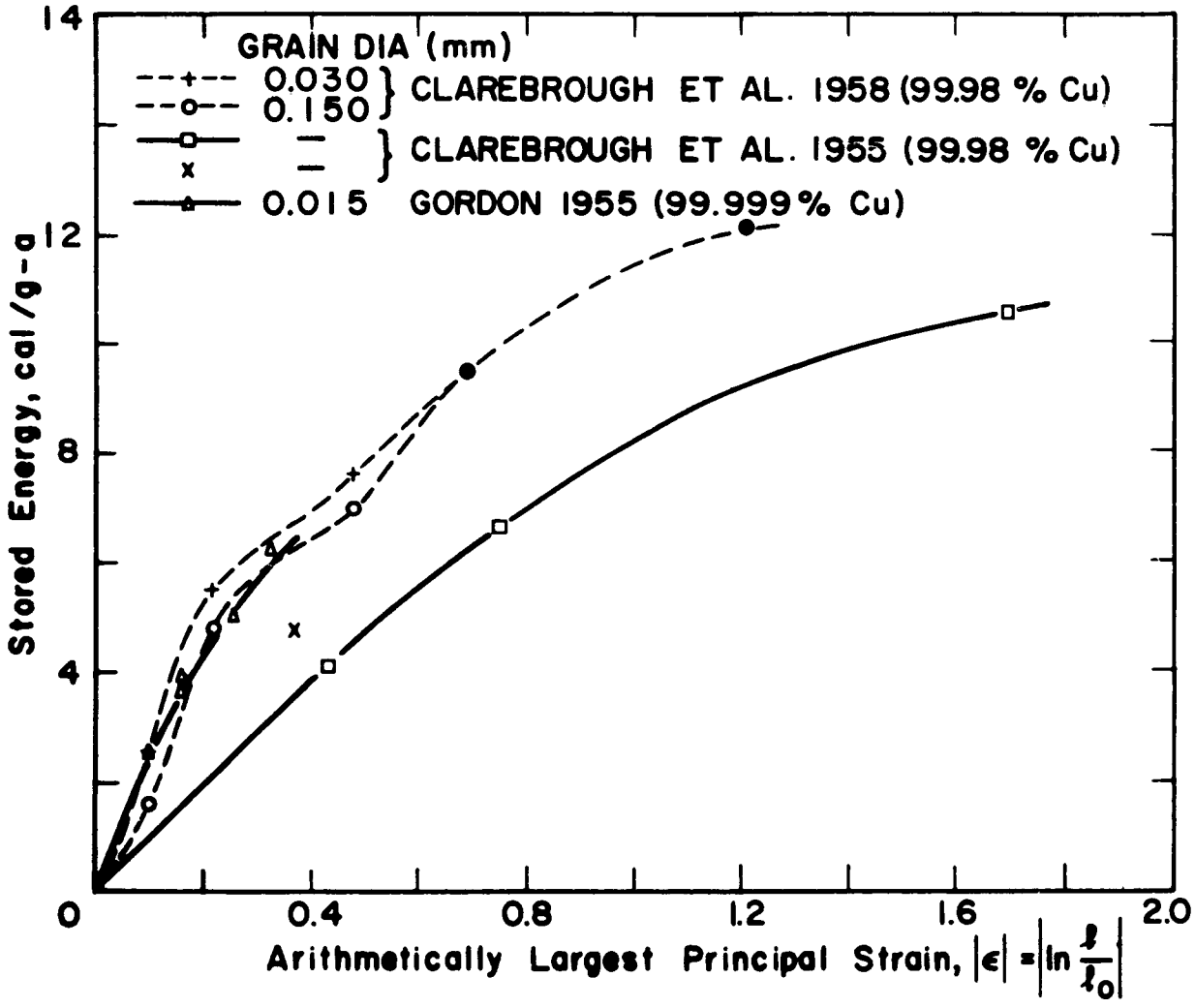

Fig. 1 Energy Stored in Copper as a Function of the Arithmetically Largest Value of Logarithmic Strain in Tension and Compression. (After Titchener, 1961)

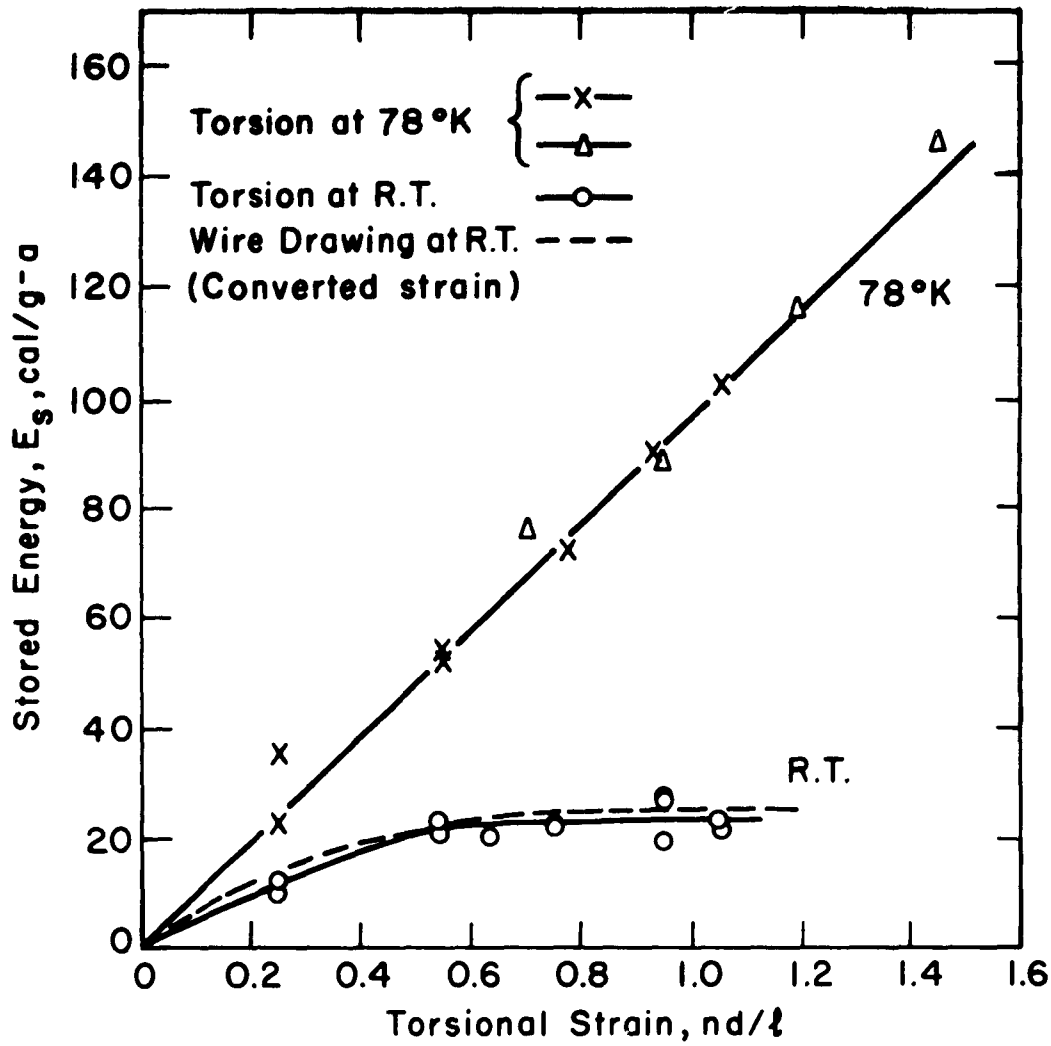

Fig. 2 The Energy Stored by an 82.6%Au-17.4%Ag Alloy at Room Temperature and 78°K as a Function of Strain. (Appleton and Bever, 1963; Titchener and Bever, 1959)

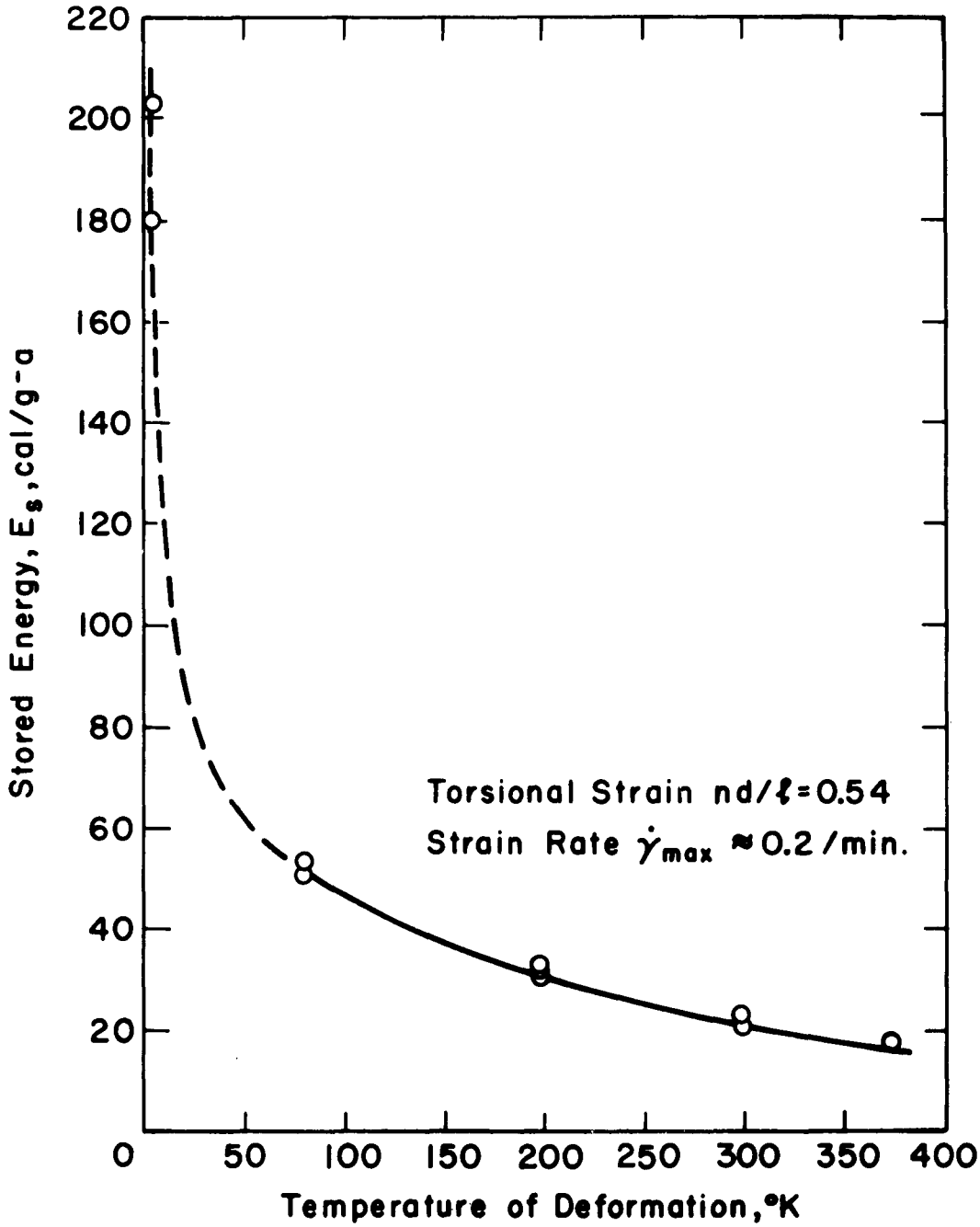

Fig. 3 The Energy Stored by an 82.6% Au-17.4% Ag Alloy at Constant Strain as a Function of the Temperature of Deformation by Torsion. (Appleton and Bever, 1963)

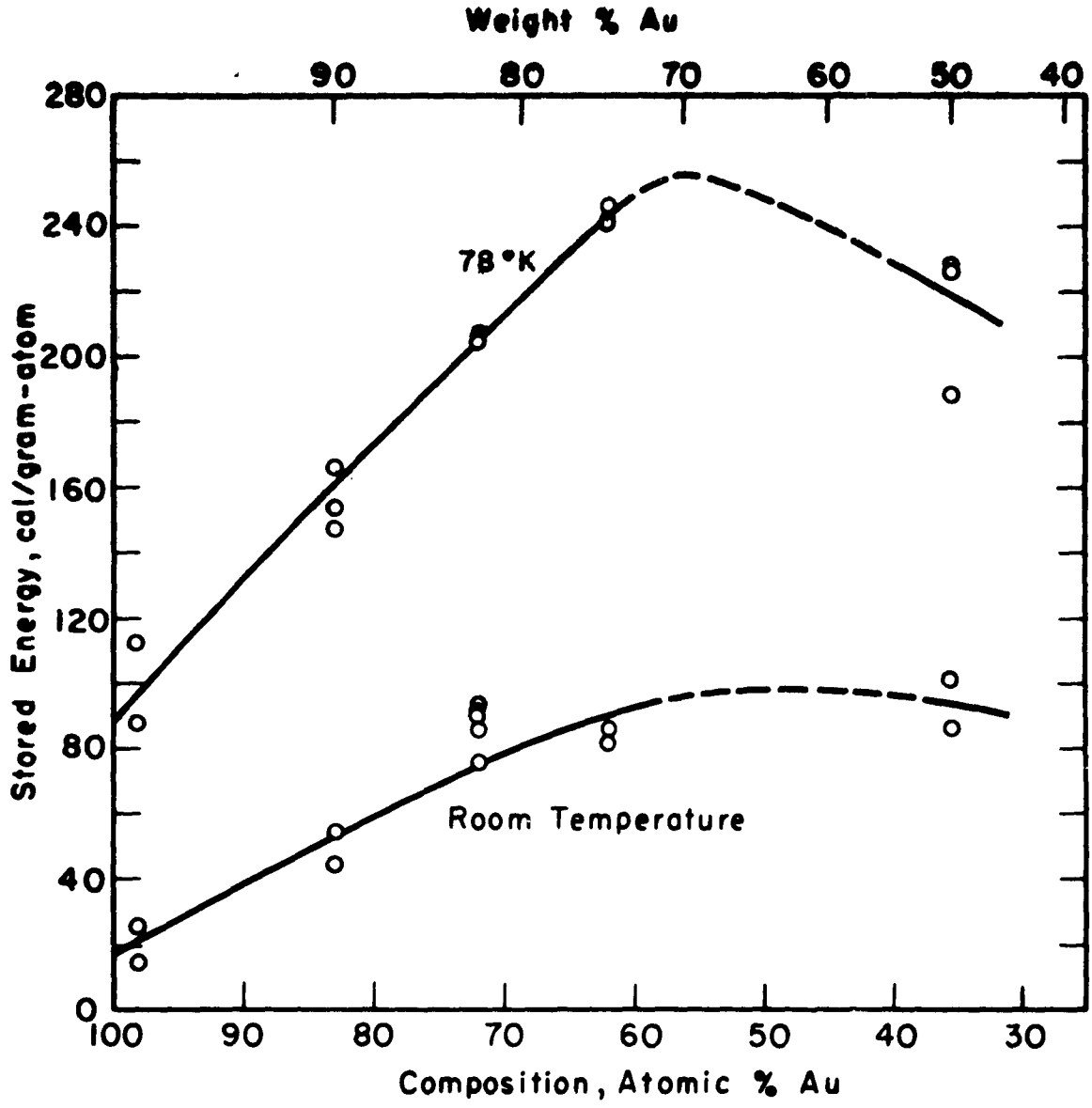

Fig. 4 The Energy Stored by Gold-Silver Alloys Cold Worked at Room Temperature and 78°K. (Greenfield and Bever, 1957)

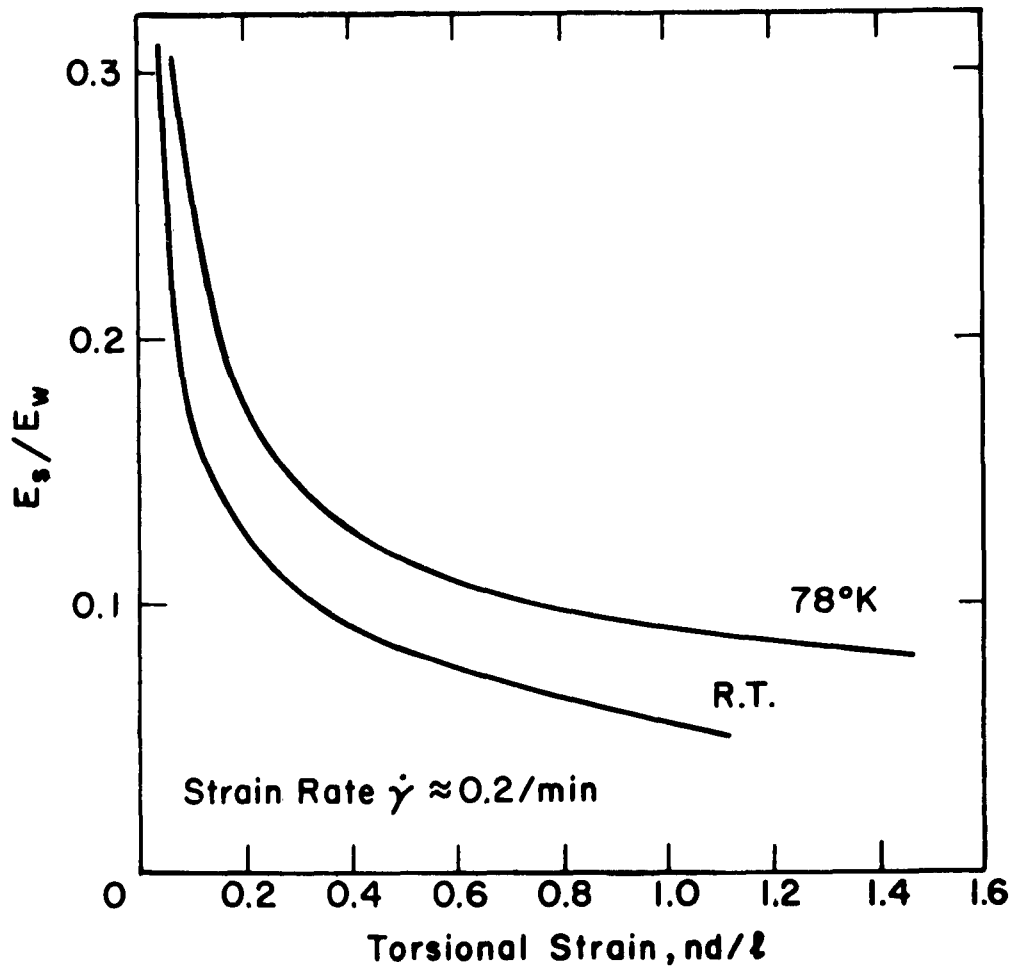

Fig. 5 The Ratio of the Stored to the Expended Energy at Room Temperature and 78°K as a Function of Torsional Strain. (Appleton and Bever, 1963)

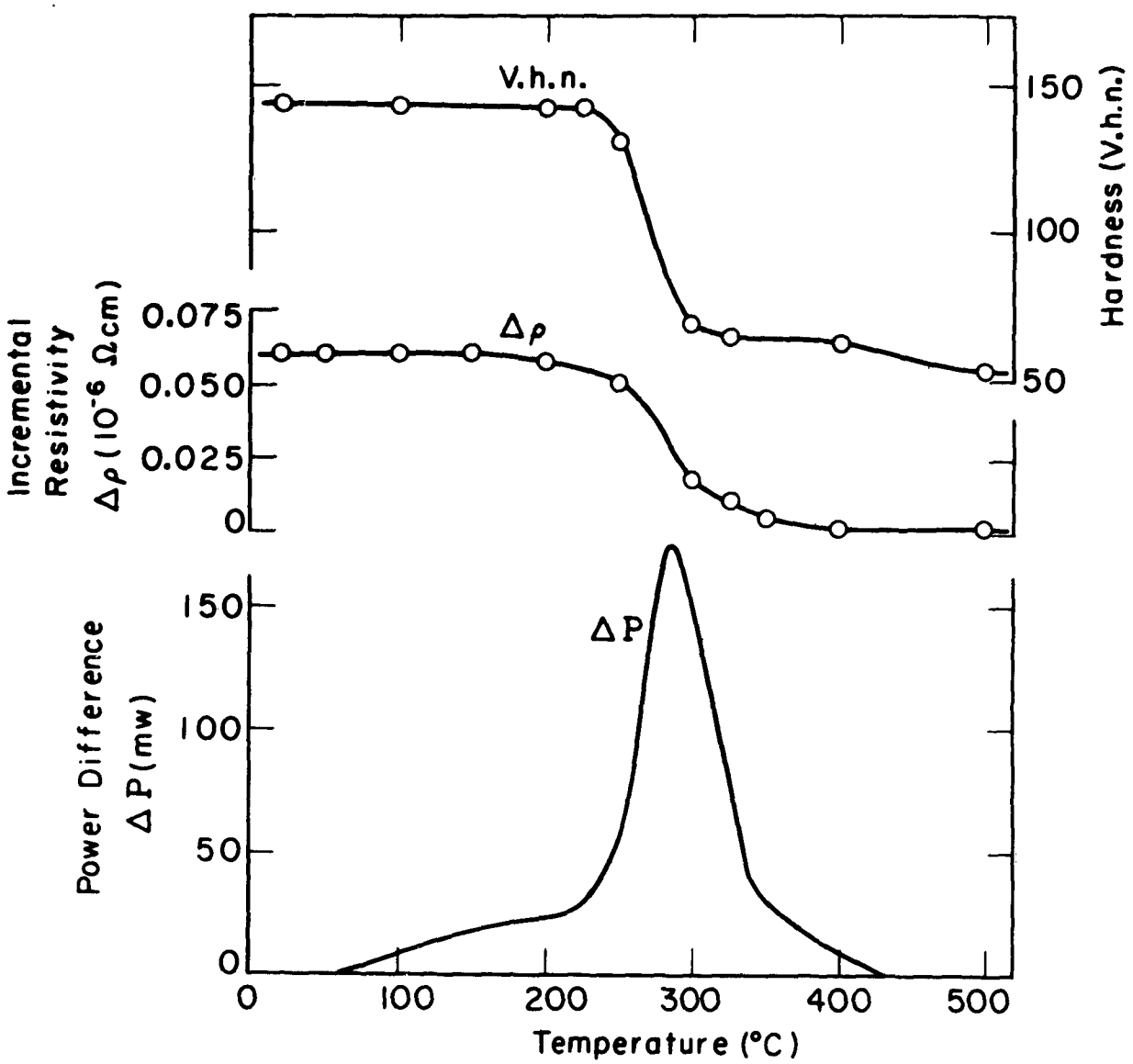

Fig. 6 Rate of Energy Release by Cold Worked Copper as a Function of Annealing Temperature. Incremental Resistivity and Hardness also Shown. Specimen Deformed in Torsion to $nd/\ell = 1.87$. (Clarebrough et al., 1955)

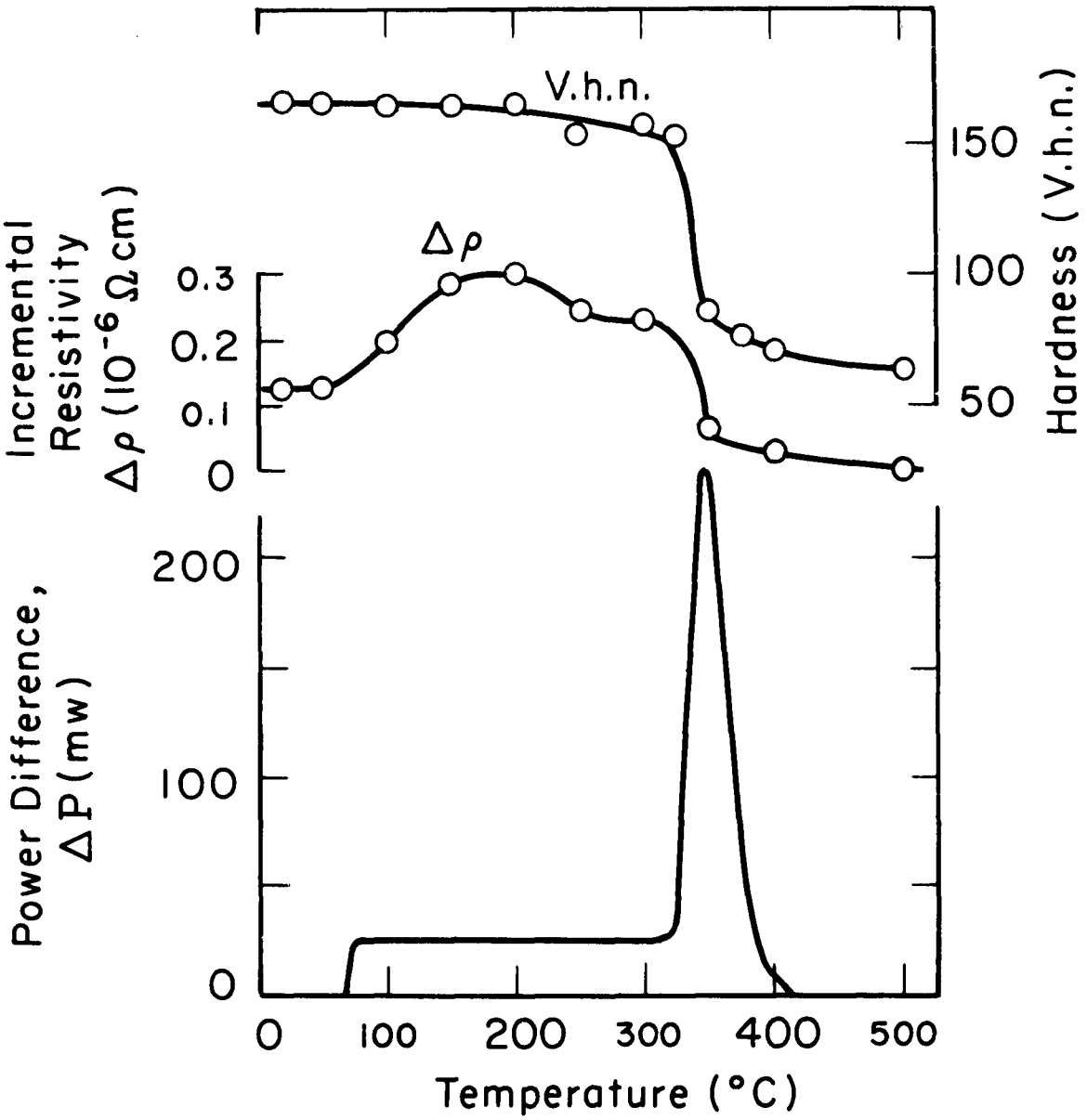

Fig. 7 Rate of Energy Release by Cold Worked Copper Containing Arsenic and Phosphorus as a Function of Annealing Temperature. Incremental Resistivity and Hardness also Shown. Specimen Deformed in Torsion to $nd/\ell = 1.87$. (Clarebrough et al., 1955)

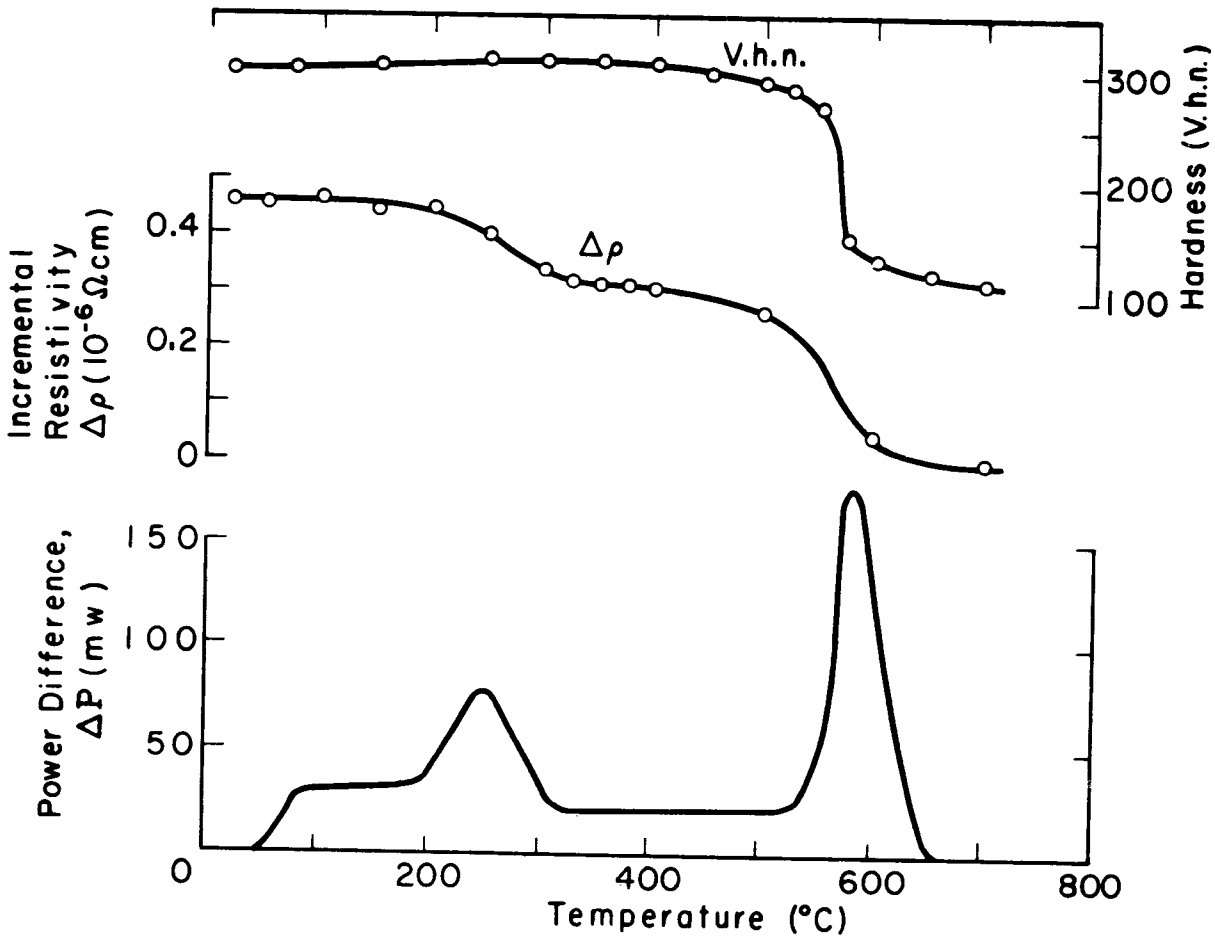

Fig 8 Rate of Energy Release by Commercial Nickel Deformed in Torsion as a Function of Annealing Temperature. Incremental Resistivity and Hardness also Shown. Specimen Deformed in Torsion to $nd/l = 2.34$. (Clarebrough et al., 1955)

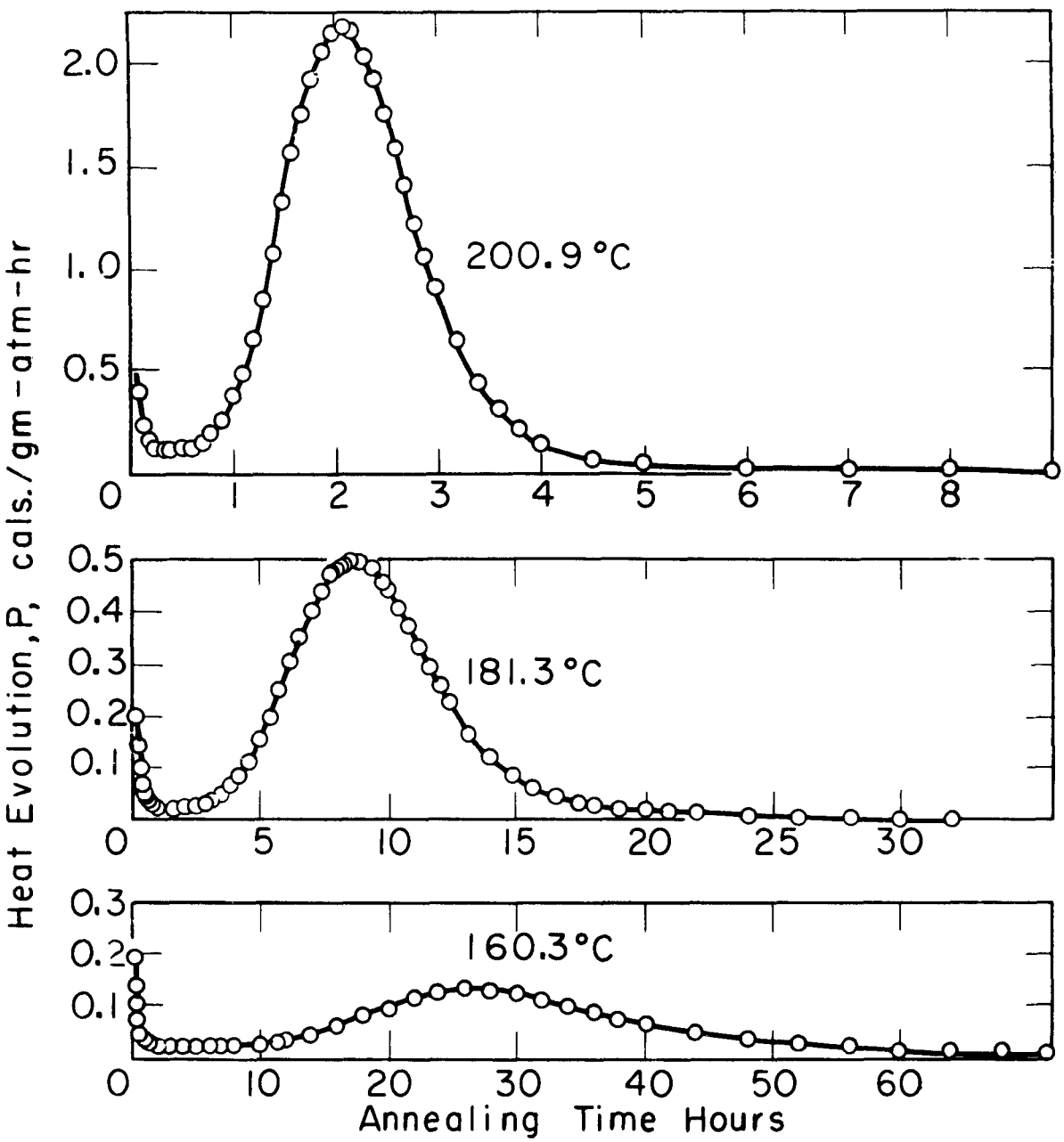

Fig. 9 Rate of Energy Release by Copper Extended 17.7% as Function of Annealing Time at Constant Temperature. (Gordon, 1955)

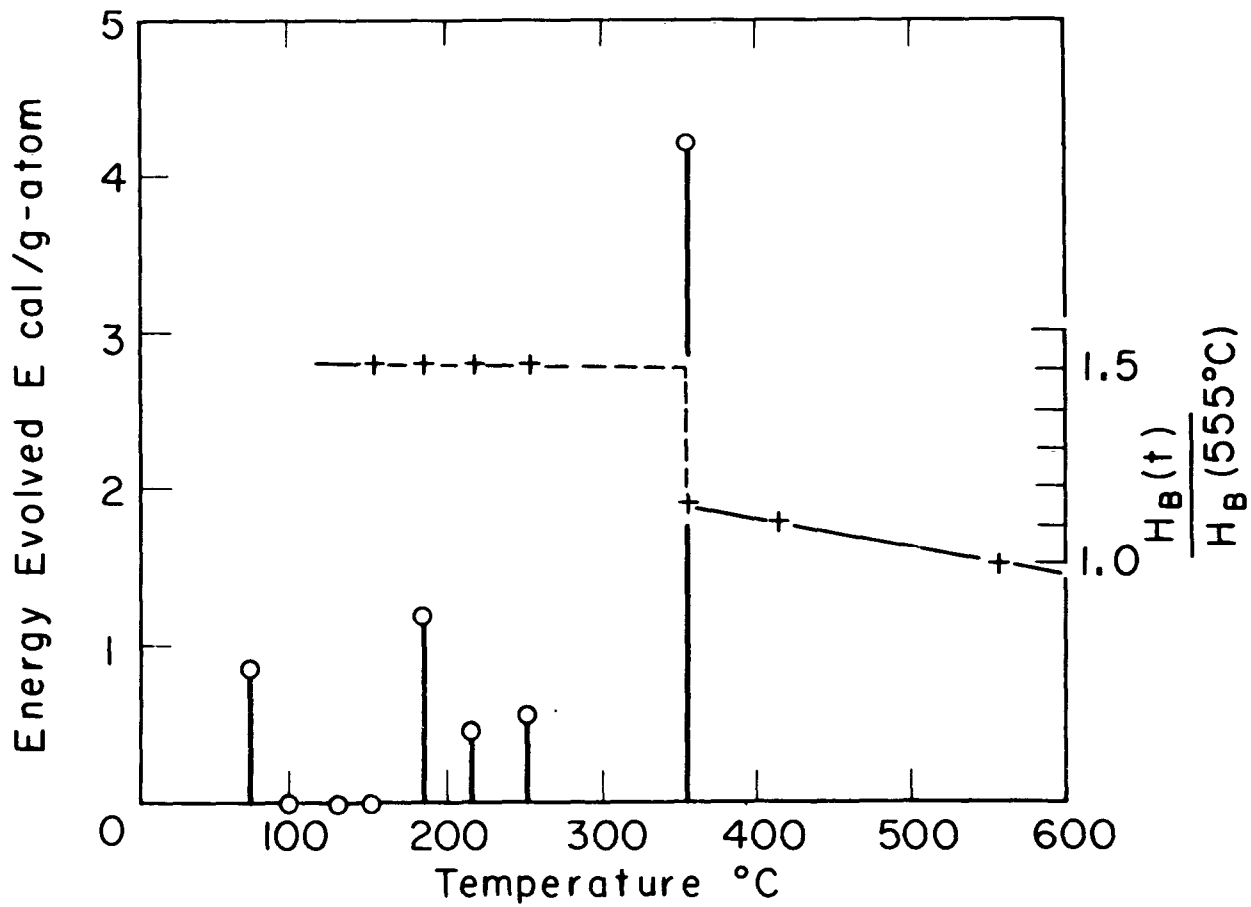

Fig.10 Energy Release by Aluminum Compressed 45% as Function of Annealing Temperature. Relative Hardness also Shown. (Åstrom, 1955)

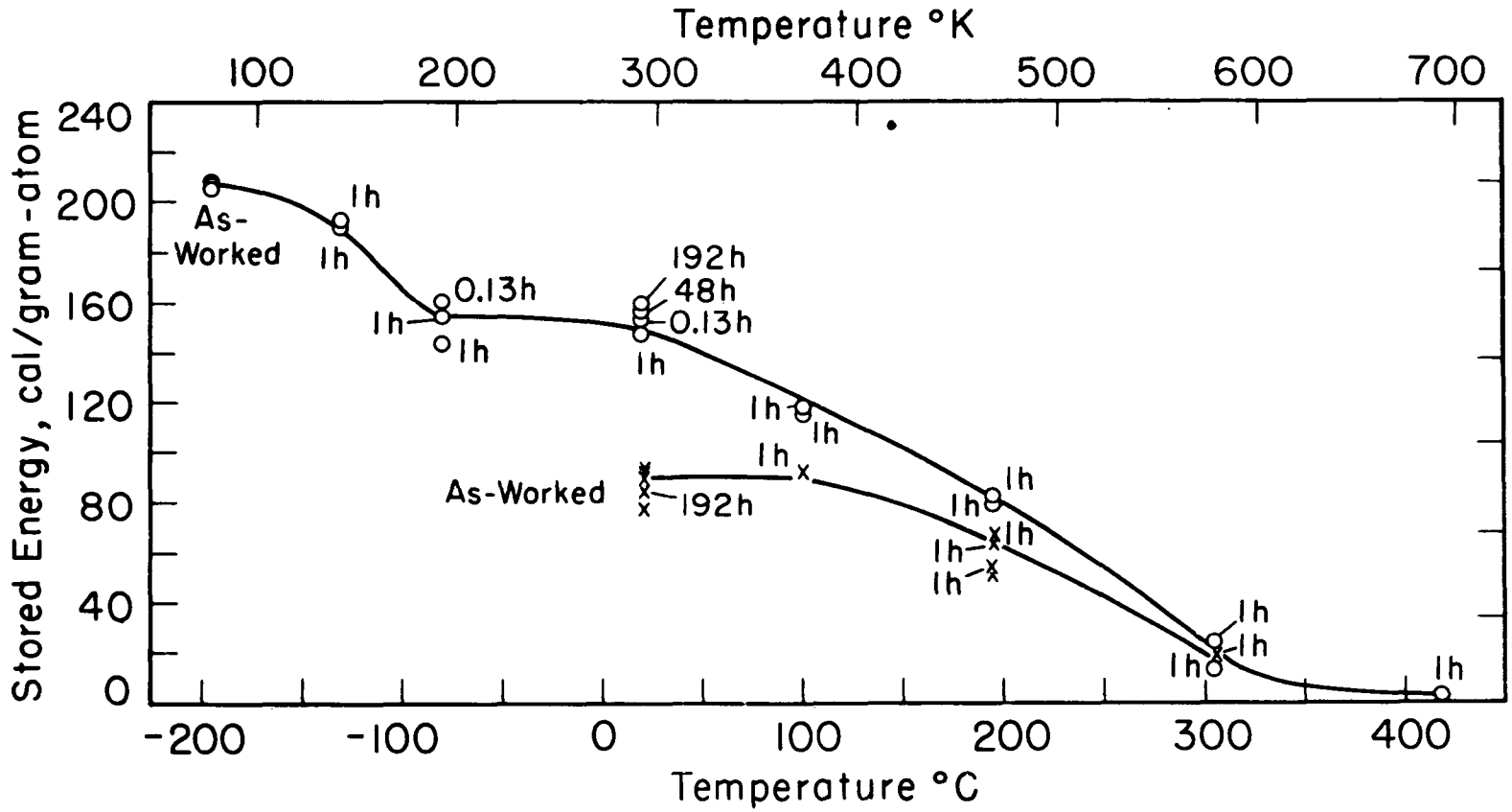

Fig. 11 Energy Stored in Samples of 82.6% Au-17.4% Ag Alloy Cold Worked at Room Temperature and 78°K as a Function of Subsequent Annealing Treatments. (Greenfield and Bever, 1956)

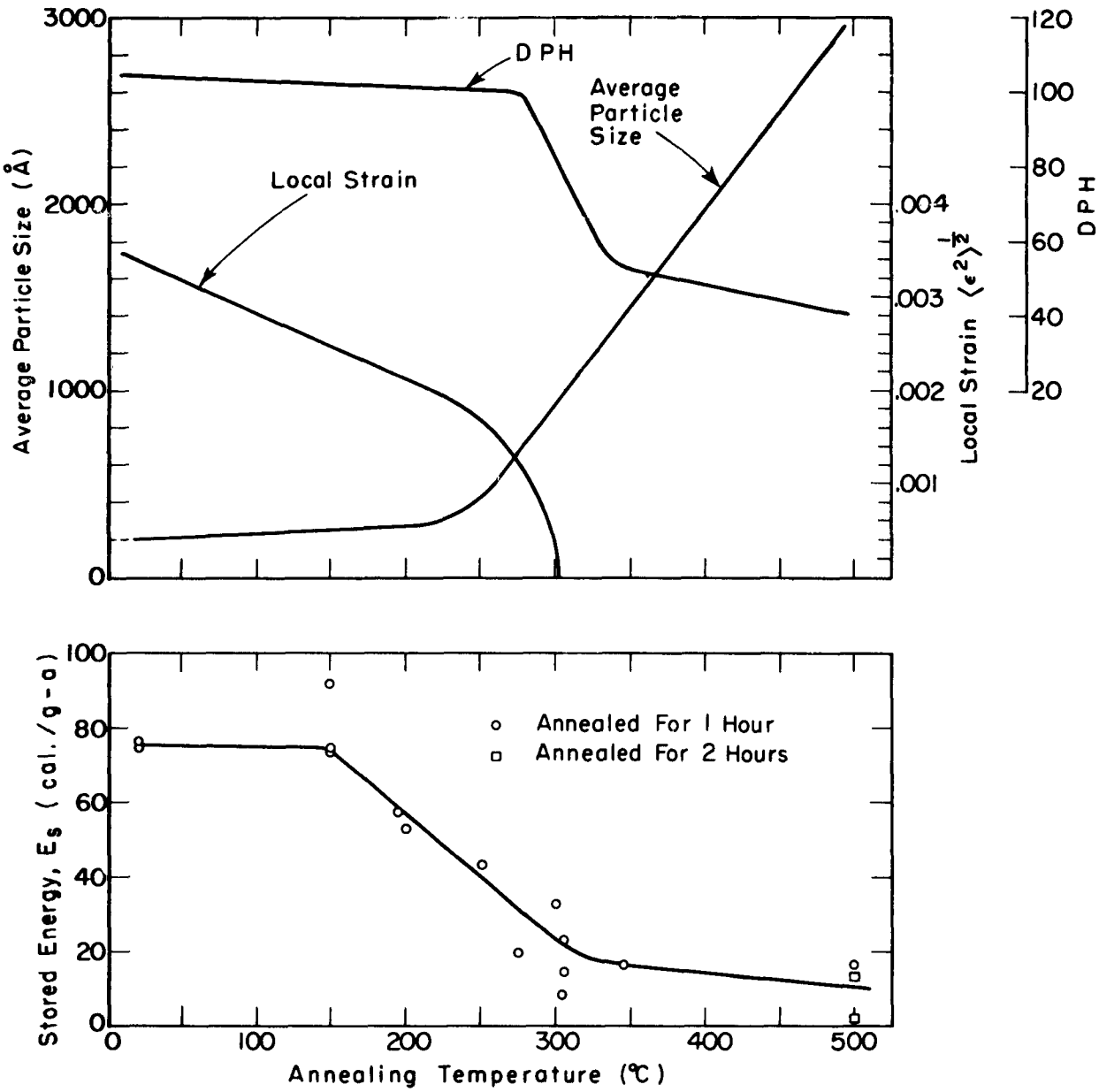

Fig. 12 Stored Energy, Particle Size, Strain and Hardness of 75%Au-25%Ag Alloy as a Function of Annealing Treatment. (Averbach, Bever, Comerford and Leach, 1956)

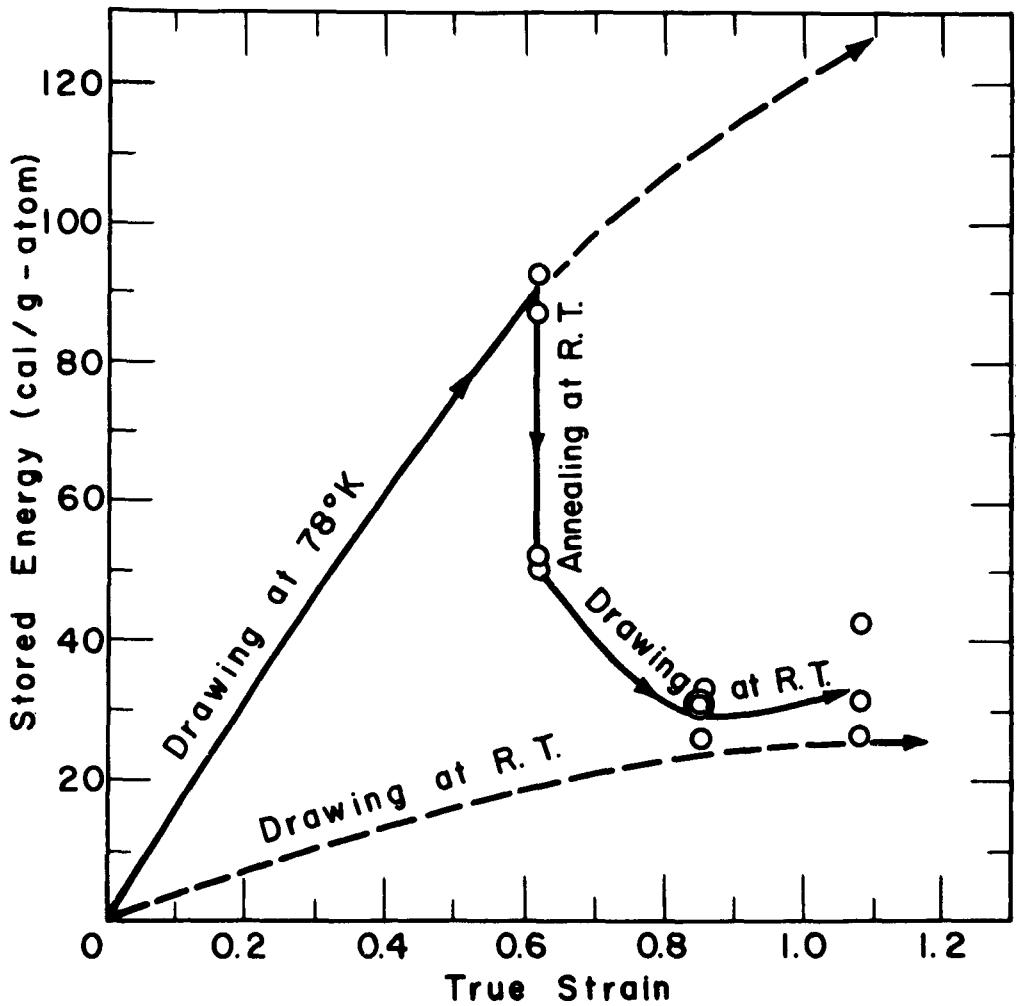

Fig. 13 Stored Energy in 82.6% Au - 17.4% Ag Alloy as a Function of Strain and Temperature History. (Titchener and Bever, 1960)

The Observation of Substructures in Crystals with the Electron Microscope

H. G. F. Wilsdorf

The Franklin Institute Laboratories
Philadelphia, Pennsylvania

The term "substructure" encompasses a variety of dislocation arrangements including the well defined sub-boundaries. Detailed aspects of substructures were covered in review articles by Hirsch (1), and Amelinckx and Dekeyser (2). As early as 1954, the electron microscope had been used for the study of dislocation boundaries by means of the replica technique (3) which will be outlined in this article. Later, this method was also applied to investigations of slip bands, pile-ups and interactions of glide dislocations with sub-boundaries (4-6). Since 1956, dislocations (7) and stacking faults (8) have been studied even more directly by a new technique called diffraction electron microscopy. Immediately after its discovery, this technique provided experimental proof for the many concepts of dislocation theory and later on was instrumental in providing new information on dislocation substructures. The two techniques will be discussed, and their applicability to the study of substructures will be critically reviewed.

Replica Technique

The use of the standard type electron microscope became of interest to metallurgists with the development of replica techniques in 1940 (9). Since that time numerous variations of this technique have been devised which have been reviewed in considerable detail in the literature (10).

The principle of the replica technique is to cover the metal surface which is to be investigated, with a film not thicker than, say, 500 Å, whereby the thickness of the film with respect to the normal of the surface has to be controlled. Fig. 1a indicates the production of a SiO replica (11) by vacuum evaporation. Subsequently, the film has to be separated by chemical means from the metal and then is "shadow-cast" (Fig. 1b). Since the contrast in electron images is usually due to an electron scattering mechanism depending on the thickness and mass of the specimen, the shadow-cast substance to be evaporated under an angle of, say, 30° onto the specimen ought to have a high atomic number. Now, the specimen is ready for examination in the electron microscope at magnifications from 2,000X to 60,000X. The surface area that can be screened at a time is 1 mm x 0.1 mm or about 2 mm in diameter, depending on the roughness of the surface, the microscope used, and other conditions.

Because of the inherent high resolving power of first class electron microscopes, details in the order of 25 Å can be detected. Obviously, this requires the careful preparation of metal surfaces, which, however, can be done with relative ease by applying suitable electropolishing procedures (12).

Turning to the subject matter of detecting sub-boundaries, it becomes clear that this technique permits their study at the line of intersection with the surface. For a tilt boundary with a $\theta = 5'$, the dislocations are separated by a

distance of about 2000 Å, which puts a rather stringent requirement on techniques that are used to mark the intercept of dislocations with the surface. Reference is made to the precipitation method and the etch pit technique. The former method was actually used to provide the first visible evidence of dislocations in a metal (3) and is based on the preferential nucleation of a precipitate at a dislocation site. Figs. 2a and b give examples of sub-boundaries which were found in the as-grown crystals of an Al-4% Cu alloy. Assuming that each precipitate marks the point of emergence of an edge dislocation, the misorientation between the two sub-grains can be calculated as $\theta = b/h$, where b is the Burgers vector and h the distance between the precipitates. The good agreement between measurements with the electron microscope and x-ray data (13) justifies the assumption that each dislocation gives rise to one precipitate.

Etch pit techniques have been successfully used to indicate the position of dislocations at surfaces, and many crystals have been thoroughly studied with this method using the light microscope (14). The limited resolving power of the light microscope led to the application of replica techniques and observations with the electron microscope. In particular, α-brass crystals have been studied extensively, and Figs. 3a and b demonstrate the ability of the technique (15-18). The points of emergence of dislocations are indicated by well defined etch pits which are small enough as to give a clear indication of the dislocations' arrangement. Fig. 3a shows a grown-in sub-boundary, and in Fig. 3b the interaction of glide dislocations with a sub-boundary can be seen.

The spatial distribution of sub-boundaries can be determined to some extent by repeatedly removing thin surface layers and replicating the same area with a suitable technique (19). It can be concluded that the replica method, in conjunction with precipitation and etch pit techniques, is capable of detecting the dislocation arrangements in sub-boundaries at their intersections with surfaces. Recent investigations by Young (20) and Levinstein and Robinson (21) with the light microscope indicate the possibility of applying the replica technique to etch pit studies in deformed pure f.c.c. metals which contain dislocation tangles.

Diffraction Contrast

The detection of lattice defects with the electron microscope is based on the diffraction of electrons by crystal lattices. The diffraction conditions have been given by von Laue in the fundamental equation

$$\underline{k}-\underline{k}_0 = \underline{g} \cdot \lambda \qquad (1)$$

where $\underline{k}_0$ and $\underline{k}$ are the wave vectors of the incident and diffracted beam, λ the wavelength, and $\underline{g}$ a lattice vector in the reciprocal lattice which is equal to $g_1 \underline{a}^* + g_2 \underline{b}^* + g_3 c^*$, g_1, g_2, g_3 being integers and a^*, b^*, c^* unit vectors in the reciprocal lattice. Fig. 4 represents the above relation in two dimensions in graphical form, and also shows the direction of the diffracted beam. According to Ewald's construction, diffraction occurs when a sphere with radius $1/\lambda$ and 0 as its center cuts through the intensity distribution of a reciprocal lattice point.

The amplitude of the diffracted wave can be written with the help of the structure factor F

$$A = |F| = \sum_n f_n \exp\left[2\pi i\, (\underline{k} - \underline{k}_o) \cdot \underline{r}_n\right] \qquad (2)$$

where f_n is the scattering factor for electrons and the vector $\underline{r}_n$ marks the position of the scattering atom in a column of unit cell dimensions as measured from the origin of the lattice. However, if the Ewald sphere does not exactly pass through a reciprocal lattice point G but lies at a small distance from a given G as measured by the vector $\underline{s}$, then we have to replace $\underline{k} - \underline{k}_o$ by $\underline{g} + \underline{s}$. Since $\underline{g} \cdot \underline{r}_n$ is an integer, equation (2) becomes

$$A = f_n \sum_n \exp\,(2\pi i\, \underline{s} \cdot \underline{r}_n). \qquad (3)$$

f_n has been taken out of the sum, which is permissible under the reasonable assumption that all the unit cells in the column are similar. So far, the case of a perfect crystal has been considered. Our main concern, however, is to show the formation of images of lattice defects. Following the calculations by Hirsch, Howie and Whelan (22) and in accordance with the nomenclature introduced by them, a deviation of the scattering atom from its ideal position will be defined by the vector R. Now, the amplitude of the diffracted wave is obtained by adding a phase factor $\alpha = 2\pi\, \underline{g} \cdot \underline{R}$ to equation (3), and α being a function of z (see Fig. 5) we can write

$$A \approx \int_{\text{column}} \exp\,(2\pi i\, \underline{g} \cdot \underline{R}) \cdot \exp\,(2\pi i\, s\, z)\, d\, z \qquad (4)$$

s is now the distance between the Ewald sphere and G, taken in the direction of the column.

Equation (4) provides the foundation for discussing the formation of dislocation images in the electron microscope. First, we will consider the path of electron beams in the microscope. It follows from the principle of diffraction contrast that the diffracted beam (or beams) have to be prevented from contributing to the electron image. This is effected by an objective aperture which is in the order of 10^{-3} rad.; Fig. 6 shows the path of rays for the formation of the first electron image. The distorted lattice around a dislocation is indicated by a line in the specimen, while the missing electrons in the image can be seen as the "white" line in the figure.

Next, we have to determine the displacement vector $\underline{R}$ in equation (4). Choosing a simple case, $\underline{R}$ will be given for a screw dislocation lying parallel to the z-axis of an orthogonal coordinate system and parallel to the surface of the foil. One finds that $\underline{R}_x$ and $\underline{R}_y$ are zero and that

$$\underline{R}_z = \frac{b}{2\pi}\,\theta = \frac{b}{2\pi}\,\text{arc tan}\,\frac{y}{x}, \qquad (5)$$

with $\underline{b}$ the Burgers vector of the dislocation. Inserting (5) into equation (4), a decision concerning the choice of a diffracting beam for producing an image of

the dislocation can be made immediately. The phase factor α contains a product of the reciprocal lattice vector $\underline{g}$ and the Burgers vector $\underline{b}$, which becomes zero if the family of diffracting lattice planes and $\underline{b}$ are parallel. It can, therefore, be concluded that the highest contrast may be expected when the diffracting lattice planes are perpendicular to the Burgers vector, and it would be most desirable to select a diffraction spectrum in accordance with this consideration.

From equation (4) the intensity profile of a dislocation can be obtained. Hirsch, Howie and Whelan have calculated the line width with the help of amplitude-phase diagrams (22). Recently, the values of the integral (4) have been calculated by Gevers for $\underline{g} \cdot \underline{b} = n = 1, 2, 3$ and 4 (23), and his main results for $n = 1$ and $n = 2$ are given in Fig. 7. Three features are in evidence: (i) The image of a dislocation is shifted from its true position by a distance approximately equal to its width; (ii) The width of an edge dislocation is twice that of a screw dislocation; (iii) The intensity profile of dislocations is steeper on that side which faces the center position of the dislocation.

The true position of a dislocation can be determined by changing $\underline{g}$, i.e., by choosing a different diffraction plane, or by reversing the sign of $\underline{s}$, which can be achieved by tilting the specimen around a suitable crystallographic direction (24). Fig. 8 demonstrates the shift of the dislocation image in the vicinity of an extinction contour, i.e., due to a change of sign of s.

As has been already mentioned above, the displacement vector has to have a perpendicular component with respect to the diffracting lattice planes if a dislocation image is to be obtained. On the other hand, the disappearance of the image when $\underline{g} \cdot \underline{b} = 0$ can be used to confirm the Burgers vector, which in many investigations can be presumed from experimental conditions. It is a requisite for a Burgers vector determination to have a goniometer stage for positioning of the crystal in the microscope. For a meaningful determination of the Burgers vector, one desires to have other dislocations in the specimen which have a Burgers vector different from the first set in order to ascertain that the critical diffraction condition is satisfied. A further check can be provided by employing the dark field technique. Here, the objective aperture in the back focal plane is adjusted so as to permit only the diffracted beam chosen above to form the dark field image, and, of course, those dislocations for which $\underline{g} \cdot \underline{b} = 0$ should not be seen.

The determination of the sign of s is necessary if one wishes to know the sense of the Burgers vector, since the above techniques yield only its direction. Crystals for these investigations have a thickness of more than 1000 Å and usually also show Kikuchi lines, which consist for each spectrum of a dark and a light line, parallel to each other, against the background of inelastically scattered electrons. For $s = 0$ the Kikuchi lines go through the center of the reciprocal lattice point, but for a positive or negative s (see Fig. 4) the Kikuchi lines are displaced to the right or to the left of the reciprocal lattice point, respectively, The location of the dislocation's image for a given lattice position with respect to the incident beam is given in Fig. 9 for a dislocation loop. Slight rotations of the specimen and the additional observation of the actual diffraction pattern together with the electron micrograph enable the unambiguous determination of the direction and the sense of the Burgers vector.

Any discussion concerning diffraction contrast in electron micrographs must include the formation of fringes. Integration of equation (3) yields for

a thin crystal

$$A \sim \frac{\sin \pi ts}{\pi s} \tag{6}$$

which shows immediately that the intensity of a diffracted beam depends on both the thickness t as well as on s. The first case is realized in crystals with varying thickness, and in particular, in wedge-shaped specimens (Fig. 10a); the second occurs when a thin film is bent and the Ewald sphere cuts the reciprocal lattice point at different distances. The resultant contrast pattern is called an "extinction contour", and an example of it is shown in Fig. 10b.

A two-dimensional lattice defect resulting from a "mistake" in the stacking of closest-packed planes in a crystal lattice is of considerable importance and can easily be detected with this technique. In the f.c.c. lattice, a mistake in the stacking of octahedral planes, for example ABCAB/ABC..., can be described as a displacement of the two parts of the crystal by a vector $R = a/6 \langle 112 \rangle$, a being a lattice translation. Fig. 11a shows the two parts of the crystal divided by the stacking fault AB. The amplitude of the diffracted wave is calculated by means of equation (4), adding to the term for the perfect crystal (above the line AB) a term that contains the displacement $a/6 \langle 112 \rangle$. The resultant phase angle, α, equals 0° or $\pm 120^\circ$, which leads to a set of light-dark fringes from A' to B with a spacing

$$D = t_o \operatorname{cotan} \phi \tag{7}$$

where t_o is the so-called extinction distance. t_o is related to the electrons' wavelength λ, the accelerating voltage U and the lattice potential V_g.

Similar fringes may be observed when twin and grain boundaries lie under an oblique angle in the specimen (Fig. 12).

The above discussion of the diffraction contrast was based on the kinematical theory of electron diffraction. The validity of this theory breaks down for s approaching zero, i.e., when the Laue conditions are fulfilled exactly. Then use must be made of the dynamical theory of electron diffraction which takes into account the interaction of electron waves with the wave field inside the crystal. The latter treatment provides quantitative results for many of the problems discussed above. According to the dynamical theory (25), the fringe distance for stacking faults is half of that obtained for $s > 0$ (see Fig. 11b), which is an important result concerning the possibility of distinguishing between stacking faults and grain boundaries and other diffraction fringes. So far only dislocations lying parallel to the plane of the foils have been considered. While their image showed uniform contrast, dislocations inclined against the surface of the foil have a dotted appearance (Fig. 12) which has been explained by the dynamical theory as intensity oscillations.

Reliability of Results Obtained by Diffraction Electron Microscopy

The high scattering power of matter for electrons demands the preparation of specimens for diffraction electron microscopy in the thickness range of a few thousand Angstroms. Usually this is done by electropolishing (12), and techniques for electromachining electron transparent crystal wafers from bulk specimens have been described in the literature (26).

Because of the reduction of thick metal crystals to very thin foils, one immediately raises the question of how representative the observed dislocation patterns really are. In a recent paper Ham claims that 60% of the dislocations in a rolled aluminum-silver alloy are lost in the preparation of the thin specimens (27). This conclusion is based on comparisons between dislocation densities of unaged and aged Al-0.5% Ag alloys which had been deformed by rolling 18% or 45%. Because of the formation of small silver aggregates in the aged alloy, it can be assumed that the free motion of dislocations is reduced. Since the aged specimens contained more than 2 times as many dislocations than the unaged specimens, Ham argues that at least 60% of dislocations in Al-0.5% Ag and, by inference in Al, are lost during the preparation of the thin specimen. If this result be correct, one would have to conclude that dislocation rearrangements during electropolishing would take place to an extent that the patterns observed in the microscope would not bear much resemblance to the dislocation arrangement in the bulk specimen.

The change of dislocation patterns in deformed aluminum single crystals has been investigated with the diffraction electron microscopy method, selecting specimen thickness as the variable (28). Indeed, a considerable loss of dislocations and their rearrangement was clearly measurable below a thickness of 1500 Å. However, it was found that the dislocation patterns did not change noticeably in foils from 2000 Å up to 8000 Å, the latter specimen thickness being the largest which permitted discernible dislocation contrast to be obtained at an acceleration voltage of 100 KV. It has been pointed out (28) that "image forces" will tend to pull dislocations out of the specimen, if they are parallel or almost parallel to the surface, and provided that the slip plane is sufficiently inclined against the foil's surface, which should not be covered with an elastically harder layer. The other major influence on dislocations is due to their tendency to reduce their line energy. This can be achieved by dislocations moving perpendicular to the surface while remaining in their slip planes. Clearly, the above considerations will be influenced by the frictional forces the dislocations have to overcome, which will vary greatly from metal to metal.

Before we return to the problem of measuring dislocation densities by the thin film technique, some experimental findings will be discussed which are related to the mobility of dislocations near the surface of a thin foil. Under certain experimental conditions, dislocations form patterns that are repeated throughout the specimen. As a first example, I am referring to square-shaped loops in Al-0.5% Mg which are obtained after annealing quenched specimens. In Fig. 13 a number of these loops are shown. The plane of the loops is only slightly inclined to the surface, which in one instance cuts through the loop (see arrow in Fig. 13). Although the shape of the loop has not been changed markedly, a short dislocation is seen to connect one end of the cut-off loop with the surface. Undoubtedly, this part of the dislocation has been moved out of the original plane of the loop by the driving forces discussed in the previous paragraph. However, no further changes seem to have taken place. A second example can be provided with the help of Fig. 14 which shows dislocation loops in a deformed molybdenum single crystal. Loops of this type are prismatic and apparently have been "punched out" by stress concentrations due to precipitates in the matrix. They number from five to approximately twenty and are mostly of similar diameter, which decreases somewhat with increasing distance from its origin. Again, the surface has cut through most of the loops without affecting their shape to a major degree.

One might also refer at this point to the numerous investigations carried out on many pure metals and alloys which have yielded much information as to the different dislocation behavior in these materials. From the above discussion it is concluded that, provided certain precautions are observed, the technique provides reliable information on dislocation arrangements in crystals.

Since the knowledge of dislocation densities in deformed crystals is of utmost importance to the understanding of the flow characteristics, the measurement of this quantity deserves to be given special attention. Most specimens for diffraction electron microscopy are prepared from large single crystals or test specimens by electrolytic cutting and polishing. In general, the final film has a thickness of a few thousand Angstroms and contains in an area of, say, $10\mu^2$, a number of macroscopic wrinkles. Although the angular deviation between adjacent areas may only be in the order of one minute of arc, it is sufficient to upset the diffraction condition. This in turn does not permit the observer to see dislocations in a large area without continuously adjusting the orientation of the specimen against the incident beam. Also, the diffracting lattice planes may contain the direction of the Burgers vector of one set of dislocations which would lead to too small a dislocation count. Again, tilting the specimen could correct this possible error in measurement.

In case the inherent difficulties of the technique have been overcome, the success of a dislocation count will also depend on the particular arrangement of these defects. Since the majority of dislocations will not be straight but kinked and curved, the actual measurement of dislocation lines per ccm is difficult. Moreover, this measurement requires the knowledge of the thickness of the specimen, the dislocation's glide plane and the angle of this glide plane to the foil's surface; often the experimental determination of the Burgers vector is needed. In principle, all of these measurements can be performed, but the process is cumbersome and time consuming. Only few instances are known where glide dislocations are distributed uniformly throughout the crystal, which is the main assumption for the discussion so far.

The agglomeration of dislocations into tangles or "diffuse" cell walls during plastic flow is more frequent. Here, the density of dislocations may become so high that cell walls or tangles appear as dark areas in the micrographs, which condition will not allow a dislocation count at all, or only over smaller areas. Of course, thinning the foil to 1000 Å or possibly less would enable the detection of single dislocations; however, this appears not to be possible without losing many of them to the surface and/or from their ararrangement. This is exactly what seems to have happened in the foils studied by Ham (27). His paper contains three electron micrographs which exhibit cell walls containing glide dislocations in (i) pure aluminum, (ii) unaged Al-0.5% Ag, and (iii) aged Al-0.5 Ag. While the latter micrograph shows dislocations not only in the cell walls but also in the areas between walls, the volume between cell walls in the first two micrographs is empty. It is known from other investigations (29) that aluminum contains small prismatic loops near glide dislocations. The absence of prismatic loops and some odd dislocations within the cells indicate that the final foils were too thin to permit reliable dislocation counts, while thicker foils would have obscured single dislocations in the cell walls. It stands to reason that diffraction electron microscopy is a suitable technique for dislocation counts in lightly deformed crystals with reasonably uniform dislocation density. However, for heavily deformed crystals the error of measurement is quite considerable, and Ham's data

on Al-0.5% Ag are not acceptable until the measurements have been repeated with single crystals which permit the counts in known crystallographic planes and an accurate determination of the specimen's thickness.

Summary of Applications

Many applications of the techniques discussed above to the numerous problems of substructures in crystals have been reported (30). It has been pointed out in the previous paragraph that diffraction electron microscopy is particularly useful for accurate measurements in the range of a few microns and less. This is the reason why the most significant results have been obtained on substructures in deformed metals, characterizing their role in yielding phenomena, plastic flow, by translation as well as twinning, and fracture. Since this method offers the highest resolution of all known experimental techniques for the study of dislocations, even sub-boundaries with spacings of less than 500 Å can be analyzed in great detail, provided the arrangement is fairly regular. This applies to all tilt and twist boundaries, and the investigation of recovery and recrystallization processes with this method can be very useful. Recently, the formation of dislocation networks in crystals with layer structures has received considerable attention. Since these crystals cleave easily parallel to their basal planes, specimen preparation is thus facilitated and, of course, it is of great advantage that the dislocations are lying parallel to the plane of the specimen. Usually, diffraction conditions are satisfied for areas larger than the field of view, and very beautiful micrographs have been taken from graphite, mica, talc, the bismuth-tellurides and others (31).

Certain substructures found in crystals grown by solidification methods have spacings in the order of 1 mm, and electron microscopy is not likely to contribute much to their explanation. The chances of coming across grown-in sub-boundaries in a thin film are rather small, and x-ray and etch pit techniques are more suitable for their study. However, in the field of epitaxial overgrowth diffraction microscopy could play an important role. According to Frank and van der Merwe (32), the misfit between two different lattices can be described in terms of interfacial dislocations, and interesting observations on PbS and PbSe and chromium bromide have recently been reported in the literature (33, 34).

The most interesting observations of substructures have been made on deformed crystals, and we will limit ourselves to a brief discussion of dislocation patterns in metal crystals. The state of the art until 1959 was summarized by Hirsch in a review article (35). In agreement with earlier surface studies on deformed metals (36), it was found that α-brass and the pure fcc metals respectively show different dislocation structures indeed. In α-brass and stainless steel (37) pile-ups were observed while in gold, copper and nickel the dislocations are arranged "in very complex three-dimensional networks at low deformation, and in poorly developed sub-boundaries at higher deformations." (35) Experimental evidence to this effect due to Tomlinson and Partridge was given in the above-mentioned review article by Hirsch (35) and by Whelan (38). These results were explained by considering dislocation interactions.

In 1959, Wilsdorf and Kuhlmann-Wilsdorf (29) pointed out that small prismatic dislocation loops were present near the irregularly arranged glide dislocations in lightly deformed aluminum and nickel. For several reasons, including the observation that the nature of these loops is the same as that of quenched-in loops (39-41), it was concluded that point defect interactions with

glide dislocations are responsible for the formation of the irregular and kinked dislocations in fcc pure metals. Along an individual dislocation line many curvatures of very small radii can be observed which are too small to be in equilibrium with the applied stress; i.e., dislocation lines are lying not in one slip plane but contain many super jogs. The fact that tangles occur at a glide strain of 0.05 in crystals oriented for single glide is strong proof that the responsible mechanism is based on point defect interactions and not on "forest cutting" (42-44).

Another unexpected dislocation phenomenon, discovered with the help of diffraction electron microscopy, is the presence of long, narrow dislocation loops which form behind screw dislocations parallel to $\langle 112 \rangle$. They were seen in aluminum (45), magnesium oxide (46), in zinc (47), copper (48,49,50), and in fatigued metals (48). In particular, the presence of these dislocation "dipoles" is most frequent in stage I of the stress-strain curve of f.c.c. crystals deformed at low temperatures (43,49,50). The reason that they are not seen at higher deformations under conditions of multiple slip or at elevated temperatures presumably is two fold: (i) intersecting dislocations will break up the dipoles; (ii) as shown by Price (47), the dipoles disintegrate into sequences of prismatic loops at temperatures which permit conservative climb.

Electron diffraction microscopy is the only technique which enables one to see the movement of dislocations. Hirsch, Horne, and Whelan (7) were the first to observe moving dislocations in aluminum foils. In these experiments an increase in intensity of the illuminating electron beam was used to induce the stresses which moved the dislocations. Soon afterwards, small straining devices were built for the deformation of thin foils in the electron microscope (51,52,53). This technique made possible the direct observation of dislocation propagation, their interactions with each other and with obstacles, cross-slip, pile-ups, dislocation sources and fracture (54,55,56). Later experiments made use of ribbons grown by vapor techniques and showed the formation of prismatic loops in the wake of glide dislocation. Information on climb was obtained by following the motion of R-dislocations (39) during the annealing of thin quenched aluminum foils in the microscope (57). Even the formation of precipitates in an aluminum-copper alloy and their dissolution at will by controlling the temperature cycle was possible (58).

Acknowledgement

I wish to thank my wife, Professor Doris Wilsdorf, University of Pennsylvania, Philadelphia, for valuable discussions.

The partial financial support by the Aeronautical Research Laboratory, Office of Aerospace Research, USAF, under Contract No. AF 33(616)-6996 is gratefully acknowledged.

References

1. Hirsch, P. B., Progress in Metal Physics 6, 236 (1956).

2. Amelinckx, S. and Dekeyser, W., Solid State Physics 8, 327 (1959).

3. Wilsdorf, H. and Kuhlmann-Wilsdorf, D., Phil. Mag. 45, 1096 (1954).

4. Wilsdorf, H. and Kuhlmann-Wilsdorf, D., Report of Conference on Defects in Cryst. Solids (London, Phys. Soc.), 1955, pp. 175.

5. Thomas, G. and Nutting, J., Institute of Metals Symposium on "Mechanism of Phase Transf. in Metals" (London), 1955, pp. 57.

6. Takeyama, T. and Koda, S. Nature (London) 179, 777 (1957).

7. Hirsch, P. B., Horne, R. W., and Whelan, M. J., Phil. Mag. 1, 677 (1956).

8. Bollmann, W., Phys. Rev. 103, 1588 (1956).

9. Mahl, H., Z. techn. Phys. 21, 17 (1940).

10. Muller, H., Praparation von Technisch-Physikalischen Objekten fur die Elektronenmikroskopische Untersuchung. Akad. Verlagsges., Leipzig, 1962.

11. Wilsdorf, H., Z. Metallkd. 45, 14 (1954).

12. Jacquet, P.A., Met. Reviews 1, 156 (1956).

13. Guinier, A., Imperfections in Nearly Perfect Crystals, Wiley 1952, p. 402.

14. Johnston, W. G., Progress in Ceramic Science 2, 1 (1961).

15. Sun, R. and Wilsdorf, H. G. F., J. Franklin Inst. 265, 413 (1958).

16. Wilsdorf, H. G. F., Internal Stresses and Fatigue in Metals, Elsevier, 1959, pp. 178.

17. Meakin, J. D. and Wilsdorf, H. G. F., Trans. AIME 218, 737 (1960).

18. Meakin, J. D. and Wilsdorf, Trans. AIME 218, 745 (1960).

19. Fourie, J. T., J. Appl. Phys. 29, 608 (1958).

20. Young, F. W., J. Appl. Phys. 33, 3553 (1962).

21. Levinstein, H. J. and Robinson, W. H., J. Appl. Phys. 33, 3149 (1962).

22. Hirsch, P. B., Howie, A., and Whelan, M. J., Phil. Trans. A 252, 499 (1960)

23. Gevers, R., Phil. Mag. 7, 59 (1962).

24. Howie, A. and Whelan, M. J., Proc. Roy. Soc. A 267, 206 (1962).

25. Whelan, M. J. and Hirsch, P. B., Phil. Mag. 2, 1121 (1957).

26. Strutt, P. R., Rev. Sci. Instr. 32, 411 (1961).

27. Ham, R. K., Phil. Mag. 7, 1177 (1962).

28. Wilsdorf, H. G. F. and Schmitz, J., J. Appl. Phys. 33, 1750 (1962).

29. Wilsdorf, H. G. F. and Kuhlmann-Wilsdorf, D., Phys. Rev. Letters 3, 170 (1959).

30. Thomas, G., Transmission Electron Microscopy of Metals, Wiley, 1961.

31. Amelinckx, S. and Delavignette, P., Direct Observations of Imperfections in Crystals, AIME, 1961, pp. 295.

32. Frank, F. C and van der Merwe, J. H., Proc. Roy. Soc. A 198, 205 (1959); Ibid. 200, 125 (1950); Ibid. 201, 261 (1950).

33. Matthews, J. W., Phil. Mag. 6, 1347 (1961).

34. Delavignette, P., Tournier, J., and Amelinckx, S., Phil. Mag. 6, 1419 (1961).

35. Hirsch, P. B., Met. Reviews 4, 101 (1959).

36. Kuhlmann-Wilsdorf, D. and Wilsdorf, H. G. F., Acta Met. 1, 394 (1953).

37. Whelan, M. J., Hirsch, P. B., Horne, R. W., and Bollmann, W., Proc. Roy. Soc. A 240, 524 (1957).

38. Whelan, M. J., Proc. Roy. Soc. A 249, 114 (1958).

39. Kuhlmann-Wilsdorf, D., Phil. Mag. 3, 125 (1958).

40. Hirsch, P. B., Silcox, J., Smallman, R. E., and Westmacott, K. H., Phil. Mag. 3, 897 (1958).

41. Kuhlmann-Wilsdorf, D. and Wilsdorf, H. G. F., J. Appl. Phys. 31, 516 (1960).

42. Kuhlmann-Wilsdorf, D., Maddin, R., and Wilsdorf, H. G. F., "Strengthening Mechanisms in Solids", ASM, 1962, pp. 175.

43. Kuhlmann-Wilsdorf, D. and Wilsdorf, H. G. F., Symposium on Electron Microscopy, Wiley, 1963.

44. Wilsdorf, H. G. F. and Schmitz, J., J. Appl. Phys. 33, 1750 (1962).

45. Fourie, J. T. and Wilsdorf, H. G. F., J. Appl. Phys. 31, 2219 (1960).

46. Washburn, J., Graves, G. W., Kelly, A., and Williamson, G. K., Phil. Mag. 5, 991 (1960).

47. Price, P. B., Phil. Mag. 5, 873 (1960).

48. Quoted by Hirsch, P. B. and Warrington, D. H., Phil. Mag. 6, 735 (1961).

49. Fourie, J. T. and Murphy, R. J., Phil. Mag. 7, 1617 (1962).

50. Basinski, Z. S., Proc. 5th Int. Congress Electron Microscopy, Academic Press 1962, B-13.

51. Wilsdorf, H. G. F., Rev. Sci. Instr. 29, 323 (1958).

52. Berghezan, A. and Fourdeux, A., Fourth Int. Conf. on Electron Microscopy, 567, Springer, 1960.

53. Kear, B. H., Rev. Sci. Instr. 31, 1007 (1960).

54. Wilsdorf, H. G. F., ASTM Special Technical Publication No. 245, 43 (1958).

55. Berghezan, A. and Fourdeux, J. Appl. Phys. 30, 1913 (1959).

56. Wilsdorf, H. G. F., Proc. Int. Conf. on Structure and Prop. of Thin Films, John Wiley, 1959, pp. 151.

57. Silcox, J. and Whelan, M. J., Proc. Int. Conf. on Structure and Prop. of Thin Films, John Wiley, 1959, pp. 164.

58. Thomas, G. and Whelan, M. J., Phil. Mag. 6, 1103 (1961).

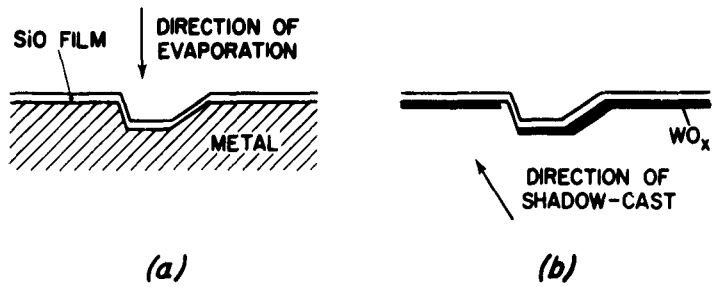

Fig. 1 Schematic representation of the preparation of a so-called "direct" replica. For details of the SiO replica technique, see reference (11).

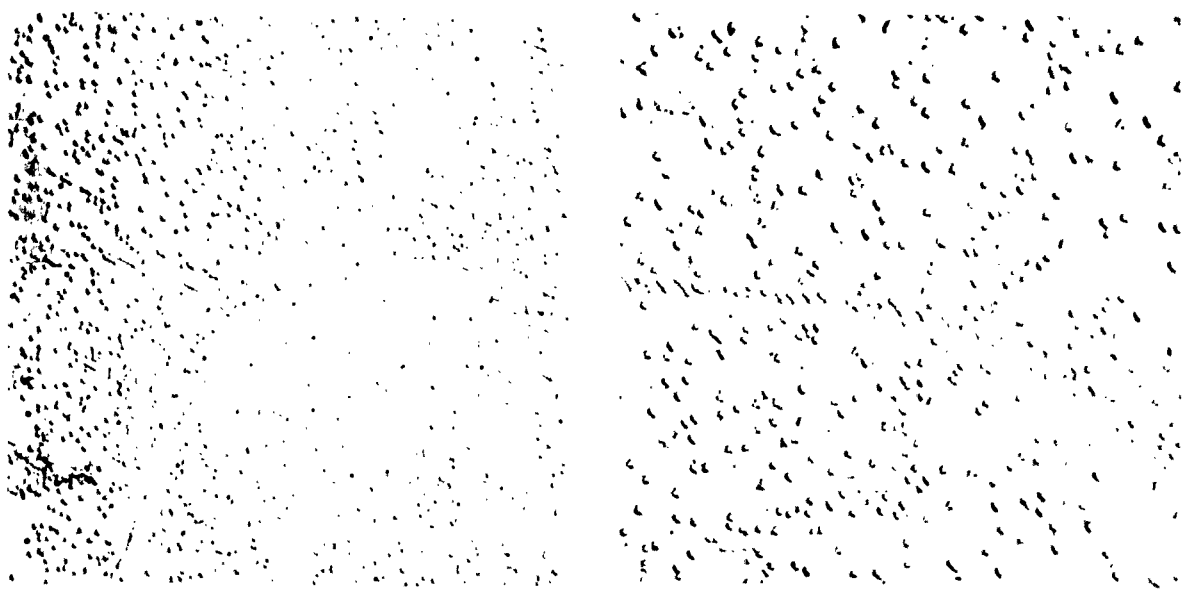

Fig. 2 Detection of the emergence of dislocations at the surface by a combined precipitation and replica technique.
(a) 9000:1; (b) 18000:1

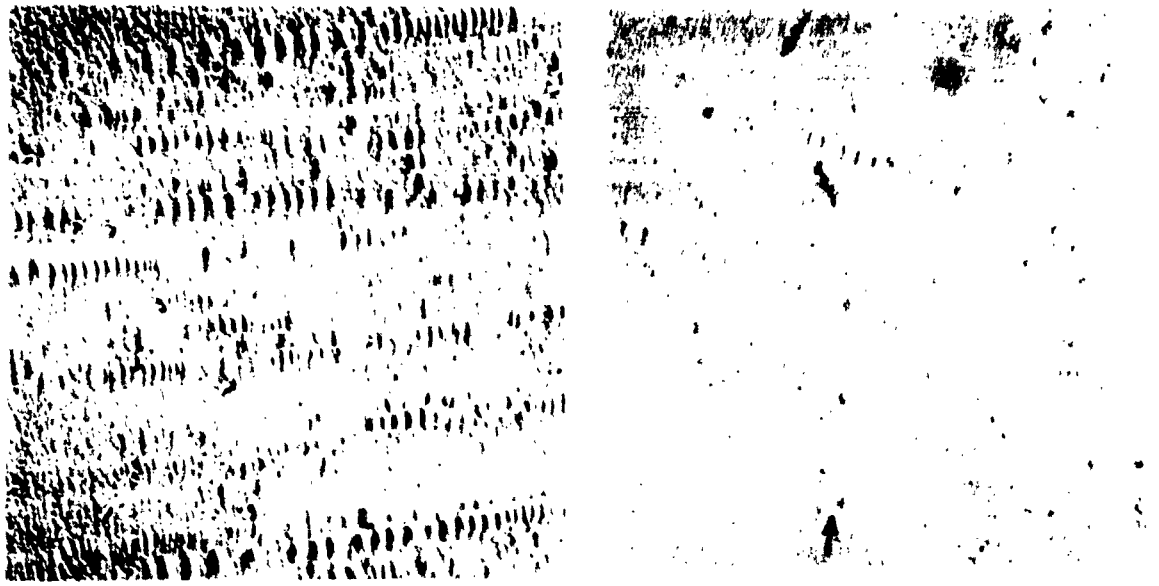

Fig. 3 Etch pits marking the sites of dislocations in deformed α-brass (Meakin and Wilsdorf (17,18)).
(a) 20000:1; (b) 15000:1 (arrows indicate sub-boundary)

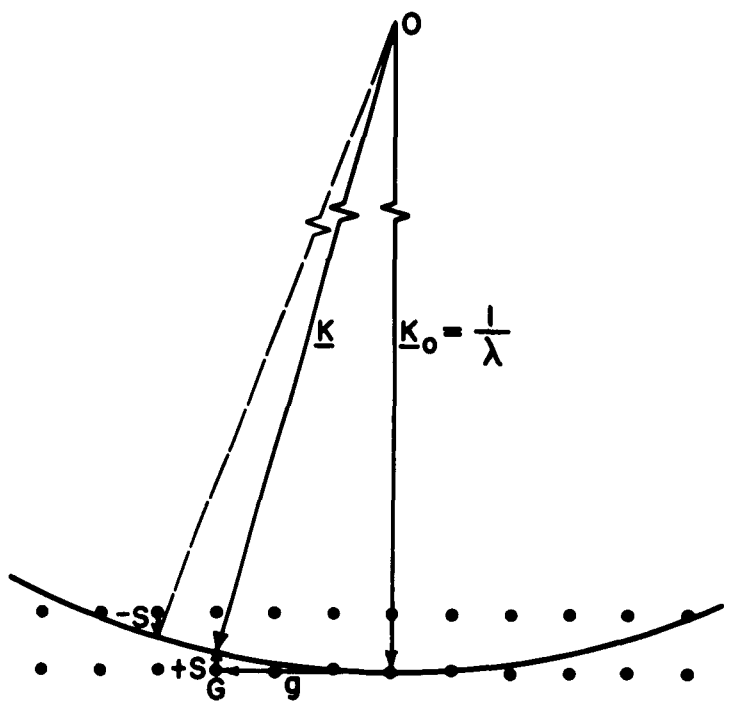

Fig. 4 Ewald's construction of the conditions for the diffraction of electrons in crystals. For explanation of symbols, see text.

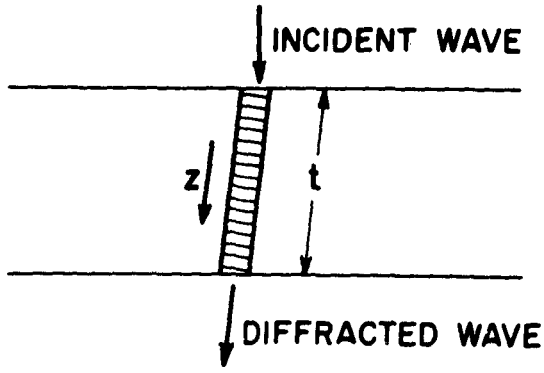

Fig. 5 Column in crystal used for the calculation of diffraction contrast.

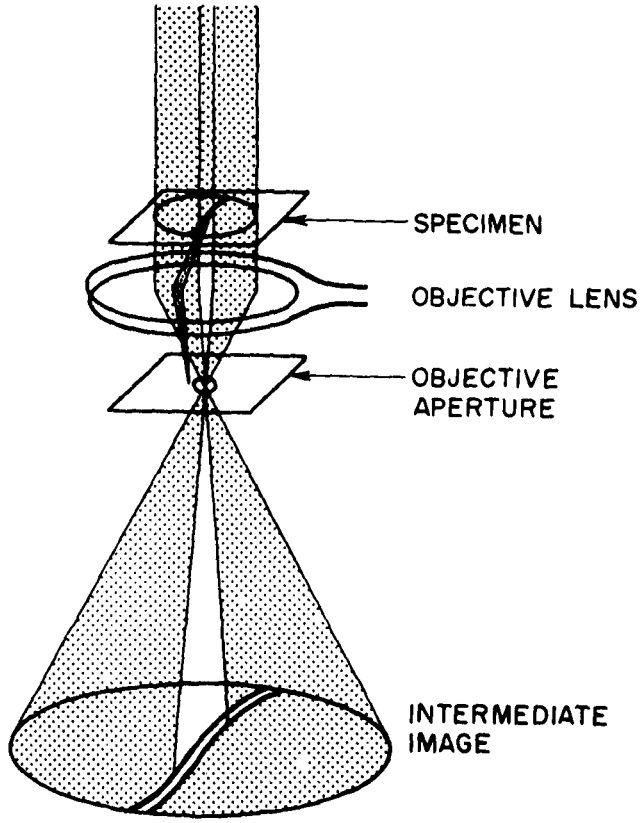

Fig. 6 Path of electrons passing through the specimen, or being diffracted into an angle larger than the objective aperture, forming the intermediate image. Dislocation is indicated as dark line in specimen.

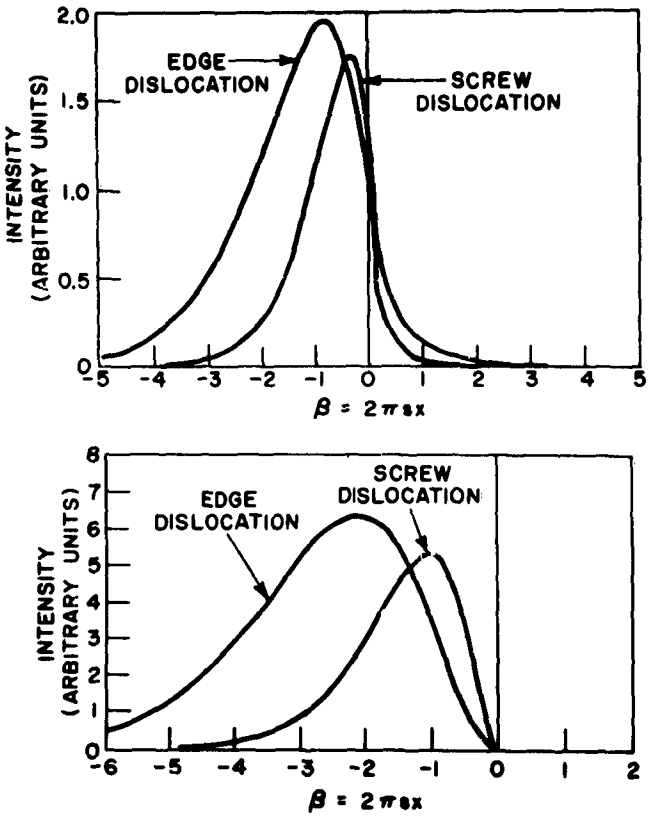

Fig. 7 Intensity profiles for dislocations with n = 1 (top) and n = 2 (bottom) (after Gevers (24)).

Fig. 8 Shift of the image of dislocations due to a change of s. 40000:1

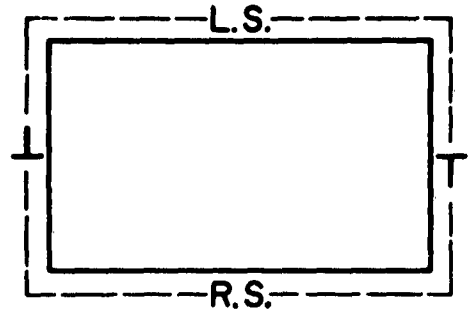

Fig. 9 Sketch illustrating that the image of a dislocation loop is lying either "inside" or "outside" of the true location of the dislocation loop. L.S. and R.S. indicate left and right-handed screw dislocation respectively.

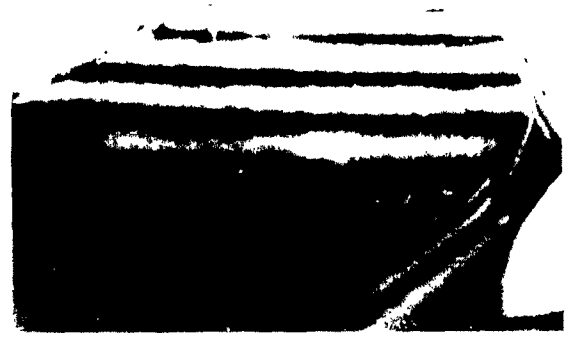

Fig. 10a Diffraction fringes due to changing thickness of specimen. 13000:1

10b Fringes due to bent specimen, named "extinction contour". 20000:1

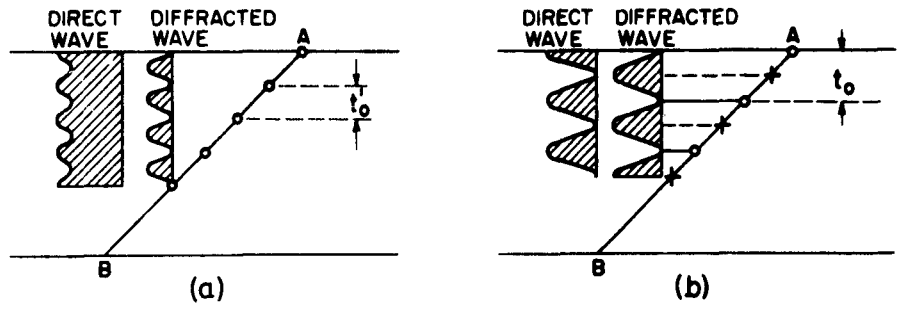

Fig. 11 Origin or diffraction fringes caused by a stacking fault. (a) Spacing of fringes according to kinematical theory and (b) due to the dynamical theory of electron diffraction (after Howie and Whelan (24)).

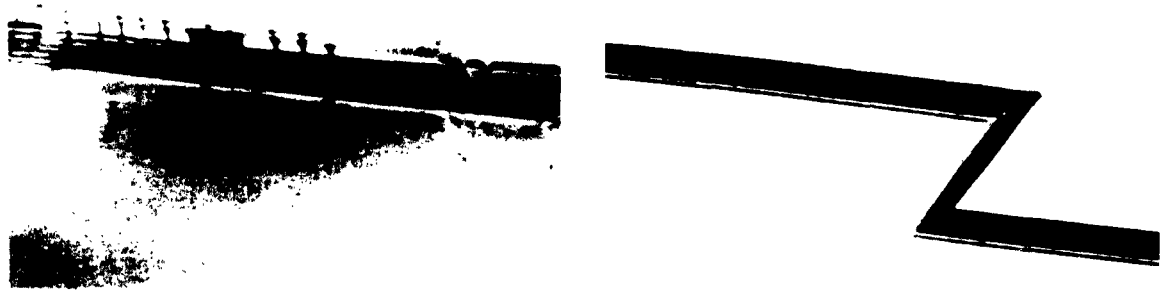

Fig. 12 Diffraction fringes due to (a) a stacking fault, 40000:1; and (b) a grain or twin boundary, 40000:1

Fig. 13 Square-shaped dislocation loops in quenched and aged Al-0.5% Mg specimen. 40000:1
Micrograph by courtesy of I. G. Greenfield

Fig. 14 "Punched-out" loops in molybdenum single crystal. 40000:1
Micrograph by courtesy of H. Gaigher and A. Lawley

THE OBSERVATION AND MEASUREMENT OF SUBSTRUCTURES IN CRYSTALS BY X-RAY TECHNIQUES

by S. Weissmann
College of Engineering, Rutgers · The State University, New Brunswick, N. J.

1. INTRODUCTION

It is universally recognized that a great many properties of solids are significantly affected by small changes in the perfect arrangement of atoms of which the solid is composed. Such properties are said to be structure-sensitive. The three most important classes of structure-sensitive properties of crystalline matter are mechanical, electric and magnetic. Thus the strength and plastic properties of metals and many other crystals, the phenomena of crystal growth and recrystallization, the diffuse properties, optical and dielectrical behavior of insulating crystals, photoconductivity, luminescence and the coercive force are typical structure-sensitive properties. Generally, a relatively small number of lattice defects exerts disproportionately large effects on these properties.

It is proposed to discuss in this paper various x-ray methods used for disclosing crystal imperfections and lattice inhomogeneities and to show how these methods can be effectively linked to light and electron microscopic studies. For it is the belief of this author that through the interplay of these methods a detailed, quantitative elucidation of the defect structure can be achieved. Furthermore, it is proposed to show briefly in the manner of an illustrated travelogue highlights of some applications of these methods to problems of scientific and technological importance alike. Because of the limited scope of this paper the reader will be referred to special publications if details concerning the methods, applications and research results are desired.

2. X-RAY BACK-REFLECTION DIVERGENT BEAM METHOD AND STRAIN ANALYSIS

The divergent beam method is principally a precision method for the determination of lattice parameters and anisotropic lattice distortions of single crystals. It yields also information with regard to local lattice misalignment and, if the patterns are properly interpreted, one may even obtain a topographical mapping of lattice misorientations in the crystal with a limiting resolution of about 3'-4' of arc.

As practiced by the author the divergent beam method utilizes a horizontal capillary x-ray tube designed by T. Imura (1). An electron beam originating from an electron gun is focussed by means of electromagnetic lenses onto the tip of a long capillary tube, where a thin metal foil is placed as an x-ray target. By operating the tube at a suitable voltage an x-ray beam with characteristic radiation emerges from the tip of the x-ray tube, exhibiting a divergence of nearly 180°. When this beam impinges on the test crystal which is placed at a distance of 1-3 mm from the tip of the capillary tube, diffraction patterns of the characteristic

(1) T. Imura, Part I, II, III; J. Jap. Inst. of Metals, 16, 10 (1952); Naniwa Univ. Ser. A, 2, 51 (1954); Bull. Univ. of Osaka Prefecture, Ser. A, 5, 1 (1957).

spectrum in transmission as well as in the back-reflection region are obtained (Fig. 1). These patterns are analogous to the well-known Kossel patterns, except that in the case of the capillary x-ray tube the patterns are produced by an x-ray source which is outside instead of inside the specimen. For want of a better name these patterns were termed pseudo-Kossel patterns.

Of particular interest are the back-reflection patterns which can be obtained with much greater ease than the transmission patterns. Only a few minutes' exposure time is required. Figure 2 is a back-reflection pattern of an Al-3.85% Cu crystal solution heat-treated and water-quenched. Each ellipse corresponds to a definite (hkl) set of planes. By measuring the long axis of the ellipses and the specimen-to-film distance, the interatomic distance, d, of the various (hkl) planes can be determined (1). In a new development a quartz crystal, a few microns thick, is used as an internal calibrator. The quartz crystal is placed in front of the test crystal and both patterns, that of quartz and that of the test crystal, are simultaneously recorded. Using the a_0 parameter of quartz as an internal standard the d-spacings can be measured with a precision of $\pm 0.02\%$.

Hosokawa, Padawer and Weissmann (2) have recently developed an alternative method achieving nearly the same degree of precision. In this method the pseudo-Kossel patterns are recorded on the same film at different specimen-to-film distances and the diffraction angle θ of the (hkl) reflection is directly determined from the precisely known distances between consecutive film positions. Let β represent the dip angle, that is, the angle between the optical axis of the capillary tube and the normal of the diffracting (hkl) planes, $\alpha = 90 - \theta$, and let m and n be the measured distances of the corresponding points on the elliptical pseudo-Kossel patterns recorded at film positions a_2 and a_1, respectively, as shown in Fig. 1, where $c = a_2 - a_1$; then the following relationship holds:

$$m/c = \tan(\alpha + \beta) \qquad (1)$$

$$n/c = \tan(\alpha - \beta) \qquad (2)$$

From these two equations α and therefore θ and d(hkl) can be determined directly.

Modifications of the interatomic spacings resulting from physical or chemical processes can be well studied by the divergent beam method, and since individual (hkl) reflections are being measured the anisotropic changes in structure can be uniquely determined. For example, the (hkl) and ($\bar{h}kl$) reflections in a cubic structure give rise to two different ellipses and consequently if anisotropic changes in structure occur the d-values of the two reflections may no longer be identical. One may become larger and the other may indeed become smaller (Fig. 3). By measuring the changes of lattice spacings, Δd, of more than six independent (hkl) reflections and referring them to the d values of the original state, strain values, $\frac{\Delta d}{d}$, are obtained which are used as the raw data for a recently developed strain analysis (3). This analysis, carried out with the aid of a computer, gives the strain distribution in terms of three principal strains, namely, the maximum strain

(2) N. Hosokawa, G. Padawer and S. Weissmann, "Precision Measurements by the X-Ray Back-Reflection Divergent Beam Method," (to be published).

(3) T. Imura, S. Weissmann and J. J. Slade, Jr., Acta Cryst. 15, 786 (1962).

ε_1, the intermediate strain ε_2 and the minimum strain ε_3. The magnitude and direction of the principal strains define completely the strain ellipsoid and consequently the strains in any other desired direction can be computed.

2.1 Applications

A. Lattice Distortions in Age-Hardening of Alloys

The strain analysis based on the back-reflection divergent beam method was applied to the study of age-hardening of an Al-3.85% Cu alloy (3). Various modes of quenching and various stages of age-hardening were investigated. The results of the analysis are given in Table I. The maximum strain corresponding to the ageing stage associated with the formation of the Guinier-Preston zones coincided with one of the [100] directions and shifted about 20° when the θ' phase was predominant. The anisotropy of strain distribution was interpreted in terms of a preferred vacancy migration due to thermal and concentration gradients introduced by quenching.

B. Lattice Defects Induced by Neutron Irradiation

Another interesting application of the method was the determination of the strain distribution in thin quartz crystals induced by fast neutron irradiation(4). Major strain differences were found between crystals cut parallel to the basal (00.1) plane (z-cut) and those cut perpendicular to it (x-cut) (Table II). The x-ray results were interpreted in terms of a mechanism of dynamic crowdions involving the formation of clusters of interstitial atoms aligned in specific directions relative to the open screw channels of the quartz structure, and in terms of a thermal spike mechanism giving rise to cluster formation. It was indeed gratifying when subsequent studies of transmission electron microscopy, carried out on the identical specimens after appropriate thinning by etching, disclosed directly the existence of clusters of point defects. Furthermore, it was found that the alignment of the clusters as determined by means of selected area diffraction coincided with the maximum strain direction deduced from the x-ray study (Fig. 4). Good agreement was also found between the average size of defect clusters determined by transmission electron microscopy and that determined by small-angle x-ray scattering (Table III). This study may serve as a good example for illustrating the interplay of x-ray and electron microscopy techniques, which are not competitive but complementary to each other.

C. Plastic Deformation of Solids

Local misorientations of lattice domains show up as discontinuities in the pseudo-Kossel line pattern. Such discontinuities, indicated by arrows, were made more conspicuous in Fig. 5 by employing a multiple exposure technique in which the specimen-to-film distance was slightly varied between exposures. Whereas ductile metals such as f. c. c. aluminum or b. c. c. tantalum deform at room temperature on many slip systems and therefore exhibit broadening and discontinuities for practically all elliptical lines, brittle metals, viz. molybdenum, deform essentially on few or only on a single slip system and therefore show broadening and discon-

(4)S. Weissmann, T. Imura, K. Nakajima and S. E. Wisnewski, "Lattice Defects of Quartz Induced by Fast Neutron Irradiation" (to be published in Proc. of Symposium on Point Defects, Kyoto, 1962, J. Phys. Soc. Japan).

Table I. Principal strains in age-hardened Al-3.85% Cu crystal, water-quenched after solution treatment.

Heat Treatment	Phases Present	Maximum Strain ε_1			Intermediate Strain ε_2			Minimum Strain ε_3		
		Magnitude in %	Direction Number	Direction	Magnitude in %	Direction Number	Direction	Magnitude in %	Direction Number	Direction
205° C for 20 hours	G. P. [I] -trace + G. P. [II]	0.41	n_1 0.05 n_2 1.00 n_3 -0.18	u 0 v 1 w 0	0.18	n_1 0.17 n_2 0.17 n_3 1.00	u 0 v 0 w 1	-0.10	n_1 1.00 n_2 -0.08 n_3 -0.15	u 1 v 0 w 0
Additional annealing at 320° C for 1/2 hr.	θ'	0.47	n_1 0.04 n_2 1.00 n_3 -0.37	u 0 v 3 w 1	0.15	n_1 0.15 n_2 0.37 n_3 1.00	u 0 v 1 w 3	-0.03	n_1 1.00 n_2 -0.08 n_3 0.12	u 1 v 0 w 0
Additional annealing at 430° C for 23 hrs.	Matrix + incoherent θ (equilibrium phase)	0.29	n_1 1.00 n_2 -0.18 n_3 -0.13	u 1 v 0 w 0	-0.08	n_1 0.16 n_2 1.00 n_3 -0.09	u 0 v 1 w 0	-0.02	n_1 0.14 n_2 0.06 n_3 1.00	u 0 v 0 w 1

Table II

Effect of Fast Neutron Irradiation on the Principal Strains in Quartz Crystals

Irradiation nvt (Fast)	Natural Quartz Z-Cut	Z-Face Synthetic Z-Cut	Z-Growth Synthetic Z-Cut	Natural Quartz X-Cut	Z-Face Synthetic X-Cut
	* Magnitude % (h k . l)	Magnitude % (h k . l)	Magnitude % (h k . l)	Magnitude % (h k . l)	Magnitude % (h k . l)
1×10^{19}	ϵ_1 = -0.2812 (2 $\bar{1}$. 0) ϵ_2 = +0.2338 (0 0 . 1) ϵ_3 = +0.0703 (0 1 . 0)	+0.6113 (2 $\bar{1}$. 0) -0.0883 (0 0 . 1) -0.0070 (0 0 . 1)	+0.3850 (3 $\bar{1}$. 1) +0.1777 ($\bar{1}$ 2 . 2) -0.0309 (0 0 . 1)	+1.8070 (1 $\bar{1}$. 0) +0.5607 (0 0 . 1) +0.0246 (1 1 . 0)	+1.6809 (2 $\bar{2}$. 1) +0.3694 (1 $\bar{1}$. 2) -0.0579 (2 1 . 0)
3×10^{19}	ϵ_1 = +0.5793 (0 1 . 0) ϵ_2 = +0.3993 (2 0 . $\bar{1}$) ϵ_3 = +0.0654 (0 0 . 1)	+0.6139 (2 $\bar{1}$. 0) +0.3732 (0 1 . 0) -0.1022 (0 0 . 1)	+0.4372 (1 1 . 0) +0.3172 (1 $\bar{1}$. 0) +0.1511 (0 0 . 1)	+1.8219 (2 $\bar{2}$. 1) +0.4143 ($\bar{1}$ 0 . 2) +0.1705 (0 1 . 0)	+0.9083 (1 $\bar{1}$. 0) +0.2870 (2 4 . $\bar{1}$) -0.0742 (0 0 . 1)
6×10^{19}	ϵ_1 = +0.6142 (2 $\bar{1}$. 0) ϵ_2 = +0.3715 (0 1 . 0) ϵ_3 = +0.0235 (0 0 . 1)	+0.6143 (2 $\bar{1}$. 0) +0.3665 (0 1 . 0) -0.0333 (0 0 . 1)	+0.3913 (1 0 . 0) +0.3258 (0 1 . 0) +0.0584 (0 0 . 1)	+0.7935 (1 $\bar{1}$. 3) +0.4520 (2 $\bar{2}$. $\bar{1}$) +0.0207 (2 1 . 0)	+1.1814 (1 $\bar{1}$. $\bar{1}$) +0.3380 (2 $\bar{1}$. 2) -0.1329 (1 2 . 0)
8×10^{19}			ϵ_1 = +0.3166 ($\bar{1}$ 2 . 0) ϵ_2 = +0.1766 (1 0 . 0) ϵ_3 = -0.1534 (0 0 . 1)		

Legend

*ϵ_1 = maximum strain
ϵ_2 = intermediate strain
ϵ_3 = minimum strain

(h k . l) are Miller indices of planes perpendicular to the direction of strain.

TABLE III

Effect of Neutron Irradiation on Size of Interstitial Clusters and Density in Quartz

Type of Crystal	Irradiation nvt	Mean Radius of Cluster, $\bar{r}$, (Small-Angle X-Ray Scattering) cm	Mean Radius of Cluster, $\bar{r}$, cm (Transmission Electron Microscopy, T. E. M.)	Total Volume of Cluster, Nv, per cm^3 (T. E. M.)	Fractional Change in Density $-\frac{\Delta\rho}{\rho}$ % *
z-cut	1×10^{19}	--	8×10^{-7}	0.008	0.8
	6×10^{19}	12×10^{-7}	21×10^{-7}	0.04	4.2
	8×10^{19}	--	21×10^{-7}	0.093	9.8
	1×10^{20}	9×10^{-7}	11×10^{-7}**	0.098**	10.4
	1.5×10^{20}	--	8×10^{-7}***	0.053***	--
x-cut	6×10^{19}	9×10^{-7}	6×10^{-7}	0.015	1.6

* $-\frac{\Delta\rho}{\rho} = 1.06Nv$

**In addition to isolated clusters a hexagonal network was observed resulting from the interactions of clusters. Size of hexagon ≈ 1000Å.

***Extensive network formation.

tinuities for only a few (hkl) reflections, leaving the other (hkl) reflections virtually unaffected. This opens up an exciting possibility of studying the change in strain distribution during the ductile-brittle transition of a metal. Such studies are currently in progress. For initial stages of deformation of metals the strain distribution on all active slip planes can be determined from the principal strains and the increase or decline of strain can be followed as a function of deformation. The strain distribution measurements of this type are made possible either because of an effective build-up of strains taking place at the specimen surface, where dislocations are being prevented from escaping presumably by barriers of oxide layers, or because of the existence of residual strains resulting from the deformation process.

If a binary alloy foil is used as x-ray target the pseudo-Kossel pattern will consist of two sets of lines corresponding to the target material. Consequently, precision lattice parameter measurements can then be carried out not only as a function of wavelength but also as a function of depth penetration. It is also possible to extend the divergent beam method further by carrying out microphotometric measurements of the line profiles followed by a Fourier transform analysis in order to determine particle size and average local strain (5). Such studies are also currently in progress.

3. COMBINATION OF X-RAY DOUBLE-CRYSTAL DIFFRACTOMETER AND X-RAY DIFFRACTION MICROSCOPY

The double-crystal diffractometer is a precision instrument capable of resolving lattice misorientations of a few seconds of arc. It is, therefore, very well suited for the study of the misfit angle of adjacent subgrains and its modifications induced by mechanical stress or annealing.

In this instrument the incident beam falling on the test crystal is first reflected from a monochromatizing crystal and the beam reflected by the rotating test crystal is registered by an electronic radiation detector. Perfect test crystals will reflect over a very narrow range of specimen rotation, while imperfect crystals having a wider spread of lattice misorientation will reflect over an extended range. In the case of crystals possessing subgrains which are brought successively into reflecting position, the reflection curve will exhibit multiple peaks instead of a single peak (6). Such a reflection curve is illustrated in Fig. 6, where the angular separation of $\approx 30'$ between peaks 3 and 9 defines the misfit angle between two adjacent coarse subgrains. It is interesting to note that in this specific case the misorientation of the coarse subgrains is not large enough to be resolved by conventional x-ray techniques. Thus the back-reflection Laue diagram of this crystal exhibits no visible break-up of the spots.

The most characteristic and useful feature of the double-crystal diffractometer method as employed in this laboratory is the combination of electronic radiation detector and supplementary film technique (6). Although the radiation detector is highly sensitive in registering slight variations in x-ray intensities, it is insensitive in discriminating between the location of different lattice domains on the specimen surface which contribute to a registered intensity value. A film

(5)B. E. Warren, Progress in Metal Physics, 8, Ch. 3, 147, Pergamon Press (1959).
(6)J. Intrater and S. Weissmann, Acta Cryst. 7, 729 (1954).

placed in front of the radiation detector, however, functions as a "guiding eye" to the counter and pins down the location of the reflecting lattice domains which give rise to a specific registered intensity value.

The analysis of the reflection curve of Fig. 6 by means of the supplementary film technique is shown in Fig. 7. This figure exhibits the reflection images of the magnesium crystal recorded photographically in front of the radiation detector at discrete rotation positions of the specimen. The corresponding positions are indicated by numbers. The break-up of the reflection images discloses the existence of microscopic subgrains of which the coarse subgrains are composed. By tracing the reflection images to the specimen surface photographically a topographical mapping of the substructure can be achieved by x-ray diffraction microscopy and correlated to the quantitative analysis of the double-crystal diffractometer method (6, 7, 8).

The topographical mapping of lattice inhomogeneities by x-ray diffraction microscopy was first suggested by Berg (9) and later extended by Barrett (10). It is based upon differences in diffracting power from point to point in the specimen to produce contrast and to enhance the topographical detail of the image. In imperfect crystals image intensification is obtained by diffraction from adjacent lattice domains which are curved or misaligned in a concave manner, while diffraction from lattice domains curved or misaligned in a convex manner will give rise to a dispersion of the diffracted beam. In the former case the image will be darker, whereas in the latter case it will be lighter than the background.

Figure 9 shows the instrument with the aid of which the analysis of the magnesium crystal (Figs. 6, 7) was carried out. Not only single crystals but also polycrystalline materials can be analyzed by the combination method. By means of the movable upper platform, which can be rotated around an axis coincident with that of the monochromatizing first crystal, the test specimen can be irradiated successively with unfiltered and crystal-monochromatized radiation (8). In the case of a polycrystalline specimen this technique permits one to trace the reflection curves to the corresponding grains on the specimen surface and to analyze these grains for their substructure characteristics (8).

Depending on the perfection of the grains, the specimen is rotated in angular intervals of seconds or minutes of arc and the spot reflections of the grains, recorded for each discrete specimen rotation, are separated by film shifts. This multiple exposure technique gives rise to an array of spots for each reflecting grain. Since each grain may be regarded as the test crystal of a double-crystal diffractometer, the array of spots is analogous to the reflection (rocking) curve of a single crystal and can be analyzed in a similar manner. Thus, if the grains contain a substructure the intensity distribution of the array of spots shown in Fig. 8 will be multi-peaked in complete analogy to the reflection curves obtained from single crystals containing substructure. In the case of single crystals indi-

(7) S. Weissmann, J. Appl. Phys., 27, 389 (1956).
(8) S. Weissmann, Trans. Am. Soc. for Metals, 52, 599 (1960).
(9) W. Berg, Naturwissenschaften 89, 286 (1934).
(10) C. S. Barrett, Trans. Am. Inst. Min. and Metall. Engrs. 161, 15 (1945).

vidual subgrain boundaries can even be analyzed if an exposure superposition technique is used (11).

3.1 Applications

A. Substructure and Dislocation Networks in Tungsten (11)

The existence of three orders of magnitude of subgrains was disclosed in a single crystal of tungsten produced by the arc fusion method. Two orders of subgrains, namely, the macroscopic and microscopic subgrains--also termed first and second order subgrains--are shown in the reflection micrograph of Fig. 10. This micrograph was taken with unfiltered copper radiation using a microfocussing tube with an effective focal spot size of 40 μ. Both the specimen as well as the fine-grained photographic plate, placed 1 mm from the specimen, were oscillated over a range of $\approx 1^{\circ}$ of arc. Applying the exposure superposition technique shown in Fig. 11, which consists of the successive application of unfiltered and crystal-monochromatized radiation, the individual sub-boundaries such as those separating the macroscopic subgrains A and B were directly analyzed. The reflection curve taken with crystal-monochromatized radiation, shown in Fig. 12, consists of two major peaks, one pertaining to subgrain A and the other to subgrain B. Since the sub-boundary was so oriented that it coincided with the specimen rotation axis, the peak-to-peak separation of 16.5' yielded directly the disorientation angle between the subgrains. From this angle the dislocation density in the sub-boundary was computed to be 8.8×10^5 per cm^2. By employing the supplementary film technique at the rotation positions indicated by numbers in Fig. 12, the microscopic subgrains, marked by the small letters a→f in the corresponding metallograph of Fig. 11a, were analyzed. The disorientation angle of the microscopic subgrains ranged from 1'-4' of arc and the dislocation density in the sub-boundaries from 7.7×10^5 to 2.2×10^6 per cm^2. The smallest subgrains (third order), about 10 μ in size, were directly disclosed by transmission electron microscopy after the specimen was appropriately thinned by electropolishing. The average dislocation density in the sub-boundaries turned out to be 1.8×10^6 per cm^2 (11).

B. Mechanical and Thermal Stability of Low-Angle Boundaries (12)

The mechanical and thermal stability of low-angle boundaries in zinc single crystals were studied by methods combining light microscopy with the x-ray combination method described above. The modifications of the x-ray reflection curves during isothermal annealing were studied by means of a special timing device attached to the reversible motor which controls the rotation of the precision goniometer head holding the test specimen. The time intervals for reversible specimen rotation were controlled by an interchangeable cam system. Consequently, the entire reflection curve or portions of the reflection curve could be repeated as desired during isothermal annealing and the modifications in the x-ray profile could be studied as a function of annealing time. Thus, if no detectable change in substructure occurred, the consecutive curves obtained as a function of annealing time appeared as perfect mirror images of each other, since by means of the reversible motor the direction of the specimen rotation was reversed. Conversely, if changes in the substructure occurred the consecutive rocking curves exhibited corresponding modifications in shape. For the annealing of the specimens, which was carried out

(11) Y. Nakayama, S. Weissmann and T. Imura, Direct Observations of Imperfections in Crystals, p. 573, Interscience Publ., div. of John Wiley & Sons, New York, 1962.
(12) S. Weissmann, M. Hirabayashi and H. Fujita, J. Appl. Phys. 32, 1156 (1961).

on the x-ray unit without removal of the specimen, an elliptical reflector lamp was used.

It was found that low-angle boundaries perpendicular to the basal plane did not offer any appreciable resistance to a shearing force parallel to the basal plane if they were pure tilt boundaries, but constituted substantial barriers if they were asymmetrical, that is, made up of screw and edge dislocations. If the external force exceeded a critical value these asymmetrical, low-angle boundaries became sites where fracture occurred. The strengthening effect of the asymmetrical low-angle boundaries was attributed to the effective stress field of the screw dislocations, which were mechanically stabilized by the edge dislocations. The stress field of the screw dislocations was also responsible for the thermal instability of the asymmetrical low-angle boundaries, which on annealing were gradually converted into pure tilt boundaries. A coarse substructure established after annealing was thermally very stable. On solidification after partial melting of the crystal, the coarse substructure was re-established, whereas the fine substructure was entirely modified (12).

C. Structural Changes Associated with Recrystallization and Grain Growth (13)

Growth processes of 99.998% aluminum were studied by the combination method discussed in section 3. The recrystallized grains were shown to be the product of preferential subgrain growth whereby subgrains subtending large disorientation angles with respect to their neighbors exhibited the highest velocity of growth. The recrystallized grains emerging from the deformed matrix showed at first a high degree of lattice perfection. However, as growth proceeded lattice imperfections were incorporated into the growing grain and the lattice misorientation of the grain increased. These lattice imperfections arose either from grain impingement and adaptation to orientation differences which might have existed between the growing grain and the grain being consumed, or they might have been generated by overcoming barriers such as impurity-locked dislocations. The recrystallized grains exhibited occasionally a fine net of sub-boundaries which usually emanated from the advancing interface. In any case, the lattice defects were not survivals of defects introduced during the deformation process but were by-products of the growth process. However, owing to the large volume increase of the growing grain the number of dislocations per unit volume, that is to say, the dislocation density, steadily declined.

4. DIRECT OBSERVATION OF LATTICE DEFECTS IN CRYSTALS OF LOW DISLOCATION DENSITY BY X-RAY DIFFRACTION MICROSCOPY

In crystals of low dislocation density the direct observation of lattice defects by x-ray diffraction microscopy can be achieved in two different ways. One method is based on the effect of primary extinction contrast, while the other is based on the anomalous transmission effect of the x-ray beam.

4.1 X-Ray Diffraction Microscopy Based on Extinction Contrast

In highly perfect crystals contrast is governed by the effect of primary extinction. If a perfect crystal is set in reflecting position the energy of the

(13) S. Weissmann, Trans. ASM 53, 265 (1961).

incident, primary beam gets rapidly extinguished as the beam passes through the crystal, because the energy diverted into the secondary or reflected beam interacts intimately with the primary beam. One can see in a general way how this diminution may come about. The wave reflected by each crystal plane suffers a phase change of $\pi/2$ relative to that of the primary beam, so that the twice-reflected waves which again travel in the direction of the primary waves will have a phase difference of π relative to the primary waves. This phase difference results in a reduction of the amplitude of the primary beam. In a perfect crystal the definite phase relationship set up between the incident, the reflected and multiple-reflected waves leads to a constant interchange of energy between the primary and diffracted beams. The process results in a dynamic equilibrium which extinguishes the primary beam after penetrating to a depth of 0.1μ to 10μ for strong reflections and a larger distance for weaker reflections.

If a crystal contains a few dislocations the rupture of coherence in the perfect periodicity of the reflecting planes as well as the lattice strains associated with the dislocation lines decrease the primary extinction effect. The diffracted image of a lattice domain will, therefore, be enhanced in the vicinity of a dislocation line and this is the underlying reason why in nearly perfect crystals the dislocations can be made visible by x-ray diffraction microscopy.

The contrast, that is, the intensity above background I_D will depend on the direction of the lattice strain (Burgers vector b in the case of a dislocation) relative to the orientation of the reflecting (hkl) planes. The relation is given by

$$I_D = k(\vec{g} \cdot \vec{b}) \qquad (1)$$

where $\vec{g}$ = reciprocal lattice vector
$\vec{b}$ = displacement or strain vector (Burgers vector in case of a dislocation)
k = constant.

It will be seen that maximum contrast is achieved if the lattice strain is normal to the reflecting (hkl) planes and will be zero if it is parallel to them.

By applying the Berg-Barrett reflection method to crystals of LiF Newkirk (14) has successfully shown on the basis of extinction contrast individual dislocation lines and fine details of dislocation networks.

A refined variation of the Berg-Barrett method, the projection topography method of Lang, has found interesting application for the study of the dislocation structure in semiconducting crystals (15, 16, 17). The basic principle of this method is shown in Fig. 13. A collimated x-ray beam a impinges on a crystal b, which is so oriented and of such thickness as to permit the Bragg-reflected beam to pass in transmission. The diffracted beam is recorded on a fine-grained film c,

(14) J. B. Newkirk, Trans. Am. Inst. Min. & Metall. Engrs., 215, 483 (1959).
(15) A. R. Lang, J. Appl. Phys. 29, 527 (1958); 30, 1748 (1959).
(16) A. E. Jenkison and A. R. Lang, Direct Observation of Imperfections in Crystals, p. 471, Interscience Publ., div. John Wiley & Sons, New York (1962).
(17) G. H. Schwuttke, Direct Observation of Imperfections in Crystals, p. 497, Interscience Publ., div. John Wiley & Sons, New York (1962).

placed close to the crystal. Since the image of the specimen is larger than the width of the interposed slit, the specimen is moved synchronously with the film. A stationary screen d is provided which prevents the direct beam from striking the film.

Figure 14 shows a Lang camera commercially produced by the Rigaku-Denki Co. which is so designed that its greatest effectiveness is achieved when attached to a microfocussing x-ray source, preferably 10μ in size. Figure 15 illustrates an x-ray diffraction topograph of a silicon crystal produced by a Lang camera, disclosing clearly the pattern of the dislocation structure of the crystal.

X-ray topography is not only applicable to disclosure of the dislocation structure of crystals but is also capable of revealing segregation effects such as oxygen banding in silicon crystals (17). If the crystals to be analyzed contain, however, a large dislocation density, viz. larger than $10^6/cm^2$, or a large density of impurities, the x-ray topographs become so complicated that no unequivocal interpretation can be rendered and their usefulness becomes greatly reduced.

4.2 X-Ray Diffraction Microscopy Based on Anomalous Transmission Effects

An extensive review article on the anomalous transmission of x-rays has been published by Borrmann (18). The essential principles of this effect will be briefly outlined here. Anomalous transmission occurs only in nearly perfect crystals and consists of enhanced transmission of the direct beam if the crystal is held in diffracting position. When the crystal is rotated to any non-diffracting position the intensity of the transmitted direct beam is considerably reduced. This effect was discovered by Borrmann (19) and subsequently explained by Von Laue (20).

If a plane monochromatic x-ray wave enters a perfect crystal set for diffraction position, two standing waves are generated. The flow of energy takes place principally along the lattice planes and the direction of the standing waves is perpendicular to the flow direction. Taking the case of a simple lattice, one of these standing waves (A) may have its nodal planes coincide with the position of a family of (hkl) planes, while the other standing wave (N) has its nodes halfway between. If the crystal is assumed to consist of point absorbers taking the place of real atoms, the N wave will rapidly be absorbed due to its interactions with the point absorbers, while the A wave is transmitted with undiminished intensity through the crystal. Upon leaving the crystal the A wave splits into two equal components, namely, the transmitted beam R_o and the diffracted beam R (Figs. 16 and 17).

In the case of a real crystal consisting of scattering atoms whose scattering factor is known, the A wave has a finite absorption coefficient. The intensity of the x-ray beam emerging from the crystal will depend greatly on crystal perfection. Lattice defects destroying the periodicity of the crystal will reduce the intensity of the A wave, since the critical conditions necessary for the Borrmann (anomalous) transmission are being destroyed and normal absorption will then occur. Figure 16 shows schematically a simple experimental arrangement used by Schwuttke (21) to ob-

(18) G. Borrmann, Beitraege zur Physik und Chemie des 20 Jahrhunderts, edit. by Frisch, Paneth, Laves and Rosbaud, p. 262, Vieweg. Braunschweig, (1959).
(19) G. Borrmann, Z. Physik 42, 157 (1941); ibid. 127, 297 (1950).
(20) M. Von Laue, Acta Cryst. 2, 106 (1949).
(21) G. H. Schwuttke, J. Appl. Phys. 33, 2760 (1962).

tain anomalous transmission topographs of the dislocation structure of semiconducting crystals such as those shown in Fig. 17. In this picture the R and R_o images are completely identical, as expected from the theory of anomalous transmission. The dislocation lines are clearly visible as shadows because the anomalous transmitted wave field is not propagated in the strain field associated with the dislocations.

Segregation and precipitation of copper in silicon and arsenic in highly doped germanium crystals could also be disclosed by this method (21).

4.3 Comparison of Extinction and Anomalous Transmission Methods

The results obtained by the two methods are virtually identical. While both methods are restricted to the study of lattice defects of nearly perfect crystals, the conditions of obtaining maximum contrast of the image differ greatly. For best contrast the anomalous transmission method requires that the product of $\mu \times t \geqq 20$, while for the extinction method $\mu \times t \leqq 1$, where μ is the linear mass absorption coefficient and t (cm) is the thickness of the specimen. As a direct consequence of this condition soft radiation, viz. copper or cobalt, is used for the anomalous transmission method and penetrating radiation, viz. silver or molybdenum, for the extinction method if applied in transmission (Lang method).

The contrast images of lattice defects differ also in both methods. In the anomalous transmission method defects show up by absorption contrast, whereas in the extinction method the contrast is produced by enhancement of the transmitted intensity. If equal areas are recorded, the scanning extinction method requires approximately one half the exposure time necessary for the stationary anomalous transmission method (21).

5. DETERMINATION OF SUBSTRUCTURE CHARACTERISTICS BY IMAGE TRACING

A method has been recently developed by Weissmann, Gorman and Zwell (22) by which the substructure characteristics and dislocation densities of crystalline materials can be rapidly determined. The method is based on spatial tracing of reflection images and their extrapolation onto the specimen surface, using the method of least squares.

If a Bragg reflection is photographically recorded at increasing specimen-to-film distance, the parametric equations of the reflected ray are given by

$$\begin{aligned} x &= x_o + \beta_x h \\ y &= y_o + \beta_y h \end{aligned} \qquad (1)$$

where (x_o, y_o), (x, y) are the coordinates of the reflection images on the crystal surface and on the film, respectively, h is the specimen-to-film distance and (β_x, β_y) are the slope parameters. From measurements of the coordinates x_i, y_i corresponding to the distances h_i, the x_o, y_o coordinates on the specimen surface are determined by the method of least squares, using the equations (22)

(22) S. Weissmann, L. A. Gorman and L. Zwell, J. Appl. Phys. 33, 3131 (1962).

$$x_o = \frac{\Sigma x \Sigma h^2 - \Sigma h \Sigma hx}{n\Sigma h^2 - (\Sigma h)^2}$$

$$y_o = \frac{\Sigma y \Sigma h^2 - \Sigma h \Sigma hy}{n\Sigma h^2 - (\Sigma h)^2} \qquad (2)$$

Similarly, the slope parameters are determined by the method of least squares from the expressions

$$\beta_x = \frac{n\Sigma hx - \Sigma h \Sigma x}{n\Sigma h^2 - (\Sigma h)^2}$$

$$\beta_y = \frac{n\Sigma hy - \Sigma h \Sigma y}{n\Sigma h^2 - (\Sigma h)^2} \qquad (3)$$

Referring to Fig. 18, the size of the images is measured in terms of Δy and Δx for various values of h, and the dimensions on the specimen, Δx_o and Δy_o, are determined by the application of Eq. (2).

If a parallel, crystal-monochromatized radiation is used the change of the size parameters Δy and Δx for various h values gives information about the vertical lattice misalignment, $\Delta\beta_y$, and the horizontal lattice misalignment $\Delta\beta_x$. These can be computed with the aid of Eq. (3).

The disorientation angle between subgrains can be computed from the measurements of the vertical separation, Δt, and the horizontal separation, Δs, of the images as a function of h and substituting these values in Eq. (3).

For this method the requirements of instrumentation are reduced to a minimum. Its application should be within the reach of any laboratory having standard diffraction equipment.

ACKNOWLEDGMENT

Thanks are due to Dr. G. H. Schwuttke for his generous contribution of Figs. 15, 16 and 17.

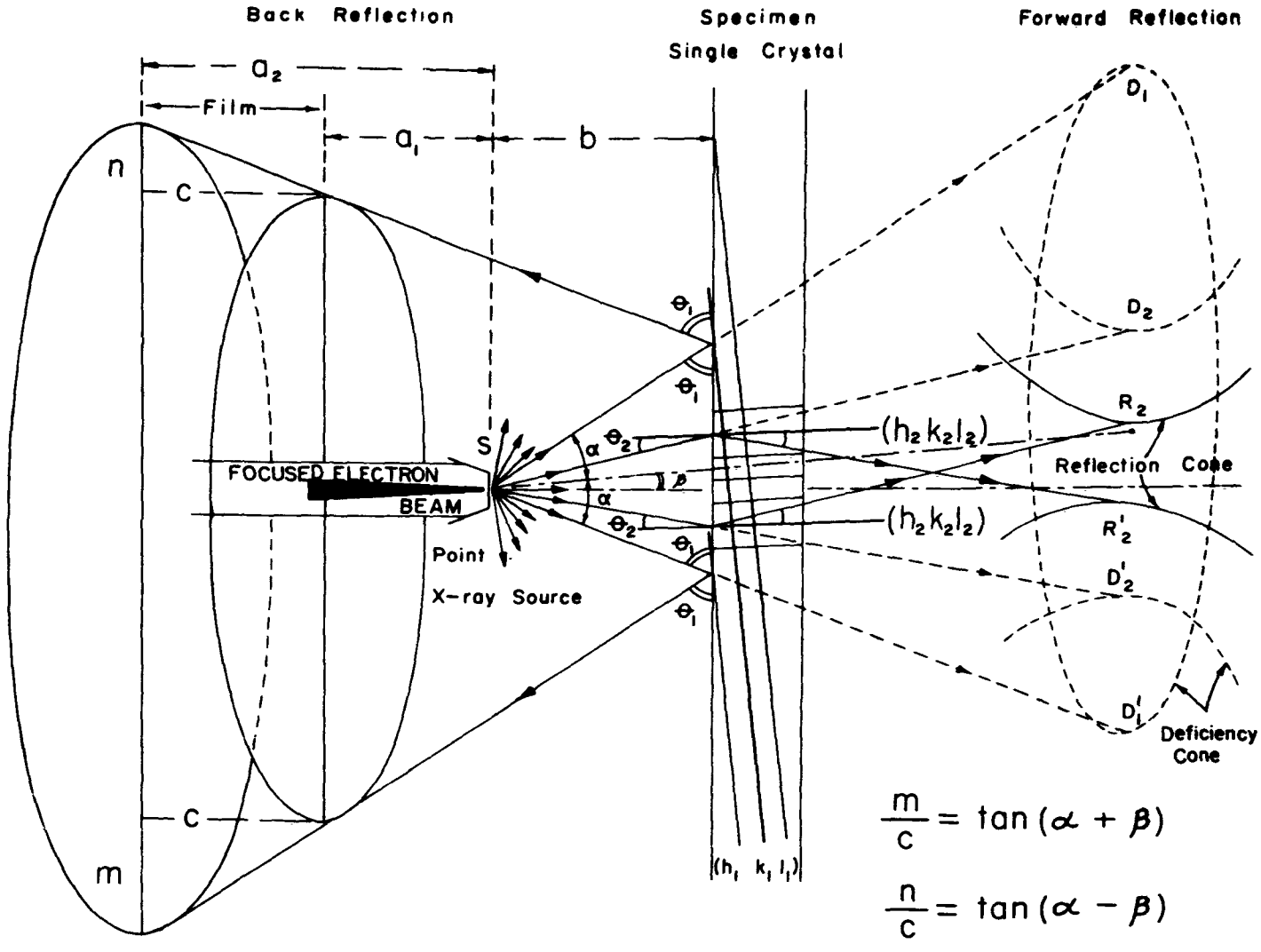

Fig. 1--Schematic representation of the generation of pseudo-Kossel patterns by the divergent beam method.

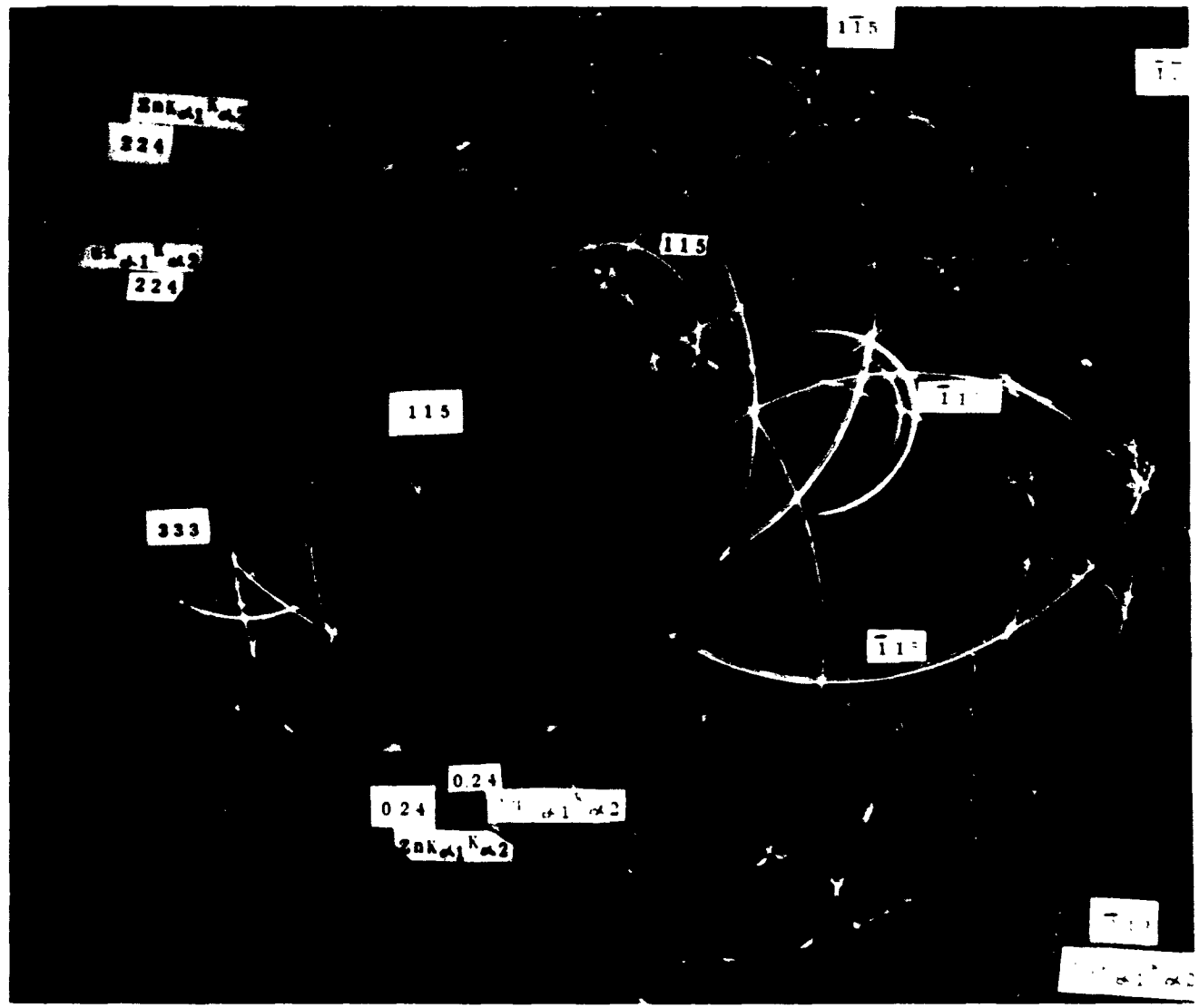

Fig. 2--Back-reflection divergent x-ray beam photograph of Al-3.85% Cu crystal. Solution heat-treated at 540° C and water-quenched. A brass target was employed, giving rise to sets of CuK_α and ZnK_α lines.

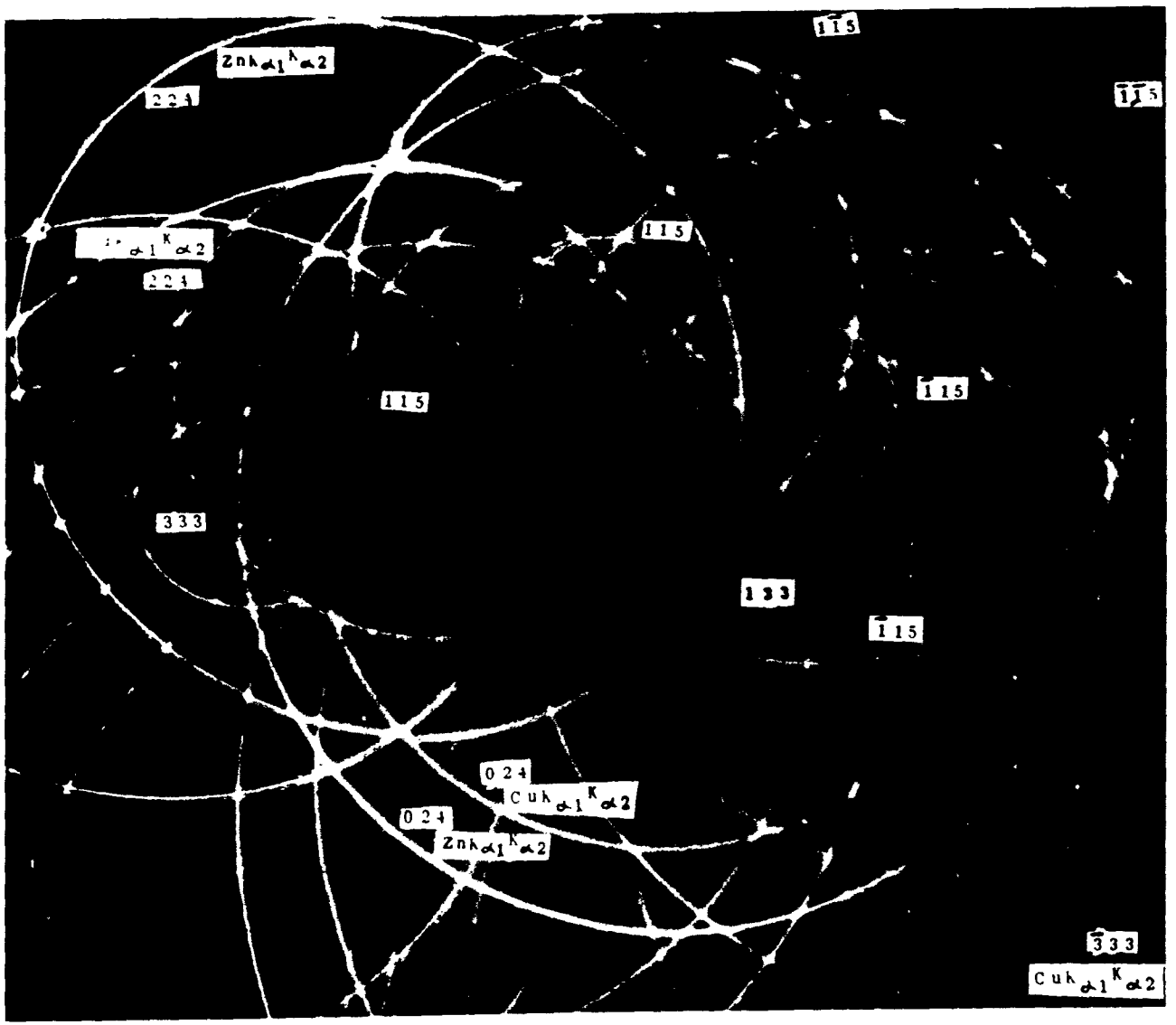

Fig. 3--Superposition of two back-reflection divergent x-ray beam photographs of Al-3.85% Cu crystal, as quenched and aged at 320° C for 1/2 hour, illustrating anisotropic lattice expansion induced by age-hardening.

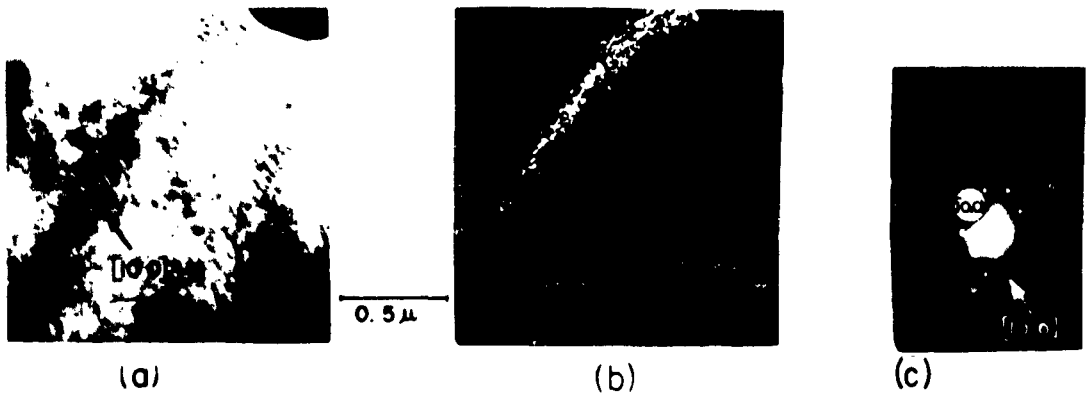

Fig. 4--Transmission electron micrograph of z-cut quartz crystal irradiated 1×10^{19} nvt. (a) Bright field. (b) Dark field. (c) Selected area diffraction. Dark field taken from (10.0) reflection.

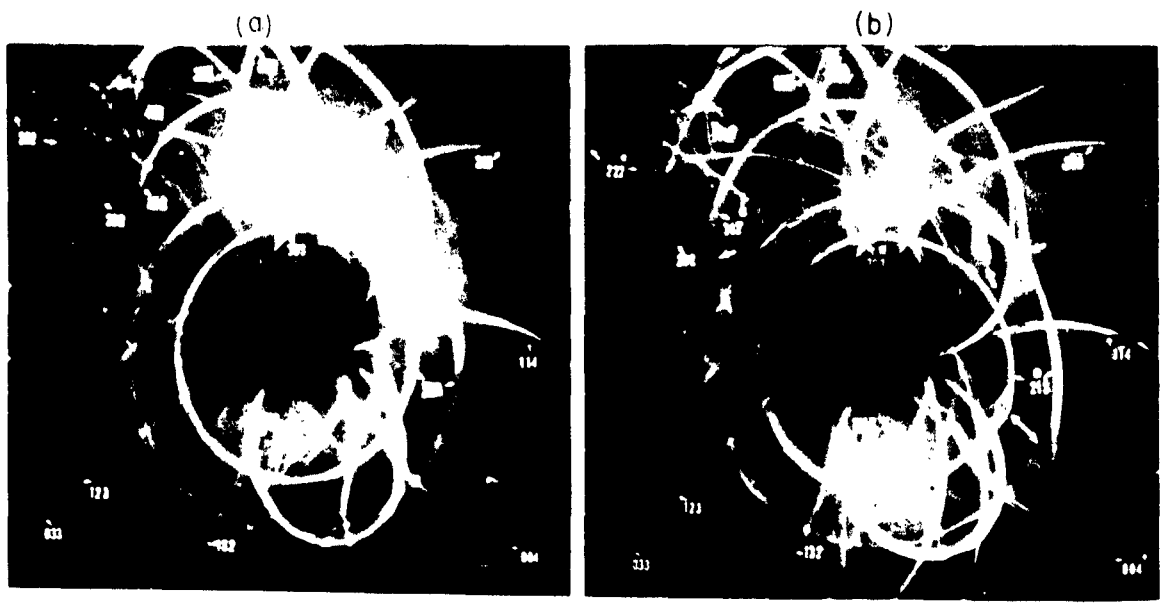

Fig. 5--Back-reflection x-ray divergent beam photographs of Mo crystal. a) Undeformed. b) Deformed 5.8% at room temperature. Note: Irradiation of adjacent lattice domains by multiple exposure technique. Distorted lattice domains indicated by arrows.

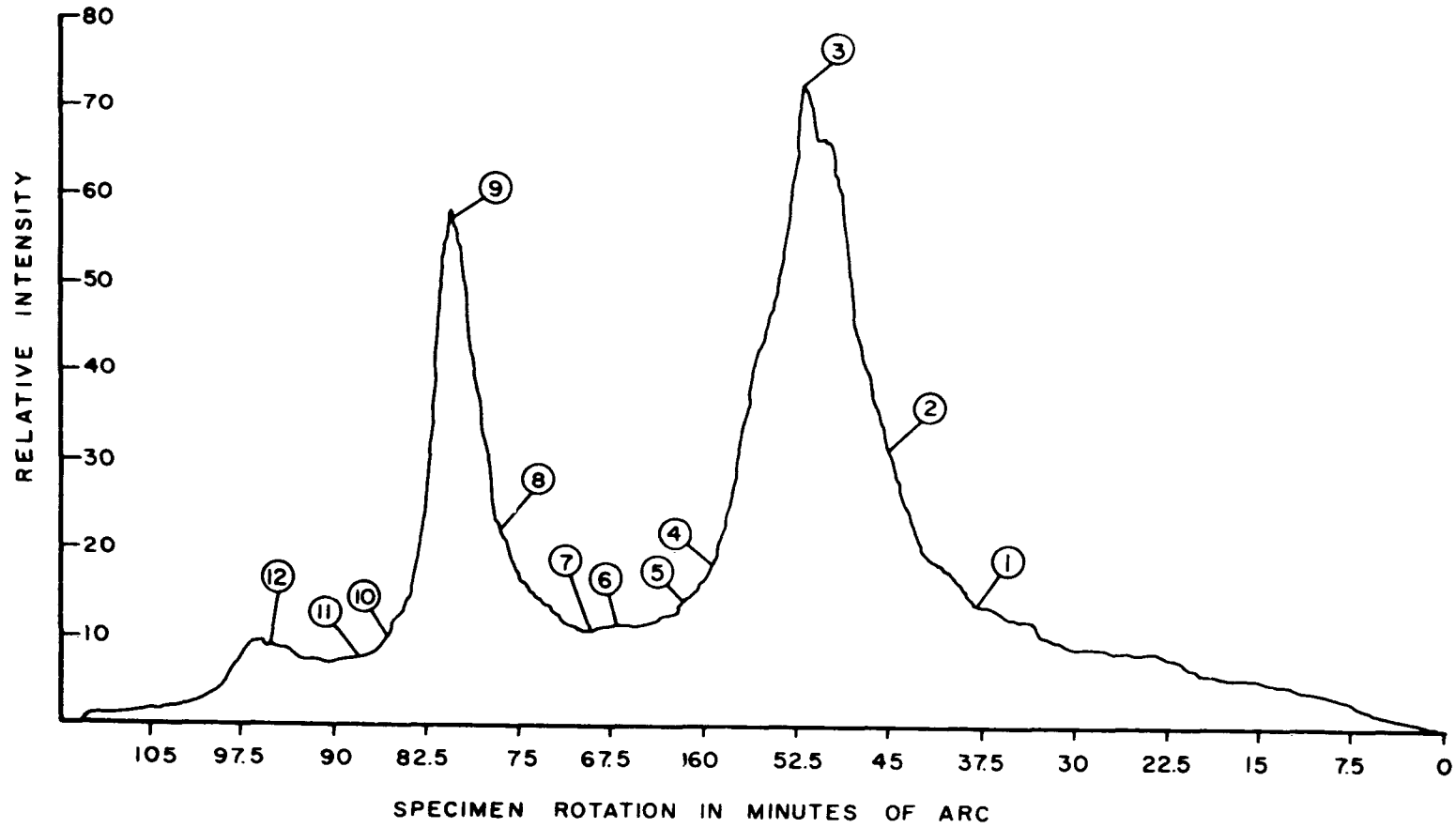

Fig. 6--Reflection curve of magnesium single crystal as obtained by the double-crystal diffractometer method. $CuK_{\alpha 1}$ radiation. (1, -1) position.

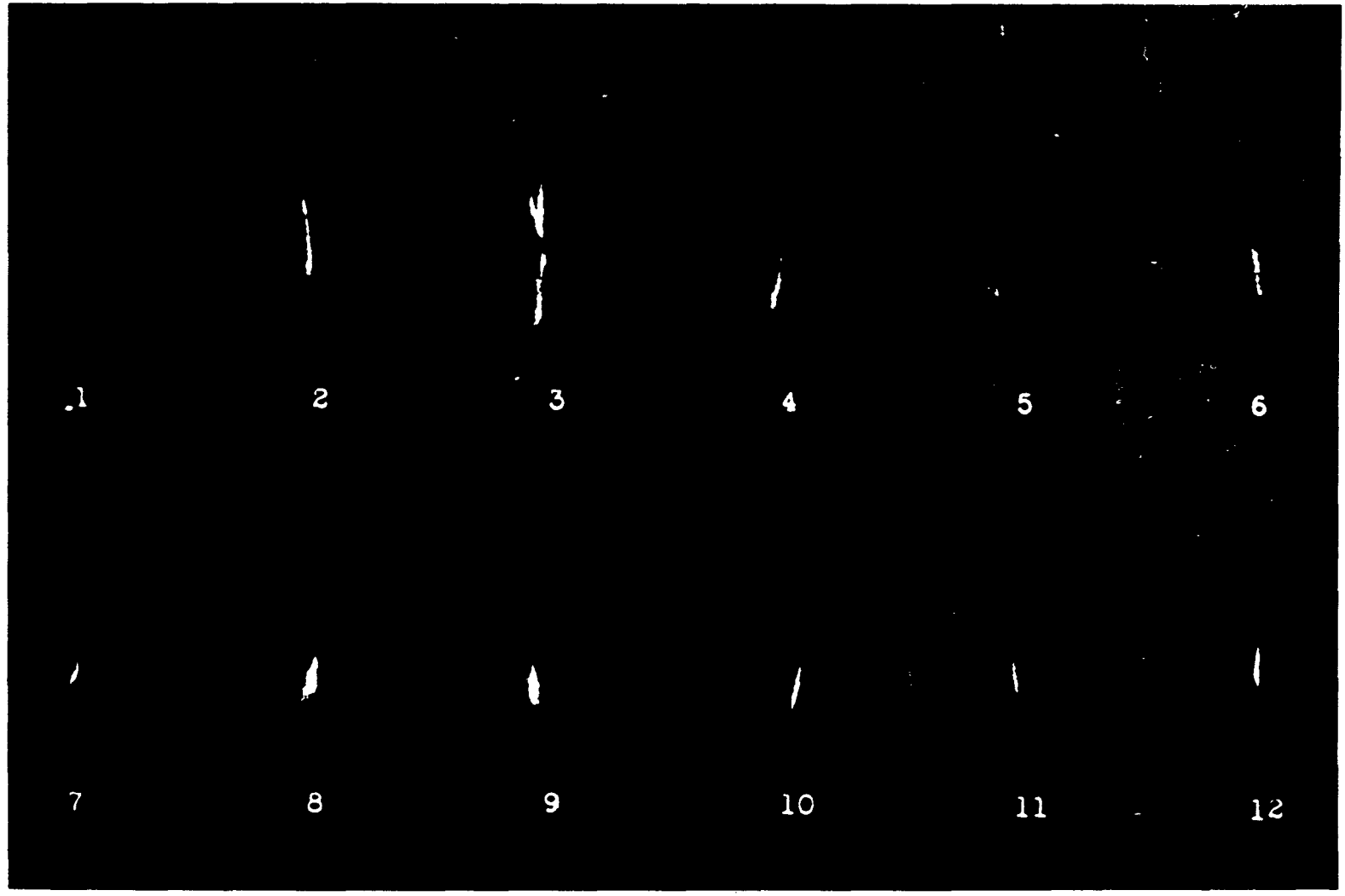

Fig. 7--Reflection images of magnesium crystal taken in front of radiation counter. The numbers refer to the corresponding discrete rotation positions of the specimen shown in Fig. 6

Fig. 8--Detailed view of (422) reflection of multiple-exposure diagram exhibiting multi-modal intensity distribution curves typical of subgrain structure. Al 99.95% pure, 96% reduced and annealed 1 hour at 300° C. Specimen rotation interval 4'.

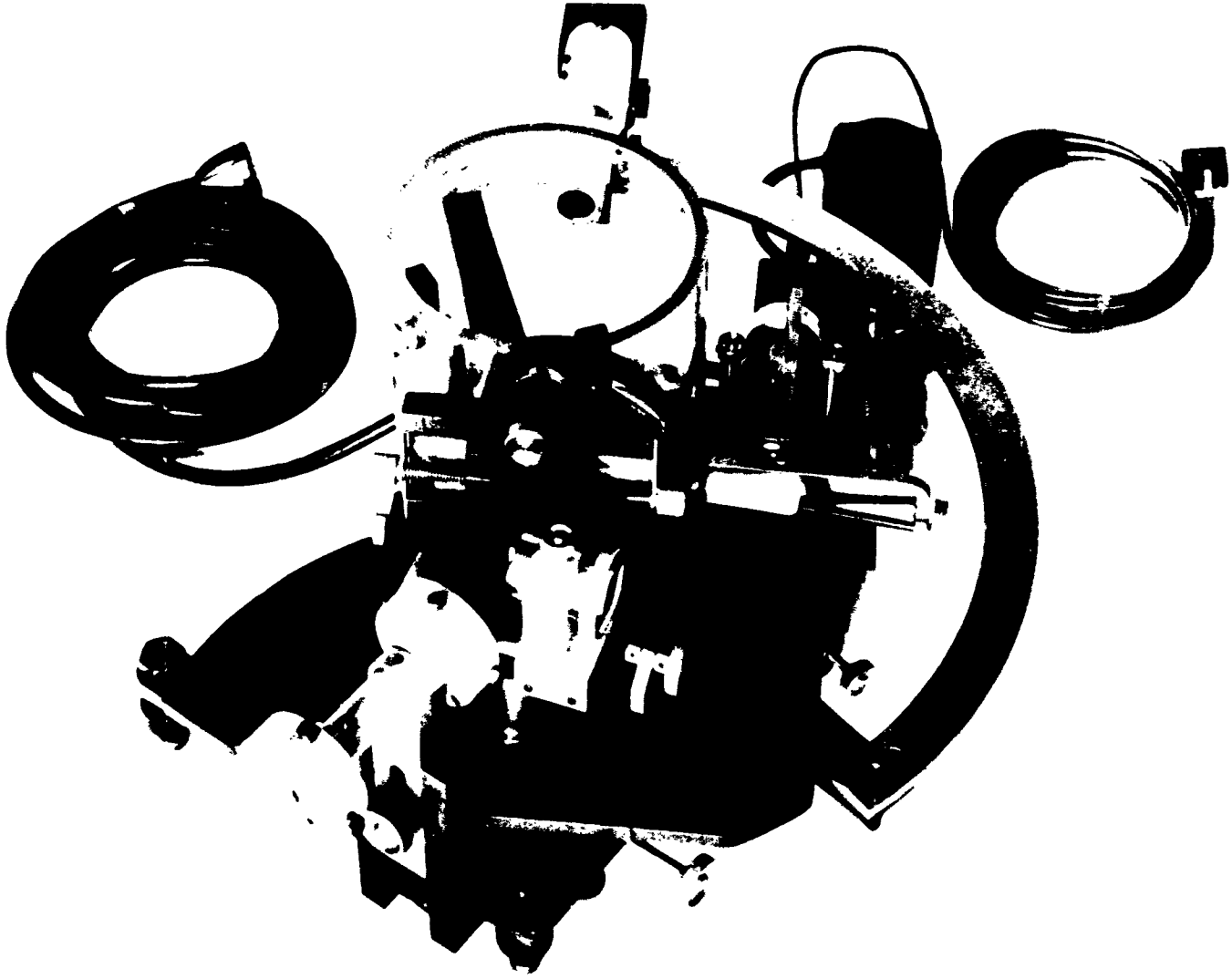

Fig. 9--X-ray double-crystal diffractometer. Experimental arrangement for use of crystal-monochromatized radiation.

Fig. 10--X-ray oscillation reflection micrograph of tungsten single crystal grown by arc fusion. Effective focal spot size 40μ. Disclosure of macroscopic and microscopic substructure. Magnification 40 x.

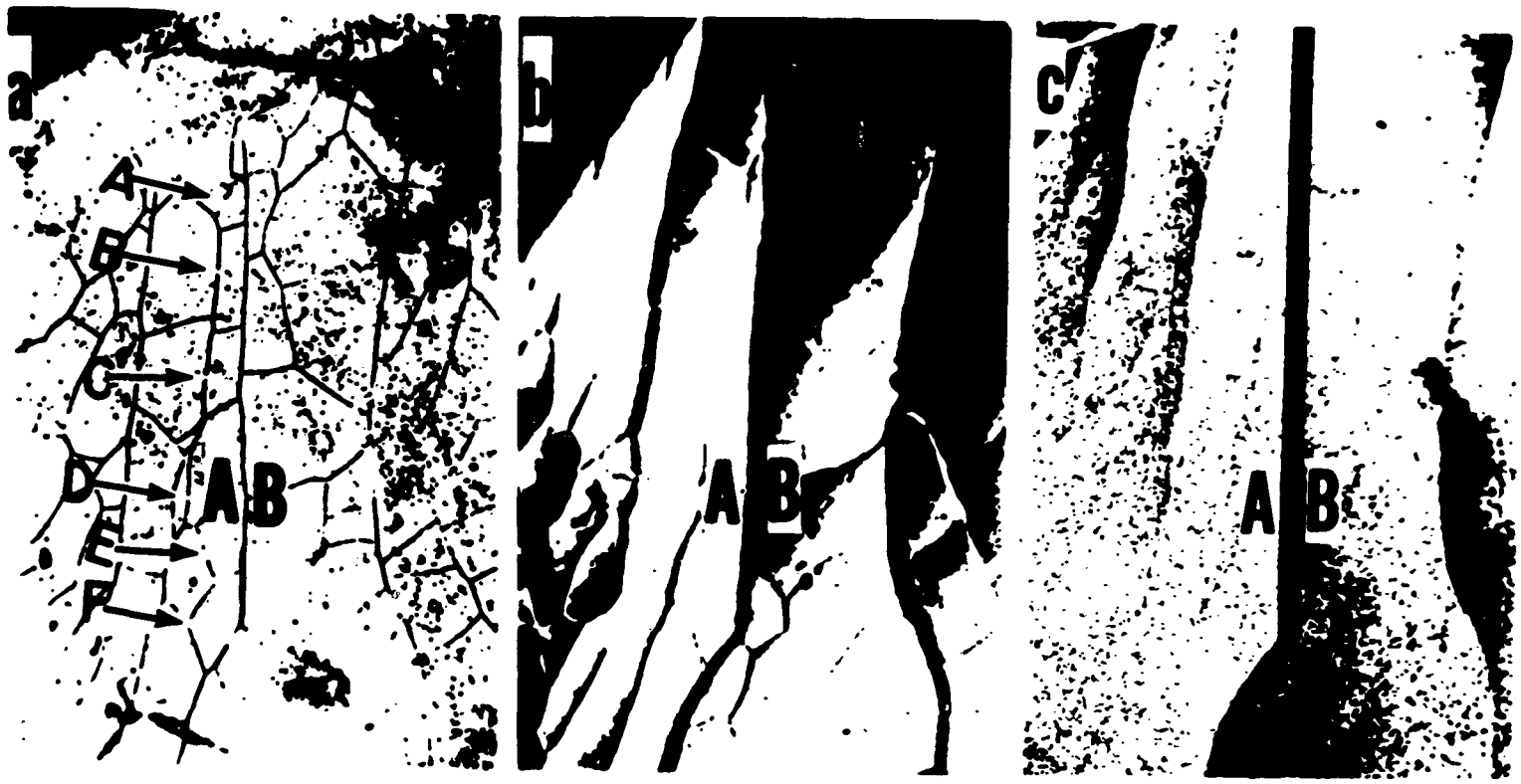

Fig. 11--Correlation of substructure in tungsten crystal (18.5x). a) Light micrograph of substructure disclosed by etching with 3% boiling H_2O_2. b) X-ray rotation reflection micrograph. Unfiltered radiation, Cu target. Effective size of focal spot, 40 μ. c) X-ray rotation reflection micrograph. Unfiltered radiation with superimposed crystal-monochromatized $CuK_{\alpha 1}$ radiation.

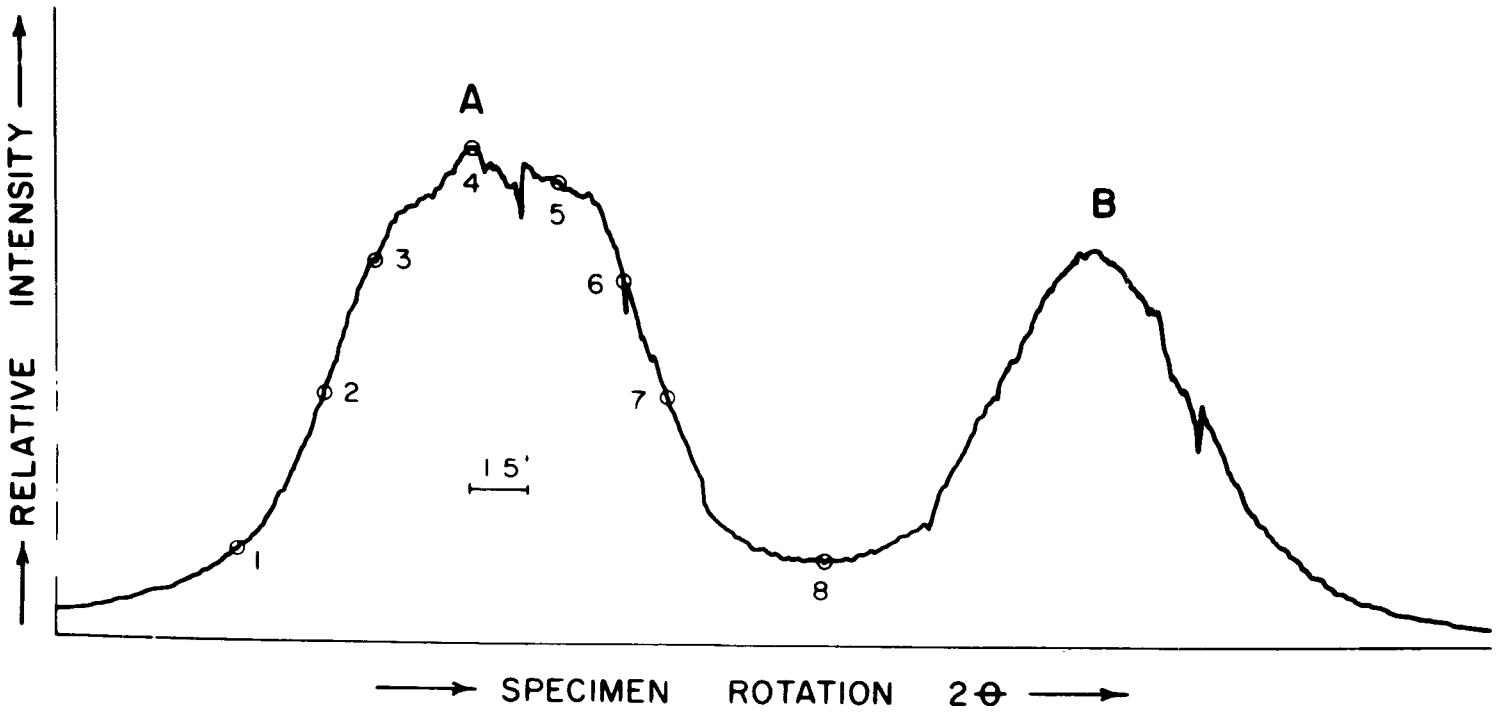

Fig. 12--Double-crystal diffractometer curve of macroscopic subgrains A and B of Figs. 10 and 11.

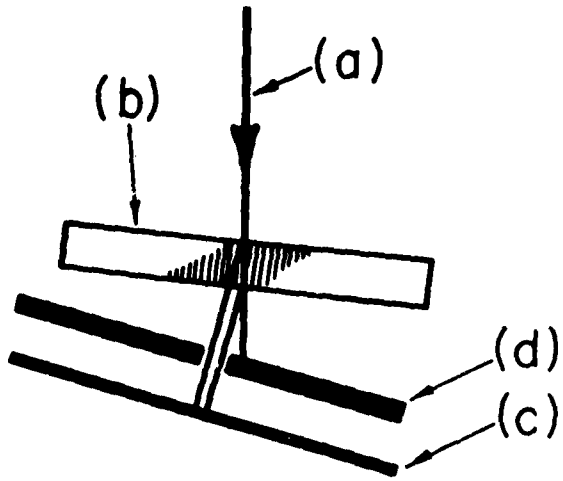

Fig. 13--Principle of Lang's x-ray projection topography. (a) Collimated x-ray beam. (b) Crystal. (c) Film. (d) Stationary screen.

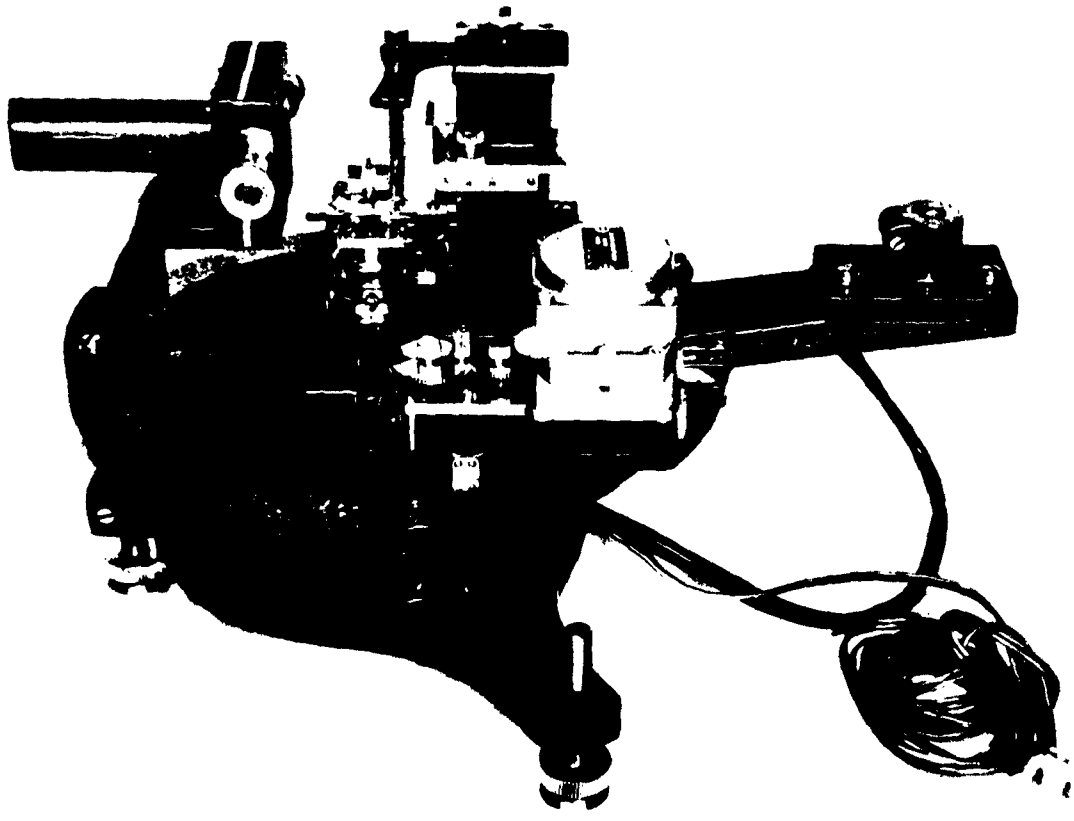

Fig. 14--Commercial Lang camera for x-ray diffraction topography (courtesy of Rigaku-Denki Co.).

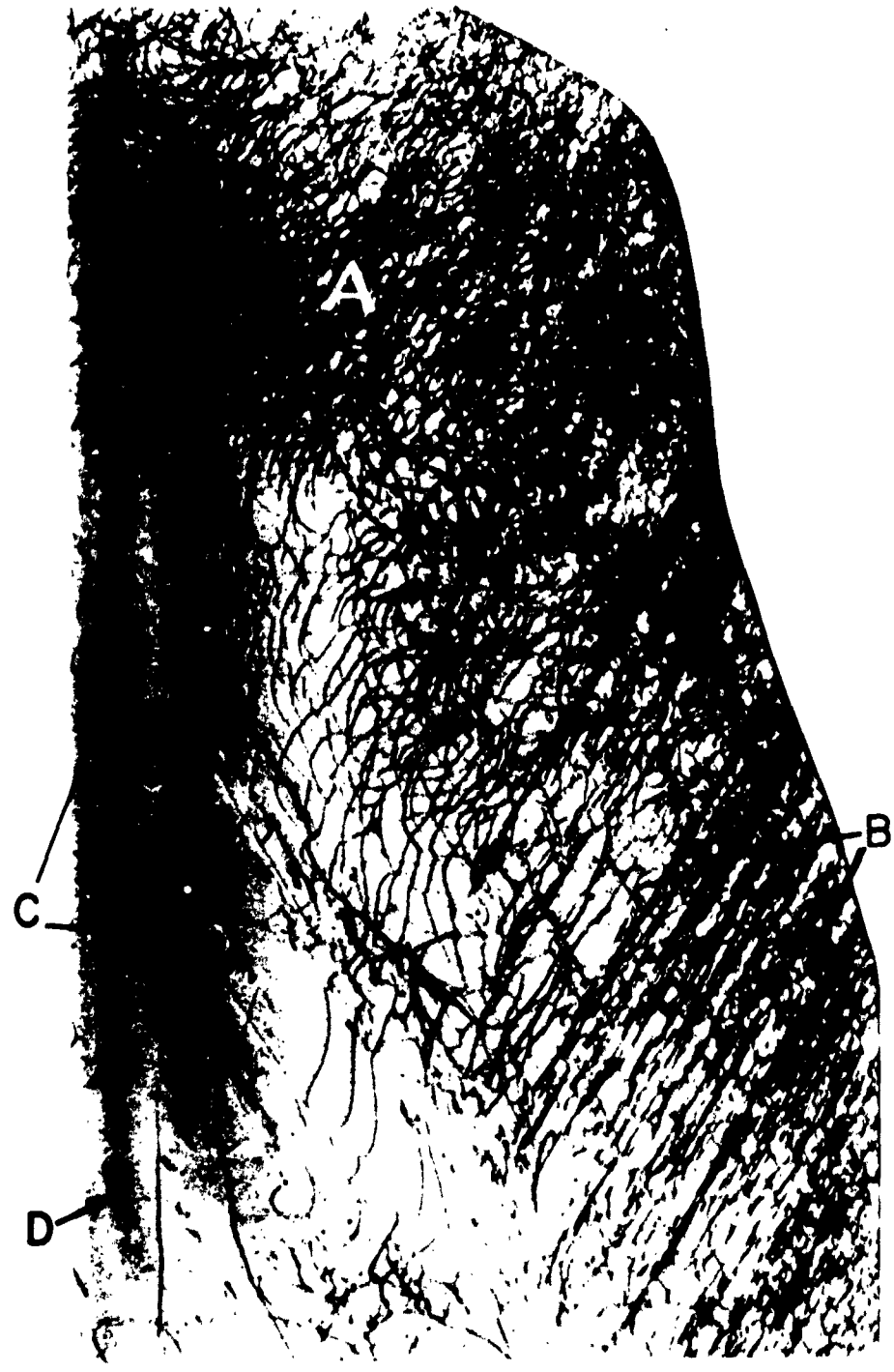

Fig. 15—X-ray diffraction topograph of silicon (220 reflection). Growth axis ⟨111⟩ (courtesy of G. H. Schwuttke). The dislocation density at A is approximately 10^5 lines/cm^2. Alignment of edge dislocations at D. Long dislocation lines with maximum contrast at C. The short lines at D have 60° Burgers vector lying in the plane perpendicular to (110).

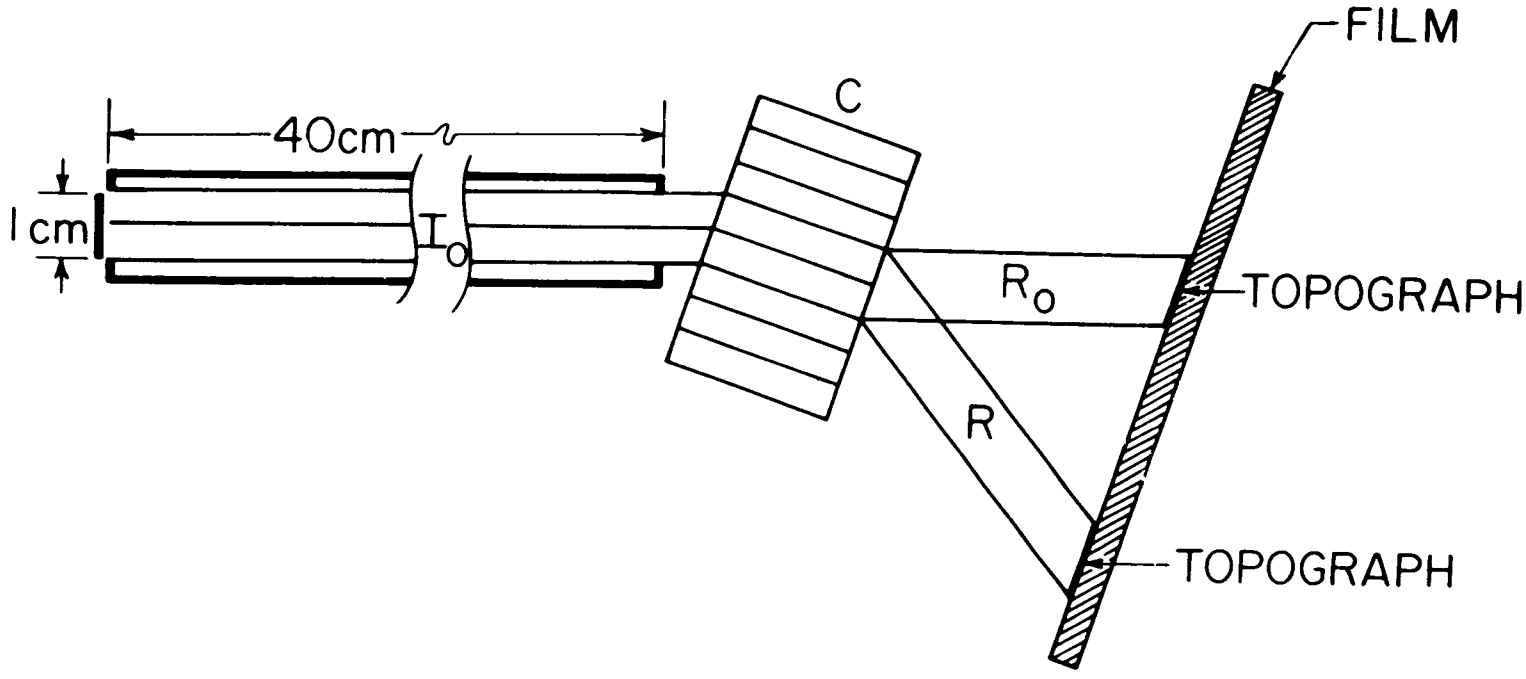

Fig. 16--Sketch of experimental arrangement for the anomalous transmission method (after Schwuttke[21]).

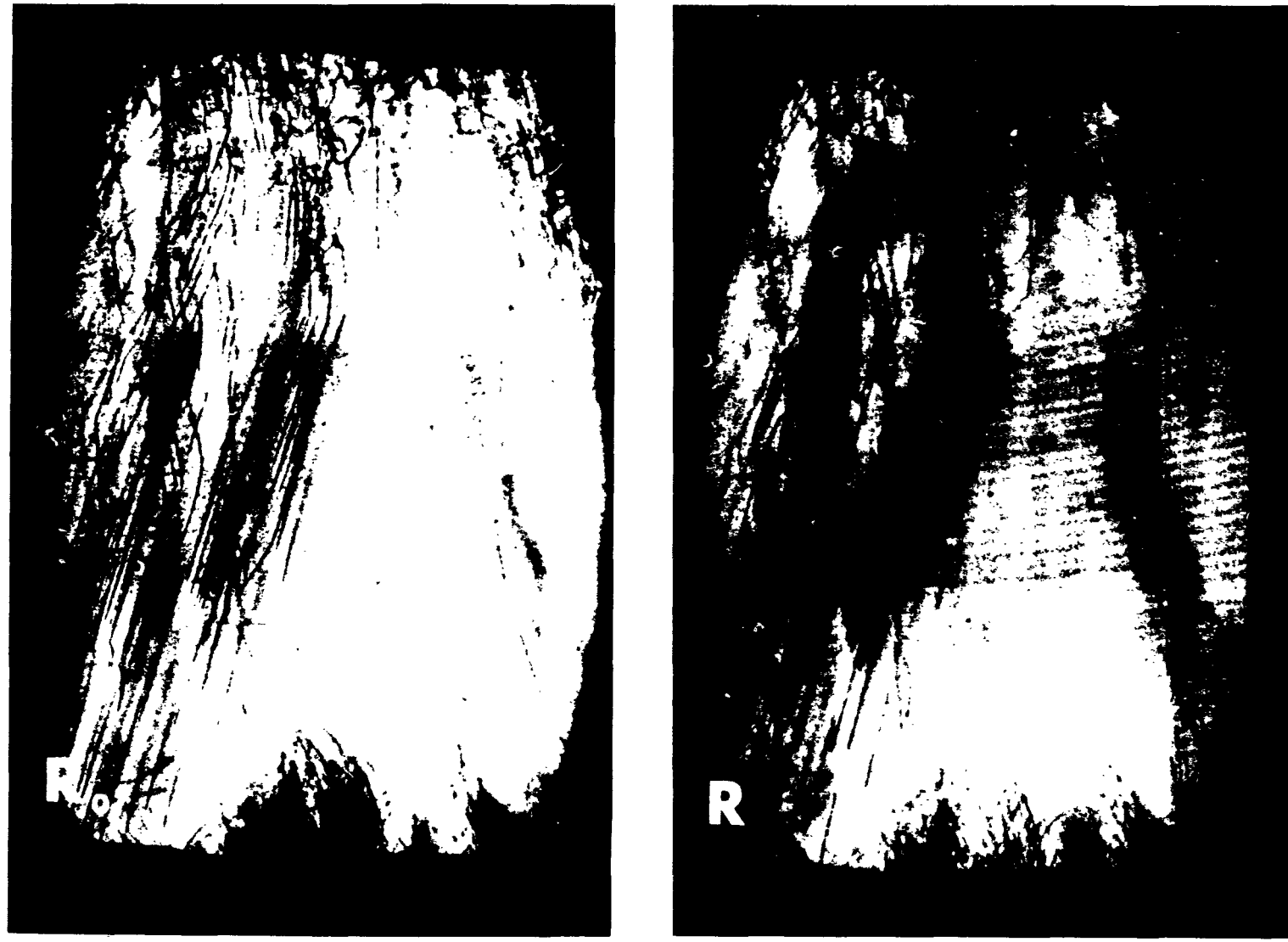

Fig. 17--R and R_o image of germanium wafer showing dislocations and segregation of arsenic. (220) reflection. 12 x. (After Schwuttke[21]).

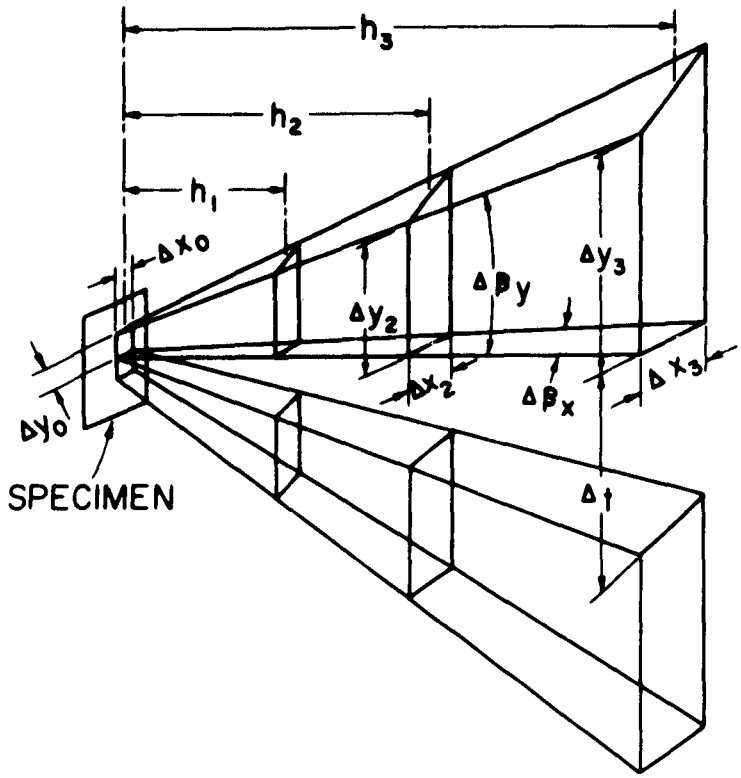

Fig. 18--Schematic representation of spatial image tracing showing dependence of image size and separation on substructure characteristics.

Discussion of Paper by S. Weissmann

The Observation and Measurement of Substructures
In Crystals by X-Ray Techniques

by

W. P. Evans
Research Department
Caterpillar Tractor Company, Peoria, Illinois
and
J. B. Cohen
Department of Materials Science
The Technological Institute
Northwestern University
Evanston, Illinois

We would like to point out that another x-ray technique, the Fourier analysis of shapes of diffraction peaks, is useful in characterizing substructures. This method was originally proposed by Warren and Averbach[1] and was recently reviewed by Warren[2]. One obtains from the coefficients of a Fourier series representing a peak the mosaic size $(D_{eff})_{<hk\ell>}$, determined by substructure and fault density, and the rms strains $<\varepsilon^2_{x\mathring{A}}>^{1/2}_{<hk\ell>}$ averaged over various distances ($x\mathring{A}$) normal to the diffracting planes, i.e., in specific crystallographic directions. Additional information concerning faulting and long-range strains can also be obtained from peak positions and peak asymmetry[2, 3]. The information obtained is averaged over the area under the x-ray beam and thus good statistical data is obtained to relate to properties which do not depend on a local state of imperfection (such as in a failure or in recrystallization). In addition to being non-destructive and not very restrictive as to sample geometry, it is also especially helpful after moderate deformation, in which case present resolution with the electron microscope is not adequate. In fact, we have even found it useful after only a few percent elongation in tension of fine grained materials. Apparently the method has not been used extensively because of the work involved in obtaining the Fourier coefficients. However, this can be done quickly and cheaply with computers[4]; in fact it is possible to feed the x-ray data directly to

punched cards or tape, or to use a chart reading device with the computer and hence to eliminate almost all the time for analysis.

Two recent theoretical investigations have shown the nature of some of the errors in the analysis and how to simply correct for these[5, 6].

In order to demonstrate the usefulness of the method, we wish to briefly present two examples:

1) Relationships between the substructure and properties of electrodeposits are not at all clear, for example, it is known that macro-residual stresses and hardness do not correlate well[7]. In Table I data is presented concerning the effect of potassium ethyl xanthate (KEX) additions on the substructure of Ag electrodeposits, as determined by the Fourier technique, and some of the properties of the deposit[8]. These results clearly illustrate that in this case the mosaic size and twin fault probability (β) control the hardness but are not important in determining the residual stresses, especially after large additions of KEX.

2) The fatigue life of steels seems to increase and pass through a maximum with increasing hardness[9]. It is also known that introducing surface compressive stresses, for example by peening, will improve fatigue life[10]. In Table II, some x-ray data on a 1045 steel is presented for two heat treatments and for the effects of peening[11]. At low hardness levels, peening affects both the long-range residual stresses and the substructure (mosaic size and microstrains) whereas at a high hardness level, only the long-range stresses are strongly affected. This data suggests that in low hardness steels, the substructure is important in retarding ductile fracture. However, this substructure also lowers cleavage strength or raises the flow stress above the cleavage strength; hence as hardness increases cleavage fracture becomes more important, resulting in the maximum in fatigue life. The role of long-range compressive residual stresses at high hardness is then to

retard clevage fracture.

It is also worth pointing out that with polycrystalline b. c. c. metals and alloys (such as low carbon steel) the diffraction pattern contains a third order of one peak, the 440, which does not overlap with any other peak. (This does not occur with polycrystalline f. c. c. materials.) As a result of this, enough data is available in the diffraction pattern to obtain the actual strain distribution without assumptions[1] and thus to see how the distribution is affected by treatment. The results can be compared with distributions arrived at from theoretical considerations. For example, if the strain distribution is thought to be Gaussian, the standard deviation (σ) is simply related to the microstrain and the long-range residual strains:

$$\sigma^2_{<hk\ell>} \quad \text{at } X\,\text{Å} = \langle \varepsilon^2_{xA} \rangle_{<hk\ell>} - \langle \varepsilon \rangle^2_{<hk\ell>}$$

where $\langle \varepsilon \rangle_{<hk\ell>}$ is obtained from peak shifts.

Thus it is possible to calculate the Gaussian distribution from some of the Fourier data and to compare it to the actual distribution determined from the Fourier analysis, and perhaps with electron microscopy as well, to understand why and how the distribution is affected.

Finally, we would like to point out that electron microscopy could be especially useful in establishing the exact meaning of the mosaic size determined by x-ray diffraction. Some work along these lines has been done[12] but much more is needed.

REFERENCES

1. B. E. Warren and B. L. Averbach, J. Appl. Phys. 21 (1950) 595; 23 (1952) 497.
   B. E. Warren and B. L. Averbach in "Modern Research Techniques in Physical Metallurgy." (ASM Cleveland 1954) p. 95.

2. B. E. Warren, in "Progress in Metal Physics" (Pergamon Press, New York, 1959) Vol. 8, p. 147.

3. J. B. Cohen and C. N. J. Wagner, J. of Appl. Phys. 33 (1962) 2073.

4. R. J. De Angelis, L. H. Schwartz and J. B. Cohen, Amer. Cryst. Assoc., Mark I Computer Listing; to be published in detail.

5. V. Kukol., Sov. Phys. Solid State 4 (1962) 528.

6. B. Ya Pines and A. F. Sirenko, Sov. Phys. Cryst. 7 (1962) 15.

7. H. Fischer, P. Hubse and F. Pawlek, Zelt. fur Metallkunde, 47 (1956) 43.

8. R. W. Hinton, L. H. Schwartz and J. B. Cohen, J. Electrochem Soc., in press.

9. M. F. Garwood, H. H. Zurburg and M. A. Erickson in "Interpretation of Tests and Correlation with Service" (ASM, Cleveland, 1941) pp. 12, 16.

10. J. Morrow and J. F. Millan, SAE TR - 198 (SAE, Inc. New York, 1961) pp. 5, 17.

11. W. Evans and R. W. Buenneke, Trans. AIME, in press.

12. E. Hofer and P. Javet, Journal Suisse D'Horlogerie No. 7-8 (1962) p. 1.

TABLE I

STRUCTURE AND PROPERTIES OF SILVER ELECTRODEPOSIT*

Conc. KEX mg/l	0.00	0.34	0.84	1.9	3.5
$\langle \varepsilon^2_{50\text{Å}} \rangle^{1/2}_{\langle 111 \rangle}$	1.4×10^{-3}	1.7	1.4	1.7	1.8
$\langle \varepsilon^2_{50\text{Å}} \rangle^{1/2}_{\langle 200 \rangle}$	1.9×10^{-3}	1.6	1.7	1.75	-
Surface Stress (in psi) error: $\pm$ 2560 psi	+ 3750	1250	10,750	11,900	9,000
VHN error $\approx \pm$ 7 pct.	92	103	95	111	116
β	0.001	0.011	0.005	0.015	-
$D_{eff\,\langle 111 \rangle}$	560A	250	340	150	170
$D_{eff\,\langle 200 \rangle}$	260A	140	180	85	-
$D_{f\,\langle 220 \rangle}$ +	4000A	370	820	280	-
Plating Efficiency	75%	85%	76%	85%	89%

* Plating Conditions: 1.4N KCN + 0.4N KCN, 10 ma/cm^2, room temperature.

+ Calculated contribution of β to D_{eff}

TABLE II

EFFECTS OF PEENING ON THE SUBSTRUCTURE AND PROPERTIES OF SAE 1045 STEEL

	Not Peened		Peened*	
	RC - 21	RC - 50	RC - 21	RC - 50
$\langle \varepsilon^2_{4\text{Å}} \rangle^{1/2}_{\langle 110 \rangle}$	4.5×10^{-3}	10.7×10^{-3}	8×10^{-3}	11×10^{-3}
$\langle D_{eff} \rangle_{\langle 110 \rangle}$	1900Å	315Å	420Å	260Å
$\langle \varepsilon_{av.} \rangle_{220}$ peak shift	0.2×10^{-3}	-0.5×10^{-3}	0.9×10^{-3}	1.3×10^{-3}
$\langle \varepsilon_{av} \rangle$ sine coeff. 220	0.2×10^{-3}	0.4×10^{-3}	1.1×10^{-3}	1.6×10^{-3}
Surface residual macro-stresses	-15,000psi	-1200psi	-67,000psi	-95,000psi
*Peened to 0.010 A-2 intensity				

Experiments on Substructure in Iron

by

G. V. Smith, P. M Kranzlein and M S Burton
Cornell University

ABSTRACT

The development of substructure by recovery annealing in several high purity irons and in an iron 3.5% chromium alloy was studied by optical metallography. The subgrain size was found to be essentially independent of tensile prestrain within the range of 5 to 30% strain, and no appreciable growth occurred until annealing temperatures causing partial recrystallization were reached. The subgrain size for the several irons was approximately 1 to 2 microns and that of the iron-chromium alloy slightly less In partially recrystallized material, subgrain growth was observed in the unrecrystallized matrix.

Initial flow strength was evaluated in a zone-refined iron and in the same iron after treatment in pure wet hydrogen, as dependent on prestrain, and recovery annealing temperature For the zone-refined iron, the yield strength after annealing at intermediate temperature was significantly higher than the prestrain stress, whereas the hydrogen-purified iron showed a lower yield stress for similar treatment Hence, it is concluded that the strengthening of the zone-refined iron is to be attributed to interstitial-substructure interaction rather than to substructure as has been suggested by some earlier work reported in the literature.

The effect of grain size on flow strength was also studied, with results showing that interstitial-grain boundary interaction contributes importantly to the strength of iron.

Introduction

Considerable interest has developed in recent years in the possible influence of substructure on flow and fracture of metals Parker and Washburn[1] found that by straining mild steel from 4 to 8% and annealing at temperatures of 427 to 690°C, the ultimate strength was increased to above that of the cold worked material. In some cases the recovered lower yield strength was greater than the prestrain stress, and in others it was less The recovered yield strength was always greater than the initial yield point These effects were attributed to a strengthening influence of substructure boundaries introduced during annealing and this conclusion has been widely accepted (see for example Ref. 2). However, when the evidence supporting this view is carefully examined, it is not clear that the data are free of question. Thus, it may be asked whether the results of Parker and Washburn have been influenced by quench-aging or strain-aging phenomena.

Since Parker and Washburn's early work, others have examined the possible role of substructures, with somewhat controversial conclusions. Washburn[3] introduced dislocation arrays into zinc crystals, and observed that the strengthening effect depended upon the temperature of annealing of the specimen containing such boundaries. A pair of 1° boundaries introduced by bending at the temperature of liquid nitrogen caused no strengthening if the crystal was heated only to room temperature, only a small strengthening on heating to 300°C, but considerable increase of yield stress (up to 50%) on heating to 400°C. Li[4] concluded from theoretical considerations that polygonized edge dislocation walls should not significantly increase flow strength. Meakin and Wilsdorf[5] experimentally observed that although subboundaries in single crystals of alpha brass occasionally offered definite impedance to the motion of gliding dislocations, this was not generally true. Michalak[6], in studies of hydrogen purified, zone-refined iron observed a continuous decrease in strength on annealing plastically strained samples in the recovery range. However, no substructure was detected.

In view of the confused evidence, further experimental study seemed desirable, and consequently the present study was made. In order to assess the results of past or current studies, it is desirable to attempt to establish what might properly be accepted as evidence of a strengthening role for substructure. Certainly, the introduction of additional dislocations and vacancies during deformation at temperatures below the recovery range leads to strengthening (strain-hardening), and until the density of these defects is lowered to the original level, by an annealing process designed to develop substructures, it is reasonable to expect residual strengthening, even when the defects are rearranged into small angle boundaries. Thus the exact role of substructure is difficult to assess. However, if the rearrangement into small angle boundaries leads to an increase of flow strength beyond that of the as-strained material, as some investigators have claimed (for example, Parker and Washburn[1]), then a strengthening effect of substructure cannot be questioned, unless an alternative source of strengthening can be suggested. In the case of iron, interstitial impurity atom-dislocation interaction[8] is an alternative strengthening mechanism.

EXPERIMENTAL PROCEDURE

A conventional method of introducing substructure into metals involves plastic straining followed by annealing below the recrystallization temperature range. The development of substructure in iron has recently been reviewed by Keh[9], who also reported additional experimental results using electron transmission microscopy. A cell-like structure, comprised of tangled dislocations, forms in iron plastically strained at room temperature. Annealing at temperatures above 400°C resulted in the formation of regular dislocation networks and a decrease in dislocation density. There was no significant subgrain growth during recovery at temperatures below that necessary to initiate recrystallization.

For most of the present investigation, the base material was a zone-refined iron which was obtained from Battelle Memorial Institute, where it had been prepared under the auspices of the American Iron and Steel Institute. This

material received six passes in an alumina boat. The chemical analysis of this material is reported in Table I. However, preliminary experiments to characterize the dependence of substructure on prestrain, time and temperature were made with a vacuum-melted and cast electrolytic iron* and a similarly processed iron-3.6% chromium alloy. Since our early studies suggested important interstitial effects in the zone-refined iron[8], the zone-refined iron was purified by annealing in wet hydrogen to obtain a lower interstitial content. Pure hydrogen was obtained by diffusion through a palladium-silver coil and saturated with distilled water at room temperature. Treatment was prolonged to a time beyond which further lowering of the yield strength was not observed. Carbon was analyzed by the Fundamental Research Laboratory of United States Steel Corporation in the specimens after purification and reported as 13 ppm for the hydrogen-purified iron, as compared with 19 ppm for the non-purified material (Battelle analysis, 10 ppm, Table I).

Wire tensile specimens were prepared from the zone-refined iron bar by cold rolling and drawing. During preparation of the wire, great care was taken to avoid contamination; no lubricant was used and the wire was degreased with acetone between all stages of preparation and prior to annealing. After rolling to 100 mil. diameter rod (86% reduction of area), part of the zone-refined iron was wet-hydrogen-purified for 50 hours at 750°C to reduce the interstitial impurities, and part was annealed (for recrystallization) at 750°C in vacuum. The rods were cold drawn to 50 mil. diameter wire (75% reduction of area) and specimens 3 inches long were cut from the wire stock. To obtain uniform small grain size, the wire specimens were recrystallized at 625°C for 5 hours, in vacuum for as-received zone-refined iron and in wet hydrogen for hydrogen-purified iron. The resulting grain size of both materials was about 80-100 microns (ASTM 4-5). After prestraining, the heat treating of both materials was performed in thoroughly outgassed vycor capsules in a vacuum of about 10^{-5} mm Hg; the capsules were withdrawn from the furnace and cooled in still air.

Tensile tests were conducted at room temperature using an Instron testing machine. Specimens with a gage length of 1.60 inches between grips were loaded at a crosshead speed of 0.02 inches per minute, which gave an initial strain rate of 1.25×10^{-2} min.$^{-1}$. The yield strength was defined as the lower yield stress in zone-refined iron, for which a well-defined yield point was always observed. In some cases, small yield points were observed in the hydrogen-purified iron, but the maximum length of the yield was 0.1% strain in hydrogen-purified iron as compared to 2.7% strain for zone-refined iron. For hydrogen-purified iron, the yield strength was defined as the stress at 0.1% offset.

---

*C, N and O contents of this iron were respectively 0.005, 0.001 and 0.031 per cent by weight.

EXPERIMENTAL RESULTS

Delineation of Substructure

A special metallographic technique was developed to reveal substructure in iron regardless of purity. Specimens were mechanically polished and then electropolished in a stirred solution containing 65 parts of orthophosphoric acid, 35 parts of ethyl alcohol and 35 parts water for 4 minutes at 1 volt D. C. It was discovered that an etchant developed by Gorsuch[10] for studying dislocations in iron whiskers revealed substructure by etching the subboundaries and decorating them by preferentially depositing a thin layer of copper at the dislocation wall. To avoid copper deposition over the entire specimen, the etching time was limited to one second, and the specimen was rinsed immediately under flowing water The composition of the etchant was

2.5 gms picric acid
4.0 gms anh. cupric chloride
100 ml ethyl alcohol
10 ml hydrochloric acid
3 ml nitric acid

This etchant exhibits an orientation sensitivity, so that not all grains in a polycrystalline specimen can be etched to show substructure

In vacuum-melted electrolytic iron with a carbon concentration of about 50 ppm, a picral etchant satisfactorily reveals substructure and is not orientation dependent, allowing the number of grains containing substructure to be determined.

Characterization of Substructure

To explore the effect of the strain and recovery temperature on the development of substructure in iron, a series of tensile specimens of vacuum-melted and cast electrolytic iron and an iron-3.6% chromium alloy (referred to earlier) were prepared and recrystallized at 840°C for two hours For electrolytic iron the resulting grain size was about 500 microns, and for the iron-3.6% chromium alloy the grain size was about 250 microns Specimens were strained in tension different amounts in the range 6 to 10%. Samples were cut from the gage section and annealed one hour at various temperatures in the range 600 to 835°C

No significant variation in subgrain size in vacuum-melted electrolytic iron was observed with strains from 6 to 10% for constant annealing temperature. The subgrain size was approximately 1 to 2 microns for annealing at 600°C Above 650°C partial recrystallization was observed and as the temperature was increased to 800 C subgrain growth occurred in the unrecrystallized grains. Figure 1 shows typical substructures observed in electrolytic iron.

For the iron-3.6% chromium alloy, the substructure developed after annealing at 600°C was slightly finer, 0.5 to 1.5 microns, than that observed in iron and not quite as well defined. Again, no dependency of subgrain size on strain was observed within the range of 6 to 10%. As the annealing temperature was increased from 700 to 835°C, partial recrystallization occurred and subgrain growth was observed in the unrecrystallized matrix. Typical substructures observed in the iron-3.6% chromium alloy are shown in Figure 2.

Since no significant difference in subgrain size was observed in the range of 6 to 10% strain in vacuum-melted electrolytic iron and iron-3.6% chromium, a wider range of 5 to 30% strain was studied in as-received and in hydrogen-purified, zone-refined iron wire. In initial experiments with zone-refined iron wire, the development of substructure was evaluated for strains of 10 and 30% and annealing temperatures of 350, 450 and 500°C for 16 hours. Figure 3 shows the progress of the development of substructure in the 30% specimen with increasing annealing temperature. Substructure appeared to form directly in the slip traces. During annealing the slip traces appeared to become more sharply defined and discrete cells became recognizable. In the 30% specimen, the cell size remained essentially uncoarsened even after annealing 16 hours at 500°C. Thus, the picture obtained of the nature of substructure in iron is a "perfecting" of the deformation structure (see also Ball[11] and Keh[8,9]). In general, the degree of definition of substructure was heterogeneous throughout the polycrystalline specimens; in the same specimen sharply defined cells were observed in some grains while other grains showed only slip traces.

In this fine-grained iron, recrystallization occurred simultaneously with the development of well-defined subgrains, and the specimens were largely recrystallized before significant subgrain growth occurred. The subgrain size was essentially independent of prestrain between 10% and 30% strain.

With 30% strain, recrystallization nucleation was observed after annealing 16 hours at 450°C. Substructure was best defined in the 30% specimen annealed at 500 C, where considerable recrystallization had already occurred elsewhere in the specimen. For the specimen strained 10%, higher annealing temperatures were required to obtain a degree of definition comparable to the 30% specimen, but the subgrain size was approximately the same for the same annealing temperature.

For subsequent study of the effect of substructure on flow strength of the zone-refined iron and of hydrogen-purified, zone-refined iron, prestrains of 5, 10, 15 and 25% were employed. To obtain maximum recovery and subgrain definition for this range of strain, without recrystallization, the specimens were annealed at 450°C for 4 hours. With this heat treatment, well-defined substructures were observed in the strained specimens 15 and 25%. However, in the specimens strained 5 and 10%, the substructure remained ill-defined after this annealing treatment. Well-defined substructure was observed in the 5% strain specimen only after annealing at 600°C, which brought about concurrent recrystallization nucleation.

The substructures observed in the hydrogen-treated and the nontreated

zone-refined irons were essentially identical for the same conditions of strain and annealing below the recrystallization temperature.

Mechanical Properties

To evaluate the relative effects of interstitial impurities and dislocation substructures on flow strength, the tensile behavior of as-received and hydrogen-purified zone-refined iron was studied after a series of strain and recovery-anneal treatments. Annealing temperature was varied from 200 to 600°C, and for most of the study the holding time was four hours. The prestrain was varied from 5 to 25%. Results are tabulated in Table II for hydrogen-purified iron and in Table III for zone-refined iron.

Hydrogen-purification of zone-refined iron has a major effect on the stress-strain curve as shown in Figure 4, reducing the yield strength from 16000 to 6500 psi. As mentioned earlier, chemical analysis of these materials showed that treatment in hydrogen had reduced the carbon by 6 ppm. Over 50% of the yield strength of annealed zone-refined iron is therefore presumably attributable to the interaction of interstitials with dislocations. Hydrogen-purification also decreased the ultimate strength, from about 31,600 to 28,000 psi, increased the elongation, and increased the reduction of area at fracture (not reported in Tables II and III) from 53 to 69%. It is of interest that the zone-refined iron exhibited a sharp yield point, which extended to 2.7% strain whereas after hydrogen purification yield points less than 0.1% strain were observed.

Since yield strength data for single crystals of hydrogen-purified iron were available for the same test conditions from the work of H. H. Kranzlein[12], it is possible to differentiate the factors contributing to the measured strength of polycrystalline zone-refined iron. Figure 5 illustrates schematically the relative proportions of strengthening due to the intrinsic strength of zone-refined iron (yield stress of a single crystal), due to grain boundary strengthening, and due to interaction of interstitials with grain boundaries. In Figure 5, line A represents the yield strength of polycrystalline zone-refined iron, line B is the yield strength of polycrystalline, hydrogen-purified, zone-refined iron of the same grain size, and line C is the yield strength of a hydrogen-purified, zone-refined iron single crystal.* As can be noted from the figure, the effect of grain boundaries on strength at low interstitial concentrations is relatively small. In addition, no effect on strength was observed when unstrained specimens were annealed at temperatures up to 550 C as is indicated by the figure.

---

*The yield strength of the single crystals did not vary appreciably with orientation within the range examined[12], owing presumably to the multiplicity of possible slip systems in iron.

After straining followed by annealing within the recovery range, hydrogen-purified iron exhibited a continuous decrease in yield strength with increasing temperature, as shown in Figure 6. Values for percentage recovery are given in Table IV. Even at 200°C where large increases in strength due to strain aging are observed for many irons and steels, more than 5% recovery was observed for the purified material that had been strained 5%. At 450°C, the maximum recovery temperature possible while avoiding recrystallization nucleation following 25% strain, the recovered yield strength was a function of prestrain, as shown in Figure 7, and was about 30% less than the prestrain stress. It is interesting that the ultimate tensile strength of the hydrogen-purified material remained essentially fixed throughout these annealing treatments (Table II and Fig. 12).

In contrast to the hydrogen-purified iron, a strong interstitial dislocation interaction (strain-aging) was observed in zone-refined iron after the strain-anneal treatments, as shown in Figure 8. After prestraining 5% and annealing at 200°C, the yield strength was 40% greater than the flow stress for 5% strain. For prestrains of 10, 15 and 25% the percentages of strain - aging (at 200°C) were 29, 24, and 18% respectively. The observed strain-aging was also reflected in an increase in ultimate tensile strength (Table II and Fig. 12).

If the data for hydrogen-purified iron are taken as a base, it is possible to separate, for a given prestrain and annealing temperature, the portion of strengthening due to interstitial-dislocation interaction from that intrinsic in iron. Table V presents values for the "inherent strength" and for the interaction strength obtained in this manner for zone-refined iron. Further lowering of carbon could be expected only to lower the inherent strength; hence the interaction strengths of Table V are minimal.

Figures 9 and 10 illustrate graphically the intrinsic strength, and dislocation-interstitial interaction strengthening of zone-refined iron after straining 5 and 10% and annealing. Although the contribution to the strength of zone-refined iron by interaction is reduced by annealing at the higher temperatures, this factor is still a major fraction of the strength observed at the highest temperature studied. As shown in Figure 11, the yield strengths of the 5 and 10% specimens after annealing at 450°C were still slightly greater than the prestrain stresses. For this same annealing temperature, the yield strengths of the 15 and 25% specimens were slightly less than their prestrain stresses. The levelling may be explained in terms of the saturation of interaction strengthening due to insufficient interstitial impurities, the relatively small effect of unpinned dislocations on strength, and to faster recovery at higher strains.

The variation with prestrain of ultimate tensile strength of the zone-refined and hydrogen-purified irons is shown in Fig. 12 for several annealing temperatures. Unfortunately data are not available for large prestrains and annealing temperatures of 200 and 550°C for the hydrogen-purified iron. Also the datum for this iron for the prestrain of 10% and annealing at 200°C represents 1 hour, rather than 4 hours, as do the other data. However, it is reasonable to assume no difference in yield strength for 1 to 4 hours.

(See e.g. data in Table III for 1 and 4 hours at 200°C for zone-refined iron)

Discussion of Results

Investigators have generally tended to overlook the possibility of "strain aging" in iron after higher temperature anneals (above perhaps 300°C). In some cases, the high yield strength observed after annealing just below the recrystallization temperature in iron has been attributed to the formation of substructure[1]. However, the present results suggest that important interstitial-dislocation interaction strengthening may persist in iron to relatively high temperatures (see e.g. Fig. 9) Moreover, the present results as well as other results reported in the literature have shown that the sharpening of substructure in iron by recovery annealing results in a decrease in strength. This has been shown in the present investigation by two irons which with similar substructures but different interstitial impurity contents show completely opposite behaviors. For hydrogen-purified iron, recovery of yield strength was observed after prestrain anneal treatments; moreover, no increase in the ultimate strength was observed. However, for as-received zone-refined iron, identical pre-treatments resulted in substantial increases in both the yield strength and the ultimate strength. Thus, the ultimate tensile strength of the zone-refined iron was increased from 31,600 to 38,200 psi by prestraining, 10-25%, followed by heating at 200°C.

The mechanical behavior of iron containing interstitial impurities after prestrain and annealing treatments must be considered as the net result of two processes. When a strained specimen is annealed below the recrystallization temperature, recovery occurs by the straightening, annihilation and rearrangement of dislocations and vacancies. With increasing prestrain, the cells became more sharply defined even for room temperature deformation.[13] Increasing the annealing temperature causes sharpening and perfecting of the cell structure developed during deformation. However, in polycrystalline iron, recrystallization begins before significant subgrain growth can be obtained throughout the entire specimen. The formation of well-defined substructures by annealing is associated with a decrease in strength. Concurrent with recovery, interstitial impurity atoms associate with the new dislocations introduced by the straining, with a resultant strengthening*.

The net effect of the softening and strengthening processes may be expected to depend upon the dislocation density, the concentration of interstitial impurities, and the annealing temperature The present results show that interaction strengthening is greatest at about 200°C, but that interaction makes an important contribution to flow strength, even for fairly high annealing temperatures. Furthermore, it is unjustified to look upon the formation of substructure, in the absence of impurity interactions, as causing strengthening. To the contrary, as the substructure becomes "perfected", flow strength progressively decreases.

---

*The nature of the association is presumably that of the Cottrell "cloud" at low annealing temperatures[14], but might be one of precipitate particles at high annealing temperatures.

It is of interest that the analysis of the zone-refined iron before and after treatment in pure wet hydrogen showed that the carbon content had been reduced from 19 to 13 ppm. It is difficult to understand how such a reduction could cause such large change in the flow curve of the annealed iron, as well as change in the response to recovery annealing

That polygonization boundaries do not provide an important strengthening influence in the absence of interstitial impurities is also suggested by the results of a related research program concerned with the influence of grain size on the flow strength of the same materials, some results of which are summarized in the Petch type of plot, Figure 13 The slope of the plot of yield strength at room temperature versus the reciprocal of the square root of the grain size for the hydrogen-purified iron of the present study (0.381 Kg $mm^{-3/2}$) is the lowest of which we are aware in published literature, whereas, complex interaction is indicated in the non-hydrogen-treated iron. If large angle boundaries have so little effect on strength of iron (see also Fig. 5) it seems unreasonable to expect a small angle polygonization boundary to be an important barrier.

It also seems noteworthy that the yield strength of single crystal iron does not appear to be substantially different for the hydrogen-purified material or the unpurified material, suggesting that the interaction of interstitials with randomly dispersed dislocations at least in the densities prevalent in the materials of this study is not an important strengthening influence, in contrast to the situation as regards either small or large angle dislocation boundaries.

SUMMARY

1. Subgrain size produced in high-purity iron by recovery annealing is essentially independent of tensile prestrain within the range 5 to 30 per cent strain.

2. Substructure appeared to develop along markings that formed during deformation, and sharpened with increase of annealing temperature.

3. The substructures observed in the hydrogen treated and the non-hydrogen treated irons were essentially identical for the same strain and annealing conditions.

4. No appreciable growth of subgrains was observed until annealing temperatures causing partial recrystallization were reached, whereupon coarsening occurred.

5. The subgrain size for annealing temperatures not causing coarsening was about 1 to 2 microns.

6. A large fraction of the flow strength of the recrystallized, zone-refined iron of this investigation is attributable to interaction between interstitial impurity atoms and grain boundaries.

7. Considerable strengthening attributable to interstitial substructure interaction was observed in zone-refined iron containing 19 ppm of carbon, by analysis, when plastically strained and annealed in the recovery range.

8. Zone-refined iron in which carbon had been reduced from 19 to 13 ppm by treatment in wet hydrogen, showed progressive softening on annealing after plastic straining, even though the substructure appeared to be identical with that of iron not treated in hydrogen.

9. The rearrangement of dislocations into increasingly perfect subgrains by annealing in the recovery range results in a progressive decrease of yield strength from the level reached during prestraining, when the interstitial content is reduced to low level, leading to the conclusion that substructure does not make an important contribution to the strength of iron in the absence of interstitial-dislocation interactions. This conclusion is supported by the observation that the yield strength of the hydrogen treated iron is not greatly different in the mono- and polycrystalline conditions, indicating that large angle boundaries are not important barriers.

10. The similarity in strength of single crystals of zone-refined iron, whether hydrogen-purified or not, suggests that interaction of interstitial impurity atoms with dispersed dislocations is not an important strengthening influence for the dislocation densities and interstitial contents here studied.

11. The present results suggest that studies of recovery of iron, after plastic deformation are likely to be confused by interstitial-dislocation interactions.

Acknowledgments

We gratefully acknowledge that the program of research of which these results are a part is being carried out with the financial support of the American Iron and Steel Institute and the Advanced Research Projects Agency of the Defense Department. We are also grateful to Dr. J. T. Michalak of the Fundamental Research Laboratory of the United States Steel Corporation for arranging for several chemical analyses. The zone-refined iron studied in the investigation was furnished by Battelle Memorial Institute, where it had been prepared for the American Iron and Steel Institute.

References

1. E. R. Parker and J. Washburn: "Impurities and Imperfections";1955, page 155, American Society for Metals, Cleveland, Ohio.

2. G. E. Dieter, Jr.; "Mechanical Metallurgy" p. 127 (1961) McGraw-Hill Book Company, New York.

3. J. Washburn; Trans. AIME 203 (1955) p. 675.

4. J. C. M. Li; Acta Met. 8 (1960) p. 563.

5. J. D. Meakin and H. G . F. Wilsdorf; Trans. AIME (1960) 218 p. 739.

6. J. T. Michalak; Ph. D. Thesis, Carnegie Institute of Tech. 1959.

7. W. C. Leslie, J. T. Michalak and F. W. Aul; The Annealing of Cold Worked Iron; AIME Fall Meeting 1961; to be published-Metallurgical Society Conference.

8. G. V. Smith, P. M. Kranzlein and M. S. Burton; discussion to Ref. 7.

9a. A. S. Keh and S. Weissman; Conference on the Impact of Transmission Electron Microscopy on Theories of the Strength of Crystals; Berkeley, Calif., July 1961.

9b. A. S. Keh; Symposium on The Direct Observation of Lattice Defects in Crystals, AIME, 1961.

10. P. D. Gorsuch; Research on the Behavior of Nearly Perfect Crystals; Progress Report No. 3, General Electric Company Research Laboratory, Oct. 1959.

11. C. J. Ball; Jnl. Iron and Steel Institute, March 1959, 191 p. 232.

12. H. H. Kranzlein; Solid Solution Strengthening of Iron; M. S. Thesis, Cornell University, Sept. 1962.

13. A. S. Keh; Dislocation Arrangement in Alpha Iron during Deformation and Recovery; U. S. Steel Corp. Fundamental Research Laboratory, December (1960).

14. W. C. Leslie and A. S. Keh; An Electron Transmission Study of the Strain Aging of Iron; U. S. Steel Corp. Fundamental Research Laboratory. June 1961.

TABLE I

ANALYSIS OF ZONE-REFINED IRON

(As reported by Battelle Memorial Institute)
Amounts are given as parts per million
(1 ppm equals 0.0001 per cent)

Aluminum	15	Magnesium	5
Antimony	5 ND (a)	Manganese	0.5
Arsenic	10 ND	Molybdenum	5 ND
Beryllium	0.2	Nickel	12
Boron	5	Nitrogen	2
Calcium	10 ND	Oxygen	17
Cadmium	5 ND	Phosphorus	5
Carbon	10	Silicon	10
Chromium	5	Sulfur	9
Cobalt	1	Tin	5 ND
Copper	2	Titanium	0.5 ND
Hydrogen	2	Tungsten	10 ND
Lead	1 ND	Vanadium	1 ND
		Zinc	10 ND
		Zirconium	0.5 ND

(a) ND means not detected. Detection limits are given.

TABLE II

EFFECT OF PRESTRAIN-ANNEAL TREATMENTS ON THE MECHANICAL PROPERTIES OF HYDROGEN-PURIFIED IRON

Prestrain %	Initial Yield Strength psi	Prestrain Stress psi	Annealing Temp. °C	Annealing Time hr	Recovered Yield Strength psi	Ultimate Strength psi	Total Elongation %
0	6400					28,300	51.6
0	6500					27,600	48.0
4.9	7500	18,900	200	4	17,900	25,500	19.5
5.0	7000	18,700	200	4	18,100	26,400	23.4
5.0	6700	18,600	450	4	14,800	27,800	55.7
5.0	6800	19,100	450	4	15,600	28,100	53.6
4.9	7500	19,400	550	4	14,700	27,600	38.0
5.1	7000	18,900	550	4	14,000	27,500	36.4
10.0	6500	22,900	200	1	22,100	27,500	47.2
9.8	7100	22,700	450	4	17,600	26,500	47.1
9.9	6600	23,200	450	4	17,700	27,500	53.9
14.9	6700	25,300	450	4	19,200	26,700	49.6
15.0	6600	25,200	450	4	19,100	27,000	51.9
24.8	6400	27,000	450	4	19,900	26,400	33.4
23.0	6600	26,800	450	4	20,500	27,900	57.1

TABLE III

EFFECT OF PRESTRAIN-ANNEAL TREATMENTS ON THE MECHANICAL PROPERTIES OF ZONE-REFINED IRON

Prestrain %	Initial Yield Strength psi	Prestrain Stress psi	Annealing Temp. °C	Annealing Time hr.	Recovered Yield Stress psi	Ultimate Strength psi	Total Elongation %
0	13,700					31,300	40.5
0	15,900					31,900	35.8
4.8	14,000	20,600	200	4	28,900	33,800	36.3
4.9	13,700	20,300	200	4	28,000	31,900	35.9
5.0	14,000	20,300	450	4	23,300	32,300	36.4
5.0	14,000	19,800	450	4	22,500	31,700	37.7
4.9	14,000	20,100	550	4	21,100	30,900	29.7
5.0	14,000	20,000	550	4	20,600	30,700	37.5
4.9	14,400	20,100	600	4	19,600	*	*
5.0	13,700	20,300	600	4	19,100	*	*
9.6	15,300	27,200	200	1	34,100	38,100	28.5
9.7	17,300	27,100	200	4	34,700	38,400	28.8
9.9	13,800	25,200	450	4	26,500	33,300	31.6
9.7	13,800	26,000	450	4	27,300	33,500	36.2
14.8	15,000	29,200	200	4	36,200	38,800	29.4
14.8	14,000	28,100	450	4	27,000	32,900	34.9
14.7	14,500	28,100	450	4	28,600	33,100	28.8
24.6	16,100	32,000	200	4	37,800	38,300	32.9
24.6	14,000	29,100	450	4	27,800	31,600	40.4
24.8	13,800	29,200	450	4	28,300	31,600	35.1

*Failed at the grip.

TABLE IV

FLOW-STRESS RECOVERY OF HYDROGEN-PURIFIED IRON

Prestrain	Annealing		Recovery of Flow Stress
	Temp. °C	Time hr.	%
4.9	200	4	8.8
5.0	200	4	5.3
5.0	450	4	31.9
5.0	450	4	28.4
4.9	550	4	39.5
5.1	550	4	41.2
10.0	200	1	4.9
9.8	450	4	32.7
9.9	450	4	33.1
14.9	450	4	32.8
15.0	450	4	32.8
24.8	450	4	34.7
23.0	450	4	31.2

TABLE V

Analysis of Strength of

Zone-Refined Iron

Prestrain	200°C Anneal		450°C Anneal	
%	Inherent Strength* psi	Interaction Strength psi	Inherent Strength* psi	Interaction Strength psi
5	18,000	10,400	15,200	7,700
10	22,100	12,600	17,600	9,300
15			19,200	8,500
25			20,200	7,800

*The "inherent" strength is here taken as the sum of the single crystal strength, and the grain boundary and residual strain hardening contributions, all measured for the hydrogen-purified material.

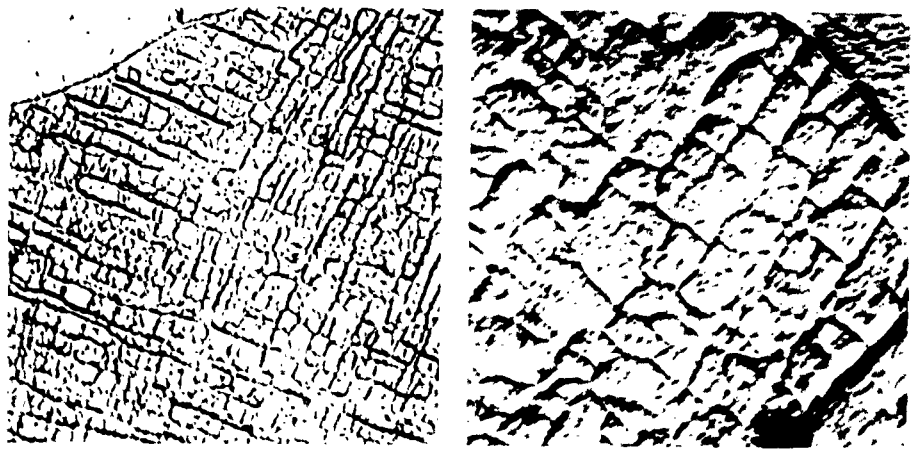

6% strain
600°C - 1 hr.

6% strain
800°C - 1 hr.

Substructure in vacuum-melted electrolytic iron; Gorsuch etchant; x 1000

Fig. 1

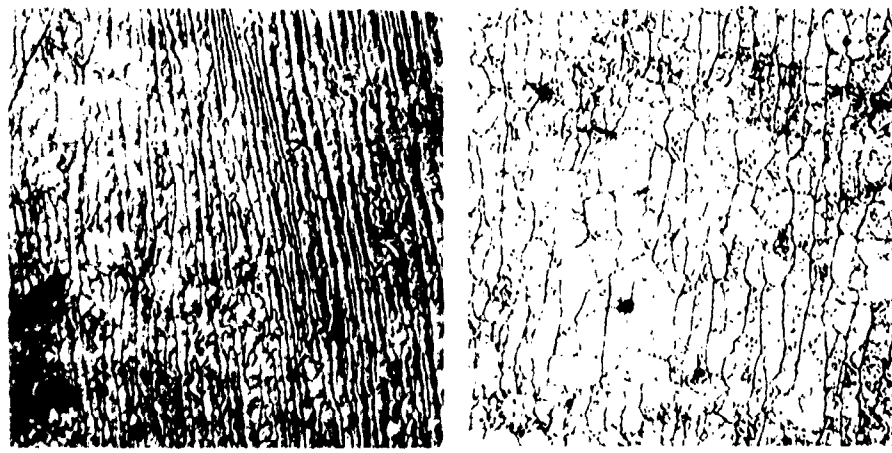

6% strain
600°C-1hr

8% strain
775°C-1hr

Substructure in vacuum-melted iron-3.6 % chromium alloy; Gorsuch etchant; x 1000

Fig. 2

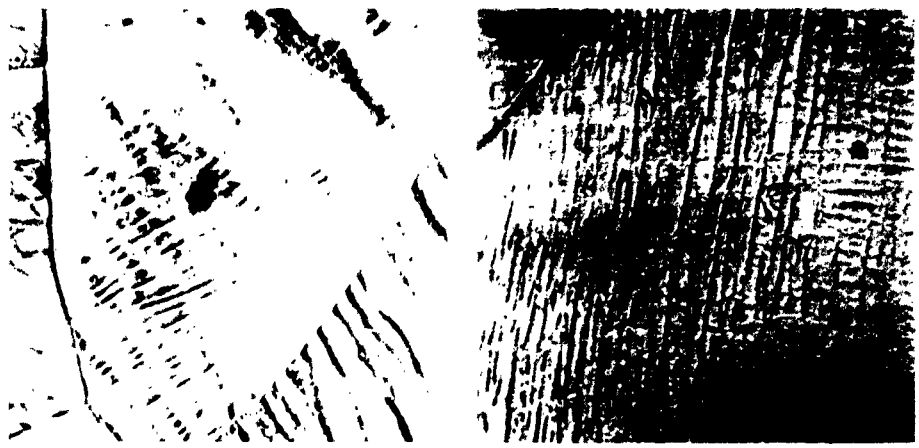

As strained 350°C 16 hrs

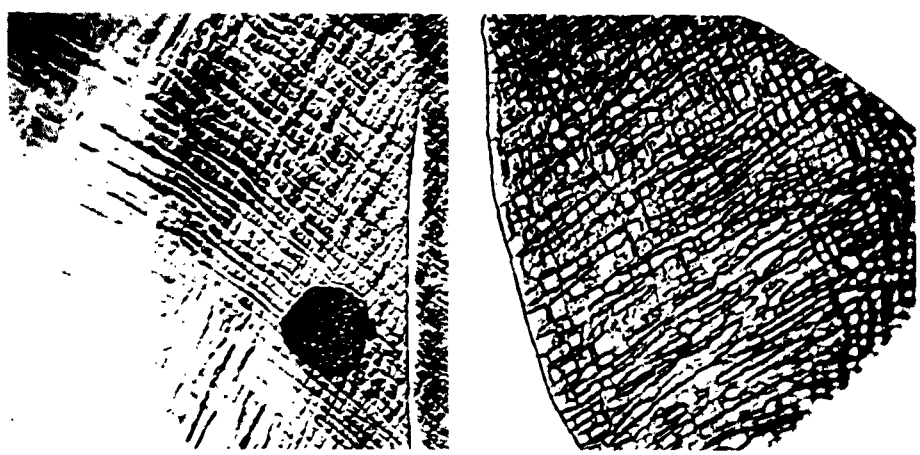

450°C 16 hrs 500°C 16 hrs

Substructure development in zone refined iron; 30 % strain; Gorsuch etchant; x 1000

Fig. 3

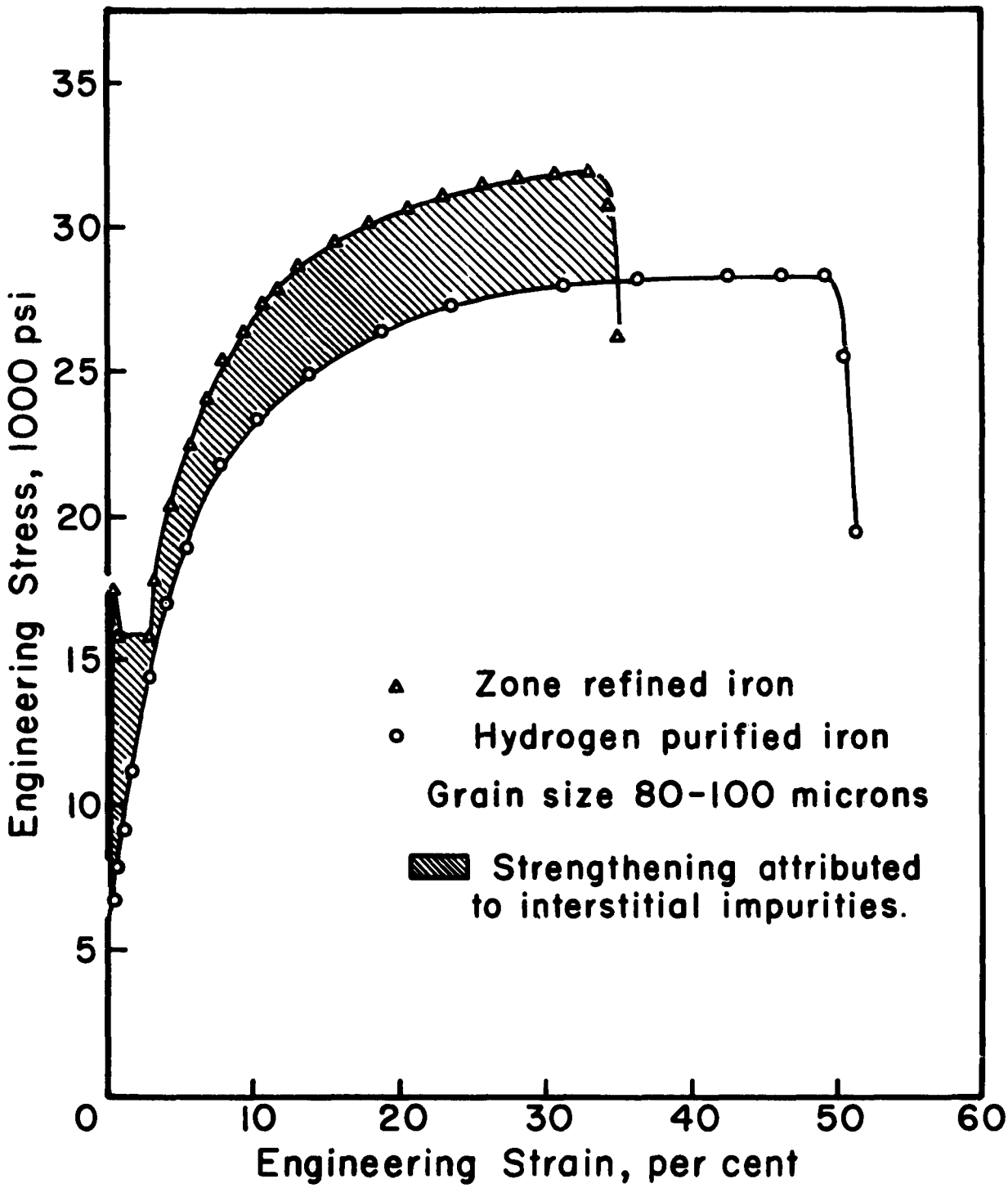

Figure 4. Stress–strain behavior of high-purity iron.

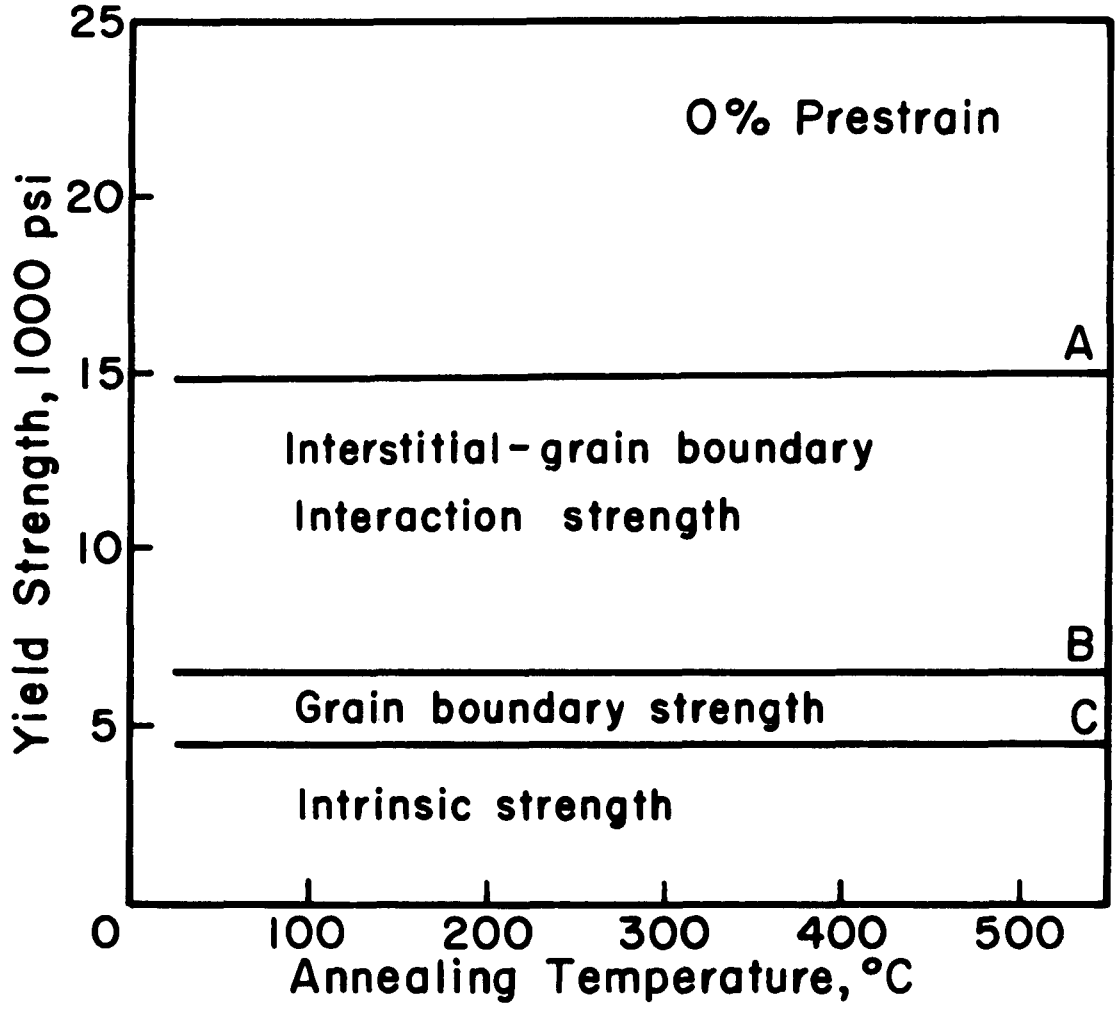

Figure 5 Analysis of the yield strength of zone refined iron.

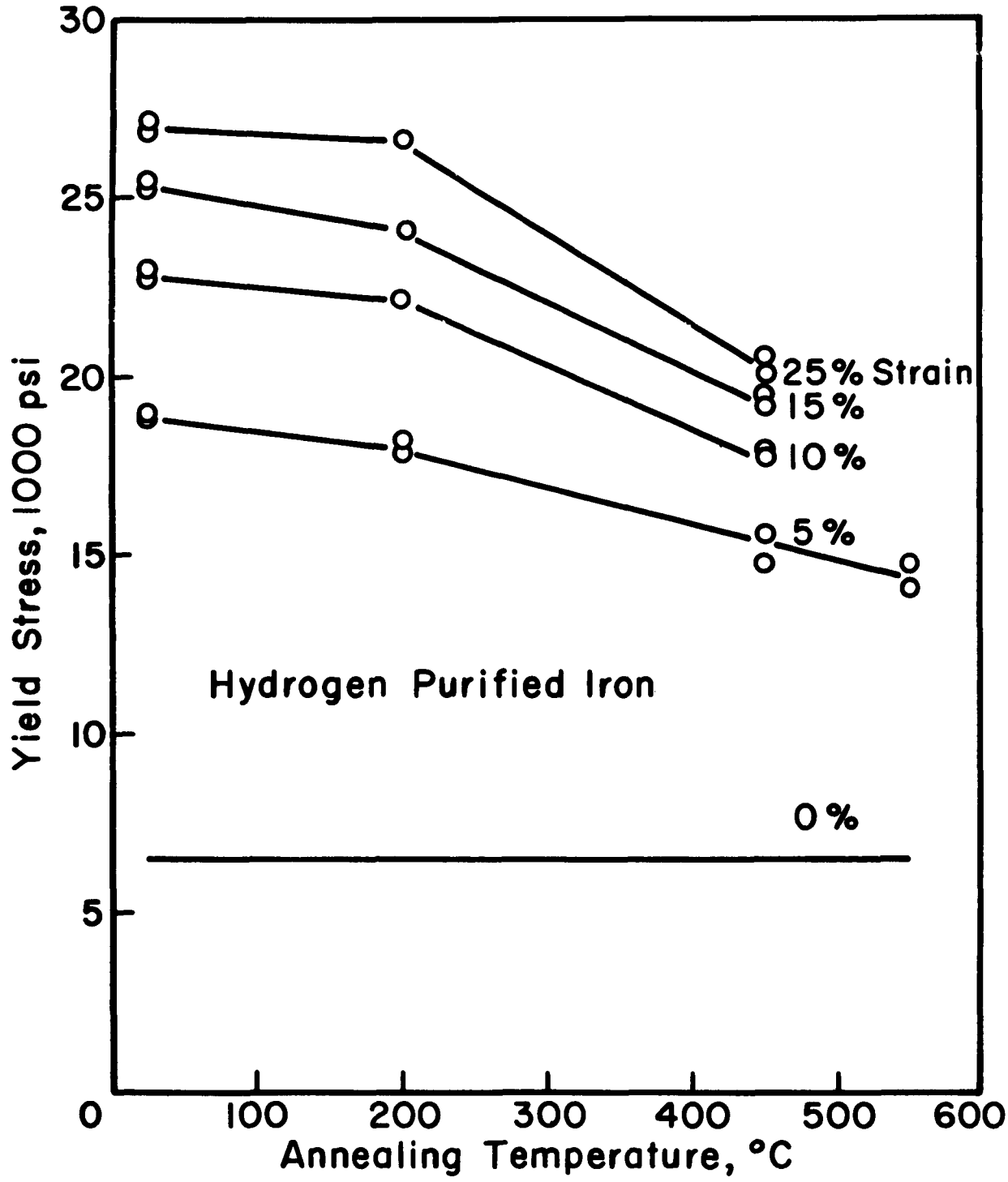

Figure 6 Effect of straining and annealing on yield strength.

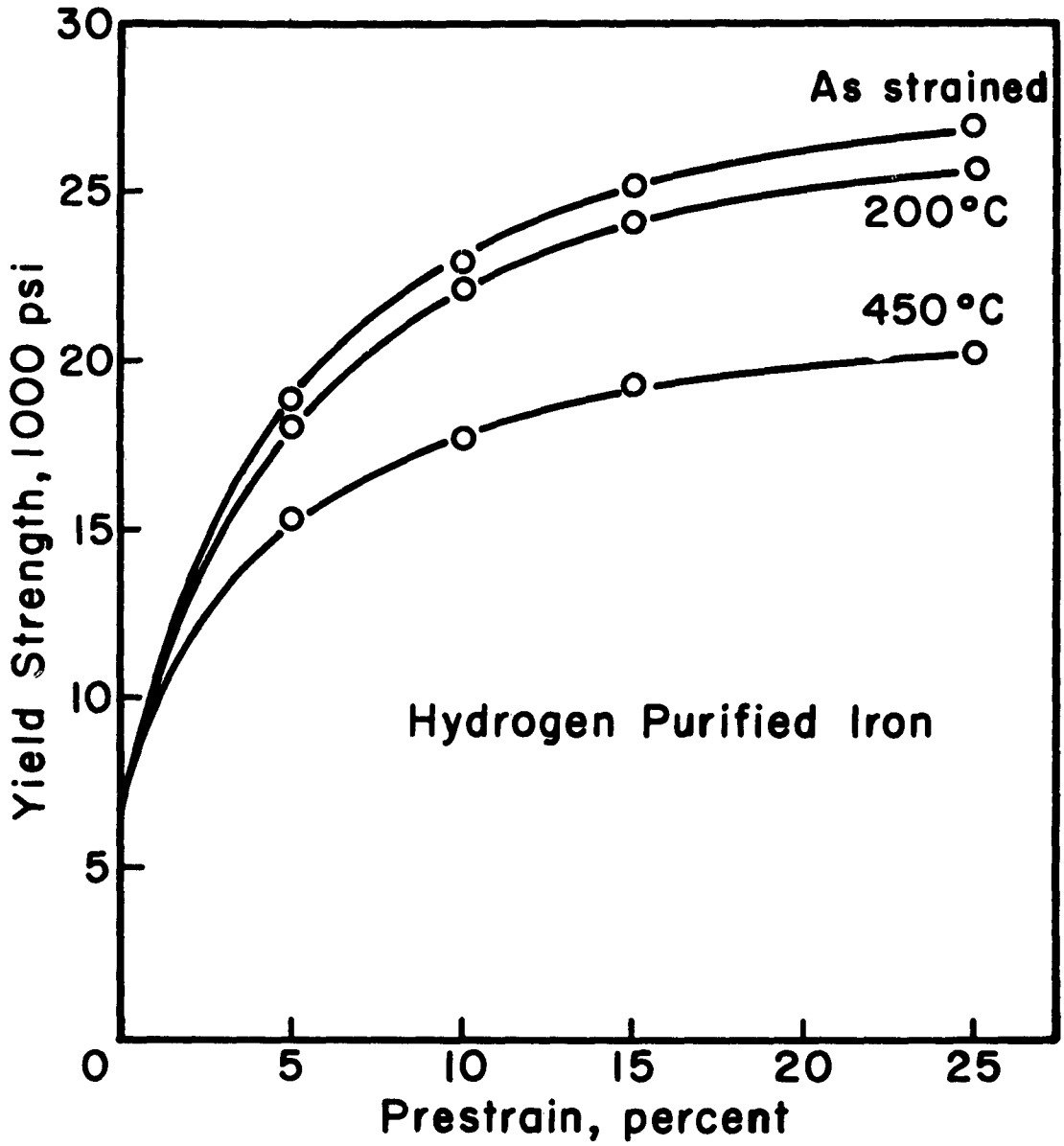

Figure 7 Effect of Prestrain on Yield Strength after Annealing

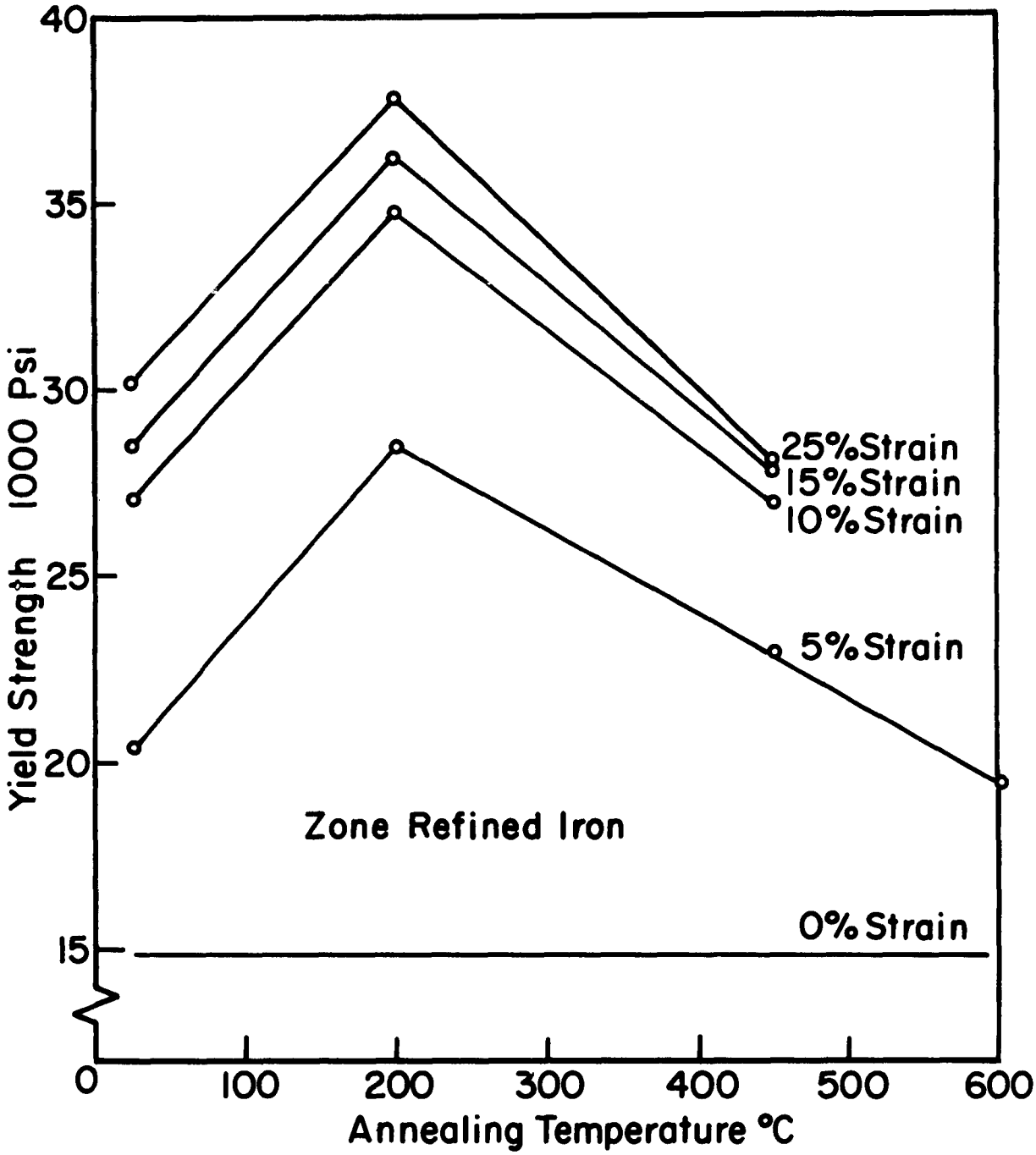

Figure 8. Effect of straining and annealing on yield strength.

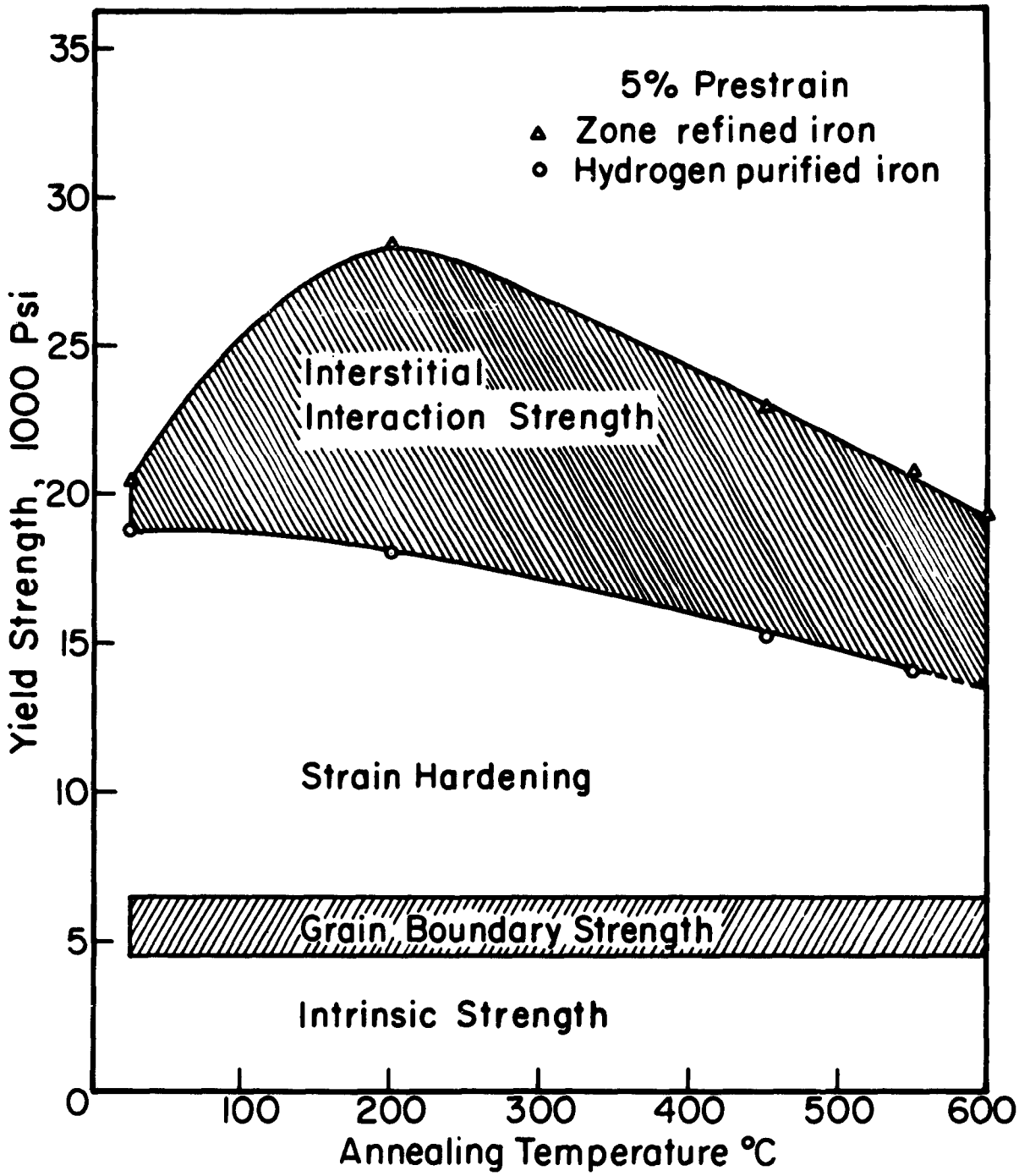

Figure9. Analysis of yield strength of zone refined iron after strain-anneal treatments

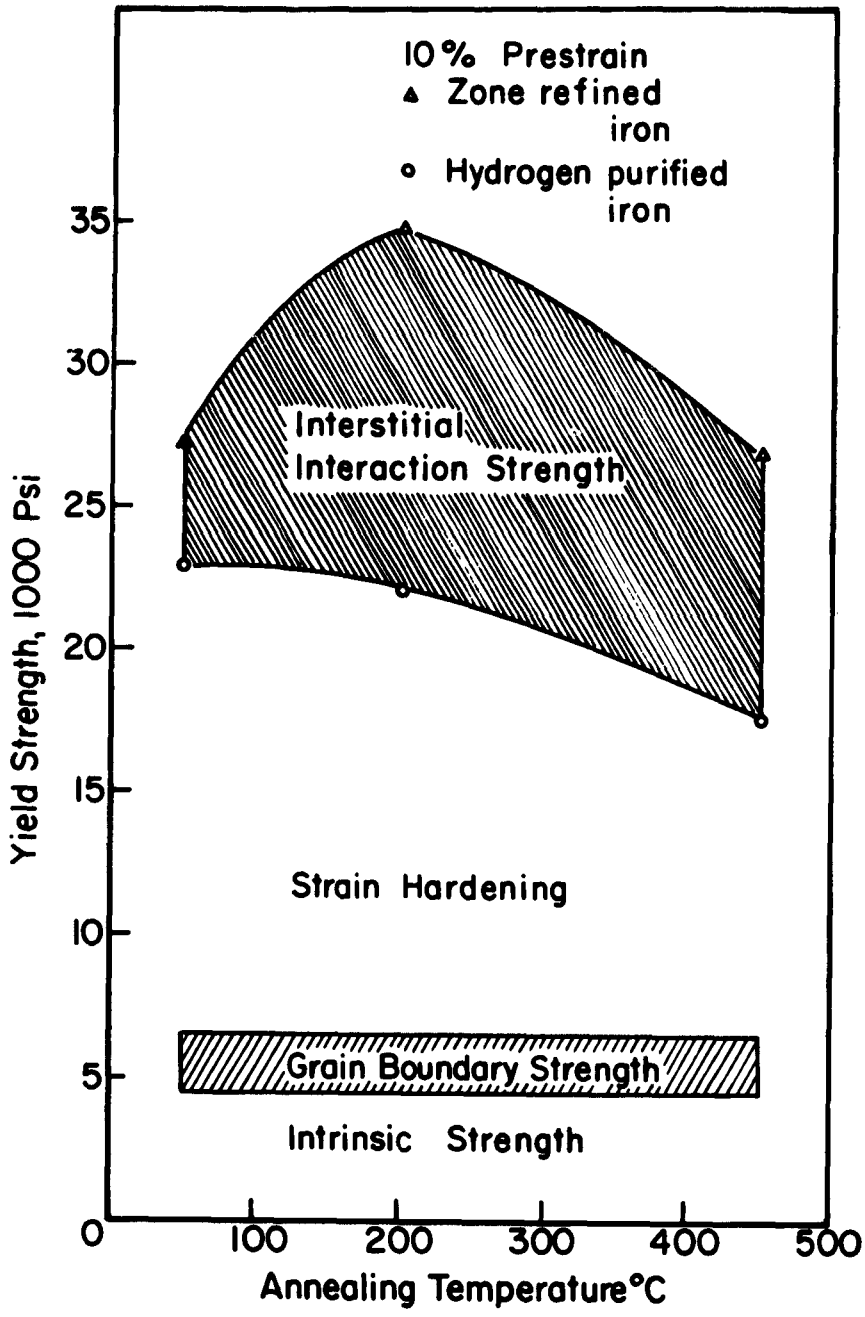

Figure 10. Analysis of yield strength of zone refined iron after strain-anneal treatments.

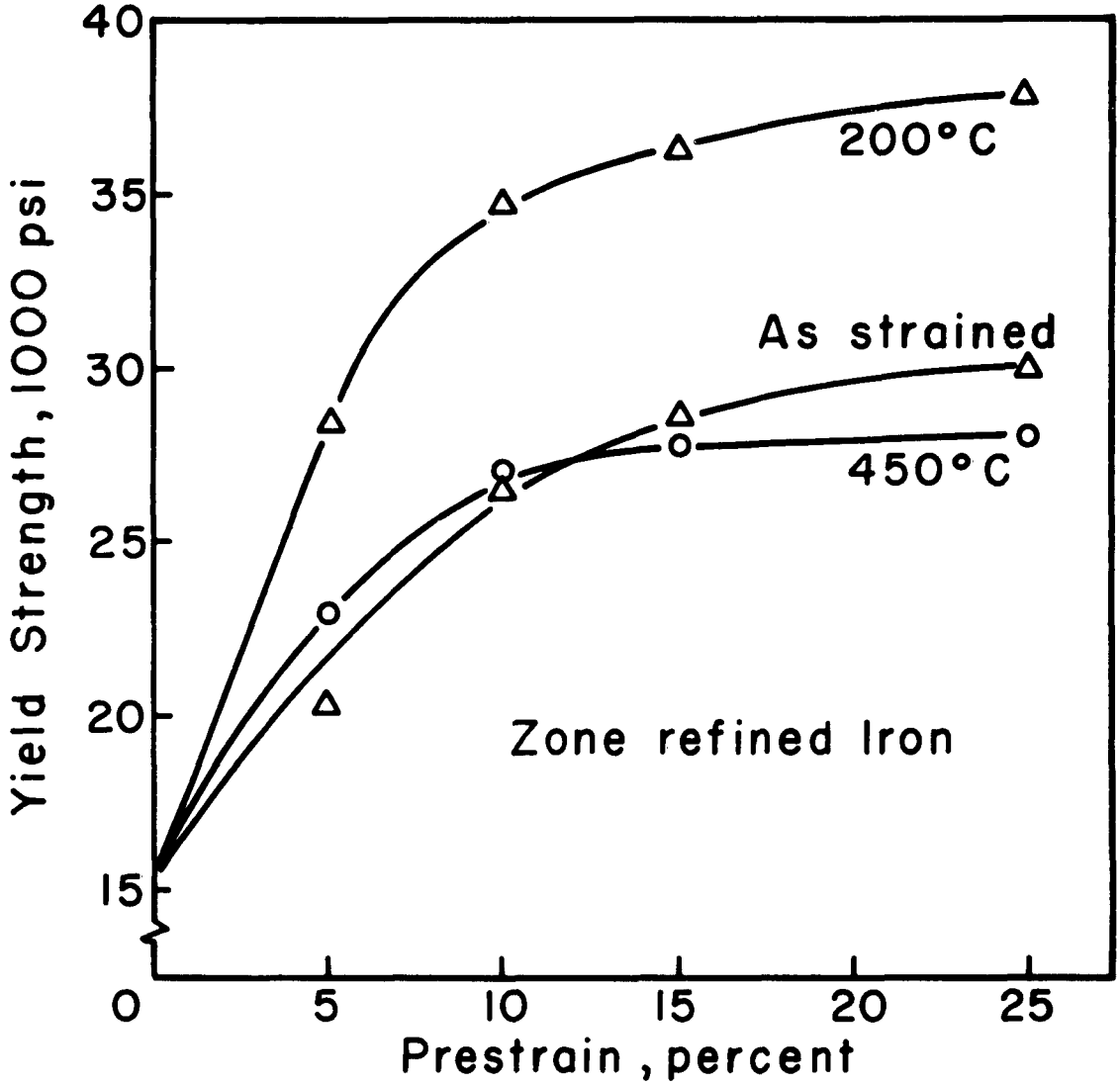

Figure 11 Effect of Prestrain on Yield Strength after Annealing

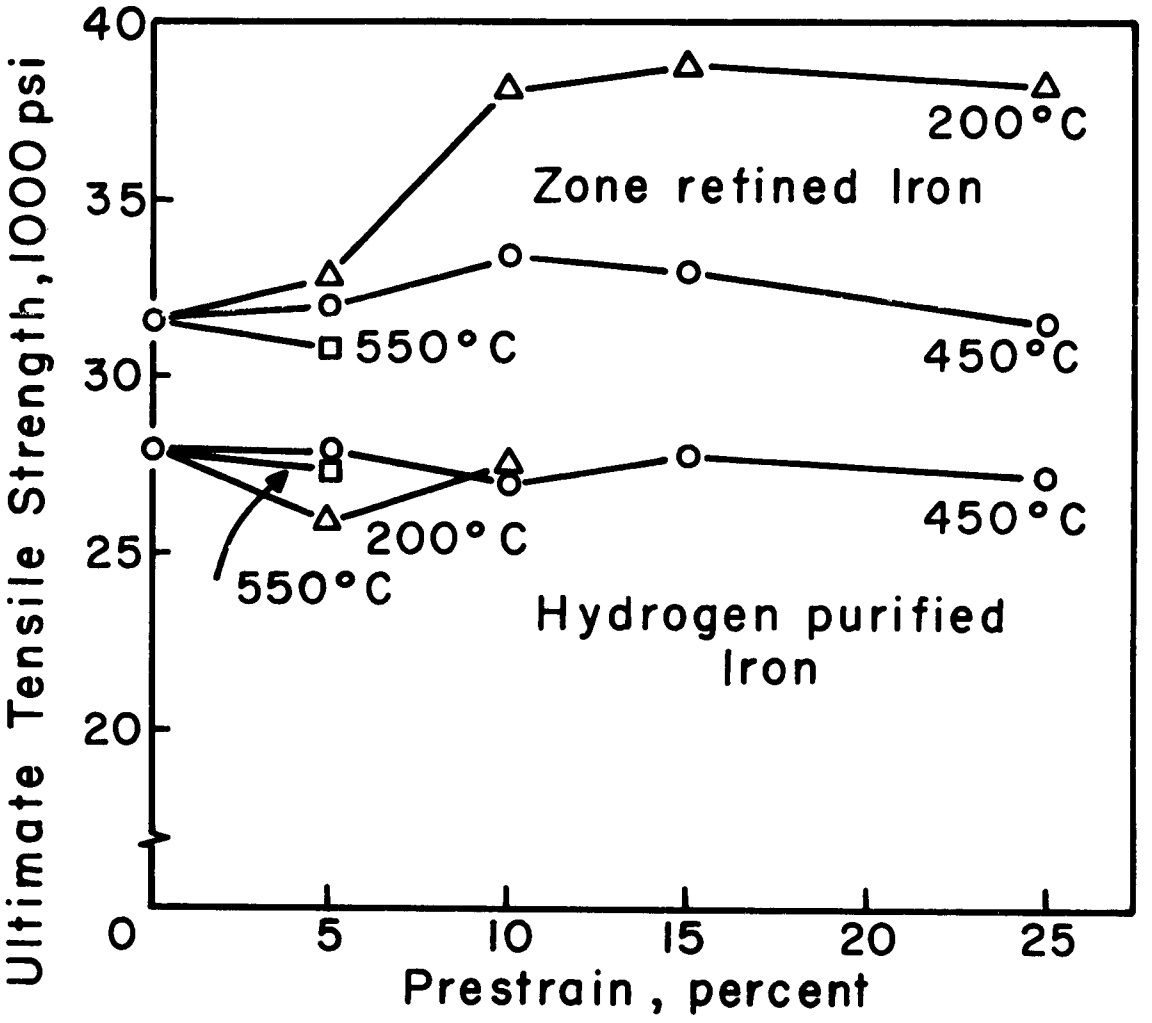

Figure 12 Variation of Ultimate Tensile Strength with Prestrain and Annealing Temperature

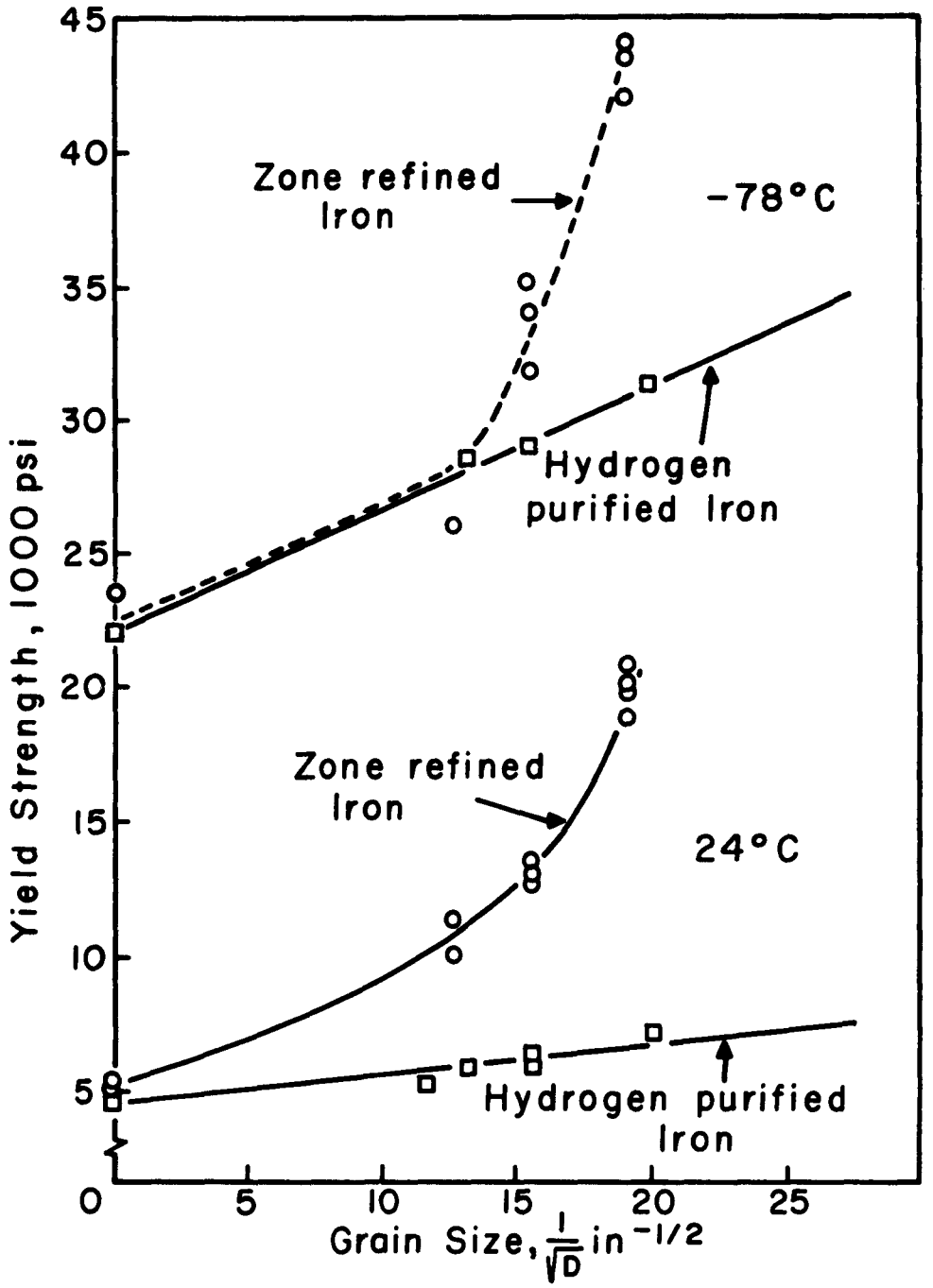

Figure 13 Variation of Yield Strength with Grain Size

Some Observations on the Development of Deformation Substructure in Zone-Refined Iron

J. T. Michalak and L. J. Cuddy
Edgar C. Bain Laboratory for Fundamental Research
United States Steel Corporation Research Center
Monroeville, Pennsylvania

Abstract

The development of the deformation substructure of zone-refined iron is similar to that observed for less pure vacuum-melted iron. Qualitative differences with increased purity are noted and are associated with a decrease in the dislocation sources and the necessity for cross-slip. Evidence is presented to show that, in the purest iron investigated, dislocation movement in the foil prepared for transmission electron microscopy is quite unrestricted and that the observed structures may not be typical of the dislocation density and distribution in the bulk.

Introduction

The importance of the substructure developed during plastic deformation of a body-centered-cubic metal cannot be denied. Keh (1) and Keh and Weissmann (2) have established experimentally a direct correlation of the dislocation density and distribution with the flow behavior of iron at 25 and -78°C. The relation between deformation substructure and mechanical properties of tantalum (3) and niobium (4) will be presented later in this Symposium. The role of substructure in recovery and recrystallization of iron and silicon-iron has been discussed by Leslie et al (5), Hu (6), and Walter (7). Substructure effects on strain aging in body-centered-cubic metals have been reviewed by Keh and Leslie (8), and by Rosenfield and Owen (9). The relations between substructure and precipitation phenomena are reviewed in other presentations of this Symposium (4,10).

The subject of this paper is the development of substructure during plastic deformation. Keh and Weissmann (2) have summarized the studies on the deformation substructure in body-centered-cubic metals and concluded that the dislocation structures of all of those investigated, which included iron, molybdenum, tungsten, tantalum and niobium, were similar. Dislocations were kinked and nonuniformly distributed in the early stage of deformation. As the amount of deformation was increased the distribution became more nonuniform and a cell structure was developed. This sequence of events is shown in Fig. 1. The walls of the cells are tangles of dislocations. For iron, the dislocation density was found to increase linearly with strain, and at a constant strain, to be independent of the deformation temperature below the temperature of recovery. The dislocation distribution in iron, however, was found to be temperature dependent; the distribution was more uniform and the tendency to form cells was decreased as the temperature of deformation was lowered. Keh and Weissmann (2) also showed that the relation between the dislocation density and the flow stress of iron was:

$$\sigma_f = \sigma_o + 0.17\ Gb\sqrt{N_f} \qquad (1)$$

where σ_f is the flow stress, σ_o is the frictional stress, G is the shear modulus ($=7.8\times10^3 kg/mm^2$), b is the Burgers vector of the slip dislocation in iron ($=2.5$ Å), and N_f is the dislocation density in the tangled regions. The change of the dislocation distribution with temperature, that is, the change in density within the tangles, accounts for the difference in flow behavior at different temperatures. Finally, it was observed that the dislocation density was dependent on grain size; a fine-grained iron exhibits a higher density of dislocations than does a coarse-grained iron strained to the same extent.

Materials and Experimental Procedure

The zone-refined iron and Fe-Mn alloy that have been studied by the present authors are listed in Table I, together with the method of purification and the final grain size obtained after cold work and recrystallization. In Table II the nominal content of carbon, nitrogen, hydrogen and oxygen is given in parts per million. All the materials were deformed in tension in bulk form and then thinned by electrolytic polishing to a final thickness suitable for examination by transmission electron microscopy.

Results and Discussion

A. Stress-Strain Behavior

The stress-strain curves for the polycrystalline, high-purity irons at several temperatures are given in Figs. 2-4. The results of tests at 25°C shown in Fig. 2 indicate that for the same grain size, there is not much difference in the tensile deformation of two irons of different overall purity. Reference to Table I indicates that iron B-3 had ten zone-refining passes compared to iron B-13 which received only one pass. It would be expected that the B-3 iron is the purer material, and although mechanical tests at 25°C do not support this, other differences in the behavior of these two irons do suggest that iron B-3 has less overall impurity. In processing these irons to a fine-grained aggregate from the zone-refined condition it was found that, after the same conditions of cold-rolling, iron B-13 required a recrystallization anneal at 650°C to produce a completely recrystallized uniform grain size of 43μ whereas iron B-3 could be recrystallized in the same time to the same uniform grain size at 600°C. The effects of small amounts of impurities on the recrystallization of iron have been investigated (11-13), and it has been observed that the purer the iron the lower the recrystallization temperature. It would appear, then, that room temperature tensile tests are not a reliable basis for evaluating the purity of iron. The lower stress levels of iron S-1, which is the least pure material on the basis of method of purification, can be accounted for by the larger grains in this iron, compared to the other two.

It will be noted from Fig. 3 that at -78°C a rather pronounced yield point drop becomes evident and that the rate of strain-hardening has decreased compared to room temperature tests. The pronounced yield point of the irons is a manifestation of an increased binding between interstitial atoms and potential dislocation sources as a result of a decrease in temperature. The increased yield point drop is not associated with a tearing away of dislocations from impurity atmospheres of increased binding, but rather with the decrease in the number of active sources of dislocations resulting from the increased binding. Keh and Weissmann (2) have suggested that the change in strain-hardening behavior with a change in temperature is associated with differences in the dislocation distribution during deformation at different temperatures. Although the average dislocation density is independent of test temperature, the dislocation distribution becomes more uniform as the temperature is decreased. Since the rate of work-hardening depends on

the density of dislocations within the tangled regions of the cell walls the more uniform distribution of dislocations results in a decreased rate of work hardening. The lower stress level and lack of a Lüders extension for iron S-1 is most probably a result of the larger grain size of this material.

The results of a temperature change during tests for iron B-3 are also shown in Fig. 3. They are consistent with the interpretation of Keh (1). He proposed that if a nonuniform distribution of dislocations is established by deformation at some temperature, then on subsequent testing at a lower temperature, characterized by a more uniform distribution, the flow stress at the lower temperature is greater than it would be if the specimen were strained to the same extent at the lower temperature only. The curvature of the stress-strain curve at the beginning of deformation at -78°C, after a prestrain at 25°C, makes it difficult to establish a well-defined initial flow stress at -78°C, but as can be seen, the flow stress at increasing strain rises above that for deformation only at -78°C, and the difference increases slightly with increased amount of prestrain at 25°C. As will be noted later, a strain of 3.75% at 25°C does not develop a gross nonuniform distribution of dislocations so that only a small difference in flow stress might be expected on subsequent straining at -78°C. Straining 7.5% at 25°C does develop some cell structure and a more nonuniform distribution so that continued deformation at -78°C results in the observed increase in flow stress.

Iron B-3 was the only high-purity iron which exhibited any plastic deformation at -196°C, and the results of testing at this temperature are shown in Fig. 4. Irons B-13 and S-1 failed predominantly by intergranular fracture at -196°C at stress levels of about 45-55 kg/mm^2.

Curve A in Fig. 4 represents the stress-strain behavior of iron B-3 deformed only at -196°C. Considerable twinning, as well as slip, was evident only during the Lüders extension. The Lüders extension in Fig. 4 is shown as a smooth line only for convenience. Fig. 5 is a light micrograph from a specimen, strained at -196°C, in which the Lüders front was allowed to pass through only about one-half of the gauge section. It is apparent from Fig. 3 and Fig. 4 that the rate of strain hardening, after the Lüders strain, is greater at -196°C than at -78°C, indicating a minimum in the temperature dependence of the rate of strain-hardening and a possible change in the mechanism of deformation at very low temperatures. A similar behavior has been observed by Keh and Weissmann (2).

Curves B, C and D of Fig. 4 are stress-strain curves at -196°C after a prestrain at 25°C of 0.75, 1.9 and 7.5% respectively. The prestrain at 25°C has eliminated completely the formation of twins at -196°C and, contrary to tests between 25 and -78°C, the flow stress at -196°C, after prestrain at 25°C, has not been increased above that for deformation only at -196°C. This observation also suggests a change in the mechanism of deformation as the temperature of deformation is decreased. This change in mechanism may be closely related to several observed factors: (a) the active

slip plane in iron becomes more restricted to the {110} planes (14) as the temperature is decreased; (b) the temperature dependence of the stress-velocity relationship for edge dislocations is greater for {112} planes than for {110} planes (15); (c) cross-slip of the screw dislocations becomes more difficult as the temperature is decreased (1,2).

B. Dislocation Sources

Before considering development of the deformation substructure it is necessary to establish what major source or sources of dislocations exist in the material prior to deformation. The sources of dislocations in any metal are: (a) random matrix dislocations, (b) the interfaces between the matrix and second-phase particles, (c) subboundaries within the grains, and (d) the grain boundaries. The random matrix dislocations which are not of the Frank-Read source type and which are not immobilized by impurity atmospheres will generate dislocations by the double cross slip mechanism (16), as has been shown by Low and Guard (17). The generation of dislocations at an inclusion-matrix interface under an applied stress has been reported (5,18). The formation of well-defined cell walls, after only light deformation, as a result of interaction of dislocations generated from closely spaced particles is illustrated in Fig. 6 from the work of Leslie, et al (5). Li (19) has considered the theoretical aspects of subboundary and grain boundary sources; Hornbogen (20) and Keh (1) have reported experimental evidence for subboundary and grain boundary sources. An example of dislocations originating from a grain boundary in an Fe-1.78 wt.% P alloy is shown in Fig. 7.

In fully recrystallized high-purity iron it has been observed that the number of second phase particles and subboundaries is so small as to be inconsequential as effective sources of dislocations. Likewise, the density of random dislocations, as measured by transmission electron microscopy and an X-ray technique discussed by Weissmann (21), is low and of the order of $10^6/cm^2$. Fig. 8 is a typical electron transmission micrograph of recrystallized high-purity iron illustrating this low dislocation density. Observations of dislocation loops emanating from grain boundaries (20), the "hairy" appearance of grain boundaries and the formation of irregular dislocation networks adjacent to the boundaries (1) after small deformations suggest that the grain boundaries and not the random matrix dislocations are the primary source of dislocations in high-purity iron. Li (19) has postulated that grain boundary ledges (or jogs) are the source of dislocations in the grain boundary. An example of the generation of a dislocation from a grain boundary ledge is shown in Fig. 9. The strain field of the ledge is shown only in one grain, although it could exist in both grains. It should be noted that this type of source is not a dislocation mill of the Frank-Read type which is capable of continuous generation. The grain boundary ledge is only a "donor" of dislocations and subsequent generation of dislocations within the grain can take place by the double cross-slip mechanism. According to Li's correlation between the density of grain boundary ledges and the Hall-Petch (22) slope, the decarburized Swedish iron studied by Codd and Petch (23) would have a ledge density of about 8×10^5 cm of ledge per cm^2 of grain boundary area. For a grain size of 100μ this would mean approximately 240 cm of ledge per grain, whereas the

nominal dislocation density within the grain of 10^6 cm/cm^3 provides about 0.5 cm of dislocation line within the grain. It is not unreasonable, then, that the primary source of dislocations is the ledges in the grain boundaries. Fig. 10 illustrates that ledges do in fact exist in the grain boundaries of a well annealed high-purity iron. The density of ledges in this micrograph is about 8×10^4/cm, a factor of ten less than that calculated for the Codd and Petch iron. A lower density of grain boundary ledges in a purer material is consistent with Li's analysis of the effect of impurities on the density of grain boundary ledges.

The micrographs of Fig. 11 illustrate the dislocation arrangements near grain boundaries in a sample strained 0.375% at 25°C. Fig. 11a is the arrangement near a boundary away from grain boundary junctions. It is characterized by few dislocation intersections. Fig. 10b shows that near a grain boundary junction there are more dislocations and more interactions due to the stress concentration at the junction. Occasionally a severe tangle can be found emanating from a grain boundary junction or from a region of change in orientation of the boundary, such as in Fig. 12.

C. Formation of Dislocation Tangles and Cell Structure

1. General Features

The change in dislocation density and distribution with increasing strain for iron S-1 is qualitatively similar to the changes in the less pure vacuum-melted iron previously reported (2). In the early stage of deformation the dislocations are generally kinked and nonuniformly distributed; as the amount of strain is increased, the distribution becomes more nonuniform, dislocation tangles are formed and finally a cell structure is developed. This sequence of events for iron S-1 is illustrated in Figs. 13 and 14. The deformation substructure in the higher purity iron is characterized by the more frequent observation of unkinked dislocations in areas removed from tangles, fewer tangles and less severe tangling at small amounts of strain as shown in Fig. 13a. The increased purity of the iron has reduced the tendency for the formation of jogs by reducing the interaction of dislocations with point defects (24), or by reducing the necessity for cross-slip of dislocations (25). The somewhat parallel arrangements of these unjogged dislocations would suggest that cross-slip, the more likely mechanism of jog formation, is reduced. This is probable, since the barriers which necessitate the cross-slip of dislocations are reduced with increased purity. Keh and Weissmann (2) have concluded that tangle formation is the result of interaction of dislocations of a secondary slip system with the jogs formed on primary slip dislocations by the cross-slip mechanism. The observation of fewer and less severe tangles is consistent with a reduction in density of interaction sites, the jogs, and a reduction in the density of grain boundary sources. Tangles may form by direct interaction of slip dislocations of two systems without the requirement of jog formation. In this case, the initial tangle is expected to consist of a rather regular network of dislocations. The arrangement could be a crossed grid (26) or an hexagonal network as observed in molybdenum (27). The hexagonal network arises from the dislocation

reaction

$$\frac{a}{2}[111] + \frac{a}{2}[1\bar{1}\bar{1}] = a[100]$$

Regular networks in individual tangles and cell walls have not been observed frequently in an as-strained vacuum melted iron, but they seem to be a common feature in the higher purity material, as can be seen in Fig. 13a and Fig. 15. The frequency of observation of these fairly regular networks in the tangles and in the cell walls developed from tangles indicates that interaction of dislocations on at least two slip systems is necessary for tangle formation and the development of the cell structure.

The zone axis of the possible crystallographic planes of a cell wall may be determined by means of selected-area diffraction and single-surface trace analysis. The zone axis is that crystallographic direction, in the plane of the foil, which is parallel to the trace of the cell wall in the plane of the foil. With very few exceptions, at least one of the planes of the zone has been of the $\{110\}$, $\{112\}$ or $\{123\}$ type. No other low-index planes have shown such a trend or occurred with the same frequency. This result strongly suggests that the plane of the cell wall in iron is then $\{110\}$, $\{112\}$ or $\{123\}$. The development of cell walls on these planes could be the result of the interaction of the dislocations of two slip systems to form the initial tangles on these planes or the result of cooperative motion of the tangles leading to alignment in the slip planes (2,28).

The development of deformation substructure in iron B-13 is similar to that in iron S-1. Lesser amounts of strain to produce a comparable structure were required since the grain size of B-13 was smaller.

The ten-pass zone-refined iron B-3 has presented two serious experimental difficulties which hinder study of this material by electron transmission microscopy. The production of usable thin foils has been sporadic and their preparation has required precise control of composition of polishing solution and polishing conditions. The more serious difficulty has been a decrease in the density of dislocations and an almost certain rearrangement as a result of the thinning operation. An excessive amount of dislocation motion, not typical of less pure iron, has been noted during examination of foils in the microscope. Fig. 16 is an illustration of the degree of movement of dislocations in foils of iron B-3. The variation of dislocation density and distribution in this iron is considerably more than normally encountered in this type of study. Irons S-1 and B-13 did not show such a large variation and the structures observed in these irons can be considered "typical". The inconsistency of the deformation substructure in a foil of B-3, as shown in Fig. 17, makes it difficult to define any single structure as typical of this material. For the purpose of discussion, the typical unaltered structure of this iron after deformation will be considered as that structure with the greatest dislocation density, the most severe tangles and the best developed cell structure. The change in deformation substructure with increasing strain for iron B-3 is shown in Figs. 18 and 19. A significant degree of tangling

and cell formation is accomplished only after about 5% strain at room temperature. An appreciable change in the flow stress at -78°C, after prestrain at room temperature, would not be expected for prestrains less than about 5%, in agreement with the tensile test results given in Fig. 3. Comparison with the structures of iron S-1, in Figs. 13 and 14, indicates that the distribution of dislocations is more uniform and the cell structure not as well developed in iron B-3. The limiting cell size for the vacuum-melted iron was 1.5μ whereas in this investigation the limiting cell size increases somewhat with increasing purity from 2μ for S-1 and B-13 to about 2.5μ for B-3. As the purity increases, the density of grain boundary ledge sources decreases and the necessity for cross-slip decreases. A decrease in these two factors leads necessarily to a decreased dislocation density, fewer and less severe tangles, and consequently a larger cell structure with a more regular distribution of dislocations within the cell walls. Dynamic recovery at room temperature in the purer irons could also result in a larger cell size with cell walls of somewhat regular networks of dislocations.

2. Effect of Deformation Temperature on the Dislocation Distribution

As previously reported (2), the tendency for cell formation becomes less and the dislocation distribution becomes more uniform for a given strain as the temperature of deformation is decreased. The dislocation structures of iron S-1 deformed at 25 and -78°C to about the same strain are shown in Fig. 20. The dislocation distribution at -78°C is considerably more uniform and the dislocations are more uniformly kinked than at 25°C. This structure has been explained on the basis of more frequent cross slip, but over smaller distances than at room temperature (2). Figs. 21 and 22 illustrate that the same temperature effect on the distribution of dislocations is present in iron B-3. In this iron, however, the dislocations formed by low temperature deformation do not appear to be severely kinked as in iron S-1, nor as uniformly distributed, and occurrence of loose tangles is also more frequent. These observations are consistent with dislocation movement, resulting from the thinning operation. Such movement could cause a decrease in the density of jogs on the dislocations and rearrangement of a uniform distribution to a less uniform distribution.

The dislocation structures developed in iron B-3 by deformation at -196°C are shown in Fig. 23. The distribution is much more uniform consisting of at least two sets of parallel dislocations; tangles are not formed up to the point of fracture of this iron at about 14% strain. The curvatures at dislocation intersections, such as shown in Fig. 24, suggest that possibly three slip systems were active in this particular grain. Two of the sets of dislocations have the same Burgers vector and at the point of intersection there is mutual annihilation and a rounding off of the intersection point, as indicated in area A in Fig. 24. The third set of parallel dislocations has a different Burgers vector, such that there is interaction to form an a[100] segment at the point of intersection. In this case, the sharp points of the dislocation interaction remain, and examination of Fig. 24 reveals that the a [100] segments have two directions as is expected. This interaction is noted at points B and C in Fig. 24.

3. Effect of Strain Rate on the Dislocation Distribution

The effect of increasing the strain rate of deformation is analogous to decreasing the temperature of deformation, that is, the tendency for cell formation becomes less pronounced and the dislocation distribution becomes more uniform for a given strain as the strain rate is increased. The degree of change in dislocation distribution with a change in strain rate is not as marked as for a change in temperature. Differences are most apparent at small amounts of deformation and for changes in strain rate of several orders of magnitude. Fig. 25 illustrates the difference in dislocation distribution in iron S-1 strained 2.5% at strain rates of 2.5×10^{-5} sec^{-1} and 1.25×10^{-2} sec^{-1}. These structures may also be compared with that shown in Fig. 13a. The dynamic theory of yielding proposed by Johnston and Gilman (29) requires either an increase in the number of mobile dislocations or an increase in the average velocity of dislocations to accommodate an increase in strain rate. The more uniform distribution of dislocations could be accomplished by an increase in the amount of cross-slip to increase the number of mobile dislocations or an increase in the velocity of the edge components of dislocations relative to the velocity of the screw components. The latter would result in mainly screw dislocations being left in the structure. Since the densities of dislocations are not very different, as is also the case for low temperature deformation (2), it may be assumed that the uniform distribution is more likely the result of an increase in the velocity of edge dislocations.

As the amount of strain is increased the differences due to strain rate become less apparent and a well developed cell structure is formed.

4. Effects of Alloying on Dislocation Distribution

The influence of alloy additions on the dislocation arrangements in iron has not received much study except for iron-silicon (30), iron-phosphorus (20), and iron-manganese (5) alloys. In the first two cases the effect of alloy addition was to decrease the tendency for cell formation and to produce a more uniform distribution of dislocations. The effect is analogous to lowering the temperature or increasing the strain rate of deformation. It is well known that silicon and phosphorus are very pronounced solid-solution strengtheners and substantially increase the tendency for mechanical twinning. Manganese is not nearly as potent a solid-solution strengthener and has been reported (5) to result in a less uniform distribution of dislocations and to increase the tendency for cell formation at room temperature, as shown in Fig. 26. An increase in alloy content would result in an increase in grain boundary sources thus leading to increased dislocation density and enhanced cell formation. The differences in dislocation distribution for different alloy additions cannot be explained solely on changes on the density of grain boundary sources. In the case of silicon or phosphorus additions the random distribution has been attributed to a decreased mobility of the dislocations and, in particular, a greater decrease in the mobility of screw components. The decrease could be the result of an increased frictional stress or an increase in the density of vacancies which might interact with the screw dislocations to form jogs. The addition of

0.6 wt.% manganese apparently does not markedly influence the relative mobilities of the edge and screw dislocations and therefore the distribution of dislocations does not tend to be random. The effect of manganese, therefore, is primarily to increase the average density for a given strain by increasing the density of grain boundary sources. The binding effect of manganese on these sources is small since the difference in yield stress of pure iron and iron-0.6 wt.% manganese is not large (5).

The increased tendency for retention of a nonuniform distribution and the formation of tangles and cell walls in the manganese alloy is also observed at lower temperatures or increased strain rates. This may be seen by comparison of Fig. 27a with Fig. 20b and Fig. 27b with Fig. 25b.

4. Summary

1. The development of deformation substructure in zone-refined iron is similar to that reported for vacuum-melted iron and other body-centered cubic metals.

2. The primary effect of increased purity is to decrease the density of grain boundary sources and to decrease the necessity for cross-slip. This results in fewer and less severe tangles of dislocations and a small increase in the size of cells.

3. The cell walls in the purer iron consist of somewhat regular networks of dislocations, as do the initial tangles.

4. In a very high-purity iron the dislocation density may decrease and the dislocations may change their distribution as a result of the thinning process.

5. A decrease in the temperature of deformation or an increase in the strain rate decreases the tendency for cell formation and produces a more uniform distribution of dislocations.

6. The addition of an alloying element which is not a strong solid-solution strengthener increases the dislocation density and tendency for cell formation primarily by increasing the density of grain boundary sources.

Acknowledgment

The authors wish to thank J. C. Raley and R. D. Schoone for their assistance in this investigation. The zone-refined materials prepared by Battelle Memorial Institute under the sponsorship of the American Iron and Steel Institute were obtained through the courtesy of J. W. Halley. The ten-pass zone-refined iron was prepared by B. F. Oliver of the E. C. Bain Laboratory, U. S. Steel Corporation. We are indebted to A. S. Keh and J. C. M. Li, also of this Laboratory, for helpful discussions.

References

1. A. S. Keh, Direct Observations of Imperfections in Crystals, Interscience, New York, 1962, 213.

2. A. S. Keh and S. Weissmann, to be published.

3. W. S. Owen, this symposium, paper 9.

4. A. Berghezan, this symposium, paper 17.

5. W. C. Leslie, J. T. Michalak and F. W. Aul, to be published, Iron and Its Dilute Solid Solutions, Interscience.

6. H. Hu, to be published, Recovery and Recrystallization of Metals, Interscience.

7. J. L. Walter, this symposium, paper 8.

8. W. C. Leslie and A. S. Keh, J. Iron Steel Inst. 200, 722 (1962).

9. A. R. Rosenfield and W. S. Owen, this symposium, paper 14.

10. A. S. Keh, W. C. Leslie and G. R. Speich, this symposium, paper 16.

11. W. C. Leslie, F. J. Plecity and J. T. Michalak, Trans. AIME 221, 691 (1961).

12. W. C. Leslie, F. J. Plecity and F. W. Aul, Trans. AIME 221, 982 (1961).

13. E. P. Abrahamson, II and B. S. Blakeney, Jr., Trans. AIME 218, 1101 (1960).

14. J. J. Cox, G. T. Horne and R. F. Mehl, Trans. ASM 49, 118 (1957).

15. J. S. Erickson, J. Appl. Phys. 33, 2499 (1962).

16. J. S. Koehler, Phys. Rev. 86, 52 (1952).

17. J. R. Low, Jr. and R. W. Guard, Acta Met. 7, 171 (1959).

18. W. C. Leslie, Acta Met. 9, 1004 (1961).

19. J. C. M. Li, to be published, Trans. AIME.

20. E. Hornbogen, to be published, Trans. ASM.

21. S. Weissmann, Trans. ASM 52, 599 (1960).

22. E. O. Hall, Proc. Phys. Soc. B64, 747 (1951).

23. I. Codd and N. J. Petch, Phil. Mag. 5, 30 (1960).

24. J. T. Fourie and H. G. T. Wilsdorf, J. Appl. Phys. 31, 2219 (1960).

25. W. G. Johnston and J. J. Gilman, J. Appl. Phys. 31, 632 (1960).

26. J. C. M. Li, J. Appl. Phys. 32, 1873 (1961).

27. R. Benson, G. Thomas, and J. Washburn, Direct Observation of Imperfections in Crystals, Interscience, New York, 1962, 375.

28. J. C. M. Li, Direct Observation of Imperfections in Crystals, Interscience, New York, 1962, 234.

29. W. G. Johnston and J. J. Gilman, J. Appl. Phys. 30, 129 (1959).

30. J. R. Low, Jr. and A. M. Turkalo, Acta Met. 10, 215 (1962).

Table I

High-Purity Materials Investigated

Material	Designation	Method of Purification	Grain Size
Fe*	S-1	Zone-melted in horizontal boat. Two passes.	90μ
Fe*	B-13	Zone-refined by floating-zone technique. One pass.	43μ
Fe**	B-3	Zone-refined by floating-zone technique. Ten passes.	42μ
Fe-0.60 Mn*	S-8	Zone-melted in horizontal boat. One pass.	60μ

* Supplied by Battelle Memorial Institute.

** Supplied by B. F. Oliver, United States Steel Corporation.

Table II

Nonmetallic Impurity Contents, PPM

Material	C	N	H	O
S-1	15	6	0.2	25
B-13	10	<0.05	0.9	1.2
B-3	15	5	<1	<5
S-8	15	6	0.4	25

(a) INITIAL, RECRYSTALLIZED

(b) 1 % STRAIN

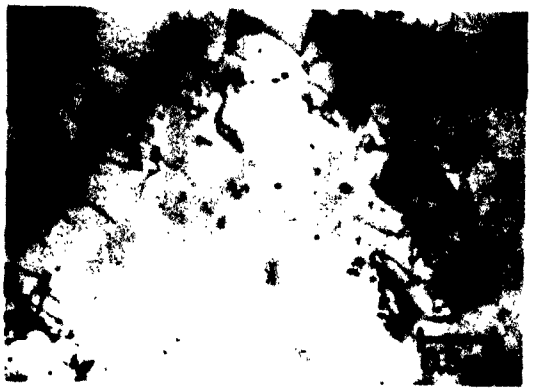

(c) 3 1/2 % STRAIN

(d) 9 % STRAIN

(e) 20 % STRAIN

FIG. 1 -- DEVELOPMENT OF DEFORMATION SUBSTRUCTURE IN IRON. (See ref. 2).

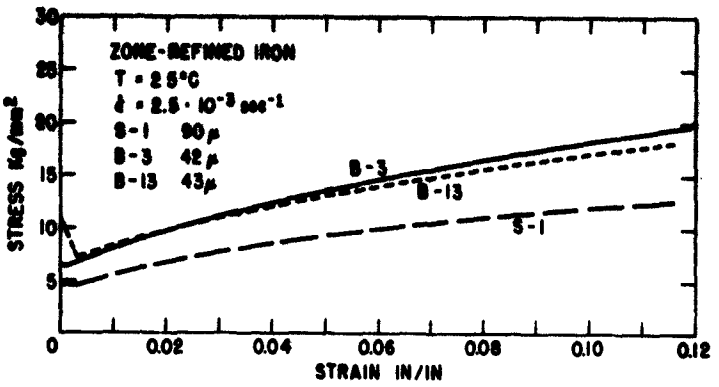

FIG. 2 -- STRESS-STRAIN CURVES FOR POLYCRYSTALLINE HIGH-PURITY IRON DEFORMED AT 25°C.

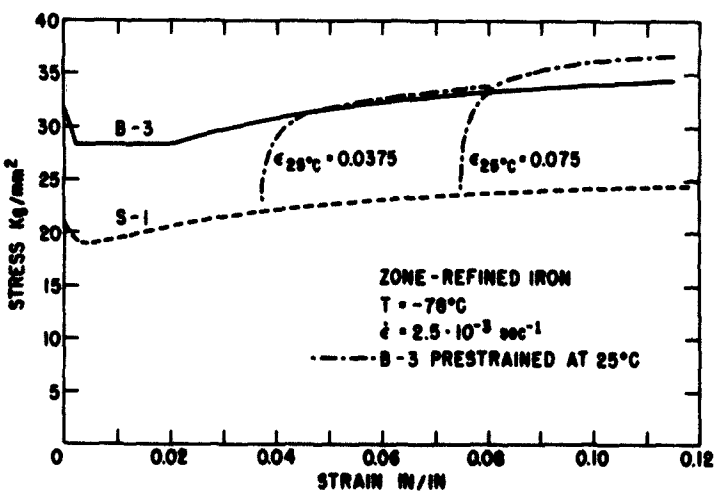

FIG. 3 -- STRESS-STRAIN CURVES FOR POLYCRYSTALLINE HIGH-PURITY IRON DEFORMED AT -78°C.

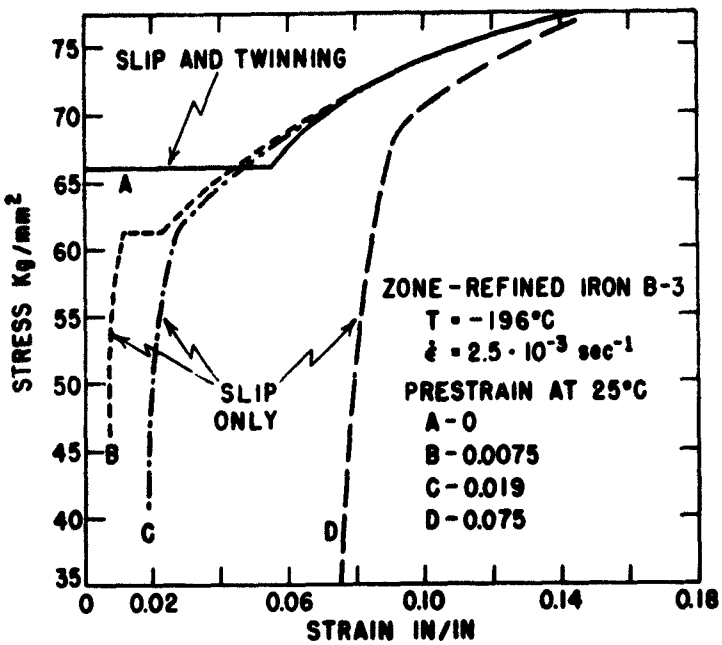

FIG. 4 -- STRESS-STRAIN CURVES FOR POLYCRYSTALLINE HIGH-PURITY IRON DEFORMED AT -196°C.

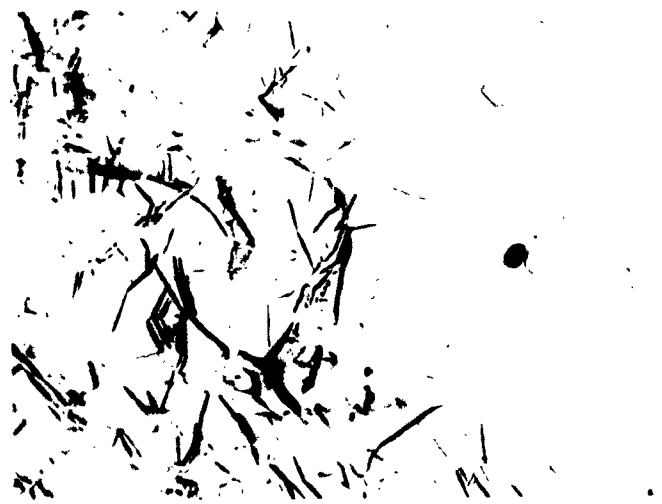

FIG. 5 -- LUDERS FRONT IN IRON B-3 STRAINED AT -196°C. 100X. UNETCHED SURFACE.

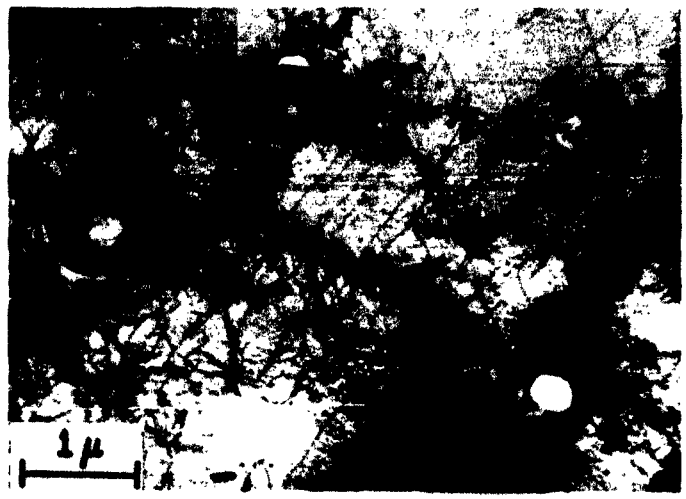

FIG. 6 -- WELL-DEVELOPED CELLS AROUND LARGE PRECIPITATED PARTICLES. Fe-0.015% Bi, C. R. 10%, LONGITUDINAL SECTION. (See ref. 5).

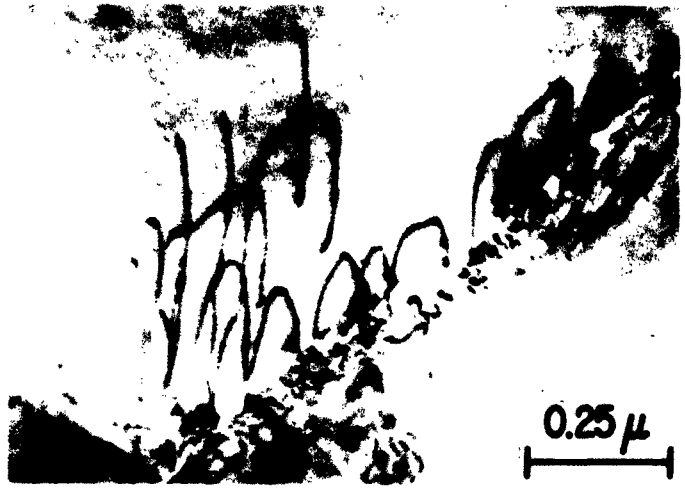

FIG. 7 -- DISLOCATIONS ORIGINATING AT A GRAIN BOUNDARY. Fe-1.78 wt. % P, 1.0% STRAIN. (See ref. 20).

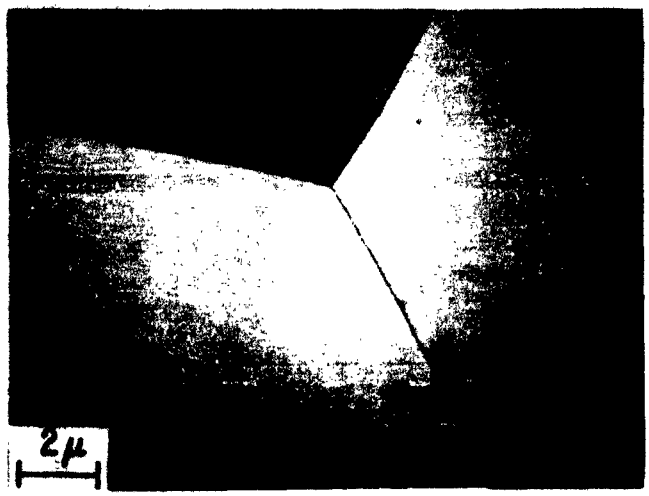

FIG. 8 -- STRUCTURE OF RECRYSTALLIZED GRAINS IN IRON.

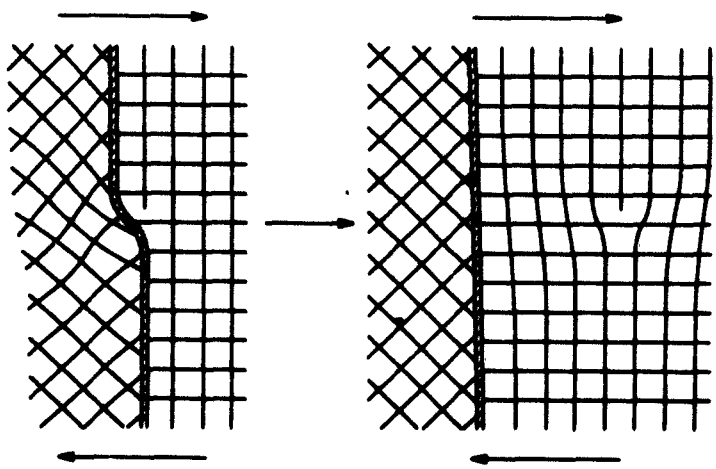

FIG. 9 -- GRAIN BOUNDARY LEDGE ACTING AS DONOR OF DISLOCATION. (See ref. 19).

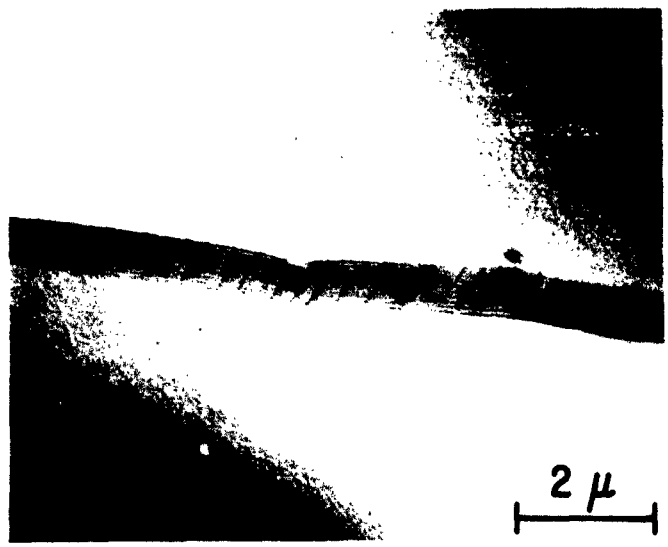

FIG. 10 -- GRAIN BOUNDARY LEDGES IN RECRYSTALLIZED IRON.

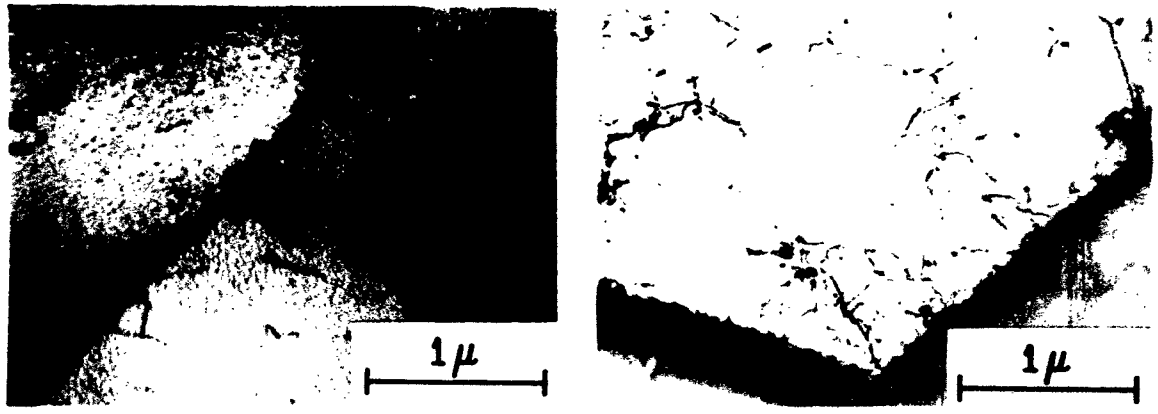

FIG. 11 -- DISLOCATION ARRANGEMENTS IN IRON STRAINED 0.375% AT 25°C, (a) AT GRAIN BOUNDARY, (b) AT GRAIN BOUNDARY JUNCTION.

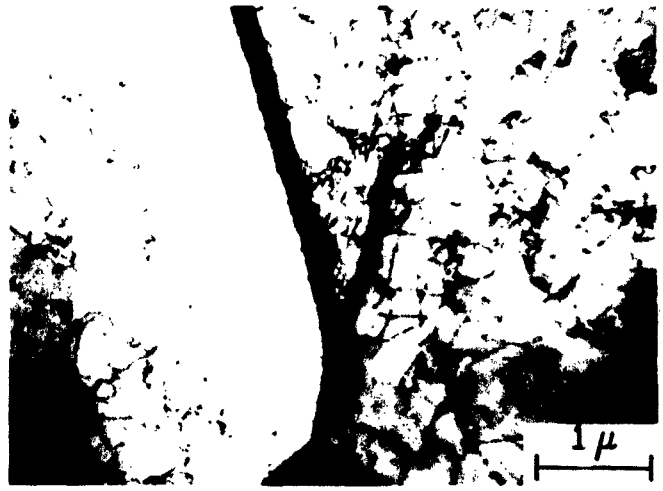

FIG. 12 -- DISLOCATION TANGLE INITIATED FROM A GRAIN BOUNDARY KINK.

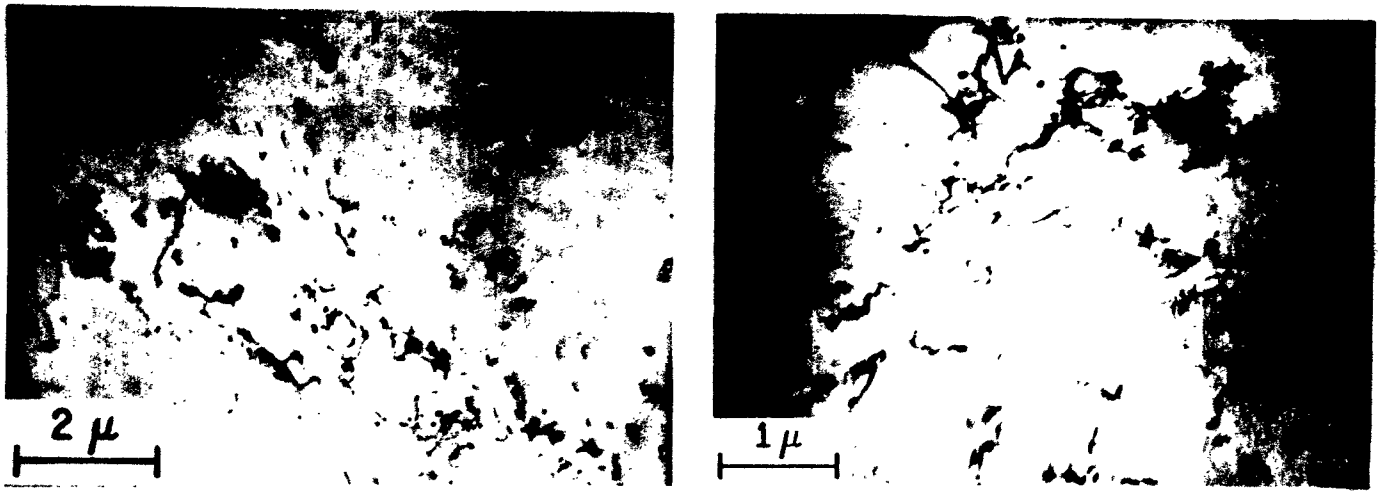

FIG. 13 -- DISLOCATION STRUCTURE IN IRON S-1 STRAINED AT 25°C. (a) 2.5% STRAIN, (b) 4% STRAIN.

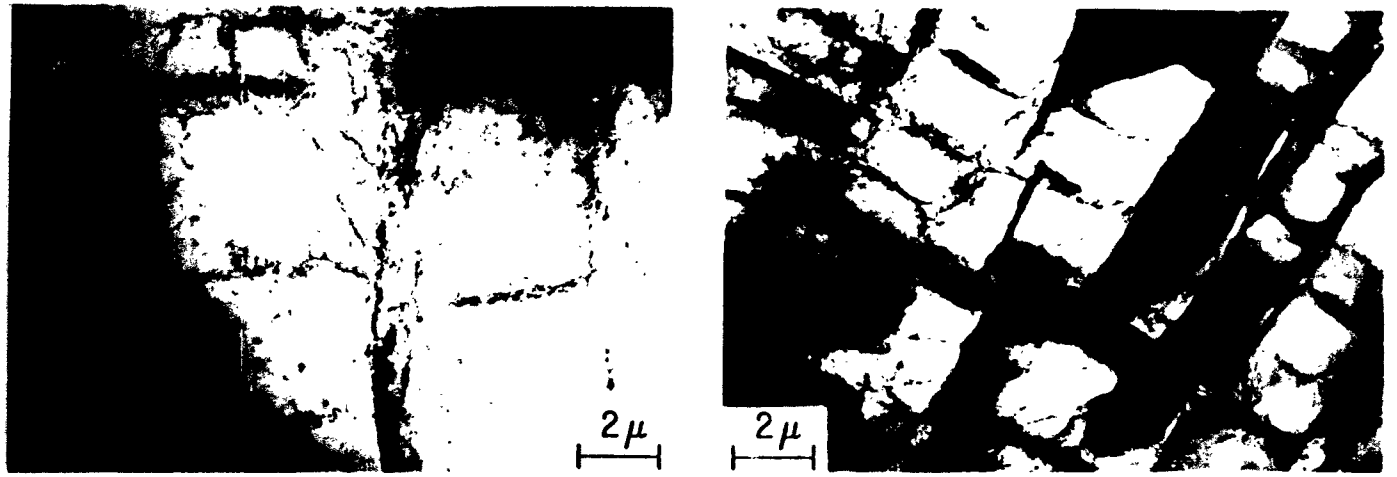

FIG. 14 -- DISLOCATION STRUCTURE IN IRON S-1 STRAINED AT 25°C. (a) 7.0% STRAIN, (b) 15% STRAIN.

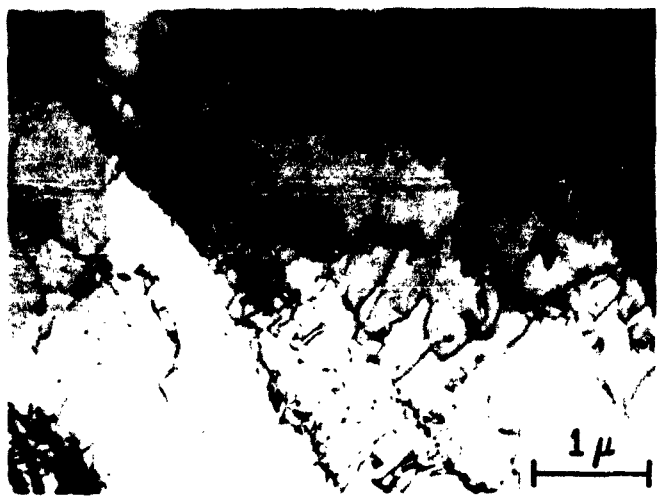

FIG. 15 -- REGULAR NETWORKS OF DISLOCATIONS IN CELL WALLS OF IRON.

FIG. 16 -- TRAILS OF MOVING DISLOCATIONS IN IRON B-3.

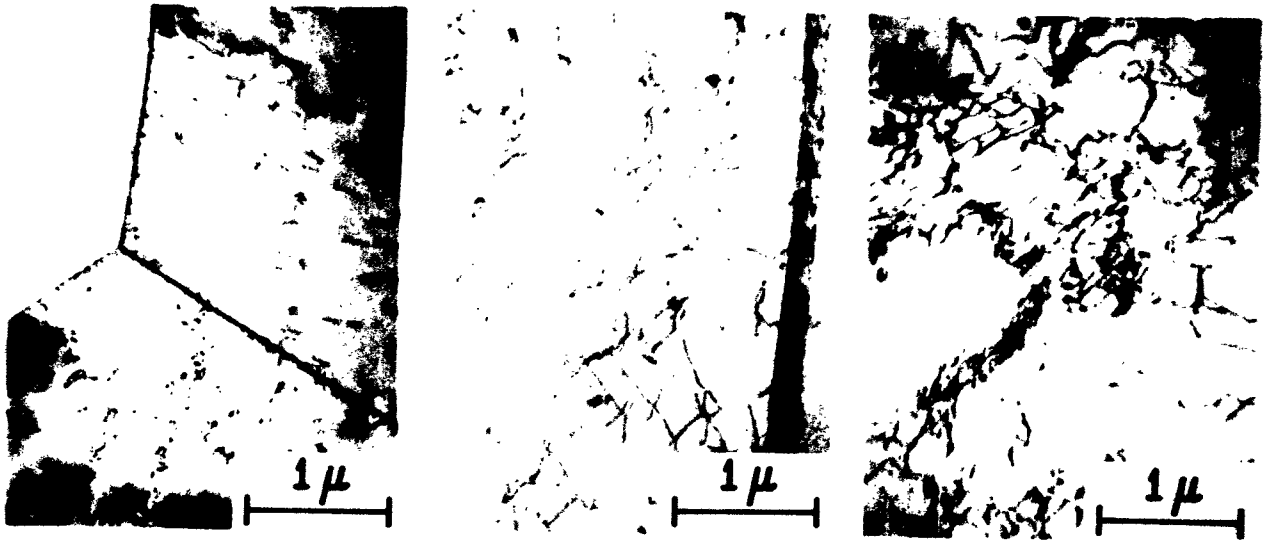

FIG. 17 -- VARIATION OF DISLOCATION STRUCTURE IN IRON B-3 AFTER 5.5% STRAIN AT 25°C.

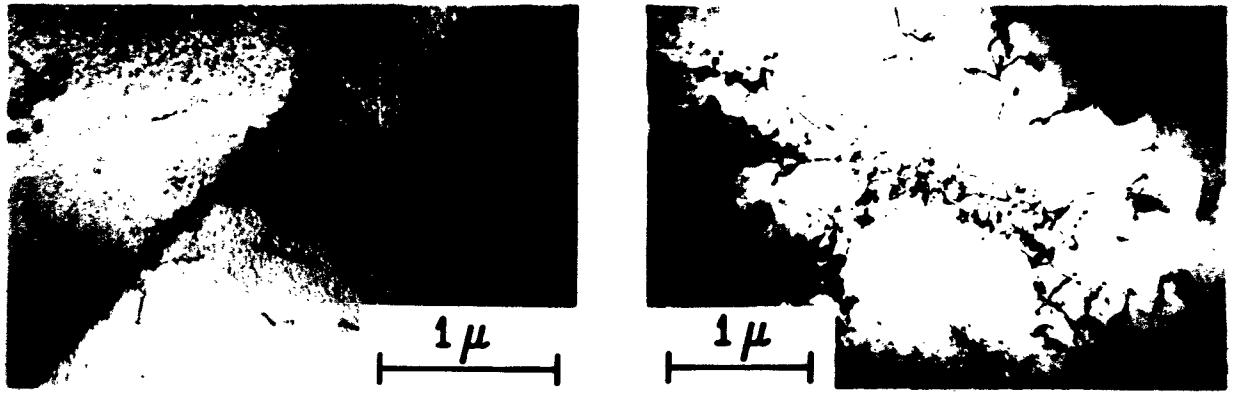

FIG. 18 -- DISLOCATION STRUCTURE IN IRON B-3 STRAINED AT 25°C. (a) 0.375% STRAIN, (b) 2.5% STRAIN.

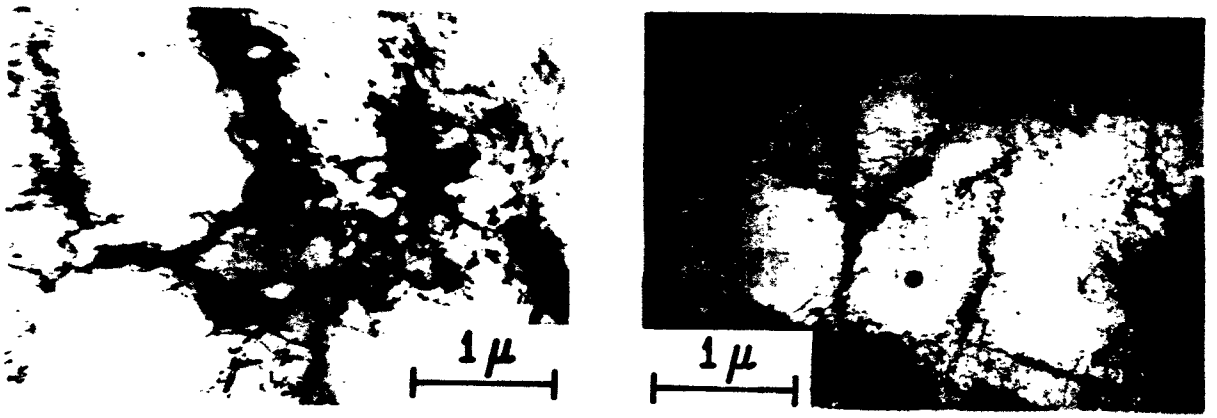

FIG. 19 -- DISLOCATION STRUCTURE IN IRON B-3 STRAINED AT 25°C. (a) 5.5% STRAIN, (b) 15.5% STRAIN.

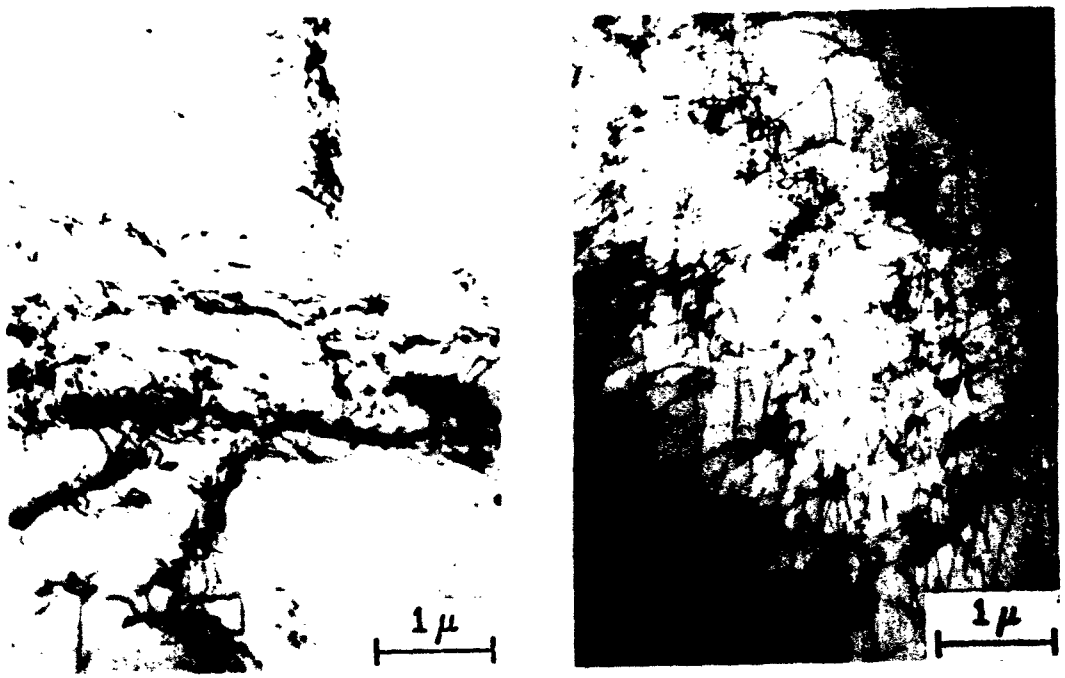

FIG. 20 -- DISLOCATION STRUCTURE IN IRON S-1 STRAINED 7.0% AT (a) 25°C AND (b) -78°C.

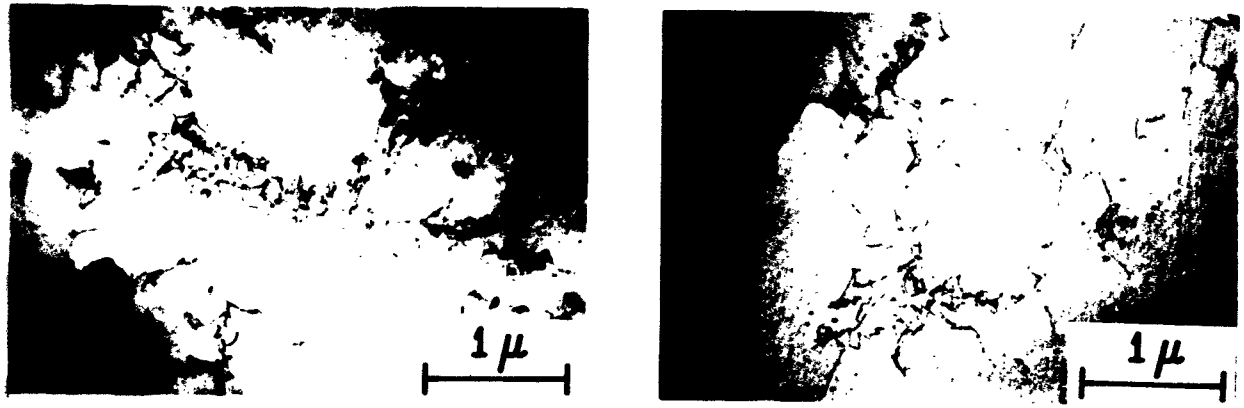

FIG. 21 -- DISLOCATION STRUCTURE IN IRON B-3 STRAINED 2.5% AT (a) 25°C AND (b) -78°C.

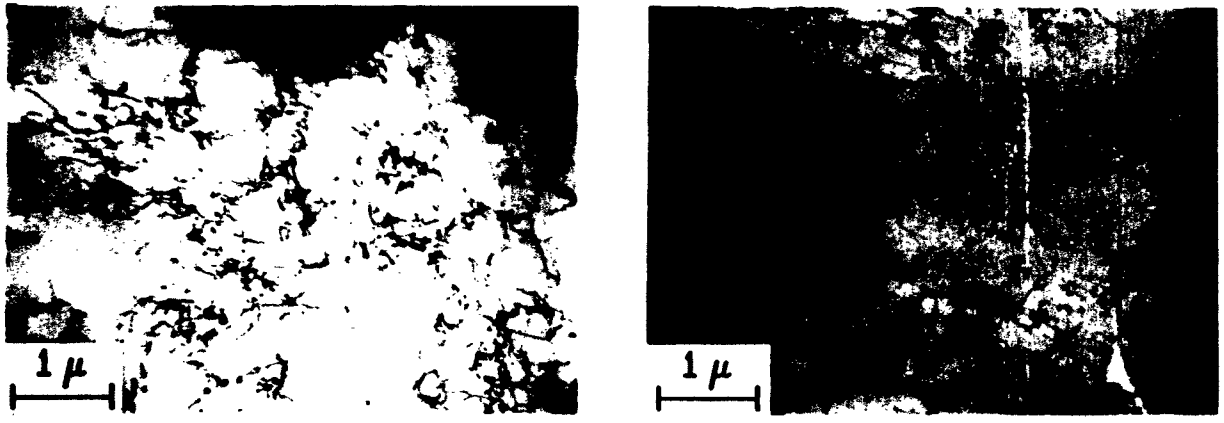

FIG. 22 -- DISLOCATION STRUCTURE IN IRON B-3 STRAINED 5.5% AT (a) 25°C AND (b) -78°C.

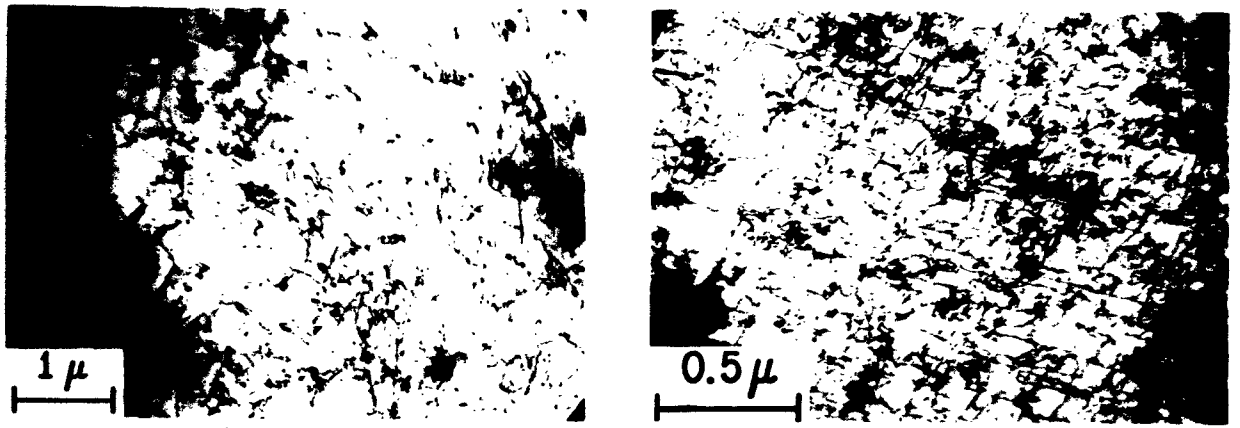

FIG. 23 -- DISLOCATION STRUCTURE IN IRON B-3 STRAINED AT -196°C. (a) 5.5% STRAIN, (b) 14.0% STRAIN.

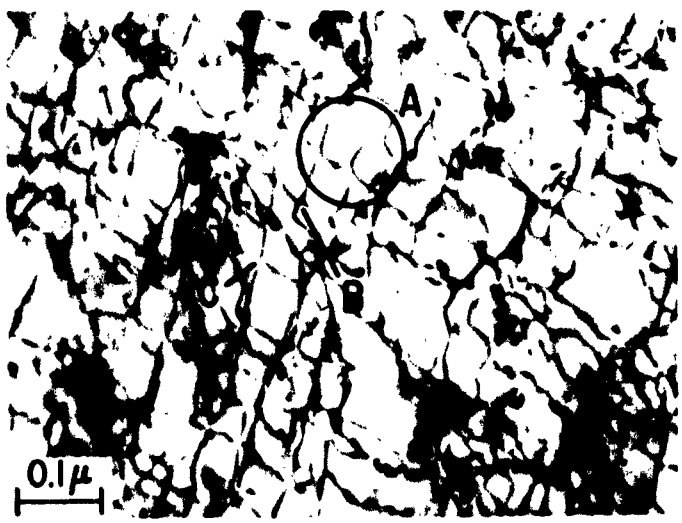

FIG. 24 -- DISLOCATION INTERACTIONS IN IRON B-3 STRAINED 14.0% AT -196°C.

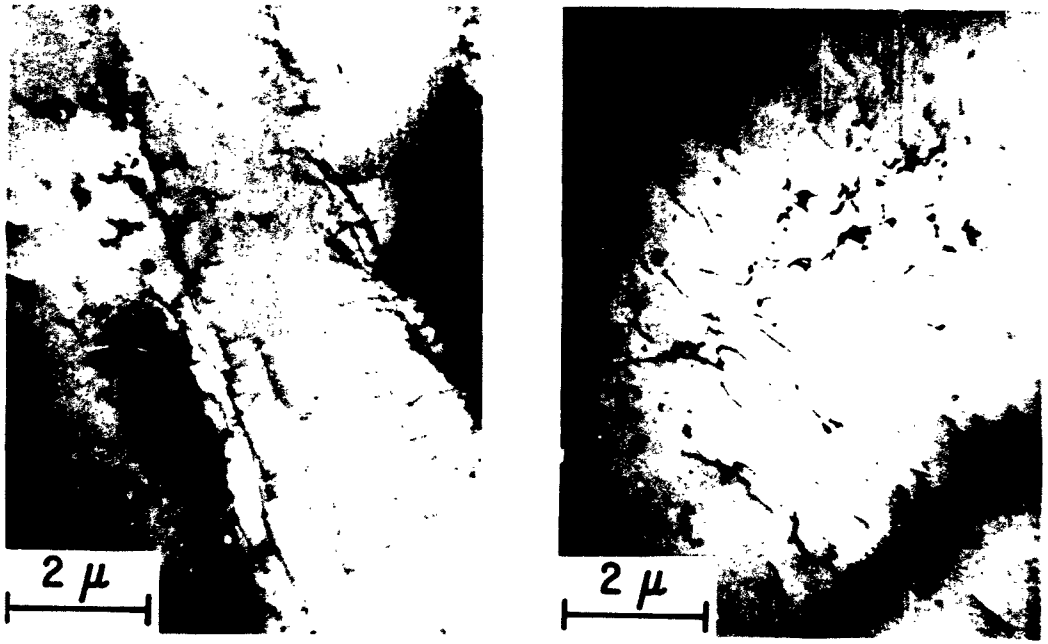

FIG. 25 -- DISLOCATION STRUCTURE IN IRON S-1 STRAINED 2.5% AT 25°C AT STRAIN RATES OF (a) 2.5×10^{-5} sec^{-1} AND (b) 1.25×10^{-2} sec^{-1}.

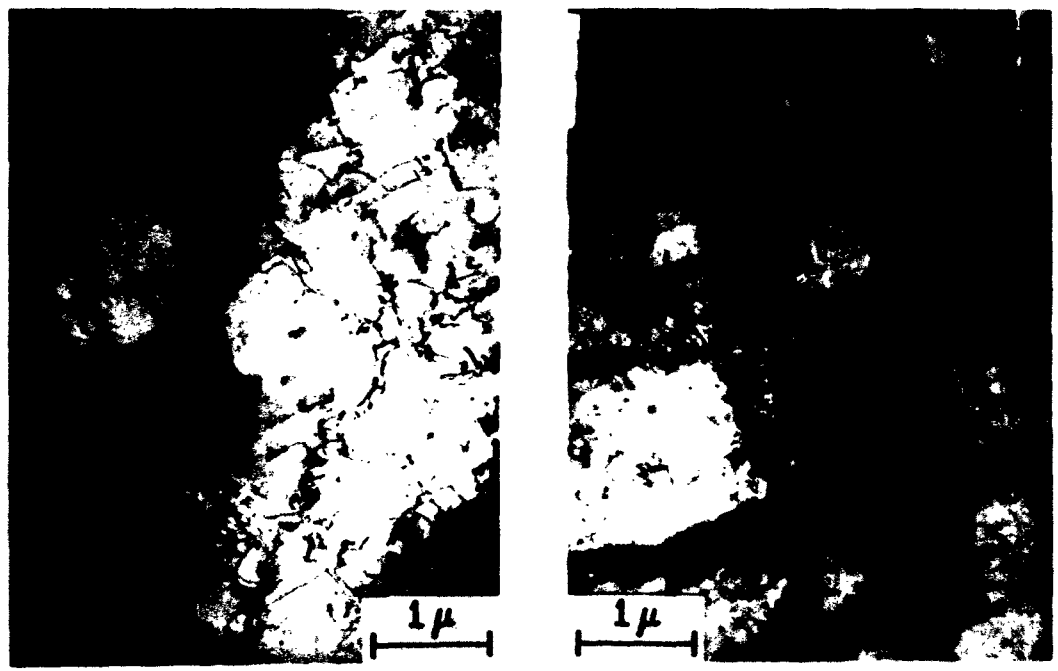

FIG. 26 -- DISLOCATION STRUCTURE IN (a) IRON S-1, AND (b) IRON-0.60 wt. % MANGANESE S-8, STRAINED 15% AT 25°C.

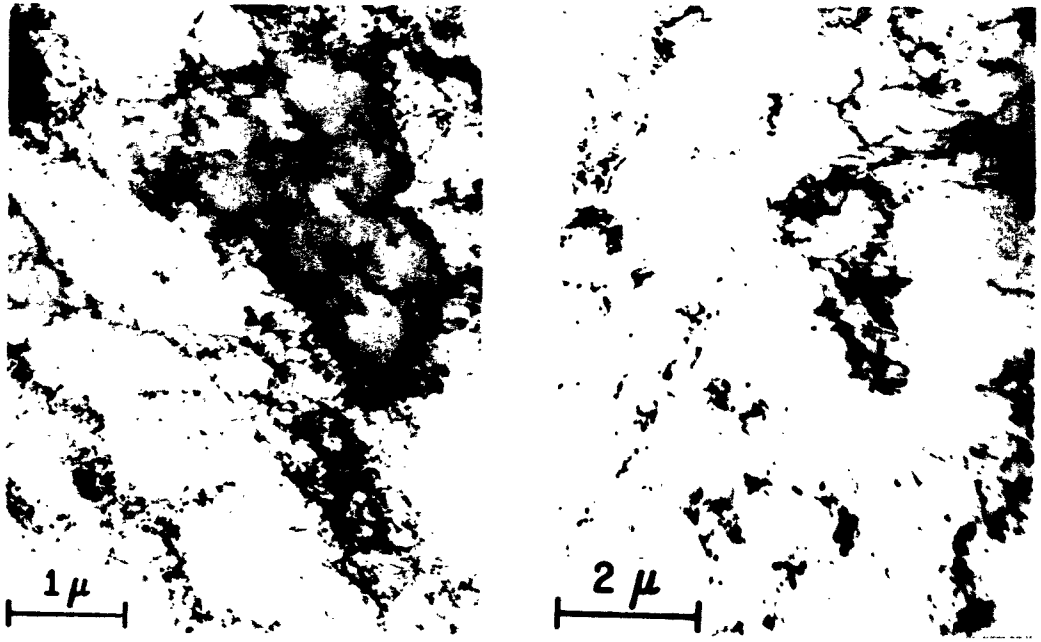

FIG. 27 -- DISLOCATION STRUCTURE IN IRON-0.60 wt. % MANGANESE. (a) 9.5% STRAIN AT -78°C, (b) 2.5% STRAIN AT 25°C AND STRAIN RATE OF 1.25×10^{-2} sec^{-1}.

SUBSTRUCTURE AND RECRYSTALLIZATION OF DEFORMED CRYSTALS OF HIGH-PURITY SILICON-IRON

John L. Walter
General Electric Company
Research Laboratory

I. INTRODUCTION

Recent advances in the techniques of transmission electron microscopy have made it possible to directly observe the dislocation substructures of metals.

Many studies have been undertaken to relate the mechanical behavior of metals to the substructure during plastic deformation. Some investigators have followed the changes in the substructure and mechanical properties during annealing treatments. As a result of these studies, various mechanisms for recrystallization have been proposed based on observations of the modification of the substructure when the deformed metals are heated.

It is not the purpose of the present paper to examine the several proposed mechanisms for recrystallization but, rather, to describe in some detail the derivation and modification of substructure in a deformed and annealed single crystal of silicon iron. It will be shown that the substructure, as evolved during deformation, directly prescribes the state and orientation of nuclei for primary recrystallization. This is not to say that the presently described mechanism for recrystallization holds for all metals and all crystal orientations, however. Additional effort will be required to determine whether there is a single mechanism for recrystallization or whether the mechanism is dependent upon the initial orientation of the crystal being deformed and the type and extent of deformation. This aspect of the situation will be briefly explored in context with the proposed mechanisms for recrystallization.

II. EXPERIMENTAL PROCEDURE

The single crystals used in this study all had a (100) [001] orientation with respect to the rolling plane and rolling direction. The crystals contained 3% silicon and were prepared as follows. High-purity iron and silicon were melted and cast, in vacuo, into slab ingots. The ingots were hot-and cold-rolled to sheet, 0.012" thick. Portions of the sheet were annealed in vacuum, hydrogen, or argon at 1200°C to effect growth of grains with (100)

planes parallel to the sheet surface by means of the surface energy driving force (1-4). Crystals with (100) planes within 1 degree of the plane of the sheet were removed from the sheet and rolled, at room temperature, parallel to the [001] direction to reductions of 10% to 90% of thickness.

Samples of the rolled crystals to be used for transmission electron microscopy were thinned by electropolishing successively smaller areas of the sample until a small hole formed (5). The thinnest parts of the sample, adjacent to the hole, were removed and placed in the microscope. Other portions of the rolled crystals were annealed in a salt bath at temperatures from 535°C to 700°C. These were thinned after annealing. The majority of the transmission microscopy was performed on a Phillips electron microscope type EM-100B at 100 KV.

III. EXPERIMENTAL RESULTS

a. Substructure of Rolled Crystals

Figure 1 shows the dislocation substructure and the beginning of cell formation in a crystal rolled to 10% reduction. The planar orientation, as determined by selected area diffraction, is (100) and a <011> direction of the crystal is parallel to the <011> trace superimposed on the figure. It appears that the dense tangles and incipient cell walls consist of short segments of edge dislocations parallel or nearly parallel to the <112> directions (short traces in Fig. 1). There are also some longer segments of screw dislocations (areas marked a) parallel to the <011> trace. The bent dislocations in areas b and c are probably screws that are cross-slipping on to other {110} planes. The configuration of cross-slipping screw dislocations has been described by Swann and Nutting (6).

Rolling to 20% reduction leads to the formation of distinct cells, 0.2-0.3 microns in diameter as shown in Fig. 2. These cells are a factor of 5 smaller than the cells found in iron deformed a comparable amount (7)*.

---

* It is possible that the addition of silicon to iron results in a decrease in cell size as is the case for the addition of aluminum to copper (8).

The cell walls contain a higher density of dislocations than was the case for the crystal rolled to 10%. The disorientation across the cell walls is less than 1 degree. Surveys of the crystal with the diffraction beam showed no differences of orientation greater than 1 degree within the crystal in agreement with X-ray diffraction data.

When rolled to 50% reduction, the cells are found to be elongated and the cell walls are aligned parallel to the rolling direction. The elongated cells can be seen in Fig. 3. The cell elongation is roughly a factor of 2 and appears to occur not so much by the enlargement of the cells in the rolling direction as by the breaking of cross tangles or walls to combine two cells into one. Several examples of cross-wall breaking may be seen in the figure. The width of the cells remains constant at 0.2-0.3 microns.

While the same elongated cell structure exists everywhere within the sample, in certain regions of the crystal substantial reorientations are found. The diffraction pattern in Fig. 3 illustrates the nature of the reorientation which may amount to as much as 25 degrees. The diffraction pattern, which shows a rotation of 10°, encompassed approximately 15 cells. Since the (100) plane is parallel to the plane of the sample, the reorientation may be characterized as a rotation about an axis normal to the (100) or rolling plane. The average angle of disorientation per cell wall is 0.6-0.7°.

The regions containing the reorientations we have called "transition bands". The transition bands alternate with regions wherein there is no orientation shift and we have classified these latter regions as "deformation bands". As far as can be determined, the substructure in the transition bands is identical to the substructure in the deformation bands. This situation changes, however, with increasing deformation.

Figure 4 shows the structure of a transition band in a crystal rolled to 60% reduction. The further elongation of the cells into sub-bands is apparent as is the narrowing and sharpening of the walls between the sub-bands. However, as seen in Fig. 5, the cell structure within the deformation bands has altered considerably in that the average cell diameter has been reduced to 0.1-0.2 microns and in many areas the cells have been filled with dislocations. The diffraction pattern, obtained from this deformation band, shows no significant orientation shifts.

Elimination of cells in the deformation bands is virtually

complete at 70% reduction and the width of the transition bands is considerably reduced as shown in Fig. 6a. This figure shows a transition band and the orientations of the deformation bands on either side of it (Figs. 6b and 6c) in a crystal rolled to 70%. The transition band now consists of clearly defined sub-bands, still only 0.2-0.3 microns wide, running parallel to the rolling direction. Diffraction patterns show the deformation bands to have (100) planes parallel to the plane of the sample and a change in orientation of the [001] direction of about 40 degrees across the transition band. This rotation occurs as a series of small, discrete orientation changes associated with the individual low-angle boundaries of the transition band. Since there are 18-20 sub-bands within the transition band, the average angle of disorientation of the low-angle boundaries is approximately 2 degrees. The [001] direction of the center sub-band is parallel to the direction of the transition band and hence, parallel to the rolling direction. The structure of the low-angle boundaries is shown in Fig. 7 at high magnification. The structure of these boundaries varies considerably from place to place as does the density of dislocations within the sub-bands. Further examples of the structures of the low-angle boundaries will be given later.

When rolled to 90% reduction, the transition bands become even narrower although the width of the sub-bands remains constant. The average angle of disorientation of the low-angle boundaries has increased to 3-4 degrees. Figure 8a shows a typical example of a transition band in a crystal rolled to 90% reduction. The deformation bands have (100) planes parallel to the sample (diffraction patterns, Figs. 8b and c)and there is a change in orientation of the [001] direction across the transition band of 15 degrees. This relatively small change in orientation across the transition band is frequently observed for crystals rolled to 90% reduction. In many cases, in the more heavily rolled crystals, the transition bands are split and the [001] direction of the center sub-band does not always coincide with the rolling direction. In some cases, where the transition bands are closely spaced, the deformation band between them contains an elongated cell structure similar to that observed in crystals rolled to 50% reduction. This effect is not understood.

Repeated diffraction surveys of all the deformed crystals show that the majority of the crystal is comprised of regions with the (100) planar orientation but other orientations are occasionally found that have their origin in the formation of mechanical twins during rolling. Figure 9a shows a transition band and deformation bands in a crystal rolled to 70% reduction. The diffraction

patterns (Figs. 9b and c) show that the deformation bands have (111) planes parallel to the rolling plane. The change in orientation across the transition band is 21 degrees about an axis normal to the (111) plane.

Many twins have been observed after reductions of 10-20% and these should reorient during subsequent cold-rolling to place (111) planes nearly parallel to the rolling plane. Diffraction patterns of deformed twins observed in the electron microscope show these to have (111) planes in the rolling plane and a <011> direction parallel to a <011> direction of the matrix (9).

b. Textures of the Rolled Crystals

Up to about 50% reduction, the reorientation during rolling may be characterized as a spread of the initial single crystal in two directions about an axis normal to the rolling plane. At 50% reduction, this spread is approximately 15 degrees in both directions. Beyond about 50% reduction, the crystal begins to form two texture components. The components are shown in the pole figure of Fig. 10 which shows the (200) poles of a crystal after rolling to 70% reduction. The initial orientation of the single crystal is given by the open squares. The central portion of the pole figure was not obtained since the symmetry of the orientation made this unnecessary.

The two components, A and B, are related to the initial orientation by rotations of 25 degrees, both clockwise and counterclockwise, mainly about an axis normal to the rolling plane. The dashed lines arbitrarily delineate the orientations of the major components from the transition region (TR), the region of continuous spread from the initial single crystal to the orientations of the components.

Rolling to 90% reduction increases the rotation of the major components away from the rolling direction to about 35° while slightly increasing the spread away from the periphery of the pole figure. There is a decrease in the volume fraction of material in the transition region and an increase in the volume fraction contained within the major components.

The presence of the major components in the rolled crystal can be seen directly by proper etching of the rolled crystal. Figure 11 shows the macroetched surface of a (100) [001] crystal rolled to 70% reduction. The etchant reveals the cube faces; thus, the edges of the pits are parallel to <001> directions. A [001] direction in the region marked A lies at an angle of about 20

degrees counterclockwise to the rolling direction, whereas, in the region marked B, the [001] direction lies at an angle of about 12 degrees clockwise to the RD. The regions A and B, of single but different orientation, are the deformation bands. The narrow band between A and B is the transition region of Fig. 10 across which the change in orientation between adjacent deformation bands is accomplished. As has already been shown in the examination of the transition bands, the change in orientation between the deformation bands is gradual and spread over a distance of about 5 microns in crystals rolled to 50% to as little as 1 micron in crystals rolled 90%.

c. Substructure of Annealed Crystals

The changes that occur in the substructure upon annealing crystals that have been rolled to reductions of 50% or greater may be generalized as follows: a) a decrease in the width of the transition bands (particularly in the case of crystals rolled to 50%), b) a sharpening of the low-angle boundaries, c) nucleation of recrystallization grains within the transition bands, and e) polygonization to sub-grains within the deformation bands.

Figure 12a shows a transition band in a crystal rolled to 50% reduction and annealed for 15 min. at 600°C. The elongated cell structure that comprised the entire substructure of the rolled crystal is no longer present; instead, the transition bands consist of numbers of clearly defined sub-bands, 0.2-0.3 microns wide, separated by sharply defined low-angle boundaries. The deformation bands are structureless, the cells having been replaced by a general distribution of dislocations.

While the total width of the transition bands has decreased for comparable changes in orientation of the [001] directions (compared to the width of the transition bands in the rolled crystal), and the width of the sub-bands remains constant, the average angle of disorientation of the low-angle boundaries has increased to 1.3 to 1.5 degrees.

The diffraction patterns in Figs. 12b and c show that the deformation bands, Band C and B, on either side of the transition band, have (100) planes parallel to the plane of the sample. The change in orientation of the [001] direction across the transition band is 28 degrees.

The nature of the rotation across the transition band is shown more clearly by referring to Fig. 13 which shows a transition

band in a crystal rolled to 70% reduction and annealed for 5 min. at 700°C. Diffraction patterns were obtained at points 1-5 and show that within the deformation bands (points 1 and 5) and the transition bands (points 2, 3, 4) (100) planes are parallel to the rolling plane. The change in orientation of the [001] direction occurs as step-wise rotations about the normal to the rolling plane, for a total rotation of 47 degrees. The [001] direction in the center of the transition band coincides both with the rolling direction and the direction of the transition band. The number of sub-bands in this transition band is 22; dividing by the total orientation change of 47 degrees gives an average angle of disorientation per low-angle boundary of 2 degrees. The nature of the rotations across the transition band suggests that the low-angle boundaries are tilt boundaries and should, therefore, consist of edge dislocations. The structure of the low-angle boundaries is shown more clearly in Fig. 14. This shows another area of the same transition band shown in Fig. 13, but at much higher magnification. The transition band is traversed by a very narrow twin (400 Angstroms wide) which was formed at the time the sample was being thinned or cut in preparation for electron microscopy. The twin changes direction where it crosses a low-angle boundary; the change in direction is a bend with the bend axis normal to the sample surface. There is no apparent twist at the low-angle boundary. Measurements of the twin's angular change at the low-angle boundaries range from 1 to 3 degrees with an average bend of 2 degrees.

If one counts the number of dislocations per cm length of boundary, then, from $Db = \theta$ (10) for a simple tilt boundary, values of 1 to 2 degrees are obtained. D is the number of dislocations per cm of boundary and b is the Burger's vector (2.5 angstroms). Thus, electron diffraction, the change in direction of the twin, and dislocation counts confirm the tilt nature of the low-angle boundaries.

As was pointed out earlier, the transition bands in crystals rolled to 90% reduction contain low-angle boundaries with angles of disorientation of 3-4 degrees. When annealed, the angle of disorientation remains constant as does the width of the sub-bands.

Figure 15a shows a typical transition band in a crystal rolled to 90% reduction and annealed for 30 sec. at 657°C. The deformation bands, B and D, have (100) planes in the plane of the sample (diffraction patterns 15b and d). The change in orientation of the [001] direction across the transition band is approximately 35 degrees.

d. Recrystallization

The most striking characteristic of recrystallization in the rolled crystals is that of nucleation; nuclei are observed to arise only within the transition bands. This is illustrated in Fig. 16 which shows the polished and etched surface of a crystal rolled to 90% reduction and annealed for 1 min. at 650°C.

The broad bands are deformation bands and the narrow bands are the transition bands. The recrystallization grains are either contained within or are contiguous to the transition bands. Recrystallization did not occur within the deformation bands; however, growth of new grains into the deformation bands occurred readily.

Recrystallization grains were easily identified in the electron microscope by 1) the general configuration of the grain within the transition band, 2) a very low density of dislocations, 3) a tendency to polish through at the boundary between the new grain and the transition band, and 4) the presence of Kikuchi lines in the diffraction pattern. Kikuchi lines indicate greater perfection of the new grain as compared to the sub-bands of the transition band (11).

One such new grain, approximately 1.5 microns wide, in a sample rolled to 70% and annealed for 5 min. at 700°C, is shown in Fig. 17a. Diffraction patterns, obtained at point 1 (within the transition band), at point 2, within the grain, and at point 3, within the deformation band to the right of the transition band, are given in Figs. 17b, c, and d, respectively. All three areas of the crystal have (100) planes parallel to the plane of the sample. Across the boundary between points 1 and 2 there is a change in orientation of the [001] direction of only 2 degrees. Across the boundary between the new grain (point 2) and the deformation band, however, there is a change of 10 degrees in the [001] direction. Since the planar orientation is the same, it is evident that the new grain originated as a part of the transition band. Furthermore, the disparity of the angles of disorientation across the boundaries between 1 and 2 and between 2 and 3 indicate that the point of origin of the new grain was adjacent to point 1. The grain increased in width and the boundary 2-3 increased its angle of disorientation as it migrated toward point 3.

The new grain, marked C, in Fig. 15a also has a (100) plane in the plane of the sample as do the deformation bands on either side of the transition band. It is obvious that grain C originated near the right hand side of the transition band since the difference in orientation of the [001] direction between C and D is only 3-4

degrees.

The recrystallization grain always has the same planar orientation as the transition band from which it originates. For instance, Fig. 18a shows a recrystallization grain in a crystal rolled to 90% reduction and annealed for 1 min. at 650°C. The new grain, C, has a (111) plane parallel to the plane of the sample (diffraction pattern, Fig. 18c), as do the deformation bands, B and D, on either side of the transition band (Figs. 18b and d). Regions and grains of this orientation are the result of the formation of mechanical twins during the early stages of rolling. The deformed twins recrystallize completely before recrystallization even begins in the matrix. At the points of intersection of the twins, grains of many different orientations are found.

It has been observed that nucleation occurs more often near the edges of the transition bands than in the center. That this is to be expected will be discussed later.

IV. DISCUSSION

a. Origin of Primary Recrystallization Nuclei

It is characteristic of the nucleus for primary recrystallization, in this particular system, to have the same orientation as the orientation of the particular sub-band which served as the point of origin of the nucleus.

This characteristic suggests that the nucleation event is the result of the enlargement of a portion of a sub-band by migration of the low-angle boundary separating the growing sub-band from adjacent sub-bands in the transition band. Figure 19 gives an example of low-angle boundary migration leading to formation of a recrystallization nucleus in a crystal rolled to 70% and annealed for 5 min. at 700°C. The low-angle boundary, which originally separated the sub-band marked X from the adjacent left-hand sub-band, has migrated to the point marked by the arrow 1. It has combined with the existing boundary to form another boundary of higher angle of disorientation. With this migration, a curvature has been imparted to the connecting boundaries (arrows 2) such that they must move in the direction of the arrows. Thus, X-block will widen and lengthen at the expense of neighboring sub-bands.

The angle of disorientation of the migrating boundary progressively increases as it crosses successive sub-bands; it

encounters the polygonized deformation band as a relatively high-angle grain boundary (see, for instance, Fig. 17). The arrows marked 3, near the bottom of Fig. 19, show a region where parts of a low-angle boundary have migrated across an adjacent sub-band in an irregular fashion.

The driving force for migration of the low-angle boundary derives from the difference in energy-density across the boundary (12). The sub-band boundaries within the transition band add to the driving force for growth of the nucleus. Thus, the recrystallization grains are generally long and narrow with points at one or both ends (see Fig. 16).

The sub-grain boundaries within the polygonized deformation bands also add to the driving force for growth once the nucleus boundary reaches the deformation band; there are cusps where the grain boundary intersects the sub-grain boundaries. These cusps cause a curvature to be imposed upon short segments of the grain boundary with the centers of curvature in the direction of migration of the boundary.

This description of the nucleation event is based on the supposition that the low-angle boundaries are mobile. As the photomicrographs and the diffraction patterns show, the low-angle boundaries are tilt boundaries and, as such, they should be mobile, according to Cottrell (13). Thus, it remains to determine the mechanism by which such low-angle tilt boundaries and the transition bands are formed during deformation and how these boundaries might be changed during the anneal. The following section considers a mechanism for formation of the transition bands.

b. Formation of Transition Bands

The formation of the transition bands appears to occur as a result of interactions of edge dislocations of different Burger's vectors approaching each other along the two operative <111> glide directions in each {110} glide plane.

In the early stages of deformation, the <111> glide directions are symmetrically disposed with respect to the rolling direction and {110} glide planes have the highest resolved shear stress. Thus, dislocations with $[\bar{1}11]$ and $[\bar{1}\bar{1}1]$ Burger's vectors, gliding in the (101) plane, for instance, approach each other, the leading edge components meeting to form a wall. This wall is shown schematically as the center wall in Fig. 20. The following screw components undergo cross glide on to $(10\bar{1})$ and other {110} glide

planes and meeting another screw dislocation of opposite sign, are annihilated. Left behind, then, in the original glide plane are equal numbers of edge dislocations with different Burger's vectors. This basically is the mechanism of formation of cells as described by Seeger (14) and examined by Swann and Nutting (15).

Thus, after a 10% reduction (see Fig. 1), the incipient cell walls and tangles appear to consist of edge dislocations parallel to several <112> directions. Also, the small number of screw dislocations (parallel to the <011> trace) and the evidence for abundant cross-glide appear to substantiate the annihilation of screw dislocations. The cell walls represent the early stages of formation of the transition bands.

As the amount of deformation is increased, the <111> glide directions begin to rotate away from the symmetrical glide position to a position where glide occurs more readily along one of the <111> directions than along the other. This rotation occurs in different directions in different regions of the crystal. That is, on the right-hand side of the cell wall, the rotation will be clockwise and on the left hand side, counterclockwise. Referring to Fig. 20, the succeeding dislocation walls will then contain more edge dislocations of one Burger's vector and fewer of the other Burger's vector. As the rotation increases, each succeeding wall will contain fewer and fewer dislocations of one type. Eventually, the low-angle boundaries near the edge of the transition band will contain only one family of edge dislocations. If the amount of deformation is sufficient to cause rotations of about 30 degrees (reductions beyond about 70%) the edge dislocations in the low-angle boundaries along the edge of the transition band will have Burger's vectors parallel to the rolling direction. In Fig. 20 these walls are adjacent to the deformation bands.

The dislocation structure of these outer low-angle boundaries can be clearly seen in Fig. 21 where the boundaries in the bottom left-hand corner of the photograph are adjacent to the deformation band. This sample was rolled to 70% reduction and annealed for 1 min. at 700°C.

Within the deformation bands, glide occurs along a single <111> direction and the cells are eventually filled with dislocations. Because of this single glide, the deformation bands retain a single orientation which gradually changes with increasing deformation beyond about 50% reduction to provide the major components of the texture. Since there are no significant variations of orientation within the deformation bands there is no nucleation

of recrystallization grains.

c. Effect of Annealing on Structure of Transition Bands

Annealing short of recrystallization results in some modifications of the structures of the transition bands.

In the case of the crystals rolled to 50% reduction, the transition bands become narrower and the low-angle boundaries straighten and become more sharply defined. Also, the angle of disorientation of the low-angle boundaries increases from 0.6-0.7 degrees (in the as-rolled crystal) to 1.5-1.7 degrees after the anneal. The total change in orientation across the transition band remains constant, however. There must be some combination of the low-angle boundaries during the anneal to produce the higher-angle boundaries.

In the case of the crystals rolled to 70% and 90% reduction, however, there is no significant change in the angle of disorientation of the low-angle boundaries during the anneal. In fact, the only change in the structure of the transition bands in the more heavily rolled crystals is the simplification of the structure of the low-angle boundaries. This simplification is probably due to the expulsion of whatever screw dislocations might be contained within the low-angle boundaries (16, 17) to convert them to pure tilt boundaries during the anneal.

Since the boundaries near the edge of the transition band are more likely to consist of a single family of edge dislocations, it is expected that nucleation would occur in the sub-bands adjacent to the deformation bands rather than within the center of the transition band. The present observations indicate this to be the case. However, the limited number of instances in which nucleation is far enough along to be recognizable yet not so far along that the new grain traverses the transition band prevents making a sweeping generalization.

d. Other Mechanisms

It is possible that the above proposed mechanism for recrystallization holds only for the (100) [001] orientation in a body centered cubic crystal or for other crystals under similar conditions of symmetrized glide. Hu (18), in a study of the structures of rolled (110) [001]-oriented crystals of silicon-iron, observed, upon annealing, rapid formation of sub-grains followed by a slow increase in sub-grain size prior to recrystallization. He postulated that sub-grains coalesced as a result of the disap-

pearance of some of the sub-grain boundaries, the coalescence being followed by rotation of the sub-grains. This same coalescence and rotation mechanism was applied by Hu in an independent study of the structures of rolled and annealed (100) [001]-oriented crystals of silicon-iron (19). In that study he observed a grain with the (113) orientation in a transition band with the (100) orientation and suggested that the grain was formed as a result of very large rotations of some of the sub-bands of the transition band.

In the present study, the recrystallization grains were always observed to have the same planar orientation as the transition band from which the grains originated, at least within the accuracy of the electron diffraction measurements.

Weissmann, et al (16), and Fujita (20), in studies of the substructures of cold-worked aluminum, observed that growth of sub-grains during an anneal appeared to proceed by a gradual disappearance of sub-boundaries, i.e., by coalescence of sub-grains. The sub-grains became surrounded by high-angle boundaries, presumably as a result of migration of dislocations from the sub-grain boundaries to some point outside the coalescing group of sub-grains.

Votava (21) observed a cell structure in cold-worked copper which polygonized to sub-grains upon annealing. However, the recrystallization nuclei appeared suddenly and simultaneously with polygonization. Baily (22) suggests that recrystallization in deformed silver results from the migration of already present grain boundaries but could not determine the source of the necessary high-angle boundaries in heavily worked silver.

It seems that additional study will be required to provide a detailed description of formation of high-angle boundaries when sub-grains coalesce. Particular attention must be paid to the presence and conditions of local curvature (23) at the points of nucleation in view of the body of evidence suggesting that nuclei are formed in regions where turbulent glide has occurred (24), i.e., where the lattice has become curved.

In the present study and in the study by Hu (19), the observations confirm the presence of the necessary regions of disorientation required for nucleation.

V. SUMMARY AND CONCLUSIONS

1. (100) [001]-oriented crystals of high-purity 3% silicon-iron were rolled, at room temperature, to reductions of 10-90% of

thickness. The structures of rolled and annealed crystals were observed by means of transmission electron microscopy.

2. Cells are formed at low reductions (10-20%). The cell walls consist mainly of edge dislocations parallel to <112> directions.

3. With heavier reductions (up to 50%), the cells elongate in the rolling direction. In certain regions of the crystal there are significant reorientations. The reorientation is characterized as a rotation about an axis normal to the (100) or rolling plane. These regions have been called "transition bands". The regions in which there are no reorientations are called "deformation bands".

4. At 60-70% reduction, the elongated cells in the transition bands become sub-bands separated by low-angle tilt boundaries which have angles of disorientation of about 2 degrees. The elongated cell structure in the deformation bands is replaced by a general distribution of dislocations.

5. The low-angle boundaries in the transition bands in the crystals rolled to 90% reduction have angles of disorientation of 3-4 degrees.

6. When annealed, the low-angle boundaries of the transition bands are converted to pure tilt boundaries. The deformation bands undergo polygonization to sub-grains.

7. Nucleation of recrystallization grains occurs only within the transition bands by a process of migration of low-angle boundaries across adjacent sub-bands. The driving force for migration derives from differences in dislocation density from sub-band to sub-band.

8. The recrystallization grains have the same orientation as the sub-band which served as the point of origin of the nucleus.

9. The majority of recrystallization grains have (100) planes parallel to the plane of the sample. Occasional recrystallization grains are observed to have orientations near (111). These are found in conjunction with (111)-oriented transition bands and deformation bands located within deformed twins.

10. The proposed mechanism for recrystallization in (100) [001]-oriented crystals of high-purity silicon-iron may not hold for crystals of other orientations or for metals with different deformation characteristics.

ACKNOWLEDGEMENTS

The author is indebted to E. F. Koch for sample preparation and electron microscopy. The gratitude of the author is extended to J. R. Low, (Miss) A. M. Turkalo, and J. C. Fisher of this Laboratory and to Professor B. Chalmers of Harvard University and Professor F. C. Frank of the University of Bristol for stimulating discussion and valuable comments.

REFERENCES

1. J.L. Walter and C.G. Dunn, Trans. Met. Soc. AIME, 215, 465 (1959).

2. J.L. Walter, Acta Met., 7, 424 (1959).

3. J.L. Walter and C.G. Dunn, Trans. Met. Soc. AIME, 218, 914 (1960).

4. J.L. Walter and C.G. Dunn, Acta Met., 8, 497 (1960).

5. V.A. Phillips and J.A. Hugo, J. Sci. Instr., 37, 216 (1960).

6. P.R. Swann and J. Nutting, J. of Inst. of Metals, 90, 133 (1961).

7. A.S. Keh and S. Weissmann, to be published in Proc. of 1961 Conf. on "The Impact of Trans. Electron Microscopy on Theories of Strength of Crystals", Interscience Pub., New York.

8. See Ref. 6, p. 134.

9. For additional information concerning twins in high-purity silicon-iron crystals see J.L. Walter and E.F. Koch, Acta Met., 10, 1059 (Nov. 1962).

10. W.T. Read, Dislocations in Crystals, McGraw-Hill Book Co., Inc., New York (1953) p. 158.

11. Z.G. Pinsker, Electron Diffraction, Butterworths Sci. Publ., London (1953) p. 217.

12. C.G. Dunn and K.T. Aust, Acta Met., 5, 368 (1957).

13. A.H. Cottrell, Dislocations and Plastic Flow in Crystals, Oxford Univ. Press, London (1953) p. 188.

14. A. Seeger, Dislocations and Mechanical Properties of Crystals, Wiley, New York and London (1956) p. 243.

15. See Ref. 6, p. 135.

16. S. Weissmann, T. Imura, and N. Hosokawa, to be published in the Proceedings of the Symposium on "Recovery and Recrystallization of Metals", AIME Annual Meeting, Feb. 1962.

17. J.C.M. Li, to be published.

18. H. Hu, Trans., Met. Soc. AIME, 224, 75 (1962).

19. H. Hu, Letter to Ed., Acta Met., 10, 1112 (Nov. 1962).

20. H. Fujita, J. Phys. Soc. Japan, 16, 397 (1961).

21. E. Votava. Acta Met., 9, 870 (1961).

22. J.E. Bailey, Phil. Mag., 5, 833 (1960).

23. R.W. Cahn, Proc. Phys. Soc. A63, 323 (1950).

24. R.W.K. Honeycombe, J. Inst. Metals, 80, 45 (1951).

1. Incipient cells and dislocation tangles in crystal rolled to 10% reduction. X 110,000.

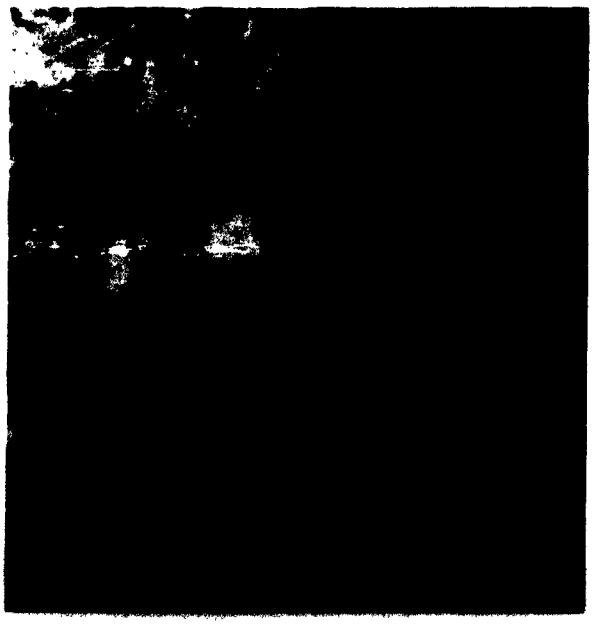

2. Cells in crystal rolled to 20% reduction. X 100,000.

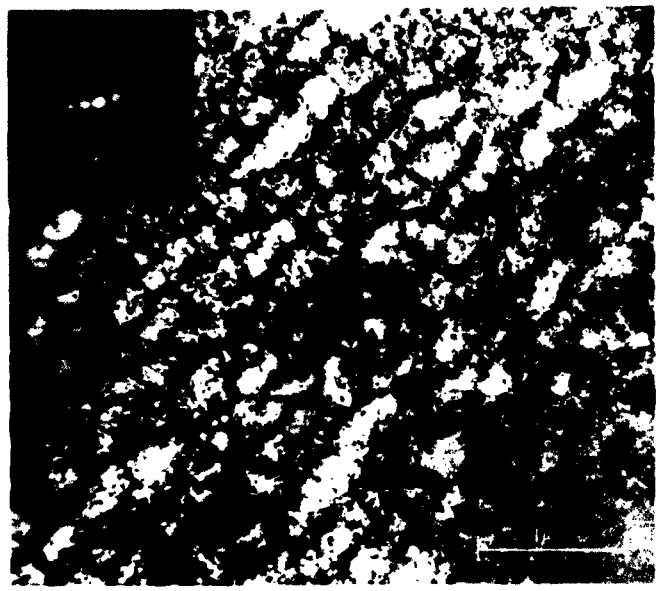

3. Elongated cells in transition band in crystal rolled to 50% reduction. Diffraction pattern shows nature of reorientation. X 48,000.

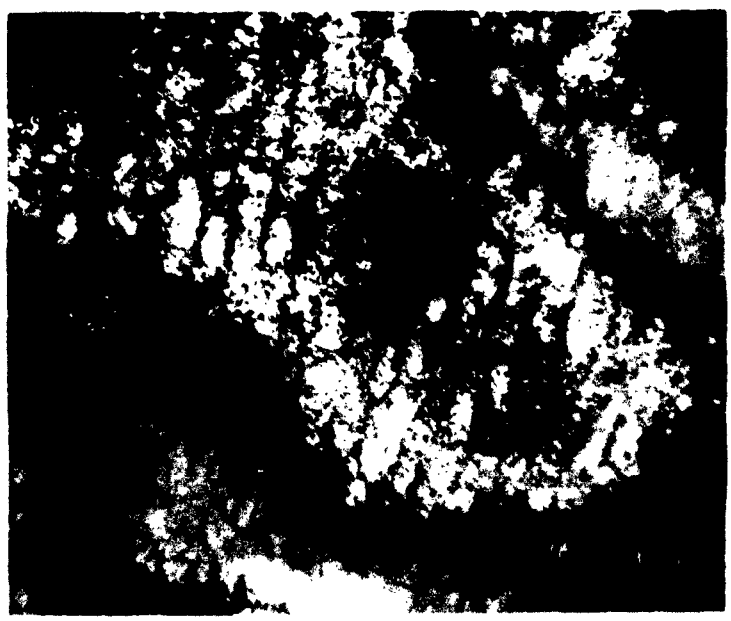

4. Sub-bands in transition band in crystal rolled to 60% reduction. X 50,000.

5. Dislocation structure and diffraction pattern of deformation band in crystal rolled to 60% reduction. X 84,000.

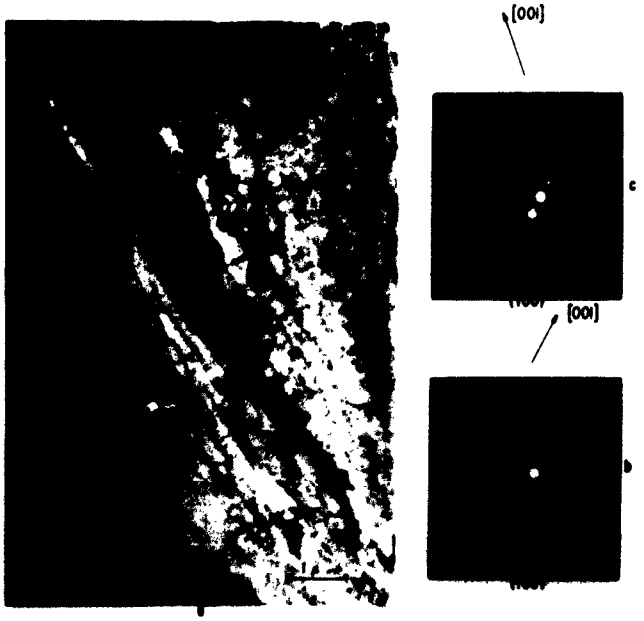

6. Transition band and diffraction patterns of deformation bands, B and C, in crystal rolled to 70% reduction. X 19,000.

7. Structure of low-angle boundaries in transition band in crystal rolled to 70% reduction. X 100,000.

8. Transition band and diffraction patterns of deformation bands, B and C, in crystal rolled to 90% reduction. X 90,000.

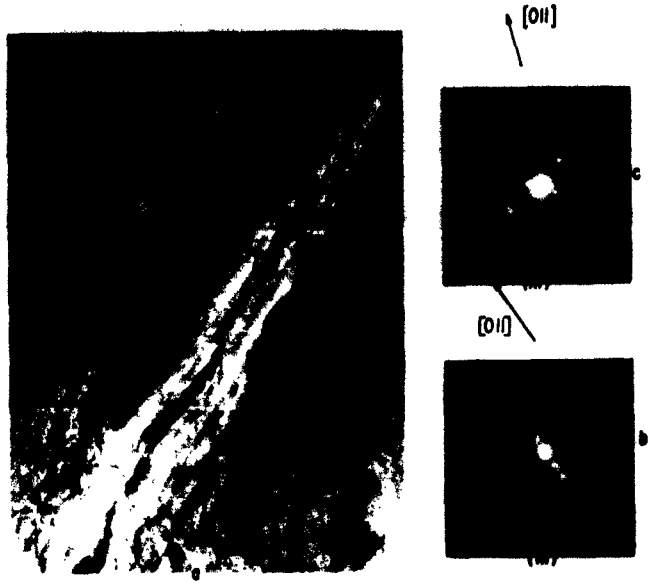

9. Transition band and (111)-oriented deformation bands B and C, (diffraction patterns b and c) in crystal rolled to 70% reduction. X 24,000.

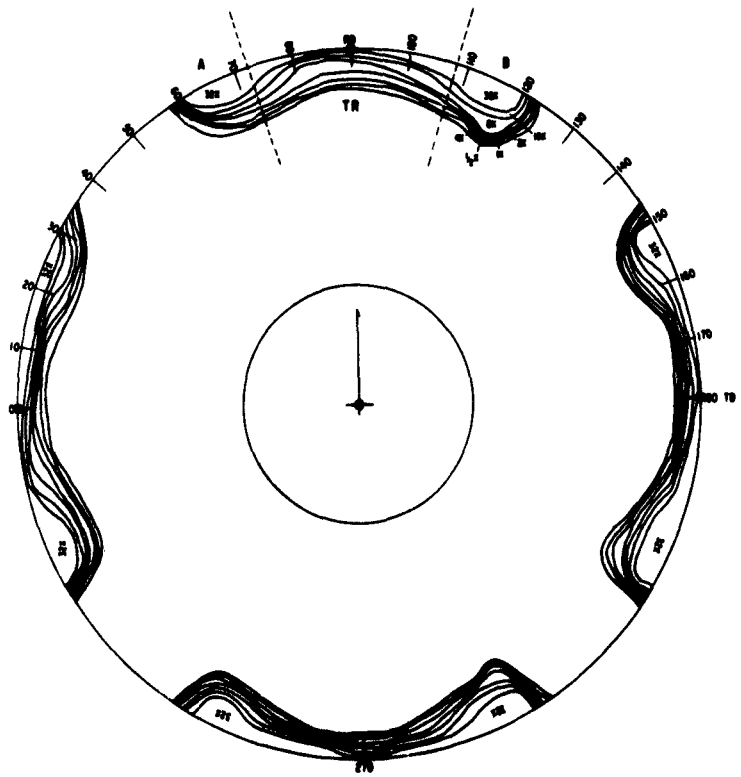

10. (200) pole figure of crystal rolled to 70% reduction. Open squares give initial orientation, (100) [001].

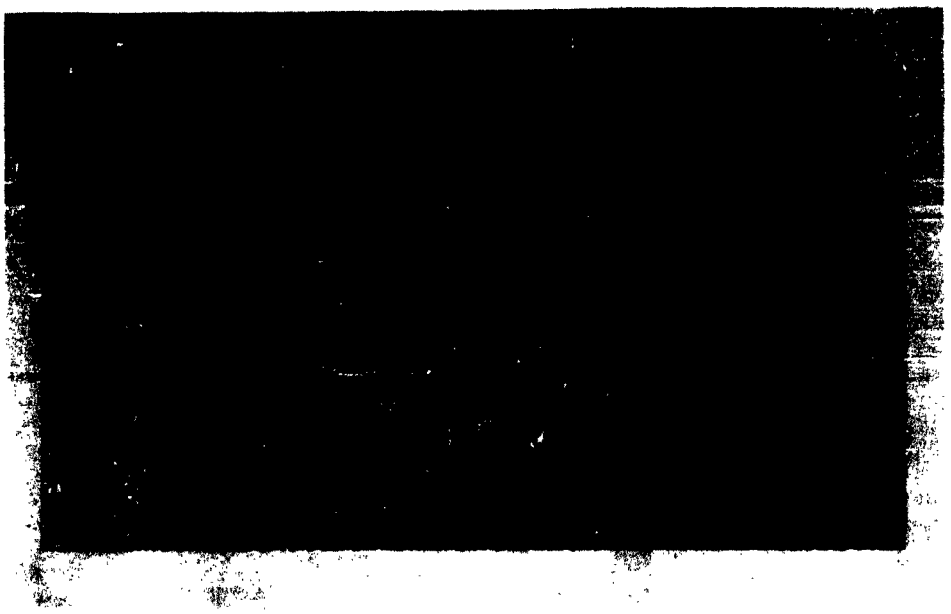

11. Macroetched surface of crystal rolled to 70% reduction. Shows variety of orientations. A and B are deformation bands. X 500.

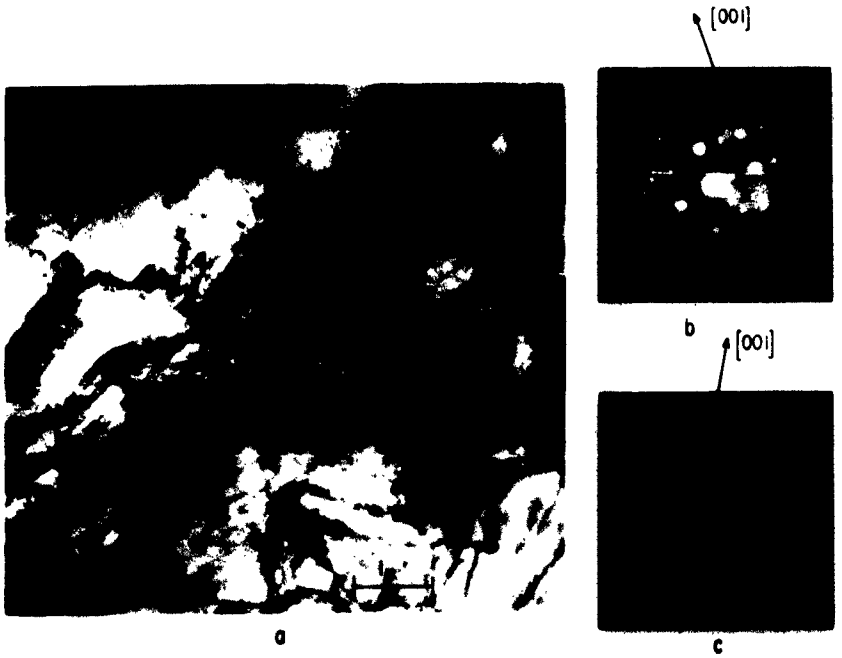

12. Transition band and diffraction patterns of deformation bands, B and C, in crystal rolled to 50% and annealed 15 min. at 601°C. X 25,000.

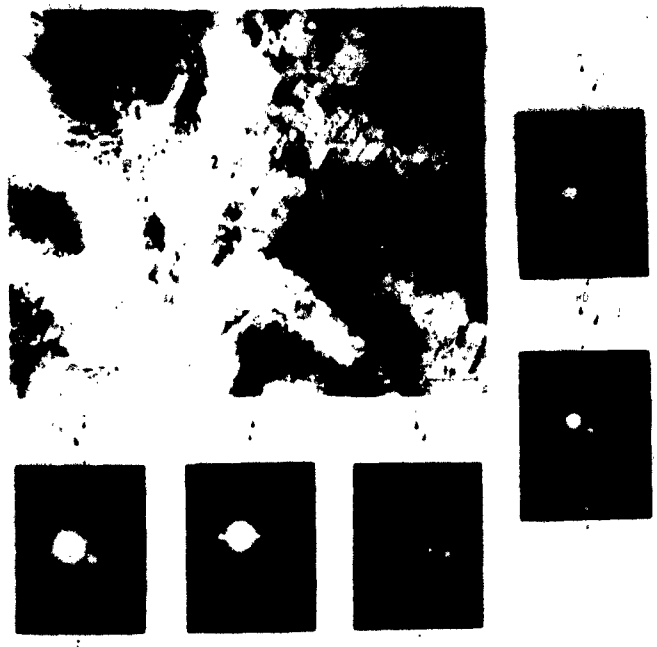

13. Transition band in crystal rolled to 70% reduction and annealed for 5 min. at 700°C. Diffraction patterns taken at points 1-5 to show change of orientation of [001] direction across transition band. X 17,000.

14. Structure of low-angle boundaries in transition band in crystal rolled to 70% and annealed for 5 min. at 700°C. Narrow band traversing transition band is twin. X 108,000.

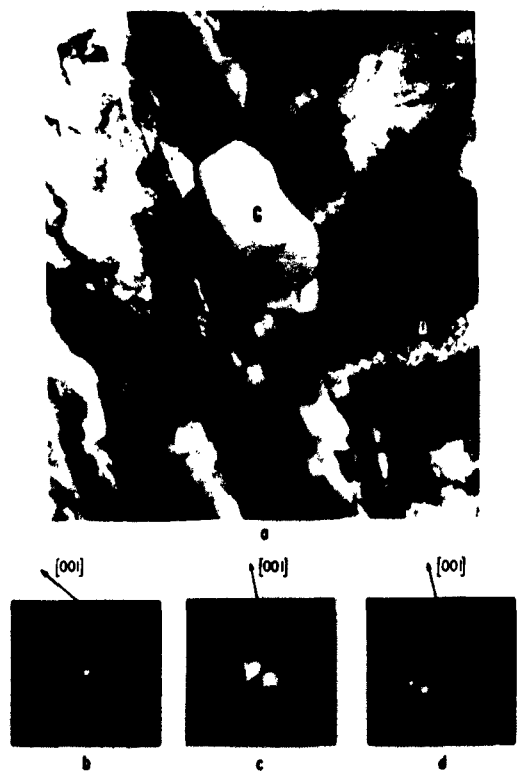

15. Transition band and recrystallization nucleus in crystal rolled to 90% and annealed 30 sec. at 657°C. Diffraction patterns b, c, d show (100) orientations of deformation bands, B and D, and nucleus, C.

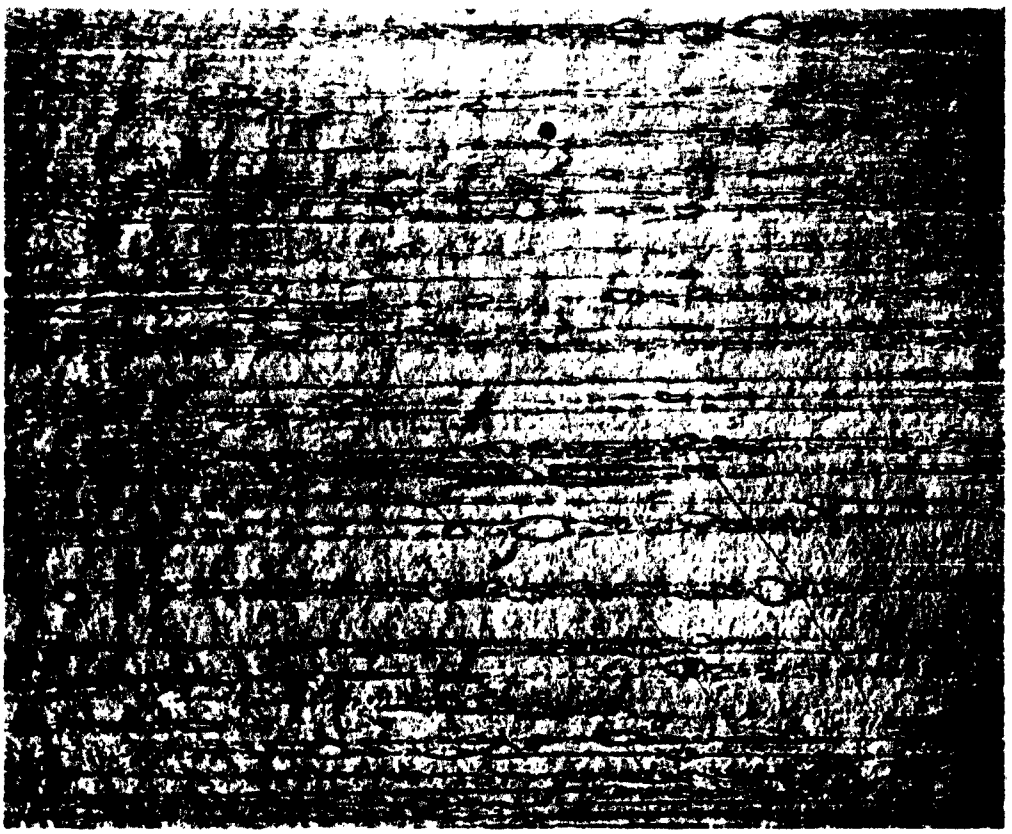

16. Polished and etched surface of crystal rolled to 90% and annealed 1 min. at 650°C. Wide bands are deformation bands and narrow bands are transition bands. Nucleation occurs within transition bands. X 150.

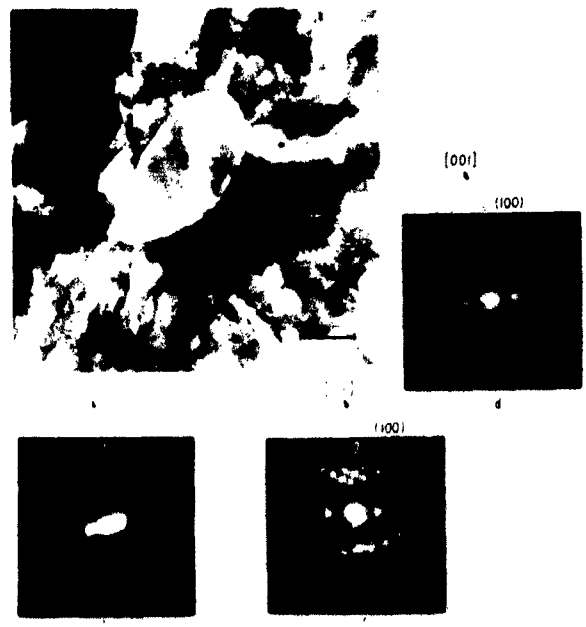

17. Transition band, recrystallization nucleus (2) and polygonized deformation bands in crystal rolled to 70% and annealed 5 min. at 700°C. Diffraction patterns show orientations at points 1-3. X 19,000.

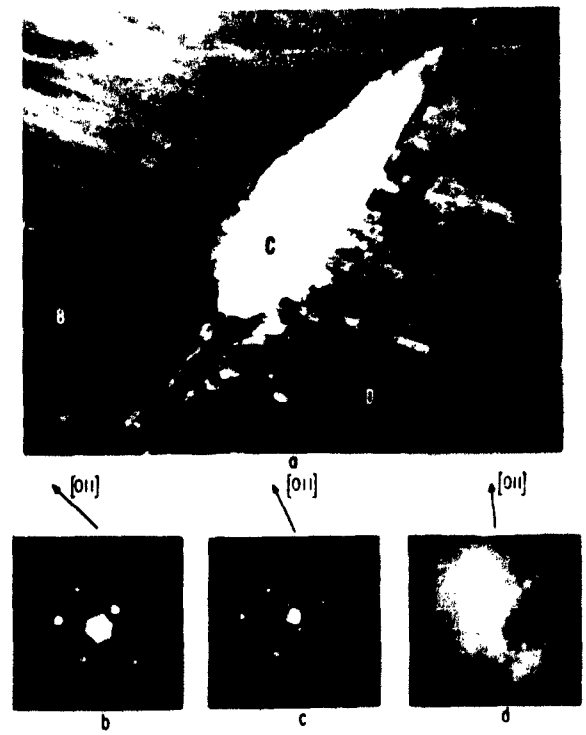

18. (111)-oriented recrystallization grain and deformation bands in crystal rolled to 90% and annealed 1 min. at 650°C. Diffraction patterns b and d show orientation of deformation bands. X 10,000.

19. Origin of recrystallization nucleus within transition band in crystal rolled to 70% and annealed 5 min. at 700°C. X 53,000.

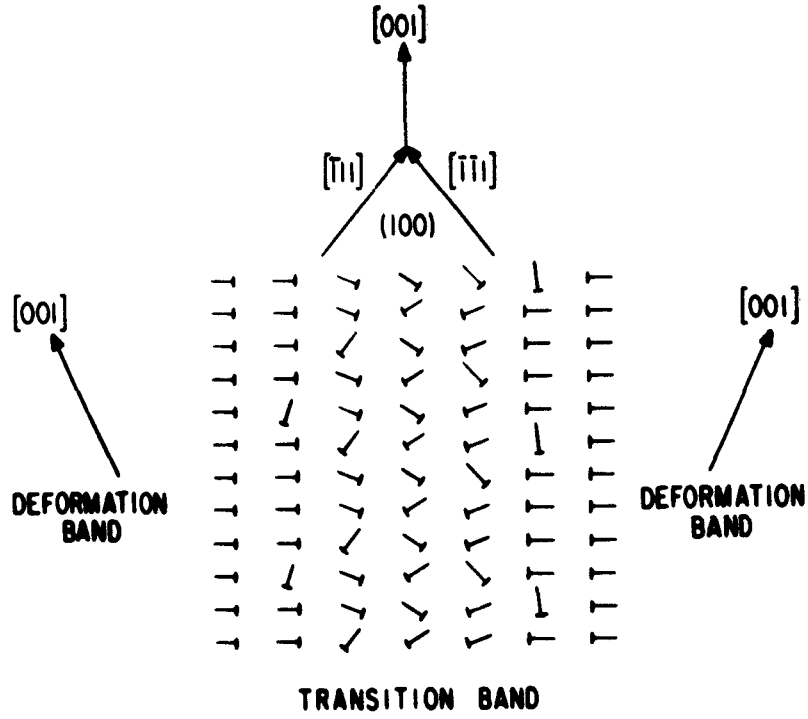

20. Schematic diagram of dislocation structure of low-angle boundaries of transition bands.

21. Dislocation structure of low-angle tilt boundaries adjacent to deformation band in crystal rolled to 70% and annealed 1 min. at 700°C. X 100,000.

The Variation of Flow Stress with Substructure in Tantalum

Walter S. Owen
Department of Metallurgy
University of Liverpool.

1. General Features

On annealing cold worked (90 percent reduction at 20°C) tantalum (less than 160 ppm total interstitial impurity) at successively higher temperatures four effects were observed[1]. In order of increasing annealing temperature:

1. The dislocation density of the cold-worked foils was very high (greater than 3×10^{11} cm^{-2}). It was difficult to resolve the individual dislocations and no clear cell structure was observed. On annealing for 30 minutes at 900°C there was some rearrangement and annihilation of dislocations but no formation of sub-boundaries. The density decreased to about 9×10^{10} cm^{-2}.

2. Annealing at temperatures between 950° and 1200°C produced sub-boundary networks which were very regular at the higher temperatures in the range (Figure 1). More than 60 percent of the networks were of the ⟨111⟩/⟨100⟩ type.

3. At higher annealing temperatures coarser networks were produced, corresponding to a decrease on the angular misorientation across the boundary. There was a small decrease on the average dislocation density.

4. No networks were found in specimens annealed at still higher temperatures (up to 1700°C) and there was a very marked decrease in the average dislocation density.

The processes overlap somewhat and the annealing temperature at which each effect was observed varied appreciably with the purity of the tantalum. In the most impure material (147 ppm oxygen, 160 ppm total impurity) effects 2 and 4 occurred at the lowest temperatures and the average dislocation density decreased most rapidly with increasing annealing temperature.

2. The Change of Substructure on Deforming Annealed Foils in Tension

The sequence of changes in the substructure on deforming annealed foils in tension at constant temperature is similar to those observed in iron[2,3,4], but there are differences in detail.

After 1.6 percent strain at 293°K many straight dislocations were observed and the start of network disintegration was detected in relatively pure tantalum (Ta-21 containing less than 35 ppm total interstitial impurity) with a high initial dislocation density (5×10^{10} cm^{-2}). In the annealed specimen most of the dislocations were in well developed networks although there were an appreciable number of random dislocations. Very few regular networks remained after 2.0 percent strain and a number of tangles of dislocations had formed. There was some indication of cell formation although it was not possible to estimate the cell size. After 4.6 percent strain the cell structure was better defined, the cell diameter being about 0.3μ, and there were extensive dislocation tangles. The cells were clearly defined after 7.3 percent strain and the diameter was about 0.2μ(Figure 2). However, unlike iron deformed at the same temperature, after further strain the cells started to break-up. Although some evidence of cells remained after 10.6 percent strain the dislocation distribution was much more uniform than after 9.2 percent. After 12.2 percent strain the cell structure had disappeared and the dislocation density was uniform throughout the specimen (Figure 3).

The strain at which tangles and cells form is greatly influenced by the initial substructure. A dilute tantalum-oxygen alloy (Ta-24 containing 147 ppm oxygen) annealed to give a low dislocation density (1×10^{9} cm^{-2}) arranged randomly showed only slight evidence of cell formation after 10.0 percent strain at 293°K although there was a marked increase in the dislocation entanglement (Figure 4). This contrasts with the same alloy annealed to a high dislocation density, with all the dislocations in well-formed networks, which proved remarkably resistant to disintegration on straining. Even after 11.0 percent strain some of the original networks could still be observed. In Figure 5 a network surviving after 6.7 percent strain is shown. Although the network is still intact the surrounding areas show obvious signs of deformation. Thus, it seems that, in general, high dislocation density specimens form tangles and subsequently cells more readily than those with low initial density, but annealed-in networks vary significantly in their ability to withstand disintegration. Comparing the general deformation structures in tantalum with those described for iron[2-4] it seems that tantalum deformed at 293°K corresponds to iron deformed at a temperature 100°K or more higher. Since the melting point of tantalum is appreciably higher than that of iron this difference is not surprising.

Several sources of dislocation multiplication have been identified. Profuse generation of dislocations has been observed in the vicinity of the

intersection of a slip band with a dislocation network (Figure 6). It seems that when a network is broken up by a slip band cutting through it many new dislocations are produced. In addition, it was observed in all the specimens that as the deformation was increased the grain boundaries became thicker and more fuzzy due to the accumulation of dislocations along the boundary (Figure 7). It is not clear where these dislocations originate but it seems unlikely that they are formed by the blocking of a slip band because when this occurs the new dislocations can be clearly seen and they are more widely dispersed (Figure 8).

3. The Variation of Flow Stress with Dislocation Density

The average dislocation density was measured, by the method described by Keh and Weissman[4], as a function of flow stress for two specimens of Ta-E4 with the same grain size, one (Ta-E4 LD) with a low (1×10^{9} cm^{-2}) and the other (Ta-E4 HD) with a high density of dislocations (1.6×10^{10} cm^{-2}). In the low density material the dislocations were random and in that with a high dislocation density almost all of the dislocations were in well-developed networks. The mechanical and thermal treatments are given in Table 1. Ta-E4 LD was tested at 293°K, and 240°K and the other specimens at 293°K only.

The stress-strain curves are shown in Figure 9. As with all polycrystalline dilute tantalum alloys tested in this and other investigations the logarithm of the true stress σ varied linearly with the logarithm of the true strain ε when the strain was greater than the Luders strain. Thus, the strain-hardening curve could be accurately represented by:-

$$\sigma_f = K\varepsilon^n \qquad (1)$$

where K is the strength constant and n the strain-hardening index. Values of the flow stress at zero plastic strain σ_{fo} were obtained by logarithmic extrapolation of the strain hardening curve to the intersection with the elastic line[5,6]. Values of the lower yield stress σ_y, σ_{fo}, K and n are listed in Table 1. Changing the initial substructure (compare Ta-E4 LD and Ta-E4 HD) produces only a very small difference in the yield stress at 293°K but the difference in σ_{fo} is appreciable. Clearly, σ_{fo}, K and n are markedly affected by the initial substructure. Many determinations of σ_i, which is equivalent to σ_{fo}[6], have been made on other materials using the Petch extrapolation which depends on

$$\sigma_y = \sigma_i + k_y d^{-\frac{1}{2}} \qquad (2)$$

where 2d is the grain size and k_y a locking parameter. This method cannot be used to study the effect of substructure on the yield parameters because of the practical difficulty of maintaining a constant dislocation arrangement

and density in a series of specimens with an appreciable range of grain size. When the grain size range is established by annealing cold-worked tantalum at successively higher temperatures the Petch method measures some averaged value of σ_i which is higher than σ_{fo} measured by extrapolation of the strain hardening curve[5]. In iron specimens, which usually go through a phase change during the annealing to establish the grain size, the variation of substructure with annealing temperature is not marked and there is good agreement between σ_i by the Petch method and σ_{fo} by extrapolation of the strain-hardening curve[7].

Following Keh and Weissman[4] the flow stress for Ta-E4 LD and Ta-E4 HD was plotted as a function of $\sqrt{N}$, where N is the average dislocation density, and all the tantalum specimens were found to approximate to the empirical relationship

$$\sigma_f = \sigma_o + \alpha G b \sqrt{N} \qquad (3)$$

where σ_o and α are constants, G is the shear modulus and b the Burgers vector (Figure 10). A relationship of this form is predicted by several different strain hardening theories but the models on which the theories are based relate to the second stage of linear hardening of a single crystal and the extension of these ideas to the non-linear hardening of polycrystals is of doubtful significance. Further, to interpret equation 3 in these terms an assumption is necessary about the fraction of dislocations which are mobile or the ratio between the dislocation density of the tangled regions and the average density. In polycrystalline tantalum specimens the dislocation geometry changes markedly with the preliminary mechanical and thermal treatment and with strain during testing and thus a simple assumption of this type does not appear to be justified. The problem has been discussed in detail by Keh and Weissman[4]. However, equation 3 is a useful empirical representation of the results and it enables the flow stress at zero strain σ_{fo} to be obtained by a third method. σ_{fo} is the stress corresponding to the initial dislocation density N_i. Values of σ_{fo} obtained in this way are given in Table 1. The values from equation 3 are a little greater than those from the stress-strain curve but the agreement is fair.

The variation of average dislocation density with strain could be represented by a simple power relationship (Figure 11)

$$N = C \varepsilon^a \qquad (4)$$

values of C and a are given in Table 1. A similar result has been found for iron and, by etch-pit counting, for mild steel[6]. Hahn replaces the total strain ε by the elastic strain ε_p, but as the elastic strain is small compared with ε over the range of the experimental measurements this substitution does not make a significant difference. Hahn[8] has advocated the use of

$$N - N_i = C' \varepsilon^{a'} \qquad (5)$$

The data for tantalum are plotted in this way in Figure 12. Each increment of strain is proportional to the number of moving dislocations N_m and the slip distance l, $\varepsilon = N_m b l$. At 293°K a or a' is nearly unity for both the high and low initial density specimens indicating that the product $N_m l/N$ is constant or, if the difference in the slip distance is assumed to be small, that the ratio of moving to static dislocations is independent of initial substructure. The fraction of dislocations moving can be assumed to be independent of the strain only if the slip distance is independent of the average dislocation density. At 240°K the situation is quite different, the strain varying approximately as the square root of the dislocation density. Thus, the product $N_m l/N$ varies with strain but without exact knowledge of the change in slip distance with strain and temperature no deduction about the effect of these variables on the fraction of dislocations moving can be made.

If equations 1 and 4 are judged to be a correct representation of the data then, eliminating ε,

$$\sigma_f = K C^{\frac{a-n}{n}} N^{\frac{n}{a}} \qquad (6)$$

Not surprisingly, since σ_f, N and ε are all taken from the same collection of interrelated data, the experimental results fit this relationship (Figure 13 and Table 1). Of course, equation 6 is not compatible with equation 3 since $\frac{n}{a} \neq 0.5$. The values of σ_{fo}, the stress corresponding to a dislocation density N_i, obtained from the data plotted in Figure 13 (equation 6) are given in Table 1. These are probably more reliable than those obtained from equation 3.

The Significance of σ_o

In the equation used by Keh and Weissman (equation 3) $\sigma_f = \sigma_o$ when $N = 0$ and σ_o might be considered to be the Peierls stress. However, σ_o defined in this way varies over a wide range when the initial substructure is changed (Figure 10 and Table 1). This, together with the objections to the application of this formula to polycrystalline material, suggests that no physical meaning can be given to this σ_o. Equation 6 is also unsatisfactory because neither of the equations from which it is derived (equations 1 and 4) take account of the Peierls stress. However, the fact that these equations appear to be a good representation of the experimental data indicates that the Peierls stress is small compared with σ_{fo}.

In the absence of a firmly-based equation relating the flow stress and the average dislocation density an attempt to assess the Peierls stress by a

more circuitous route appears justified. Previously, σ_{fo} has been defined as the point satisfying simultaneously equation 1 and the elastic equation

$$\sigma = E\varepsilon \tag{7}$$

where E is Young's modulus (Figure 14) and

$$\sigma_{fo} = K^{\frac{1}{1-n}} E^{\frac{n}{n-1}} \tag{8}$$

However, if it is assumed that σ_{fo} is the sum of two stresses, the Peierls stress σ_o and the stress σ_s required to move a dislocation through the annealed-in substructure, the relation between the elastic line and the strain-hardening curve may be as represented in Figure 15. σ_o is the strain introduced into the specimen by building up the dislocation density from zero to N_i. Hypothetically, if this is done without any dislocation interaction the stress required would be σ_o. Then, σ_{fo}, now defined as the stress at which the elastic line (equation 7) is tangential to the strain-hardening curve

$$\sigma_f - \sigma_o = K(\varepsilon - \varepsilon_o)^n \tag{9}$$

becomes

$$\sigma_{fo} = \sigma_o + K^{\frac{1}{1-n}} E^{\frac{n}{n-1}} n^{\frac{n}{1-n}} \tag{10}$$

Experimentally, the stresses σ_f and strains ε can be measured only at strains larger than the Luders strain. In these circumstances, if it is assumed that $\sigma_f \gg \sigma_o$ and $\varepsilon >> \varepsilon_o$ equation 9 reduces to equation 1 and n and K can be determined experimentally. Equation 1 fits the strain hardening curve very closely suggesting that at large strains this approximation is reasonable. The second term on the right-hand side of equation 10 differs from the right-hand side of equation 8 only by the factor $n^{\frac{n}{1-n}}$. For tantalum tested at 293°K n has values between 0.1 and 0.3 depending upon the initial substructure and $n^{\frac{n}{1-n}}$ varies between 0.77 and 0.60. Probably the least ambiguous method of determining σ_{fo} experimentally is from the data in Figure 13, taking σ_{fo} as the stress corresponding to N_i. Since the value from equation 8 (that is logarithmic extrapolation of the stress-strain curve) agrees fairly well with this value the decrease due to $n^{\frac{n}{1-n}}$ must be approximately compensated by the introduction of σ_o into equation 10. That is, between about 60 and 75 percent of σ_{fo} at 293°K is due to dislocation interaction.

Values of σ_o from the tantalum data obtained by taking σ_{fo} from the plots of ln σ_f versus ln N, and n and K from the application of equation 1 at large values of ϵ are given in Table 1. The values of σ_o for the high and low density specimens tested at the same temperature agree within the experimental error and it appears that further exploration of these ideas is justified.

The experimental results quoted in this paper are taken from work by Dr. D. Hull and Mr. I. McIvor which is still in progress. The work is supported by the United States Air Force under contract AF33(616) - 6838 Materials Laboratory, W.A.D.C., Wright-Patterson Air Force Base, Ohio; Manlabs Inc., Subcontract No. 105.

References

1. D. Hull, I. McIvor and W.S. Owen, J. Less Common Metals, 1962 (to be published).

2. W. Carrington, K.F. Hale, and D. McLean, Proc. Roy. Soc. 1960, 259A, 203.

3. D.G. Brandon and J. Nutting, J. Iron Steel Inst., 1960, 196, 160.

4. A.S. Keh and S. Weissman, Conference on the Impact of Transmission Electron Microscopy, California 1961

5. A. Gilbert, D. Hull, W.S. Owen and C.N. Reid, J. Less Common Metals, in press.

6. A.R. Rosenfield, J. Inst. Met. in press.

7. I. Mogford and D. Hull, private communication.

8. G.T. Hahn, Acta Met., 1962, 10, 727.

Table 1

	Ta-E4 LD		Ta-E4 HD
Treatment	Cold-worked 90 percent. Annealed 1750°C for 6 min.		Cold-worked 90 percent. Annealed 1750°C, 6 min. Cold worked 2 percent Annealed 1000°C, 1 hour
Grain-size $d^{-\frac{1}{2}}$ $mm^{-\frac{1}{2}}$	2.8		2.8
Initial dislocation density N_i, cm^{-2}	1.0×10^9		1.6×10^{10}
Initial dislocation arrangement	Random		Networks
Test Temperature	240°K	293°K	293°K
Stress-strain curve			
σ_y Kg mm^{-2}	26.8	22.2	22.6
σ_{fo} Kg mm^{-2}	19.6	14.7	19.9
K c.g.s.	8.3×10^7	8.5×10^7	3.2×10^7
n	0.12	0.25	0.13
Equation 3			
σ_o Kg mm^{-2}	21.6	15.0	19.0
α	0.07	0.34	0.08
σ_{fo} Kg mm^{-2}	21.7	15.8	21.7
Figure 13			
σ_{fo} Kg mm^{-2}	22.5	16.4	22.4
Equation 4			
C	5.3×10^{13}	5.3×10^{11}	1.3×10^{12}
a	2.2	1.2	0.8

Table 1 (continued)

Equation 5:	C'	5.3×10^{13}	5.3×10^{11}	1.9×10^{12}
	a'	2.2	1.2	0.9
n/a from equation 6		0.06	0.21	0.16
n/a from Figure 13		0.07	0.17	0.15
Equation 10				
σ_o Kg mm^{-2}		7.9	7.1	7.6

Figure 1. TaE1 Anealed 1200°C.
X50,000

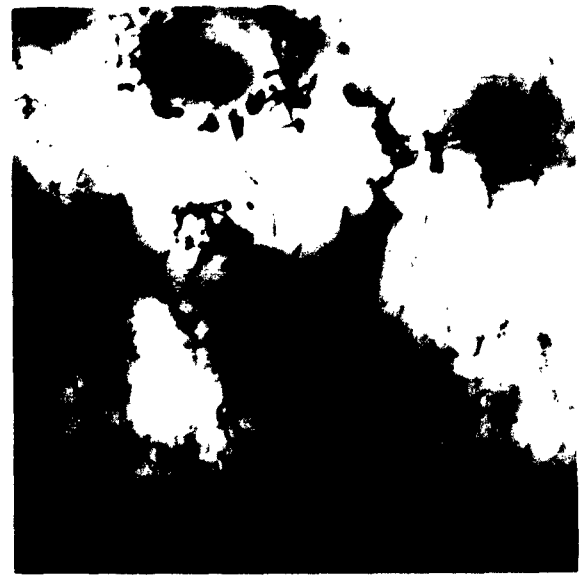

Figure 2. TaE1 Annealed 1200°C,
Deformed 7.3% in tension.
X40,000

Figure 3. TaE1 Annealed 1200°C,
Deformed 12.2% in tension.
X40,000

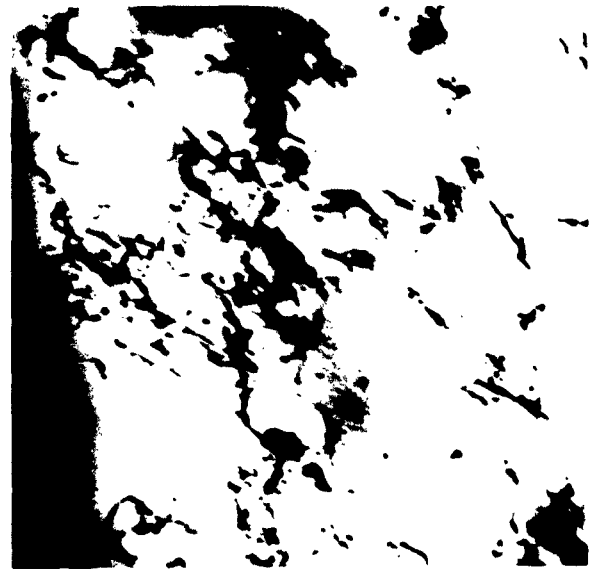

Figure 4. TaE4 Annealed 1750°C
Deformed 10.0% in tension
X40,000

Figure 5. TaE4 Annealed 1000°C, Deformed 6.7% in Tension X40,000

Figure 6. TaE4 Annealed 1000°C, Deformed 6.7% in Tension X40,000

Figure 7. TaE1 Annealed 1200°C, Deformed 10.6% in Tension X20,000

Figure 8. TaE4 Annealed 1750°C, Deformed 4.3% in Tension X60,000

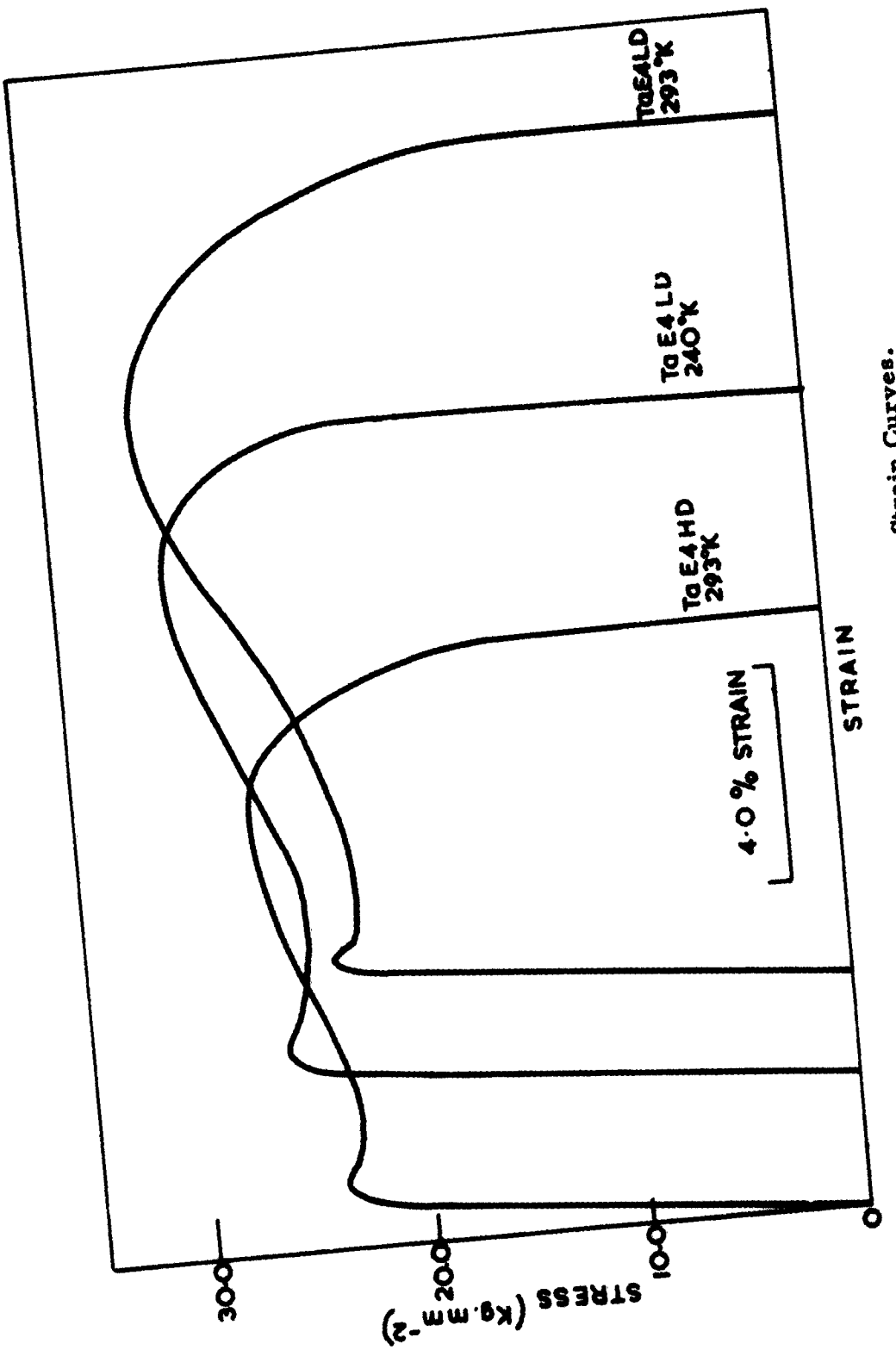

Figure 9. Experimental Stress - Strain Curves.

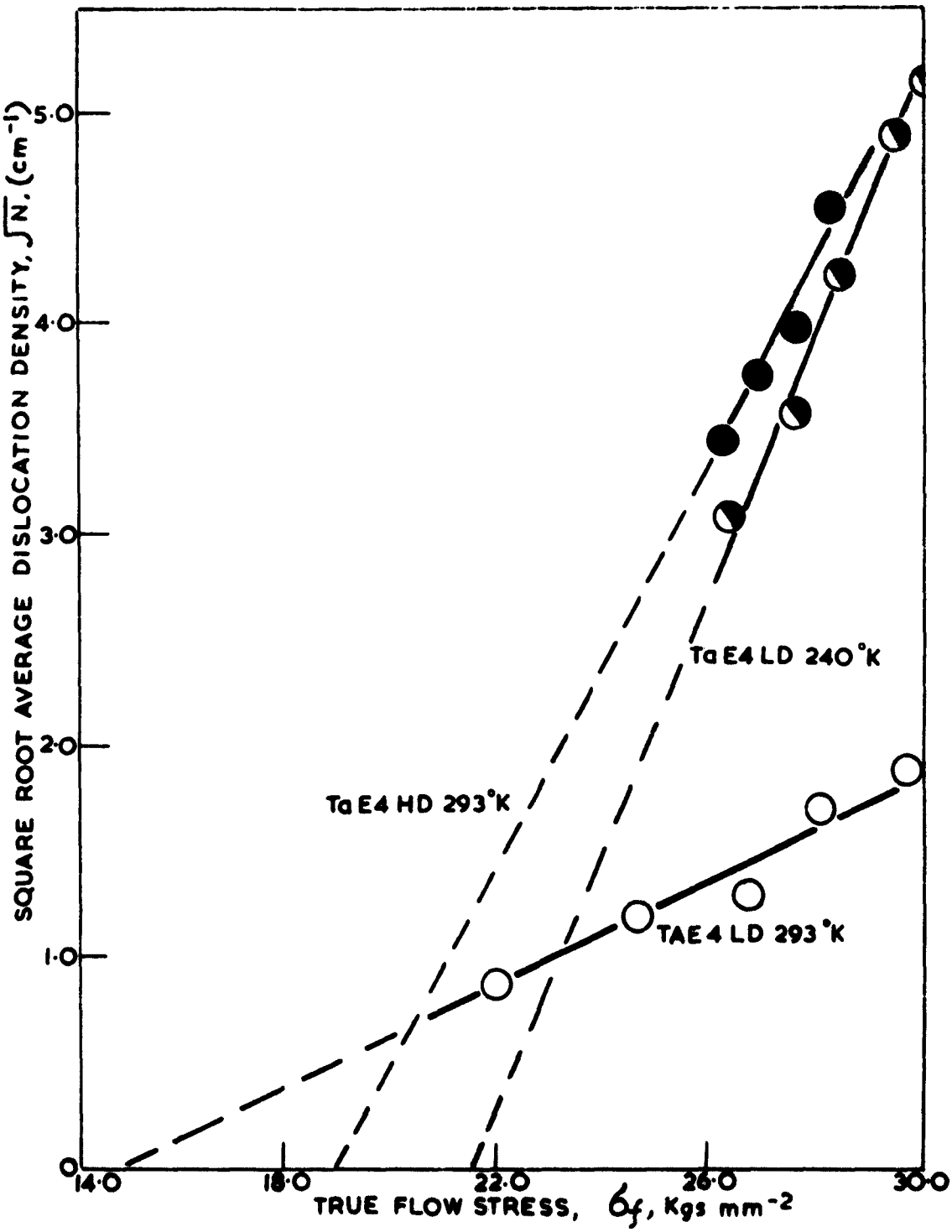

Figure 10. Dislocation Density as a Function of Flow Stress According to Equation 3.

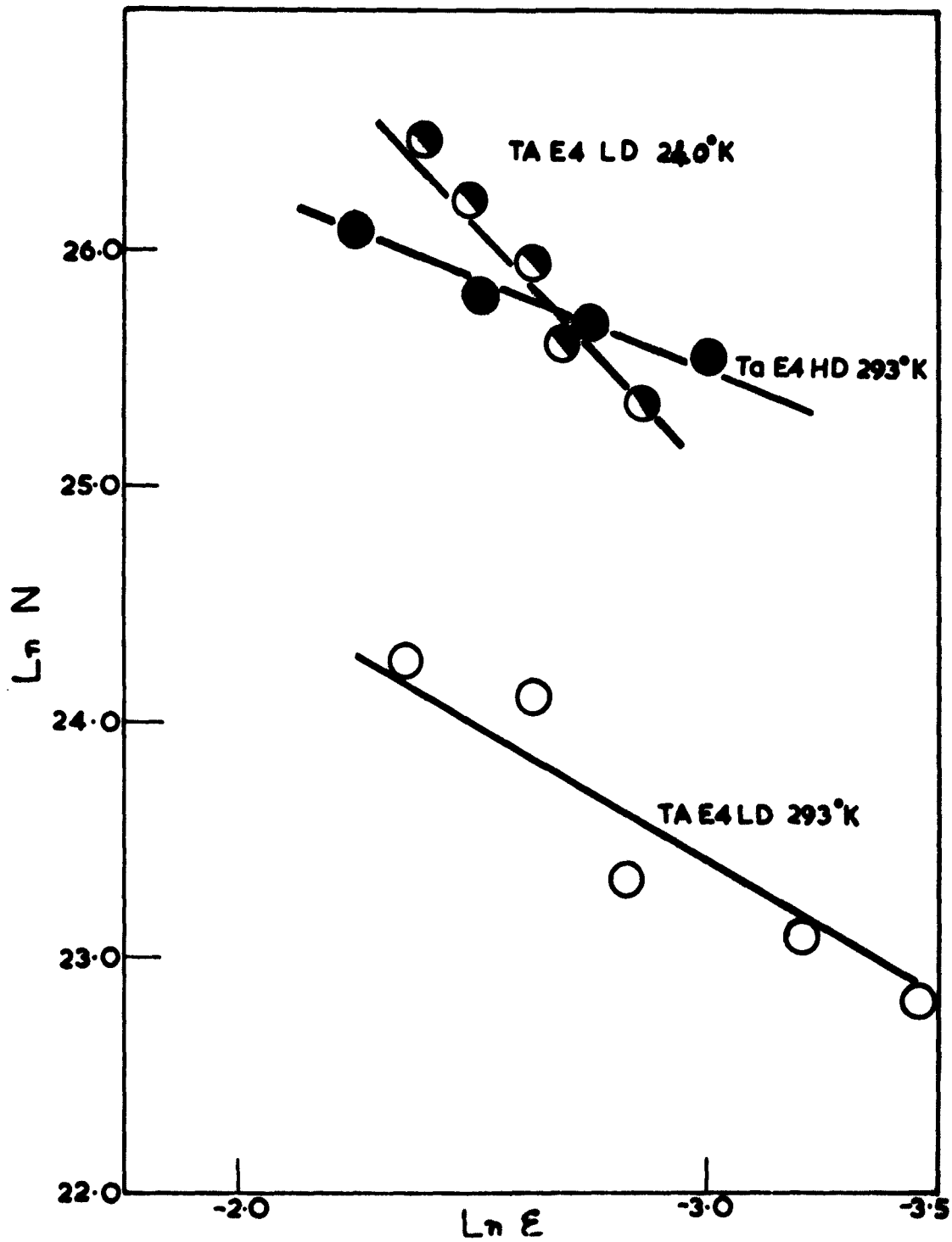

Figure 11. Dislocation Density as a Function of Strain According to Equation 4.

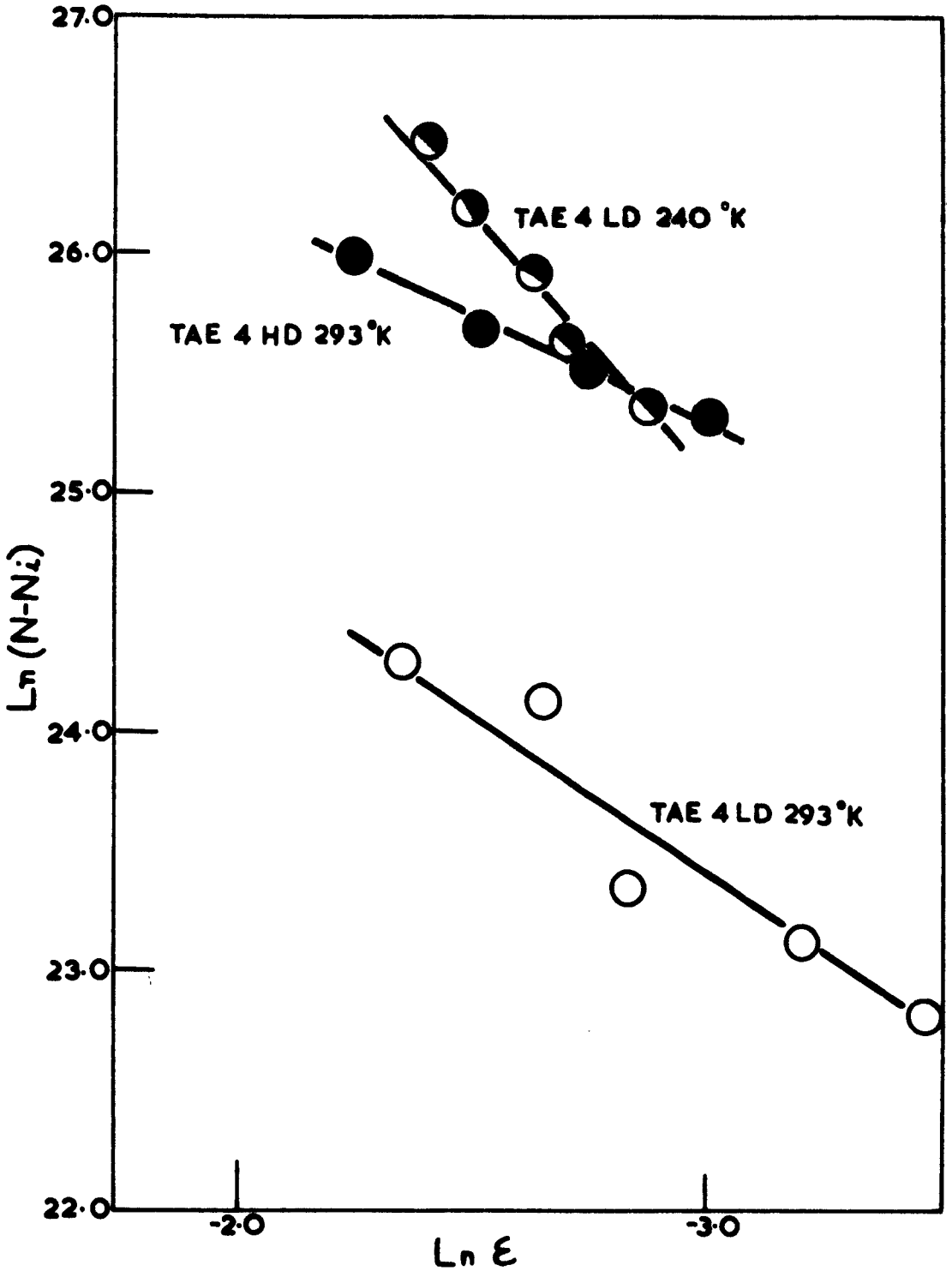

Figure 12. Dislocation Density as a Function of Strain According to Equation 5.

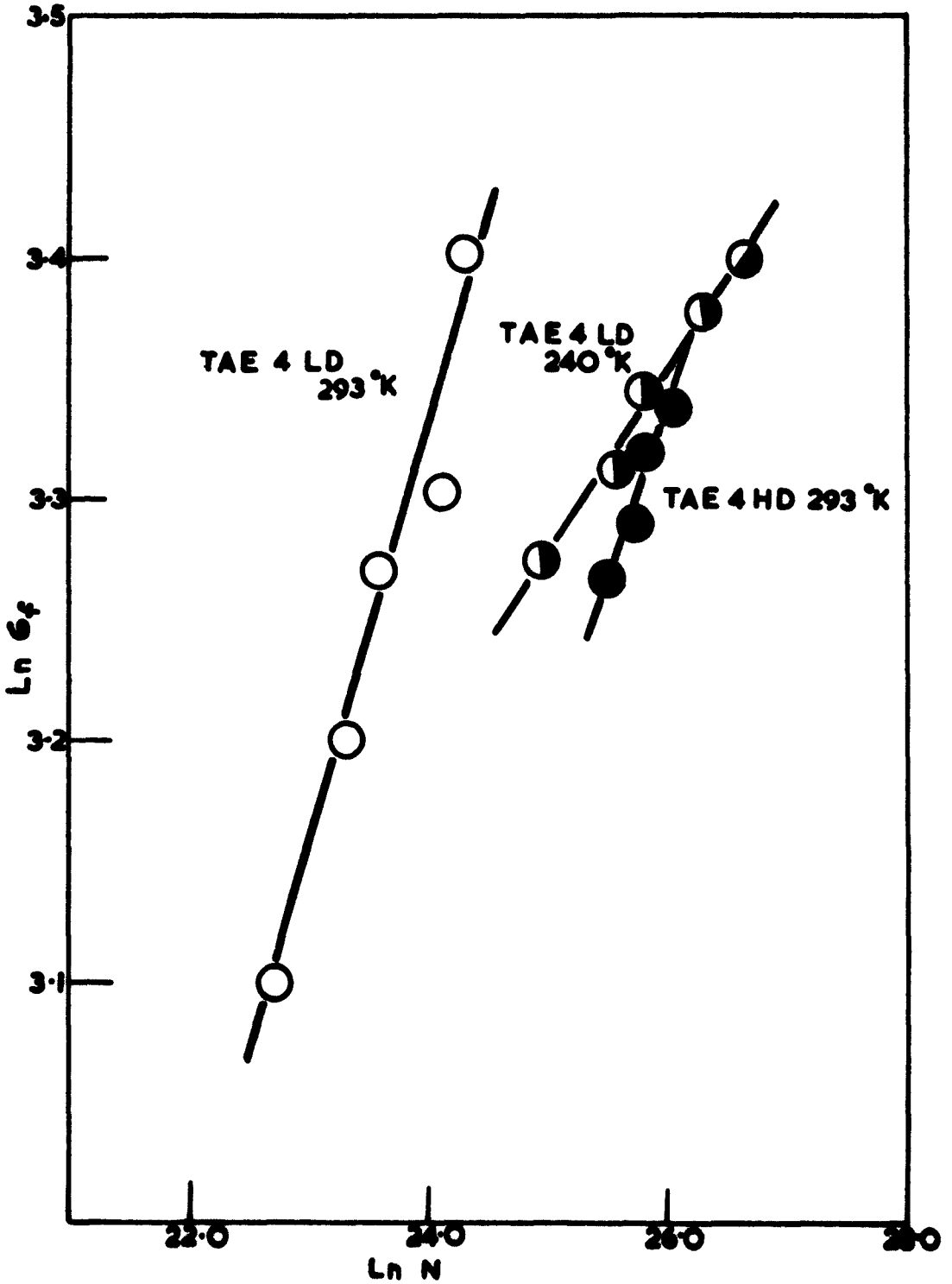

Figure 13. Flow Stress as a Function of Dislocation Density According to Equation 6.

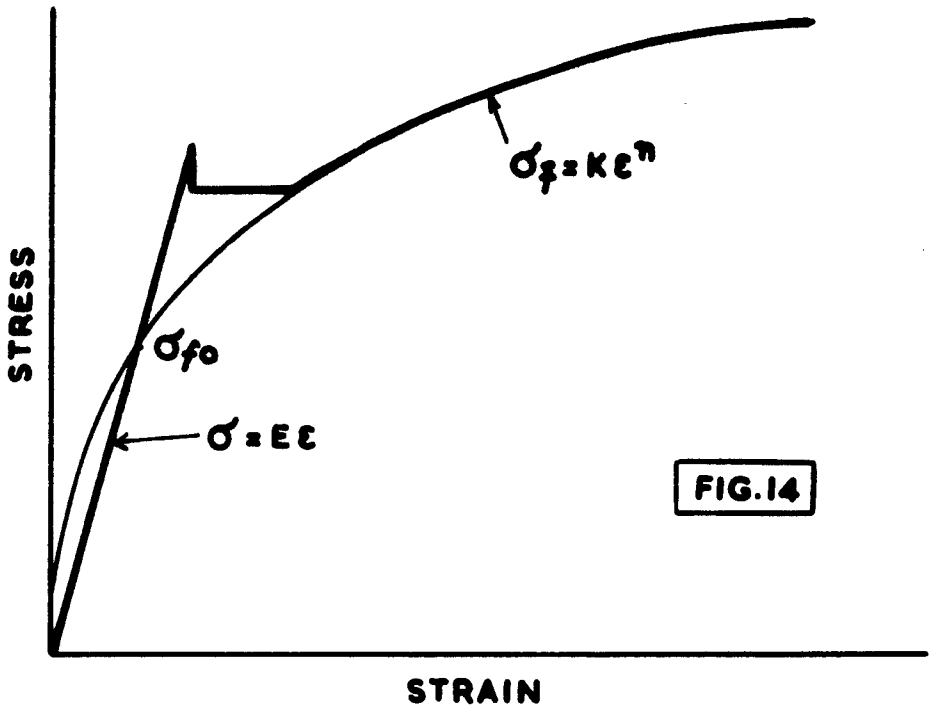

FIG. 14

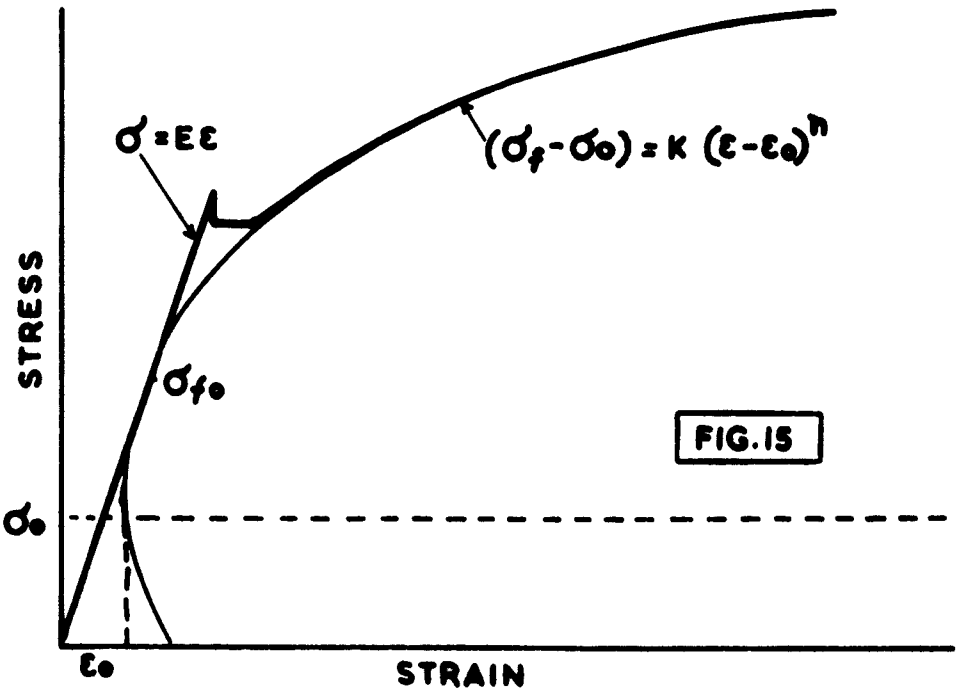

FIG. 15

Figures 14 and 15. Schematic Stress - Strain Curve.

DISLOCATION ARRANGEMENT IN COPPER SINGLE CRYSTALS DEFORMED AT LOW TEMPERATURES

Z. S. Basinski
National Research Council, Ottawa, Canada

The phenomenon of the plastic deformation of crystals, and, in particular, the aspect of work hardening, presents a very complex problem. To understand it we must explain the macroscopic observations, such as the stress strain curve with its dependence on temperature, strain rate, crystal orientation and impurity content, and also account for the various microscopic features such as the development of particular substructure, surface observations, etc. This would apply even if we are trying to explain the behaviour only of a particular crystal type, e.g., f.c.c.

In recent years, direct observation of thin sections of deformed crystals by transmission electron microscopy has been added to the already large arsenal of methods used in the study of plastic deformation, and, for a while, it appeared that the problem was almost solved. However, it now seems that the additional data only show that the process is much more complex than had been envisaged. The existing explanations of the work hardening process fall into several groups based on different structural models, and it should be possible to assess the validity of these on the basis of experimental observations. However, very often the experimental observations are inconclusive and critical experiments, for many reasons, are lacking.

Thin foil techniques suffer from the danger that the observed dislocation distribution may not be representative of the bulk material. Slip line measurements, on the other hand, are made on the surface region which may be atypical. Macroscopic deformation behaviour can be influenced by even minute amounts of impurity. It therefore seems advisable to collect as much information as possible and assess it carefully.

The present work deals with the deformation behaviour of Cu single crystals as studied by a combination of slip line observations, etch pit techniques and transmission electron microscopy. Copper crystals of preselected orientations were grown from the melt in graphite molds. The copper used was 99.999%, from American Smelting and Refining Company. To reduce the number of possible variables, the stress strain curve was obtained at low temperatures (usually 4.2°K), the effect of diffusion during deformation could then be neglected. Since warming copper specimens to room temperature for subsequent study did not affect either the flow stress or rate of strain hardening (Blewitt et al, 1957), subsequent changes are therefore not considered to be of major importance. After deformation the crystal was sliced to desired

orientations using a Servomet spark cutter modified to give a spark energy of about 1 erg per spark. The temperature rise 1/10 mm from the face being cut was less than 15°C, and the spark damage determined by dislocation etch pit counts on well annealed crystals was confined to a depth of less than 1/10 mm. Specimens were prepared from the slices by the method of Wilsdorf et al (1958) and examined in a Siemens Elmiscope I operating at 100 K.V. Specimens were examined in various reflections to determine the Burgers vectors of the dislocations present. The relative distribution of dislocations in three dimensions was determined by preparing stereo-photographs, (Basinski, 1962), using a Valdré goniometer stage (1962).

Etch Pit Measurements

The variation of dislocation density and distribution was studied by various authors, (e.g. Livingston, 1962; Young, 1961; Hordon, 1962). Livingston's data show that the flow stress correlates quite well with dislocation density except in the early stages of deformation of crystals oriented for single glide, where the etch pit density is somewhat high.

The orientation of the crystals used in the present work was almost identical with the single glide crystals of Livingston, the tension axis lay 8° away from the <110> direction on the great circle between the corner of the standard triangle and the slip direction. Etch pits were examined both on the cross glide plane and on the main glide plane to examine the difference between dislocation density lying in and threading the primary glide plane.

Fig. 1 shows the plot of the etch pit density versus flow stress. Livingston's data are included for comparison. In general the forest density is somewhat lower than the dislocation density lying in the main glide system; this difference decreases at higher stresses. No sign of a systematic deviation in the flow stress-density relation occurs for the forest dislocations although it is desirable to check this point further by making more measurements at lower stresses. The distribution of the etch pits on the cross and main glide planes is markedly different. Those on the cross glide plane are nonuniformly distributed and show alignment along the traces of the main glide plane, glide polygonisation, and an increase in etch pit density near sub-grain boundaries. These observations are in agreement with Livingston's work. The distribution of etch pits on the main glide plane, on the other hand, is much more uniform, no increase in etch pit density near sub-boundaries is observed (Fig. 2).

The absence of an increase in etch pit density near the sub-boundaries on the main glide plane indicates that dislocations of the secondary system move a distance short in comparison with the mean sub-grain size, and in spite of their comparatively large number presumably do not contribute appreciably to the overall

strain. This would appear to remove an important difficulty facing the observations, arising from the fact that the lattice rotations produced during deformation are well accounted for by assuming deformation on the primary system only, (e.g. Ahlers and Haasen, 1962), especially since the X-ray measurements would be insensitive to small amounts of strain occurring on other systems.

Further evidence for the activity of slip systems other than the primary one, even in the early stages of deformation, can be obtained from slip line observations. Fig. 3 shows slip lines on the cross slip plane of a specimen deformed to 345g/mm^2. Since the slip direction here lies in the plane of observation the primary system cannot produce any visible surface changes.

Foil Observations

Specimens deformed in easy glide show mainly edge dislocations belonging to the primary glide system. These, as expected from etch pit data, are distributed extremely unevenly with large areas of the foil being completely free of dislocations. Fig. 4 shows a region having a high density of dislocations. The primary glide direction here is vertical, and the dislocations have a form strongly resembling the "dipoles" observed in fatigued specimens (e.g., Segall, 1959), and in specimens deformed in tension, (e.g. Wilsdorf and Wilsdorf, 1961). On closer examination it is apparent that these are arranged in dense walls which contain not only dipoles but also single edge dislocations.

Occasionally the dislocation-free regions on either side of the wall have different contrast resulting from an excess of one sign of Burgers vector causing lattice tilting; but in most cases no difference in contrast is observed, indicating that the Burgers vectors of the dislocations in the wall add approximately to zero.

Another type of defect visible at this stage are straight faint segments of dislocation which end within the crystal. These invariably run along two of the <110> directions lying in the slip plane other than the slip direction. They have been shown (Howie, 1962) to be very narrow dipoles bounded by Frank sessile dislocations.

A very characteristic feature recurring in most of these photographs is the coincidence of dipole ends and other features along certain cross slip planes. The imperfect alignment of these ends in the two dimensional photographs can be seen in three dimensions to be due to the different depth of dipoles in the foil. These "slicing planes" are indicated by arrows in Fig. 4. Long dipoles must therefore have been cut into shorter pieces by slip occurring on cross slip planes. Since there is no evidence left at the ends of cut dipoles of trails which would indicate distributed slip, relatively large amounts of slip must have occurred on isolated or very closely spaced planes. The direction of this slip must have

had at least a component normal to the glide plane to account for the cutting of the dipoles, and displacing single dislocations into planes above or below their original plane (e.g. A in Fig. 4).

The dense regions of dipoles invariably show complex interactions along such a "slicing plane" (B in Fig. 4) and very often show there dislocations with different Burgers vectors (Fig. 5). These types of interaction can also be clearly seen in Fig. 6 obtained from a specimen strained to 340g/mm^2, and in fact on most photographs at this, and higher strains. This observation strongly suggests that the short dipole loops commonly seen, especially at higher strains, in deformed crystals result from chopping much longer dipoles probably formed originally by the lining up of edge dislocations, and not by repeated cross slip mechanisms (e.g., Johnston and Gilman, 1960) or dislocation interaction mechanisms proposed by Tetelman (1962).

A large number of short dipoles were usually observed in the vicinity of sub-grain boundaries, as can be seen in Fig. 7. The sub-grain boundary was identified by developing etch pits on the specimen after observation in the microscope, the boundary was seen to cross the carbonised region. These dipoles would appear as dense etch pits near a sub-boundary on the cross slip plane, but not on the main glide plane.

Stage II General Features

The following section refers mainly to work carried out with Dr. D. B. Dove, (to be published).

Electron microscopic observations on copper specimens from strip crystals deformed at low temperatures (78°K and 4.2°K) in Stage II show dense dislocation tangles which tend to lie on planes parallel to those for which the resolved shear stress is high. Similar observations were made by Howie (1960) in CuAl alloy crystals deformed at room temperature.

For crystals oriented for single glide most of the tangles are parallel to the primary glide plane, but some do lie on other planes; the frequency with which they occur being approximately in proportion to the resolved shear stress on that particular plane. Fig. 8.

The presence of strong contrast indicates that the dislocations in a tangle cause appreciable lattice rotation across it. This rotation was analysed in the electron microscope by examining the relative displacement of Kikuchi lines resulting from scattering by portions of the crystal on either side of a dense dislocation tangle. In every case examined the rotation axis appeared to lie in the slip plane (i.e. the plane of the tangle) normal to the slip direction. This, in fact corresponds to the rotation axis which is known to occur in the kink bands. Here,

however, the boundary lies in the slip plane and not in the plane normal to it. The displacement of Kikuchi lines gives information on only two components of rotation, the component parallel to the electron beam is difficult to determine, and in order to check this, some slices were cut having normals, (a) in the slip direction, and (b) lying in the main glide plane and perpendicular to the slip direction. Strong contrast across dislocation walls in specimens of the first type, and almost complete absence of such contrast in specimens of the second type, viewed in various reflections, supports the original conclusion.

When the crystals are oriented for double glide the dislocation tangles present a very striking cross-grid pattern (Fig. 9).

There does not seem to be much reliable evidence on the Burgers vectors of dislocations lying in these tangles. One important question is what proportion of the dislocations have Burgers vectors belonging to the primary slip system. Fig. 10 shows a specimen photographed in the reflection of the primary slip plane; all dislocations having Burgers vectors lying in this plane are therefore not visible. It is apparent that there is a very large number of dislocations belonging to systems other than the primary glide system. A striking feature of this figure is that even though the primary glide dislocations are absent, it is very easy to pick out the traces of the primary glide plane. It may be concluded from this feature that a relatively large number of sources on the secondary systems emit a small number of dislocations which travel short distances, rendering the deformation here much more homogeneous, and making its detection by either slip line studies or lattice rotation extremely difficult.

Photographs of specimens obtained from the surface regions of crystals deformed in Stage II show that the dislocation distribution there is quite different from that in the interior of the crystal. Fig. 11 shows part of a foil polished from one side only. Slip lines, due to changes in thickness, are clearly visible. In spite of the close correlation between the prominent directions on the surface and in the interior of the crystal, there is very little correlation between slip lines and the crystal just underneath them. The dislocations here are less tangled and are arranged approximately at random. That the material just under the surface is atypical is hardly surprising since not only are the dislocations near the surface subjected to image forces which may modify their behaviour, but also a large number of dislocations leave the crystal to produce slip bands. Whereas in the interior of the crystal dislocations travel in both directions, unless a large number of additional sources operates at the surface (corresponding to the number contained in a slab whose thickness is equal to the dislocation mean free path), the loss of dislocations at the surface must be compensated by an increase in the distance travelled by the dislocations in this region.

Dislocation Networks in the Main Glide Plane

To attempt to elucidate the nature of the dense dislocation tangles sections of the crystal were cut parallel to the main glide plane, from crystals stretched up to about 1.7kg/mm^2. Several distinct types of dislocation arrangements were to be observed. One feature is the three dimensional networks containing a large number of short segments of Cottrell-Lomer dislocations. These result from reaction at the intersection with both the conjugate and critical slipplanes, however, specific areas usually contain a predominance of one type. Fig. 12a shows a typical example of such a region. In Fig. 12b, the Cottrell-Lomer dislocations are invisible.

In some regions, portions of the crystal which are reasonably free of dislocations are separated by long narrow tangles lying along the traces of the highly stressed secondary slip plane (Fig. 13). These presumably occur when sections are cut between the dense networks of the main glide system, and show a section through a steeply inclined secondary glide tangle. Here a large number of edge dislocation dipoles belonging to the primary glide system is visible, and suggests quite an extensive crossing of these tangles by primary glide dislocations. This is rather similar to the large number of primary glide dislocation dipoles associated with the sub-grain boundary, as in Fig. 7.

In some areas dense patches of short dipoles were observed. As expected the Burgers vectors of the dislocations comprising them always lay in the slip direction.

Preliminary observations on a crystal whose tension axis lay in the <211> direction indicate that the distribution of dislocations here is not fundamentally different from that in crystals oriented for single glide. In this case, however, mainly Cottrell-Lomer dislocations resulting from interaction with the conjugate system were observed. So far, no dense networks were seen in which the Cottrell-Lomer dislocations completely predominate. This may not be significant since the number of specimens of this orientation examined was small.

Sections parallel to both of the active glide planes showed also dipole patches in each case lying in the plane of observation. Here too, as in easy glide of crystals oriented for single slip, the "slicing" on the cross slip plane could clearly be seen. An example is shown in Fig. 14.

Discussion

From the data presented it appears that in copper crystals deformed at low temperatures in Stage I most of the dislocations remaining in the lattice are edge dislocations belonging to the primary slip system. Comparison of the dislocation densities obtained from etch pit data, with the strain, gives for the

dislocation mean free path, $\lambda \simeq \frac{\epsilon}{\rho b}$, the surprisingly large value of 2-4 mm. This may be compared with a value of about 25μ obtained by Wilsdorf and Schmitz (1962) in aluminium deformed at room temperature. Although the estimate for copper may be somewhat high, since dense clumps of edge dislocations may not be resolvable into individual etch pits, it is improbable that this would account for a difference of a factor of 10^2. It is difficult to estimate the dislocation density in Stage I from thin foils because of the very nonuniform distribution. However, in Stage II the densities from thin foil counts and etch pit counts agree to within a factor of 2. It therefore appears that the discrepancy must lie in a difference in both material and the temperature of deformation. The large mean free path of the dislocations in easy glide is also indicated by the large scale crossing of sub-boundaries. It is not clear at present whether screw dislocations are not visible because they cross slipped during deformation or because they are lost from the foil during thinning.

In spite of the long mean free path, the dislocation density on the primary glide plane is still larger than would be expected from the flow stress. These dislocations therefore cannot harden the crystal very effectively. It is often asserted (Seeger et al, 1961) that the forest density does not increase during easy glide and only slowly even in Stage II. These authors assume that the temperature dependent flow stress comes from the forest contribution and the lack of its increase in easy glide is taken as evidence of no increase in the forest density. Recent work (Basinski and Dove, to be published) has shown, however, that the flow stress ratio in the early stages of deformation is extremely sensitive to small amounts of impurity, and therefore the forest contribution to the temperature dependent flow stress may be completely swamped by the impurity contribution during easy glide.

The present results leave little doubt that the forest density does increase during deformation.

Several mechanisms have been proposed for the formation of dislocation dipoles, sometimes called prismatic loops, during deformation. The first mechanism considered by various authors, (e.g. Johnston and Gilman, 1960; Price, 1960; Wilsdorf and Fourie, 1960) envisages cross slip by a screw dislocation with the formation of a large jog which during subsequent glide gives rise to a dislocation dipole. Cross slip to the original plane then completes the process producing a prismatic dislocation loop. It is difficult to see how a large length of dislocation would cross slip simultaneously; and cross slip by a short segment would produce two dipoles of opposite sign close to each other, which could then easily annihilate by gliding during subsequent deformation. Furthermore, recross-slipping of a screw dislocation to its original plane appears to be a rather improbable process. A more plausible mechanism proposed by Tetelman (1962) envisages an elastic interaction between

dislocations having an edge component and lying on a parallel glide plane, followed by cross slip of the screw components separating a prismatic loop.

The perfect alignment of dipole ends on a particular cross slip plane almost invariably observed, however, supports the view that the mechanism of this loop formation may be much simpler. Edge dislocations mainly during Stage I of the deformation get stopped by other edge dislocations producing reasonably long dislocation walls, which subsequently get cut into shorter pieces by slip on the cross glide plane. A large number of short dipoles could be produced by such a process. Since the long range stresses would favour the formation of edge dislocation tangles composed of dislocations of opposite signs we would expect that dipoles would predominate over single dislocations in such a wall.

With increasing deformation in Stage II the relative prominence of the dipoles decreases rapidly and it is quite probable that not many of them are formed once the other systems become more active, and that the dislocations in Stage II are stopped by other interactions.

Stage II

The most noticeable change in the dislocation arrangements with the onset of Stage II is the increasing appearance of dislocations with Burgers vectors other than that of the main glide system, until, at stresses of about 2 - 3kg/mm^2 the predominance of dislocations of the primary system over any other seems to be almost lost. At first sight this observation may seem rather surprising in view of the fact that most of the strain appears to have been produced by the operation of the primary systems in crystals oriented for single glide. But, unless the slip on the primary system is distributed extremely homogeneously, or the slip displacement continues in each packet right across the crystal, large accommodation stresses will be present which can only be relieved by glide on secondary systems. Reactions between the primary and secondary dislocations then could produce the networks observed in Stage II. The presence of tangles in crystals deformed at liquid helium temperature shows that interaction with point defects (Wilsdorf and Wilsdorf, 1961) is not necessary for their formation.

The lattice rotations observed around the $\langle 211 \rangle$ direction are surprising since it is not easy to see how a simple dislocation network could produce them without involving a prohibitive amount of long range stress. However, Cottrell-Lomer barriers lying in both of the possible directions were observed and it can be shown that a combination of these with some screw dislocations derived from the two other slip directions lying in the primary glide plane could produce a network free of long range stresses and giving the required lattice rotation. It may be that this type of rotation is preferred by

the lattice to the twist type boundary, because it does not require very large additional accommodation at the ends of a cell.

Much additional work, however, especially involving careful analysis of all the components of the dislocation networks is required before all the aspects of deformation mechanisms can be understood.

REFERENCES

Ahlers and Haasen, P. 1962 Acta Met. 10, 977 (L).
Basinski, Z. S. 1962, 5th Int. Cong. Elec. Microscopy, Philadelphia, 1, B13.
Blewitt, T. H., Coltman, R. R. and Redman, J. K. 1957, J. Appl. Phys. 28, 651.
Fourie, J. T. and Wilsdorf, H. G. F. 1960, J. Appl. Phys. 31, 2219.
Hordon, M. J. 1962, Acta Met. 10, 999.
Howie, A. 1960, Ph.D. Thesis (Cambridge) and European Regional Conference on Electron Microscopy, Delft 1960, 383.
Howie, A. 1962, Private communication.
Johnston, W. G. and Gilman, J. J. 1960, J. Appl. Phys. 31, 632.
Livingston. 1962, Acta Met, 229.
Price, P. B. 1960, Phil. Mag. 5, 873.
Seeger, A., Kronmuller, H., Mader, S. and Trauble, H. 1961, Phil. Mag. 6, 639.
Segall, R. L. and Partridge, P. G. 1959, Phil. Mag. 4, 912.
Valdré, U. 1962, J. Sci. Inst. 39, 278.
Wilsdorf, H. G. F., Cinquina, L. and Varker, C. J. 1958, 4th International Conference on Electron Microscopy, Berlin, 559.
Wilsdorf, H. G. F. and Schmitz, J. 1962, J. Appl. Phys. 33, 1750.
Wilsdorf, H. G. F. and Wilsdorf, D. 1961 Proc. 1st Int. Mat. Conf. Berkeley.
Young, F. W. 1961, J. Appl. Phys. 32, 192.

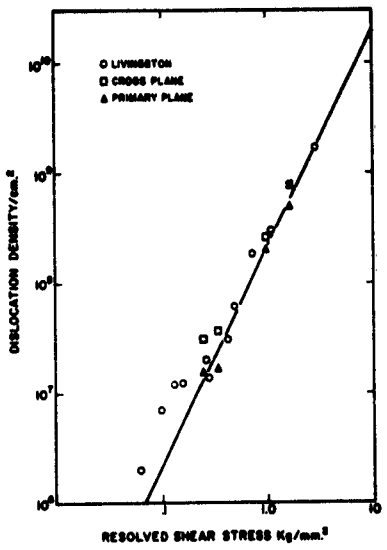

Figure 1 Etch pit density versus stress.

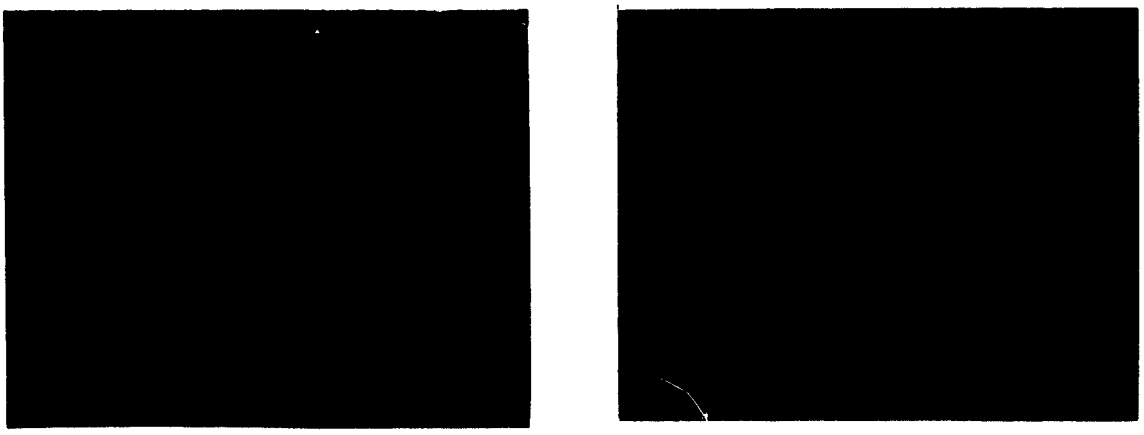

(a) (b)

Figure 2. Dislocation etch pits; (a) cross slip plane; (b) main glide plane, note absence of increased density near sub-boundary.

Figure 3. Slip lines on cross slip plane. (x 225). Resolved shear stress 345g/mm².

Figure 4. Stereo pair of a dislocation clump in the early stage of deformation. σ = 245g/mm²., deformed at 4.2 K.. Section parallel to main glide plane. Slip direction vertical. (x 15,000).

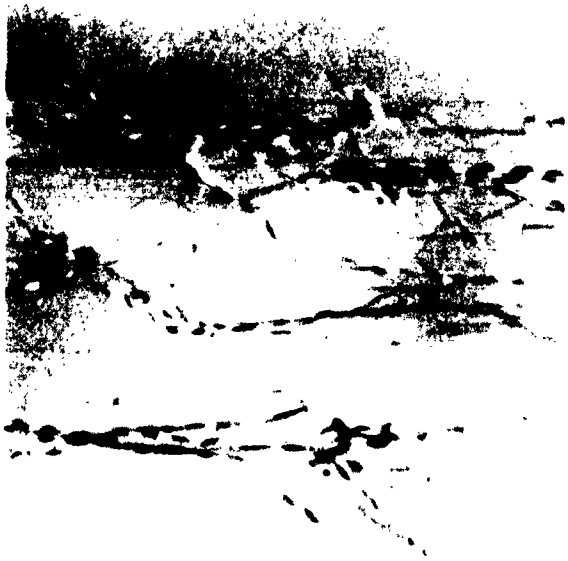

Figure 5. Same as 4, g.b = 0 for main glide system.

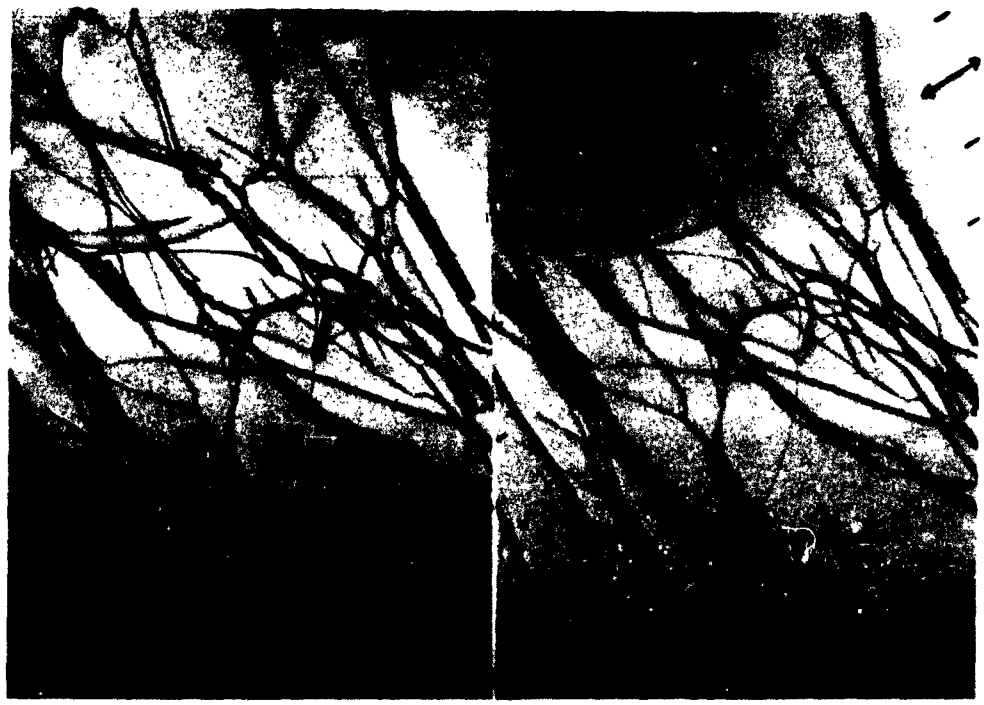

Figure 6. Stereo pair later in easy glide. Section parallel to main glide plane, slip direction indicated by arrow. (x 15,000)

Figure 7. Section showing sub grain boundary. (x 15,000)

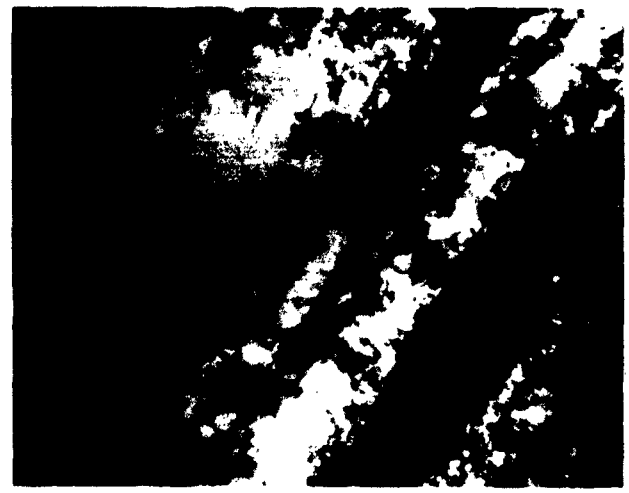

Figure 8. Strip crystal deformed at 4.2°K in stage II. Single glide orientation. Not dislocation tangles and contrasts parallel to main glide plane. (x 15,000) (Basinski & Dove, to be published.)

Figure 9 Crystal deformed at 78°K. Double glide orientation. (x 15,000) (Basinski & Dove, to be published.)

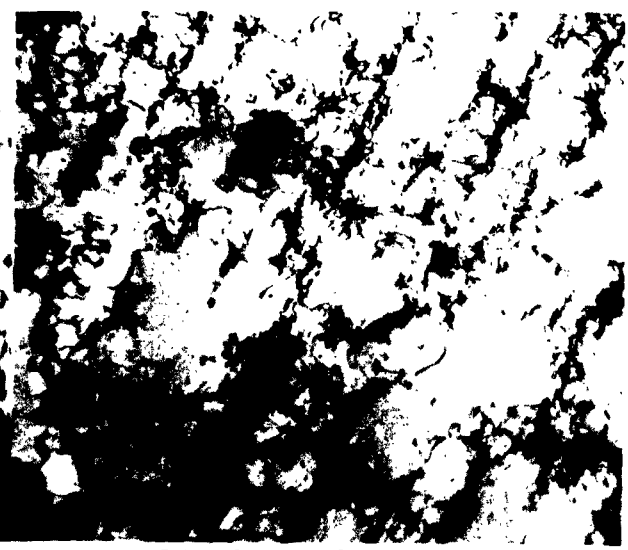

Figure 10. Crystal in single glide orientation, deformed at 4.2°K. Contrast from reflection in main glide plane; dislocations with Burgers vectors lying in this plane are invisible. (15,000) (Basinski & Dove, to be published)

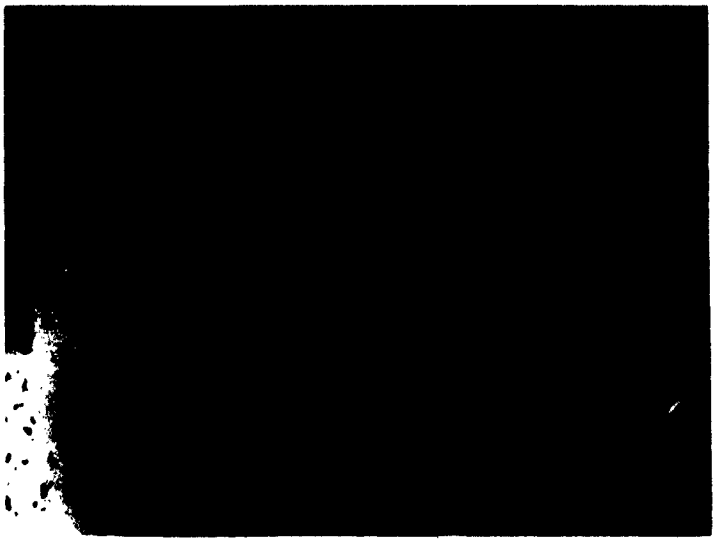

Figure 11. Copper, single glide orientation, deformed at 4.2°K. Polished from one side only. Note the absence of correlation between slip lines and dislocation arrangement. (x 15,000).

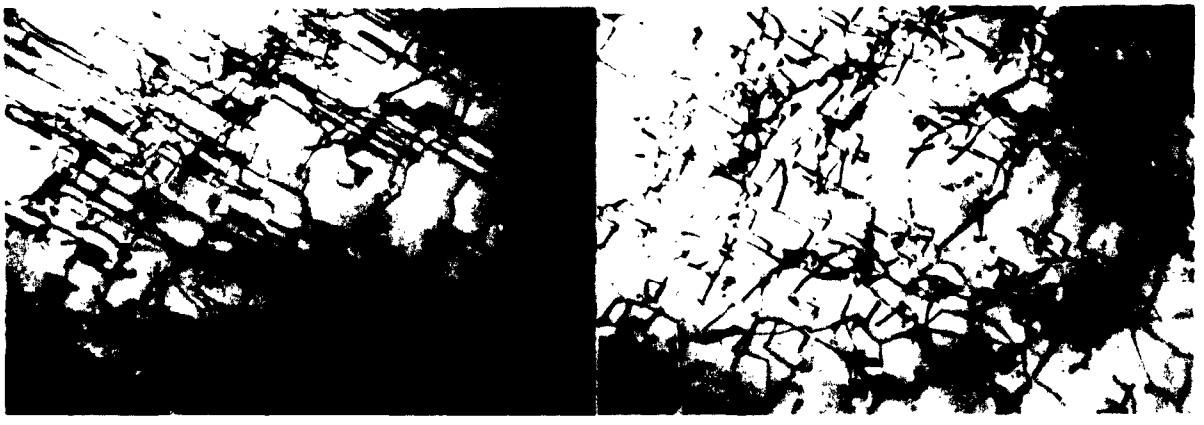

(a) (b)

Figure 12. Network containing a large number of Cottrell-Lomer dislocations. Section parallel to main glide plane. In 12 (b) g.b for Cottrell-Lomer dislocations is zero. $\sigma = 995 g/mm^2$. (x 15,000)

Figure 13 (x 15,000)

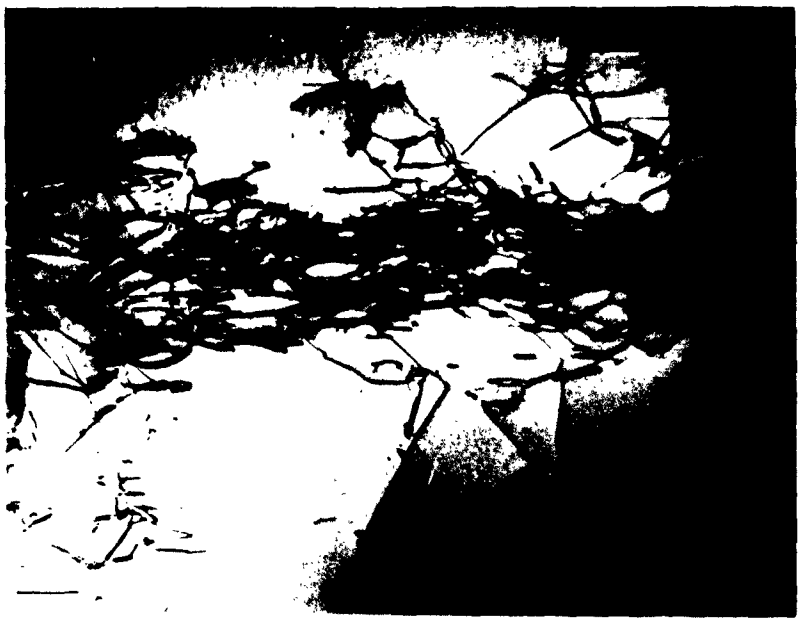

Figure 14. Section parallel to one of the glide planes. Crystal oriented for double glide. Slip direction in this plane is vertical. (x 15,000).

SUBSTRUCTURE AND THE FLOW STRESS OF POLYCRYSTALS

by

J.D. Meakin* and N.J. Petch,

University of Durham, King's College, Newcastle upon Tyne, England.

ABSTRACT

From a study of polycrystalline alpha brasses, it is shown that the dislocation structure developed in the high Zn alloys (low stacking fault energy) during a strain ε gives a hardening $\alpha\varepsilon + \beta\varepsilon^{\frac{1}{2}}\ell^{-\frac{1}{2}}$, where α and β are constants and ℓ is the grain diameter. Thus, in the equation for the flow stress σ_f at constant strain, $\sigma_f = \sigma_o^f + k_f \ell^{-\frac{1}{2}}$, where σ_o^f is the friction stress and k is a constant, σ_o^f increases linearly with strain and k_f also increases with strain because of the inclusion in it of the strain hardening $\beta\varepsilon^{\frac{1}{2}}\ell^{-\frac{1}{2}}$. At high strains or low Zn contents, cross-slip and cell formation occurs; the significance of the grain size in the flow stress then diminishes and k_f falls.

The present paper describes a study of the effect of substructure on the flow stress of polycrystalline α-brasses. The term substructure is here used in a very general sense to denote the dislocation structure produced by the plastic deformation during the flow stress measurement. There is no attempt to restrict the term to mean the presence of definite subgrain networks.

The α-brass system was chosen for this work because it presents the possibility of a wide variation of dislocation locking strength and of stacking fault energy with composition, and because there is a long range of almost linear hardening, at least with high zinc contents. It was felt that these qualities might simplify the interpretation of the results and this proved to be the case.

First, the experimental facts. Prior to the present work, it had been shown (1) that the equation relating the lower yield stress σ_y of a polycrystalline material to the grain diameter ℓ, namely,

$$\sigma_y = \sigma_o + k\ell^{-\frac{1}{2}} \qquad \ldots\ldots\ldots (1)$$

where σ_o and k are constants, has a counterpart in the equation relating the flow stress σ_f at a given strain with the grain diameter, so that

$$\sigma_f = \sigma_o^f + k_f \ell^{-\frac{1}{2}} \qquad \ldots\ldots\ldots (2)$$

* Now at the Franklin Institute, Philadelphia.

This applies to the flow stress after the yield point and also to the flow stress in the absence of a yield point.

The present work has examined the effect of substructure through the application of equation (2). Figure 1, which plots the yield stress and the flow stresses at various strains for a 25% Zn alloy at 77°K as a function of grain size, illustrates the type of result obtained. It will be seen that equations(1) and (2) fit the measurements closely. Also, as the strain increases, σ_o^f increases and there are alterations in k_f. This type of measurement was made on a series of brasses up to 35% Zn. The measurements extended to strains just below the onset of necking.

Figure 2 shows the variation with composition and strain of the slope k_f extracted from these measurements at 77° and 295°K. Three points are clear.

(a) The value of k at the yield point increases with zinc content, except for a final decrease at 35%.

(b) With the high zinc alloys, k_f increases with strain up to a maximum and then decreases. The maximum occurs at a strain of 0.1/0.15 for alloys with 25% Zn and above, but it occurs at lower strains with lower zinc contents, and at 10% Zn and below no initial increase in k_f was detected, only a progressive decrease.

(c) The value of k at the yield point is independent of temperature, but the increase of k_f with strain in the high zinc alloys is less at the higher temperature.

Values of σ_o were also extracted from the measurements. At the yield point, these showed an increase with zinc content and quite strong temperature-dependence, but the increase in σ_o^f with strain is of greater interest in the present connection and this is plotted in Figure 3 for 77° and 295°K. With 20% Zn and above, the increase with strain is accurately linear at 77°K up to the highest strain used and the slope is practically independent of composition. Some departure from linearity occurs with the lower zinc alloys. The measurements at 295°K show that the linear slope is practically independent of temperature, but the departure from linearity is more marked at this temperature, and it occurs at smaller strains and in alloys of higher zinc content.

INTERPRETATION

In the simplest interpretation (1) of equation (2), derived from its relationship to equation (1), σ_f represents the "friction stress" in a slip band. That is, the stress a slip band could sustain if the displacement in it could move out freely at the grain boundary, so producing a step in the boundary. The other term $k_f \ell^{-1/2}$ then represents the limiting value of the additional stress the slip band can sustain because such step formation is opposed by the next grain. The limiting value of this additional stress arises when the stress generated at the end of the slip band induces plastic deformation in the next grain.

On this view, the increase of σ_o^f with strain represents simply the effect of strain-hardening and the alterations in k_f must represent other complicated changes in the grain boundary resistance to slip band formation.

To maintain compliance with equation (2) and yet retain this simple interpretation, it will be noted that the rate of strain-hardening must be independent of grain size, so that all sizes have the same friction stress at a given strain. It is not obvious that this should be true. Unless the average distance a dislocation travels is the same for all grain sizes, the dislocation structure at a given strain will depend upon grain size and this may well give rise to a variation in the friction stress.

In the present paper, it is suggested that such a variation does happen in the α-brasses. The argument is that the strain-hardening has a grain-size-dependent component, so that part of the friction stress becomes incorporated in the $k_f \ell^{-1/2}$ term in equation (2) and this accounts for the increase in k_f with strain.

To develop this argument, the details of the strain-hardening have to be considered.

It is clear from Figure 1 that the principal strain-hardening effect appears in σ_o^f. Figure 3 shows that it is a linear hardening. Further, it is, of course, independent of grain size (since grain size effects are extrapolated out in obtaining σ_o^f), and it is independent of temperature and of composition, except that linearity breaks down at smaller strains the higher the temperature and the lower the zinc content. The rate of hardening is in the range $\mu/230$ - $\mu/290$, where μ is the rigidity modulus. All this suggests close similarity to Stage II hardening in f.c.c. single crystals. Enough has been argued about the mechanism of such hardening to make further comment unnecessary, and possibly unwise here.

Consider now the possibility of a grain-size-dependent strain-hardening. In the high zinc alloys, the stacking fault energy is low, so the wide separation of the partials confines them to the slip plane and inhibits cross-slip. In this circumstance, grain boundary pile-ups rather than dislocation networks should form in the strained condition. Consequently, L, the average slip distance of a dislocation, should be comparable to the grain diameter ℓ.

If ρ is the dislocation density and $\underline{b}$ is the Burgers vector, then at a shear strain γ,

$$\gamma = \rho \, b \, L.$$

Thus, where $L \sim \ell$, a fine grain specimen must have a higher dislocation density at a given strain than a coarse grain one. This will affect the strain-hardening due to dislocation intersection.

Taking the shear stress τ' required for intersection as

$$\tau' = \alpha \mu b \rho^{1/2}$$

where α is a constant, it follows that

$$\tau' = \alpha \mu b^{1/2} \gamma^{1/2} L^{-1/2}$$

Using the Taylor orientation factor m to convert to tensile stresses and strains (1) and putting $L = \ell$,

$$\sigma' = \alpha m^{3/2} \mu b^{1/2} \varepsilon^{1/2} \ell^{-1/2} \quad \ldots\ldots\ldots (3)$$

Thus, on this model, which depends upon having $L \sim \ell$, there should be a parabolic strain hardening term that is proportional to $\ell^{-1/2}$

The total strain-hardening at ℓ will then be $(\chi\varepsilon + \beta\varepsilon^{1/2}\ell^{-1/2})$ where χ and β are constants and $\chi\varepsilon$ is the linear hardening that is extracted into $\sigma_0{}^f$ in equation (2) and $\beta\varepsilon^{1/2}\ell^{-1/2}$ is the parabolic hardening that will appear in k_f.

We now add to this a belief that the limiting grain boundary resistance to slip band formation arises when dislocations are forced out from the grain boundary at the end of a slip band and that the stress required depends principally on interaction with alloy atoms segregated in the boundary. This resistance should then remain fairly close, whatever the strain, to the original value $k\ell^{-1/2}$ given by equation (1) for the yield point.

With these conclusions and provided the strain does not affect the process responsible for the initial friction stress σ_0, the flow stress at should be given by

$$\sigma_f = \sigma_0 + \chi\varepsilon + (k' + \beta\varepsilon^{1/2})\ell^{-1/2} \quad \ldots\ldots\ldots (4)$$

Comparison with equation (2) gives

$$\sigma_0^f = \sigma_0 + \chi\varepsilon$$

$$k_f = (k + \beta\varepsilon^{1/2})$$

Thus, it is concluded that the increase in k_f with strain observed with the high zinc alloys arises from the incorporation in k_f $\ell^{-1/2}$ of the parabolic strain hardening $\beta\varepsilon^{1/2}\ell^{-1/2}$ in addition to the grain boundary resistance $k\ell^{-1/2}$

The value of β from (3) is $\alpha m^{3/2} b^{1/2} \mu$, which gives 1.9 kg mm$^{-3/2}$, using α = 0.2 from Bailey and Hirsch (2). The present measurements on k_f for the 25, 30 and 35% Zn alloys at 77°K agree with equation (4), and give a value of β = 1.6 kg mm$^{-3/2}$

Since the parabolic hardening is attributed here to dislocation intersection, temperature-dependence is a possibility and the smaller increase in k_f with strain at 295°K compared to 77°K, shown in Figure 2, is consistent with this.

Current theoretical ideas on the theory of strain-hardening are rather fluid and it may be that developments in this field will require a modification of the present attribution of parabolic hardening to dislocation

intersection. The point that we wish to emphasize is not so much this attribution as the existence of the parabolic grain-size-dependent term.

Consider now the drop in k_f with increasing strain that occurs with the low zinc alloys and even with the high zinc ones at larger strains (Figure 2).

The low zinc alloys have a high stacking fault energy, so cross-slip and the development of a dislocation cell structure can be expected at an early stage in the plastic deformation. Even with the low stacking fault alloys, cell formation should eventually occur.

Once cell structure is present, it is improbable that the slip distance is fixed by the grain size, so the basis for equation (4) and for the $\beta \epsilon^{1/2} l^{-1/2}$ term disappears. With a strongly developed cell structure, this, rather than the grain structure, may become the significant unit in plastic deformation. Thus, the reduced significance of grain size shown by a drop in k_f in Figure 2 is thought to be due to cell formation when cross slip occurs. This condition is also associated with the departure from linear hardening of σ_o^f.

The conclusion from this study is that when the dislocations are confined to their slip planes, the dislocation structure developed on deformation gives a flow stress that follows equation (4), but once cross-slip, leading to cell formation, occurs, the significance of the grain size decreases and σ_o^f shows departure from linear hardening.

REFERENCES

1. R. Armstrong, I. Codd, R.M. Douthwaite and N.J. Petch, Phil. Mag., Vol. 7, 45, 1962.

2. J.E. Bailey and P.B. Hirsch, Phil. Mag., Vol. 5, 485, 1960.

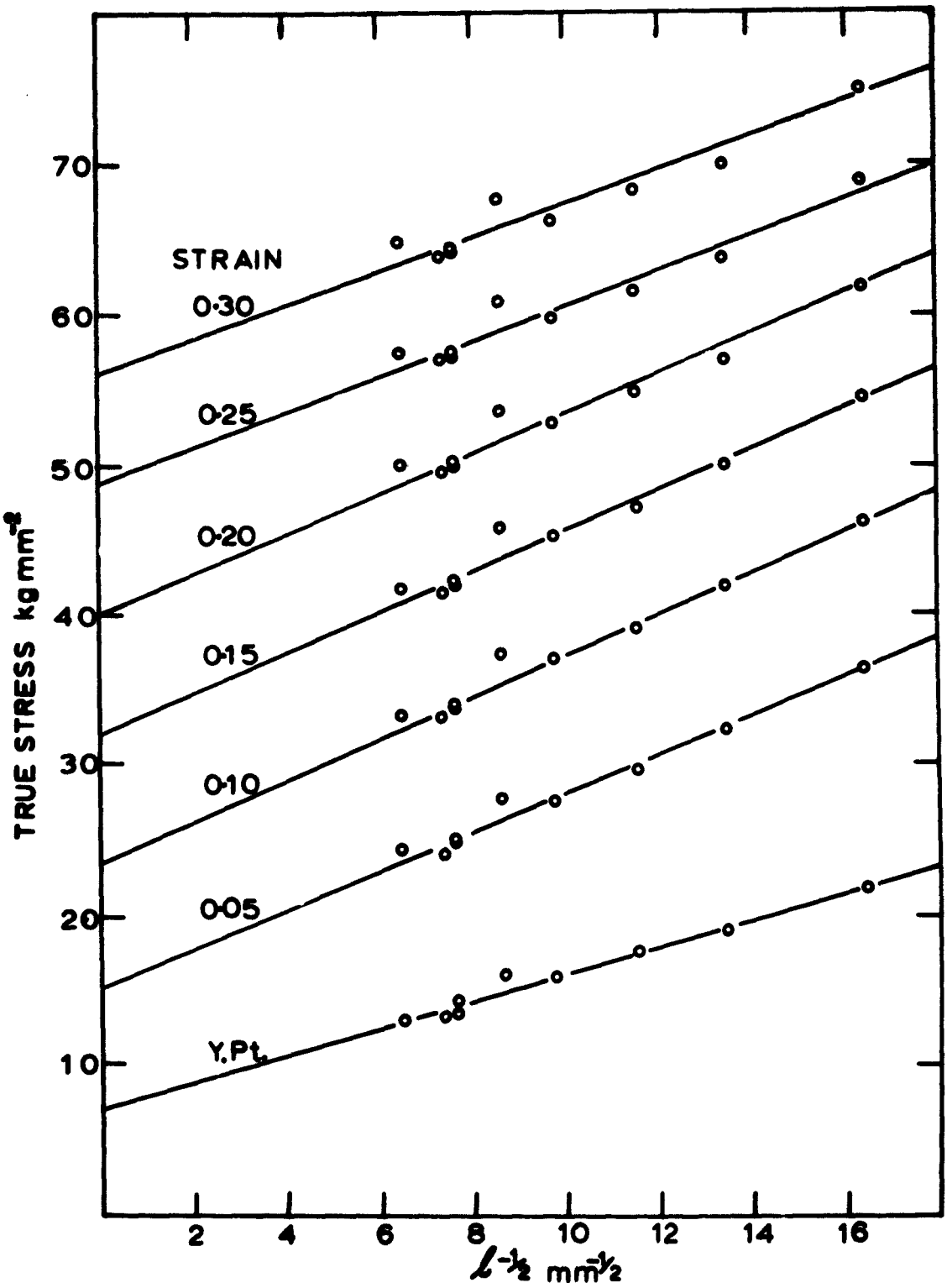

Figure 1. Yield and Flow Stress of 25% Zn alloy at 77°K as a function of grain size.

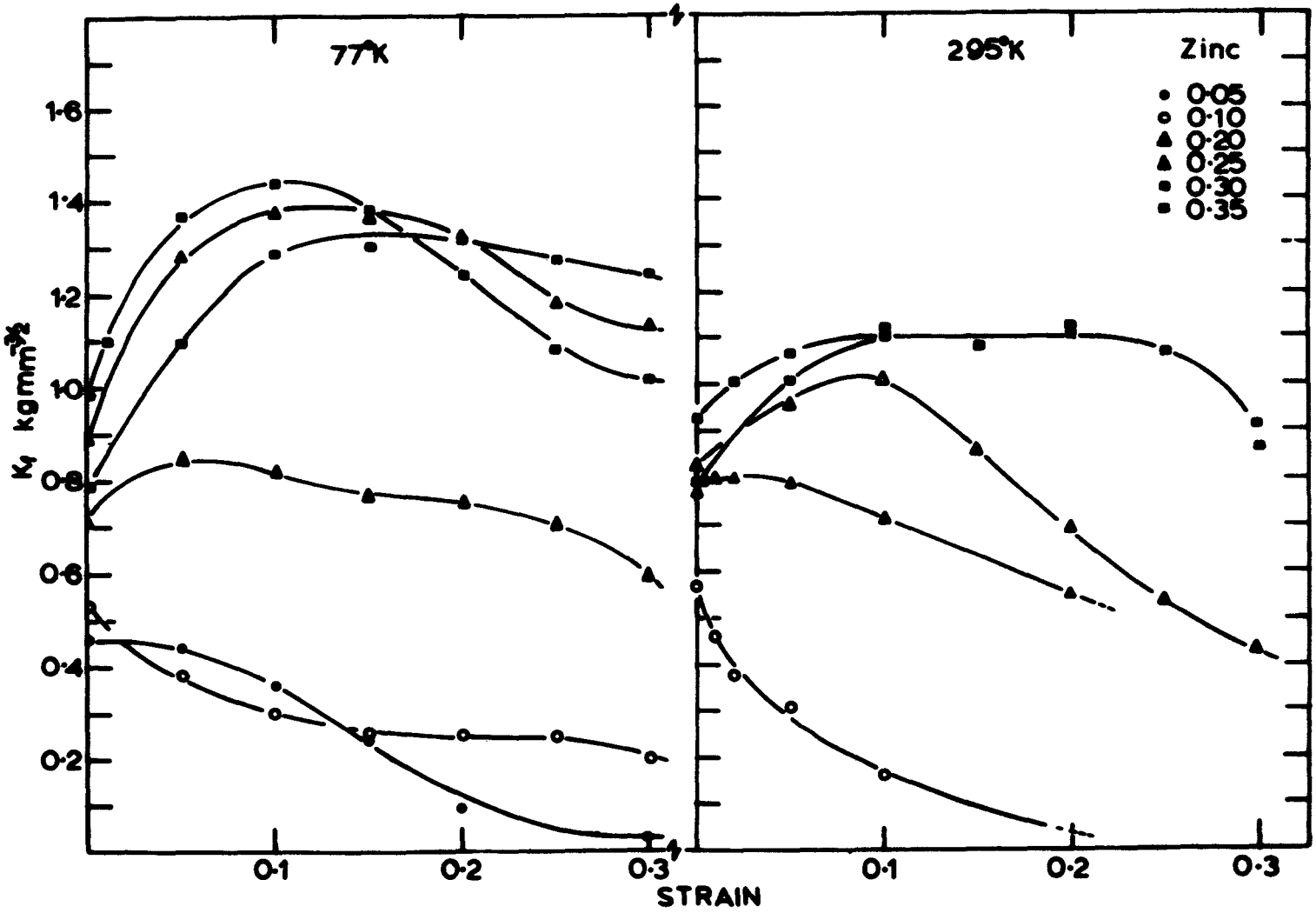

Figure 2. The variation of k_f with strain and zinc content.

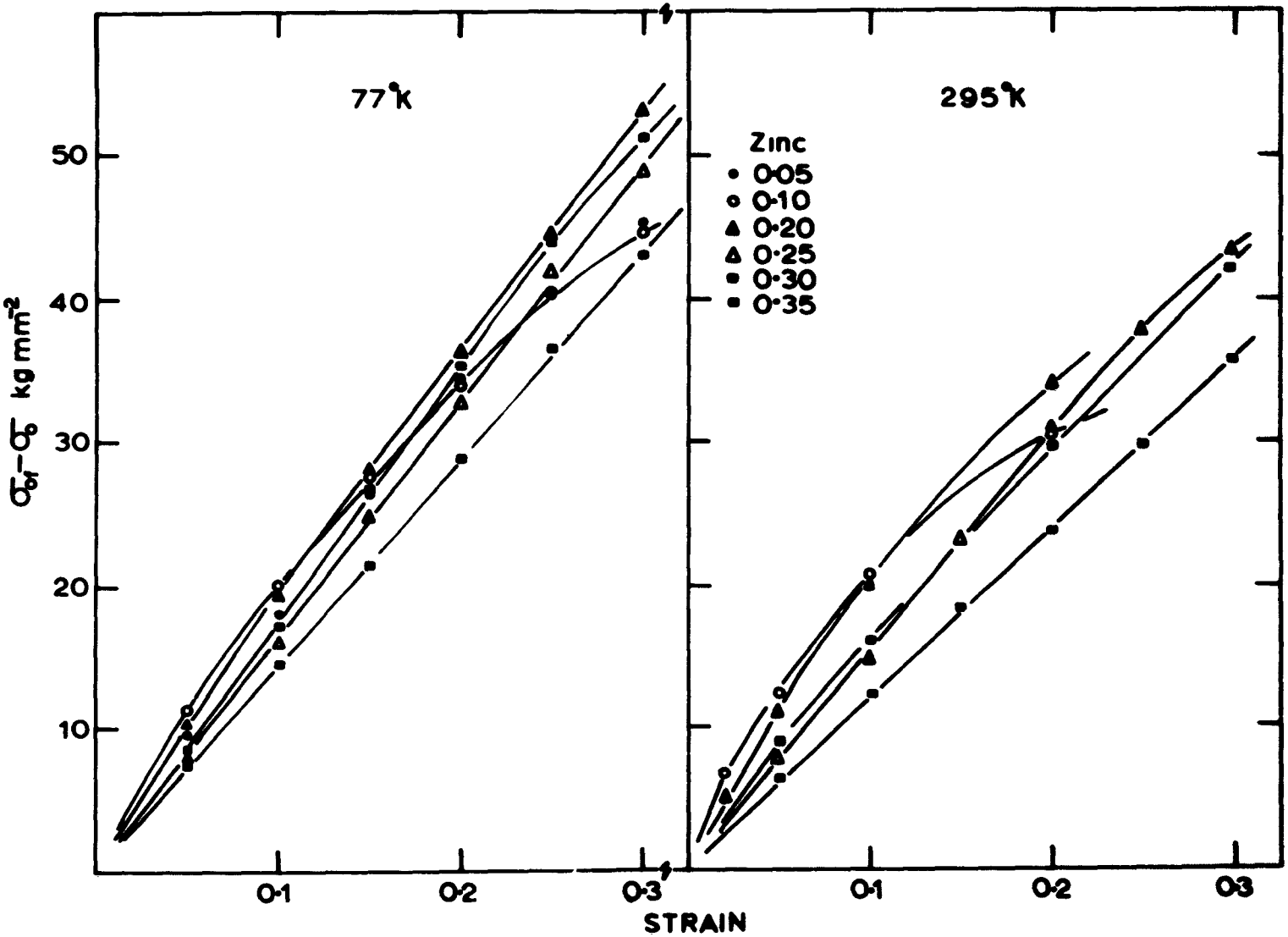

Figure 3. The variation of σ_o^f with strain and zinc content.

DISLOCATION DYNAMICS OF YIELDING AND FRACTURE

by

G. T. Hahn, C. N. Reid, and A. Gilbert
Battelle Memorial Institute

INTRODUCTION

Many recent observations on the submicroscopic scale have revealed the presence of both regular and irregular arrangements of dislocations in crystals. Such submicroscopic features fall under the general heading of substructure. Of these dislocations many are immobile, while the rest are free to move under the action of an applied stress. Study of the mobile dislocations has led to the development of a treatment which may be termed Dislocation Dynamics, the object of which is to predict deformation behavior from a knowledge of dislocation parameters.

The dislocation dynamics practiced in the 1950's accepted that the generation of mobile dislocations is difficult but their movement through the lattice is easy. Consequently, the processes for generating free dislocations--nucleation, unpinning, or multiplication--were regarded as rate controlling. More recently, however, the opposite view has gained support. This has come about largely through the work of Johnston and Gilman[1] at the G. E. Research Laboratory, who made three important contributions. First they showed by direct measurement that dislocations do not accelerate freely in lithium-fluoride crystals, but travel with a well defined velocity. Secondly, they formulated a concise statement of the dislocation dynamics of flow in terms of the velocity of the dislocations and the number moving. Finally, they used

this expression to calculate from the basic dislocation parameters a stress-strain curve of lithium-fluoride crystals. Since then, dislocation velocities have been measured in a number of other materials, including Fe-3.25Si crystals,[2,3] silicon,[4] germanium,[4,5] and tungsten,[6] and the treatment extended to describe other features of yielding such as the strain rate dependence of the yield stress, the delay time for yielding, and the Lüders' band.[7] These studies tend to identify the dislocation velocity, rather than the rate of generation, as the more important variable.

Dislocation Velocity

Johnston and Gilman measured dislocation velocity in the following way. The surface of a crystal was indented to produce free dislocations, whose positions were revealed by etch-pitting. The crystal was then stressed for a known time and re-etched. The pitting technique was such that the old and new positions of the dislocations were distinguished. They found that the distance moved at any given stress was proportional to the time duration of the stress, and from this they calculated a mean velocity. This is not to say that the dislocation moved through the lattice with constant speed, as is shown schematically in Figure 1a. For example, evidence exists that dislocation movement on the atomistic scale proceeds discontinuously by thermal activation at a succession of barriers. The motion may therefore be looked upon as a repeated sequence of release and arrest, as shown in Figure 1b. Since only one segment of the dislocation may be stopped at any one time, Figure 1c may be a truer representation.

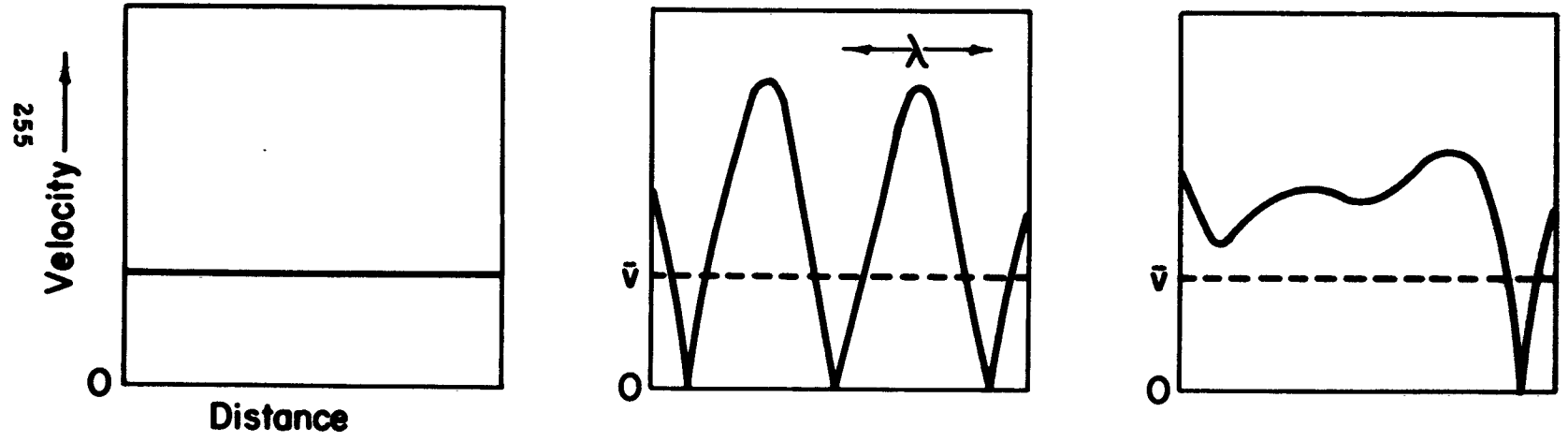

1a 1b 1c

FIGURE 1. SCHEMATIC ILLUSTRATION OF THE MOTION OF A DISLOCATION SEGMENT.

Figure 2a shows the observed variation of dislocation velocity, $\bar{v}$, with shear stress, τ, in LiF. The dependence may be described by the formulae:

$$\bar{v} = Ae^{\frac{-B(T)}{\tau}} , \tag{1}$$

$$\bar{v} = \left\{\frac{\tau}{\tau_o}\right\}^m . \tag{2}$$

Equation (1) applies to LiF over the entire velocity spectrum, whereas Equation (2) is applicable at low velocities in LiF and also over the more restricted velocity range investigated in other materials. The values assumed by m and τ_o are characteristic of a material, and Table 1 summarizes published values of m.

Johnston and Gilman were also able to measure the velocity in slightly deformed crystals. The results of these experiments, shown in Figure 2b, illustrate that the dislocations still display essentially the same velocity-stress relationship, except that the stresses associated with any given velocity are greater. This increase in stress corresponds closely with the amount of work-hardening displayed by the stress-strain curve. One may say that the effect of the applied stress is reduced by an amount equal to the work hardening increment, but more research must be done to see if this view is really justified. Assuming a linear work-hardening rate, Equation 2 can be modified as follows:

$$\bar{v} = \left\{\frac{\tau - q\epsilon_p}{\tau_o}\right\}^m \tag{3}$$

Having described the relationship between the applied stress and the resultant dislocation velocity, one other major variable remains

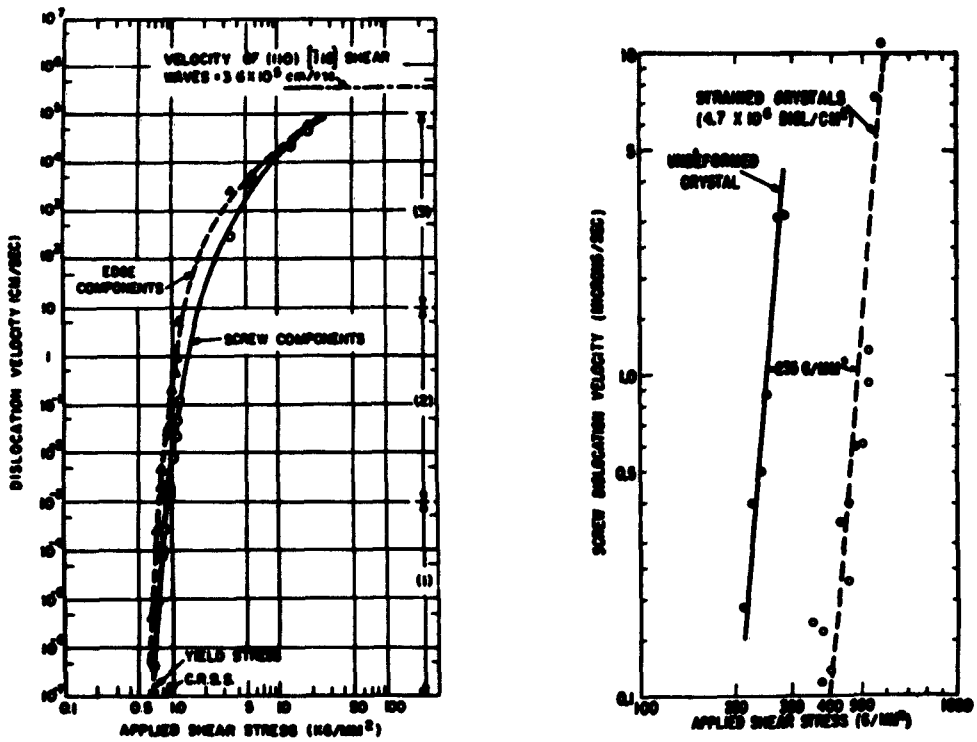

2a 2b

FIGURE 2. a. Variation of dislocation velocity with applied shear stress in LiF crystals(1).

b. Effect of strain on dislocation mobility in LiF(35).

TABLE 1. VALUES OF m PUBLISHED IN THE LITERATURE

MATERIAL	TEMPERATURE	m	REFERENCE
Si	600-900 C	1.4	4
Ge	420-700 C	1.4 - 1.9	
InSb	218 C	1.87	
GaSb	450 C	2.0	
W	R.T.	5.0	6
W	-196 C	14.0	
Fe-3.25Si, {110} SLIP	-196 C	44	2
Fe-3.25Si, {110} SLIP	-77 C	38	
Fe-3.25Si, {110} SLIP	R.T.	35	
Fe-3.25Si, {110} SLIP	100 C	41	
Fe-3.25Si, {112} SLIP	-77 C	42	3
Fe-3.25Si, {112} SLIP	-40 C	43	
Fe-3.25Si, {112} SLIP	R.T.	34	
LiF	R.T.	14.5 ± 2	1

before dislocation dynamics can be applied, namely the number of dislocations actually moving.

Dislocation Density

It is known that most annealed crystals possess a grown-in dislocation density of about 10^6 to 10^8 cm/cm^3. In certain cases, however, these dislocations are tightly bound by impurity atmospheres or precipitates, and when the crystal is stressed, these grown-in dislocations frequently do not move. Instead, mobile dislocations are produced either by heterogeneous nucleation or unpinning at points of high stress such as inclusion particles or discontinuities at the grain boundaries. Precipitate particles are particularly effective sites for nucleation. An example of this is presented in Figure 3, which shows dislocation loops produced by precipitate particles in unalloyed chromium, and revealed on the surface by etching. The dislocations produced in this way then move through the crystal and multiply rapidly, probably by the double cross-slip mechanism. As a result, the dislocation density increases rapidly as the material is deformed. The change in dislocation density with strain has now been studied in a number of materials by etch pitting and by transmission microscopy. Such studies, however, do not permit a distinction to be made between dislocations which are immobile and those which are able to move. The only experimental evidence currently in the literature concerning the fraction, f, which is mobile, is due to Patel and Chaudhuri.[4] They were able to infer the value of f in a few isolated cases involving small strains and report values in the range between 0.08 and 1. It is unlikely that f is a constant except perhaps in the early stages of yielding, and the formulation of f from experiment

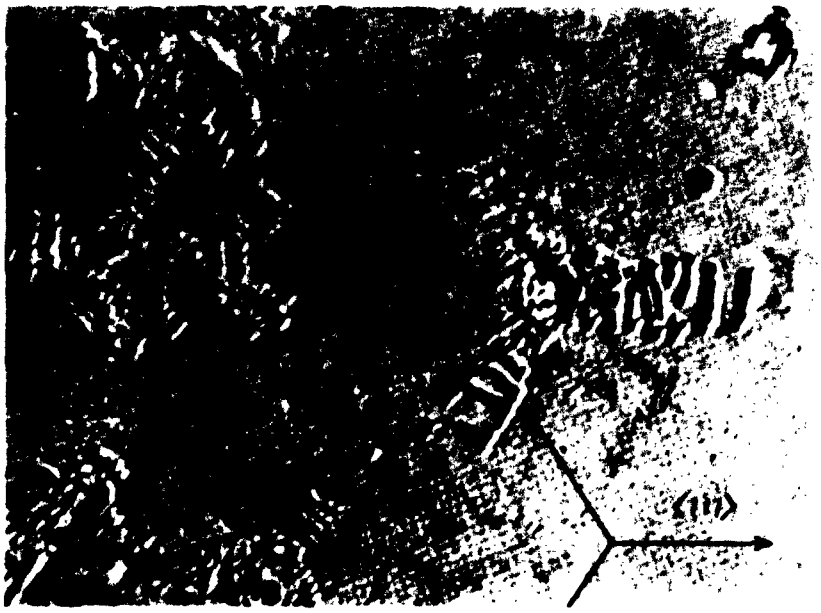

FIGURE 3. NUCLEATION OF DISLOCATIONS BY PRECIPITATE PARTICLES IN CHROMIUM[36].

or theory is a problem deserving of more attention. In the absence of such a formulation however, the assumption is made that the total density, ρ, is simply related to the mobile density, ρ'.

Typical examples of the rate of increase of total dislocation density with strain are presented in Figure 4, which shows results obtained at Battelle for a mild steel using transmission electron microscopy. The dislocation density increases from about 5×10^8 cm/cm^3 in the annealed material, to about 10^{10} after 10 per cent deformation. These experiments were carried out at three widely differing strain rates, about 10^{-5} per second, 10^{-2} per second, and 10^3 per second, a range of nearly eight orders of magnitude. The figure illustrates that the rate of multiplication in this material at least is relatively insensitive to strain rate. This is illustrated qualitatively in Figure 5, which shows examples of the transmission micrographs that were obtained at the three different strain rates. The main difference is that the dislocation segments tend to be more straight and parallel at the highest strain rate.

The experimentally measured dislocation densities can be described by an equation of the form:

$$\rho = \rho_o + C\epsilon_p^{\beta} , \qquad (4)$$

where ρ_o represents the initial dislocation density and C and β are multiplication parameters. Values of β are in the range 1/2 to 3/2, but are usually close to 1. This expression describes the total number of dislocations that have been generated and does not distinguish between

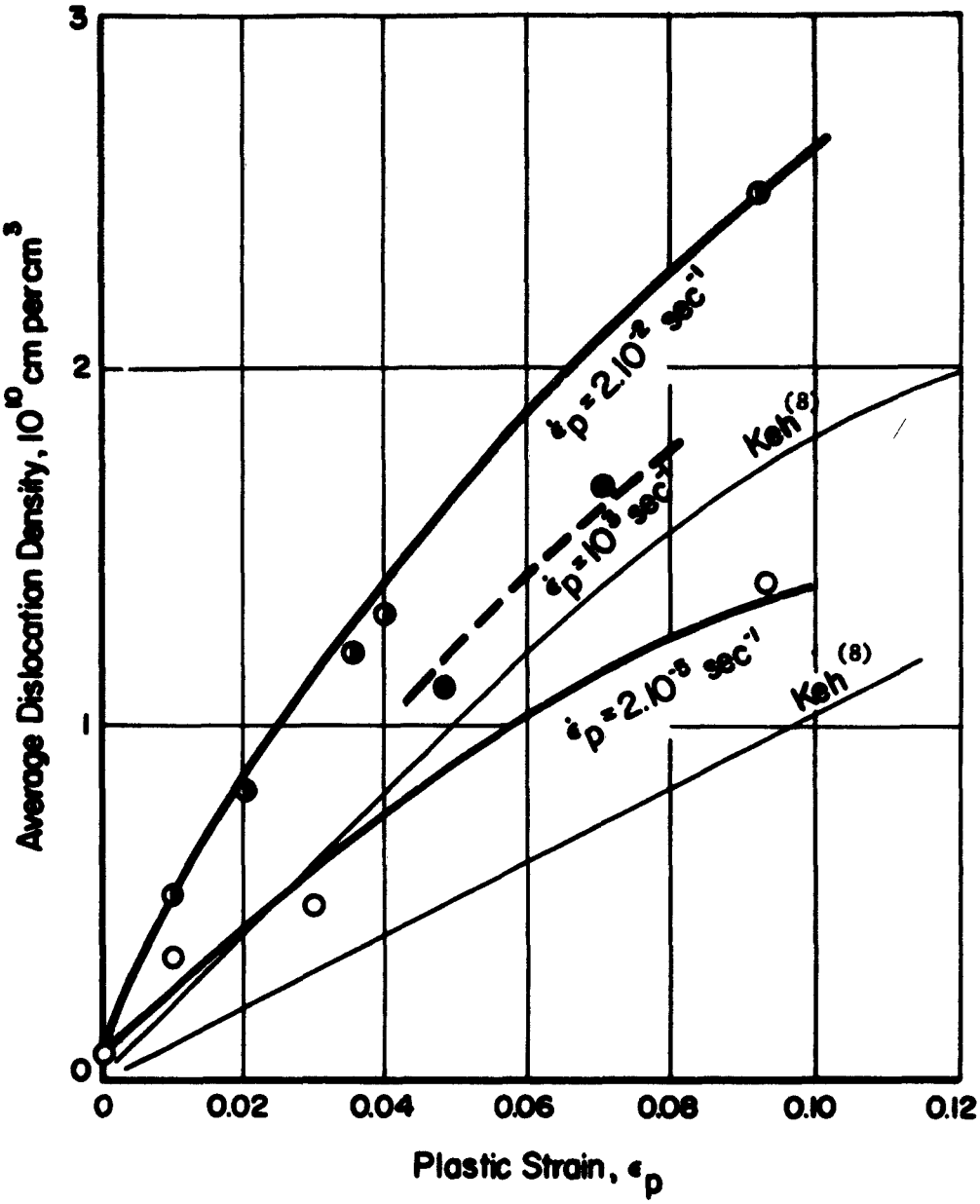

FIGURE 4. INCREASE OF DISLOCATION DENSITY WITH STRAIN IN MILD STEEL DEFORMED AT DIFFERENT RATES.

FIGURE 5. ELECTRON MICROGRAPHS OF THE SUBSTRUCTURES PRESENT IN MILD STEEL AFTER DEFORMATION AT VARIOUS STRAIN RATES, TO 3% STRAIN.

the ones that are still mobile and those that have become arrested. The relevant parameter is the mobile density, which can be described, at least in a very approximate way, by the equation,

$$\rho' = \rho_o' + fC\epsilon_p \quad , \tag{5}$$

where ρ_o' represents the number of dislocations initially mobile and f the fraction of the dislocations subsequently generated that is mobile.

Table 2 summarizes available information regarding the value of the multiplication parameter, C. These values show that there are significant differences in the rate of multiplication. The results for copper, for example, show that multiplication is more rapid in polycrystalline samples than in single crystals. Consistent with this, Keh[8] investigated the rates of multiplication in iron of two grain sizes, and found the rate to be higher in the fine grained material.

Utilizing the above data, dislocation dynamics can now be applied to describe plastic flow in response to a variety of loading conditions.

DISLOCATION DYNAMICS

The new knowledge of the velocity of dislocations and their rate of multiplication is important in its own right. However, its significance was not fully appreciated until Johnston and Gilman formulated a concise statement of the dislocation dynamics of flow. They pointed out that the deformation accompanying the application of stress consists of an elastic and a plastic contribution. For instance, in a

TABLE 2 . VALUES OF THE DISLOCATION MULTIPLICATION PARAMETER $C = \left(\frac{d\rho}{d\epsilon}\right)_{\epsilon = 1\%}$ FOR A VARIETY OF MATERIALS

MATERIAL	S: SINGLE CRYSTAL P: POLYCRYSTALLINE	C $(CMS^2 \cdot PER\ CENT)^{-1}$
COPPER [10-12]	S P	$3\text{-}9 \times 10^6$ 5×10^8
LITHIUM FLUORIDE [1]	S	1×10^7
GERMANIUM [4,5,9]	S	$4\text{-}80 \times 10^6$
NIOBIUM [13]	P	4×10^9
TANTALUM [14]	P	1.7×10^{10}
MOLYBDENUM [15]	P	8×10^8
TUNGSTEN [6]	S	2×10^7
IRON [8]	P	1.5×10^9
MILD STEEL [16]	P	$2\text{-}4 \times 10^9$

constant strain rate test, the strain rate, $\dot{\epsilon}$, imposed by the machine must be matched by the sum of the elastic and plastic components, $\dot{\epsilon}_e$ and $\dot{\epsilon}_p$, of the strain rate in the specimen.

$$\dot{\epsilon} = \dot{\epsilon}_e + \dot{\epsilon}_p \tag{6}$$

The elastic contribution can be expressed in terms of the rate of stress application and a modulus, M, which reflects the stiffness of the test bar, grips, and supporting members. The plastic contribution is given by the equation[17]

$$\dot{\epsilon}_p = 0.5\ b\ \rho'\ \bar{v} \tag{7}$$

where b is the Burgers vector for slip, and 0.5 arises from geometrical considerations. Equation (6) may therefore be written

$$\dot{\epsilon} = \frac{1}{M}\frac{d\sigma}{dt} + 0.5\ b\ \rho'\ \bar{v} \tag{8}$$

where σ refers to tensile stress. Substituting in Equation (8) from Equations (3) and (5) yields

$$\dot{\epsilon} = \frac{1}{M}\frac{d\sigma}{dt} + 0.5\ b\ (\rho_o' + fC\epsilon_p)\ (\sigma - q\epsilon_p)^m\ (\sigma_o)^{-m} \tag{9}$$

the shear stresses, τ and τ_o from Equation (3), being replaced by the equivalent tensile stresses σ and σ_o. This differential equation may be solved to describe the stress-strain relationship for a single crystal.

The behavior of polycrystalline samples is complicated by

the variation of the resolved shear stress from grain to grain owing to the different grain orientations, the anisotropy of the modulus and the constraints imposed by neighboring grains. In principle at least, the deformation of polycrystalline samples can be described by a summation over all the grains of the aggregate. It should be noted that such parameters as ρ_o, f, c, and q may depend on grain size, a fact Conrad has used to derive the yield stress grain-size relation for steel.[18]

Application to Yielding

Johnston and Gilman first used the dislocation dynamics approach to calculate the stress-strain curve of lithium-fluoride crystals. When an empirical correction is made for the effect of work hardening, and plausible values adopted for f and ρ_o', the curve calculated from Equation (9) agrees very well with that determined experimentally.

More recently, Johnston[19] has solved the equation for simple tension with the aid of a computer for various values of the parameters m and ρ_o'. Figure 6 demonstrates the influence of ρ_o' on the shape of the stress-strain curve, all other parameters being kept constant. The effect of m is illustrated in Figure 7a. These calculations show that the initial yield drop is a general feature of small values of ρ_o' and small values of m. The predicted effect of ρ_o' (Figure 6) correlates well with the observed occurrence of a yield point in annealed b.c.c. metals, and the observed absence of this phenomenon in prestrained material. Furthermore, comparison of Figures 7a and 7b illustrates that the predicted influence of m on the stress-strain curve is verified by experiment for those materials where m has been measured.

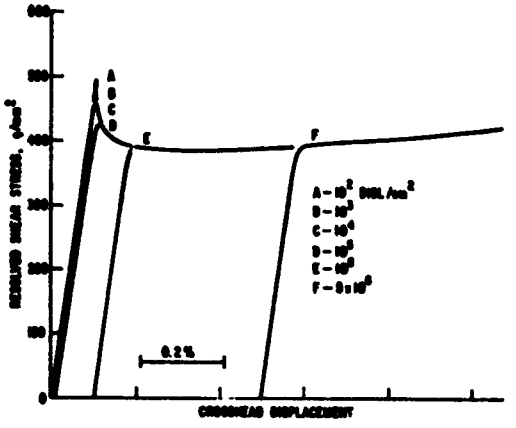

FIGURE 6. EFFECT OF ρ_o' ON THE SHAPE OF THE CALCULATED STRESS-STRAIN CURVE, ALL OTHER PARAMETERS IN EQUATION (9) BEING CONSTANT

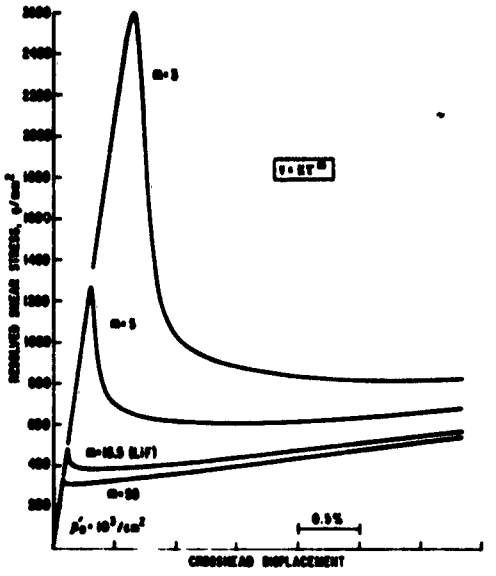

a. **Effect of m on the shape of the calculated stress-strain curve**

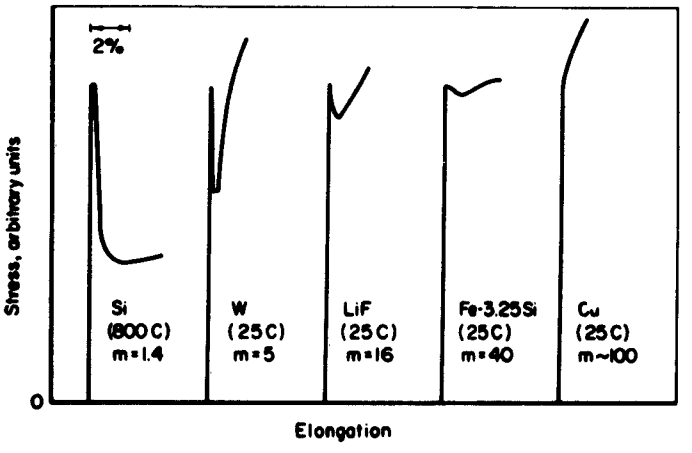

b. **Experimental stress-strain curves for materials where values of m are known**

FIGURE 7

Strain Rate Dependence of Yielding

At the upper or lower yield stress, the $\frac{d\sigma}{dt}$ term of Equation (9) is zero, and the plastic strain is so small that the work hardening term can be neglected. Equation (9) then reads:

$$\dot{\epsilon} = 0.5\ b\ \rho'\ \sigma_y^{m}\ \sigma_o^{-m} \tag{10}$$

Taking logarithms of both sides

$$\log \dot{\epsilon} = \log\ (0.5\ b\ \rho'\ \sigma_o^{-m}) + m \log \sigma_y$$

or
$$\log \dot{\epsilon} = m \log \sigma_y + \text{CONSTANT} \tag{11}$$

This may be compared to the long established empirical equation describing the strain rate dependence of the yield stress:

$$\log \dot{\epsilon} = m' \log \sigma_y + \text{CONSTANT} \tag{12}$$

A comparison of Equations (11) and (12) affords an indirect method of determining m. Table 3 compares values of m' to values of m determined directly. The agreement is good.

Delay Time

The delay time, t_d, can be regarded as the time taken for a material under constant stress to deform to the minimum detectable strain, say ϵ'. Under these conditions $d\sigma/dt = 0$ and Equation (9) can

TABLE 3. COMPARISON OF THE DIRECT AND INDIRECT METHODS OF DETERMINING m

		m	m′	m″	m‴
LiF	(S)	14.5[1]	14.5[20]		
Fe-Si	(S)	40 ± 5[2]	45[21]		
	(P)		48[21]		
W	(P)		7[32]		
W	(S)	5[6]			
Mo			14[23]	10-15[24]	14[23]
Steel	$\dot{\epsilon} < 1$		20-50[25,26]		30[27,28]
	$\dot{\epsilon} > 1$		10-15[29]	10-15[29]	
Cu			~200[30]		
Ag			~300[31]		

S = SINGLE CRYSTAL

P = POLYCRYSTALS

$$m = \frac{d \ln \bar{v}}{d \ln \sigma}$$

$$m' = \frac{d \ln \dot{\epsilon}}{d \ln \sigma}$$

$$m'' = \frac{d \ln t_d}{d \ln \sigma}$$

$$m''' = \frac{d \ln u}{d \ln \sigma}$$

be rewritten:

$$\int_{\epsilon_p = 0}^{\epsilon'} \frac{d\epsilon_p}{0.5\ b\ (\rho_o' + fC\epsilon_p)\ (\sigma_o)^{-m}\ (\sigma)^m} = \int_0^{t_d} dt \qquad (13)$$

This may be evaluated:

$$\frac{2fC}{b} \left(\frac{\sigma_o}{\sigma}\right)^m \ln\left(1 + \frac{fC\epsilon'}{\rho_o}\right) = t_d \qquad (14)$$

The delay time may thus be calculated as a function of stress. Figure 8 shows the results of such a calculation, performed using constants appropriate for steel, compared to experimental determinations.

From Equation (14) we may write:

$$\log\left\{\frac{2fC}{b}\ \sigma_o^{\,m} \ln\left(1 + \frac{fC\epsilon'}{\rho_o}\right)\right\} - m \log \sigma = \log t_d \qquad (15)$$

or since the first term is constant,

$$m = \left[-\frac{d \log t_d}{d \log \sigma} \equiv m''\right] \qquad (16)$$

The term on the right (called m'') represents another indirect method of determining m. In Table 3, a comparison is made of m, m' and m'' for instances where this is possible, and the agreement is encouraging.

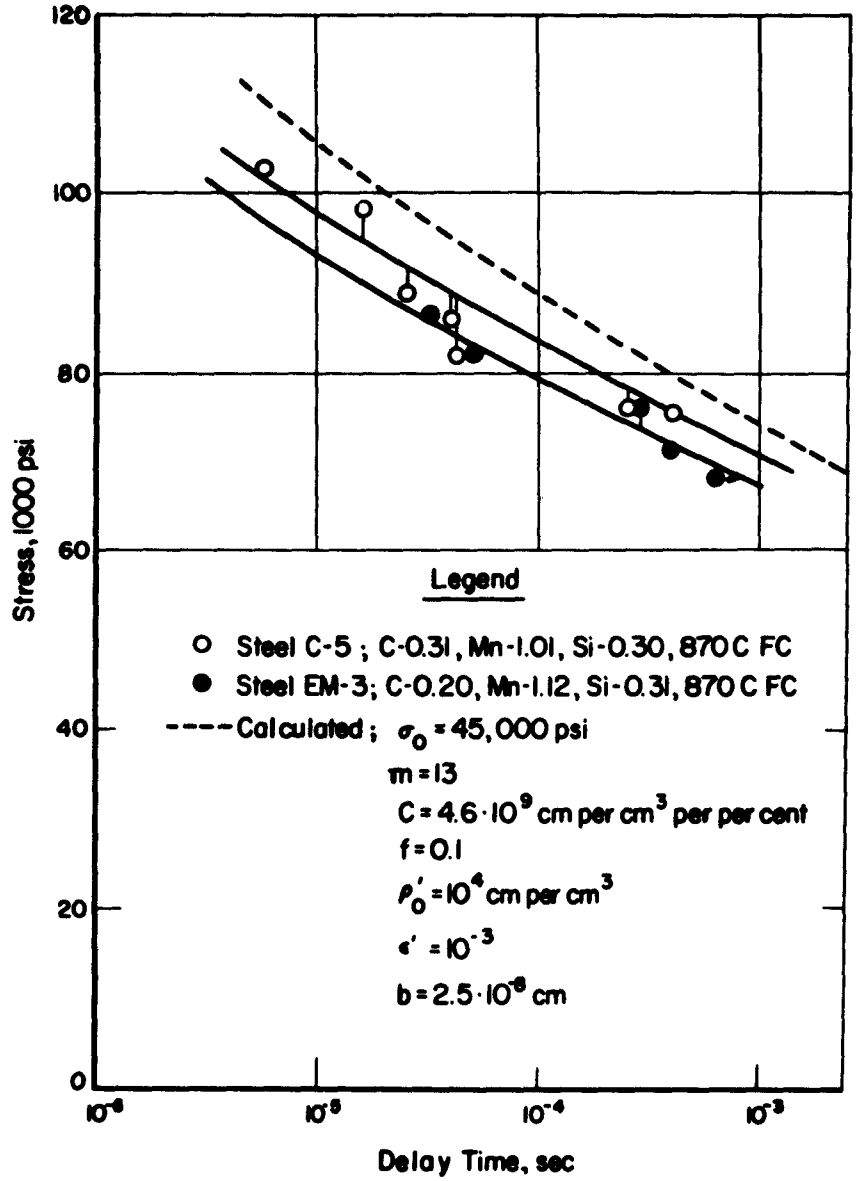

(37)

FIGURE 8. COMPARISON OF EXPERIMENTAL AND CALCULATED VALUES OF DELAY TIME FOR MILD STEEL

Lüders' Bands

The variation of strain with distance along a test piece exhibiting a Lüders' band can be calculated and compared with the results of experiments. If x is distance from the band front, then

$$\frac{d\epsilon_p}{dx} = \frac{d\epsilon_p}{dt} \cdot \frac{dt}{dx} \tag{17}$$

For steady state Lüders' band propagation, $\frac{dx}{dt}$ is constant, u. Thus,

$$\frac{d\epsilon_p}{dx} = \frac{\dot{\epsilon}_p}{u} \tag{18}$$

Thus,

$$\int \frac{d\epsilon_p}{\dot{\epsilon}_p} = \int \frac{dx}{u} \tag{19}$$

and

$$\int \frac{d\epsilon_p}{\dot{\epsilon}_p} = \frac{x}{u} \tag{20}$$

The stress, σ, at any point along the band is given by

$$\sigma = \sigma'_{LY} (1 + \epsilon_p) \tag{21}$$

where σ'_{LY} is the load on the specimen at the lower yield point divided by the initial cross section.

Substituting in Equation (20) values of $\dot{\epsilon}$ from Equation (9)

and the value of σ from Equation (21), we obtain:

$$\frac{x}{u} = \int \frac{d\epsilon_p}{.5\ b\ (\rho_o' + fC\epsilon_p)\ (\sigma_o)^{-m}\ \{\sigma'_{LY}\ (1 + \epsilon_p) - q\ \epsilon_p\}^m} \tag{22}$$

since at the lower yield point $d\sigma/dt = 0$. By graphical integration we can solve this equation and thus calculate the variation of strain with distance--that is, the strain profile of the Lüders' band. There is good qualitative agreement with experiment, as is shown in Figure 9.

There remains another indirect method of determining m. This is based on the postulate that there exists a simple relationship between the velocity of a Lüders' band front and the average velocity of the dislocations at the front. This would be the case if for example the band propagated by the injection of mobile dislocations from the band front into the otherwise undeformed matrix. Let the relationship be

$$\begin{aligned} u &= k\bar{v} \\ &= k\ \sigma^m\ \sigma_o^{-m} \end{aligned} \tag{23}$$

Therefore,

$$m = \left[\frac{d\ \log\ u}{d\ \log\ \sigma} = m'''\right] \tag{24}$$

The term on the right will be called m'''. Figure 10 gives an idea of the usefulness of this relationship: the slopes of the lines represent m' and m''' for steel and molybdenum. The agreement is good, and the numerical values appear in Table 3.

The results of Table 3 are important for two reasons. First,

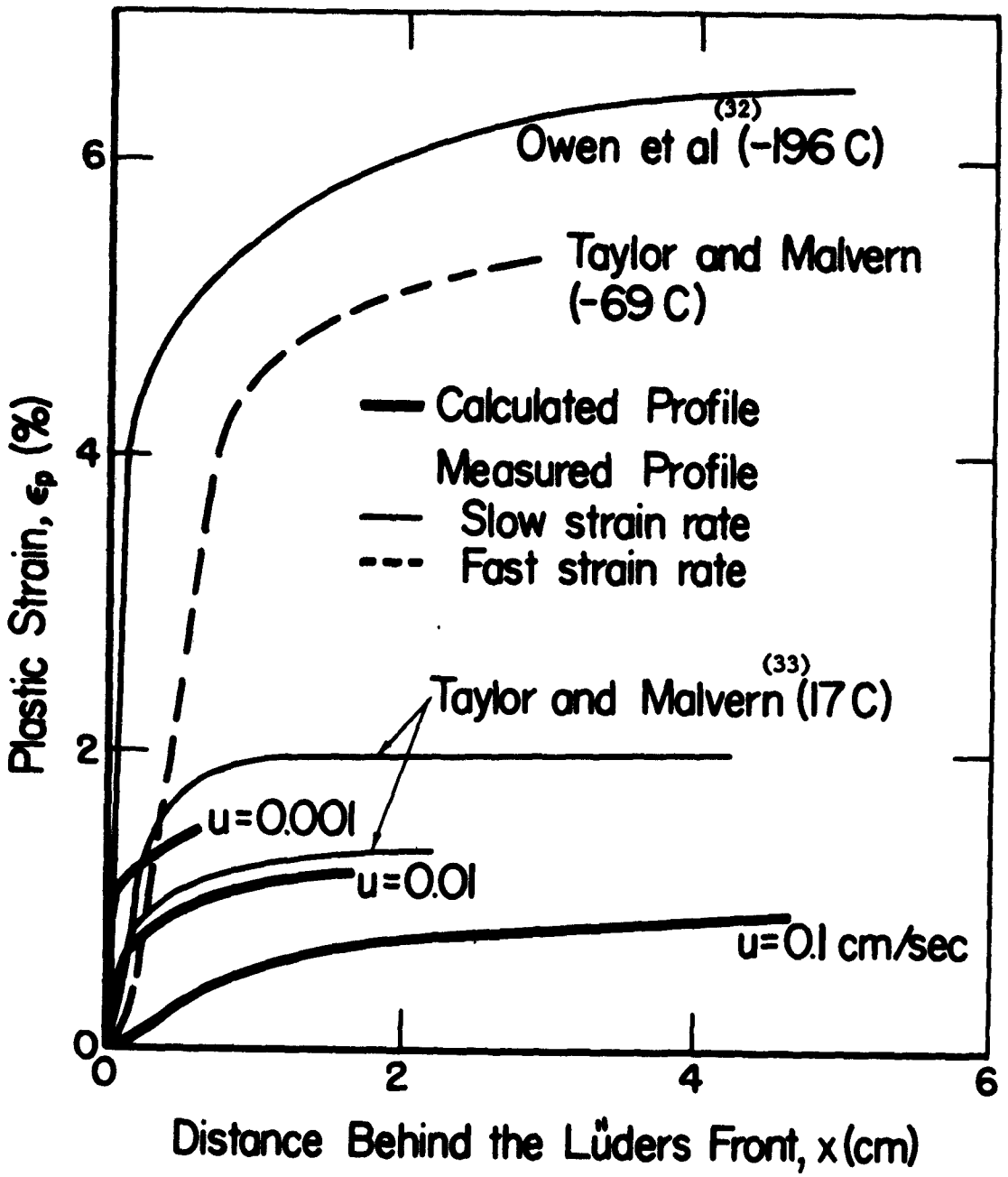

FIGURE 9. RESULTS OF LUDERS' BAND STRAIN PROFILE CALCULATIONS.[7] STRAIN PROFILES PRESCRIBED BY EQUATION (22).

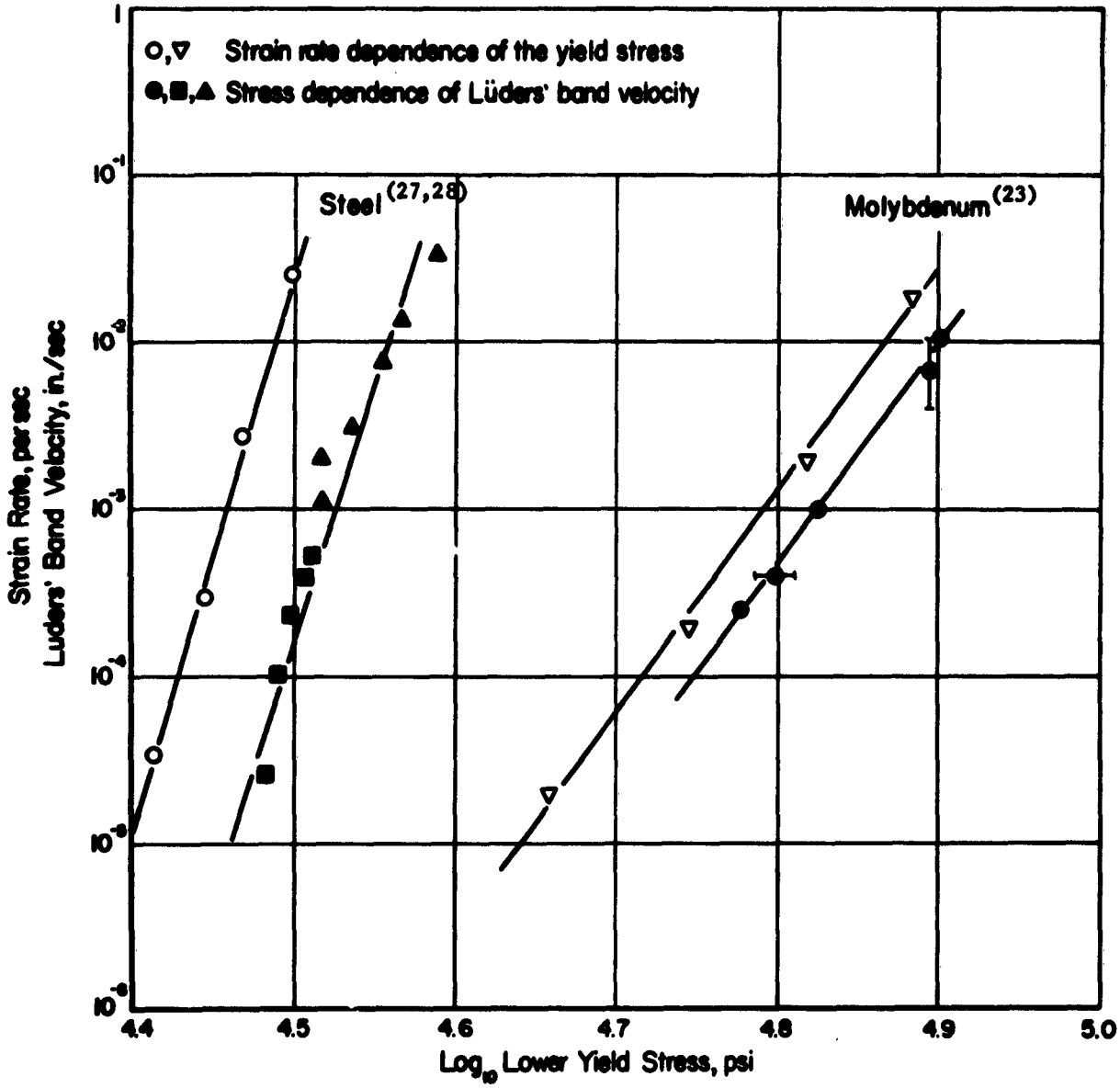

FIGURE 10. A COMPARISON OF m' AND m'''

they lend added support to the theory. Secondly, they show that the stress dependence of dislocation velocity can be inferred indirectly from other measurements which may be more convenient. For example, the values of m for copper and silver have not been measured but it can be inferred from the values of m′ that these must be relatively large numbers.

In general then, it can be said that the dislocation dynamics approach describes the yielding of metals very accurately and can therefore be used with some confidence to predict yielding under conditions that cannot be readily handled experimentally. This will be illustrated with one example, namely yielding in the vicinity of a moving crack.

Fracture

It is essential that a treatment of cleavage in plastic materials should take account of the effect of plastic flow. For example, the stresses that will cause an existing crack to grow will also tend to produce deformation at the crack tip. Such deformation will blunt the crack and redistribute the stress thereby making inappropriate the classical stress field solution of Inglis.[34] An adequate approach, therefore, demands a stress field solution that is responsive to deformation at the crack tip. Furthermore, it is necessary that the kinetics of this deformation be known, together with the fracture strength of the material.

Previous attempts at a solution have relied on a modification of the surface energy in order to account for the work done by plastic flow. Unfortunately, this approach ignores the fact that the stress field

of the propagating crack is modified by deformation, and consequently is of limited usefulness.

The model to be described attempts to fulfill all the above requirements and consists of a partially relaxed crack the relaxation of which is described by Dislocation Dynamics.

The model, illustrated in Figure 11, consists of a two-dimensional sharp crack of length 2a, whose tip is surrounded by a circular plastic zone of radius, r. Stresses within this zone are assumed to be substantially relaxed. The extent of the plastic zone is defined as the locus of points where flow begins to occur rapidly, for example where the plastic strain reaches a value of 0.1%. Under these conditions, the crack-plastic zone complex is equivalent to an elliptical hole of semi-major axis, a, and root radius, r. The stress concentration factor, α, in advance of this "hole" can be evaluated from equations derived by Inglis as a function of a/r. The variation of α with distance from the "hole" is illustrated in Figure 12, where it may be seen that the stress gradient close to the elastic-plastic boundary is very steep.

The principle of the calculation is presented in Figure 13, and is directed toward the evaluation of r, and hence α. A crack is assumed to be propagating toward a volume element dV with a velocity U. As the crack approaches, dV experiences a rising stress, (illustrated in the lower diagram) under the influence of which it flows. The condition for the solution of the calculation is that the arrival of the "hole" coincides with the strain in dV reaching a value of 0.1%. Dislocation dynamics provides a unique means of calculating this deformation.

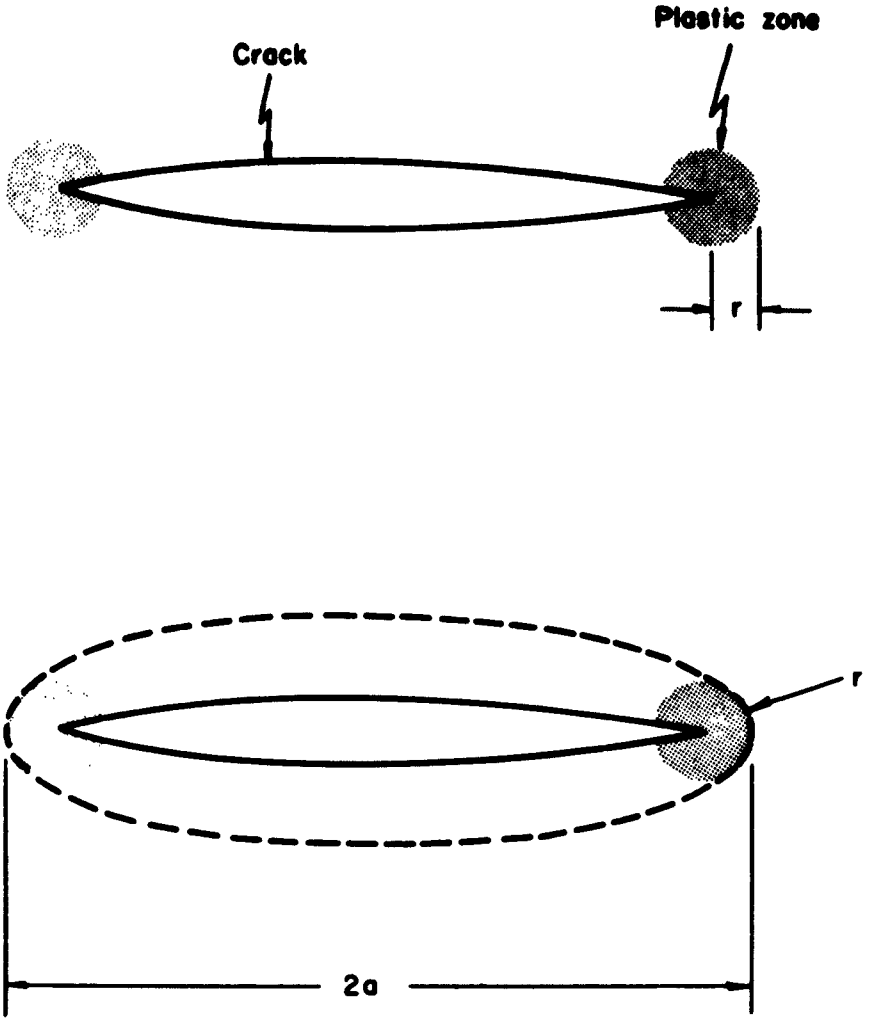

FIGURE 11. THE MODEL OF A PARTIALLY RELAXED BRITTLE CRACK

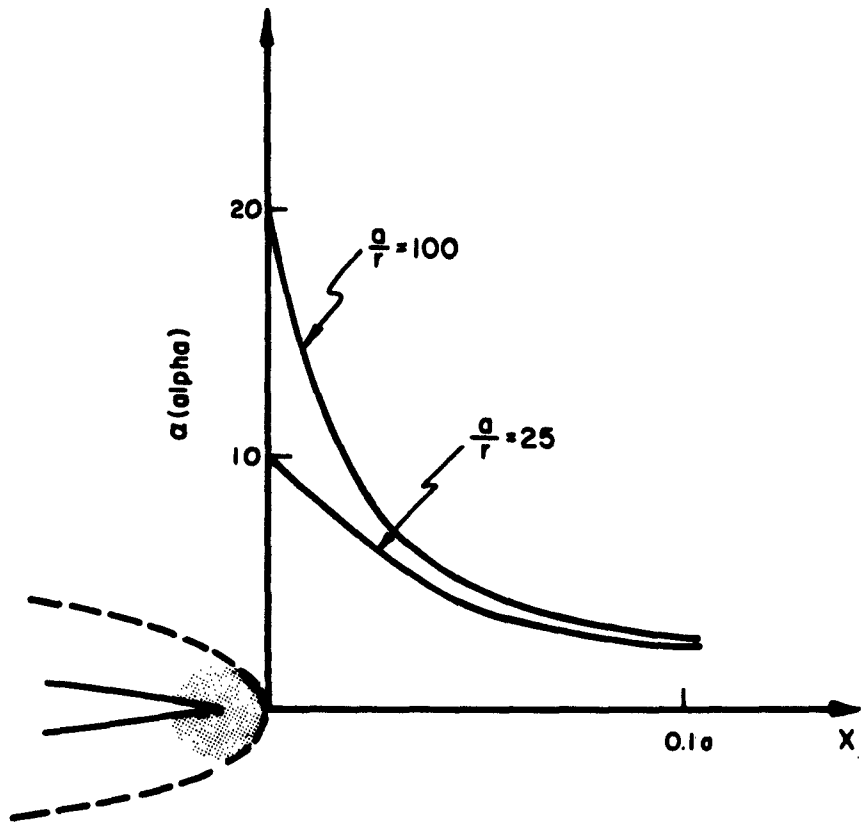

FIGURE 12. CALCULATED STRESS CONCENTRATION OF AN ELLIPTICAL CRACK FOR TWO DIFFERENT VALUES OF a/r

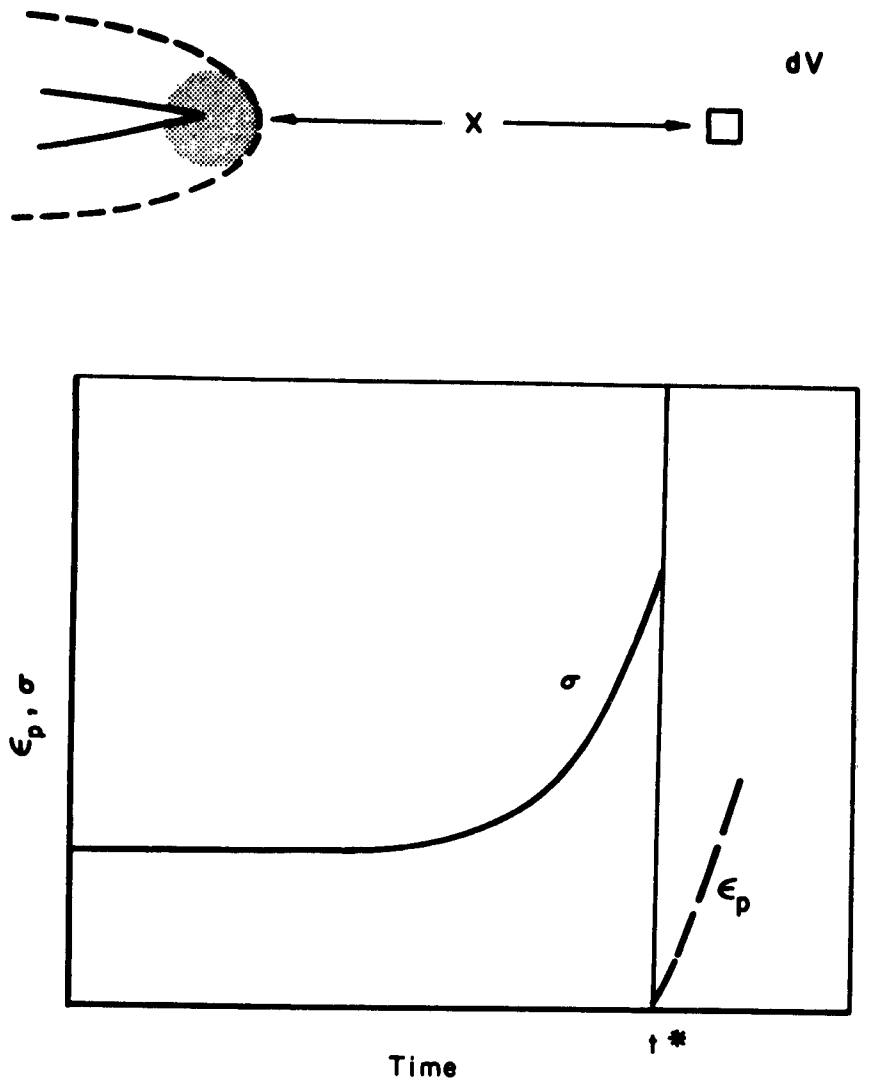

FIGURE 13. SCHEMATIC OF STRESS AND STRAIN AHEAD OF A MOVING CRACK

Recalling Equation (7), the plastic flow of dV may be written:

$$\dot{\epsilon}_p = \frac{d\epsilon}{dt} = 0.5\ b\ (\rho_o' + fC\epsilon_p)\ \left(\frac{\sigma}{\sigma_o}\right)^m \tag{25}$$

Since under the present conditions, σ is a function of t, the equation may be rearranged

$$\int \frac{d\epsilon}{0.5\ b\ (\rho_o' + fC\epsilon_p)\ (\sigma_o)^{-m}} = \int \sigma^m\ dt \tag{26}$$

The local stress, σ, experienced by dV is actually the product of the nominal stress, σ_{NOM}, and the stress concentration factor, α.

$$\sigma = \sigma_{NOM} \cdot \alpha\ (x) \tag{27}$$

where $\alpha(x)$ implies the dependence of α on the distance, x, between dV and the "hole". Since however the crack propagates toward dV with constant velocity U, x and t are related:

$$U = -\frac{dx}{dt} \tag{28}$$

The limits and base of Equation (26) can now be changed from (t) to (x).

$$\int_0^{.001} \frac{d\epsilon}{.5\ b\ (\rho_o' + fC\epsilon_p)\ (\sigma_o)^{-m}} = \frac{(\sigma_{NOM})^m}{U} \int_{x>>a}^{x=a} [\alpha(x)]^m\ dx \tag{29}$$

Let

$$\frac{(\sigma_{NOM})^m}{U} \int_{x>>a}^{x=a} [\alpha(x)]^m\ dx = I$$

The left-hand side can be integrated analytically and evaluated for given material parameters. The right-hand side must be integrated numerically and the equality of Equation (29) holds only for one value of a/r (α being a function of a/r). This may be determined by evaluating I for various values of a/r and plotting the graphical relationship between them. The magnitude of a/r corresponding to the left-hand side may then be determined.

The geometry and stress field of the propagating crack are now solved; the solution is sensitive to the values chosen for the parameters, m, U, C and ρ_o'.

In Figure 14, the plastic zone size, r/a, and the maximum stress concentration, α^*, have been determined for various values of m as a function of the crack velocity. The calculations were performed for the case where the applied stress, σ_{NOM} is half the yield stress, σ_y, in a slow tensile test. Consequently, the maximum stress, σ^*, ahead of the crack may be expressed in terms of σ_y. It can be seen that as the crack velocity increases and the time available for plastic relaxation decreases, the plastic zone size becomes progressively smaller. Effectively the crack is blunted to a lesser extent, and consequently higher stresses are generated at the crack tip. The calculation was made for different values of m. The value, m = 5, is characteristic of tungsten. It can be seen that for a fast moving crack in tungsten, stresses of the order of 100 times the yield stress are generated, which approaches plausible values for the theoretical strength. It would therefore be expected that in this material crack propagation by cleavage could occur readily. On the other hand, the stresses generated in materials characterized by higher values of m are much lower. It is, therefore, understandable that f.c.c.

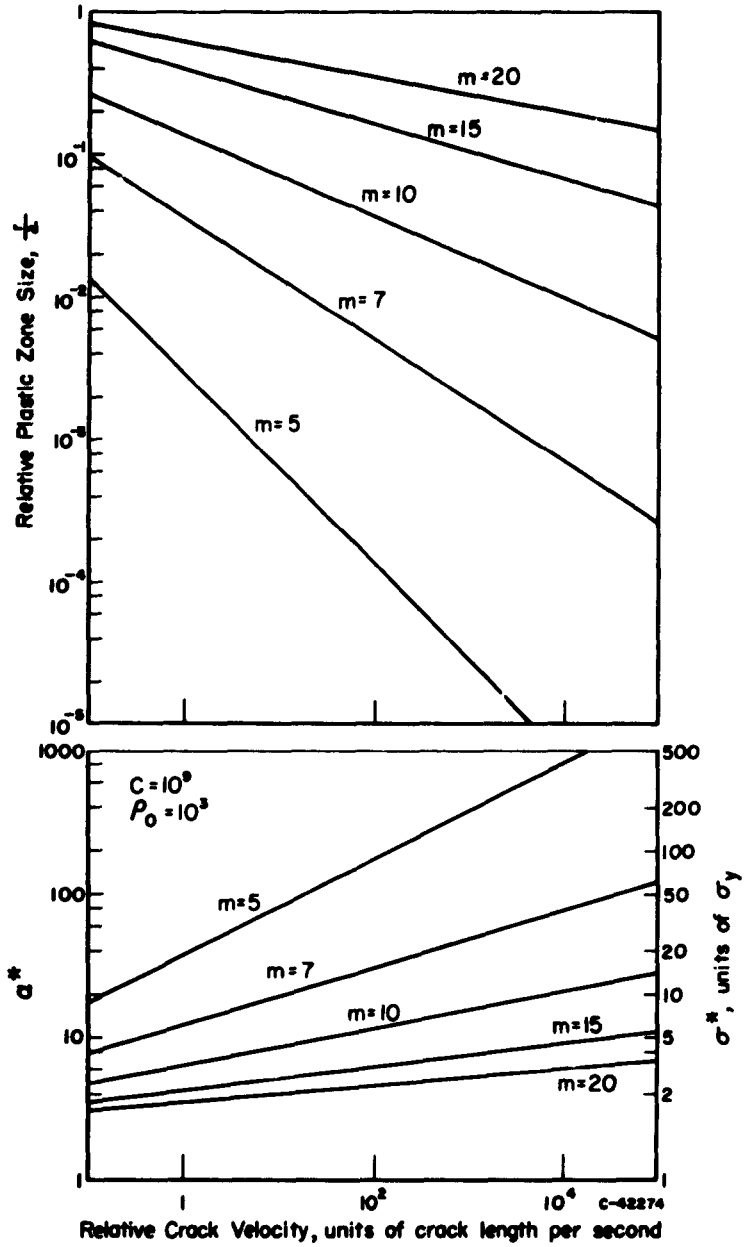

FIGURE 14. EFFECT OF m AND CRACK VELOCITY ON PLASTIC ZONE SIZE AND MAXIMUM STRESS CONCENTRATION FACTOR.

materials, such as copper or silver, that are characterized by m values of the order of 100, would be unlikely to suffer cleavage fracture.

The effect on σ^* of initial mobile dislocation density, ρ_o', and multiplication rate, C, is illustrated in Figure 15. It is apparent that dislocation locking is detrimental, giving rise to larger values of σ^*. Comparison of Figures 14 and 15 shows that for a given crack velocity, σ^* is more sensitive to m than to changes in C and ρ_o' over the range of these parameters encountered experimentally.

It must be emphasized that the treatment of crack propagation developed in this section is approximate and not rigorous. No attempt has been made to take into account constraints imposed on yielding by continuity requirements at the elastic-plastic boundary. The postulated shape of the plastic zone is in itself a basic assumption. Finally, the present calculations are valid for conditions of plane stress: the case of a through-crack in a sheet of thickness, t, when $r \gg t$, but not for plane strain, i.e., $r \ll t$. It, therefore, seems likely that the results given in Figures 14 and 15 overestimate plastic relaxation and underestimate the level of stress generated at the crack tip. In spite of these difficulties, the model does provide useful insights and serves to illustrate the potential usefulness of dislocation dynamics in the treatment of fracture.

CONCLUSIONS

1. A review has been made of current knowledge concerning dislocation multiplication and mobility. Observations are summarized of the

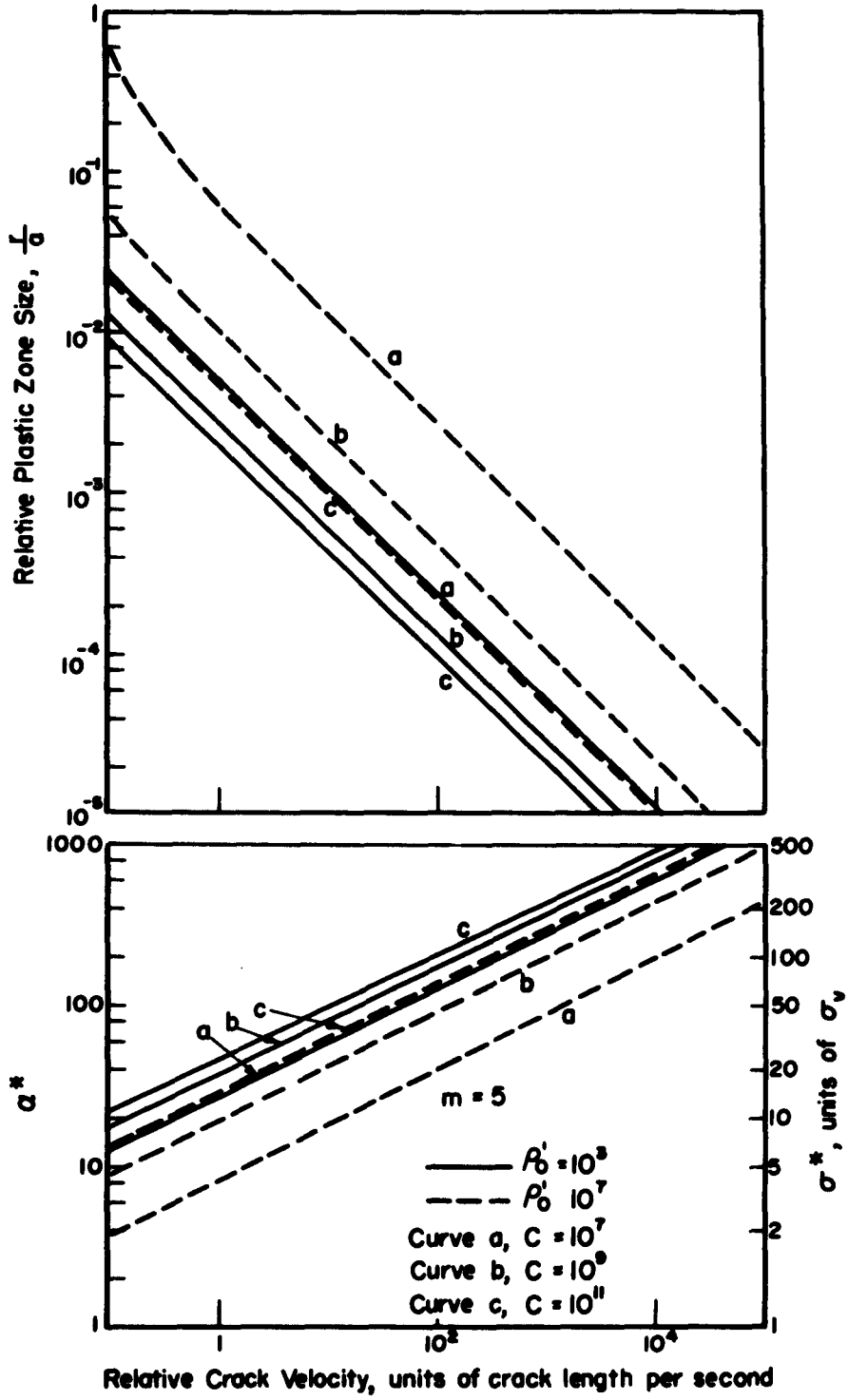

FIGURE 15. EFFECT OF MULTIPLICATION RATE AND INITIAL MOBILE DISLOCATION DENSITY ON PLASTIC ZONE SIZE AND MAXIMUM STRESS CONCENTRATION FACTOR.

increase in dislocation density produced by deformation, and the mobility of dislocations in annealed crystals. Experiments do not yet distinguish between mobile and arrested dislocations. As a consequence, the magnitudes of the initial density of mobile dislocations ρ_o and the mobile fraction f of those generated by straining are in doubt. Furthermore, the mobility of dislocations in cold-worked crystals is not known.

2. Application of Dislocation Dynamics has made possible a quantitative description of the yield point phenomenon. Although the treatment has been applied mainly to single crystals, it satisfactorily predicts the strain rate dependence of the yield stress, the delay time for yielding, and features of the Lüders' band in polycrystalline metals.

3. Dislocation Dynamics has been used to calculate the influence of deformation parameters on the response of materials to a running crack. These calculations indicate that m is the most influential material parameter, small values of m favoring cleavage crack propagation.

REFERENCES

1. Johnston, W. G., and Gilman, J. J., J. App. Phys., 30, p. 129 (1959).
2. Stein, D. F., and Low, J. R., J. App. Phys., 31, p. 362 (1960).
3. Erickson, J. S., J. App. Phys., 33, p. 2499 (1962).
4. Chaudhuri, A. R., Patel, J. R., and Rubin, L. G., J. App. Phys., 33, p. 2736 (1962).
5. Dew-Hughes, D., I.B.M. Journal, 5, p. 279 (1961).
6. Schadler, H. W., and Low, J. R., Final Report on Contract No. Nonr-2614(00) (April, 1962).
7. Hahn, G. T., Acta Met., 10, p. 727 (1962).
8. Keh, A. S., and Weissman, S., Conference on the Impact of Transmission Electron Microscopy on Theories of the Strength of Crystals, Berkeley (to be published by Interscience Publishers, New York) (1961).
9. Patel, J. R., and Alexander, B. H., Acta Met., 4, p. 385 (1956).
10. Hordon, M. J., Acta Met., 10, p. 999 (1962).
11. Livingston, J. D., Acta Met., 10, p. 229 (1962).
12. Young, F. W., J. App. Phys., 33, p. 963 (1962).
13. Van Torne, L. I., L.R.L. Report, University of California, Contract No. W-7405 eng 48 (August, 1962).
14. Owen, W. S. et al., WADD TR 61-181, Part II, p. 236 (October, 1962).
15. Benson, R., Thomas, G., and Washburn, J., "Direct Observations of Imperfections in Crystals", Wiley, p. 375 (1962).
16. Present authors, unpublished work.
17. Cottrell, A. H., "Dislocations and Plastic Flow in Crystals", O.U.P., p. 18 (1948).
18. Conrad, H., Acta Met., 11, p. 75 (1963).
19. Johnston, W. G., J. App. Phys., 33, p. 2716 (1962).

20. Johnston, W. G., Private communications.

21. Stein, D. F., Private communications.

22. Bechtold, J. H., Trans. AIME, 206, p. 142 (1956).

23. Present authors, Unpublished work.

24. Hendrickson, J. A., Wood, D. S., and Clark, D. S., Trans ASM, 48, p. 540 (1956).

25. Winlock, J., Trans. AIME, 197, p. 797 (1953).

26. Manjoine, M. J., Trans. ASME, 66, p. A-211 (1944).

27. Fisher, J. C., and Rogers, H. C., Acta Met., 4, p. 180 (1956).

28. Sylwestrowicz, W., and Hall, E. O., Proc. Phys. Soc., B64, p. 495 (1951).

29. Krafft, J. M., and Sullivan, A. M., Trans. ASM, 51, p. 643 (1959).

30. Carreker, R. P., and Hibbard, W. R., Acta Met., 1, p. 654 (1953).

31. Carreker, R. P., Trans. AIME, 209, p. 112 (1957).

32. Owen, W. S., Averbach, B. L., and Cohen, M., Trans. ASM, 50, p. 634 (1958).

33. Taylor, D. B. C., and Malvern, L. E., Response of Metals to High Velocity Deformation, p. 77, Interscience Publishers, New York (1961).

34. Inglis, C. E., Trans. Inst. Naval Arch., 55, Pt. 1, p. 219 (1913).

35. Gilman, J. J., and Johnston, W. G., J. App. Phys., 31, p. 687 (1960).

36. Present authors, Unpublished work.

37. Krafft, J. M., and Sullivan, A. M., Report to Ship Structure Committee SSC-139, "On the Effects of Carbon and Manganese Content and of Grain Size on Dynamic Strength Properties of Mild Steel".

YIELDING AND FLOW OF THE B.C.C. METALS AT LOW TEMPERATURES

Hans Conrad
Materials Sciences Laboratory
Aerospace Corporation
El Segundo, California

ABSTRACT

The available experimental data on the mechanical behavior of the B.C.C. transition metals at low temperatures ($< 0.25\ T_m$) are reviewed and analyzed to establish the rate-controlling mechanism responsible for the strong temperature and strain rate dependence of the yield and flow stresses. The activation energy H, activation volume v*, and frequency factor ν were determined as a function of the thermal component of the stress τ^*. It was found that H_o ($\tau^* = 1$ Kg/mm^2) $\simeq 0.1\ \mu b^3$ where μ is the shear modulus and b the Burgers vector, $v^* \simeq 50\ b^3$ at $\tau^* = 2$ Kg/mm^2, increasing rapidly to values in excess of $100\ b^3$ at lower stresses and decreasing to 2-5 b^3 at high stresses (50-60 Kg/mm^2) and $\nu = 10^6 - 10^{12}$ sec^{-1}, the higher values of ν generally being associated with the purer materials. H and v* as a function of stress were independent of structure. This along with other observations indicates that thermally-activated overcoming of the Peierls-Nabarro stress is the rate-controlling mechanism. The values of H_o and the change in H with stress at low stresses are in agreement with those predicted by Seeger's model for the nucleation of kinks. The Peierls-Nabarro stress and kink energy derived from the experimental data are approximately $10^{-2}\mu$ and $4 \times 10^{-2}\ \mu b^3$ respectively.

The experimental data suggest that the yield point in the B.C.C. metals is associated with the sudden multiplication of dislocations by the double cross-slip mechanism, which in turn is controlled by the motion of dislocations through the lattice. Stress-strain curves for mild steel calculated on the basis of this mechanism are in good agreement with the experimental curves.

YIELDING AND FLOW OF THE B.C.C. METALS AT LOW TEMPERATURES

Hans Conrad
Materials Sciences Laboratory
Aerospace Corporation
El Segundo, California

Introduction

A distinguishing feature of the B.C.C. metals, as compared to the close-packed (C.P.H. and F.C.C.) metals, is the strong effect of temperature and strain rate on the yield stress at low temperatures ($T < 0.2\ T_m$); see, for example, Figs. 1 and 2. (T is the test temperature and T_m is the melting temperature.) An understanding of this difference is of technological, as well as scientific interest, for the ductile-to-brittle transition in the B.C.C. metals is related to the strong temperature and strain rate dependence of the yield stress.

A number of thermally-activated dislocation mechanisms have been proposed to account for the strong temperature and strain rate dependence of the yield stress of the B.C.C. metals. In chronological order, these are:

1. Breaking away from an interstitial atmosphere (1-4)
2. Overcoming the Peierls-Nabarro stress (5-9)†
3. Non-conservative motion of jogs (11-13)
4. Overcoming interstitial precipitates (14)
5. Cross-slip (15)

There is some experimental support for each of these mechanisms, making it difficult to decide which one is actually rate-controlling. From a review

†Heslop and Petch (10) first suggested that the strong temperature dependence of the yield and flow stress in iron might be due to a high Peierls-Nabarro stress. However, they attributed the temperature dependence to a change in width of the dislocation with temperature rather than the contribution of thermal fluctuations to overcoming of the Peierls-Nabarro stress. Their suggestion does not account for the strong effect of strain rate on the yield stress.

YIELDING AND FLOW OF THE B.C.C. METALS AT LOW TEMPERATURES

Hans Conrad
Materials Sciences Laboratory
Aerospace Corporation
El Segundo, California

Introduction

A distinguishing feature of the B.C.C. metals, as compared to the close-packed (C.P.H. and F.C.C.) metals, is the strong effect of temperature and strain rate on the yield stress at low temperatures ($T < 0.2\ T_m$); see, for example, Figs. 1 and 2. (T is the test temperature and T_m is the melting temperature.) An understanding of this difference is of technological, as well as scientific interest, for the ductile-to-brittle transition in the B.C.C. metals is related to the strong temperature and strain rate dependence of the yield stress.

A number of thermally-activated dislocation mechanisms have been proposed to account for the strong temperature and strain rate dependence of the yield stress of the B.C.C. metals. In chronological order, these are:

1. Breaking away from an interstitial atmosphere (1-4)
2. Overcoming the Peierls-Nabarro stress (5-9)†
3. Non-conservative motion of jogs (11-13)
4. Overcoming interstitial precipitates (14)
5. Cross-slip (15)

There is some experimental support for each of these mechanisms, making it difficult to decide which one is actually rate-controlling. From a review

†Heslop and Petch (10) first suggested that the strong temperature dependence of the yield and flow stress in iron might be due to a high Peierls-Nabarro stress. However, they attributed the temperature dependence to a change in width of the dislocation with temperature rather than the contribution of thermal fluctuations to overcoming of the Peierls-Nabarro stress. Their suggestion does not account for the strong effect of strain rate on the yield stress.

of the experimental data available at the time for iron, Conrad (6) concluded that best overall agreement was for thermally-activated overcoming of the Peierls-Nabarro stress. Subsequent work on iron (8,16) supported this conclusion. More recently, Conrad and Hayes (9) analyzed the available data for the Group VA (V, Nb, Ta) and Group VIA (Cr, Mo, W) metals and again concluded that the rate-controlling mechanism at low temperatures was overcoming the Peierls-Nabarro stress. A similar conclusion was reached by Basinski and Christian (5) for iron and Christian and Masters (7) for the Group VA metals.

In the present paper pertinent data for all the B.C.C. transition metals are reviewed (including some more recent data [7,13,17-19])[†] and the question of the rate-controlling mechanism during low temperature deformation re-examined.

Experimental Data

I. Effect of Temperature on Yield and Flow Stresses

1. Micro-deformation

Employing a strain sensitivity of 4×10^{-6} and a strain rate of $\sim 10^{-3}$ sec^{-1}, Brown and Ekvall (15) found that the stress-strain behavior of ultrapure ($\sim$ 0.004 wt % interstitials) and impure ($\sim$ 0.04 wt % interstitials) iron consisted of three distinct regions; Fig. 3.

A. σ_E[††] is the stress where a hysteresis loop is first observed upon loading and unloading and represents the first evidence of dislocation motion. σ_E was only observed after previous straining ($\epsilon = 10^{-4}$ to 5×10^{-2}).

[†]Sources of data in addition to those mentioned in the text are given at the end of the bibliography. Also given there are the references pertaining to the Figures.

[††]Throughout the present paper σ will be used to designate tensile stress and τ shear stress. It will be assumed that $\tau = \frac{1}{2}\sigma$. Similarily, $\dot{\epsilon}$ is the tensile strain rate and $\dot{\gamma}$ the shear strain rate; $\dot{\gamma} = 0.7\ \dot{\epsilon}$.

B. σ_A is the stress at which a permanent strain first occurs; i.e. the lowest stress at which the hysterisis loop does not close. This is generally the same as the stress at which a deviation from linearity can be measured and is usually called the proportional limit.

C. σ_F is the commonly called yield or flow stress.

Brown and Ekvall found that σ_E was independent of temperature (between 300° and 78°K) for both the impure and pure irons. The variation of σ_A with temperature is shown in Fig. 4. σ_A for the locked state (undeformed impure iron) here exhibits about the same temperature dependence as that previously reported (20,21) for the lower yield stress (of annealed or strain-aged states) and the subsequent flow stress of various impure irons (C + N > 0.015 wt %) and steels.† On the other hand, σ_A for the unlocked (deformed) state has a lower temperature dependence than that for yielding or for subsequent flow. Additional evidence that the proportional limit σ_A after prestraining has a weaker temperature dependence than the flow stress σ_F of iron has been reported by Conrad and Frederick (8), Fig. 5, and Kitajima (22).

2. Macro-deformation

The yield or flow stress τ of B.C.C. metals can be considered to consist of three components (6,10,20,21):

$$\tau = \tau^* (T,\dot{\gamma}) + \tau_\mu + Kd^{-\frac{1}{2}} \qquad (1)$$

τ^* is the thermal component which depends on temperature T and strain rate $\dot{\gamma}$ and is associated with thermally-assisted overcoming of short-range obstacles. τ_μ represents the athermal component associated with long-range stress fields, is independent of strain rate, and varies with temperature only through the temper-

†Data on the other B.C.C. metals also indicate that the proportional limit of annealed impure (> 0.02 wt % interstitials) material has a temperature dependence similar to that for the subsequent yield and flow stresses (9,20).

ature variation of the shear modulus μ. $Kd^{-\frac{1}{2}}$ is the component representing the grain size effect. K is the slope of the plot of the yield or flow stress versus the reciprocal of the square root of the grain size d and for annealed impure material is relatively independent of temperature and strain rate, when compared to τ^* (21, 23-26). When K is independent of grain size, $Kd^{-\frac{1}{2}}$ gives the Hall-Petch relation (27, 28). There are, however, indications (29) that K for both the lower yield stress and flow stress is a function of the grain size and, therefore, that the effect of grain size is not given by the simple Hall-Petch equation.

In the present discussion we are principally concerned with the effect of temperature on the thermal component τ^* and wish to separate it from the others. This is accomplished by subtracting the stress at a given temperature T from that at some reference temperature T^o (6,20) (assuming that K is relatively independent of temperature), i.e.

$$\tau_T - \tau_{To} = \tau^* (T,\dot{\gamma}) - \tau^* (T^o,\dot{\gamma}) = \Delta\tau^* (T,\dot{\gamma}) \qquad (2)$$

Typical results on iron and tungsten are shown in Figs. 5 and 6. Similar plots have been developed previously for iron (20) and the Group VA and VIA metals (9, 20). τ^* as a function of temperature is then derived from such plots by taking $\tau^* = 0$ at the temperature T_o, obtained by extrapolating plots of $\log\left(\frac{\partial\tau^*}{\partial T}\right)$ versus T to a value of $\sim 5 \times 10^{-3}$ Kg/(mm^2 - ^oK), where $\frac{1}{\tau}\frac{d\tau}{dT} \approx \frac{1}{\mu}\frac{d\mu}{dT}$ and hence $\tau \approx \tau_\mu$. ($\frac{\partial\tau^*}{\partial T}$ is obtained by graphical differentiation of average curves similar to those in Figs. 5 and 6.) Plots of τ^* for yielding versus temperature for a strain rate of $\sim 10^{-4}$ sec^{-1} derived in this manner from the available experimental data are given in Figs. 7 and 8. It is here seen that for the Group VA metals the variation of τ^* with temperature is relatively independent of purity and grain size (i.e. whether the specimen is single or polycrystalline), while for the Group VIA metals and iron, τ^* as a function of temperature is clearly dependent on purity and grain

size. For the Group VIA metals and iron, the upper limit of τ^* at a given temperature is for polycrystals with interstitial contents $\geq$ 0.02 wt %; the lower limit is for single and polycrystals with less than 0.005 wt % interstitials. Single crystals and polycrystals with intermediate impurity levels exhibited a variation of τ^* with temperature between these two limits. In general, for the impure materials τ^* at a given temperature was less for single crystals than for polycrystals of the same impurity content. Figs. 5 and 10 show that previous thermal treatment and deformation may also influence the temperature dependence of τ^*.

Values of T_o (to the nearest 50°K) for a strain rate of 10^{-4} sec^{-1} are given in Table I. For the Group VIA metals and iron, T_o for the pure materials is less than that for the impure materials, whereas for the Group V metals there is no significant effect of i: ity content T_o. This difference and the difference in the effect of impurity content on the temperature dependence of τ^* may be related to the higher solubility of interstitials in the Group VA metals compared to the Group VIA metals and iron.

From Table I it is seen that the ratio T_o/T_m is 0.22 $\pm$ 0.04 for all impure polycrystalline B.C.C. metals. In a previous paper (9) it was shown that the yield stresses of all the impure polycrystalline B.C.C. metals correlate rather well on a single curve when τ^* is plotted versus the parameter $(T-T_o)/T_m$.

Values of τ_o^* obtained by extrapolating the curves of Figs. 7-9 to 0°K are given in Table II. Because of the rapid increase in τ^* at very low temperatures, there is some uncertainty associated with these values. However, if one plots the logarithm of τ^* versus temperature, an approximately linear region occurs at low temperatures (see Fig. 11) allowing for an easier extrapolation. Extrapolation of this linear region to 0°K gives values of τ_o^* slightly higher than those based on the linear plots; see Table II. Both methods yield values of τ_o^*

of the order of $10^{-2}\mu$.

II. Effect of Strain Rate on the Yield and Flow Stresses

Fig. 2 shows typical variation of the strain rate parameter $\Delta\sigma/\Delta \ln \dot{\epsilon}$, ($\Delta\sigma$ is the incremental increase in yield or flow stress for an increase in strain rate from $\dot{\epsilon}_1$ to $\dot{\epsilon}_2$) with temperature for the B.C.C. metals.† It initially increases with decrease in temperature below T_o, goes through a maximum, and then decreases again, approaching zero as the temperature goes to absolute zero. It depends on structure (i.e. on impurities and on thermal and mechanical history) in a similar manner as does the parameter $\frac{\Delta\tau^*}{\Delta T}$; compare, for example, the effect of strain on $\Delta\sigma/\Delta \ln \dot{\epsilon}$ and on $\frac{\Delta\tau^*}{\Delta T}$ for iron in Figs. 2 and 5.

Another type of experiment which also gives the relationship between the yield stress and strain rate is the so-called delay-time test employed by Wood and Clark (31) and others (32). In general, the parameter $\Delta\sigma/\Delta \ln t_d$ obtained from such tests, where t_d is the delay time for yielding, has a similar value and exhibits the same trends as does the parameter $\Delta\sigma/\Delta \ln \dot{\epsilon}$.

III. Activation Energy, Activation Volume and Frequency Factor for Deformation

1. General

It is now generally accepted that the deformation of metals may be thermally activated, and if a single mechanism is rate-controlling, one can write for the shear strain rate $\dot{\gamma}$

$$\dot{\gamma} = \rho b \dot{s} = \rho b s \nu^* \exp\left(-\frac{H(\tau,T)}{kT}\right) \qquad (3)$$

where ρ is the density of dislocations contributing to the deformation, b the Burgers vector, $\dot{s}$ the average velocity of the dislocations, s the product of the number of places where thermal activation can occur per unit length of dislocation

†More detailed data on the variation of $\frac{\Delta\sigma}{\Delta \ln \dot{\epsilon}}_T$ with temperature are found in Refs. 5,7,8, and 13.

and the area swept out per successful thermal fluctuation, ν^* the frequency of vibration of the dislocation segment involved in the thermal activation, and H the activation enthalpy (energy) which may be a function of the shear stress τ and the temperature T. For the B.C.C. metals it has been established (6,8,9,16) that H is primarily a function of the effective shear stress τ^*, (i.e. the thermal component of the yield or flow stress) given by the difference between the applied stress τ and the long range internal stress τ_μ; i.e. $\tau^* = \tau - \tau_\mu$. Further, one can show that (33)

$$H = -k\left(\frac{\partial \ln \dot{\gamma}/\nu}{\partial\, 1/T}\right)_{\tau^*} \tag{4}$$

$$= -kT^2\left(\frac{\partial \ln \dot{\gamma}/\nu}{\partial \tau}\right)_T\left(\frac{\partial \tau^*}{\partial T}\right)_{\dot{\gamma}} \tag{4a}$$

Rearranging Eq. 3 and differentiating, one obtains

$$-\frac{dH}{d\tau^*} = kT\left(\frac{\partial \ln \dot{\gamma}/\nu}{\partial \tau}\right)_T \tag{5}$$

$$= \frac{k \ln (\dot{\gamma}/\nu)}{\left(\frac{\partial \tau^*}{\partial T}\right)_{\dot{\gamma}}} \tag{5a}$$

where $\nu = \rho b s \nu^*$ and $-\frac{dH}{d\tau^*}$ is defined as the activation volume v^*. The value of ν can be obtained from the relations

$$H = kT \ln(\nu/\dot{\gamma}) \tag{6}$$

$$\text{or} \qquad -T\left(\frac{\partial \ln \dot{\gamma}}{\partial \tau}\right)_T\left(\frac{\partial \tau^*}{\partial T}\right) = \ln (\nu/\dot{\gamma}) \tag{6a}$$

i.e from the slope of a plot of H versus T or a plot of $\left(\frac{\partial \tau^*}{\partial T}\right)_{\dot{\gamma}}$ versus $\frac{1}{T}\left(\frac{\partial \tau}{\partial \ln \dot{\gamma}}\right)_T$. If ν is relatively independent of temperature and stress per se, the values of H, v^* and ν can then be derived from the relationships between stress, temperature and strain rate obtained from the usual mechanical tests.† For polycrystalline

†The values of H, v^* and the product $s\nu^*$ can also be obtained from measurements of the effect of stress and temperature on dislocation velocity by replacing the strain rate $\dot{\epsilon}$ in Eqs. 4-6 with the velocity $\dot{s}$.

B.C.C. metals (and also single crystals) a reasonable assumption is that $\tau = \frac{1}{2}\sigma$, and $\gamma = 0.7\,\epsilon$, where σ is the tensile stress and ϵ is the tensile strain; also $\left(\frac{\partial\tau^*}{\partial T}\right)_{\dot{\gamma}}$ is approximated by $\left(\frac{\partial\tau}{\partial T}\right)_{\dot{\gamma}}$, for $\frac{d\tau_\mu}{\partial T}$ is small compared to $\left(\frac{\partial\tau^*}{\partial T}\right)$.

2. Activation Energy, H

The variation of H with τ^* obtained from the available experimental data is shown in Figs. 12-18. Essentially identical results were obtained from the use of either Eq. 4 or 4a, supporting the validity of the assumptions inherent in these equations. The curves drawn in these figures represent the author's interpretation of the variation of H with τ^* indicated by the data points. There is, however, some doubt as to whether a change in curvature actually occurs at the low stress and, for the most part, the data suggest equally well a rather rapid increase in H as τ^* approaches zero. Of particular significance in Figs. 12-18 is that, within the scatter of the data, H as a function of τ^* is independent of the yielding or flow phenomena considered (microcreep, delay time, proportional limit, upper yield stress, flow and dislocation velocity) and of the structure (impurity content, grain size, and previous thermal or mechanical history) for a given metal. In Fig. 19 it is seen that H_o, the value of H at $\tau^* = 1$ Kg/mm^2, is approximately equal to $0.1\,\mu b^3$, when comparing the various B.C.C. metals.†

A number of investigators (2,6,34-36) have reported that the activation energy for yielding in iron decreases in a linear manner with the logarithm of the total applied stress τ. For comparison, plots of H versus log τ^* are given in Fig. 20 for the various impure polycrystalline B.C.C. metals.†† It is here seen that for such plots there appears to be two linear regions, one at very low stresses

†The shear modulus values were derived from the relation $\mu = \frac{3}{8}E$, where E is the Young's modulus at T_o taken from Ref. 30.

††The values of H and τ^* plotted in Fig. 20 were taken from the average curves drawn in Figs. 12-18.

and the other at high stresses, with a transition region in the vicinity of $\tau^* = 1\text{-}5$ Kg/mm^2. The slope in the high stress region is about 10 times that in the low stress region. Extrapolation of the straight lines at high stresses to H = 0 gives values of τ_o^* in reasonable agreement with those obtained by the other two methods; see Table II.

3. Activation volume, v*

Typical variation of v* with τ^* is shown for Ta, W, and Fe in Figs. 21-23. There was agreement between values obtained from Eq. 5 and Eq. 5a. and from graphical differentiation of the curves of Figs. 12-18, except at the lowest values of τ^*.† Fig. 24 shows that the activation volume as a function of stress is similar for all the B.C.C. metals. The values given here were taken from average curves such as those drawn in Figs. 21-23. It is seen from Fig. 24 that, for all of the B.C.C. metals, v* is about 50 b^3 at $\tau^* = 2$ Kg/mm^2, increasing rapidly to values in excess of 100 b^3 at lower values of stress and decreasing with stress to values as low as 2-5 b^3. Again, as for H, v* as a function of stress is independent of the yielding or flow phenomena considered and of the structure (i.e. of mechanical and thermal history).

4. Frequency Factor, ν

Typical proportionality between H and temperature obtained for the B.C.C. metals is shown in Fig. 25. Plots of the average curves of H vs T for all the impure polycrystalline B.C.C. metals are given in Fig. 26. Average values of ν derived from such plots for both pure (< 0.005 wt %) and impure (> 0.02 wt %) materials are given in Table III.

Additional evidence of the proportionality between H and temperature is provided by the variation of the ductile-to-brittle transition temperature in

†This disagreement will be discussed in a subsequent section.

the B.C.C. metals with strain rate. Generally, a straight line is obtained when the logarithm of the strain rate is plotted versus the reciprocal of the transition temperature (37,38), suggesting a rate equation of the form $\dot{\epsilon} = Ae^{-H/kT}$. Taking the logarithm of both sides of this equation and rearranging, one obtains $H = kT \ln A/\dot{\epsilon}$ (see Fig. 27), which agrees with Eq. 6 when $A = \nu$. This is consistent with the analysis of Eqs. 3-6, if the transition from ductile to brittle behavior occurs at a constant stress. The values of ν derived from the effect of strain rate on the ductile-to-brittle transition are given in Table IV. They are in reasonable agreement with those obtained from the yield and flow stress measurements listed in Table III, indicating that the ductile-to-brittle transition temperature is determined by the dynamic motion of dislocations, as has been proposed by Cottrell (40) and Petch (24).

Discussion

1. Rate-Controlling Mechanism

The fact that the various relationships of Eqs. 3-6 gave the same values of H, v^* and ν indicates that the postulated assumptions are valid, at least to a first approximation. Specifically, this supports the contention that during the low temperature deformation ($< 2.0\ T_m$) of the B.C.C. transition metals a single dislocation mechanism is rate-controlling and that ν is relatively independent of stress and temperature per se. Furthermore, the fact that identical values of H and v^* were obtained for all yielding and flow phenomena (and the ductile-to-brittle transition) indicates that the same dislocation mechanism is controlling in all cases and that this is associated with the motion of dislocations through the lattice, as distinct from a generation mechanism, such as breaking away from an interstitial atmosphere. Finally, the fact that H and v^* as a function of stress were independent of structure (i.e. thermal and mechanical history) strongly

suggests that the rate-controlling mechanism is overcoming the inherent resistance of the lattice, i.e. overcoming the Peierls-Nabarro stress. Further support for the Peierls-Nabarro mechanism is that dislocations in the B.C.C. metals are often observed to lie along the close-packed directions (41-43). A summary of the experimental evidence negating the other mechanisms mentioned in the Introduction is given in Table V.

A possible thermally-activated mechanism for overcoming the Peierls-Nabarro stress (energy) is that originally proposed by Seeger (44) to explain the Bordoni peak in F.C.C. metals and is shown in Fig. 28. It involves the formation of a pair of kinks in a dislocation line lying in a close-packed direction by the combined action of thermal fluctuations and the applied stress, and the subsequent lateral propagation of the kinks along the dislocation line, resulting in the forward motion of the dislocation. Seeger (44) calculated the activation energy for this process at low stresses to be

$$H = H_K \left[1 + \tfrac{1}{4} \log \left(\frac{16\, \tau_\rho^o}{\pi \tau^*}\right)\right]^\dagger \qquad (7)$$

where H_K is the energy of a single kink and τ_ρ^o is the Peierls-Nabarro stress at 0^oK. Furthermore, Seeger gives

$$H_K = \frac{2a}{\pi} \left(\frac{2E_o\, ab\, \tau_\rho^o}{\pi}\right)^{\frac{1}{2}} \qquad (8)$$

---

†The thermal component of the stress τ^* has been substituted for the total stress τ in Seeger's equation.

and $$H_{PN} = \frac{\tau_p^o \, ab^2}{2\pi} \tag{9}$$

$$= \frac{H_K^2 \, \pi^2 \, b}{16a^2 \, E_o} \tag{9a}$$

where $2H_{PN}$ is the Peierls-Nabarro energy per atomic length, a the distance between close-packed rows, b the Burgers vector and E_o the line energy of a dislocation. Taking the average value of τ_o^* (from Table II) for τ_p^o and taking $E_o = \frac{1}{2} \mu b^2$, one obtains from Eqs. 7 and 8, H_o ($\tau^* = 1$ Kg/mm^2) $\simeq 0.1 \, \mu b^3$, in good agreement with measured values of H_o; see Table VI. Furthermore, from Eqs. 7 and 8 one obtains $H_K = 3\text{-}4 \times 10^{-2} \, \mu b^3$ and from Eq. 9, $H_{PN} = 1\text{-}2 \times 10^{-3} \, \mu b^3$; again see Table VI. Taking the derivative of Eq. 7 with respect to τ^* gives

$$- \frac{dH}{d\tau^*} = v^* = \frac{1}{4} \frac{H_K}{\tau^*} \, . \tag{10}$$

Values of H_K derived from the values of v^* at $\tau^* = 1$ Kg/mm^2 are also given in Table VI and are in agreement with those obtained from Eqs. 7 and 8. For comparison, values of H_K derived from the slope of the plots of H vs log τ^* (Fig. 20) at low stresses (< 1 Kg/mm^2) are approximately 1/6 to 1/3 those calculated using Eqs. 7 and 8, while those derived from the slope at high stresses (> 10 Kg/mm^2) are about 3 to 4 times larger. Agreement occurs in the intermediate stress range ($\tau^* = 1\text{-}5$ Kg/mm^2), where the plots show curvature.

The good agreement between the values of H_o and H_K obtained from the various relationships (Eqs. 7-10) indicates rather strongly that the nucleation of kinks is the rate-controlling mechanism during low temperature deformation of the B.C.C. metals. Although the derived values of τ_p^o, H_K and H_{PN} are somewhat higher than those usually given for close-packed metals (45), they are in accord with those calculated using the original Peierls-Nabarro equations (46) and the

more recent calculations of Kuhlmann-Wilsdorf (47) and Hobart and Celli (48). The good agreement between the values of H_o and H_K obtained using only experimental data and those obtained using $E_o = \frac{1}{2}\mu b^2$ indicates that the line energy in the B.C.C. metals is very nearly $\frac{1}{2}\mu b^2$.

According to Seeger (44) the width w of a kink is given by

$$w = \frac{1}{2} a \left(\frac{E_o\, b}{H_{PN}}\right)^{\frac{1}{2}} \tag{11}$$

and the critical separation ℓ^* of the kinks during thermal activation is

$$\ell^* = \frac{w}{\pi} \log \left(\frac{32\, H_{PN}}{\tau^*\, b^3}\right) \tag{12}$$

$$= \frac{H - H_K}{2\, H_{PN}} \tag{12a}$$

The values of w and of ℓ^* (at $\tau = 1$ Kg/mm^2) obtained from Eqs. 11, 12 and 12a using the average values of H_K, H_{PN} and H ($\tau^* = 1$ Kg/mm^2) from Table VI and taking $E_o = \frac{1}{2}\mu b^2$ are given in Table VII. It is here seen that $w = 7\text{-}10$ b and $\ell^*(\tau^* = 1$ Kg/mm$^2) = 12\text{-}22$ b, which are quite reasonable. Again of significance is the good agreement between values of ℓ^* from Eqs. 12 and 12a.

For the Peierls-Nabarro mechanism the frequency factor can be given by

$$\nu = \rho b \left[\left(\frac{1}{\ell^*}\right)\left(Lb\right)\left(\frac{b}{\ell^*}\, v_d\right)\right] \tag{13}$$

where ρ is the density of dislocations participating in the deformation, b the Burgers vector, ℓ^* the length of dislocation segment involved in the thermal activation, L the maximum lateral spread of the kinks and ν_d the Debye frequency. The first term within the brackets represents the number of places per unit dislocation length where thermal fluctuations may nucleate a loop of length ℓ^*; the second term is the area of the slip plane swept-out per successful thermal fluctuation; the third term is the frequency of vibration of a segment of length ℓ^*. Taking $\rho = 10^9$ cm^{-2}, $\ell^* = 10b$, $L = 10^{-4}$ cm and $\nu_d = 10^{13}$ sec^{-1}, one obtains $\nu = 10^8$ sec^{-1}, in agreement with that observed experimentally for many materials; see Tables III and IV.

Since H and v* as a function of τ^* were independent of structure, the effect of impurities, precipitates, grain size, dislocations and other aspects of previous thermal or mechanical history on the temperature dependence of the yield or flow stress is then due to a change in the frequency factor ν, i.e. in the number of dislocations ρ participating in the deformation or in the lateral distance L a kink can move before encountering an obstacle. In this regard, Conrad and Frederick (8) investigated the effect of straining and of interstitial precipitates in iron on the temperature dependence of τ^*. Some of their results are given in Fig. 3, which shows that a weaker temperature dependence results from straining and from the presence of precipitates. Figs. 29 and 30 (taken from their paper) show that the weaker temperature dependence is associated with a larger value of ν, given by the slope of the plot of H vs temperature. From the relation $\nu = \rho b s v^*$ and taking the value of sv^* derived from the dislocation velocity measurements of Stein and Low (50), they obtained values of ρ, and their increase with strain (see Table VIII) in agreement with dislocation densities determined by Keh and Weissman (42) by thin-film electron microscopy, indicating

that the increase in ν was due primarily to an increase in ρ. They further concluded from their results that precipitates represented good sources for dislocations, in agreement with observations of Leslie (51) and Van Torne and Thomas (52).

From Table III it is seen that the weaker temperature dependence of τ^* for single crystals or pure polycrystals as compared to impure polycrystals in the Group VIA metals and iron is associated with a frequency factor that is larger by 3 to 5 orders of magnitude. These larger values of ν cannot be due entirely to a greater dislocation density ρ, for this would require unreasonably large values for ρ. Rather, it appears that this difference in ν is primarily due to larger values of L for the pure as compared to the impure materials, suggesting that interstitial atoms or precipitates influence the extent to which the kinks can spread before encountering an obstacle. Besides acting as obstacles to kink motion, the interstitial atoms or precipitates may induce cross-slip, which in turn limits the dislocation loop length on the slip plane. Of interest in this regard are the observations of Schadler and Low (19), who report that under some conditions dislocations in tungsten crystals can move long distances without multiplying, in agreement with the high values of ν given in Table III for single crystals of tungsten.

All of the above supports overcoming the Peierls-Nabarro stress by thermally-activated nucleation of kinks as the rate-controlling mechanism in the B.C.C. metals at low temperatures. However, explanation is needed for the fact that in the vicinity of T_o (i.e. $\tau^* = 0$) H, for the most part, does not increase as rapidly with decrease in stress (or increase in temperature) as is expected from the values of v* or the straight line portion of the H versus temperature curves at lower temperatures. As indicated earlier, the scatter in the data allow for a more rapid increase in H than is indicated by the curves

drawn in Figs. 12-18. The low values of H for stresses only slightly greater than zero may then simply reflect the difficulty in defining $\tau^* = 0$ exactly. Also, ν may actually decrease with increase in temperature (or decrease in stress).[†] On the other hand, a different mechanism may become rate-controlling in the very low stress range. Additional work is needed to resolve this problem.

Finally, one needs to explain the much smaller temperature dependence of the proportional limit after straining and the fact that σ_E, as defined by Brown and Ekvall (15), is independent of temperature. Also, in recent investigations on the determination of H as a function of stress in Ta by creep tests, Chambers (39) found a spectrum of activation energies for very small strain rates (10^{-6} - 10^{-11} sec^{-1}) rather than a single activation energy.[††] There are two possible explanations for these various effects:

(1) These phenomena represent the motion of those specific dislocations located in the most favorable internal stress fields and the applied stress primarily gives direction to the motion of these dislocations and does not contribute significantly to the thermally-activated process.

(2) Another easier mechanism is rate-controlling at the very low stress levels, for example the lateral motion of kinks, as proposed by Brailsford (53), or the lateral motion of jogs as suggested by Chambers (54). In both cases the easier motion would soon die out and, to obtain gross macroscopic flow, the more difficult mechanism of nucleating kinks would become rate-controlling. The rapid strain hardening associated with the early part of the stress-strain curve

---

[†]The change in ν may be the result of straining at different temperatures (or stresses) rather than the effect of stress or temperature per se.

[††]As an upper limit, Chambers (39) reported an H versus stress relationship in agreement with that given in Fig. 14.

would then be an exhaustion hardening rather than an interaction hardening, which occurs subsequently during macro-flow. Here, also, additional research is needed to resolve this question.

2. Yield Point and Work Hardening

The fact that K in Eq. 1 is relatively independent of temperature and that the activation energy and activation volume as a function of stress are the same for all deformation phenomena suggest that the yield point in the B.C.C. metals is not due to the thermally-assisted unpinning of dislocations from their interstitial atmosphere, as proposed by Cottrell (1), but rather results from the sudden multiplication of dislocations by the double cross-slip mechanism of Koehler (55) and Orowan (56), as proposed by Johnston and Gilman (57) for LiF. In this latter model the multiplication of dislocations is controlled by their motion through the lattice, in agreement with the experimental facts. As pointed out previously (16) three factors favor the occurrence of such a yield point in the B.C.C. metals:

(1) Initially there exists only a small number of dislocations which can contribute to the plastic flow, due to the "pegging" of the available dislocations by interstitial precipitates (as distinct from pinning by an interstitial atmosphere).

(2) The dislocation density contributing to the plastic flow increases very rapidly with strain. This is inherent in the double cross-slip mechanism for multiplication, and has been observed experimentally in iron by Keh and Weissman (42) and in molybdenum by Benson (58).

(3) The change in stress for a given change in dislocation velocity $\left[\left(\frac{\partial \sigma}{\partial \ln \dot{\varepsilon}}\right)\right.$ or $\left.\left(\frac{\partial \sigma}{\partial \ln \dot{\varepsilon}}\right)\right]$ is relatively large; see Fig. 2.

To check the proposed interpretation of the yield point, stress-strain curves for mild steel were calculated (16) using Eqs. 1 and 3 and the available

information on the activation energy as a function of stress (Fig. 18), the value of s_y^* derived from etch pit measurements in silicon-iron (6), the increase in dislocation density with strain (42) and the increase in flow stress associated with the increase in dislocation density (42). The good agreement between the calculated and experimental curves is shown in Fig. 31. Since only plastic strain was considered, the upper yield point was taken as the stress at a plastic strain of 10^{-4}, which is approximately the observed pre-yield micro-strain in iron and steel.

Acknowledgement

The author wishes to express appreciation to B. L. Mordike, G. A. Sargent, P. J. Sherwood, A. A. Johnson, R. Chambers, J. W. Christian and B. C. Masters for submitting data previous to publication. He also wishes to acknowledge the valuable assistance of G. Stone in making calculations and plotting graphs.

TABLE I

T_o and the ratio T_o/T_m for pure (< 0.005 wt % interstitials) and impure (> 0.02 wt % interstitials) B.C.C. metals for a strain rate of 10^{-4} sec^{-1}.

Metal	T_m, °K	T_o, °K		T_o/T_m	
		Pure	Impure	Pure	Impure
V	2137	---	500	----	0.23
Nb	2741	500	500	0.18	0.18
Ta	3269	600	600	0.18	0.18
Cr	2148	---	500	----	0.26
Mo	2883	450	700	0.16	0.24
W	3683	500	850	0.14	0.23
Fe	1810	300	350	0.16	0.19

TABLE II

Extrapolated values of τ^* to 0°K, τ_o^*, obtained by different methods.

Metal	$\mu^\dagger$	τ_o^*, Kg/mm^2				$\tau_o^*(Avg.)/\mu$
	$\times 10^3$ Kg/mm^2	τ^* vs T	log τ^* vs T	H vs log τ^*	Avg.	$\times 10^{-2}$
V	5.2	60	65	60	62	1.19
Nb	4.0	58	65	60	61	1.52
Ta	7.0	60	67	80	69	.99
Cr	11.4	79	90	80	83	.73
Mo	12.7	78	105	85	89	.70
W	15.7	100	165	100	122	.78
Fe	7.4	49	65	60	58	.78

†The value of the shear modulus was taken as $\mu = 3/8$ E, where E is Youngs modulus at 300°K taken from data by Tietz and Wilson (30).

TABLE III

The frequency factor ν for the B.C.C. metals obtained from yield or flow stress measurements.

Metal	Authors	ν (sec^{-1}) Pure Single or Polycrystals	Impure Polycrystals
V	Present	---	10^{6}
	Christian and Masters (7)	---	10^{10}
Nb	Present	10^{6}	10^{6}
	Christian and Masters (7)	---	10^{8}
Ta	Present	10^{8}	10^{8}
	Chambers (39)	10^{7}	---
	Christian and Masters (7)	---	10^{11}
	Mordike (13)	10^{9}	---
Cr	Present	---	10^{9}
Mo	Present	10^{11}	10^{6}
W	Present	10^{11}	10^{7}
Fe	Present	10^{11}	10^{8}
	Basinski and Christian (5)	---	10^{8}
	Conrad (6)	---	$10^{8} - 10^{9}$
	Lean, Plateau and Crussard (38)	---	$10^{8} - 10^{10}$

TABLE IV

Values of ν derived from the effect of strain rate on the ductile-to-brittle transition temperature (Data from Refs. 37 and 38.)

Metal	ν (sec^{-1})
Cr	10^{10}
Mo	$10^{8} - 10^{12}$
W	10^{12}
Fe	$10^{8} - 10^{12}$

TABLE V

Summary of evidence against specific mechanisms which have been proposed as rate-controlling during the low temperature deformation of the B.C.C. metals.

Mechanism	Contrary Evidence
Breaking-away from an interstitial atmosphere	1. All yielding and flow phenomena exhibit the same values of H and v*. 2. H and v* are independent of interstitial content. 3. H and v* are the same for the mobility of dislocations as determined by etch pits as for initial yielding.
Non-conservative motion of jogs	1. H and v* are independent of structure. 2. H and v* for yielding and flow are the same as for the mobility of edge dislocations, which do not move non-conservatively.
Overcoming interstitial precipitates	1. H and v* are independent of impurity content. 2. H and v* are independent of the quantity of interstitial precipitates. 3. τ^* decreases with increase in quantity of precipitates.
Cross-slip	1. H and v* for yielding and flow are the same as for the mobility of edge dislocations, which cannot cross-slip.

TABLE VI

Values of H_o, H_K and H_{PN} derived from the experimental data.

Metal	b Å	μb^3† ergs x 10^{-12}	$H_o(\tau^* = 1\ Kg/mm^2)/\mu b^3$ Eqs. 7 & 8 x 10^{-2}	$H_o(\tau^* = 1\ Kg/mm^2)/\mu b^3$ Figs. 12-18 x 10^{-2}	$H_K/\mu b^3$ Eq. 7 x 10^{-2}	$H_K/\mu b^3$ Eq. 8 x 10^{-2}	$H_K/\mu b^3$ Eq. 10 x 10^{-2}	$H_{PN}/\mu b^3$ Eq. 9 x 10^{-3}
V	2.63	9.4	9.5	9.3	3.8	3.9	4.2	1.9
Nb	2.86	9.5	10.7	9.3	3.8	4.4	4.5	2.4
Ta	2.86	16.6	8.9	9.3	3.8	3.6	5.5	1.6
Cr	2.50	17.6	7.8	8.5	3.3	3.1	3.7	1.2
Mo	2.73	25.5	7.6	8.3	3.3	3.0	4.1	1.1
W	2.73	31.5	8.4	8.2	3.2	3.2	4.1	1.3
Fe	2.48	11.2	7.8	8.3	3.4	3.2	2.7	1.3

†The value of μ is that given in Table II.

TABLE VII

Values of w and μ^* derived from the experimental data.

Metal	w/b	μ^*/b	
		Eq. 12	Eq. 12a
V	8	15	14
Nb	8	15	12
Ta	9	17	13
Cr	10	19	20
Mo	11	21	20
W	10	21	18
Fe	10	18	19

TABLE VIII

Effect of Strain on the Dislocation Density Participating in the Plastic Flow of Iron Determined from the Frequency Factor ν (After Conrad and Frederick (8))

Material	Strain	ν (Sec^{-1})	ρ (cm^{-2})
Vac. Melt. Electrolytic Iron-W.Q. from 920°C	1×10^{-3}	2.1×10^{7}	8.4×10^{8}
	5×10^{-2}	8.2×10^{7}	3.3×10^{9}
Ferrovac - Decarb.	2×10^{-2}	3.8×10^{6}	1.5×10^{8}
	10×10^{-2}	1.7×10^{8}	6.6×10^{9}
	20×10^{-2}	5.3×10^{9}	2.1×10^{11}
Ferrovac - Annealed	$>5 \times 10^{-2}$	5.3×10^{9}	2.1×10^{11}

References

1. A. H. Cottrell - Rept. on the Strength of Solids, Phys. Soc., London, p. 30 (1948); Conf. on High Rates of Strain, Inst. Mech. Eng. London p. 448 (1957); Trans. AIME 212 192 (1958).
2. A. H. Cottrell and B. A. Bilby - Proc. Phys. Soc. 62A 49 (1949).
3. J. C. Fisher - Trans. ASM 47 451 (1955).
4. N. F. Louat - Proc. Phys. Soc. B69 454 (1956); ibid B71 444 (1958).
5. Z. S. Basinski and J. W. Christian - Aust. J. Phys. 13 299 (1960).
6. H. Conrad - J. Iron and Steel Inst. 198 364 (1961).
7. J. W. Christian and B. C. Masters - private communication; Rept. entitled "Thermally-activated Flow in Body-Centered Cubic Metals" Res. Contract 7/Exptl/729, Nov. (1961).
8. H. Conrad and S. Frederick - Acta Met. 10 1013 (1962).
9. H. Conrad and W. Hayes - to be published in Trans. ASM.
10. J. Heslop and N. J. Petch - Phil. Mag. 1 866 (1956).
11. G. Schoeck - Acta Met. 9 382 (1961).
12. R. M. Rose, D. P. Ferris and J. Wulff - Trans. AIME 224 981 (1962).
13. B. L. Mordike - Zeit. f. Metall. 53 586 (1962).
14. B. L. Mordike and P. Haasen - Phil. Mag. 7 459 (1962).
15. N. Brown and R. A. Ekvall - Acta Met. 10 1101 (1962).
16. H. Conrad - "Yielding and Flow of Iron" to be published in AIME/Interscience-Wiley Vol. "High Purity Iron and Its Dilute Solid Solutions."
17. G. A. Sargent and A. A. Johnson - private communication; Rept. entitled "The Effects of Strain Rate and Temperature on the Plastic Deformation of Niobium"; also Fall Meeting AIME, New York City, Oct. (1962).
18. P. J. Sherwood - private communication; Rept. entitled "The Effect of Strain Rate on the Tensile Properties of Polycrystalline Tantalum at Room Temperature."
19. H. Schadler and J. R. Low - "Low-Temperature Brittleness of Refractory Metals," Contract No. Nonr-2614(00), Apr. (1962).
20. H. Conrad - Phil Mag. 5 745 (1960).
21. H. Conrad and G. Schoeck - Acta Met. 8 791 (1960).
22. K. Kitajima - Rept. Res. Inst. of Appl. Mech., Kyushu Univ., Japan, No. 15 171 (1960).
23. F. de Kazinski, W. A. Backofen, and B. Kapadia - "Fracture," Wiley p. 65 (1959).
24. N. J. Petch - "Fracture," Wiley p. 54 (1959).
25. W. Owen - AIME Refractory Metals Symposium, Chicago, Apr. 1962.
26. D. V. Wilson and B. Russel - Acta Met. 8 36 (1960).
27. E. O. Hall - Proc. Phys. Soc. B64 747 (1951).
28. N. J. Petch - J. Iron and Steel Inst. 174 25 (1953).
29. H. Conrad - to be published in Acta Met. and in AIME-Interscience Vol. on Recovery and Recrystallization.
30. T. Tietz and J. Wilson - "Mechanical, Oxidation, and Thermal Property Data for Seven Refractory Metals and Their Alloys" - Lockheed Missiles and Space Div. Rept. Code 2-36-61-1, Sept. 15, 1961.
31. D. S. Clark and D. S. Wood - Proc. ASTM 49 717 (1949); Trans. ASM 43 571 (1951); ibid 44 726 (1952); ibid 46 34 (1954).
32. J. M. Kraft and A. M. Sullivan - Trans. ASM 51 643 (1959).
33. H. Conrad and H. Wiedersich - Acta Met. 8 128 (1960).

34. C. Zener and J. H. Hollomon - J. Appl. Phys. 15 22 (1944).
35. T. Yokobori - Phys. Rev. 88 1423 (1952).
36. J. D. Campbell - Acta Met. 1 706 (1953); Trans. ASM 51 659 (1959).
37. A. W. Magnusson and W. M. Baldwin - J. Mech. & Phys. Solids 5 172 (1957).
38. J. B. Lean, J. Plateau and C. Crussard - Mem. Sci. Revise Metall. 56 427 (1959).
39. R. Chambers - Fall Meeting AIME, New York, Oct. (1962).
40. A. H. Cottrell - Trans. AIME 212 192 (1958).
41. J. R. Low and R. W. Guard - Acta Met. 7 171 (1959).
42. A. Keh and S. Weissmann - Conference on the Impact of Transmission Electron Microscopy on Theories of the Strength of Crystals," Berkeley (1961); to be published by Interscience.
43. D. P. Gregory and G. H. Rowe - "Mechanism of Work Hardening in B.C.C. Metals," PWAC-375, ASD Rept. TRD-62-354, July 12, 1962.
44. A. Seeger - Phil Mag. 1 651 (1956).
45. A. Seeger, H. Donth and F. Pfaff - Disc. Faraday Soc. 23 19 (1957).
46. A. H. Cottrell - "Dislocations and Plastic Flow in Crystals," Oxford Press (1953) p. 62.
47. D. Kuhlmann-Wilsdorf - Phys. Rev. 120 773 (1960).
48. R. Hobart and V. Celli - J. Appl. Phys. 33 60 (1962).
49. A. Seeger and P. Schiller - Acta Met. 10 348 (1962).
50. D. F. Stein and J. R. Low - J. Appl. Phys. 31 362 (1960).
51. W. C. Leslie - Acta Met. 9 1004 (1961).
52. L. I. Van Torne and G. Thomas - submitted to Acta Met.
53. A. Brailsford - Phys. Rev. 122 778 (1961).
54. R. Chambers - private communication.
55. J. S. Koehler - Phys. Rev. 86 52 (1952).
56. E. Orowan - "Dislocations in Metals," AIME, New York, p. 103 (1954).
57. W. G. Johnston and J. J. Gilman - J. Appl. Phys. 30 129 (1959); ibid 31 632 (1960).
58. R. Benson - private communication.

Sources of Data other than those Referenced in the Text

59. T. A. Trozera, O. D. Sherby and J. E. Dorn - Trans. ASM 49 173 (1957).
60. R. P. Carreker and W. R. Hibbard - Acta Met. 1 654 (1953).
61. J. H. Bechtold and P. G. Shewmon - Trans. ASM 46 397 (1954).
62. J. H. Bechtold - Trans. AIME 206 142 (1956).
63. J. W. Pugh - Proc. ASTM 57 906 (1957).
64. Metals Res. Labs, Union Carbide Co., "Investigation of the Properties of Tungsten and Its Alloys" WADD Tech Rept 60-144, May (1960).
65. H. G. Sell et al - "The Physical Metallurgy of Tungsten and Tungsten Base Alloys" Contract No. AF 33(616)-6933, Proj. No. 735101, Jan 12, 1962.
66. E. S. Tankins and R. Maddin - "Columbium Metallurgy" Interscience New York, p. 343 (1961).
67. E. T. Wessel, L. L. France and R. T. Begley - "Columbium Metallurgy" Interscience, New York, P. 459 (1961).
68. M. A. Adams and A. Iannucci - "The Mechanical Properties of Tantalum with Special Reference to the Ductile-Brittle Transition," ASD Tech. Rept. 61-203, Apr. 1, 1961.
69. M. J. Marcinkowski and H. A. Lipsitt - Acta Met. 10 95 (1962).

70. R. W. Armstrong - "The Plastic Flow of Molybdenum from -200°C to +400°C by Compression Tests" - Westinghouse Res. Rept. 60-8-01-01-R3, Nov. 7 (1955).
71. J. A. Hendrickson, D. S. Wood, and D. S. Clark - Trans. ASM 48 540 (1956).
72. D. Weinstein, G. M. Sinclair and C. A. Wert - "The Strain Rate and Temperature Dependence of the Ductile-to-Brittle Transition in Molybdenum Subjected to Torsional Loading" - Univ. Ill. T. & A.M. Rept. No.156, Dec. (1959).
73. B. Jaoul and D. Gonzalez - J. Mech. Phys. Solids 9, 16 (1961).
74. R. Guard - Acta Met. 9 163 (1961).
75. J. H. Bechtold - Acta Met. 3 249 (1955).
76. J. W. Pugh - Trans. ASM 48 677 (1956).
77. P. E. Bennett and G. M. Sinclair - Univ. of Illinois T. & A.M. Rept.No. 157, Dec. (1959).

Sources of Data listed in the Figures

Fig. No.	References
2	7, 8, 59, 60
6	12, 19, 61-65
12	7, 9
13	7, 9, 66, 67
14	7, 9, 14, 68
15	9, 69
16	9, 70-72
17	9, 12, 19, 64
18	6, 14, 16, 50, 73, 74
21	7, 14, 18, 68, 75, 76
22	12, 19, 62-64
23	6, 14, 16, 50, 73, 74
25	31, 77

FIG. 1 INITIAL YIELD STRESS OF VARIOUS POLYCRYSTALLINE METALS VERSUS T/Tm

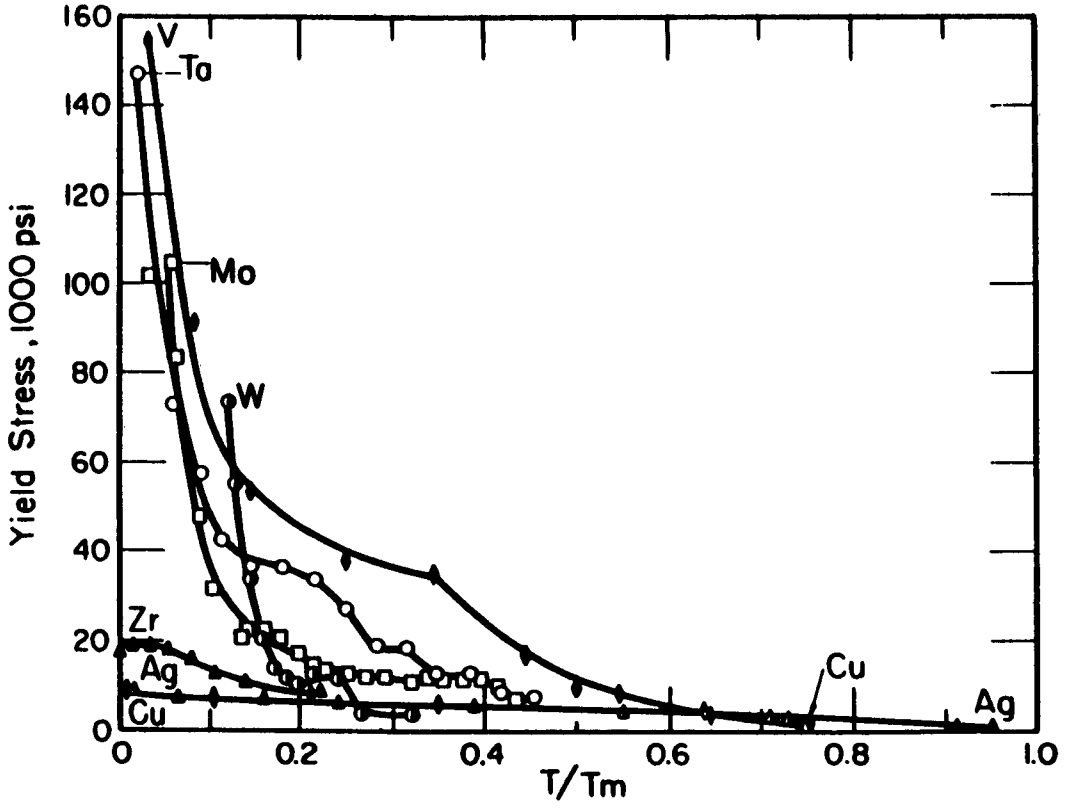

FIG. 2 EFFECT OF STRAIN RATE ON THE YIELD AND FLOW STRESSES OF F.C.C. AND B.C.C. METALS

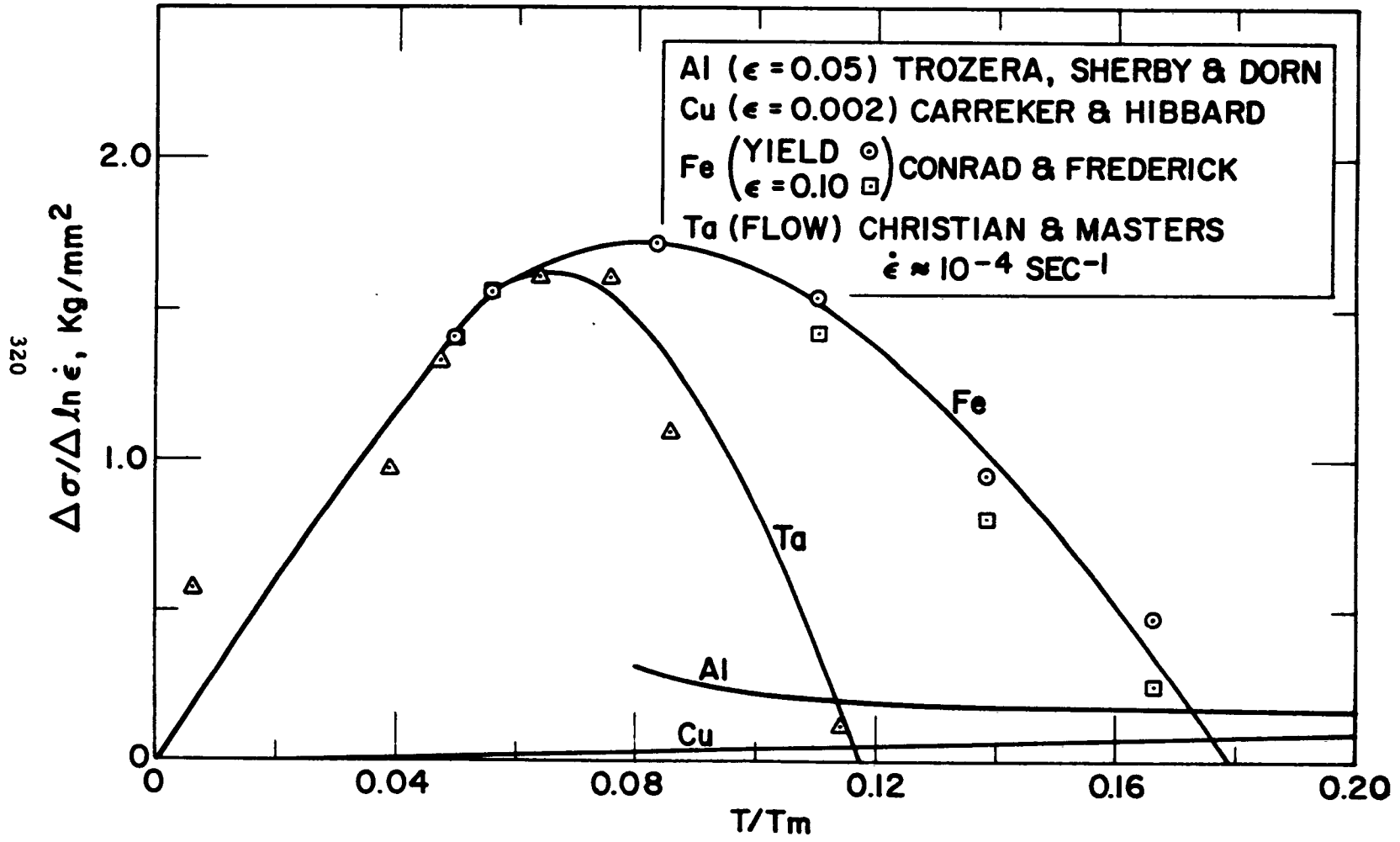

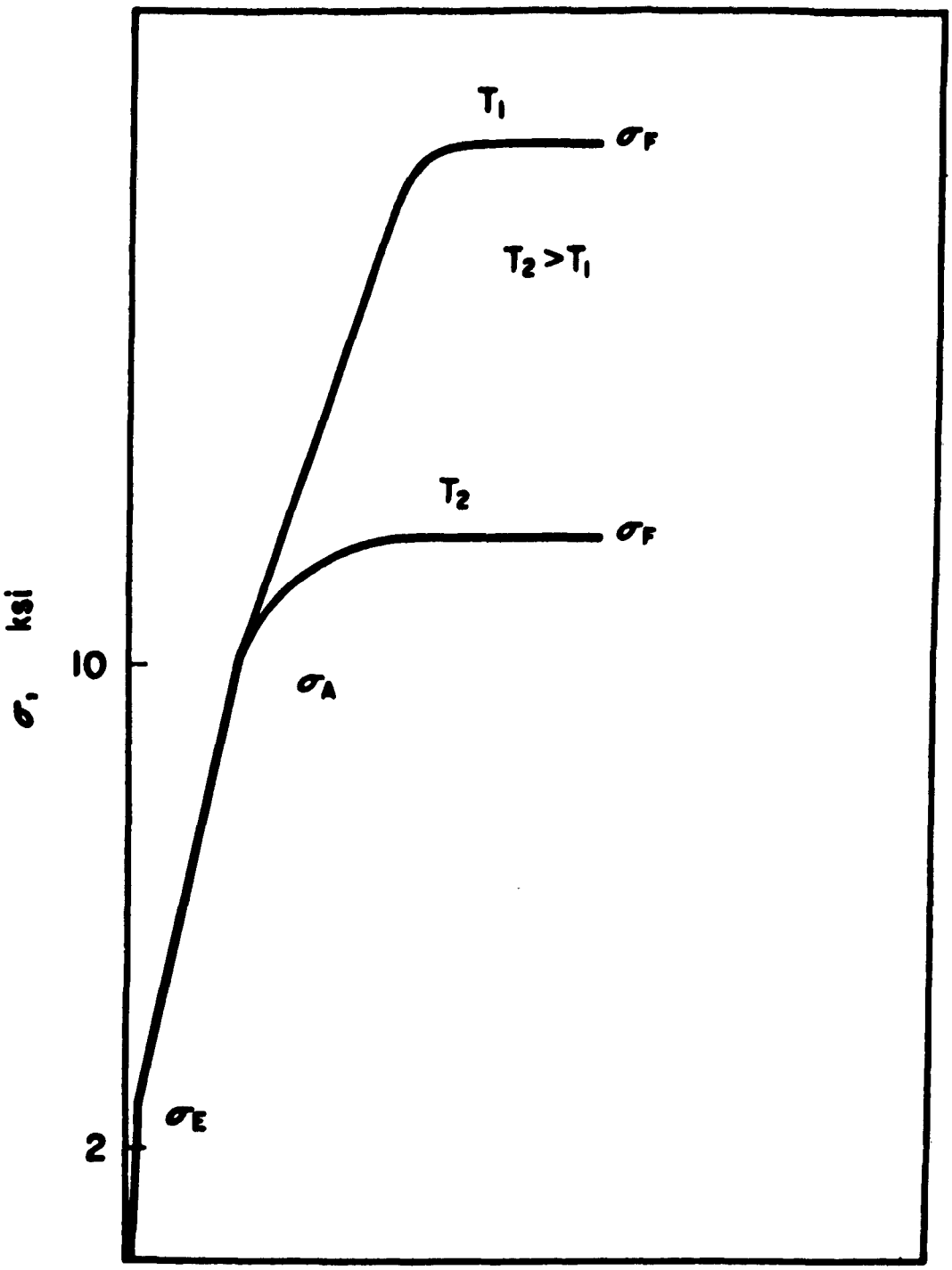

FIG. 3 Idealized stress–strain curves for an ultra-pure iron at two temperatures.
(AFTER BROWN AND EKVALL (15))

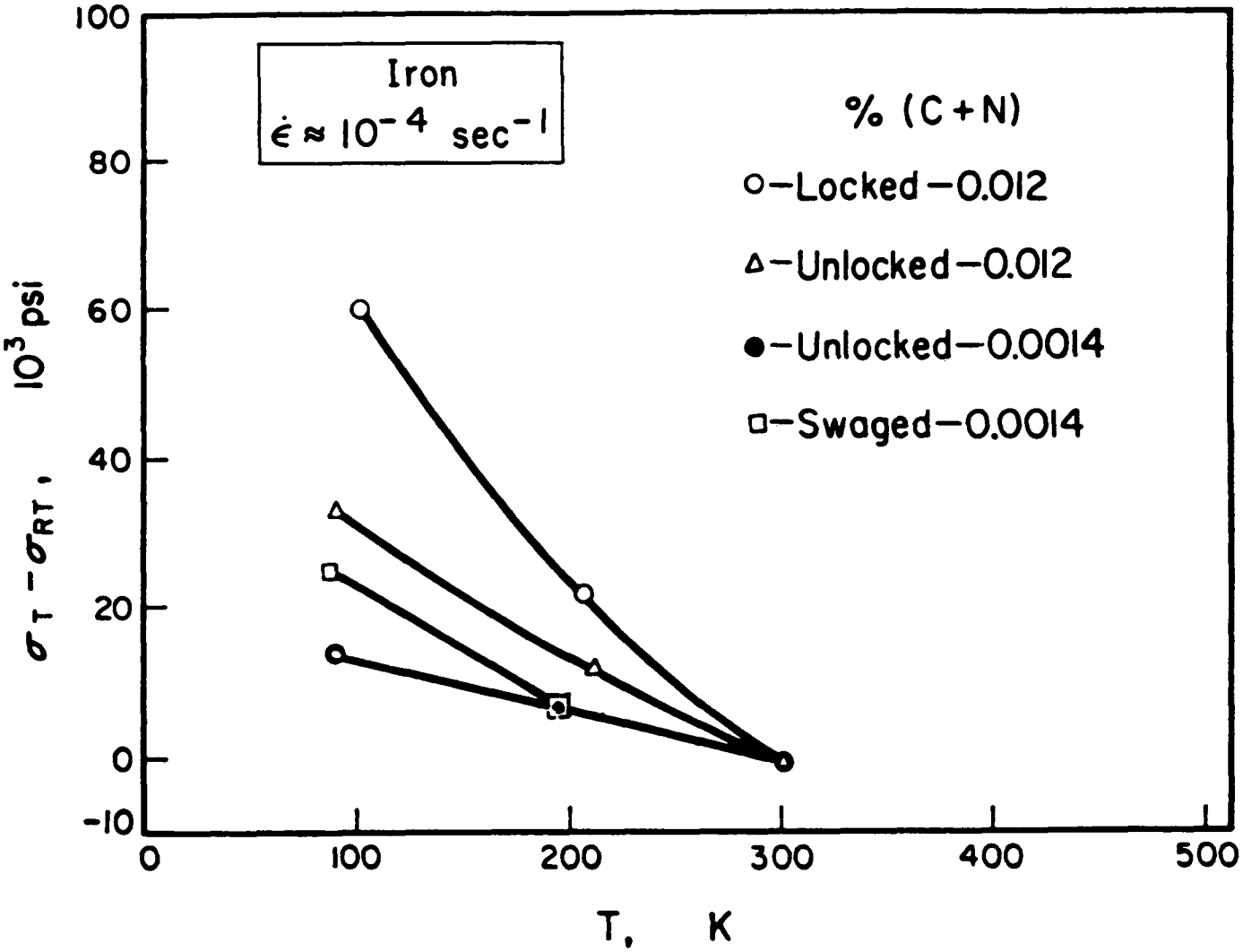

FIG. 4 Temperature dependence of σ_A for various materials and state of locking.
(AFTER BROWN AND EKVALL (15))

FIG. 5 EFFECT OF TEMPERATURE ON THE INITIAL YIELD STRESS, THE PROPORTIONAL LIMIT AFTER STRAINING AND THE FLOW STRESS OF ELECTROLYTIC IRON

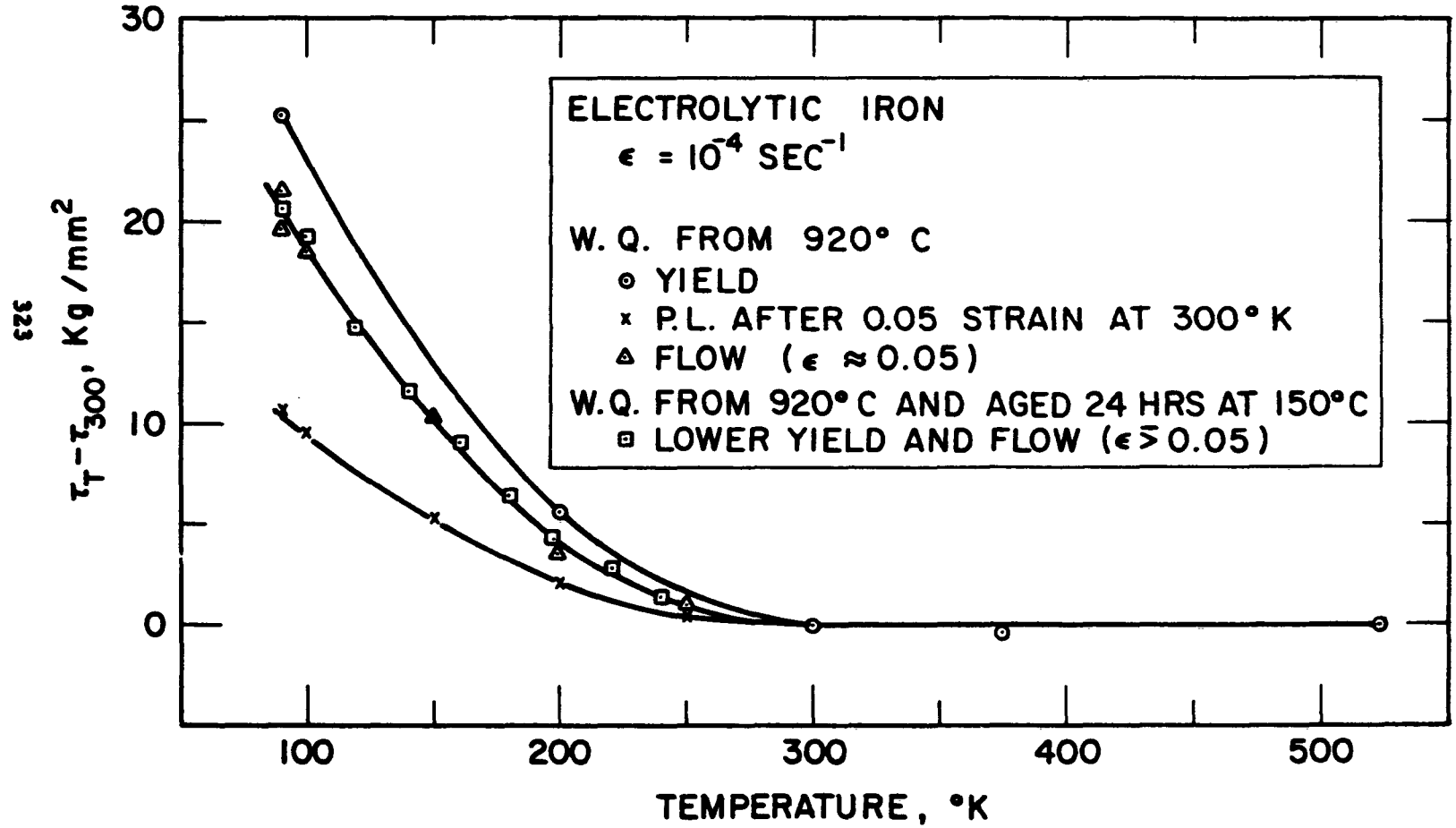

FIG. 6 EFFECT OF TEMPERATURE ON THE THERMAL COMPONENT OF THE YIELD STRESS OF TUNGSTEN

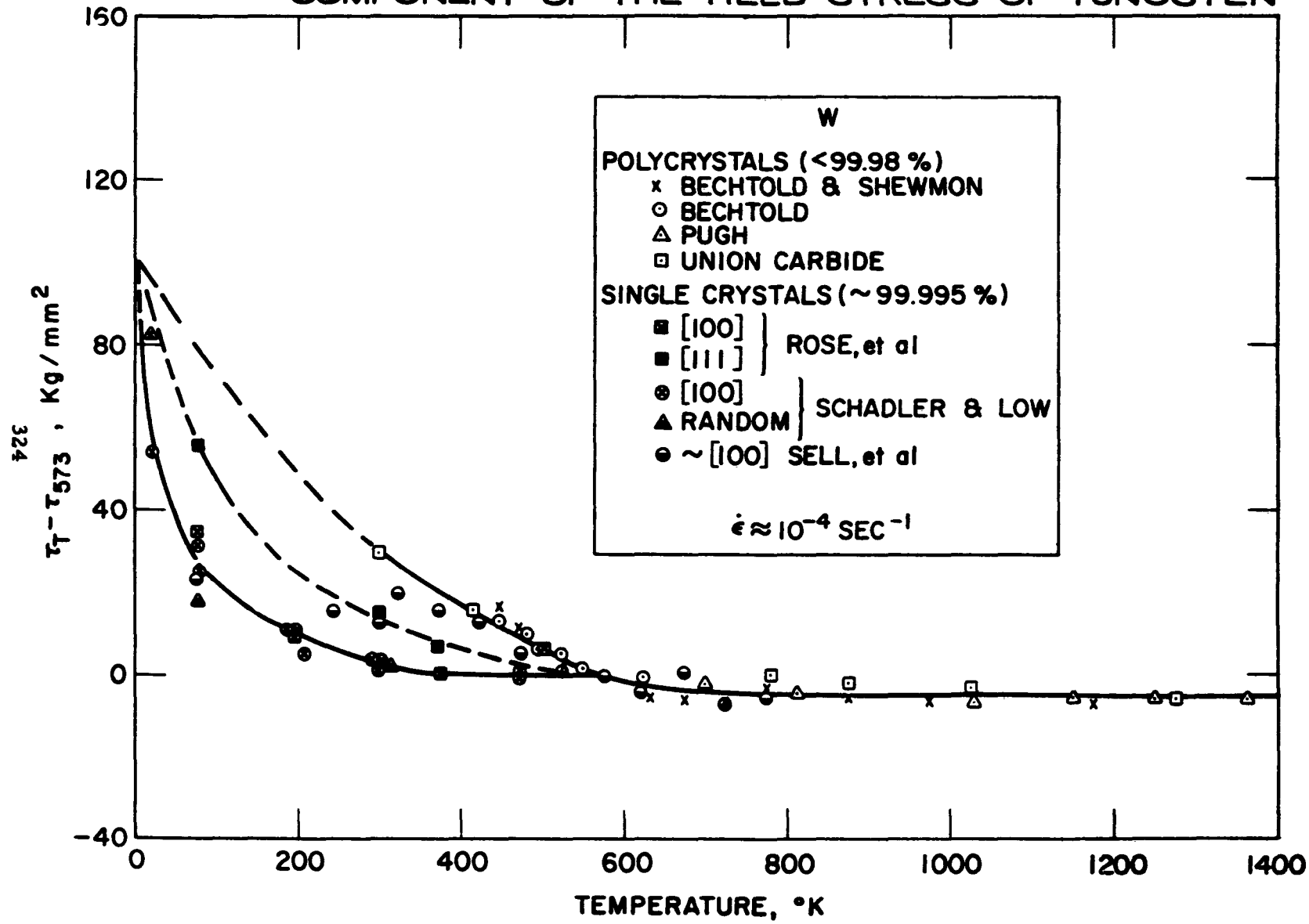

FIG. 7 VARIATION OF τ^* WITH TEMPERATURE FOR PURE (< 0.005 WT % INTERSTITIALS) AND IMPURE (> 0.02 WT % INTERSTITIALS) GROUP VA METALS. STRAIN RATE: 10^{-4} SEC^{-1}

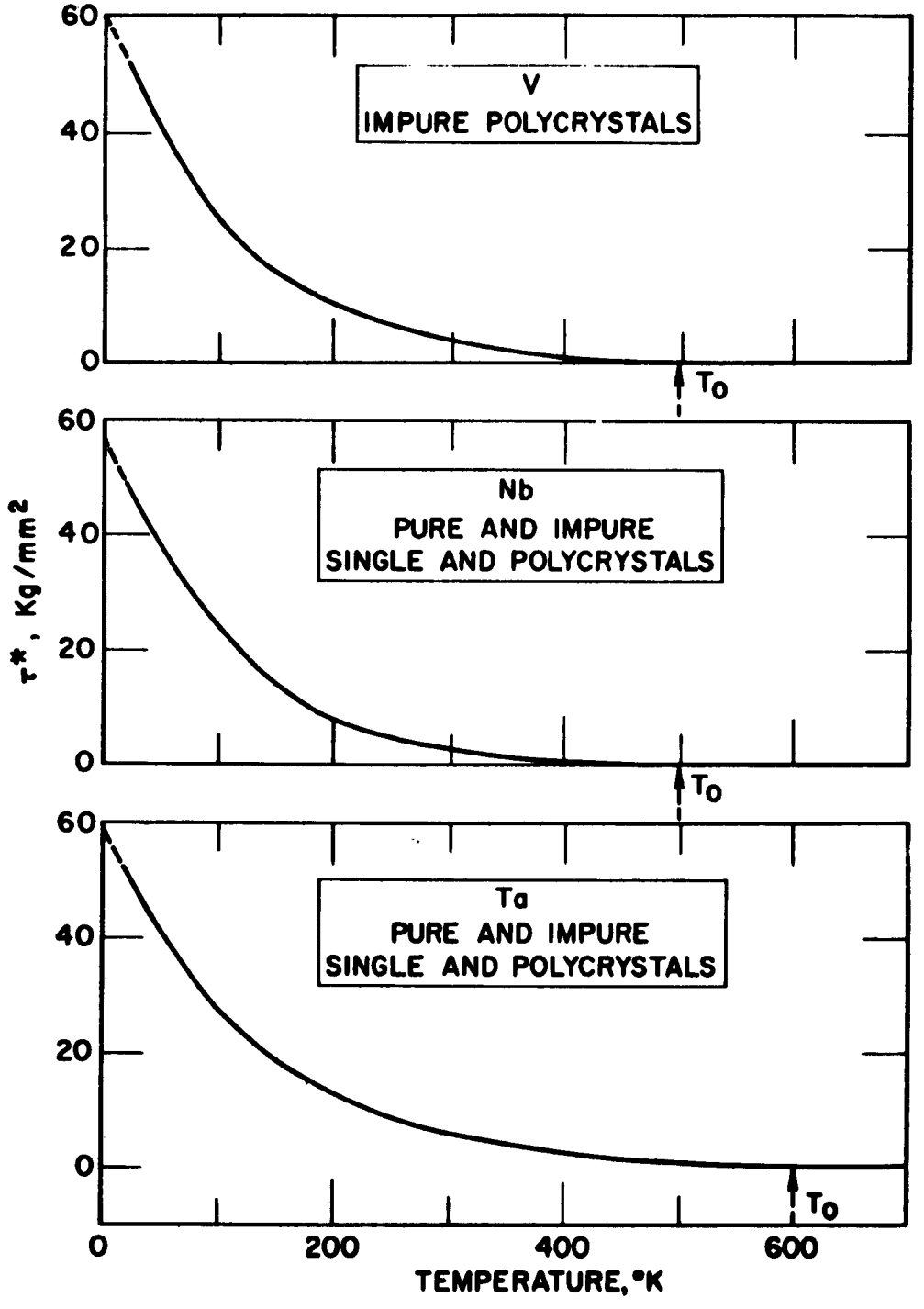

FIG. 8 VARIATION OF τ^* WITH TEMPERATURE FOR PURE (<0.005 WT % INTERSTITIALS) AND IMPURE (>0.02 WT % INTERSTITIALS) GROUP VIA METALS. STRAIN RATE: 10^{-4} SEC^{-1}

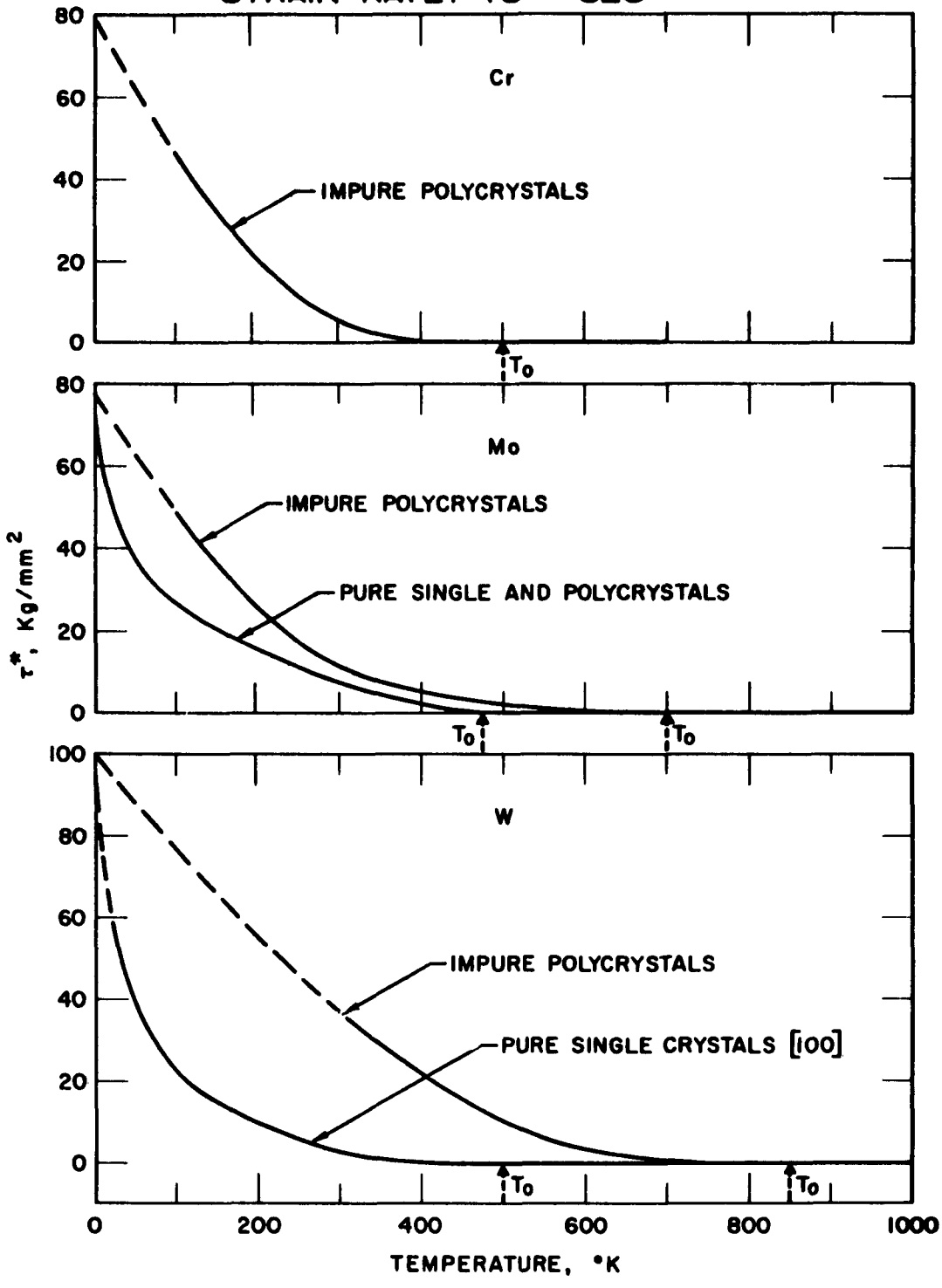

FIG. 9 VARIATION OF τ^* WITH TEMPERATURE FOR PURE (<0.005 WT% INTERSTITIALS) AND IMPURE (>0.02 WT% INTERSTITIALS) IRON

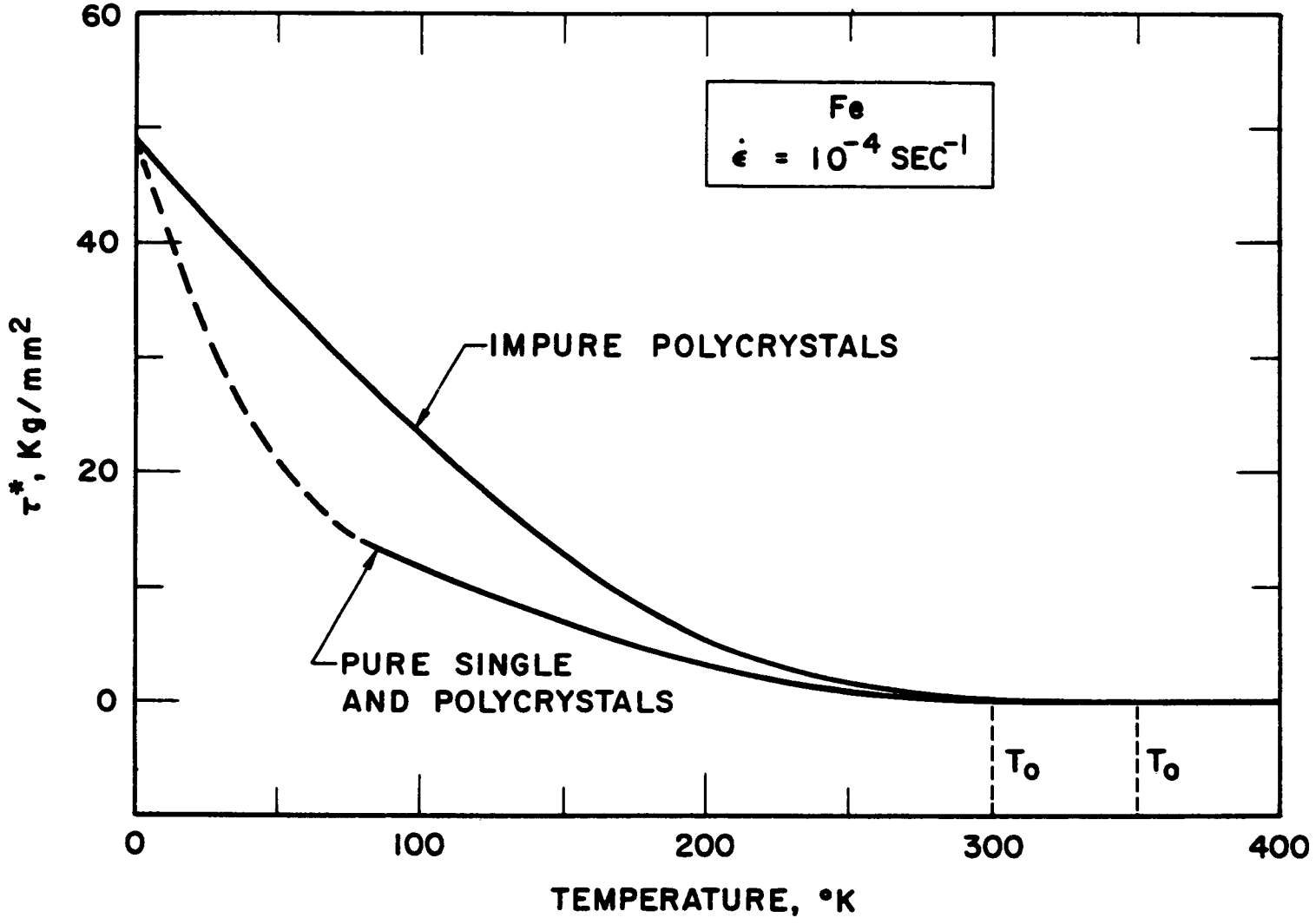

FIG. 10 TEMPERATURE DEPENDENCE OF REVERSIBLE FLOW STRESS IN IRON [AFTER BAZINSKI AND CHRISTIAN (5)]

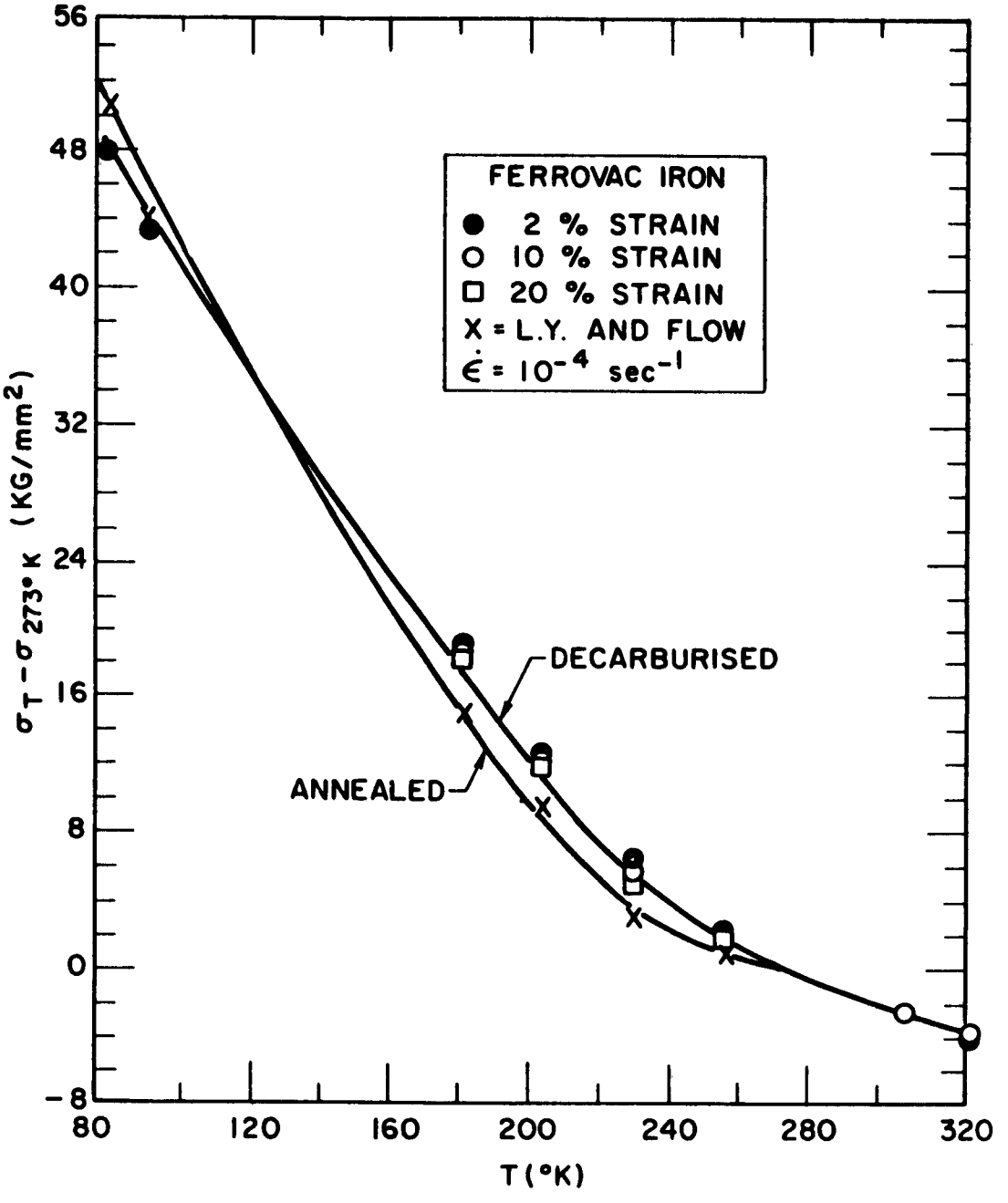

FIG. 11. LOG τ^* VS TEMPERATURE FOR IMPURE POLYCRYSTALLINE B.C.C. METALS

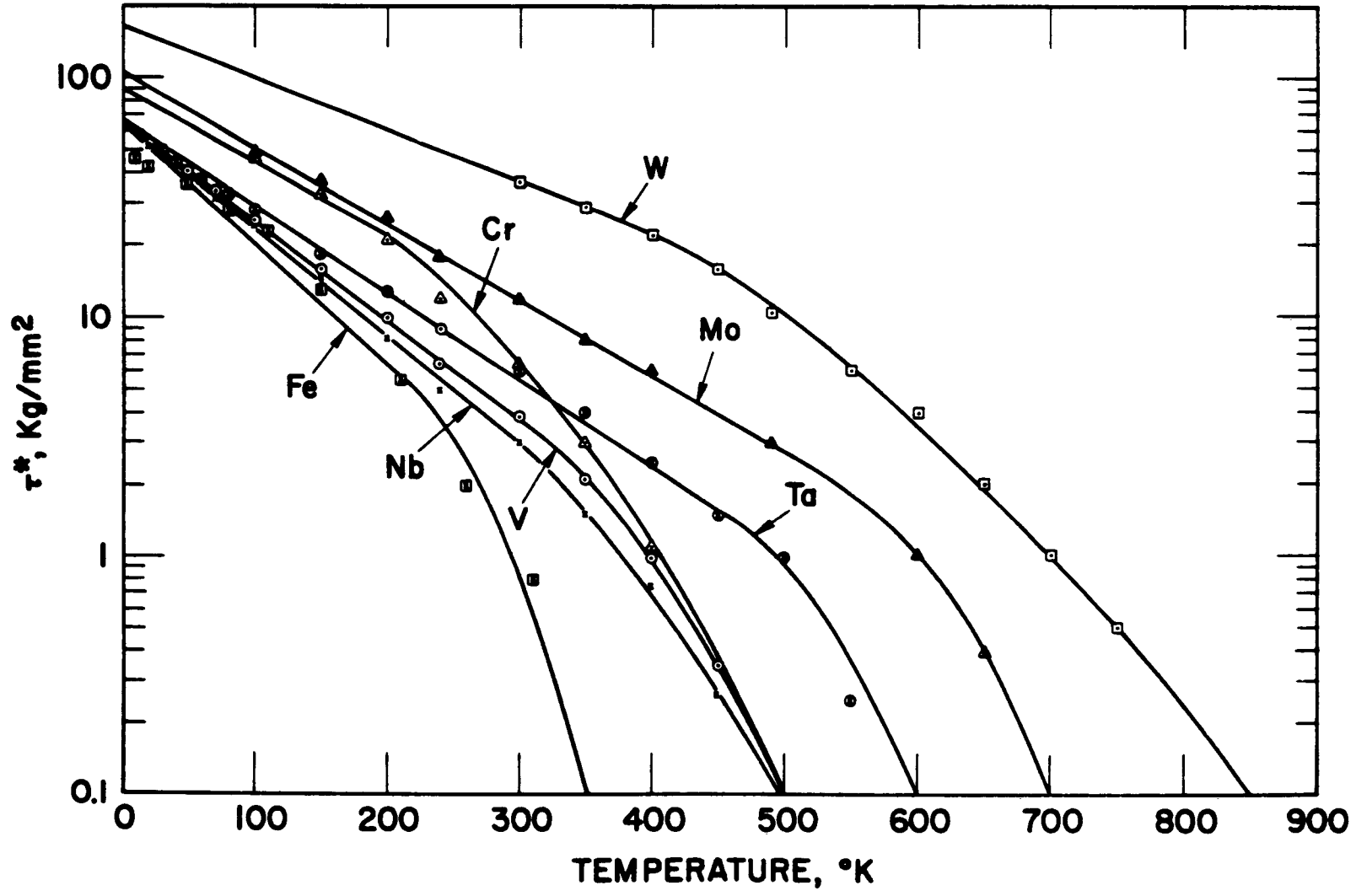

FIG. 12 EFFECT OF STRESS ON THE ACTIVATION ENERGY FOR THE DEFORMATION OF VANADIUM

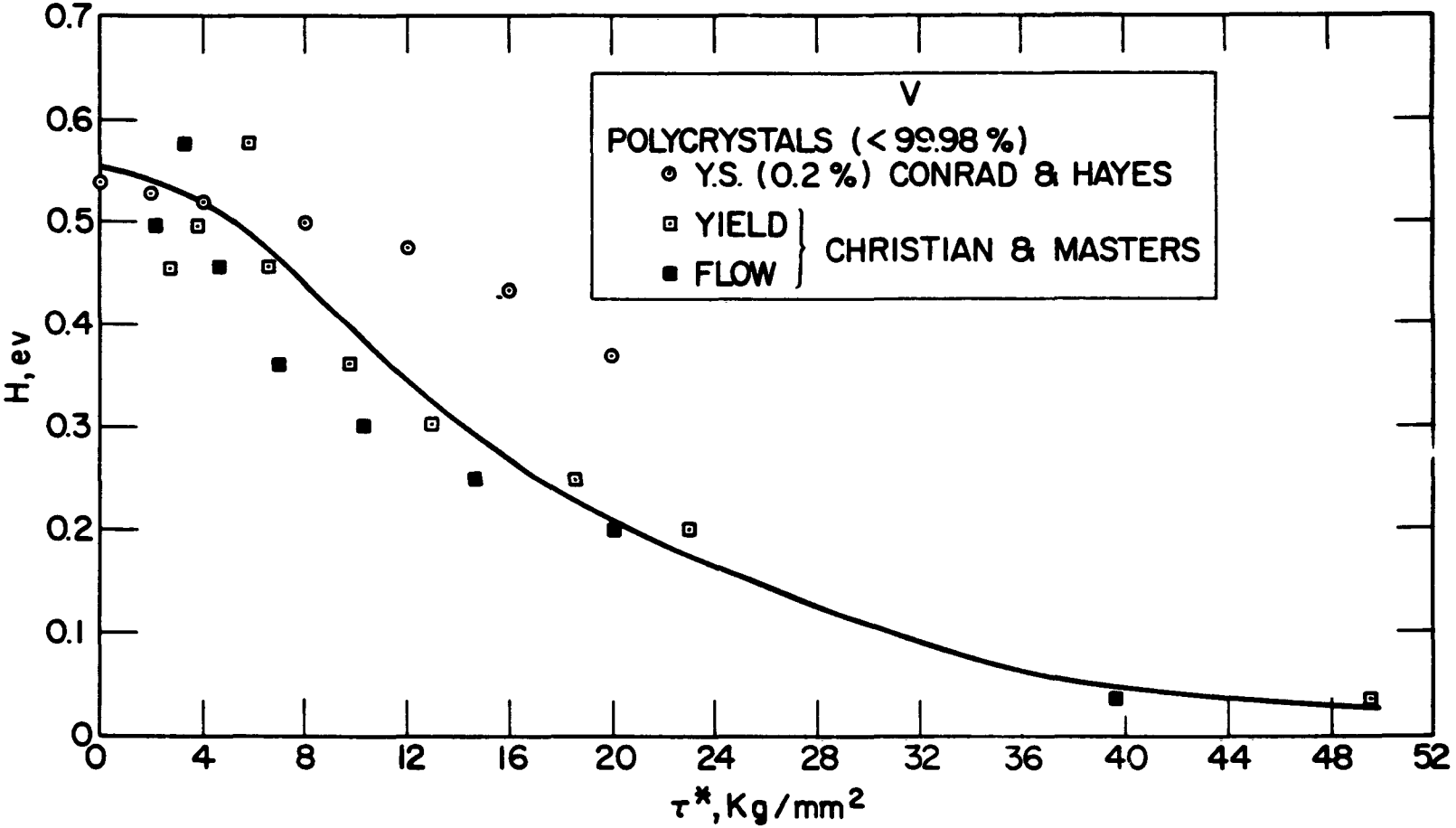

FIG. 13 EFFECT OF STRESS ON THE ACTIVATION ENERGY FOR THE DEFORMATION OF NIOBIUM

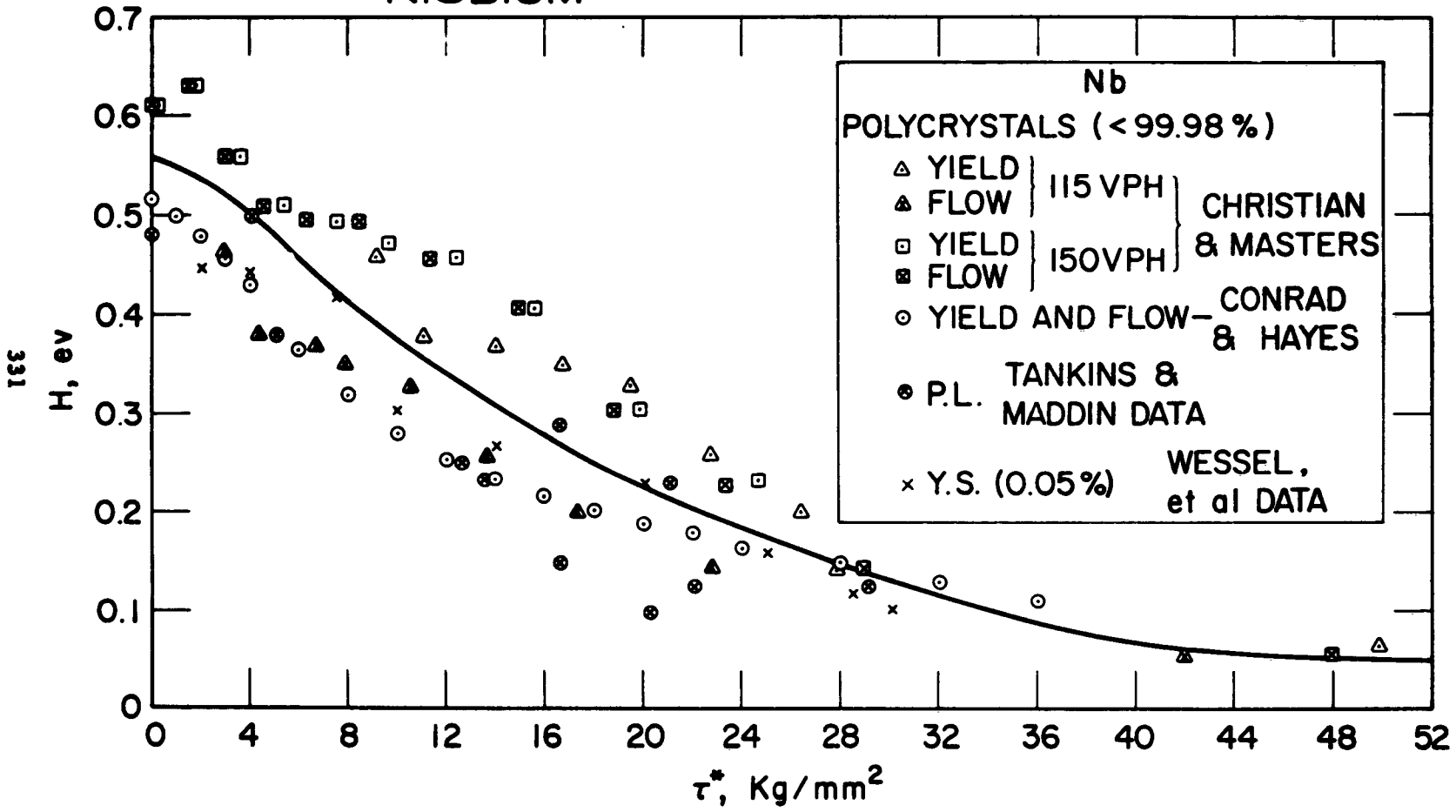

FIG. 14· EFFECT OF STRESS ON THE ACTIVATION ENERGY FOR THE DEFORMATION OF TANTALUM

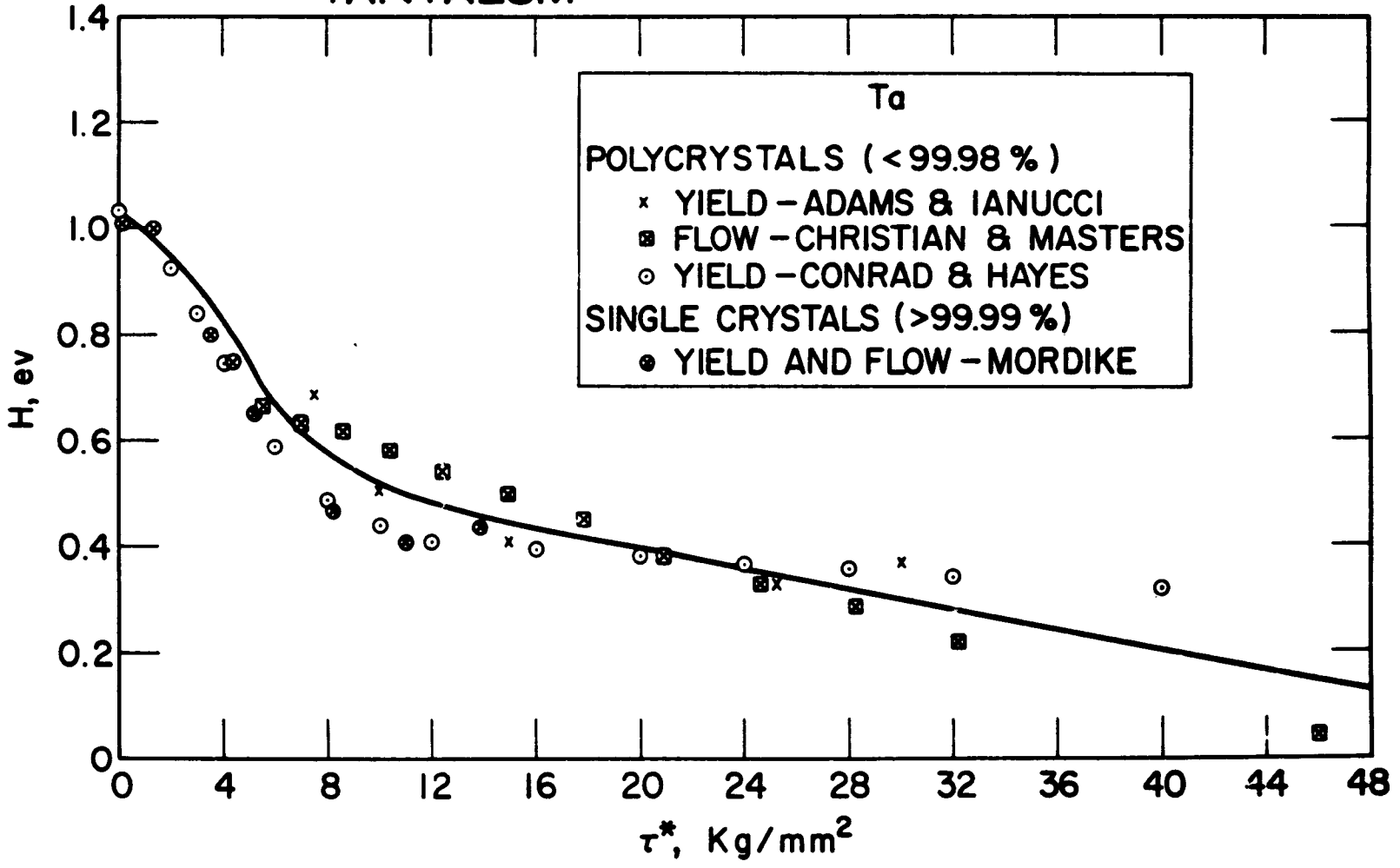

FIG. 15 EFFECT OF STRESS ON THE ACTIVATION ENERGY FOR THE DEFORMATION OF CHROMIUM

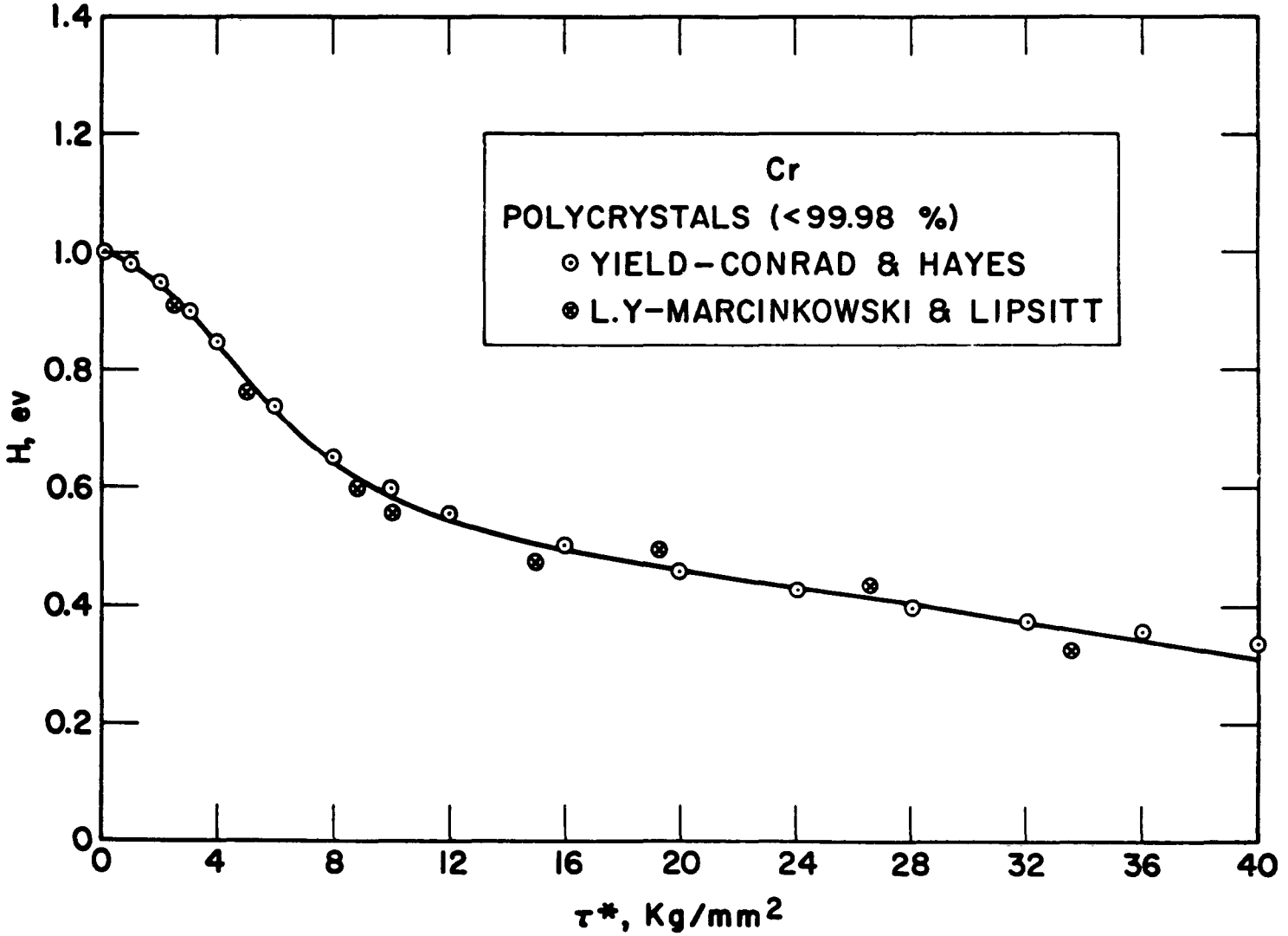

FIG. 16 EFFECT OF STRESS ON THE ACTIVATION ENERGY FOR THE DEFORMATION OF MOLYBDENUM

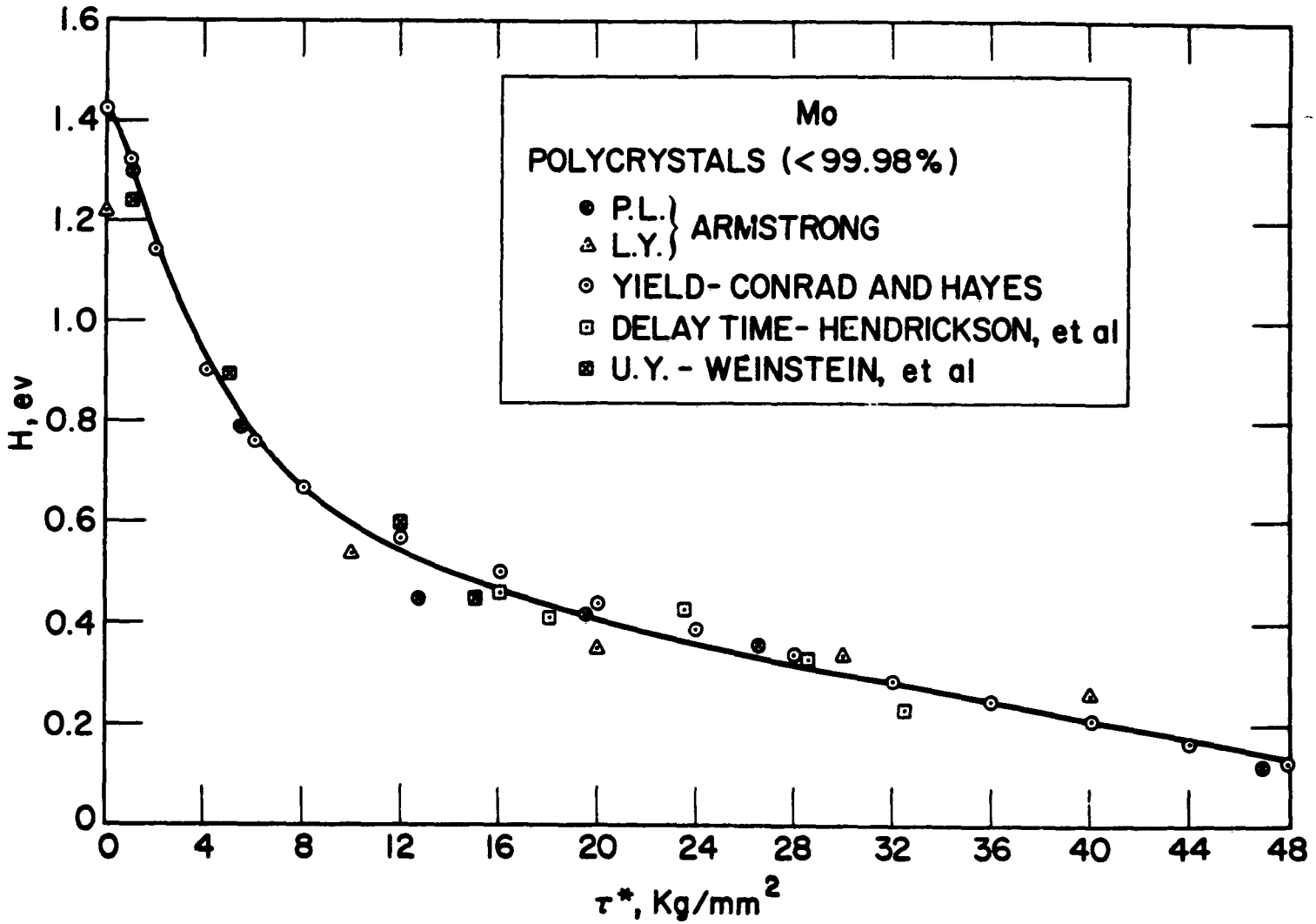

FIG. 17 - EFFECT OF STRESS ON THE ACTIVATION ENERGY FOR THE DEFORMATION OF TUNGSTEN

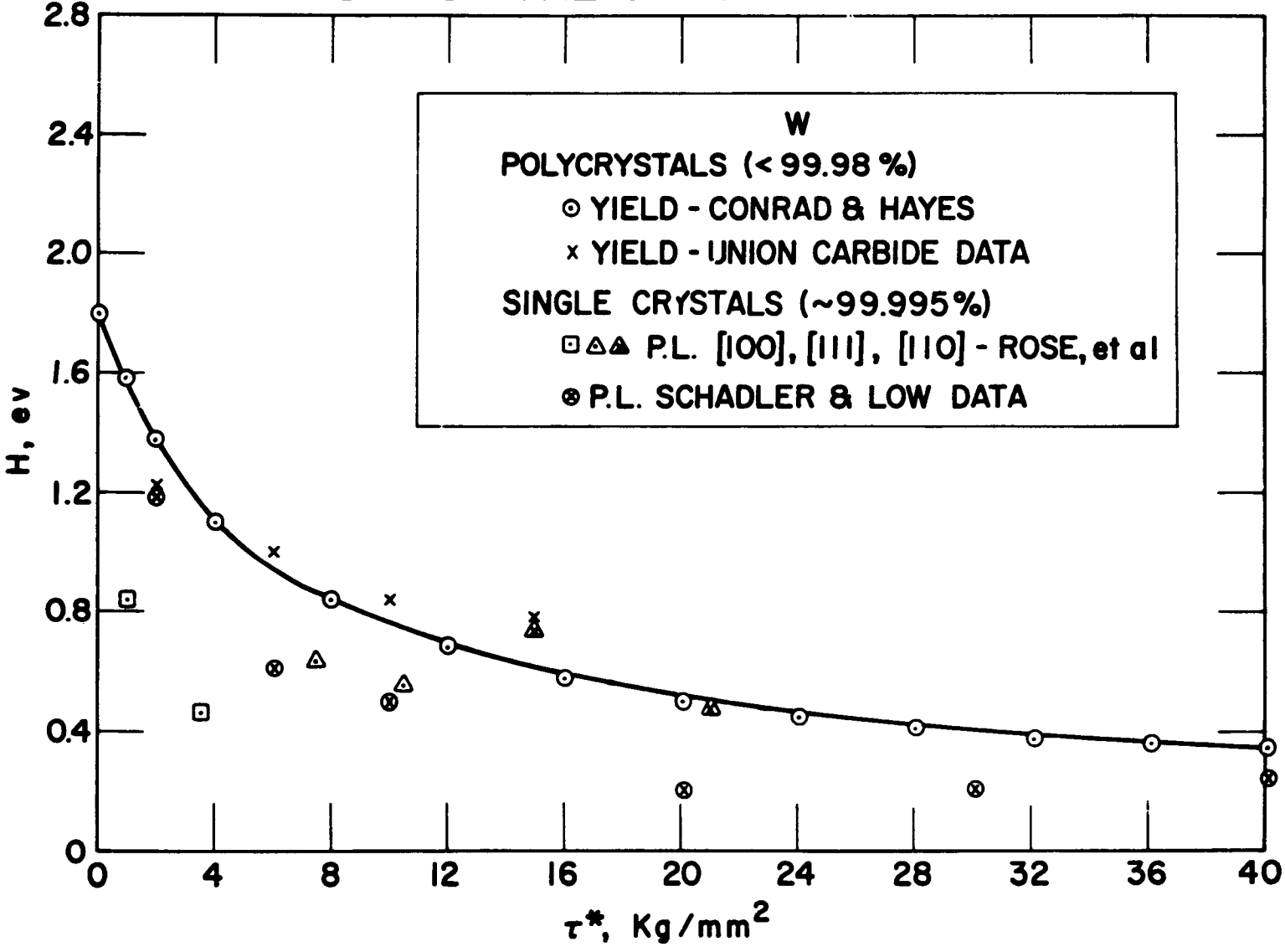

FIG. 18 EFFECT OF STRESS ON THE ACTIVATION ENERGY FOR YIELDING AND FLOW IN IRON AND STEEL

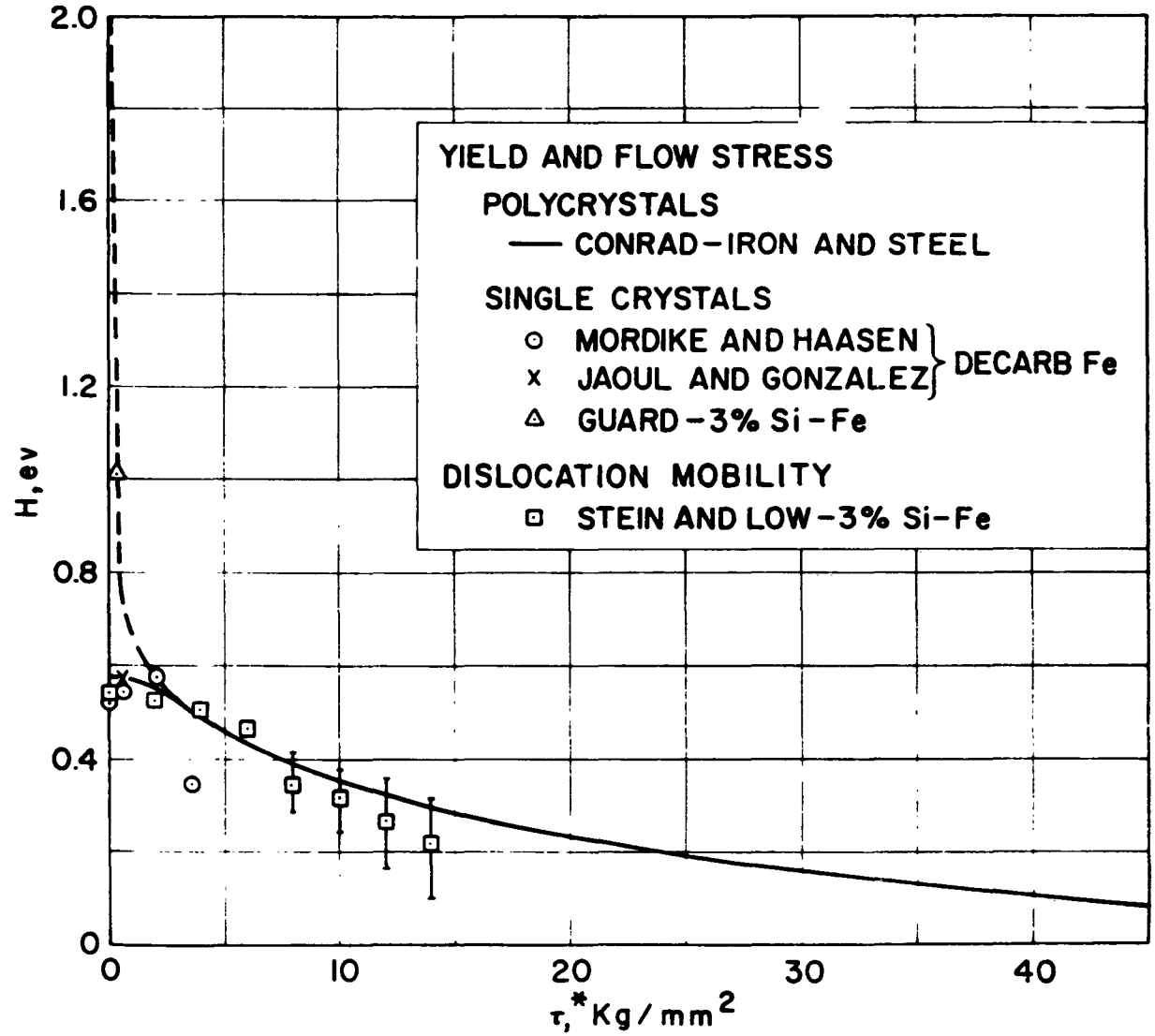

FIG. 19. RELATIONSHIP BETWEEN $H_o(\tau^* = 1 Kg/mm^2)$ AND μb^3 FOR THE B.C.C. METALS

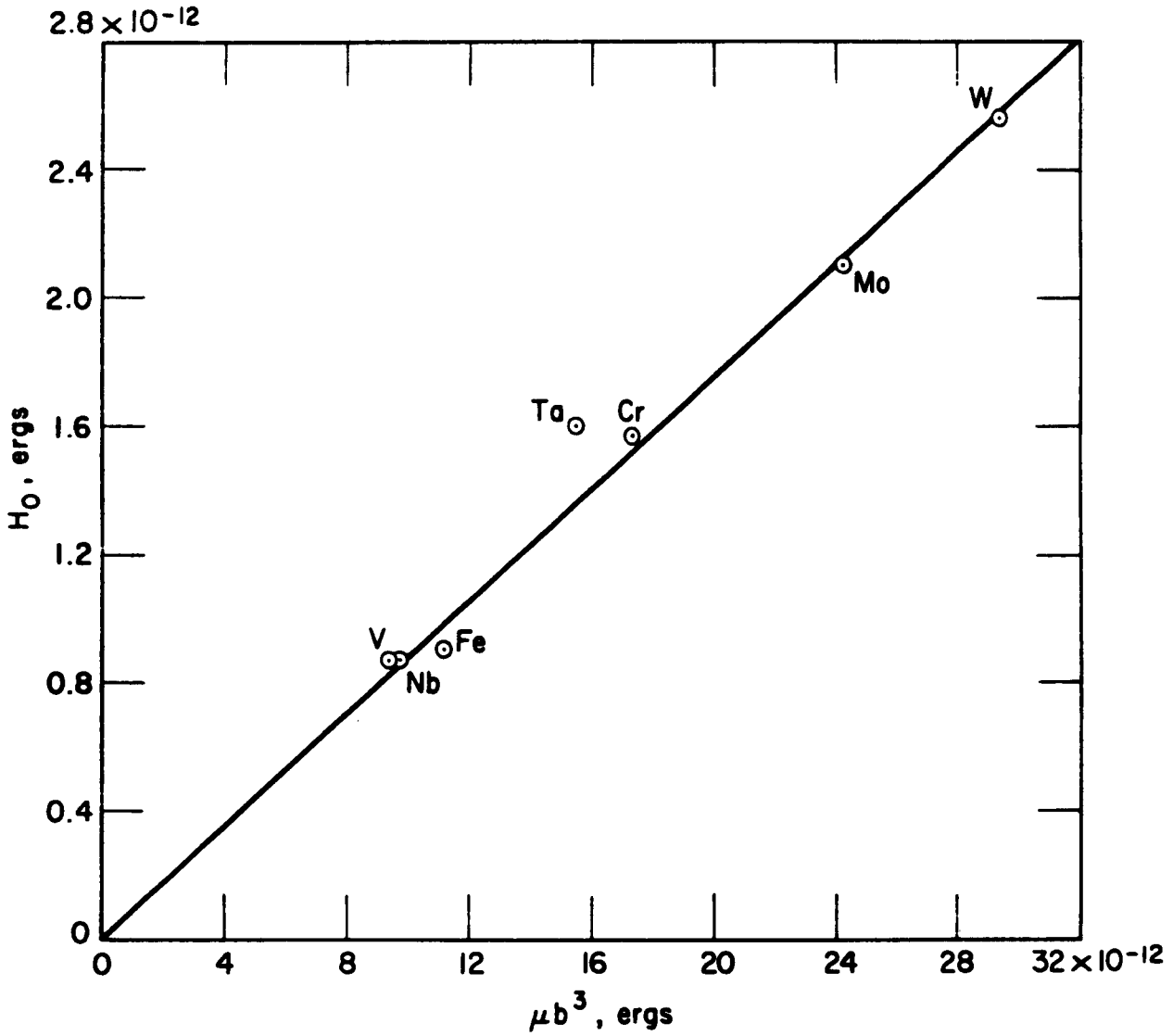

FIG. 20. ACTIVATION ENERGY VS LOG τ^* FOR THE B.C.C. METALS

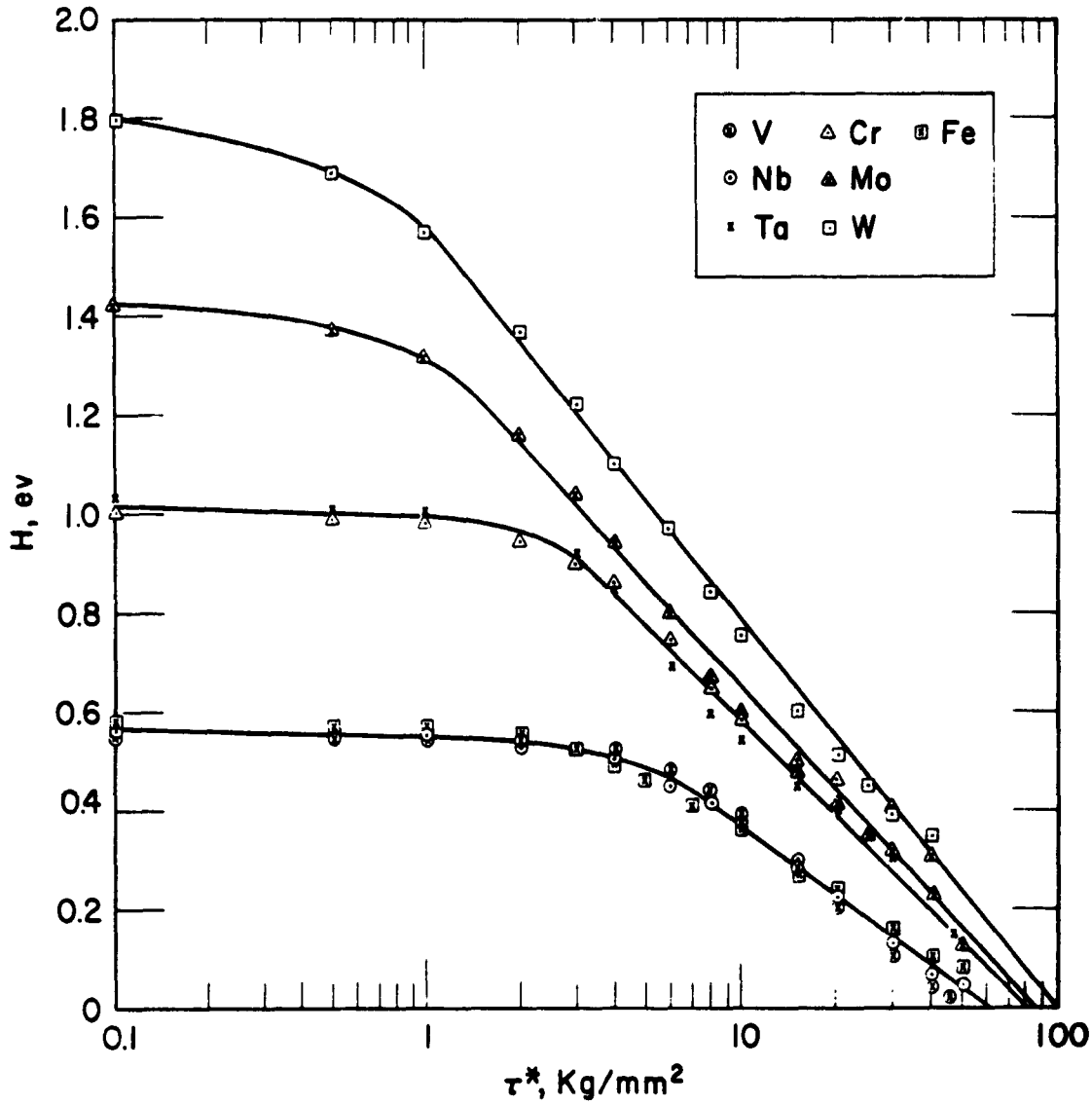

FIG. 21 EFFECT OF STRESS ON THE ACTIVATION VOLUME FOR THE DEFORMATION OF TANTALUM

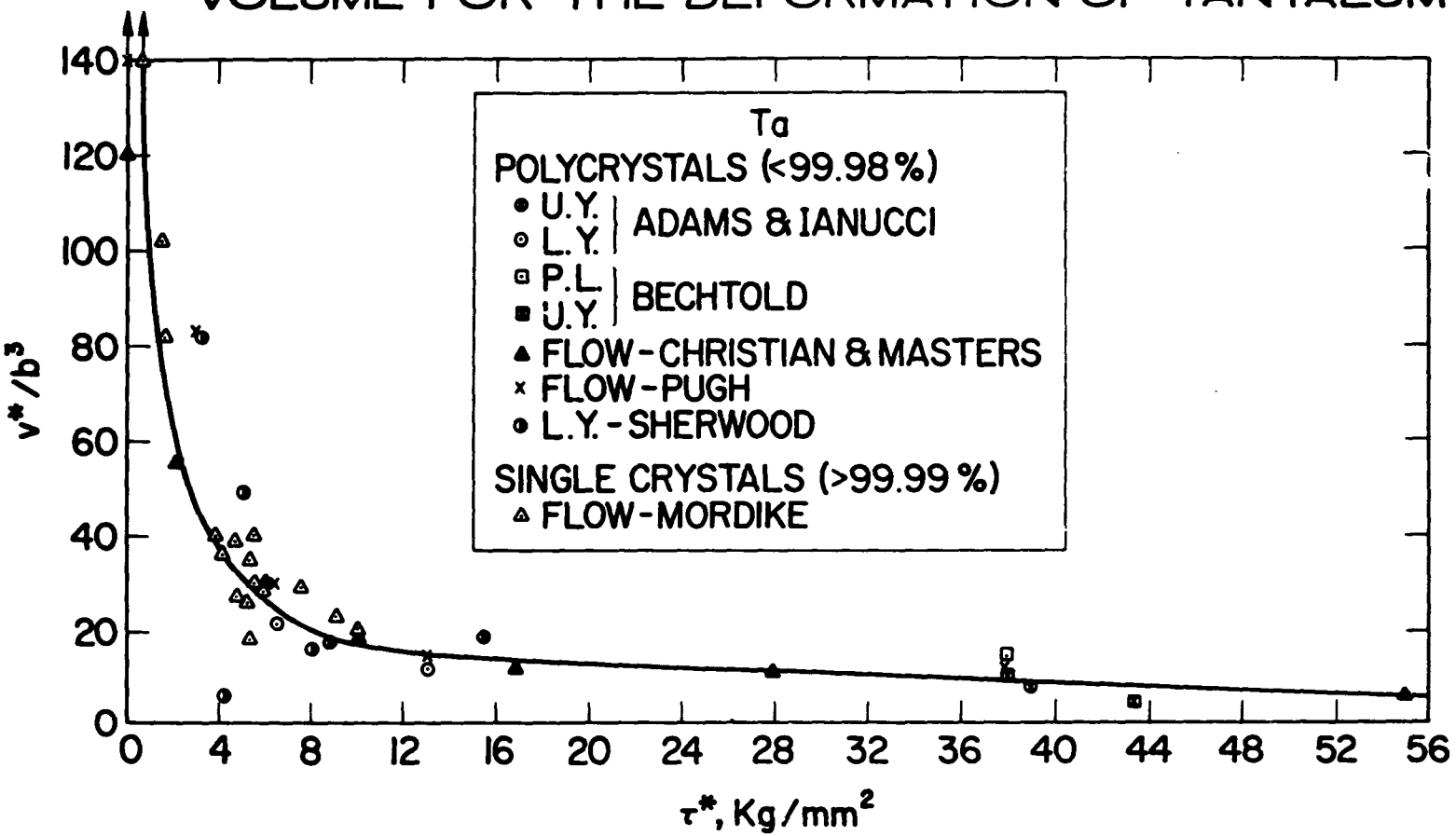

FIG. 22 EFFECT OF STRESS ON THE ACTIVATION VOLUME FOR THE DEFORMATION OF TUNGSTEN

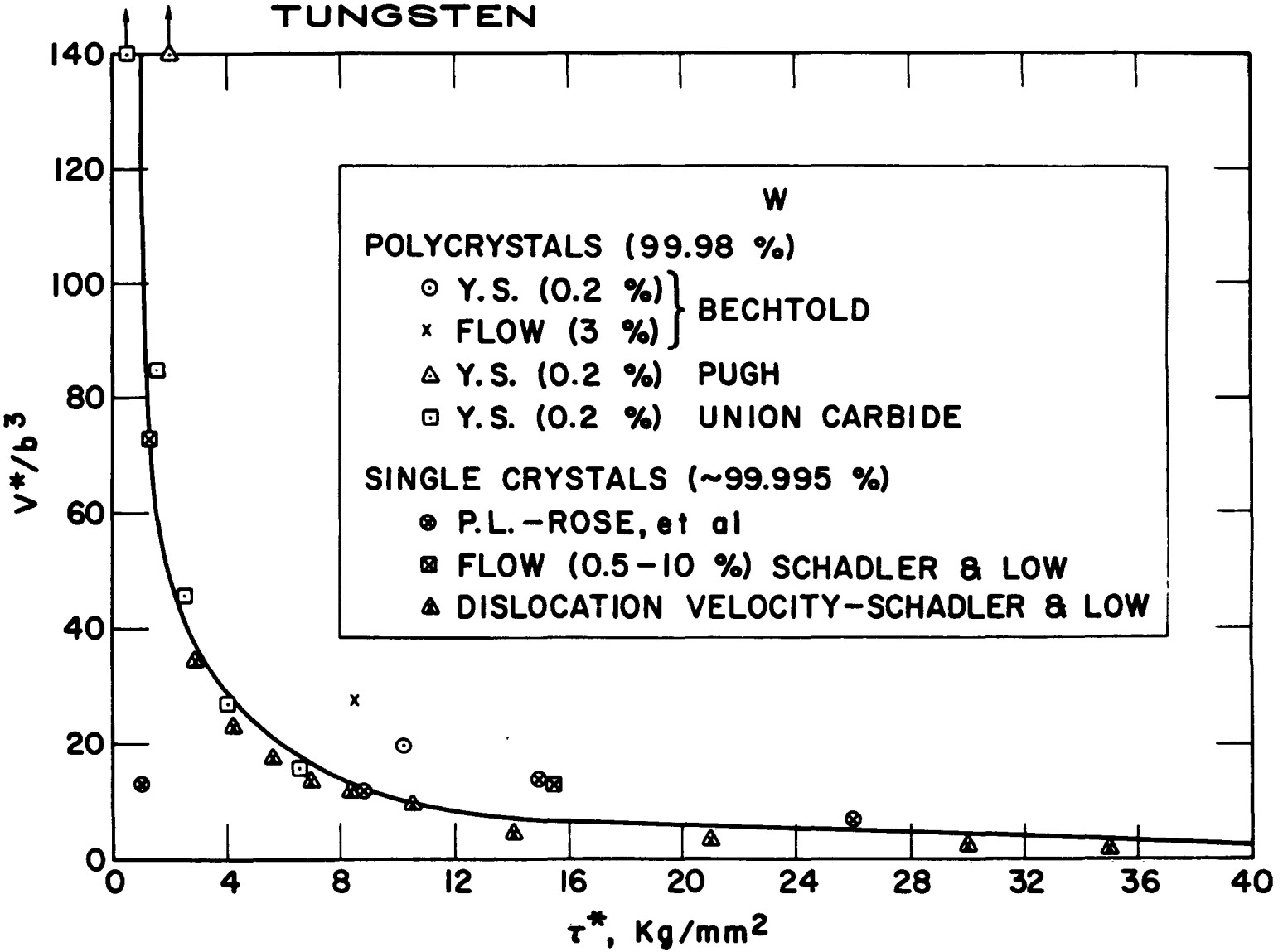

FIG. 23 EFFECT OF STRESS ON THE ACTIVATION VOLUME FOR YIELDING AND FLOW IN IRON AND STEEL

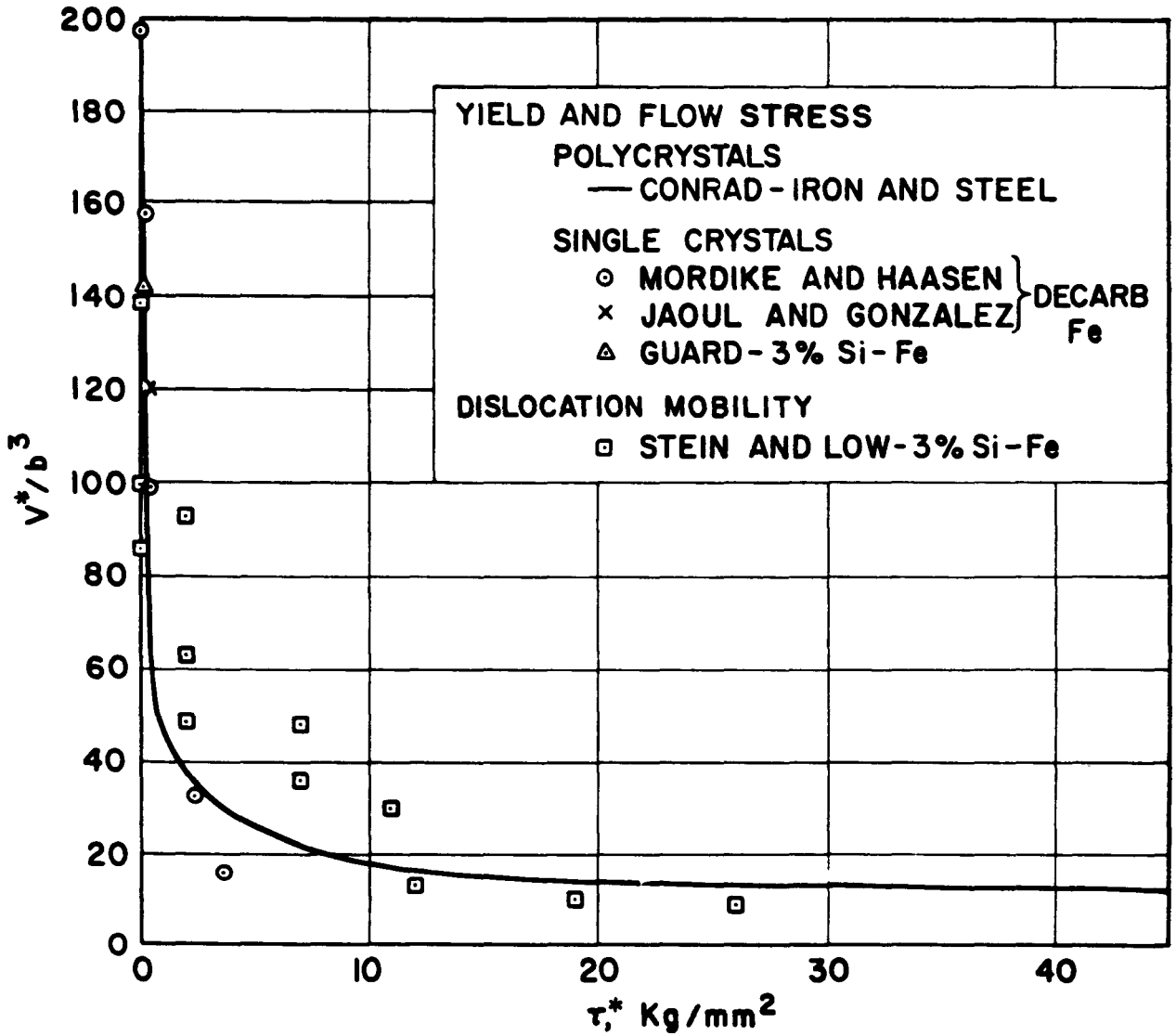

FIG. 24 EFFECT OF STRESS ON THE ACTIVATION VOLUME FOR DEFORMATION OF THE B.C.C. TRANSITION METALS

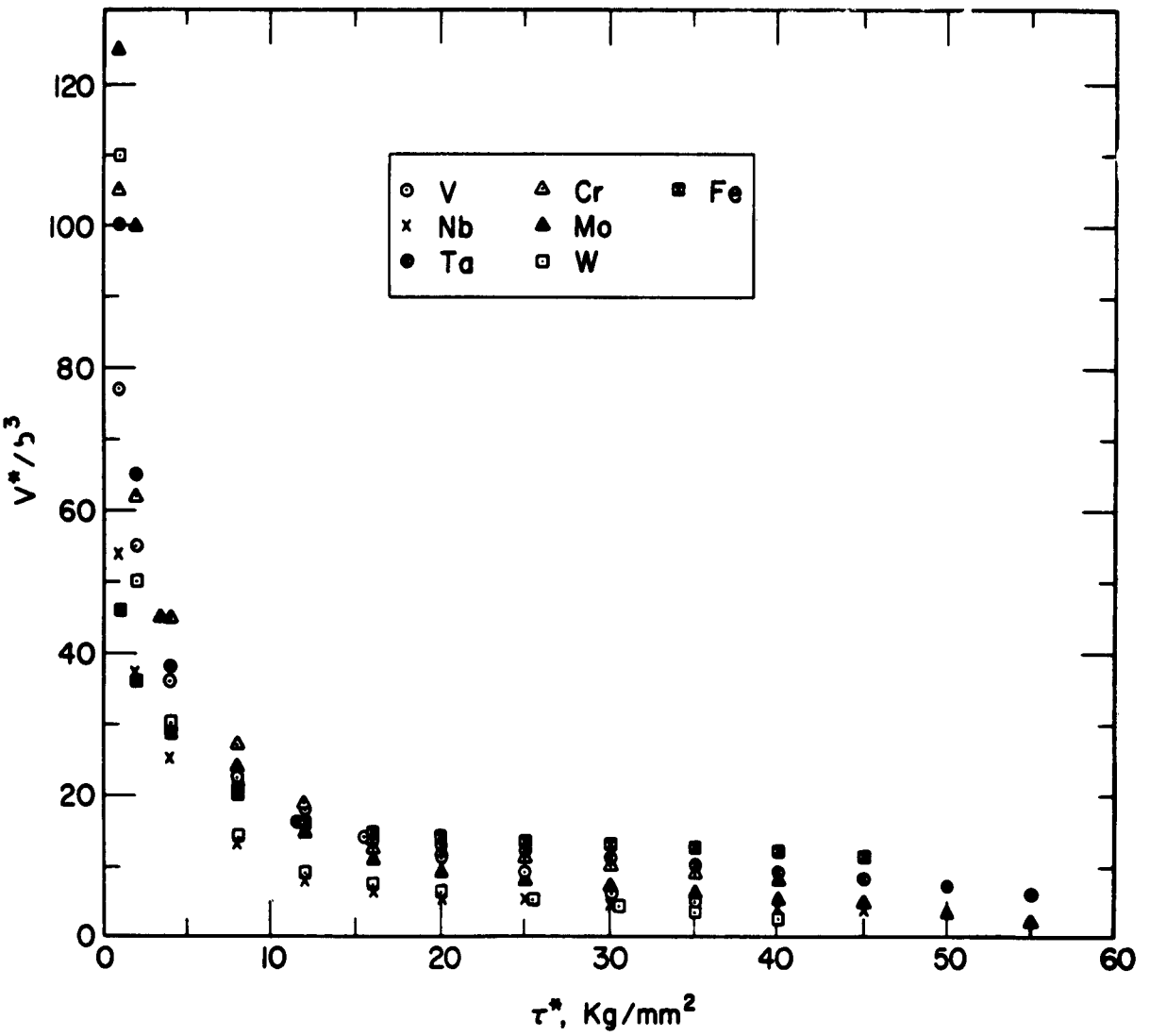

FIGURE 25

VARIATION OF ACTIVATION ENERGY WITH TEMPERATURE FOR INGOT IRON AND MILD STEEL

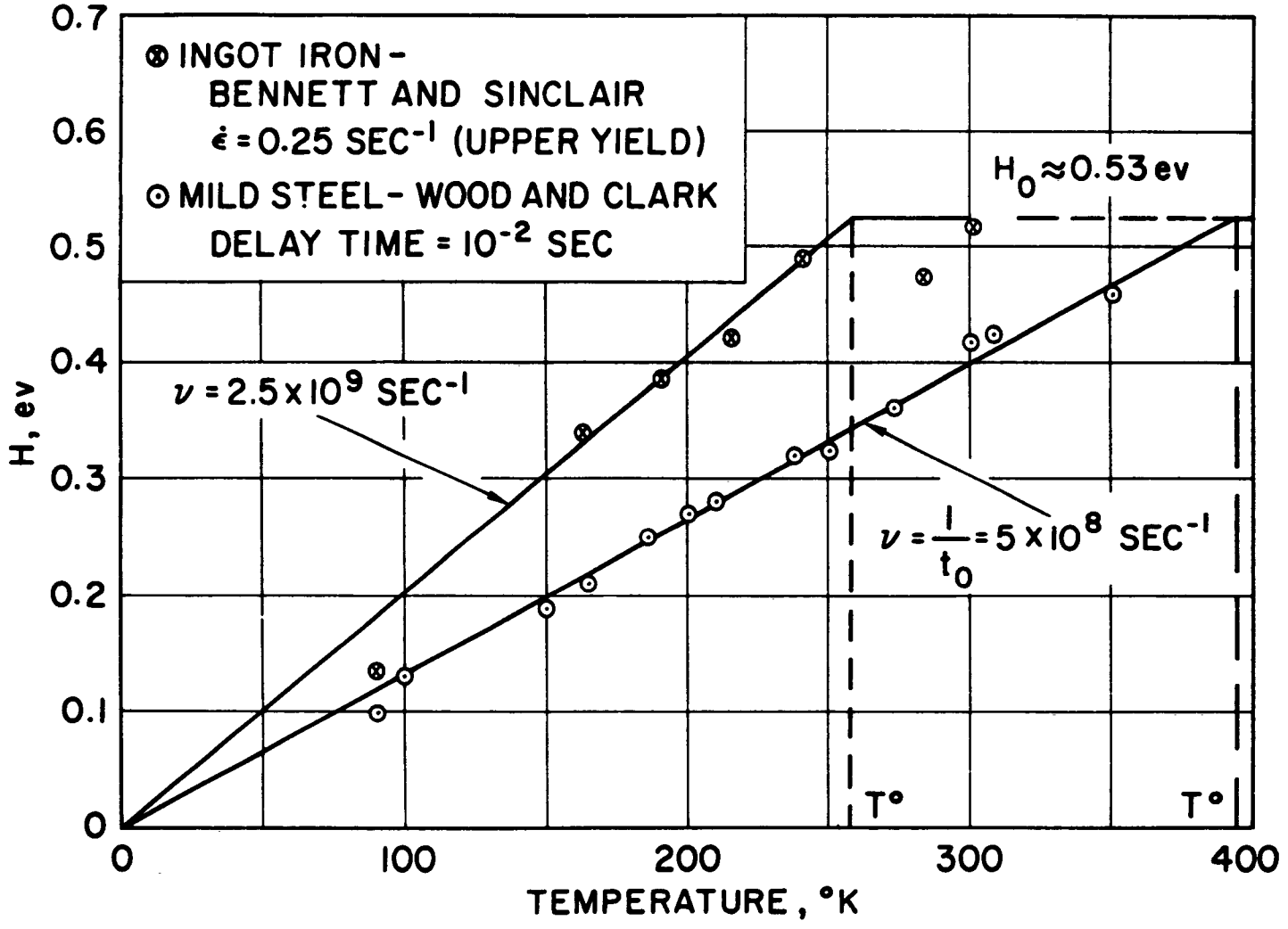

FIG. 26 VARIATION OF ACTIVATION ENERGY WITH TEMPERATURE FOR IMPURE, POLYCRYSTALLINE B.C.C. METALS

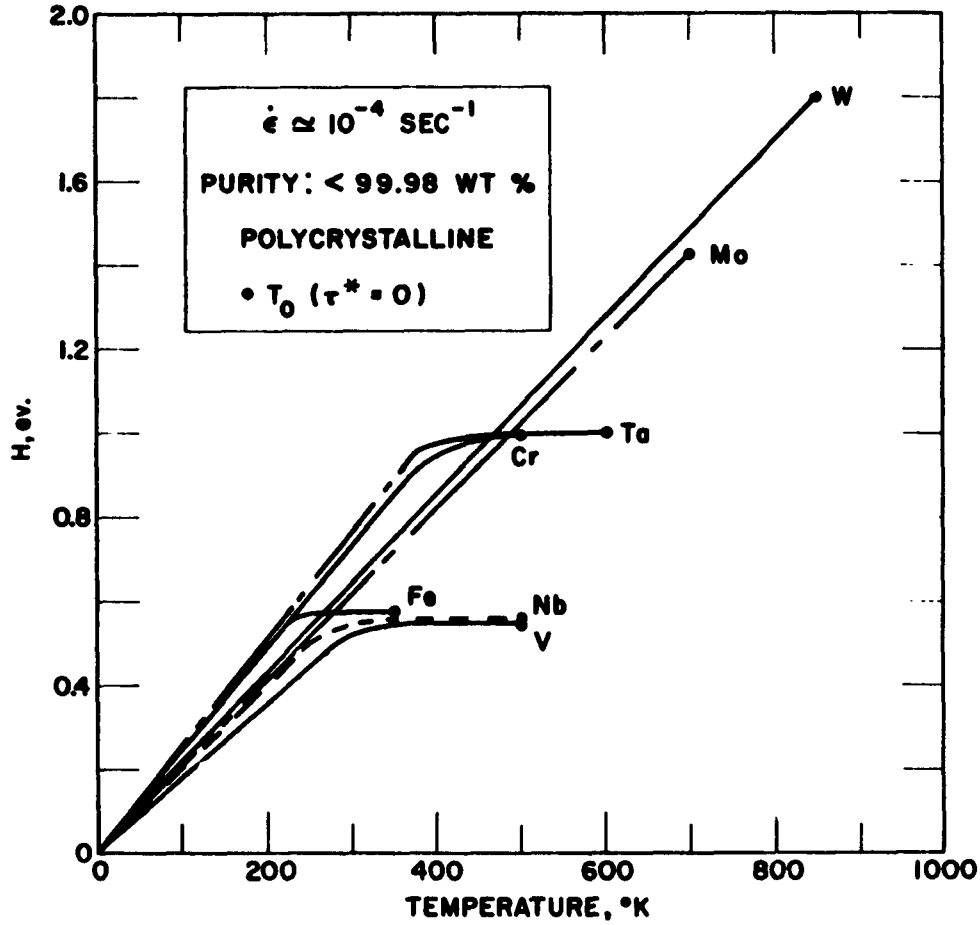

FIG. 27 VARIATION OF THE ACTIVATION ENERGY FOR BRITTLE FRACTURE WITH TEMPERATUE. (AFTER LEAN, PLATEAU AND CRUSSARD (38))

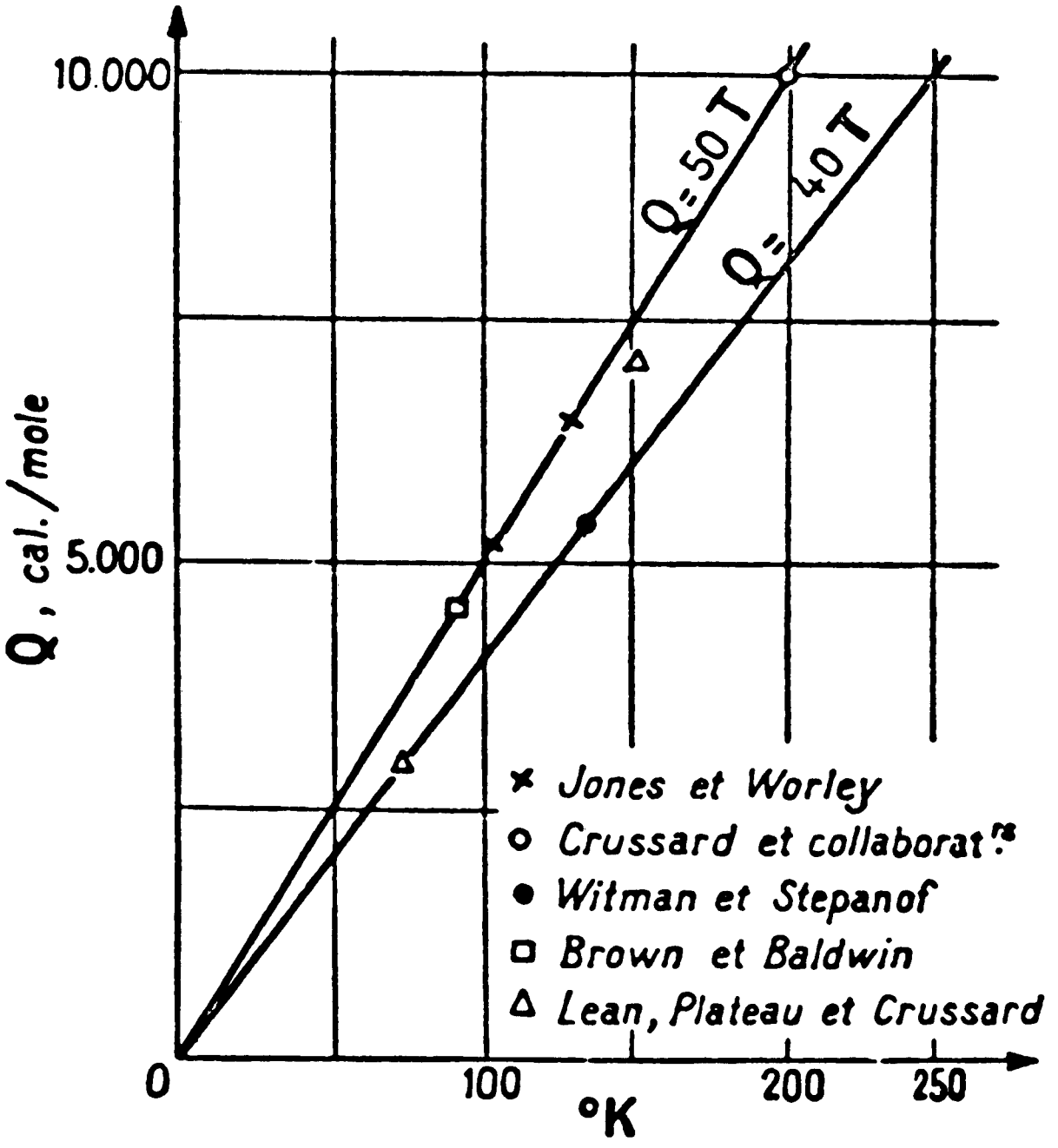

FIG. 28 SEEGER'S MODEL FOR THERMALLY-ACTIVATED OVERCOMING OF THE PEIERLS-NABARRO ENERGY. a. DISLOCATION LYING IN A CLOSE-PACKED DIRECTION. b. INTERMEDIATE STAGE IN THE FORMATION OF A PAIR OF KINKS OF OPPOSITE SIGN. c. FINAL STAGE IN THE FORMATION OF A PAIR OF KINKS. d. LATERAL MOTION OF THE KINKS UNDER THE APPLIED STRESS.

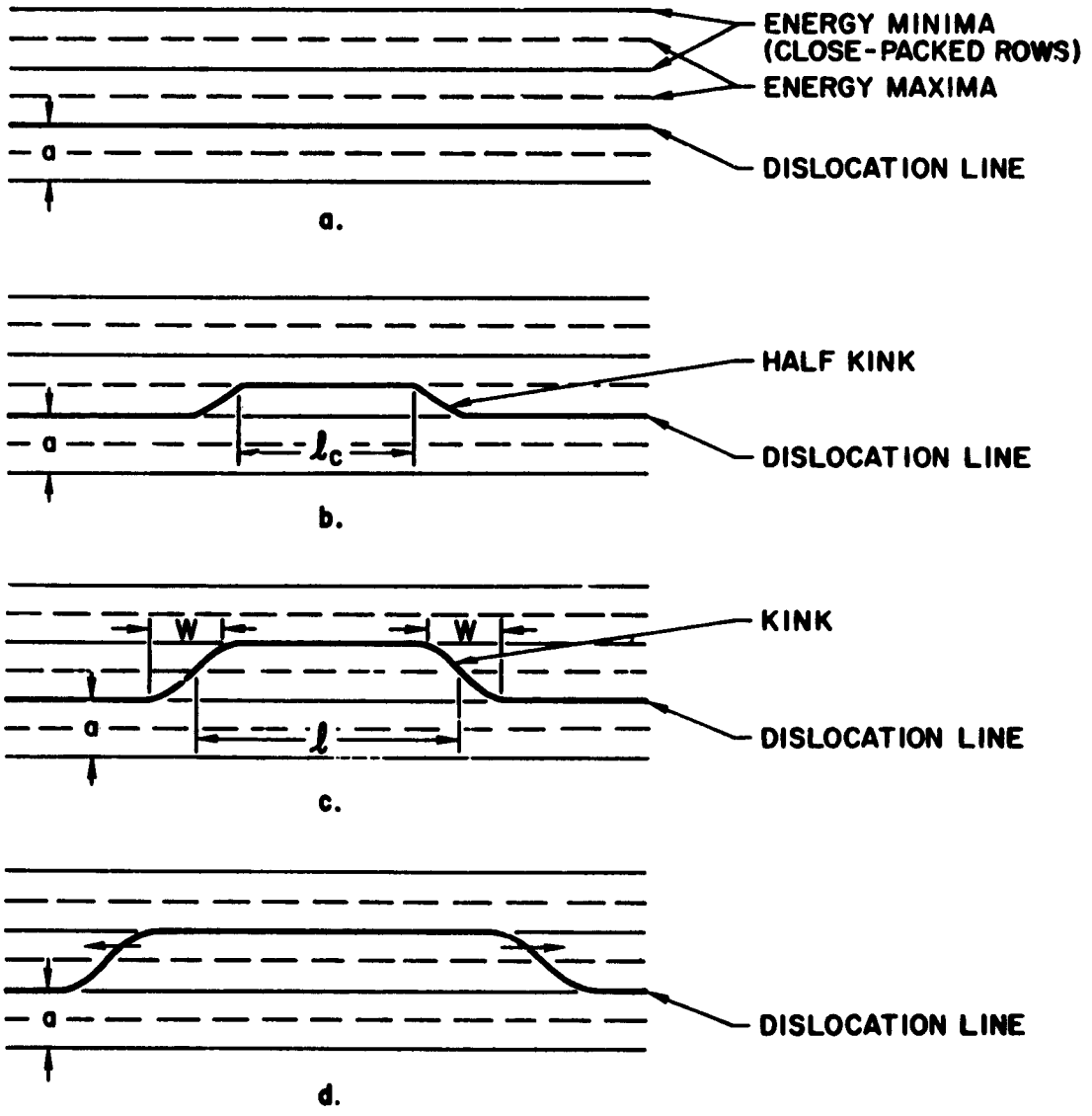

FIGURE 29

VARIATION OF ACTIVATION ENERGY WITH TEMPERATURE FOR ELECTROLYTIC IRON WATER QUENCHED FROM 920 C° (AFTER CONRAD AND FREDERICK (8))

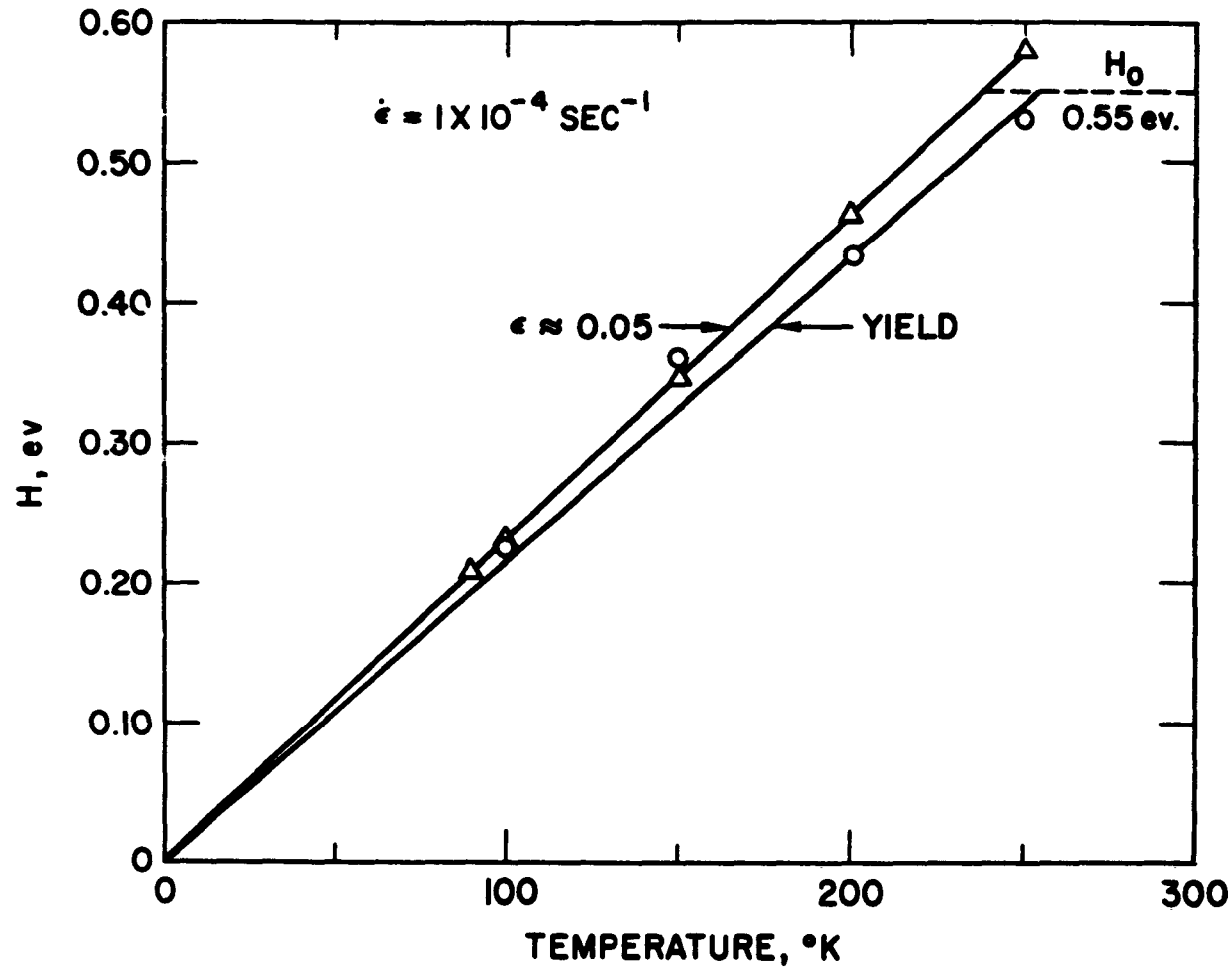

FIGURE 30

VARIATION OF ACTIVATION ENERGY WITH TEMPERATURE FOR FERROVAC IRON (FROM DATA OF BASINSKI AND CHRISTIAN (5)).

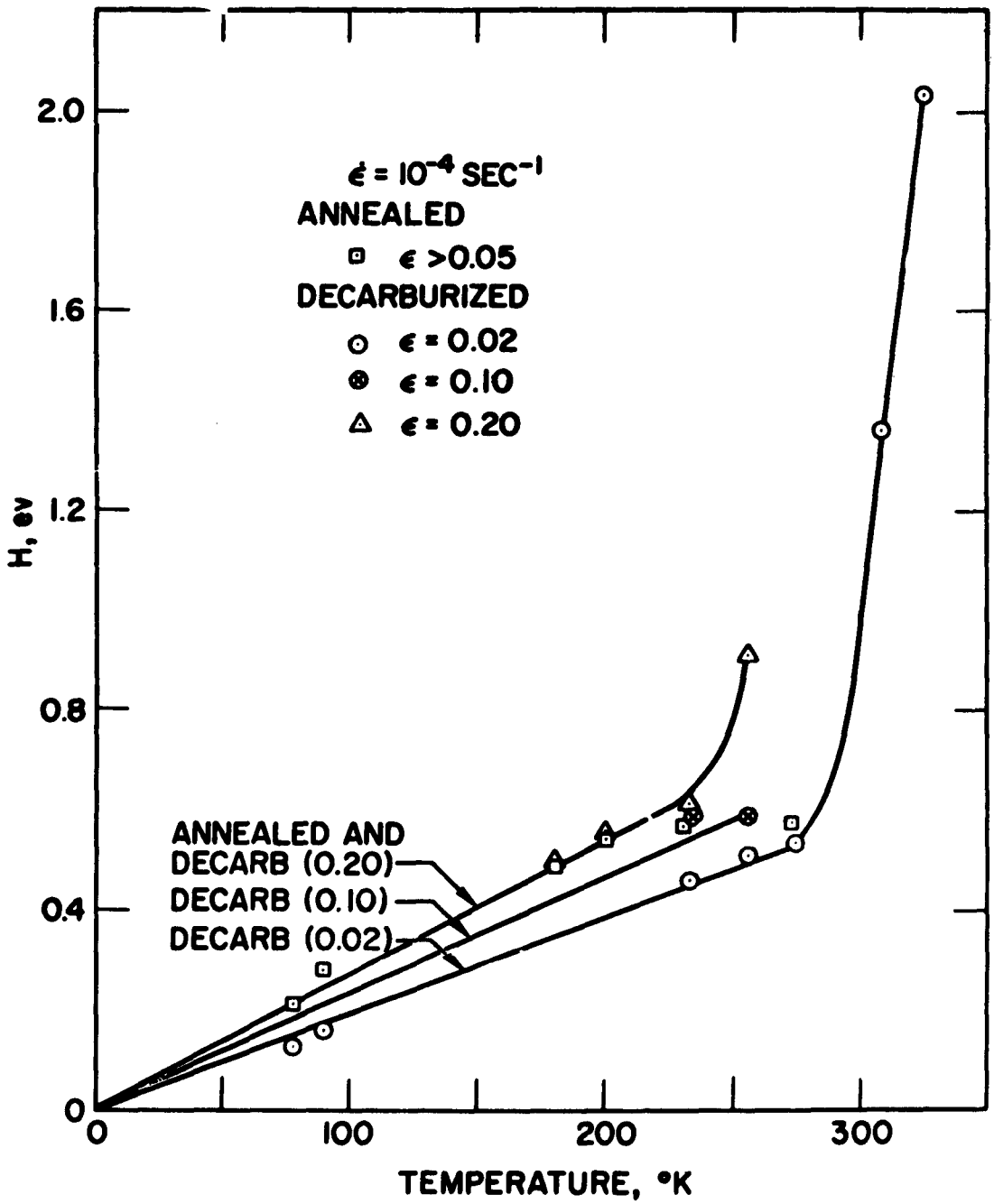

FIG. 31. COMPARISON OF CALCULATED AND EXPERIMENTAL STRESS–STRAIN CURVES FOR MILD STEEL

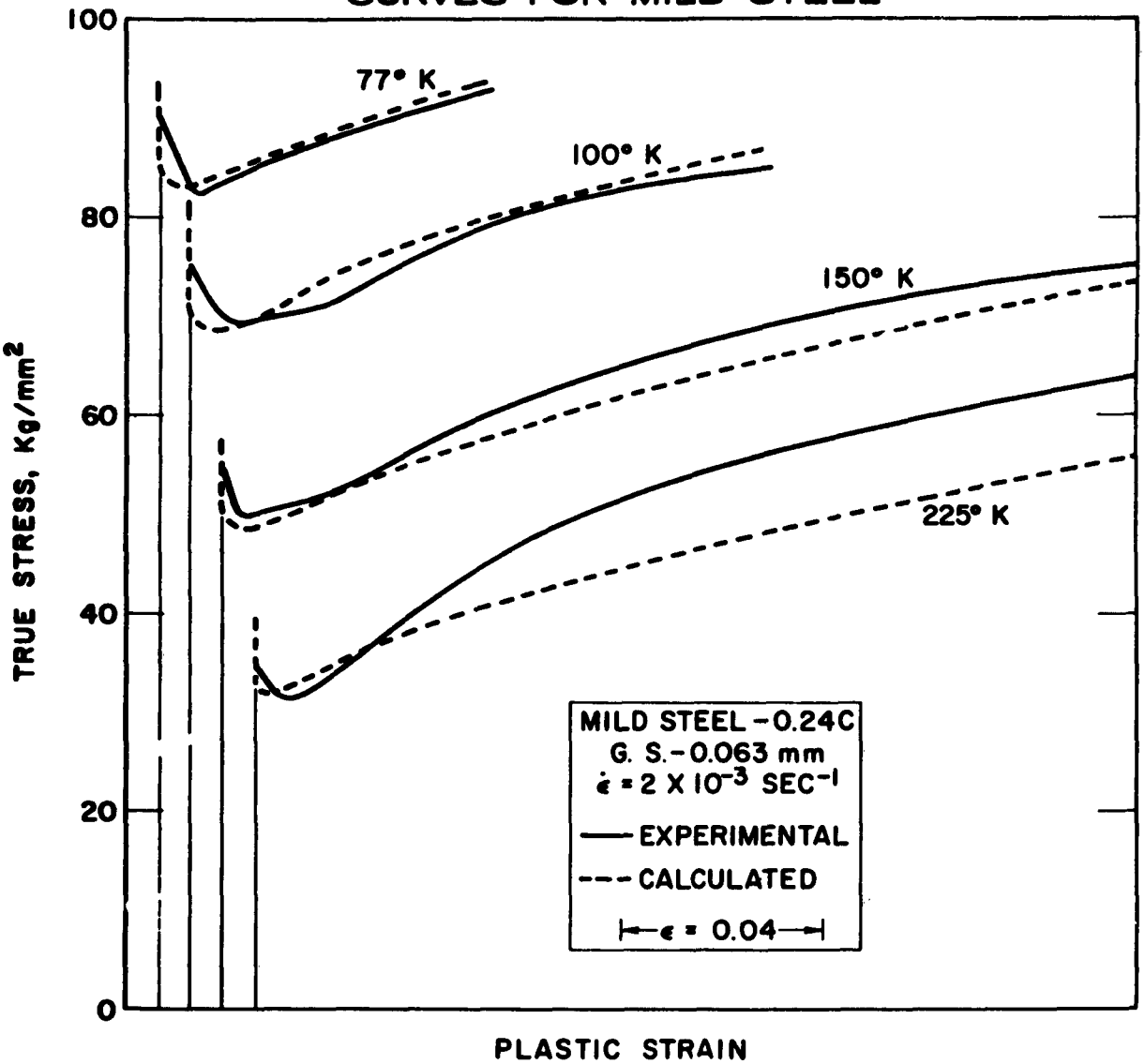

Strain-Ageing in B.C.C. Metals

by

A.R. Rosenfield and W.S. Owen
Department of Metallurgy University of Liverpool.

Most strain-ageing studies have concentrated on the kinetics of the segregation of interstitial solute during ageing, the rate of depletion of the matrix concentration being followed by the measurement of electrical resistance, internal friction or some other suitable physical property which depends only upon the presence of interstitial atoms in solution. The nature and rate of the changes in mechanical properties have been studied less extensively and in this paper attention is focussed on this aspect of the problem, but discussion of the relationships between strain-ageing and fracture properties is excluded.

Classification of Interstitial Solutes

The mechanical properties of interstitial elements in body-centred cubic lattices can be discussed systematically if a distinction is made between 'soluble' and 'insoluble' elements, the demarcation being arbitrarily chosen at 1 atomic percent solubility. The behaviour of insoluble systems, for example iron-carbon, can be described completely in terms of the hard-sphere model which assumes that the interstitial atom is not ionised. The interstitial diffusion and the interaction of the interstitial with dislocations can be explained on the basis of strain-energy considerations alone and the small solubility is a result of large local strains due to a

relatively unfavourable size-factor. When considering soluble systems, such as tantalum-oxygen, effects other than those due to strain interactions must be taken into account. Internal friction experiments reveal the existence of stress-induced interstitial atom migration[1] and on increasing the oxygen content of Group 5A metals there is a measurable increase in the lattice parameter of the solvent lattice[2,3,4]. Thus, it must be concluded that strain effects are significant. However, from the lattice parameter measurements, oxygen in tantalum, niobium and vanadium has an atomic diameter of about 2.08Å. Since the diameter of unionised oxygen atom is about 1.4Å and that of the O^{--} ion about 2.64Å, it is suggested that the oxygen in solution in the Group 5A metals is ionised with a single negative charge.

The difference between soluble and insoluble interstitials is revealed clearly by considering the activation energy for interstitial diffusion. The data in Figures 1-3 were obtained either by direct measurements of diffusion couples, measurements of stress-induced ordering (Snoek effect) by internal friction or they were deduced from measurements of blue-brittleness temperatures[5]. It is well known that the activation energy for self-diffusion increases linearly with the melting point Tm of the metal. The rate-determining step is a strain term and, because the elastic constants are related to the melting point, the activation energy increases with Tm. A similar behaviour is expected for any diffusion process in which the jumps are controlled by strain considerations and, in fact, for the interstitial diffusion of insoluble elements the activation energy does increase with the melting point of the solvent. However, for soluble interstitials the variation of activation energy with melting point is either very small or zero (Figures 1-3). This suggests that the diffusion is controlled by electronic effects and a model in these terms which provides a satisfactory qualitative explanation of this effect has been proposed by Stringer and Rosenfield[6].

Dislocation-Interstitial Binding Energies

According to Friedel[18], the binding energy W_M between a dislocation and an interstitial atom is

$$W_M = G(c) - Go(c) \qquad (1)$$

where Go (c) is the free-energy per interstitial atom dissolved in a perfect lattice and G (c) the corresponding free-energy when the lattice contains dislocations. In general, there are two ways of measuring W_M, either the solubility of the interstitial element may be measured as a function of the temperature and the dislocation density[19], or the yield drop may be measured as a function of temperature for a specimen of known interstitial content and dislocation density. The latter method depends upon the assumption that the equilibrium concentration of interstitial atoms at a dislocation line varies with temperature according to the relation[20]

$$C = C_o \exp(-W_M/kT) \qquad (2)$$

where C_o is the concentration when there is no segregation. Above some temperature T_b, C falls below the saturation value C_m at which the Fetch locking parameter k_y is just greater than zero. Thus,

$$W_M = \left[k\, T_b \ln (C_o/C_m)\right]_{k_y = 0} \qquad (3)$$

The value of C_m is somewhat uncertain as it depends on the precise model which is assumed for the unpinning of a dislocation line under the action of an applied shear stress. Estimates vary between 0.07 and 1.0. Fortunately, the value of W_M determined by this method is quite insensitive to variations in the value adopted for C_m.

Usually T_b has been determined by finding the temperature at which the discontinuous yield disappears in tensile tests carried out at successively higher temperatures. However, the conditions existing during tests at elevated temperatures do not satisfy the requirements of equation 3 and the

values of W_M deduced from them are erroneous. Yield points are observed at low temperatures because dislocations can move under the influence of an applied stress faster than interstitial atoms can diffuse. As the testing temperature is raised, the temperature dependence of the dislocation velocity is less than that of the diffusivity and at a particular temperature (and strain rate) the impurity atoms move with about the same velocity as the dislocations, producing the blue-brittleness (serrated yielding) phenomenon. This fact has been used to calculate the activation energy for interstitial diffusion[21]. The discontinuous yield point always disappears at a temperature just above the blue-brittleness temperature because at this temperature the interstitial atoms are sufficiently mobile for the moving dislocations to drag their associated interstitial atoms with them. Thus, in these circumstances the disappearance of a yield drop does not indicate the absence of segregated interstitial atoms. The temperature T_b for iron-carbon alloys is widely quoted as 700°K[22], but this was obtained from the high temperature tensile tests of Boulanger[15] and consequently the value of W_M deduced from it is incorrect.

To determine T_b it is necessary to carry out all the tensile tests at a temperature below the blue-brittleness temperature. Thus, a series of specimens must be quenched from successively higher annealing temperatures at a rate sufficient to freeze-in the interstitial distribution. The experimental difficulties are considerable since it is necessary to ensure that there is no contamination of the specimen during the annealing and the quench and that either the dislocation density is unaffected by the annealing or that the density corresponding to each annealing temperature is known. However, a number of determinations of W_M for different systems have been reported and these, together with the limited data available from measurements of solubility as a function of dislocation density are given in Table 1. When calculating W_M from T_b determined by the quenching method, the usual practice is followed of taking C_m as 1 atom per atom plane intersecting the dislocation.

The binding energy W_M has two components, W_{M1} due to strain and W_{M2} due

to electronic interaction between the dislocation and the interstitial atom. These energies are usually considered to be additive[18]

$$W_M = W_{M1} + W_{M2} \qquad (4)$$

The electronic contribution to the binding energy in the iron-carbon and iron-nitrogen systems is zero because the carbon atom is not ionised, but in systems with appreciable solubility the electronic effect is probably significant. The heterogeneous strain field around an edge dislocation produces an electric dipole[19] because electrons flow from the compressed region above the slip plane to the dilated region below. Thus, a net negative charge is created below the extra plane which attracts positively charged ions but repels ions which carry a negative charge. Thus, it is expected that W_M for tantalum-oxygen alloys will be less than W_{M1} by an amount W_{M2}.

In general, the elastic strain interaction energy is

$$W_{M1} = A/R \qquad (5)$$

where A is an interaction parameter which varies with the elastic constants, the lattice parameter of the solvent and the extent of the dilation of the lattice by the interstitial atom. R is the distance between the interstitial atom and the geometric centre of the dislocation. A can be estimated from the Cottrell-Bilby model[26] or from refinements of this model such as that due to Cochardt, Schoeck and Wiedersich[27].

The dilation caused by a carbon atom in an iron lattice can be estimated from the measured lattice parameter change of the martensite lattice with carbon content[26] and similar calculations can be made from the lattice parameter change with increasing interstitial content for those alloy systems, such as tantalum-oxygen, which do not form martensite but which have appreciable solubility. It is usual to assume that R is one Burgers vector. The calculated values of W_{M1} are compared with the experimental values of W_M in Table 1. In iron-carbon alloys W_M and W_{M1} are identical, confirming the prediction that the interaction in these alloys

is entirely due to elastic strain. However, in the tantalum-oxygen case W_M is slightly less than W_{M1} requiring W_{M2} to be negative, although the difference is probably only a little greater than the possible experimental error. The sign of W_{M2} is consistent with the concept of a negatively charged oxygen ion in the tantalum lattice and the magnitude of W_{M2} is about that expected from the electronic interaction. According to Friedel[18]

$$W_{M2} = \frac{\Delta E \, ze}{24} \qquad (6)$$

where z e is an effective value of charge and ΔE is the width of the conduction band. The value of z e in tantalum alloys depends upon a screening constant which is known only approximately, a reasonable value being 0.3. From the difference $W_M - W_{M1}$ (Table 1), W_{M2} seems to be about 0.1 eV and thus, from equation 6, ΔE is about 7 eV. This is not an unreasonable value for the width of the conduction band in transition metals. Thus, although estimates of this type are inevitably very crude, there appears to be grounds for suggesting that in tantalum-oxygen, and probably in similar alloys, there is a significant electronic contribution to the dislocation-solute interaction energy.

The Variation of the Yield Parameters with Ageing

Until recently it was generally assumed that the return of the yield point could be described completely in terms of Cottrell pinning theory; the interstitial atoms being attracted to the dislocations during ageing under the influence of the elastic strain field interactions and thermal diffusion. The difference ($\Delta\sigma$) between the lower yield stress (σ_y) of the aged specimen and the stress at which the specimen is unloaded before ageing (σp) increases with ageing time and $\Delta\sigma$ was assumed to be a direct measure of the degree of saturation of pinning sites near the dislocation. However, it is now clear that phenomenologically there are two parameters involved in the yield stress; k_y which is a measure of the local stress required to activate a new dislocation source and σ_i the friction stress opposing the propagation of a slip band[26,29]. Although it is probable that in lightly aged specimens dislocation sources are produced by the unpinning of dislocations[30] as visualised by Cottrell[20], it seems that existing dislocations are easily

completely immobilised so that the discontinuous yield occurs by the generation of dislocations from other discontinuities such as surfaces or grain boundaries. Thus, k_y is not necessarily related to unpinning. According to Petch[28]

$$\sigma_y = \sigma_i + k_y d^{-\frac{1}{2}} \qquad (7)$$

The relation between stress-strain curves for the unrestrained and the aged specimen is shown schematically in Figure 4,

$$\sigma_y = \sigma_p + \Delta\sigma_f + k_y d^{-\frac{1}{2}} \qquad (8)$$

and since, by definition $\Delta\sigma = \sigma_y - \sigma_p$

$$\Delta\sigma = \Delta\sigma_f + k_y d^{-\frac{1}{2}} \qquad (9)$$

Thus, the increase in yield stress on ageing has two components. This was first demonstrated experimentally by Wilson and Russell[31] who, by applying the Petch method, showed that in iron-carbon alloys strain-ageing is a two step process; first k_y increases to a maximum value while $\Delta\sigma_f$ remains zero and subsequently $\Delta\sigma_f$ increases. The Petch method for determining k_y and $\Delta\sigma_f$, which depends upon measuring the variation of yield stress with grain size, is valid only if the substructure and distribution of submicroscopic precipitates are unaffected by the treatments used to establish a range of grain size; a condition which is satisfied approximately for iron-base alloys which are annealed through the phase change[32], but which is not usually achieved experimentally with other body-centred cubic metals. Fortunately, σ_j (Figure 4) can be determined by a method which does not require the use of grain size as a controlled variable. The homogeneous strain-hardening curves AB and CD (Figure 4) can be represented exactly by equations of the form

$$\sigma = K\varepsilon^n \qquad (10)$$

where K is the strength constant, ε the strain and n the strain-hardening index. So that

$$\sigma_j = K\varepsilon_p^n$$

K an n are best found from a logarithmic stress versus logarithmic strain plot of CD.

Experimental studies of strain ageing which enable the changes in $\Delta\sigma_f$ and k_y to be distinguished have been reported only in the last few years, and the information available is limited. However, both soluble (tantalum-oxygen[33] vanadium with carbon and nitrogen[34]) and insoluble (iron-carbon[31] and iron-silicon-carbon[35]) systems have been examined and thus it is possible to make some comparisons. On ageing at 261°K mild steel specimens which had been quenched from 700°C and prestrained 4 percent Wilson and Russell[36] found a rapid initial increase in yield stress which they attributed to stress-induced local ordering of the interstitial atoms in the stress field of the dislocation (Snoek effect). This effect is not found in tantalum-oxygen alloys at similar temperatures and strain-rates because the jump time is too long. For carbon in iron the jump time at 293°K is about 0.6 seconds but for oxygen in tantalum it is about 468 minutes.

After an incubation period, k_y increases with ageing time. On ageing iron-carbon alloys at 60°C a maximum value is reached when the concentration of carbon at the dislocations is 1 or 2 atoms per atom plane intersecting the dislocation line, but the k_y value for tantalum-oxygen aged at the same temperature levels off when less than a tenth of the available dislocation sites are occupied by oxygen atoms. The small k_y which is developed varies very little with testing temperature. Similar results have been found for vanadium-carbon-nitrogen alloys[34]. This contrasts with the iron-carbon alloys in which the k_y is markedly temperature dependent in lightly aged specimens but insensitive to testing temperature when fully aged. It may be that these differences are a result solely of the differences in diffusivities of the interstitial elements and that parallel results to those found in iron-carbon can be found in the tantalum and vanadium alloys when ageing is carried out at higher temperatures. This aspect of the subject has not yet been explored experimentally. A striking feature of strain-ageing is that the value of k_y developed in a fully aged specimen is appreciably smaller than k_y

for the alloy in the annealed condition. This effect has been attributed to the higher dislocation density in prestrained specimens, but in all the alloys so far examined the concentration of solute is much in excess of that required to saturate the dislocations when segregation is complete and so this explanation is not tenable. Possibly, the effect is controlled by the kinetics of the strain-ageing process. In tantalum the diffusivity of oxygen is very slow and k_y for specimens fully aged at 100°C is only about one tenth of the annealed value[33]. The diffusivity of carbon in iron is appreciably faster and about one third of the annealed k_y is developed on ageing for long times at 60°C[31]. On ageing iron-silicon-carbon alloys at 150°C about two-thirds of the annealed k_y value is obtained in fully-aged specimens[35]. Again, this points to the need for extensive systematic study of ageing effects at higher ageing temperatures.

The experimental data show clearly that $\Delta\sigma_f$ and k_y are independent parameters. In alloy systems in which the solubility of the interstitial element is very small there is obviously a tendency for precipitation to occur. In the iron-carbon alloys studied by Wilson and Russell the initial increase in k_y was not accompanied by an increase in $\Delta\sigma_f$, indicating that the Cottrell atmospheres or precipitates formed as a result of the carbon segregation to dislocations in the early stages of strain-ageing do not offer an effective resistance to the motion of unpinned dislocations. However, $\Delta\sigma_f$ does increase after longer ageing time but before any precipitate can be detected by electron-transmission microscopy. This increase has been attributed to carbon clusters or submicroscopic precipitates formed after all the dislocation sites are occupied. The relative changes in k_y and $\Delta\sigma_f$ with time on ageing at 60°C are shown in Figure 5. A similar sequence of changes was found by Smallman and Lindley[34] in impure vanadium. Although carbon and nitrogen have an appreciable solubility in vanadium the alloy clearly contained some insoluble element since precipitates nucleated on dislocation lines were clearly visible by electron-transmission micrography on ageing at 750°C. In alloys containing only soluble interstitial elements no increase in $\Delta\sigma_f$ due to precipitation or preprecipitation effects is likely to occur. Nevertheless, it is observed that $\Delta\sigma_f$ increases with ageing time. In

tantalum-oxygen alloys $\Delta\sigma_f$ starts to increase at the same time as, or even before, any change in k_y can be detected (Figure 6). Effects which have been suggested to account for the increase in $\Delta\sigma_f$ are the pinning of forest dislocations, thus increasing their resistance to the passage of glide dislocations, and the jogging of glide dislocations by the segregation of vacancies to dislocation lines. The observation that, in tantalum-oxygen prestrained at 293°K, aged at 373°K and tested at 252°K, $\Delta\sigma_f$ increases long before there is any change in k_y seems to eliminate the first suggestion. The vacancy segregation hypothesis has not been tested adequately. Preliminary experiments on tantalum-oxygen alloys indicate that the increase in $\Delta\sigma_f$ with ageing time is much less marked in quench-aged specimens than in prestrained specimens aged at the same temperature and, because the vacancy concentration in the latter specimens is expected to be higher, this suggests that the role of vacancies is important. However, it is not feasible to carry out parallel experiments on quenched and prestrained specimens with the same dislocation density, nor is the change in strain-hardening index compatible with a simple vacancy segregation model, so that for the present this hypothesis must also be considered to be tentative.

The Rate Controlling Step

It is usual to calculate a heat of activation ΔH from experimental data relating the change of some physical property with ageing time to the ageing temperature, assuming an Arrhenius relationship. The values of ΔH measured by changes in the yield stress ($\Delta\sigma$), electrical resistance and internal friction peaks are in surprisingly good agreement. Data which would enable ΔH to be calculated independently for changes in k_y and $\Delta\sigma_f$ are not available. However, from measurements taken during the period when only k_y is changing, it is clear that the rate of diffusion of the most rapidly diffusing interstitial element controls the segregation to dislocations during the early stages of strain agein . Thus, the fact that reasonably good agreement between ΔH for the change in $\Delta\sigma$ and ΔH from measurements which depend upon the rate of depletion of the matrix interstitial solid-solution is maintained at later stages of ageing when the change in $\Delta\sigma_f$ is significant

suggests that the controlling activation energy for $\Delta\sigma_f$ is either that for the fastest moving interstitial or for some other process with nearly the same activation energy.

Johnson[37] has claimed that the rate of change of electrical resistivity on ageing niobium can be explained by vacancy migration because the measured activation energy is 0.25-0.30 times the activation energy for self-diffusion. When all the available values of ΔH for strain ageing processes are plotted as a function of the melting point (Tm) of the solvent metal the best fit is given by $\Delta H \cong 0.3$ Tm (Figure 7). Brooks[38] has estimated theoretically that $\Delta H \cong 0.2$ Tm. Thus, either the theoretical estimate of the proportionality constant is incorrect or the rate controlling step is not vacancy migration. Some support for the concept of control by vacancy migration is available from the limited data on the rate of recovery of irradiated materials. ΔH derived from measurements of the isothermal recovery of electrical resistance after irradiation in an atomic pile are listed in Table 2. Considerable ageing occurs in the pile and freshly irradiated specimens have well-developed yield points but, although there is no subsequent change in k_y, on isothermal annealing the flow stress increases, corresponding to a change in $\Delta\sigma_f$. This lattice hardening is usually considered to be the result of vacancy migration. For the metals for which data are available (Nb, Mo, W), the values of ΔH for the recovery of electrical resistance after irradiation agree closely with those for the change in $\Delta\sigma$ on strain ageing.

The other possibility is that all stages of strain-ageing are controlled by the diffusion of the fastest-moving interstitial element. As shown by the data collected in Table 2, in general there is good agreement between ΔH derived from measurements of the rate of change of $\Delta\sigma$ and ΔH for diffusion of the appropriate interstitial.

Thus, it must be concluded that the available data are insufficient to enable an unambiguous distinction to be made between interstitial element diffusion and vacancy migration. It is possible that the rate controlling step varies with the alloy system and with the different stages of strain ageing. However, before these questions can be answered it is clear that much more precise data on the activation energies for interstitial diffusion,

vacancy migration and the change in mechanical properties during strain ageing are required. It is particularly important that in future work experiments are designed which separate effects producing changes in k_y from those affecting $\Delta\sigma_f$.

Acknowledgements

This work is supported by the United States Air Force under contract number AF33(616)-6838 Materials Laboratory A.F.L.D.C. Wright-Patterson Air Force Base, Ohio; Hanlabs Inc. Subcontract number 105. We had useful discussions with Dr. O. Stringer, Dr. D. Hull and other colleagues at the University of Liverpool.

Table 1

Measured and Calculated Binding Energies

System	Reference	W_M Measured eV	W_{M1} Calculated eV	W_{M2} Calculated eV	A_4 Calculated $\frac{dynes}{cm^2}$
Fe-C, Fe-N	23	0.80	0.76	0	3.0×10^{-20}
	24	0.73			
	19	0.71			
Ta-O	25	0.54	0.64	-0.10	2.9×10^{-20}

Table 2

Measured Activation Energies for Strain-Ageing Processes, Interstitial Diffusion and Recovery of Radiation Damage in B.C.C. Metals

Material	Method	Reference	Ageing Temperature °C	ΔH for strain ageing eV/atom	ΔH for Interstitial Diffusion Element	ΔH for Interstitial Diffusion eV/atom	ΔH for Recovery after Irradiation eV/atom
α-Fe	Change in Δσ. Internal Friction	23	25-60	0.78 0.89			
					N	0.81	
					C	0.89	
V	Change in Δσ	2	125-200	1.20			
	Change in Δσ	34	100	1.09			
					C	1.19	
Cr	Internal Friction	39	30-330	~1-1.5			
					C or N	1.26	
Nb	Change in Δσ	40	100-162	1.17			
	Electrical Resistance	41	100-180	1.22			
					O	1.17	
	Electrical Resistance	41	100-180				1.22
Mo	Electrical Resistance	42	100-180	1.25			
	Internal Friction	43	300-400	1.3-1.5			
	Change in Δσ	44	575-700	1.58			
	Electrical Resistance	45	~150	1.3			
					C	1.45	
	Electrical Resistance	41	140-200				1.25

Table 2 (continued)

Mo	Electrical Resistance	45	150				1.30
Ta	Electrical Resistance	45	120-180	1.25	0	1.11	
W	Electrical Resistance						
	'Pure'	46	325-650	1.7			
	'Doped'	46	325-650	2.3			
	Electrical Resistance	47	~350	1.7	C	1.72	
	Electrical Resistance	48	320-450				1.7

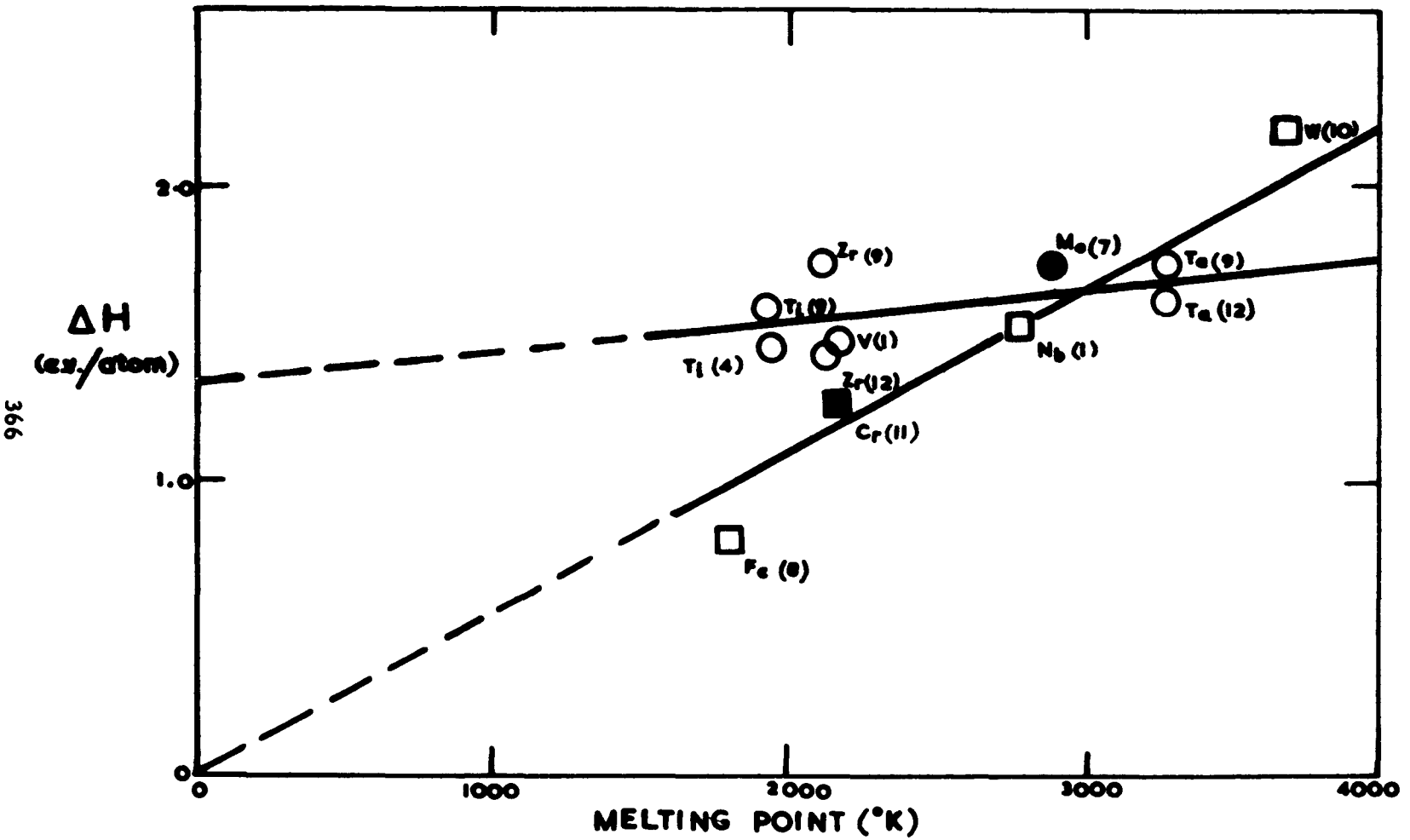

Figure 1 The variation of activation energy for the diffusion of nitrogen with the melting point of the solvent. Circles, high solubility; squares low solubility. Full points evaluated from Portevin-le Chatelier effect. Stringer and Rosenfield (6).

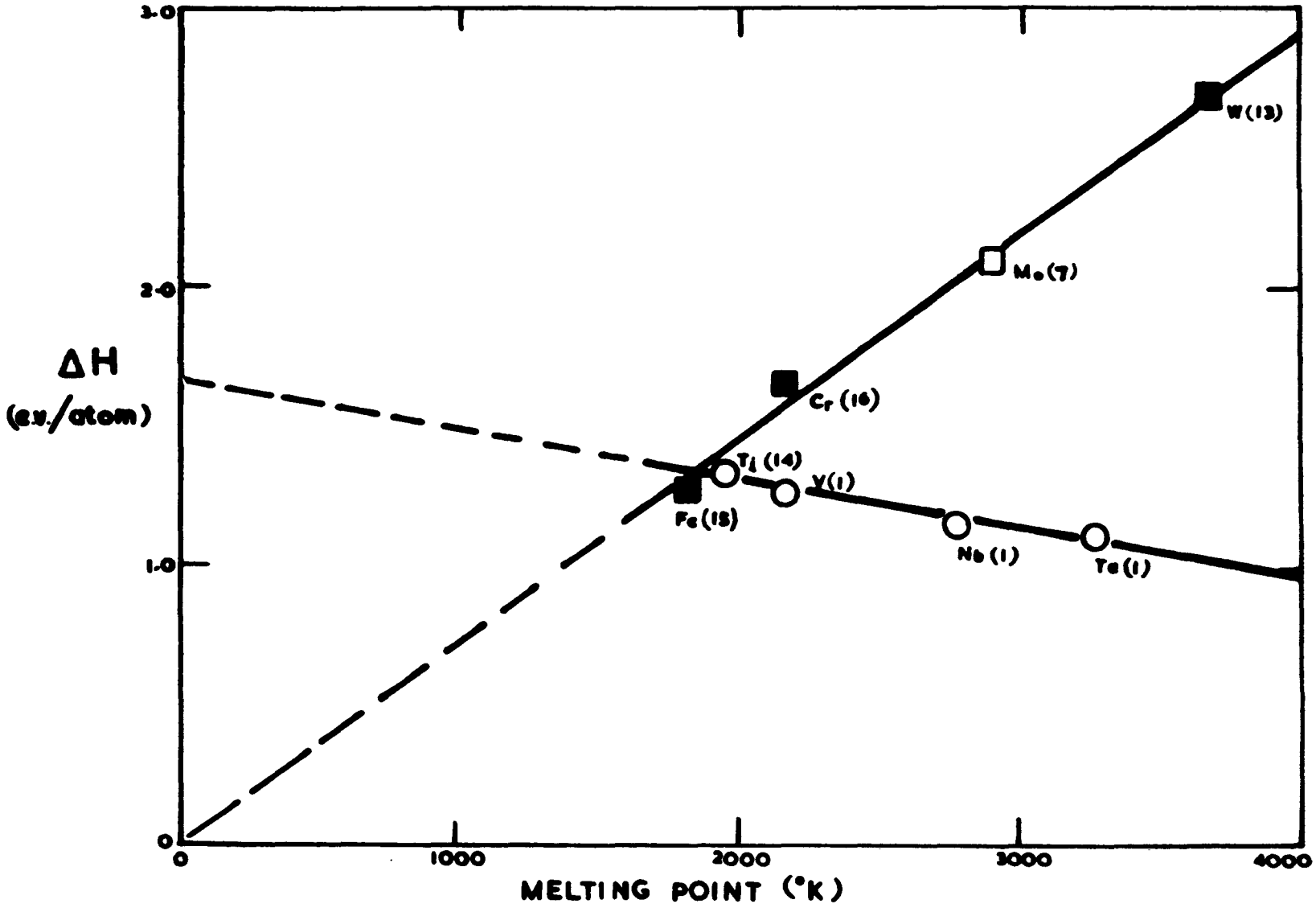

Figure 2 The variation of activation energy for the diffusion of oxygen with the melting point of the solvent. Circles, high solubility; squares, low solubility. Full points evaluated from Portevin-le Chatelier effect. Stringer and Rosenfield (6).

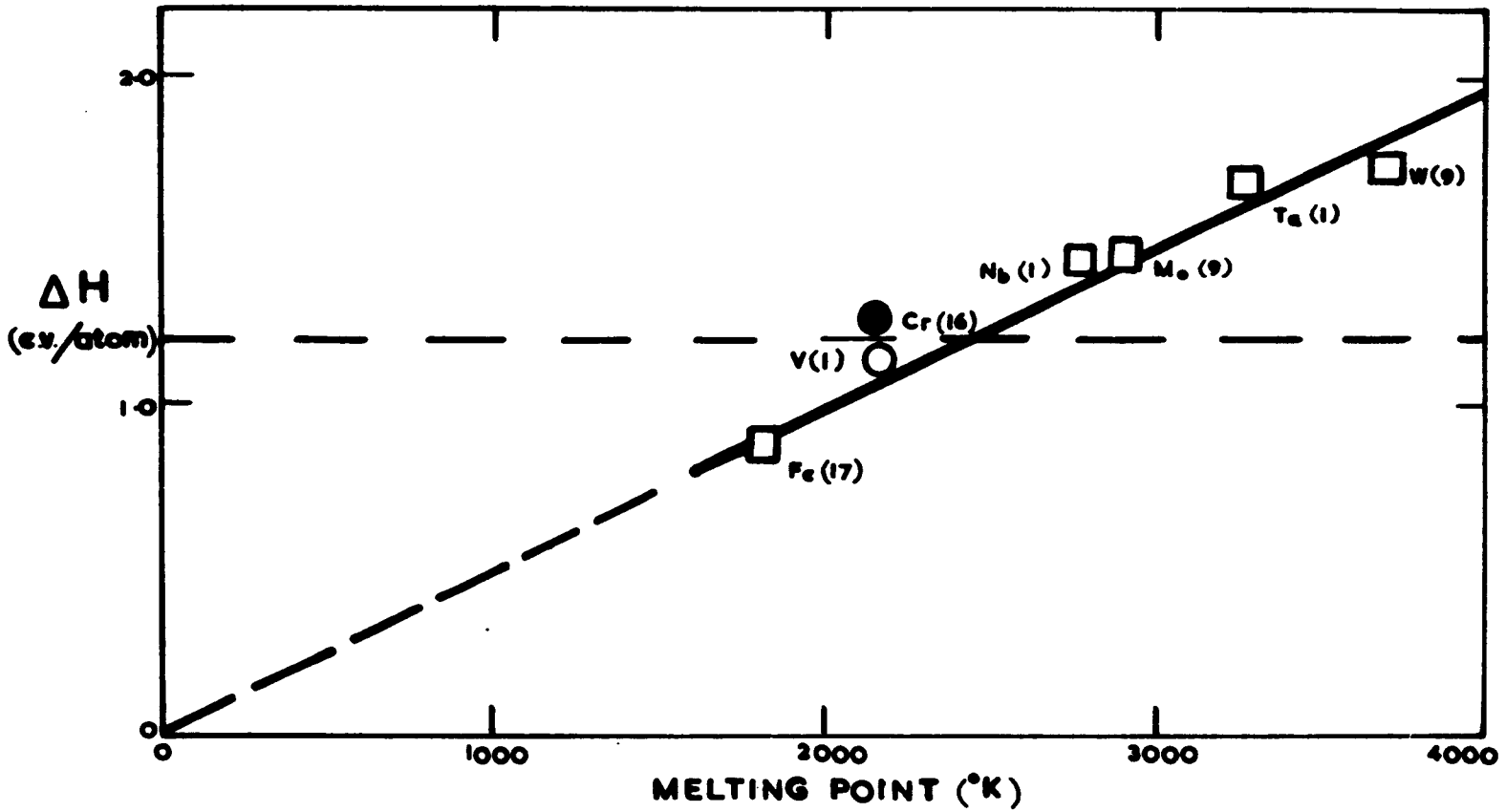

Figure 3 The variation of activation energy for the diffusion of carbon with melting point of the solvent. Circles, high solubility; squares low solubility. Full points evaluated from Portevin-le Chatelier effect. Stringer and Rosenfield (6).

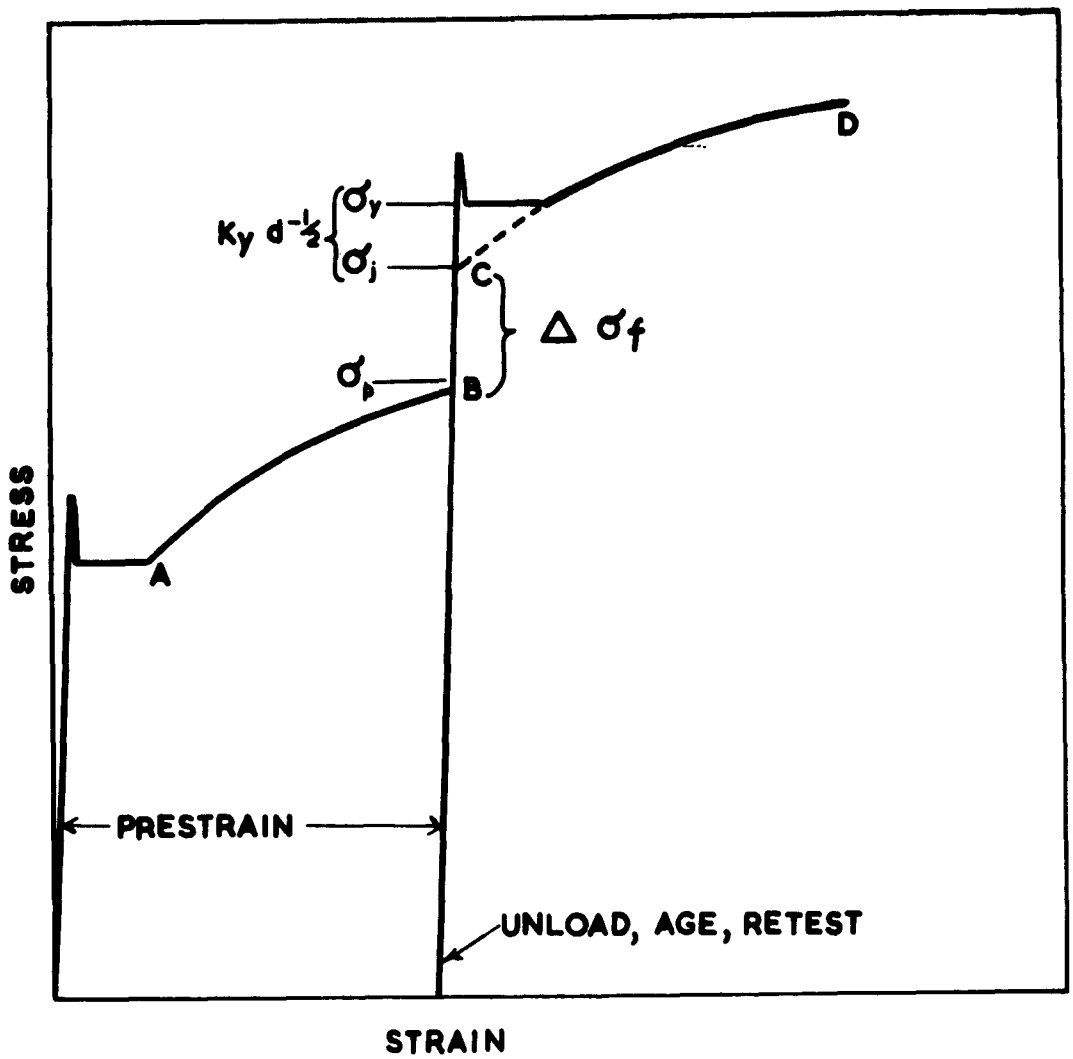

Figure 4 Schematic stress-strain curve for a prestrain, age and retest sequence.

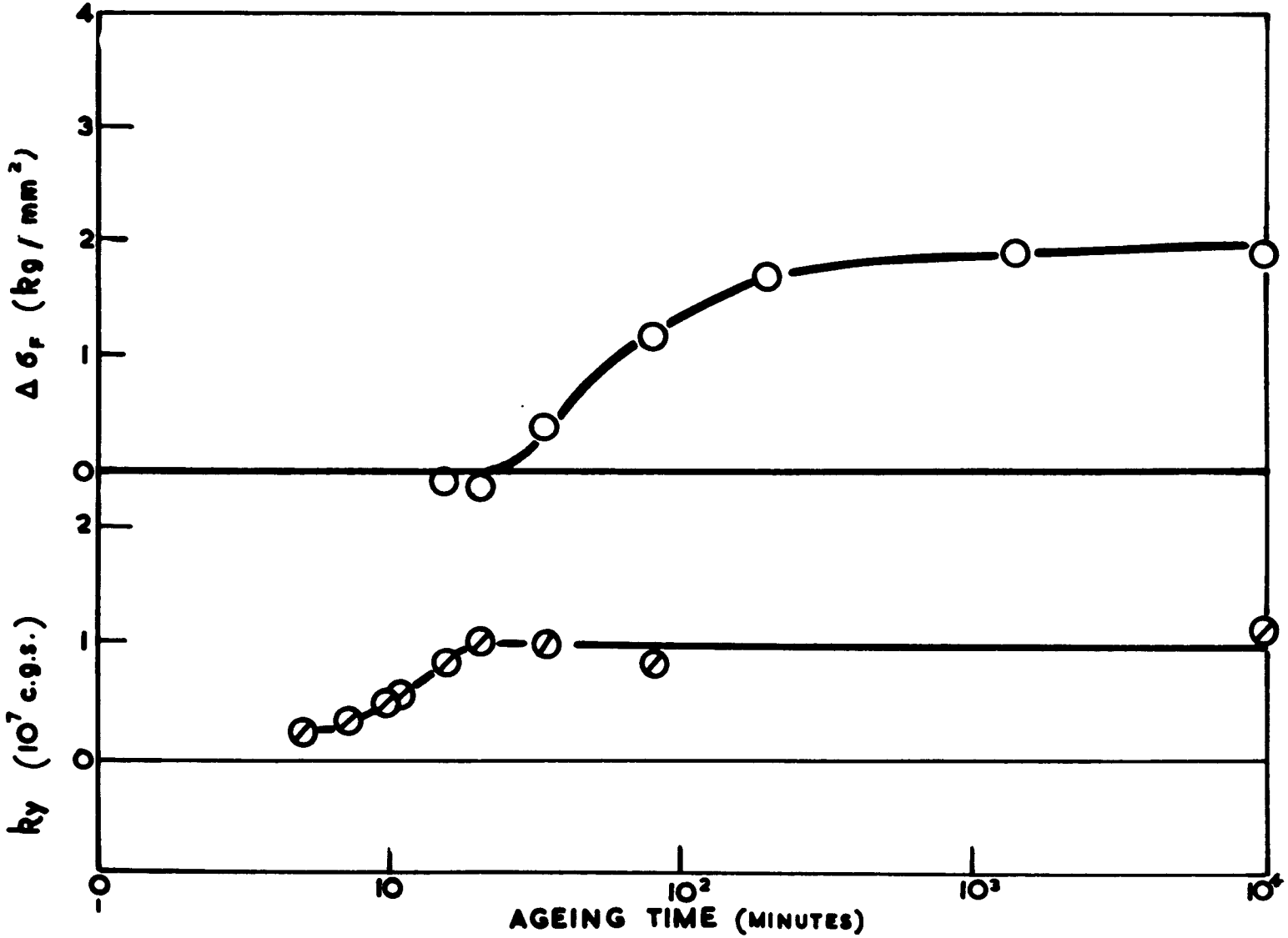

Figure 5 $\Delta\sigma_f$ and k_y for iron-carbon as a function of ageing time at 600°C. Prestrained and tested at 293°K. Wilson and Russell(36).

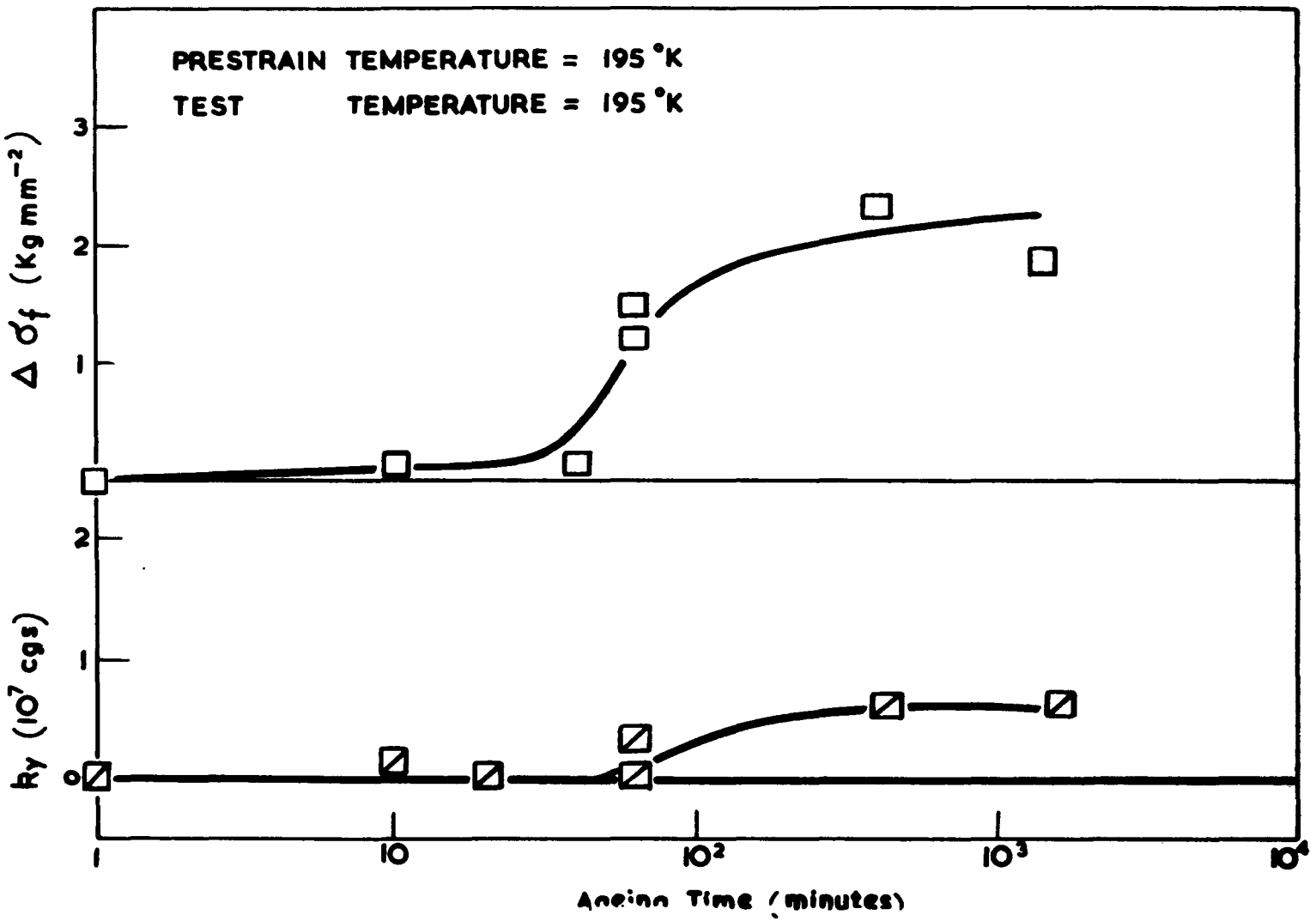

Figure 6 $\Delta\sigma_f$ and k_y for tantalum-oxygen as a function of ageing time at 100°C. Prestrained and tested at 195°K. Rosenfield and Owen[33].

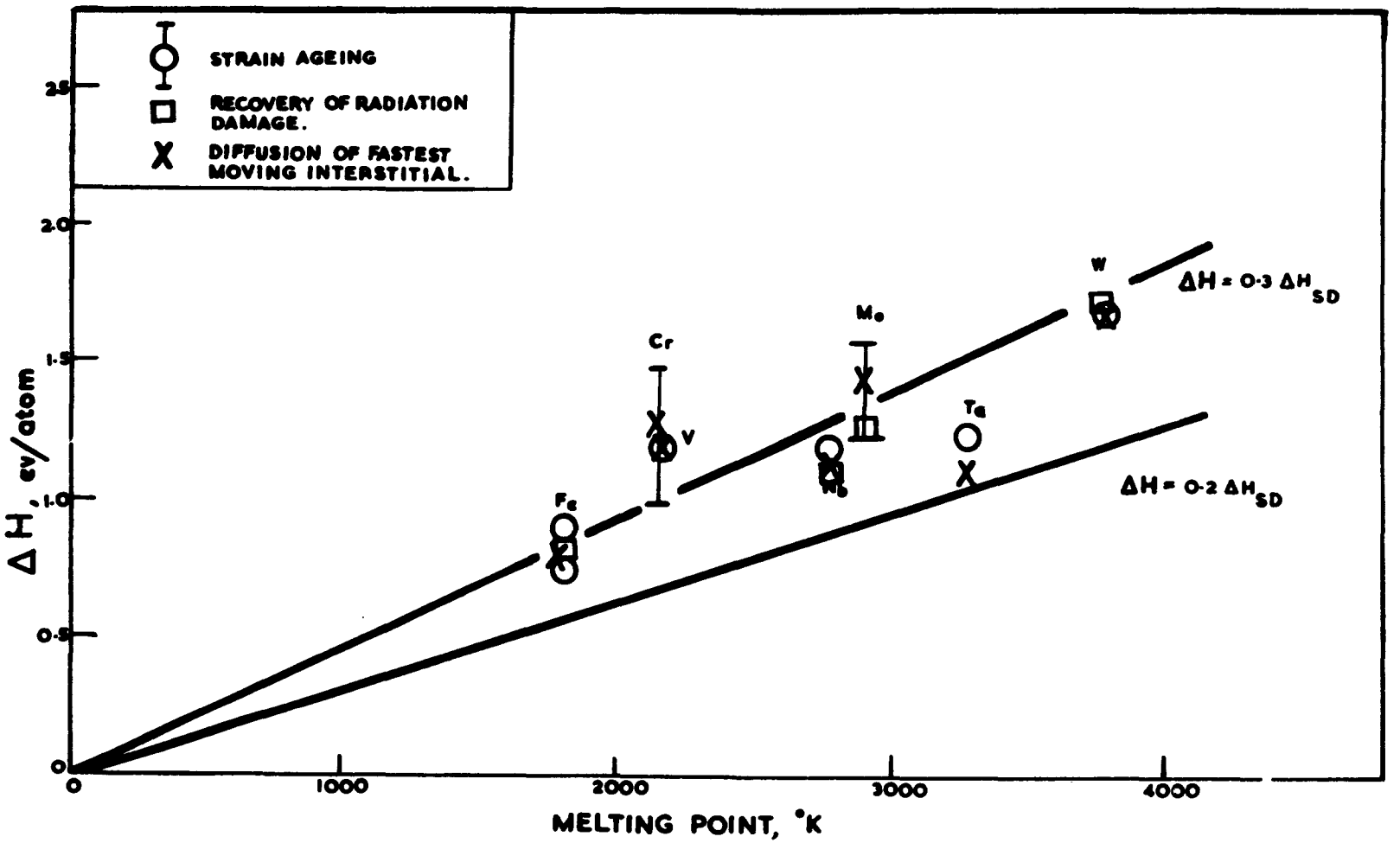

Figure 7 The variation of the activation energy for strain ageing, for recovery of radiation damage and for diffusion of the fastest moving interstitial as a function of the melting point of the solvent.

References

1. R. W. Powers and M. V. Doyle, J. App. Phys. 30 (1959), 514.
2. S. A. Bradford and O. N. Carlson, Trans. A.S.M. 55 (1962), 169.
3. A. U. Seybolt, J. Metals 6 (1954), 774.
4. E. Gilbhardt, Third Plannee Seminar (Reutte, Austria, 1958).
5. A. R. Rosenfield, Nature (1962), to be published.
6. J. Stringer and A. R. Rosenfield, to be published.
7. G. W. Brock, Trans. A.I.M.E. 221 (1961), 1055.
8. J. D. Fast and M. B. Verrijp, J.I.S.I 176 (1954), 24.
9. G. V. Samsonov and V. P. Latuisheva, Dok. Akad. Nauk SSSR 109 (1956), 582.
10. F. J. Norton and A. L. Marshal, Metals Tech. 11 (1944), T.P. 1643.
11. M. J. Marcinkowski and H. A. Lipsitt, Acta Met. 10 (1962), 95.
12. M. W. Mallett, E. M. Baroody, H. R. Nelson and C. A. Papp, J. Electrochem. Soc. 100 (1953), 103.
13. J. W. Pugh, Proc. A.S.T.M. 57 (1957), 1.
14. F. Claisse and H. P. Koenig, Acta Met. 4 (1956), 650.
15. Ch. Boulanger, Rev. Met. 47 (1950), 547.
16. J. W. Pugh, Trans. A.S.M. 50 (1958), 1072.
17. R. P. Smith, Trans. A.I.M.E. 224 (1962), 105.
18. J. Friedel, Les Dislocations (Paris, 1956).
19. L. S. Darken, Trans. A.S.M. 54 (1961), 501.
20. A. H. Cottrell, Report on Strength of Solids (London: Phys. Soc., 1948), 30.
21. A. H. Cottrell, Phil. Mag. 44 (1953), 829.
22. N. F. Mott, Imperfections in Nearly Perfect Crystals, W. Shockley, ed. New York: Wiley, 1952
23. W. R. Thomas and G. M. Leak, Proc. Phys. Soc. 68B (1955), 1001.

24. D. N. Beshers, private communication.

25. C. L. Formby, private communication.

26. A. H. Cottrell and B. A. Bilby, Proc. Phys. Soc. A62 (1949), 49.

27. A. Cochardt, G. Schoeck and H. Wiedersich, Acta Met. 3 (1955), 533.

28. N. J. Petch, J.I.S.I. 173 (1953), 25.

29. A. Gilbert, D. Hull, W. S. Owen and C. N. Reid, J. Less Common Met. 4 (1962), 399.

30. C. N. Reid and W. S. Owen, J.I.S.I. 200 (1962), 229.

31. D. V. Wilson and R. Russell, Acta Met. 7 (1959), 628.

32. I. Mogford and D. Hull, private communication.

33. A. R. Rosenfield and W. S. Owen, Trans. Met. Soc. A.I.M.E., to be published.

34. T. Lindley and R. Smallman, private communication.

35. W. Jolley and D. Hull, private communication.

36. D. V. Wilson and R. Russell, Acta Met. 7 (1959) 628.

37. A. A. Johnson, private communication.

38. H. Brooks, Impurities and Imperfections (Cleveland: A.S.M., 1955).

39. M. de Morton, Trans. A.I.M.E. 221 (1961), 395.

40. Z. C. Szkopiak, "Interim Report" (London: Battersea College of Technology, 1962).

41. D. E. Peacock, Ph.D. Thesis, University of London, 1961.

42. D. G. Martin, Acta Met. 5 (1957), 371.

43. R. H. Chambers, Acta Met. 10 (1962), 466.

44. G. W. Brock, Trans. A.I.M.E. 221 (1961), 1055.

45. G. Kinchlin and M. W. Thompson, J. Nucl. Energy 6 (1958), 275.

46. L. A. Neimark and R. A. Swalin, Trans. A.I.M.E. 218 (1960), 82.

47. H. Schultz, Z. Naturf. 14 (1959), 361.

48. M. W. Thompson, Phil. Mag. 5 (1960), 278.

HARDENING BY SPINODAL DECOMPOSITION

John W. Cahn
General Electric Research Laboratory
Schenectady, New York

ABSTRACT

The effect of the internal stresses produced by spinodal decomposition on dislocation behavior is investigated for several slip systems in cubic materials.

INTRODUCTION

There has been much work on the effect of precipitation on mechanical properties[1-4]. Almost all of the theoretical work has been concerned with discrete particles, either coherent or incoherent. There exist, however, a number of precipitating systems in which the early stages of precipitation resemble long-range coherent composition fluctuations with no abrupt changes in composition. This kind of precipitation results from a thermodynamic instability called the spinodal. The theory of spinodal decomposition has been developed for both isotropic[5, 6] and cubic[7] materials. There is good reason to believe that a number of important age hardening alloys[8] belong to this class, among them the nickel base Inconel 80 and Nimonics. It is the purpose of this paper to explore theoretically how the mechanical properties of a cubic crystal should be affected by the long-range coherent composition fluctuations resulting from spinodal decomposition.

At a first glance a structure of such composition fluctuations might seem too vague to give any hope of calculating much about its properties. Actually just the reverse is true. There is a great deal of regularity in this structure. In cubic crystal the composition fluctuations are best described as interpenetrating stationary (non-propagating) {100} plane waves. This has been derived theoretically[7] and the sharp directionality has long been known[8] experimentally from the streaking of X-ray spots. We will therefore assume that we are dealing with fluctuations all of whose Fourier components have <100> wave vectors.

For some of the calculations it will also be assumed that the structure consists of only three perpendicular {100} waves all having the same wavelength. Again there is good experimental and theoretical justification for choosing a single wavelength to describe the structure in the early stages of decomposition. Such a structure consists of two interpenetrating simple cubic arrays (a large CsCl structure) of pseudo particles (maxima and minima in composition), connected

by an interpenetrating simple cubic lattice work of <100> pseudo rods.

The experimental variables at our disposal are amplitude of the Fourier components and wavelength of the most prominent ones. Temperature of aging primarily affects the wavelength, while time, at temperature, primarily affects amplitude. Thus we can change the spacing and resistance to deformation of our pseudo particles. The spacing ranges from 10Å to 10μ, and the amplitude is usually limited by the loss of coherence which occurs when the lattice parameter variations due to the composition variations result in strains of the order of percents.

In this paper we will discuss the force on a single dislocation due to the internal stresses and composition gradients in the undeformed structure.

THE INTERNAL STRESSES

Consider first a single Fourier component of the composition fluctuation whose wave vector β is in the [001] direction (z direction) and whose amplitude is $A(\beta)$

$$c - c_o = A(\beta) \cos \beta z \tag{1}$$

in a cubic alloy of average composition c_o. Let $\eta = \frac{\partial \ln a}{\partial c}$ describe the compositional variation of stress-free lattice parameter a. The internal stress σ produced by this plane wave[7] is given by

$$\begin{aligned} \sigma_{xx} &= \sigma_{yy} = (\eta \Delta c Y) = A\eta\, Y(100) \cos \beta z \\ \sigma_{zz} &= \sigma_{xz} = \sigma_{yz} = \sigma_{xy} = 0 \end{aligned} \tag{2}$$

where $Y(100) = (C_{11} + 2C_{12})(C_{11} - C_{12})/C_{11}$.

Consider next the superpositioning of all Fourier components whose wave vectors are in the [001] direction

$$\begin{aligned} \sigma_{xx} &= \sigma_{yy} = S_3(z) \\ \sigma_{zz} &= \sigma_{xz} = \sigma_{yz} = \sigma_{xy} = 0 \end{aligned} \tag{3}$$

where $S_3(z)$ is given by integrating equation 2 over all Fourier components in the z direction

$$S_3(z) = \eta Y \int A(\beta) e^{i\beta z}\, d\beta \,.$$

For the [100] and [010] components we may define similar quantities for the internal stress, $S_1(x)$ and $S_2(y)$ respectively. Thus the internal stress resulting from all Fourier components is

$$\sigma = \begin{pmatrix} S_2(y) + S_3(z) & 0 & 0 \\ 0 & S_3(z) + S_1(x) & 0 \\ 0 & 0 & S_1(x) + S_2(y) \end{pmatrix} \quad (4)$$

For the particular case of three equal perpendicular waves of the same wavelength $2\pi/\beta$

$$\begin{aligned} S_1(x) &= A\eta Y(100) \cos \beta x \\ S_2(y) &= A\eta Y(100) \cos \beta y \\ S_3(z) &= A\eta Y(100) \cos \beta z \ . \end{aligned} \quad (3')$$

The stress pattern is a tessellated stress in the literal sense. Although the literature on tessellated stresses is voluminous[9], there appear to be only a few papers[10-12] which consider internal stresses that vary sinusoidally.

THE FORCE ON DISLOCATIONS DUE TO THE INTERNAL STRESSES

In this section we shall derive the forces exerted on a dislocation by the internal stress field. These forces are superimposed on those resulting from an externally applied stress. We shall follow the sign convention of Nabarro[4] throughout, and thereby eliminate ambiguity regarding the sign of the force. For simpler stresses it is sometimes convenient to rotate axes so that the Burgers vector is parallel to x and the slip plane is the xy plane and then determine the magnitude of the force from $b\sigma_{xz}$ and the sign from physical intuition. For the present case intuition is not quite as easy to apply, and Nabarro's convention applied to the Peach and Koehler formulation will be used since it gives, in a quite straightforward manner, not only the magnitude of the force but also its direction.

The force $\bar{F}$ on a dislocation per unit length produced by a stress field σ is

$$\bar{F} = (b \cdot \sigma) x \zeta \quad (5)$$

where b is the Burgers vector and ζ the unit tangent to the dislocation line. The sign of b depends on the direction in which the Burgers circuit is taken which in turn is related by convention to the direction of ζ so that the sign

of $\bar{F}$ depends only on the physical situation and not on the direction of the Burgers circuit. Reversing ζ also reverses b.

The force on a dislocation is always at right angles to ζ, and for edge dislocations consists of both climb and glide components. The glide component F_g is given by

$$F_g = (n \times \zeta)(b\sigma n) \tag{6}$$

where n is the normal to the glide plane. Reversing the sign of n leaves F_g unaltered. The product $b\sigma n$ is $b\sigma_{xz}$ if the coordinate axes are rotated so that b coincides with the x axis and n with the z (slip on the xy plane). The vector product $(n \times \zeta)$ is a unit vector in the slip plane at right angles to the dislocation. According to equation 6 the magnitude of the force on a dislocation is independent of the direction of the dislocation line. The product of resolved shear stress $(1/|b|)(b\sigma n)$ and the Burgers vector determines the magnitude of the force, and the remainder of the expression serves to determine its direction.

Equation 6 applies equally well to screw dislocations but since these can glide on a number of planes it is sometimes convenient to use equation 5 which for screw dislocations becomes

$$\bar{F} = \frac{1}{|b|}(b \cdot \sigma \times b) \ . \tag{7}$$

This gives the force on the dislocation and its direction, rather than the force resolved in some plane n.

Let us now apply these equations to the internal stress given by equation 4 to a dislocation whose Burgers vector has components (b_1, b_2, b_3) and which slips on a glide plane whose normal has components (n_1, n_2, n_3). The scalar force $b \cdot \sigma \cdot n$ is

$$b \cdot \sigma \cdot n = n_1 b_1 (S_2 + S_3) + n_2 b_2 (S_1 + S_3) + n_3 b_3 (S_1 + S_2) \ . \tag{8}$$

Bearing in mind that b is perpendicular to n

$$b_1 n_1 + b_2 n_2 + b_3 n_3 = 0 \tag{9}$$

we may rewrite equation 8

$$b \cdot \sigma \cdot n = -(n_1 b_1 S_1 + n_2 b_2 S_2 + n_3 b_3 S_3) \ . \tag{10}$$

For screw dislocations we have from equation 7

$$F = \frac{1}{|b|}\{ib_2b_3(S_3 - S_2) + jb_1b_3(S_1 - S_3) + kb_1b_2(S_2 - S_1)\} \quad (11)$$

where i, j and k are unit vectors along [100], [010] and [001] respectively. Equation 11 may be rearranged as the sum of three vectors, each one depending only on waves in a single direction.

$$F = b_1S_1\left(0 + \frac{jb_3}{|b|} - \frac{kb_2}{|b|}\right) + b_2S_2\left(-\frac{ib_3}{|b|} + 0 + \frac{kb_1}{|b|}\right) + b_3S_3\left(\frac{ib_2}{|b|} - \frac{jb_1}{|b|} + 0\right) . \quad (12)$$

Here $b_1/|b|$, $b_2/|b|$ and $b_3/|b|$ are simply the cosines of the angle that b makes with the three <100> directions. Each Fourier component produces an alternating force on the screw dislocation which is both perpendicular to the Burgers vector and the wave vector, and whose magnitude is zero, if the Burgers vector and wave vector are either perpendicular or parallel to each other.

OTHER FORCES ON THE DISLOCATIONS

In these inhomogeneous alloys there exist several other sources of forces on dislocations that are not present in a homogeneous alloy of the same composition. These relate mainly to the composition gradients. For very small gradients the self energy γ of a dislocation is approximately given by

$$\gamma \sim Gb^2 \sim Yb^2 \quad (13)$$

where G is the shear modulus. If γ varies with position there will be a force on the dislocation [13] given by

$$\bar{F}_c = tx(\text{grad } \gamma \times t) = \left(\gamma\left(\frac{d\ln G}{dc} + 2\eta\right)(\nabla c \times t)\right)xt . \quad (14)$$

The corresponding glide force in a plane whose normal is n

$$\bar{F}_{cg} = \gamma\left(\frac{\partial \ln G}{\partial c} + 2\eta\right)(\nabla c \times t \cdot n)(t \times n) \quad (15)$$

As before the last factor just expresses the direction; the magnitude is given by the remaining factors.

For the three equal perpendicular waves in composition

$$c - c_o = A(\cos \beta x + \cos \beta y + \cos \beta z) \quad (16)$$

equation (15) gives for the magnitude of F_{cg}

$$|F_{cg}| = A\gamma_\beta\left(\frac{\partial \ln G}{\partial c} + 2\eta\right)[\sin\beta x(t_2 n_3 - t_3 n_2) + \sin\beta y(t_3 n_1 - t_1 n_3)$$

$$+ \sin\beta z(t_1 n_3 - t_3 n_1)] \; . \qquad (17)$$

Comparison with equations 11 or 12 and 3' shows that this force is on the average smaller than the force due to the internal stresses by a factor of $b\beta$, but that it differs in phase and direction. It is therefore negligible except where, because of symmetry, the forces due to internal stresses are zero.

Another source of resistive forces in a composition gradient comes from the fact that after slip through an inhomogeneous region, the two opposing faces of a slip plane now differ in composition by a

$$\Delta c = b \cdot \nabla c. \qquad (18)$$

Such an interface requires an additional energy and gives rise to a force proportional to $(\Delta c)^2$. It is the analogue of chemical hardening model suggested by Kelly and Fine[15]. Since it is quadratic in amplitude A it is negligible whenever there are dominant terms of lower power in A.

DISCUSSION OF SEVERAL SLIP SYSTEMS

(100) Slip Plane

Equation 10 reveals that if either the slip plane normal or the Burgers vector are either parallel or perpendicular to the wave vector of a Fourier component, the internal stresses resulting from that Fourier component will exert no glide force on that dislocation. (This result is not restricted to <100> wave vectors but holds true for all orientations). Thus slip involving either <100>b or {100} slip planes will be unaffected by the internal stress field. This result is somewhat unexpected, if one bears in mind that we have here an assembly of psuedo particles and large internal stresses resulting from them. Consider, for example, the {100} slip plane.

If we examine the special case of three perpendicular waves of the same wavelength one sees that one of the (100) slip planes could have encountered a square array of the peaks in composition (pseudo particles of one phase). A parallel plane half a wavelength down would have encountered all the lows in composition (pseudo particles of the other plane). Another parallel plane, a quarter wavelength down, would have encountered no extremes in composition. One might have expected large differences in forces, but there are none. A simple insight into why this is so is provided by equation 4, which shows that the cube axes are

principal stress axes and therefore there is no shear on any cube plane.

For such a slip system we are left only with the forces due to the variations in line tension due to the composition changes (equations 14-17). These tend to pin the dislocations along either the maxima or minima in composition, that is inside one of the pseudo phases.

(110) Slip Plane

Consider next a (110) slip plane which is often a primary slip plane in B.C.C. Let the equation of the slip plane be

$$x + y = \sqrt{2}d, \tag{19}$$

where d is the distance of the plane from the origin. Let $\sqrt{2}x' = x - y$ and $z' = z$ be the coordinates in the plane (Fig. 1). All shear stresses in the plane are along the x' direction and alternate in sign. For the special case of 3 equal perpendicular waves of the same wavelength we have for the force on a $[11\ell]$ dislocation from equation 10

$$b\cdot\sigma\cdot n = -\frac{|b|}{(4 + 2\ell)}\gamma_2(S_1 - S_2)$$

which by equation 3' becomes

$$b\cdot\sigma\cdot n = \frac{A\eta\gamma|b|}{(4 + 2\ell)^{1/2}} (\cos \beta x - \cos \beta y) \tag{20}$$

$$= \frac{A\eta\gamma|b|}{(1 + \ell^2/2)^{1/2}} \sin(1/\sqrt{2}\beta d) \sin(1/\sqrt{2}\beta x') .$$

Dislocations in the various slip planes encounter no forces if $(1/\sqrt{2})\beta d$ is an integer and sinusoidal forces if $(1/\sqrt{2})\beta d$ is not an integer. The former correspond to slip planes through the centers of the pseudo particles. The strongest forces are encountered in slip planes that avoid the pseudo particles.

Let us next consider how these forces should affect the shape of the dislocation line. In the absence of an applied stress, the dislocation must curve and at equilibrium, assuming a string model for the dislocation, it must obey the following differential equation

$$b\cdot\sigma\cdot n = \gamma \frac{\frac{d^2z'}{dx'^2}}{[1 + (\frac{dz'}{dx'})^2]^{3/2}} . \tag{21}$$

Letting $w = \frac{dz'}{dx'}$, $b\cdot\sigma\cdot n = A'\sin 1/\sqrt{2}\,\beta x'$ where

$$A' = \frac{A\eta\gamma|b|}{(1+\ell^2/2)^{1/2}} \sin\frac{\beta d}{\sqrt{2}}$$

we obtain

$$\frac{A'}{\gamma} \sin\frac{1}{\sqrt{2}}\beta x' = \frac{\frac{dw}{dx}}{(1+w^2)^{3/2}}$$

which can be integrated to give

$$\text{const.} - \frac{\sqrt{2}A'}{\beta\gamma} \cos\frac{1}{\sqrt{2}}\beta x' = \frac{w}{(1+w^2)^{1/2}} \quad . \tag{22}$$

Since the right-hand side is bounded by ±1 a stable dislocation configuration straddling a band of force can exist only if

$$\frac{\sqrt{2}A'}{\beta\gamma} \leq 1 \quad . \tag{23}$$

If it exceeds 1, the internal stresses will align all dislocations along [001] in the stable zero force positions. Every mobile and flexible dislocation will be forced into such configurations. Using equation 13 this condition becomes

$$A\eta \sin\frac{1}{\sqrt{2}}\beta d \leq \beta b \quad . \tag{23'}$$

For example, the aligning of dislocations begins at wavelengths of 1000Å when the lattice parameter amplitude reaches 1%.

In considering slip in such a crystal one must carefully distinguish dislocations that already straddle the pseudo particles and those that do not. The former can move easily in the presence of an applied stress very much like a kink straddling a Peierls-Nabarro barrier can move sideways. On the other hand, formation of new kinks by having a section of a dislocation slip across a pseudo particle is very much more difficult and varies from plane to plane. At low stress levels only dislocations going through the centers of the pseudo particles can move. With increasing stress the planes on which slip is possible form an ever increasingly thick band about the centers.

The equations for a number of dislocations piling up on such a sinusoidal barrier have recently been derived[12].

The (111)[1$\bar{1}$0] Slip System

The (111)[1$\bar{1}$0] slip system is another one which interacts with only two of the three fluctuation components and therefore should behave as if the sample

contained an assembly of pseudo rods along [001]. In this case the slip plane cuts across the rods and all parallel (111) planes encounter the same obstacles as do the $(11\bar{1})$ cross slip planes. Therefore cross slip would be of no help in avoiding the resistance imposed by the internal stresses.

Let the equation of the slip plane be

$$x + y + z = \sqrt{3}d \ . \tag{24}$$

The resolved force on a $[1\bar{1}0]$ dislocation is

$$b\cdot\sigma\cdot n = -\frac{|b|}{\sqrt{6}}(S_1 - S_2) = \frac{A\eta|b|Y}{\sqrt{6}}(\cos\beta x - \cos\beta y)$$

$$= \sqrt{\frac{2}{3}}\, A\eta|b|Y \sin[1/2\ \beta(x + y)]\sin[1/2\ \beta(x - y)] \ .$$

Rotating the coordinate system such that x' is along $[1\bar{1}0]$ and y' along $[11\bar{2}]$ in the slip plane

$$\begin{aligned}\sqrt{2}x' &= x - y \\ \sqrt{6}y' &= x + y - 2z + 2\sqrt{3}d \ .\end{aligned} \tag{25}$$

By virtue of equation 24

$$\sqrt{6}y' = 3x + 3y$$

so that

$$b\cdot\sigma\cdot n = \sqrt{\frac{2}{3}}\, A\eta|b|Y \sin\left(\frac{1}{\sqrt{6}}\beta y'\right)\sin\left(\frac{1}{\sqrt{2}}\beta x'\right) \ . \tag{26}$$

The (111) slip plane thus resembles a rectangular checker board of alternating forces, as shown in Fig. 2. The sides of the rectangles are the locus of zero force positions and within each rectangle the force rises or falls to an extremum in the center.

Using the string model for a mobile dislocation one obtains an equation for the dislocation time at rest in the presence of such a force field.

$$\frac{\gamma\dfrac{d^2y'}{dx'^2}}{\left(1 + \left(\dfrac{dy'}{dx'}\right)^2\right)^{3/2}} = \sqrt{\frac{2}{3}}\, A\eta|b|Y \sin\left(\frac{1}{\sqrt{6}}\beta y'\right)\left(\sin\frac{1}{\sqrt{2}}\beta x' + \sigma_a|b|\right) \tag{27}$$

where we have added a term to account for an applied stress, whose resolved shear stress is σ_a.

Equations of this type are known as Duffing's equation and occur in forced vibrations.[16] One method of solution is the Galerkin-Ritz variational method in which one assumes a solution to the equation and adjusts parameters so that certain Fourier components of the error vanish.

As in all problems of this type there are two convenient extremes. If $A\eta|b|Y/\gamma\beta < 1$ the dislocation line is almost straight, the wavelength or amplitude of the internal stresses being too small to cause much bending. The other extreme is when $A\eta|b|Y/\gamma\beta > 1$. In this case the dislocation curves around all obstacles.

In the first case, assuming a sinusoidal form for the dislocation line

$$y' = C_1 + C_2 \sin \frac{\beta x'}{\sqrt{2}} \quad \text{for screw dislocation}$$

and

$$x' = B_1 + B_2 \sin \frac{\beta y'}{\sqrt{6}} \quad \text{for edge dislocations} \tag{28}$$

we obtain, using the Galerkin method

$$\cos C_1 = \frac{3\sqrt{3}\,\beta\gamma}{4\sqrt{2}\,A^2\eta^2Y^2|b|}\,\sigma_a$$

$$\cos B_1 = \frac{\beta\gamma}{4\sqrt{2}\,A^2\eta^2Y^2|b|}\,\sigma_a \tag{29}$$

$$C_2^2 = \frac{2}{9}\frac{A^2\eta^2Y^2b^2}{\beta^2\gamma^2}\left[1 + \sqrt{1 - 54\,\frac{\sigma_a^2\beta^2\gamma^2}{A^4\eta^4Y^4b^2}}\right]$$

$$B_2^2 = 6\,\frac{A^2\eta^2Y^2b^2}{\beta^2\gamma^2}\left[1 + \sqrt{1 - 2\,\frac{\sigma_a^2\beta^2\gamma^2}{A^4\eta^4Y^4b^2}}\right]$$

At small values of the applied stress the dislocation reaches equilibrium straddling the peaks in the internal stress which occur at $C_1 = B_1 = \pi/2$. There is an additional unstable solution at $C_1 = B_1 = 0$ where there are zero forces on the dislocation. However, certain small fluctuations in position cause the dislocation to move off this position.

At applied stresses exceeding

$$\sigma_a^* = \frac{A^2\eta^2Y^2b}{3\sqrt{6}\,\beta\gamma} \quad \text{for screws}$$

or (30)

$$\sigma_a^* = \frac{A^2\eta^2Y^2b}{\sqrt{2}\,\beta\gamma} \quad \text{for edges}$$

no solution exists and the dislocation should move continuously through the structure. This corresponds to the Mott and Nabarro yield stress for this structure. As in the Mott and Nabarro relation, this equation reflects the averaging of large forces that alternate in sign. The yield stress is therefore smaller by orders of magnitude than the internal stress maxima, and depend entirely on what little flexing the dislocation can do. Because of the longer apparent wavelength encountered by edges, they can flex more, and as a result are much harder to move than the screws. For the same reason the yield stress increases linearly with wavelength.

The stress is also quadratic in amplitude. This brings it to the same degree in amplitude as the chemical term arising from equation 18. Since such a chemical term is always a retarding force, it survives averaging without a change in degree in amplitude. Whether it is an important term will depend on how its coefficient compares with those given in equation 30. For a 1% lattice parameter difference ($A\eta = 1.6 \times 10^{-3}$) $\beta = 10^6$ cm^{-1} (600Å wavelength), $Y = 10^{12}$ ergs/cc, $b = 10^{-8}$ cm we obtain $\sigma_a = 10^8$ dynes/cm^2. This stress is close to the upper limit of the assumption of a straight dislocation because $A\eta Y|b|/\gamma\beta = .16$.

The other extreme, $A\eta Y|b|/\gamma\beta \geq 1$ corresponds to a dislocation that can curl around obstacles. At zero applied stress, we have a checker board of obstacles that touch each other at their corners to form a continuous obstacle. However, the forces on the dislocations at these junctions are very small and as a stress is applied these junctions separate (Fig. 3). The effective distance between obstacles increases with increasing stress and may be found by plotting the contours of zero net force on the dislocation

$$\sqrt{2/3}\,A\eta Y \sin\left(\frac{1}{\sqrt{6}}\beta y'\right) \sin\left(\frac{1}{\sqrt{2}}\beta x'\right) + \sigma_a = 0 \,. \tag{31}$$

Since one such junction is at $x' = y' = 0$ we may expand the sine terms in this equation to obtain

$$x'y' = -3\sqrt{2}\,\sigma_a/(A\eta Y\beta^2) \,.$$

The separation L between obstacles is thus

$$L = 4.6\,\sigma^{1/2}/[(A\eta)^{1/2}\beta] \,. \tag{32}$$

The dislocation can slip through this opening if

$$\sigma_a b > 2\gamma/L$$

or

$$\sigma_a > .57\ (A\eta Y)^{1/3}\ (\frac{\gamma\beta}{b})^{2/3} \quad . \tag{33}$$

This then is the analogue of Orowan[17] yielding in this structure. The stress depends on the reciprocal 2/3 power of the wavelength rather than on the reciprocal first power, because the effective distance between these soft particles is a function of the applied stress. Each dislocation that slips through will leave a loop around the obstacles, and should lead to the analogue of Fisher, Hart, Pry[18] hardening, including the possibility that the stress of successive concentric loops will cause the inner loop to cut through the obstacle.

Other Slip Systems

Only if there are no zeros in the Miller index designation of slip plane and slip direction will the structure appear as discrete particles to the dislocation. Thus, for instance, if the <110> Burgers vector in FCC splits into two <112> partials, each of the partials will be able to avoid obstacles by cross slip of the recombined dislocation, but what is an easy glide plane for one partial will abound in obstacles for the other, since the sum of the forces on the partials does not vary from plane to plane.

In BCC the {112} and {123} slip planes will behave as if the structure is particulate and slip bands should occur on the easy planes which will be spaced periodically.

SUMMARY AND DISCUSSION

A dislocation in a spinodally decomposed structure experiences a force from the internal stresses and composition gradients. The former are expected to be the more important, except for special slip systems where the internal stresses exert no force (either $\bar{b}$ or $\bar{n}$ along <100>). The details for the interaction with the internal stress have been worked out for several slip systems, and these give rise to a number of concepts analogous to those encountered in precipitation hardening by discrete particles, except that the details are sometimes quite different. Thus the $(111)[1\bar{1}0]$ slip system exhibits the analogues of both Mott and Nabarro and Orowan hardening, at small spacings a hardening linear in spacing (equation 30) and at large spacings hardening proportional to the reciprocal 2/3rd power of spacing (equation 33). The $(1\bar{1}0)[111]$ slip system resembles a Peierls-Nabarro trough with an extremely long period, so that thermal activation is almost certainly negligible.

In many respects spinodally decomposing materials should prove to be convenient for experimental studies of hardening. The two variables, wavelength and amplitude, can be varied independently to investigate separately the effects of each. They correspond in precipitation hardening to particle spacing and particle hardness, and certainly the latter is not normally an experimental variable.

There are numerous unexplored areas remaining. The subject of many dislocations on a slip plane is one. For the $[111](1\bar{1}0)$ slip system the recent paper by Chou is pertinent. A similar treatment for the $[1\bar{1}0]$ (111) should not be too difficult. The analogue of Fisher, Hart and Pry hardening should be investigated for long wavelengths. Still another subject is the mechanism and slip system operating in the loss of coherence. Since loss of coherence is usually not observed until the internal strains are of the order of a percent, the stresses approach the theoretical limit of strength.

Only cubic materials for which $C_{44} > \frac{C_{11} - C_{12}}{2}$ were discussed in this paper. These give rise to {100} plane waves and all known examples of spinodal decomposition belong in this class. There are a number of systems for which $C_{44} < \frac{C_{11} - C_{12}}{2}$ that could give rise to spinodal decomposition. These would give {111} plane waves, which would have quite different effects on dislocations.

Acknowledgement

I am indebted to R. L. Fleischer, E. W. Hart, G. Horvay, J. D. Livingston and H. W. Schadler for stimulating criticism and suggestions about various aspects of this paper. I am especially grateful to J. D. Livingston for a critical review of the manuscript.

References

1. E. W. Hart, ASM Symposium on Relation of Properties to Microstructure, p. 95 (1954).

2. J. D. Livingston, TAIME 215, 566 (1959).

3. A. Kelly and R. Nicholson, Prog. Mat. Sci., to be published.

4. F. R. N. Nabarro, Adv. in Physics 1, 269 (1952).

5. M, Hillert, Acta Met. 9, 525 (1961).

6. J. W. Cahn, (1) Acta Met. 9, 795 (1961).

7. J. W. Cahn, (2) Acta Met. 10, 179 (1962).

8. J. Manenc, Acta Met. 7, 124 (1959).

9. Symposium on Internal Stresses in Metals and Alloys, Institute of Metals (London), p. 47 and 61 (1948).

10. G. Masing, Z. Phys. 124, 586 (1948).

11. Z. S. Basinski, Phil. Mag. 4, 393 (1959).

12. Y. T. Chou and N. Louat, J. Appl. Phys. 33, 3312 (1962).

13. R. L. Fleischer, Acta Met. 8, 32 (1960).

14. R. L. Fleischer, Acta Met. 8, 598 (1960).

15. A. Kelly and M. Fine, Acta Met. 5, 365 (1957).

16. K. Klotter, Handbook of Appl. Mechanics, McGraw-Hill, 1962, W. Flugge, Ed.

17. E. Orowan, "Symposium on Internal Stresses in Metals and Alloys", Inst. of Metals, London, p. 451 (1948).

18. J. C. Fisher, E. W. Hart and R. H. Pry, Acta Met. 1, 336 (1953).

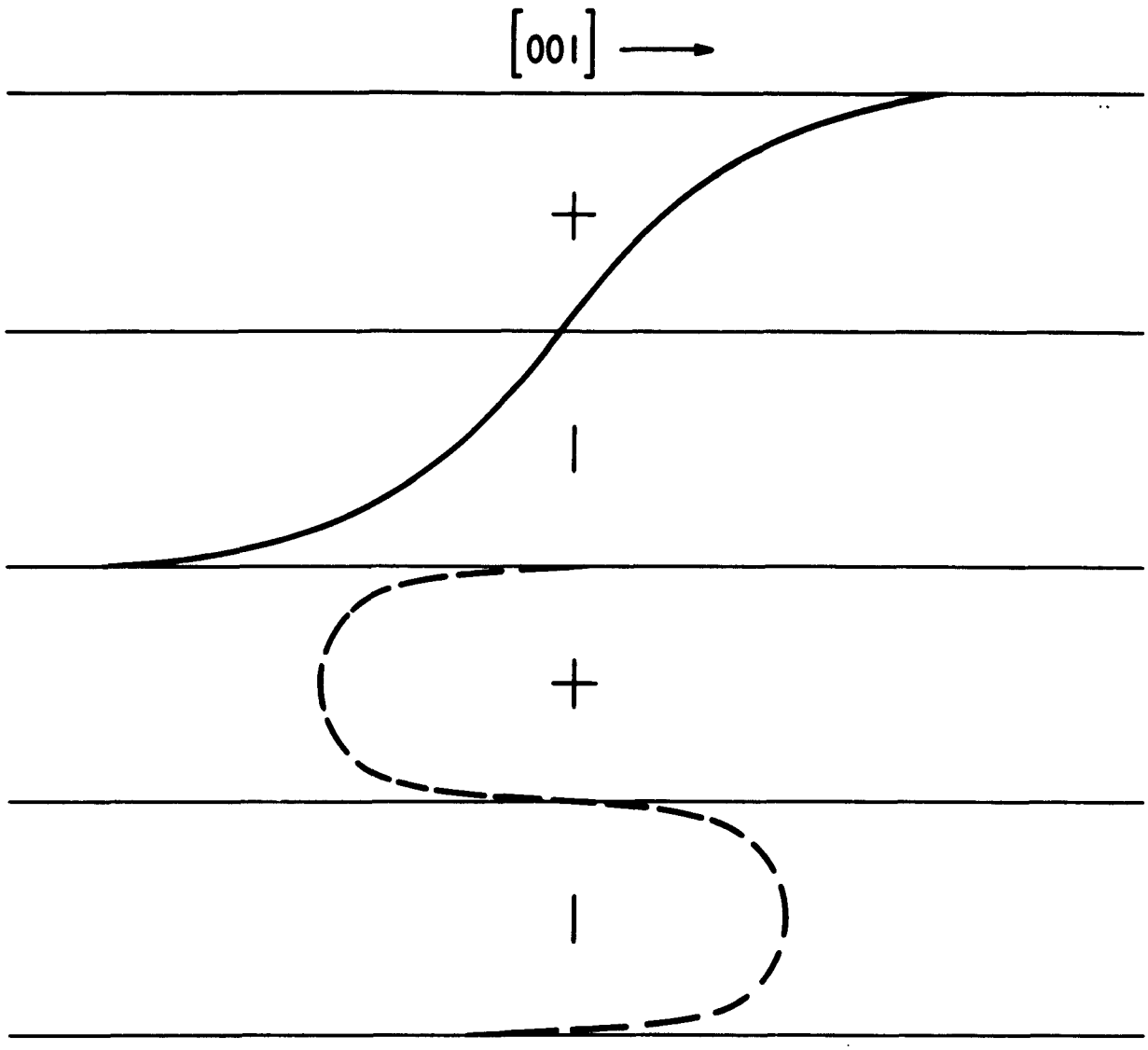

Fig. 1 - The (110) slip plane showing the forces on a dislocation and the resulting dislocation configuration. The plus and minus signs refer to the sign of the force within each region and therefore to the curvature of the dislocation line there. Left-hand dislocation is for low force amplitude (A' in equation 23) for that wavelength. Right-hand dislocation is for large A', near the limit beyond which all dislocations are forced to line up along [001].

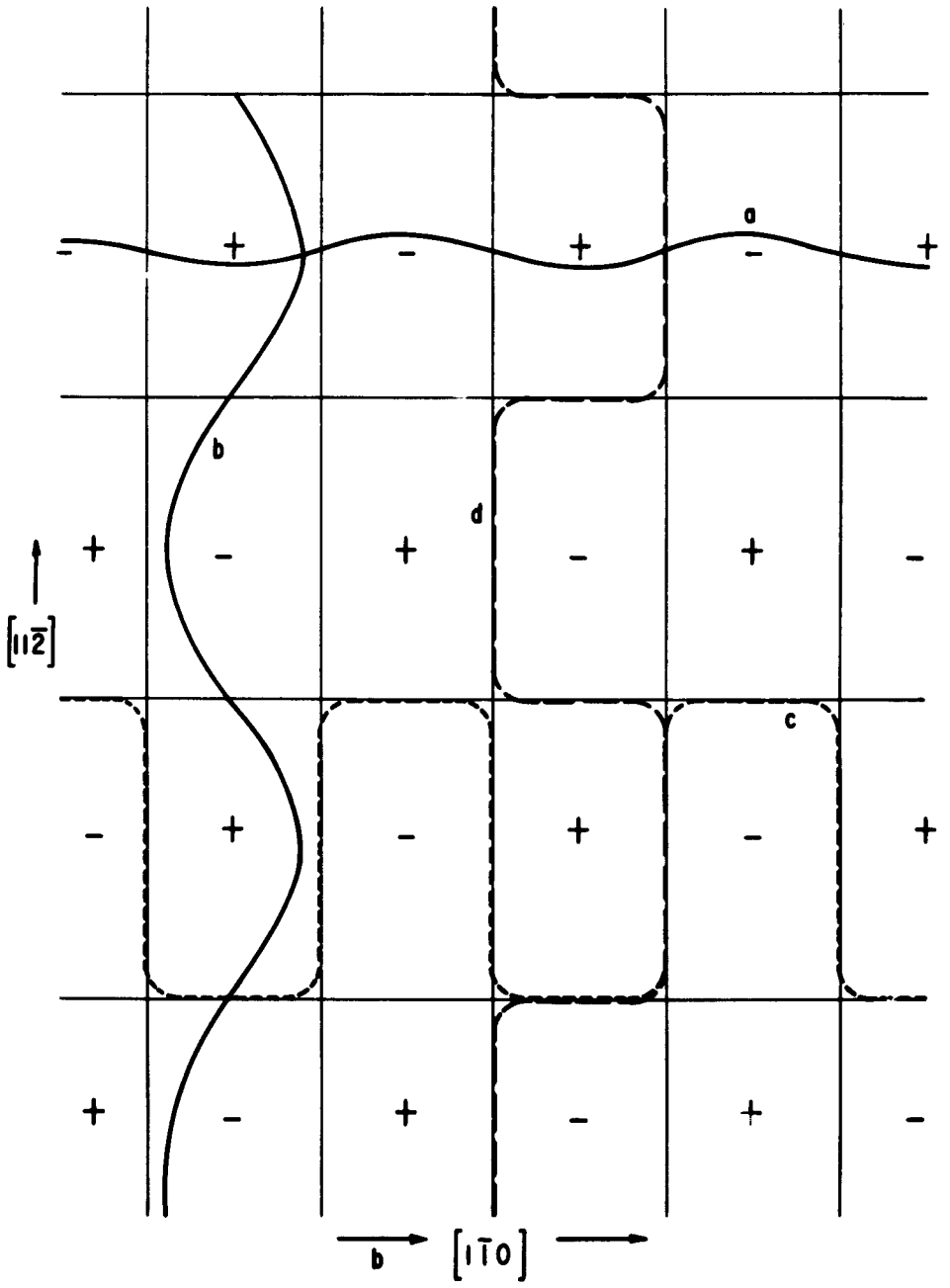

Fig. 2 - The (111)[1$\bar{1}$0] slip system in the absence of applied stress showing the forces on the dislocation and the resulting configurations. (a) screw and (b) edge at small amplitude for that wavelength; (c) "screw" and (d) "edge" at large amplitude.

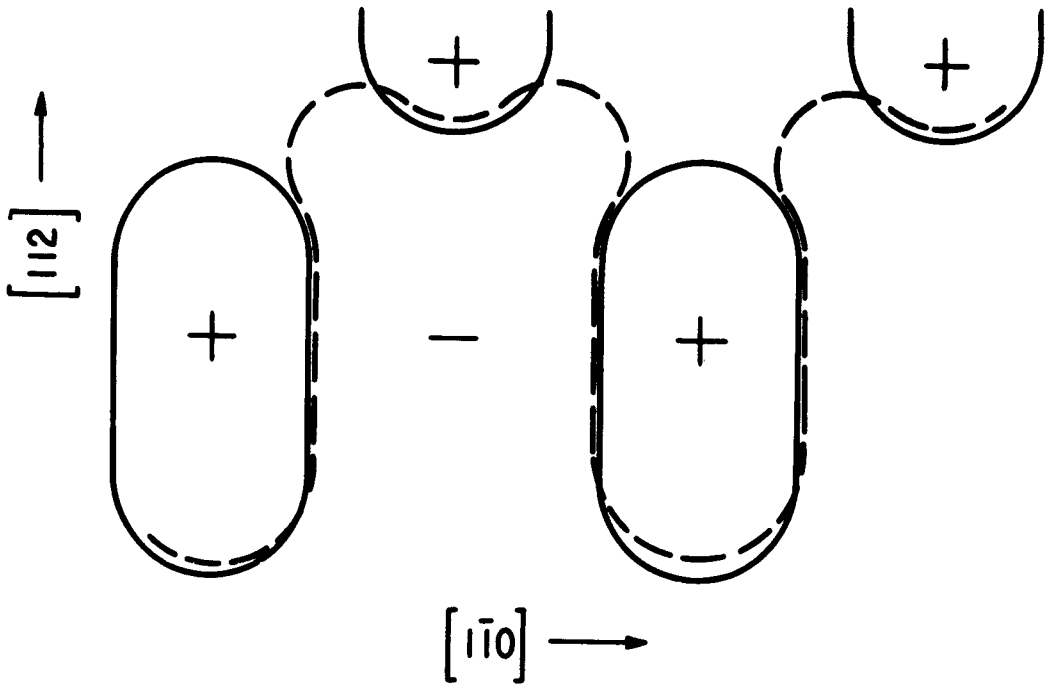

Fig. 3 - The (111)[1$\bar{1}$0] slip system in the presence of a (-) applied stress, showing the contraction of the (+) regions, and a dislocation straddling the stress dependent gap between (+) barriers.

PRECIPITATION ON SUBSTRUCTURE IN IRON-BASE ALLOYS

A. S. Keh, W. C. Leslie and G. R. Speich
Edgar C. Bain Laboratory for Fundamental Research
United States Steel Corporation Research Center
Monroeville, Pennsylvania

Abstract

An attempt is made to summarize the current state of knowledge of precipitation on defects in iron-base alloys, and the effect of precipitation on the properties of such alloys.

1. Introduction

The development and nature of substructure in metals and alloys have been described in several of the foregoing papers in this symposium. The effects of substructure on mechanical properties and recrystallization behavior have been discussed. As metallurgists, we are interested in understanding and employing as many different techniques as possible to control and improve the properties of engineering alloys. It is obvious, then, that we should consider the advantages to be gained by combining the effects produced by substructure and by precipitation from solid solution. Our understanding of these combined effects has been vastly improved in recent years by use of transmission electron microscopy, which allows us to study the details of precipitation on substructure.

Iron-base alloys are of particular interest, not only because of their paramount importance as engineering materials, but also because of the large number of possible combinations of defect structures and precipitates that exist. In cold-worked ferrite, the substructure can consist of dislocations clustered into cell walls, or of a uniform distribution of dislocations and some deformation twins. After annealing, the substructure can consist of low-angle boundaries. Cold-worked austenitic alloys can contain all the arrangements of defects that are possible in cold-worked ferrite, with the addition of stacking faults. The most complicated defect structures are those which result from the transformation from austenite to ferrite. If the rate of cooling is fairly slow, as after hot rolling, the resulting ferrite contains low-angle subboundaries. If the rate of cooling is high, as in a quench, or if the composition of the alloy is adjusted to produce a low Ms temperature, the resulting ferrite has a martensitic structure, containing a very high density of dislocations, closely-spaced boundaries produced by shear, and frequently, very fine twins within martensite plates. The purpose of this paper is to show how precipitation from solid solution is affected by substructure in ferritic, austenitic and martensitic alloys. Several examples will be cited of the use of precipitation on substructure to improve the properties of alloys.

Although research into the details of these processes is quite recent, a great deal of information is being developed very rapidly, so the authors hope they will be forgiven if they have overlooked any contributions.

2. Theory of Nucleation on Dislocations

According to the classical theory of nucleation, the total free energy change, ΔF, accompanying the formation of a nucleus of a second phase from a supersaturated solid solution can be expressed by

$$\Delta F = \Delta F_{volume} + \Delta F_{surface} + \Delta F_{strain} \cdots \qquad (1)$$

The change in volume free energy must be negative. The changes in surface free energy, $\Delta F_{surface}$, and strain free energy, ΔF_{strain}, due to formation of the nucleus, are positive. The total change of free energy is positive and increases to a maximum up to a critical size of the nucleus. When the radius of the nucleus exceeds the critical value, r_o, ΔF begins to decrease and the nucleus will then be stable.

The activation energy for precipitation is less at a dislocation than in the perfect lattice. Cahn (1) has developed a theoretical treatment of nucleation on dislocations. Assuming a cylindrical, noncoherent nucleus of radius r lying along a dislocation, he associated the strain energy of the dislocation with the strain energy required for nucleation, to reduce the barrier to nucleation. According to his treatment, the free energy per unit length of dislocation occupied by the nucleus can be expressed by

$$F = -A \log r + 2\pi \gamma r - \pi \Delta F_{volume} r^2 + C \qquad (2)$$

where

$A = \frac{Gb^2}{4\pi(1-\nu)}$ for an edge dislocation

$= \frac{Gb^2}{4\pi}$ for a screw dislocation

G = shear modulus

b = Burgers vector

ν = Poisson's ratio

γ = interfacial energy of the boundary

A minimum in free energy was found when the quantity

$$\alpha = \frac{2A \Delta F_{volume}}{\pi \gamma^2} < 1$$

This circumstance, which is analogous to the presence of a Cottrell atmosphere, is indicated schematically in Fig. 1, at A. In Cahn's model, the free energy can then increase with increasing radius of the nucleus. If the quantity $\alpha > 1$, i.e., if supersaturation is higher, this barrier can disappear, and the precipitate can nucleate and grow at a rate limited only by diffusion. Cahn's model predicts that dislocations become more effective catalysts for nucleation, relative to homogeneous nucleation, with increasing temperature and increasing supersaturation. The temperature and concentration dependence of the nucleation energy is greater at dislocations than for homogeneous nucleation.

Since Cahn's paper was written, the physical situations existing during precipitation have been found to be so complex (2) that his relatively simple model cannot be expected to correspond to many of the observations. In our own observations, for example, it has been found that the temperature and concentration dependence of matrix nucleation is greater than for dislocation nucleation.

3. Precipitation on Dislocations and Subboundaries in Ferritic Alloys

3.1 Precipitation of Interstitial Solutes

With the advent of transmission electron microscopy, precipitation in Fe-C and Fe-N alloys has been investigated extensively in several laboratories (3-8), and the effects of dislocations and subboundaries on the kinetics and morphology of precipitation have become evident. In general, dislocations are preferred sites for precipitation of carbides and nitrides in iron, but grain boundaries are preferred at high aging temperatures (low supersaturation) and matrix nucleation occurs at low aging temperatures (high supersaturation). Because of uncertainty as to the nature of the matrix sites, the term "homogeneous nucleation" will not be used. The exact mode of precipitation is critically dependent upon solute concentration, aging temperature, and dislocation density.

In both Fe-C and Fe-N alloys, a metastable phase is precipitated at low aging temperatures. In common with nearly all low-temperature precipitates in cubic metals, the particles form as disks on $\{100\}_\alpha$ planes, the disks being the configuration of minimum strain energy and $\langle 100\rangle_\alpha$ being the directions of minimum modulus of elasticity (2). These phases are not affected by the nucleation site; they are the same whether formed on dislocations or in the matrix. Most investigators have concluded that the low-temperature carbide is the hexagonal ε (7,9,10) but there remains a possibility that it may have a body-centered tetragonal structure, analogous to the structure of the α'' nitride, $Fe_{16}N_2$ (3,11). At higher aging temperatures, cementite, Fe_3C, is formed. It appears as dendrites on $\{110\}_\alpha$, with the branches growing in $\langle 111\rangle_\alpha$ (12,13). Both carbides nucleate preferentially on dislocations, although they also nucleate on unidentified matrix sites, at high supersaturation.

In the iron-nitrogen system, there appears to be no doubt of the identification of the metastable nitride precipitated from ferrite at low aging temperatures; it is the α'' phase, $Fe_{16}N_2$ (5,14,15). The γ' phase, Fe_4N, precipitated at higher temperatures, is face-centered cubic. It can nucleate at dislocations or at grain boundaries.

It is worth repeating that in both the Fe-C and Fe-N systems, the structure of the precipitate is not affected by the nucleation site. This is not necessarily true in other systems; for example, in some aluminum alloys where a sequence of precipitation occurs, the microstructure consists of GP zones in the matrix and an intermediate phase on the dislocations (2).

If the dislocation density is not very high ($\lesssim 10^8/cm^2$), and if the aging temperature is low, uniform matrix precipitation is observed, in addition to precipitation on dislocations. At higher aging temperatures, the supersaturation of the same alloy is less, and precipitates form exclusively on dislocations. Fig. 2 illustrates these differences in an Fe-0.02 wt.% N alloy, aged at 100° and at 200°C. If the dislocation density in an Fe-N alloy is high ($> 10^9/cm^2$), precipitation on dislocations

predominates, but the details of precipitation change with aging temperature. At low aging temperatures, precipitation occurs on all dislocation segments, irrespective of dislocation orientation. The precipitates thus formed are dendritic (Fig. 3a). In the same alloy aged at higher temperatures, precipitates form only on dislocations lying on $\{100\}_\alpha$, the habit plane of the precipitate (Fig. 3b). This difference is presumed to be due to the difference in chemical driving force. At the higher aging temperature, ΔF_{volume} in Eq. 1 is smaller, and dislocations must be favorably oriented for their strain energy to suffice for nucleation. At the lower temperature, the nitrogen atoms segregate to all dislocations, and since the chemical driving force is higher, precipitation occurs even on dislocations not lying on $\{100\}_\alpha$. In this circumstance, jogs probably first form on $\{100\}_\alpha$, then nitride particles grow from these jogs.

Dislocation orientation has a definite effect on the precipitation of carbides and nitrides in alpha iron. On pure screw dislocations, the precipitate can form as a spiral (Fig. 4). The alloy illustrated is Fe-0.45% Mn-0.017% C, quenched from 720°C, then aged 1 hour at 100°C. The plane of the foil is $\{110\}$ and the directions of the dislocations are $[1\bar{1}1]$ and $[1\bar{1}\bar{1}]$. It is well known that screw dislocations can be converted to helices by vacancy condensation. Such helices have not been observed in quenched, high-purity iron. Their presence in the Fe-Mn-C alloy suggests that the substitutional or interstitial solute atoms inhibit the annealing-out of vacancies, which then congregate at screw dislocations, prior to precipitation.

Precipitation can occur preferentially on one side of edge dislocations. Fig. 5 shows a simple tilt boundary, decorated with a precipitate of $Fe_{16}N_2$. It was not established whether the precipitates form on the tension or on the compression side of the dislocations. They would be expected to form on the tension side if vacancies were not involved in the precipitation process. In either case, precipitation should be confined to one of the three $\{100\}$ planes, which is what is observed in Fig. 5. The subboundary illustrated also contains a few "foreign" dislocations, which intersect and interact with the edge dislocations, forming short segments at the points of intersection. The mode of precipitation on these "foreign" dislocations and short dislocation segments differs from that on the edge dislocations.

Some dislocations on subboundaries are more favorable sites for precipitation than others. Precipitation in an Fe-3% Si-0.01% C alloy seemed to favor the [100] segments of the dislocation network formed by the reaction $a/2\ [111] + a/2\ [1\bar{1}\bar{1}] \rightarrow a[100]$, (Fig. 6). In Fig. 7, precipitation on one set of dislocations in the subboundary has a stepwise appearance and appears very dark, whereas the precipitate on the horizontal parallel set of dislocations is much lighter in shade. The zigzag dislocations are believed to be a metastable configuration formed by a dislocation interaction, as shown schematically in Fig. 7.

3.2 Precipitation of Substitutional Solutes

In a sustained effort to determine the important factors governing the precipitation of substitutional solutes from ferrite, studies have been made of the binary alloys of iron with copper and gold (16), titanium and niobium (17) and phosphorus (18). Nucleation in an alloy containing 1.1 atom per cent copper, aged at temperatures from 500 to 700°C after quenching from 840°C, was compared with nucleation in an alloy containing 1.1 atom per cent gold, similarly treated. The precipitating phase in both instances is face-centered cubic, being a dilute solution of iron in copper or in gold. In the Fe-Au alloy, nucleation occurred exclusively on dislocations and subboundaries, (Fig. 8), but in the Fe-Cu alloy, nucleation was general (Fig. 9). Hornbogen(16) attributed this difference to the difference in atomic size of the solute atoms. The copper atom is nearly the same size as the iron atom, and the atomic volumes of matrix and precipitate are almost identical. Little strain energy should be required for nucleation of the copper-rich phase. On the other hand, the gold atom is much larger than the iron atom ($r_{Au}/r_{Fe} = 1.13$) and the atomic volume of the precipitate is much greater than that of iron. In the precipitation of copper, almost the only barrier to be overcome is the surface energy. To nucleate a particle of gold, however, a large strain energy barrier must be overcome, in addition to the surface energy, so the core energy of dislocations must be utilized. Precipitation tends to be confined to dislocations and subboundaries. This conclusion of the predominant effect of solute atom size on selection of nucleation site, based as it is on one solute concentration, would be strengthened by similar studies made with other concentrations. As will be shown later, copper precipitates can be restricted to dislocations when the supersaturation is lower.

Hornbogen proposed that nucleation of gold-rich particles on dislocations occurs in several steps:

1. Segregation of gold atoms to dislocations.
2. Formation of stacking faults on $\{100\}_\alpha$ by the reaction

$$\frac{a}{2}[111] \rightarrow \frac{a}{2}[110] + \frac{a}{2}[001].$$

3. Segregation of gold to the stacking fault.

The a/2 [110] dislocation is glissile and can move as fast as gold atoms can segregate into the stacking fault. The a/2 [001] dislocation is sessile and remains in its original position as the stacking fault grows.

Speich (17) has found that dislocations and grain boundaries in ferrite are preferred sites for nucleation in Fe-Ti and Fe-Nb alloys. The precipitates are the $MgZn_2$ type Laves phases Fe_2Ti and Fe_2Nb, respectively.

Precipitation in the Fe-P system shows some interesting differences from the examples discussed previously. To obtain a high degree of supersaturation and a controlled density of dislocations, Hornbogen (18) quenched

a ferritic Fe-1.8% P alloy from 1100°C, immediately after hot rolling. The sequence of precipitation during subsequent aging at 500°C is shown in Fig. 10. The as-quenched specimen contained subboundaries and isolated dislocations (Fig. 10a). Precipitates began to form at dislocation intersections (Fig. 10b) after 4 hours at 500°C. Considerable growth had occurred after 10 hours' aging (Fig. 10c). Only after 54 hours' aging at 500°C did nucleation occur in the matrix, and then the particles differed from those formed on dislocations, being rods instead of plates. The rods grew on $\{100\}_\alpha$ in $\langle 012\rangle_\alpha$ directions.

It is a general observation (3,6,18) that precipitate particles nucleated on dislocation networks (subboundaries) do not grow to be as large as those nucleated on isolated dislocations or in the matrix. When nucleation sites are closely spaced, as in a subboundary, the volume from which a growing particle can draw solute atoms is severely limited, and growth soon stops. This limitation is not imposed on particles growing on isolated dislocations, or in the matrix. This effect is illustrated in Fig. 11.

Studies of rates of growth of precipitate particles are complicated by the general finding (3,16,19) that not all nuclei grow until the matrix has reached the equilibrium concentration of solute. Growth of larger particles occurs at the expense of smaller ones, long before the matrix is depleted of solute. A particle on an isolated dislocation can grow at the expense of smaller particles in a subboundary, or in the matrix.

It has also been found (3,18) that the temperature dependence of matrix nucleation is greater than that of dislocation nucleation. This effect, in an Fe-1.8% P alloy, is illustrated in Fig. 12. Matrix nucleation is favored by decreasing temperature, i.e., increasing supersaturation. By extrapolation of the lines in Fig. 12, matrix and dislocation nucleation of phosphides would be simultaneous at about 350°C.

4. Precipitation on Substructure in Austenitic Alloys

4.1 Precipitation on Dislocations

The factors which influence precipitation on dislocations in ferrite also affect precipitation on dislocations in austenite. The size effect discussed in Section 3.2 is apparently involved in some interesting observations made by Irani and Honeycombe (20) on precipitation of carbides on dislocations in retained austenite in Fe-4% Mo-02% C and Fe-1% V-0.2% C alloys. Specimens were quenched, then tempered at 500 and 700°C. In the Fe-Mo-C alloy tempered at 500°C helical dislocations were formed very similar in appearance to those illustrated in Fig. 4 of this paper. Additional tempering caused the formation on dislocations of a very fine precipitate, which later became recognizable as Mo_2C. On the other hand, dislocations did not play a major role in precipitation of carbides in the Fe-V-C alloy. These carbides appeared to form in the matrix from zones rich in vanadium and carbon. At least part of the difference in precipitation was attributed to the difference in atomic diameter between

molybdenum and vanadium. The larger molybdenum atom would tend more to segregate at dislocations than would the atoms of vanadium. Also, nuclei of molybdenum carbide would be less easily accommodated in the perfect lattice than would nuclei of vanadium carbide, which has a smaller unit cell. The net effect on nucleation is analogous to the differences in the precipitation of copper and gold from alpha iron.

Dislocations can be generated around large, undissolved carbide particles in austenite, or in ferrite, during the cooling of the steel, because of the stresses generated by contraction of the matrix around the particle. Such dislocation networks can serve as nucleation sites for precipitation during subsequent aging (17,21).

4.2 Precipitation on Twin Boundaries in Austenitic Alloys

Hatwell and Berghezan (22) employed a Type 316 stainless steel in a study of precipitation of $M_{23}C_6$ carbides at the boundaries of annealing twins in austenite. If the specimens are carefully handled during the solution and aging treatments, the twin boundaries remain coherent and are not preferred sites for precipitation. However, if the quench is drastic, or if the specimen is strained plastically prior to aging, dislocations pile up at the twin boundaries, i.e., coherency is lost, and these boundaries then become preferred sites for precipitation. The shape of the precipitated carbide in this instance depended upon the nucleation site; at grain boundaries the carbides were dendritic, whereas at the twin boundaries the precipitate particles were triangular, growing on $\{111\}_\gamma$ planes.

It should be noted here that the boundaries of mechanical twins in ferritic alloys always contain a high density of dislocations; matrix-mechanical twin boundaries are never coherent, so they should provide an abundance of nucleation sites for precipitation.

4.3 Precipitation on Stacking Faults in Austenitic Alloys

It was first pointed out by Suzuki (23) that solute atoms can segregate to stacking faults and thereby lower the stacking fault energy. Hendrickson (24), using the data of Howie and Swann (25), and Suzuki (26) have recently calculated the extent of such segregation. Once segregation has occurred, precipitation at the stacking fault will be favored because of the reduction of the surface energy term, $\Delta F_{surface}$, in Eq. 1. Nicholson (27) has shown that stacking faults in an Al-7% Mg alloy can act as nucleation sites for an hexagonal precipitate. More recently, van Aswegen and Honeycombe (28) have observed the precipitation of NbC on stacking faults in an 18% Cr-10% Ni-1% Nb austenitic stainless steel. After quenching from 1300°C, precipitation of NbC occurred during tempering in the range 650° to 850°C. Dislocations in the as-quenched alloy were not dissociated. Stacking faults began to appear after 5 hours at 700°C, and longer periods at this temperature resulted in formation of NbC, as shown in Fig. 13. The precipitation of the carbide at the stacking faults was attributed to the prior segregation of niobium atoms. Tempering above and below the 650°-

950°C range led to precipitation of NbC on undissociated dislocations, but the maximum strengthening corresponded to the onset of precipitation on stacking faults.

Similar observations on stacking fault precipitation in the same alloy were made by Pickering, Burns and Keown (29). They determined that the faults lie on $\{111\}_\gamma$, and the orientation relationship is $\{100\}_{NbC} \| \{100\}_\gamma$ and $\langle 100 \rangle_{NbC} \| \langle 100 \rangle_\gamma$.

5. Precipitation on Transformation Substructure

5.1 Types of Transformation Substructure

Kelly and Nutting (30,31) found principally two types of transformation substructure in iron-base alloys. The first type, characteristic of high-carbon martensites, consisted of internally twinned plates. This is illustrated by the microstructure of a quenched 1.0% C steel (Fig. 14). The twins, which are parallel to $\{112\}_M$, are about 100 Å thick and irregularly spaced. These internal twins evidently arise from the need for an inhomogeneous "second" shear accompanied by a "first" shear which is homogeneous on a macroscopic scale, to generate the martensite lattice from the austenite. The internal twins constitute this "second" inhomogeneous shear. The internally twinned plates have also been observed (30,31) in quenched 0.4 and 0.8% C steels, in martensite formed at -95° and -196°C in an Fe-20% Ni-0.8% C steel, and in Fe-30% Ni alloys by Nishiyama and Shimizu (32,33) and Warlimont (34).

The second type of transformation substructure is characteristic of quenched martensites in low-carbon steels and in 18-8 stainless steel. It consists of martensite needles with no internal twinning but with a very high dislocation density. An example from a 0.1% C steel is shown in Fig. 15. The long axis of the needles is parallel to $\langle 111 \rangle_M$. As the carbon content of the martensite is increased there is an increasing tendency for the needles to be grouped together in the form of "sheets". The orientation difference between needles in the "sheet" is usually only a few degrees although in some cases they seem to be twin related. This type of transformation substructure is also characteristic of martensite formed in Fe-30% Ni alloys and in other alloys of similar nickel content, such as the maraging steels (35). An example of the structure of an Fe-30% Ni martensite is shown in Fig. 16.

The transition from needles with a very high dislocation density in a 0.1% C steel to internally twinned plates in a 1.0% C steel occurs gradually as the carbon content is increased. Intermediate carbon contents contain mixtures of both types. Kelly and Nutting (31) postulated that the two factors controlling the type of transformation substructure are the transformation temperature and the stacking fault energy, with the composition of the steel only affecting the substructure through its effect on these two parameters. High Ms temperatures and low stacking fault energies favor the formation of martensite needles, whereas low Ms temperatures and high stacking fault energies favor the formation of internally twinned plates.

5.2 Tempering of Iron-Carbon Martensites

Kelly and Nutting (30,31) examined the structural changes during the

tempering of 0.14 and 1.0% C steels and Turkalo (36) has studied the tempering behavior of a 0.42% C steel. In the 0.14% C steel, auto-tempering occurred during quenching and Widmanstätten carbides in the form of plates or laths about 100 Å wide and 1500 Å long were visible in about 10% of the grains in the as-quenched structure. After tempering at 300°C, carbide particles were visible in all grains. Further tempering increased the thickness of the carbides.

In the 0.42% C steel studied by Turkalo (36), the primary substructure appeared to be martensite needles with a high dislocation density, although some internal twinning was evident. Although Turkalo indicated that the twins were within the "needles", the structure may actually be a mixture of internally twinned plates and twin-free martensite needles, as Kelly and Nutting (30) found in a 0.4% C steel. On tempering at 205°C carbide films appeared at the martensite needle boundaries. After tempering at 315°C, two types of carbides appeared within the grains--"streaky" carbides and "crystallographic" carbides which formed in two directions in the martensite. The latter carbides appear to be parallel to $\{110\}_\alpha$. Examples of both types are shown in Fig. 17. The carbide films at the martensite needle boundaries become thicker and less continuous at higher tempering temperatures. With further increases in tempering temperature, spheroidization of the carbides occurred, along with the formation of subboundaries in the ferrite, and eventually, recrystallization of the ferrite. The structure after tempering at 595°C consisted of fine ferrite grains and spheroidized carbides.

In 1.0% C steel the primary substructural feature that influences precipitation appears to be the internal twins (30,31). Tempering at 200°C resulted in the appearance of carbides lying along the twins in the martensite, together with tiny precipitates perpendicular to the twin plane. These small precipitates disappeared after tempering at 300°C, whereas the lath-like carbides lying along the twins became more prominent (Fig. 18).

These latter carbides were identified as cementite, with the orientation relationship:

$$(211)_\alpha \| (001)_{Fe_3C}$$

$$[0\bar{1}1]_\alpha \| [100]_{Fe_3C}$$

$$[1\bar{1}1]_\alpha \| [010]_{Fe_3C}$$

The small precipitates formed normal to the twin plane are believed to be ε carbide, although the diffraction patterns obtained by Kelly and Nutting (31) were not sufficient to allow identification.

5.3 Precipitation from Substitutional Martensites

Recently, much attention has been focused on precipitation from substitutional martensites, principally because of development of precipitation hardening stainless steels (37) and "maraging" steels (38). The structure of the martensite in these alloys is of the same type shown

in Fig. 16 for an Fe-20% Ni alloy. The martensite "needles" contain a very high density of dislocations, but no internal twins. The substructural features affecting precipitation are the boundaries between the needles and the dislocations within the needles. A polygonized substructure can be formed by recovery of the transformation substructure itself, as shown in Fig. 19 for an Fe-18% Ni-7% Co alloy aged 100 hrs. at 500°C. In this alloy no precipitation occurred since it was aged in an $\alpha + \gamma$ region.

Another process that may occur during precipitation in substitutional martensitic alloys is the formation of austenite, since the alloys are generally aged at a temperature at which austenite is stable. The structure of an Fe-20% Ni alloy aged in the $\alpha + \gamma$ region for 100 hrs. at 500°C is shown in Fig. 20. X-ray diffraction indicated that the specimen contained 40% austenite after this treatment. The extinction fringes are believed to outline the thin films of austenite, which appear to form in the martensite needle boundaries; thus, the sites for austenite formation may be controlled by the original transformation substructure. In alloys in which an intermetallic compound precipitates, recovery of the transformation substructure and formation of austenite may be occurring simultaneously with precipitation.

The precipitation of intermetallic compounds from martensitic alloys is affected principally by the dislocations within the martensite needles. Fig. 21 shows the very fine dispersion of Ni_3Ti particles that forms on aging of an Fe-20% Ni-1% Ti alloy. Fig. 22 is an example of precipitation of copper in an Fe-20% Ni-10.7% Cu alloy. Fig. 23 shows precipitation in an Fe-18% Ni-7% Co-5% Mo alloy, which has nearly the same composition as some maraging steels, but without titanium. In all three instances the precipitate occurs in an extremely fine dispersion as a result of the high density of dislocations giving a high density of nucleation sites.

6. Effects and Applications of Precipitation on Substructure

6.1 The Role of Substructure in Quench-Aging and Strain-Aging of Iron and Steel

It has been demonstrated (3,6,19) that the strengthening associated with quench-aging in Fe-C and Fe-N alloys and in commercial low-carbon steels, depends upon a uniform dispersion of fine precipitated particles in the matrix. If precipitation is restricted to the dislocations present before aging, an uneven dispersion of relatively coarse particles results, and the interparticle spacing is uaually too great for effective strengthening.

In contrast to quench aging, strain aging in iron and steels is strongly dependent upon interactions between interstitial solute atoms and the dislocations introduced before or during the aging treatment. A question frequently arises as to whether the strengthening associated with strain-aging is due to segregation of interstitial atoms to dislocations, to the actual formation of precipitates at dislocations, or both. According to Cottrell and Bilby (39) the dislocations should be saturated when the concentration of interstitial solutes reaches one atom per atom plane per dislocation line. Later experiments, especially those employing internal friction to determine the kinetics of precipitation, suggest a higher degree of segregation (40-42). These results suggested that precipitation, as well as segregation, occurred during strain aging. Wilson and Russell (43), using a replica technique,

showed some evidence of precipitation during strain aging. The Cottrell-Bilby theory has been modified by Bullough and Newman (44) to accommodate precipitation.

By means of transmission electron microscopy, Leslie and Keh (45) have shown that precipitation need not necessarily occur during strain aging. In an Fe-C alloy, slowly cooled from the annealing temperature, and in an Fe-N alloy quench-aged at a very low temperature then strained and aged, no additional precipitates were observed on dislocations, although there was a return of the yield point, and a sharp upward shift in the flow curves. The structures prior to strain aging consisted of ferrite and large carbide or small nitride particles. During straining and aging, a small fraction of the carbon and nitrogen probably re-dissolved and segregated along dislocation lines. However, in these circumstances, it is quite impossible for new particles to form. As pointed out by Kelly and Nicholson (2), a precipitate on a dislocation is not in a lower energy state than one of the same type in the matrix, and there can be no tendency for the former to grow while the latter dissolves.

On the other hand, if one starts with Fe-C or Fe-N, or with a low-carbon steel, in the condition of a supersaturated solid solution, then strains and ages the specimens, precipitation on dislocations will occur in the later stages of aging. This is superposing quench aging upon strain aging. Fig. 24 illustrates the aging of an Fe-0.02% N alloy, quenched from 500°C, then strained 3% in tension. After one minute at 100°C, no precipitates could be seen on the dislocations introduced during prestraining; however, an appreciable amount of strain aging had occurred. The strain aging index continued to increase with aging time, reaching a plateau after 10 minutes. At this point, the first fine precipitates were observed on dislocations. As aging proceeded, the alloy continued to strengthen. The precipitates on dislocations continued to grow, and particles began to form in the matrix as shown in Fig. 25a. After two hours at 100°C, the strain aging index reached a maximum. As aging progressed, the nitride particles agglomerated, freeing some dislocation segments (Fig. 25b). This change in structure was accompanied by a decrease of the strain aging index. It should be noted here that the first particles seen on dislocations are discrete platelets, lying on $\{100\}_\alpha$, with a diameter of about 30 Å. This observation differs from the theory of Bullough and Newman (44), who deduced a continuous particle, lying along the dislocation line.

The strain aging of steels is usually considered to have undesirable consequences in the way of reduced ductility, embrittlement and surface flaws, but overemphasis of these effects can serve to obscure the fact that strain aging can be an economical means of raising the strength level. The recent interest in warm-working of steels is a case in point (46). When steels are worked in the temperature range between 150 and 350°C, aging occurs simultaneously with straining. The rate of work-hardening is much greater than during straining at room temperature. It has been found (19) that the dislocation density after straining a low-carbon steel 3% at 200°C is about five times higher than in the same steel strained 4% at room temperature. This evidence supports the proposal (45) that dislocations strongly pinned during strain aging are not freed from their atmospheres, but that straining proceeds by the generation of new dislocations.

6.2 Control of Recrystallization by Precipitation on Substructure

Precipitation on substructure can be used, in a practical sense, to control the structure and properties of alloys. One such instance is the use of precipitation on substructure in a cold-worked metal to control the kinetics of recrystallization, and the grain size and shape, texture and mechanical properties in the annealed, recrystallized condition. The process depends upon solution of an alloying element or compound in the alloy. This may occur during hot rolling. Following the solution treatment, the alloy is cooled rapidly to retain the solutes in supersaturated solid solution, then cold worked and annealed. By suitable control of the annealing cycle, precipitates can be nucleated at subboundaries (cell walls) before the cells have grown to form recrystallized grains. Nucleation of such precipitates stabilizes the cell structure, greatly decreasing the number of cells which can grow, thereby decreasing the overall rate of recrystallization, and producing fewer and larger recrystallized grains.

Commercially, the most important application of this process is in the production of low-carbon, aluminum-killed sheet steels for applications involving severe forming. The precipitate in this instance is aluminum nitride. Fig. 26, taken from Rickett, et al (47), illustrates the drastic change in recrystallization kinetics that results from the precipitation of this compound during the annealing of cold-rolled low-carbon steel. The phenomenon does not depend upon precipitation of aluminum nitride alone, however. The following examples are taken from a dilute alloy of copper in iron (48). Fig. 27 illustrates the differences in structure produced in iron by precipitation during the process of recrystallization. In the high-purity iron, the recrystallized grains are nearly equiaxed. In the dilute Fe-Cu alloy, the grains are much larger and are in the shape of pancakes, with their diameter being about four times their thickness. This is the type of ferrite structure which gives aluminum-killed, low-carbon sheet steel its optimum drawing properties. The stepped annealing treatment of 3 hours at 500°C, followed by 5 hours at 700°C, initiates precipitation on the cell walls in the cold-worked alloy, then completes the process of recrystallization.

To obtain this structure of elongated recrystallized grains two factors are necessary:

1. A decrease in the number of "nuclei" for recrystallization, i.e. a decrease in the number of cells which grow to become recrystallized grains. Fewer "nuclei" results in fewer and larger recrystallized grains.

2. Barriers at the boundaries of cold-worked grains which prevent the new recrystallized grains from growing across these boundaries. The recrystallized grains tend to conform to the shape of the prior cold-worked grains.

Both factors are present when precipitation occurs preferentially on cell walls and on grain boundaries. Fig. 28, taken from Leslie, et al (49), shows preferential precipitation of copper in cell walls, which is effective in preventing migration of these walls, i.e., recrystallization is strongly inhibited. This preferential precipitation occurs despite the

fact that, as discussed in Section 3.2, there is not a strong elastic interaction between copper atoms and dislocations in iron. The effect might be even more pronounced if there were a large size difference between the iron and the solute atoms.

Fig. 29 shows the other requirement for the elongated grain ferrite structure, precipitation in grain boundaries. The growth of the few cells which do break away from the contraint of the precipitate particles in cell walls is stopped at the grain boundaries. Thus, only one of two grains may be nucleated within each prior cold-worked grain, and these grow principally within the bounds of the cold-worked grain, giving the pronounced elongation shown in Fig. 27.

Precipitation occurring after cold rolling, but before recrystallization, can also be used to control texture. The precipitation of copper in cold-rolled iron, for example, tends to increase the retention of the cold-worked texture after annealing and prevents the formation of the usual annealing texture (48).

This procedure of controlling microstructure and texture by preferential precipitation on substructure should be applicable to many metallic systems (e.g. iron in aluminum, "doped" tungsten), but to date it has not been consciously exploited to any great extent. Increased application may follow improved understanding of the process.

6.3 Use of Substructure to Reduce Grain Boundary Embrittlement

In systems wherein grain boundary embrittlement due to segregation of solutes is a problem, ductility can be improved by introducing substructure, which serves to decrease the concentration of solute at the grain boundaries. For example, it is impossible to quench an iron-1.8% phosphorus alloy from high temperatures without producing intergranular cracks (50). However, if the alloy is hot-worked immediately before quenching, the cracks are eliminated and the alloys can subsequently withstand slight plastic deformation at room temperature. The density of substructure introduced by hot rolling is illustrated in Fig. 30. After hot rolling to 80% reduction in thickness at 1100°C, the high angle grain boundaries are not visible in the welter of dislocations.

6.4 Reduction of Creep Rate by Precipitation on Substructure in Austenite

A fourth example of the practical value of precipitation on substructure is the improvement of the creep characteristics of Type 316 austenitic stainless steel developed by prestraining at room temperature, followed by aging at 480° then at 705°C (51). This pretreatment leads to the precipitation of $M_{23}C_6$ carbides at dislocation sites. In the absence of prestrain, creep testing at 705°C results in the precipitation of coarse carbides at grain boundaries. For a testing temperature of 705°C, the minimum creep rate decreases and the rupture life increases as the prestrain is increased up to 25 or 30%. At these levels of prestrain, most of the dislocations are present in broad deformation bands. Precipitation within these bands, as shown in Fig. 31, is much more effective in decreasing the minimum creep rate than is a general dispersion of particles. A pretreatment of 24 hours at 480°C and 216 hours at 705°C decreases the minimum creep rate by a factor

of 250 and increases the rupture life by a factor of 10 during creep testing at 705°C.

Hatwell and Berghezan (22), who also employed Type 316 stainless, found precipitation within grains only after 20% plastic strain. The difference between their results and those of Garofalo, et al (51), is almost certainly due to the two-stage aging treatment used by the latter. The initial treatment at 480°C nucleated carbides at dislocations and the subsequent treatment at 705°C allowed these to grow. Hatwell and Berghezan aged their specimens at 750°C after plastic deformation, a temperature too high for nucleation on dislocations, unless the dislocation density is quite high.

Irvine, Murray and Pickering (52) have shown that precipitation on dislocations and subboundaries in an austenitic stainless steel can be controlled by warm-working, as an alternative to the straining and aging sequence employed by Garofalo, et al (51), and by Hatwell and Berghezan (52).

Acknowledgment

The authors wish to thank F. W. Aul, R. C. Glenn, R. L. Miller, C. M. Owens, R. D. Schoone, and D. W. Stevens, of the staff of the Edgar C. Bain Laboratory, for their assistance in these investigations. Much of the work was carried out by E. Hornbogen, who has made substantial contributions to our knowledge in this field. The consistent encouragement of R. L. Rickett over a period of years has been of great help in the continuation of these studies.

References

1. J. W. Cahn, Acta Met. 5, 169 (1956).

2. A. Kelly and R. B. Nicholson, to be published, Progress in Materials Science, Academic Press, N.Y.

3. W. C. Leslie, Acta Met. 9, 1004 (1961).

4. E. Smith, Direct Observations of Imperfections in Crystals, Interscience, N.Y., 1962, p.203.

5. W. Pitsch, Arch. Eisenhuttenw. 32, 493 (1961).

6. A. S. Keh and H. A. Wriedt, Trans. AIME 224, 560 (1962).

7. K. F. Hale and D. McLean, to be published.

8. D. Hull and I. L. Mogford, Phil. Mag., 6, 535 (1961).

9. W. Pitsch and A. Schrader, Arch. Eisenhuttenw. 29, 715 (1958).

10. A. L. Tsou, J. Nutting and J. W. Menter, J. Iron Steel Inst. 172, 163 (1952).

11. R. H. Doremus and E. F. Koch, Trans. AIME 218, 591 (1960).

12. W. C. Leslie, R. M. Fisher and N. Sen, Acta Met. 7, 132 (1959).

13. W. Pitsch and A. Schrader, Arch. Eisenhuttenw. 29, 485 (1958).

14. K. H. Jack and D. Maxwell, J. Iron and Steel Inst. 170, 254 (1952).

15. G. R. Booker, J. Norbury and A. L. Sutton, Ibid. 187, 205 (1957).

16. E. Hornbogen, Acta Met. 10, 525 (1962).

17. G. R. Speich, Trans. AIME 224, 850 (1962).

18. E. Hornbogen, to be published, Trans. ASM.

19. A. S. Keh and W. C. Leslie, to be published, Structure and Properties of Engineering Materials, John Wiley and Sons, N.Y.

20. J. J. Irani and R. W. K. Honeycombe, 5th Inter. Con. for Electron Micros., Academic Press, N.Y., 1962, 1, p.HH-9.

21. J. Nutting and J. M. Arrowsmith, Iron Steel Inst. Spec. Report No. 70, 1961, p.147.

22. A. H. Hatwell and A. Berghezan, Iron Steel Inst. Spec. Report No. 64, 1959, p.88.

23. H. Suzuki, Sci. Rep. Res. Inst. Tohoku Univ. A1, 183 (1949).

24. A. A. Hendrickson, Acta Met. 10, 900 (1962).

25. A. Howie and P. R. Swann, Phil. Mag. 6, 1215 (1961).

26. H. Suzuki, J. Phys. Soc. Japan 17, 322 (1962).

27. R. B. Nicholson, to be published, Electron Microscopy and Strength of Crystals, John Wiley and Sons, N.Y.

28. J. S. T. van Aswegen and R. W. K. Honeycombe, Acta Met. 10, 262 (1962).

29. F. B. Pickering, K. W. Burns and S. R. Keown, 5th Int. Conq. Electron Micros. Academic Press, N.Y., 1962, 1, p.CC-4.

30. P. M. Kelly and J. Nutting, Proc. Roy. Soc. 259, 45 (1960).

31. P. M. Kelly and J. Nutting, J. Iron Steel Inst. 197, 199 (1961).

32. Z. Nishiyama and K. Shimizu, Acta Met. 9, 980 (1961).

33. K. Shimizu, J. Phys. Soc. Japan 17, 508 (1962).

34. H. Warlimont, 5th Int. Conq. Electron Micros., Academic Press, N.Y., 1, p.HH-6.

35. G. R. Speich, to be published.

36. A. M. Turkalo, Trans. ASM 54, 344 (1961).

37. A. J. Lena, Precipitation from Solid Solution, ASM Cleveland, 1959, p.244.

38. R. F. Decker, J. T. Eash, and A. J. Goldman, Trans. ASM 55, 58 (1962).

39. A. H. Cottrell and B. A. Bilby, Proc. Phys. Soc. 62A, 49 (1949).

40. S. Harper, Phys. Rev. 83, 709 (1951).

41. W. Dahl and K. Lücke, Arch. Eisenhuttenw. 25, 241 (1954).

42. W. R. Thomas and G. M. Leake, J. Iron Steel Inst. 180, 155 (1955).

43. D. V. Wilson and B. Russell, Acta Met. 8, 468 (1960).

44. R. Bullough and R. C. Newman, Proc. Roy. Soc. 266, 209 (1962).

45. W. C. Leslie and A. S. Keh, J. Iron Steel Inst. 200, 722 (1962).

46. E. Nachtman and E. B. Moore, J. Metals 10, 281 (1958).

47. R. L. Rickett, S. H. Kalin and J. T. Mackenzie, Jr., Trans. AIME 185, 242 (1949).

48. W. C. Leslie, Ibid. 221, 752 (1961).

49. W. C. Leslie, J. T. Michalak and F. W. Aul, to be published, **Metallurgical** Soc. Conf. Volumes, John Wiley and Sons, N.Y.

50. E. Hornbogen, Trans. ASM 53, 569 (1961).

51. F. Garofalo, F. von Gemmingen and W. F. Domis, Ibid. 54, 430 (1961).

52. K. J. Irvine, J. D. Murray and F. B. Pickering, J. Iron Steel Inst. 196, 166 (1960).

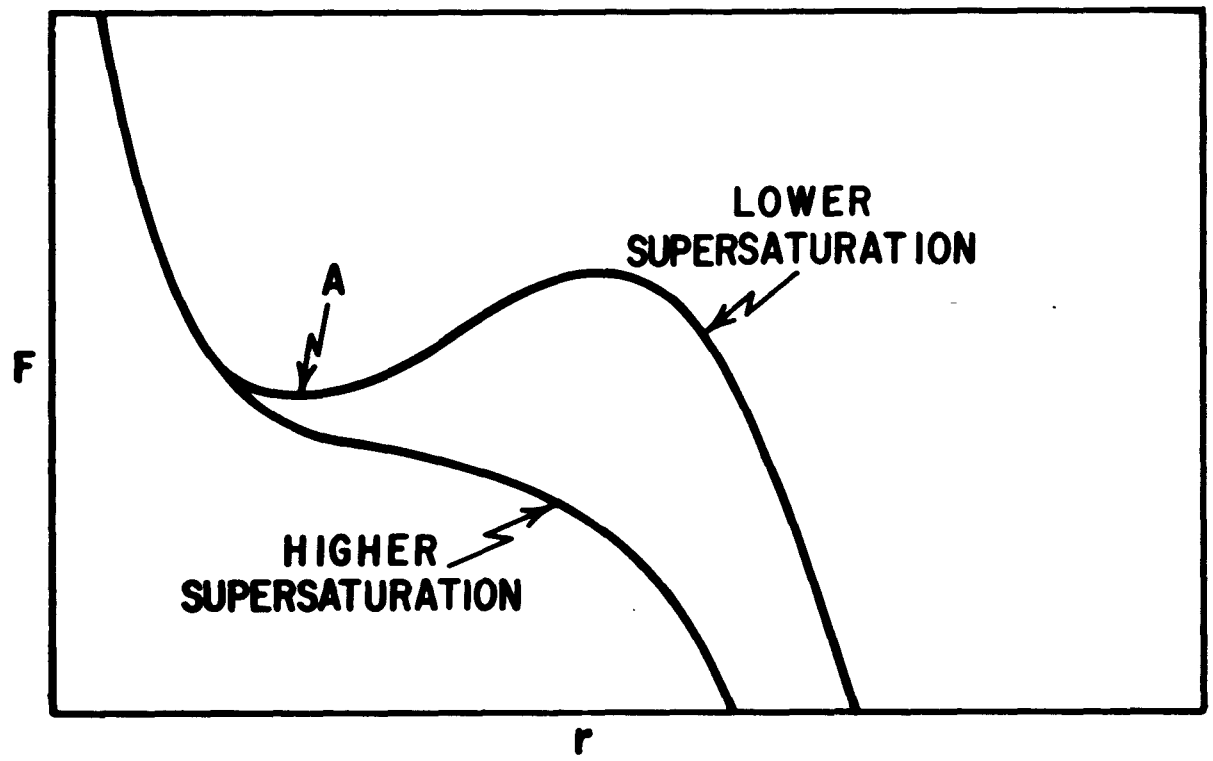

FIG. 1 -- FREE ENERGY PER UNIT LENGTH OF A CYLINDRICAL, NON-COHERENT NUCLEUS SURROUNDING A DISLOCATION[1].

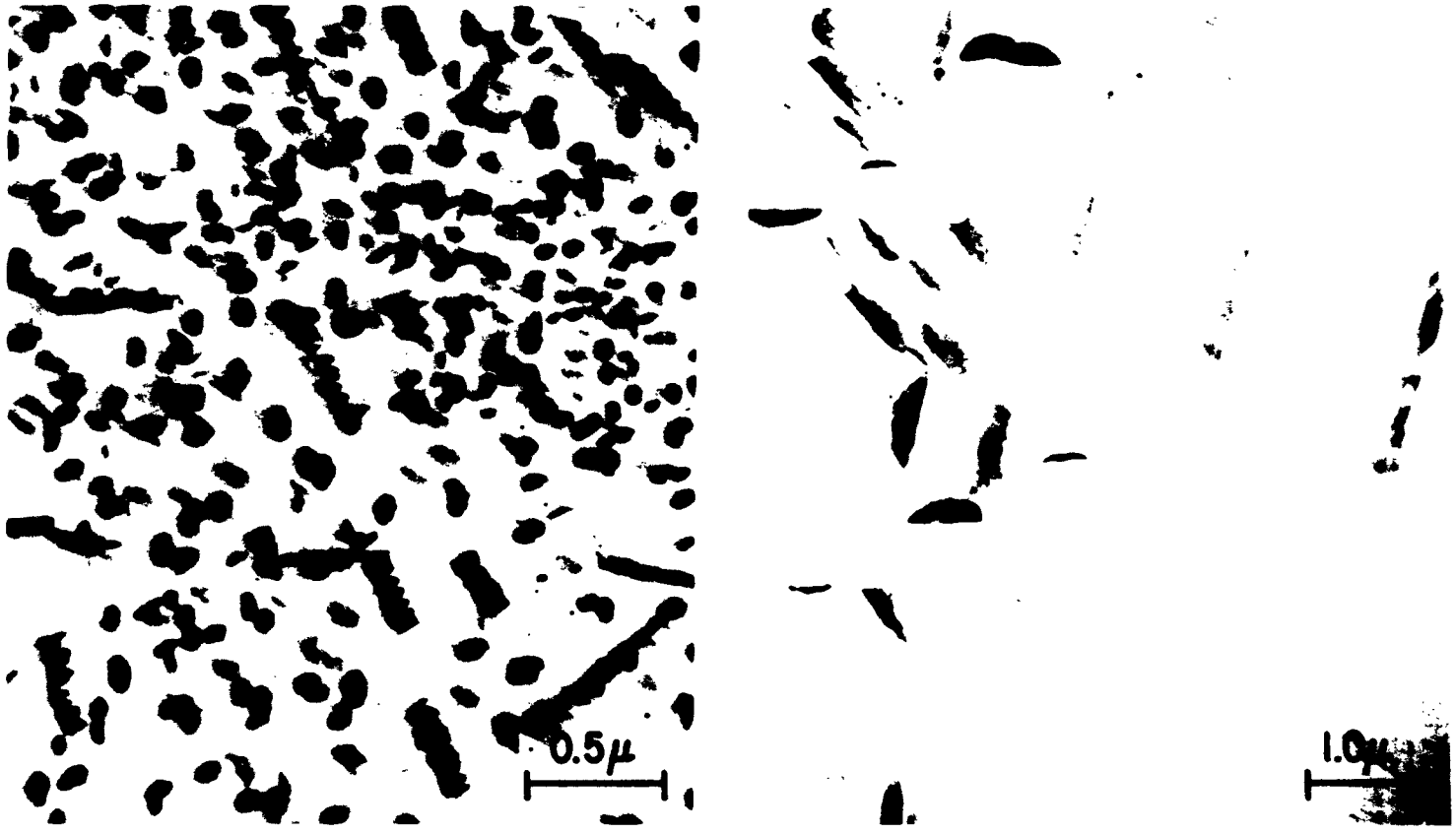

(a) 1 hr., 100°C, MATRIX PLUS DISLOCATION (b) 10 min., 200°C, DISLOCATION

FIG. 2 -- EFFECT OF AGING TEMPERATURE ON THE NUCLEATION OF $Fe_{16}N_2$ IN AN Fe-0.02% N ALLOY.

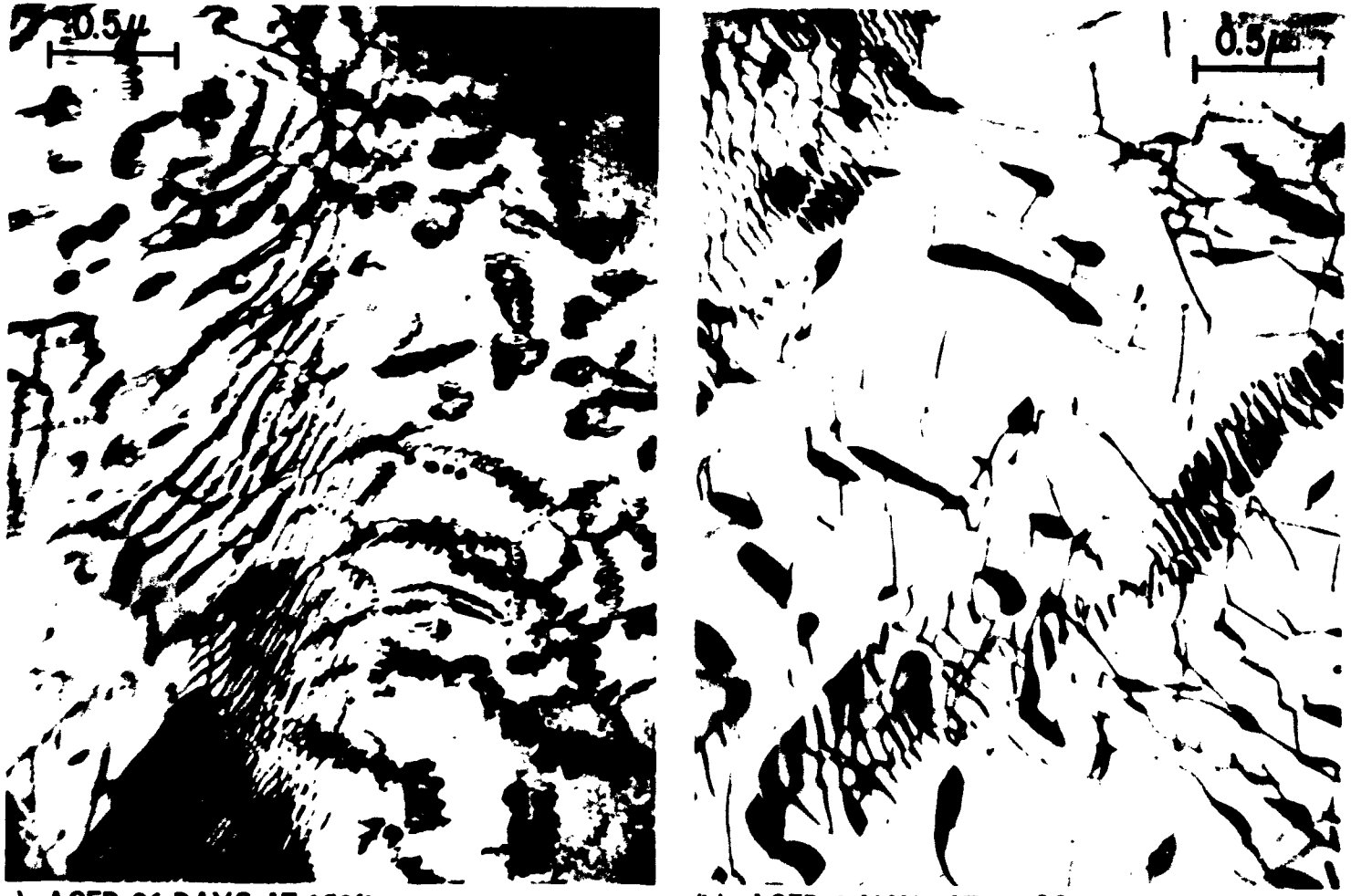

(a) AGED 26 DAYS AT 25°C

(b) AGED 2 MIN. AT 200°C

FIG. 3 -- PRECIPITATION OF $Fe_{16}N_2$ ON DISLOCATIONS AND SUBBOUNDARIES IN AN Fe-0.02% N ALLOY.

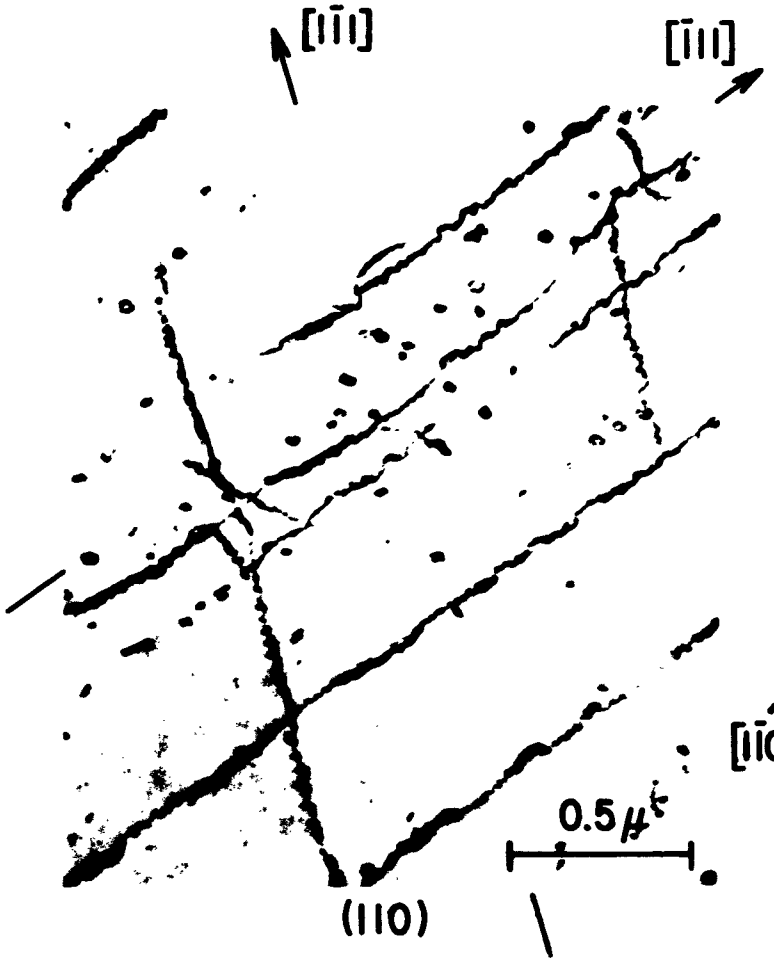

FIG. 4 -- PRECIPITATION OF CARBIDE ON SCREW DISLOCATIONS IN AN Fe-0.45Mn-0.017C ALLOY AGED 1 hr. AT 100°C.

FIG. 5 -- PRECIPITATION OF $Fe_{16}N_2$ ON EDGE DISLOCATIONS IN A SIMPLE TILT BOUNDARY OF AN Fe-0.012%N ALLOY AGED 16 MONTHS AT 25°C.

FIG. 6 -- CARBIDE PRECIPITATION ON A DISLOCATION NETWORK IN 3% SILICON STEEL AGED 256 HRS. AT 100°C.

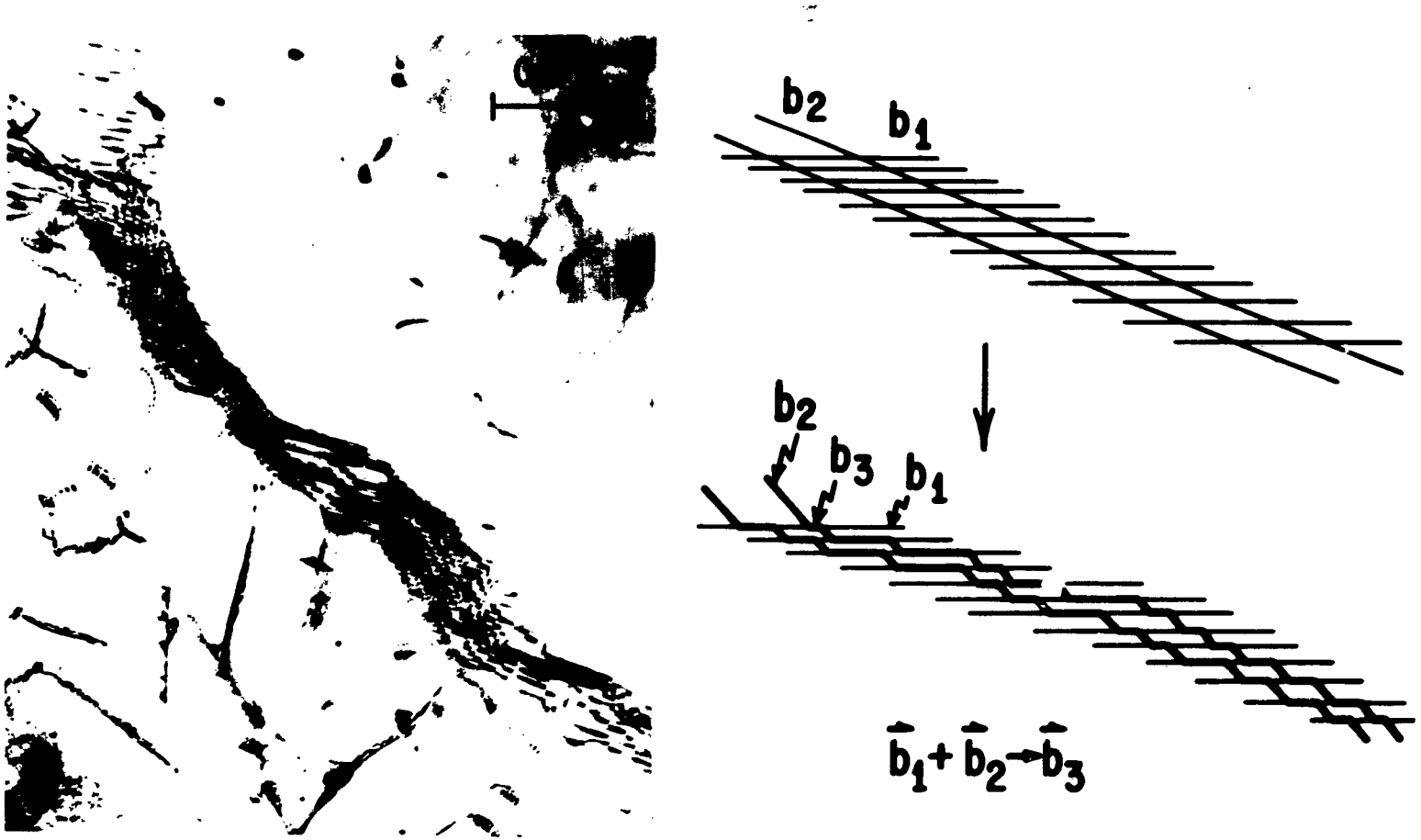

FIG 7 -- PRECIPITATION OF $Fe_{16}N_2$ ON A SUBBOUNDARY IN AN Fe-0.01% N ALLOY AGED 2 HRS. AT 100°C.

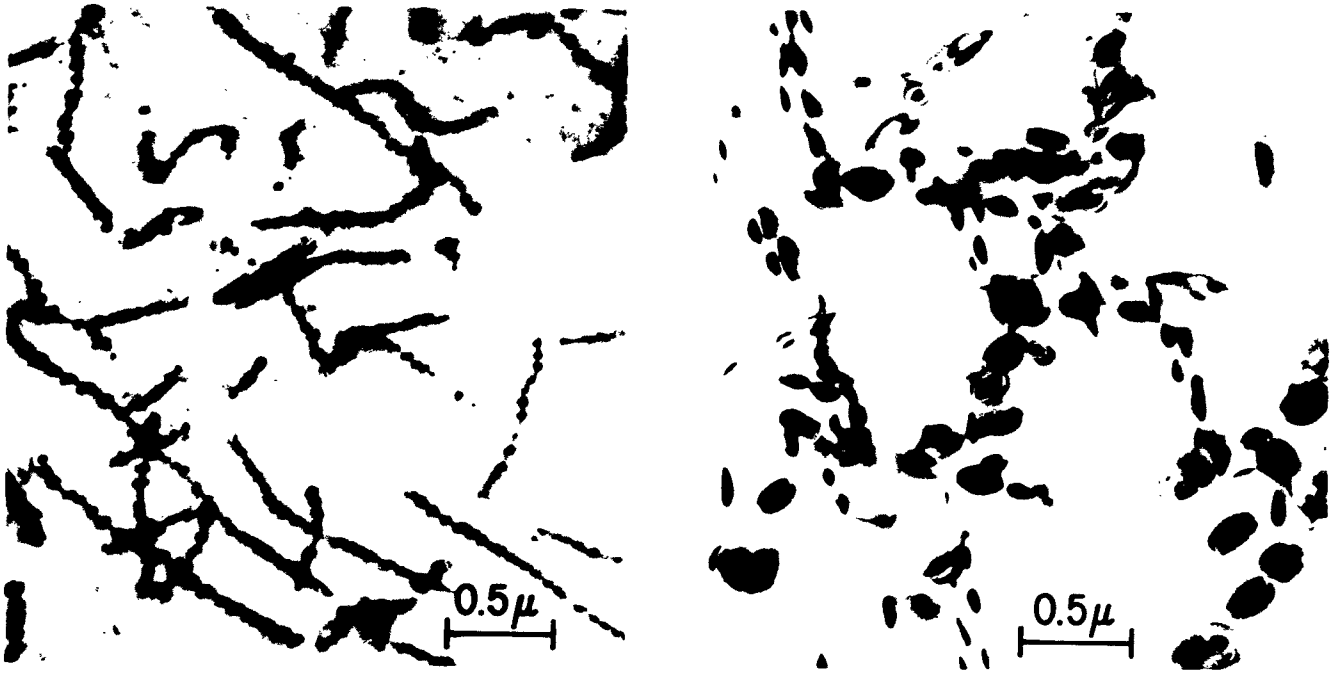

(a) 24 HRS. AT 500°C (b) 6 HRS. AT 600°C

FIG. 8 -- NUCLEATION OF GOLD PARTICLES ON DISLOCATIONS IN A 1.1 at.% Au-Fe ALLOY.

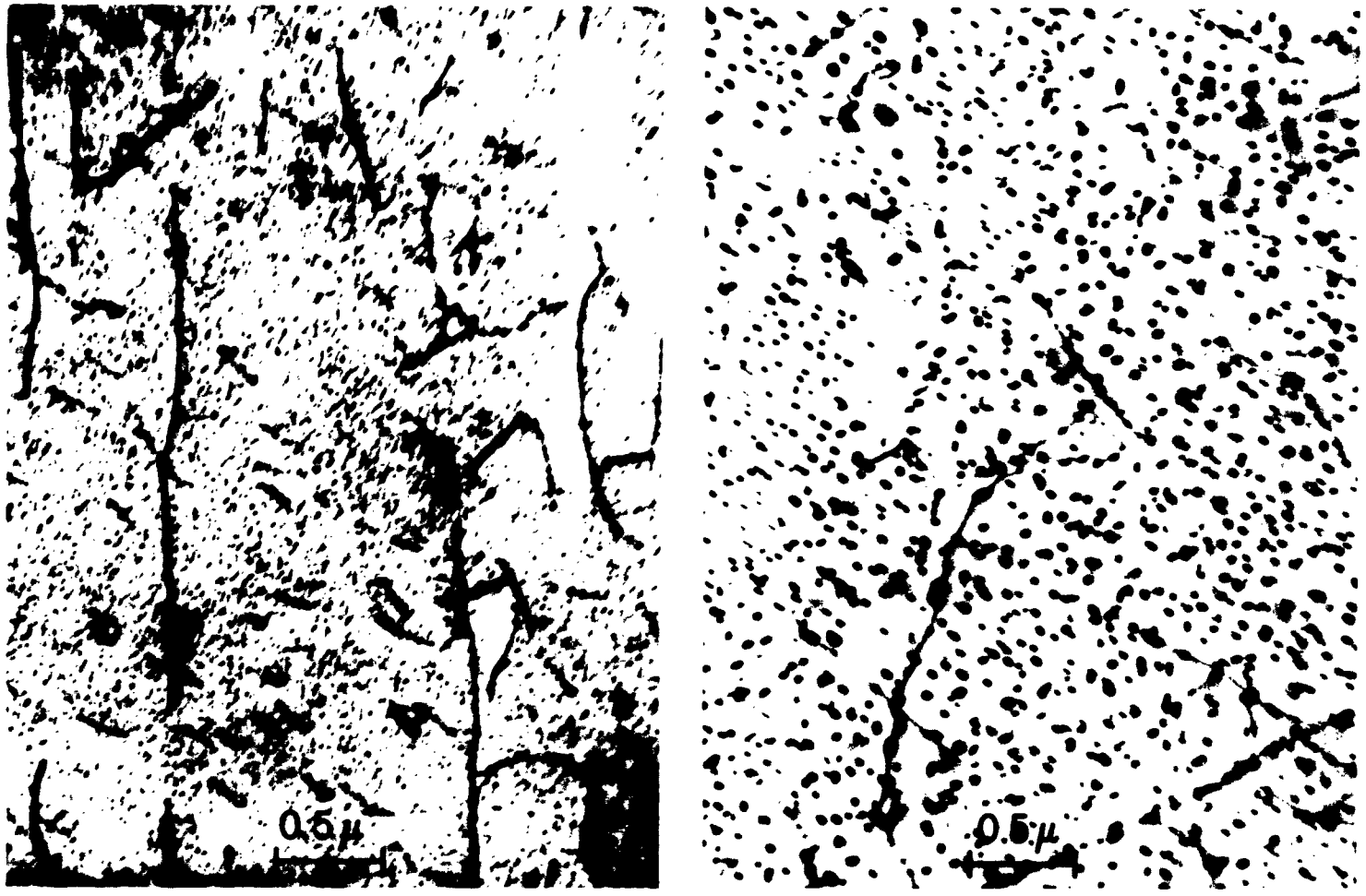

(a) 25 HRS. AT 500°C

(b) 100 HRS. AT 600°C

FIG. 9 -- PRECIPITATION OF COPPER PARTICLES IN FERRITE MATRIX IN A 1.08% Cu-Fe ALLOY.

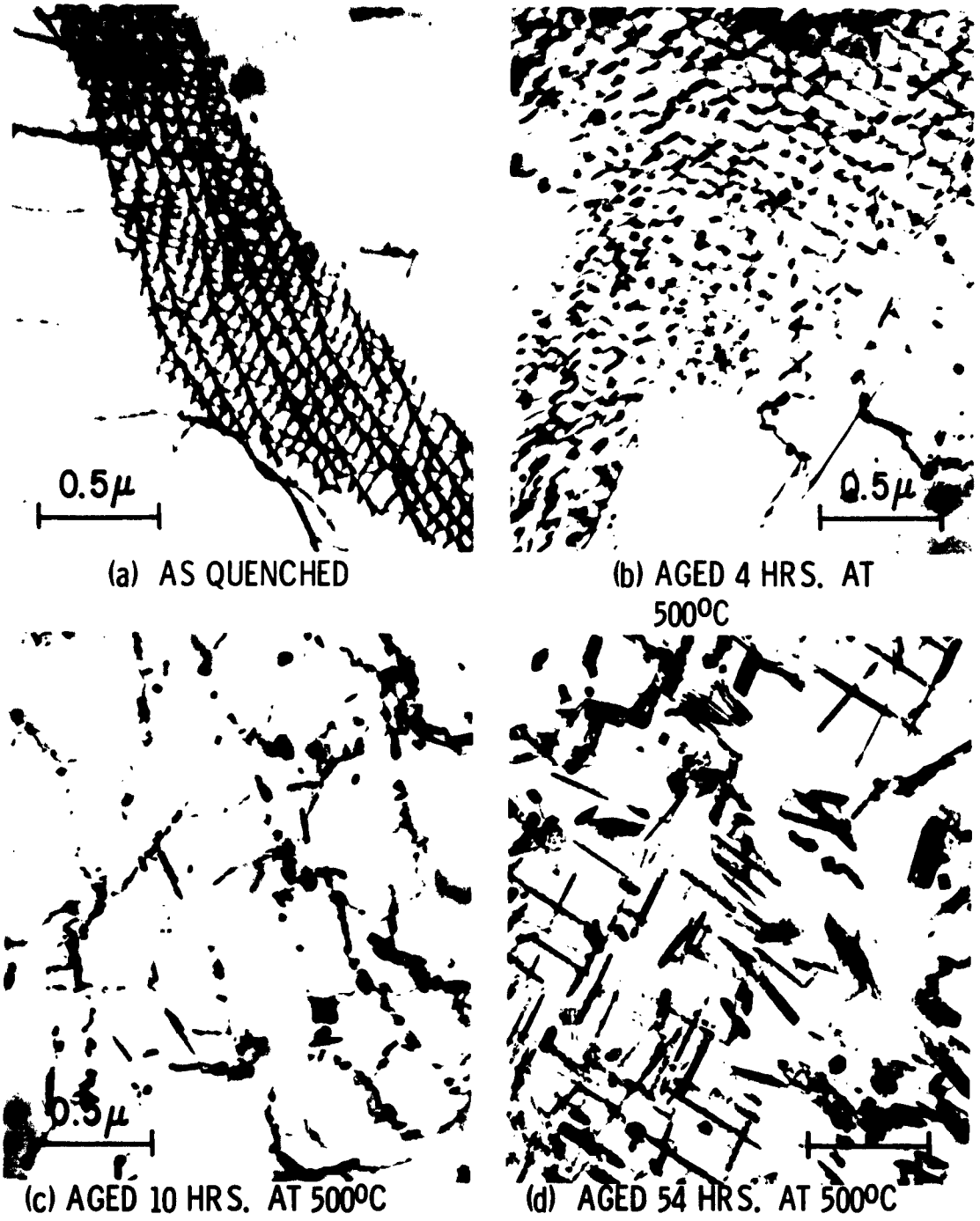

(a) AS QUENCHED

(b) AGED 4 HRS. AT 500°C

(c) AGED 10 HRS. AT 500°C

(d) AGED 54 HRS. AT 500°C

FIG. 10 -- PRECIPITATION IN AN Fe-1.8% P ALLOY, ROLLED 68% AT 1100°C, THEN QUENCHED.

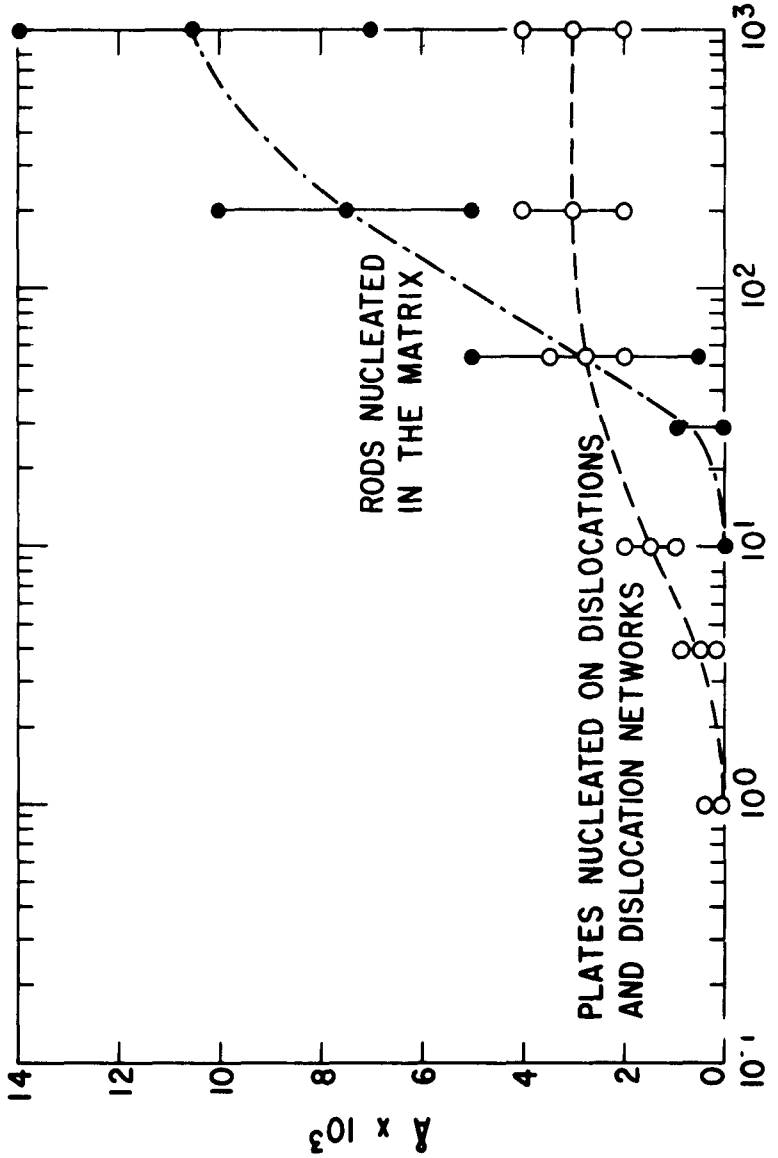

FIG. 11 -- GROWTH OF PHOSPHIDE PARTICLES AT DIFFERENT NUCLEATION SITES. Fe-1.8 wt.% P, QUENCHED FROM 1100°C AGED AT 500°C.

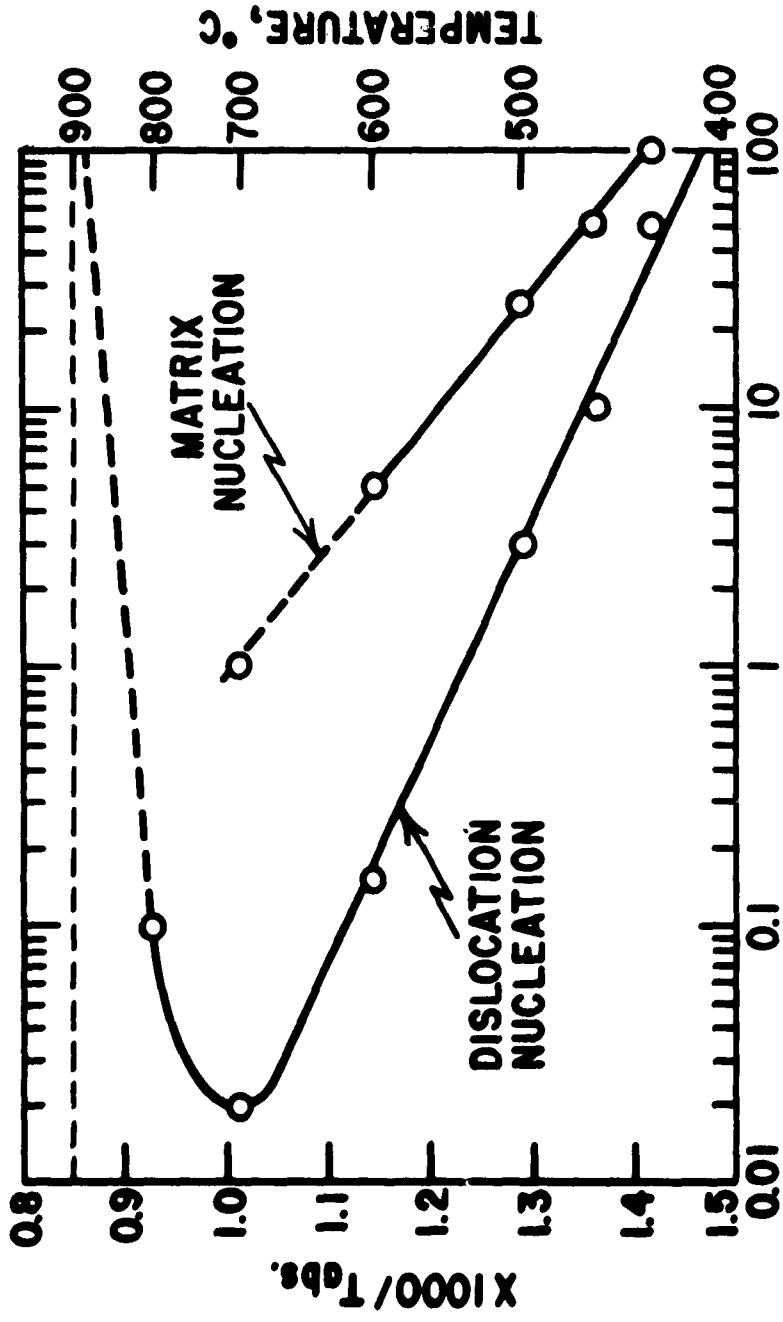

FIG. 12 -- TEMPERATURE DEPENDENCE OF DISLOCATION AND MATRIX NUCLEATION IN AN Fe-1.8% P ALLOY.

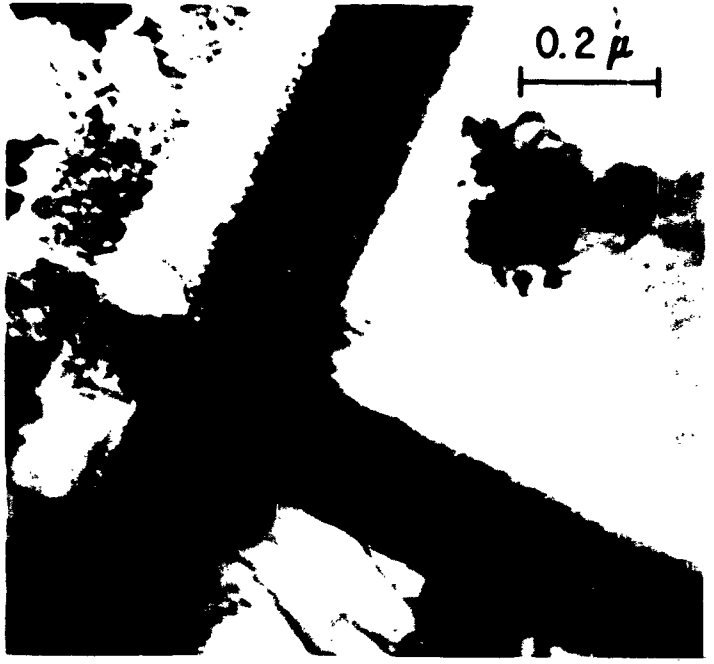

FIG. 13 -- PRECIPITATION ON STACKING FAULTS IN AN 18% Cr-10% Ni-1% Nb-0.1% C STAINLESS STEEL, TEMPERED 72 HRS. AT 700°C. (AFTER VAN ASWEGEN AND HONEYCOMBE[28])

FIG. 14 -- INTERNAL TWINNED STRUCTURE OF MARTENSITE PLATES IN A QUENCHED 1.0% C STEEL. (KELLY AND NUTTING[30])

FIG. 15 -- MARTENSITE NEEDLES WITH NO INTERNAL TWINNING BUT HIGH DISLOCATION DENSITY FORMED IN A 0.1% C STEEL. (KELLY AND NUTTING[30])

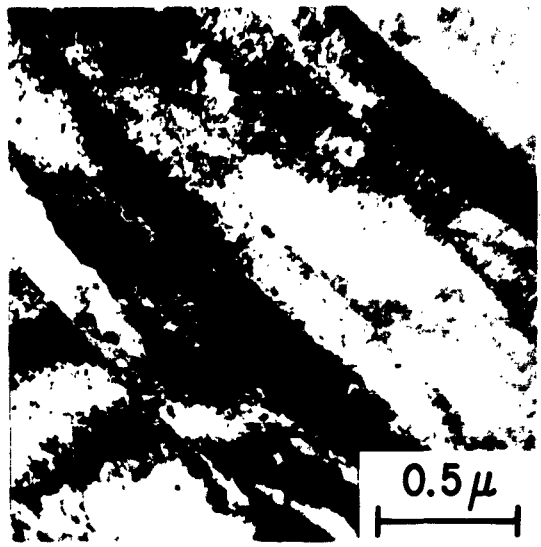

FIG. 16 -- STRUCTURE OF MARTENSITE IN AN Fe-20 Ni ALLOY.

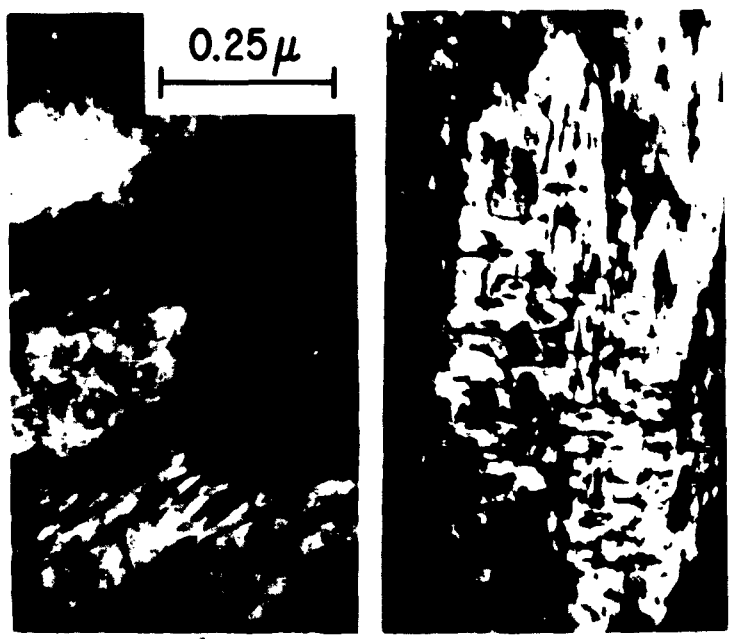

FIG. 17 -- CARBIDES FORMED IN A 0.42% C STEEL TEMPERED AT 600°F (315°C) (a) "STREAKY CARBIDES", (b) "CRYSTALLOGRAPHIC CARBIDES" (TURKALO[36])

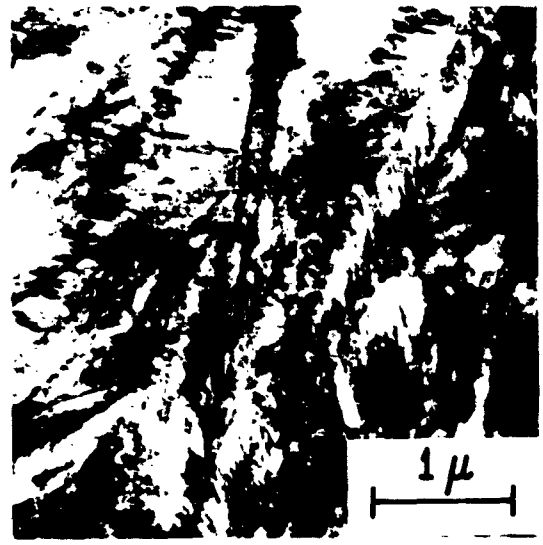

FIG. 18 -- 1.0% C STEEL TEMPERED FOR 1 HR. AT 300°C (KELLY AND NUTTING[31])

FIG. 19 -- POLYGONIZED SUBSTRUCTURE FORMED BY RECOVERY OF TRANSFORMATION SUBSTRUCTURE IN AN Fe-18 Ni-7 Co ALLOY AGED AT 500°C FOR 100 HRS.

FIG. 20 -- FORMATION OF AUSTENITE IN AN Fe-20Ni ALLOY AFTER AGING AT 500°C FOR 100 HRS.

FIG. 21 -- PRECIPITATION IN A MARTENSITIC Fe-20Ni-1Ti ALLOY AGED AT 500°C FOR 24 HRS.

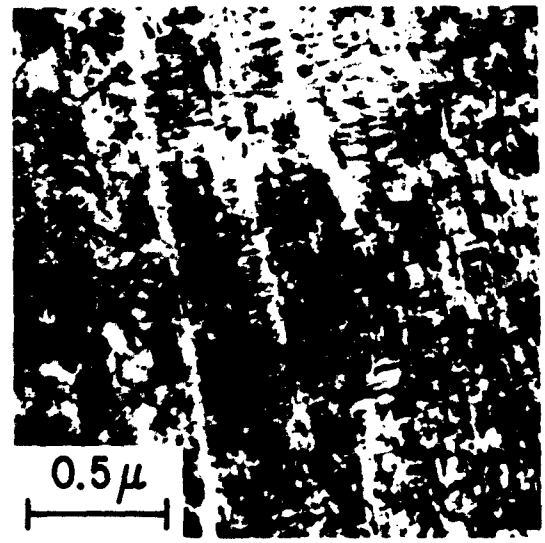

FIG. 22 -- PRECIPITATION IN A MARTENSITIC Fe-20 Ni-10 Cu ALLOY AGED AT 500°C FOR 100 HRS.

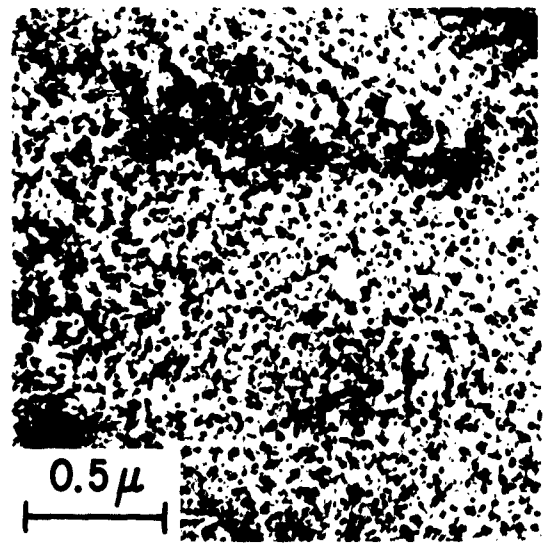

FIG. 23 -- PRECIPITATION IN A MARTENSITIC Fe-18 Ni-7 Co-5 Mo ALLOY AGED AT 500°C FOR 8 HRS.

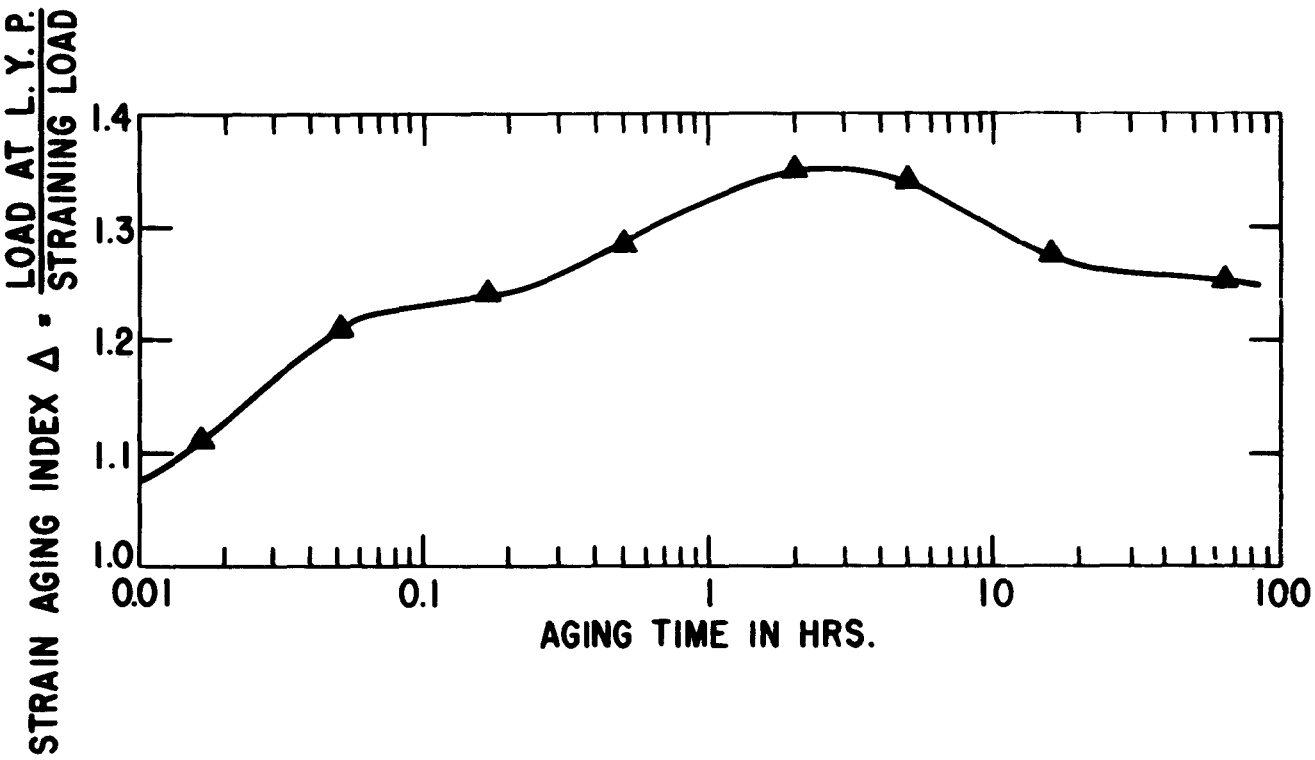

FIG. 24 -- STRAIN AGING OF A 0.022% N ALLOY, QUENCHED FROM 500°C, STRAINED 3%, AGED AT 100°C.

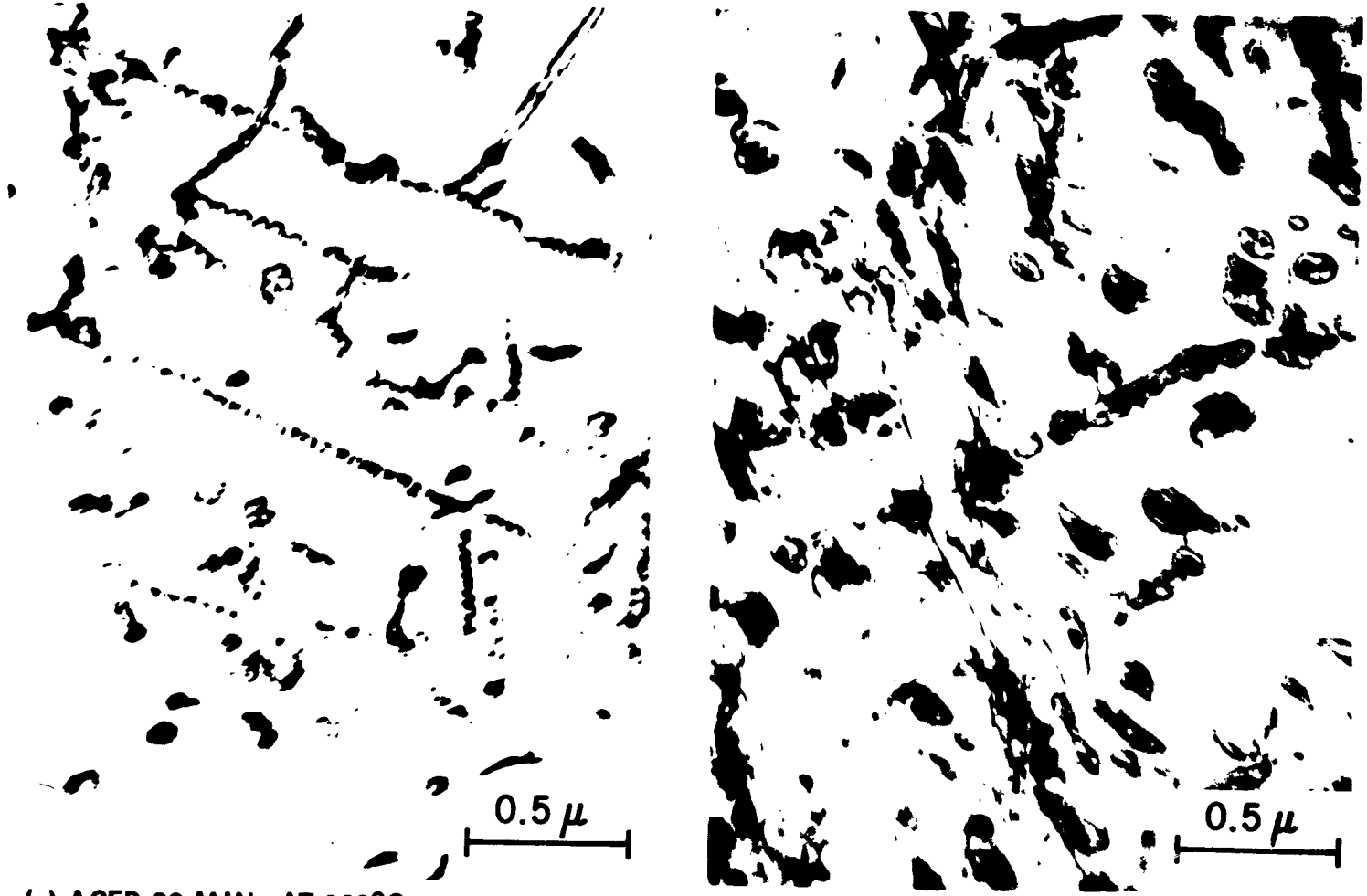

(a) AGED 30 MIN. AT 100°C

(b) AGED 16 HRS. AT 100°C

FIG. 25 -- NITRIDE PRECIPITATION AFTER STRAIN AGING OF A QUENCHED 0.022% N ALLOY, STRAINED 3%.

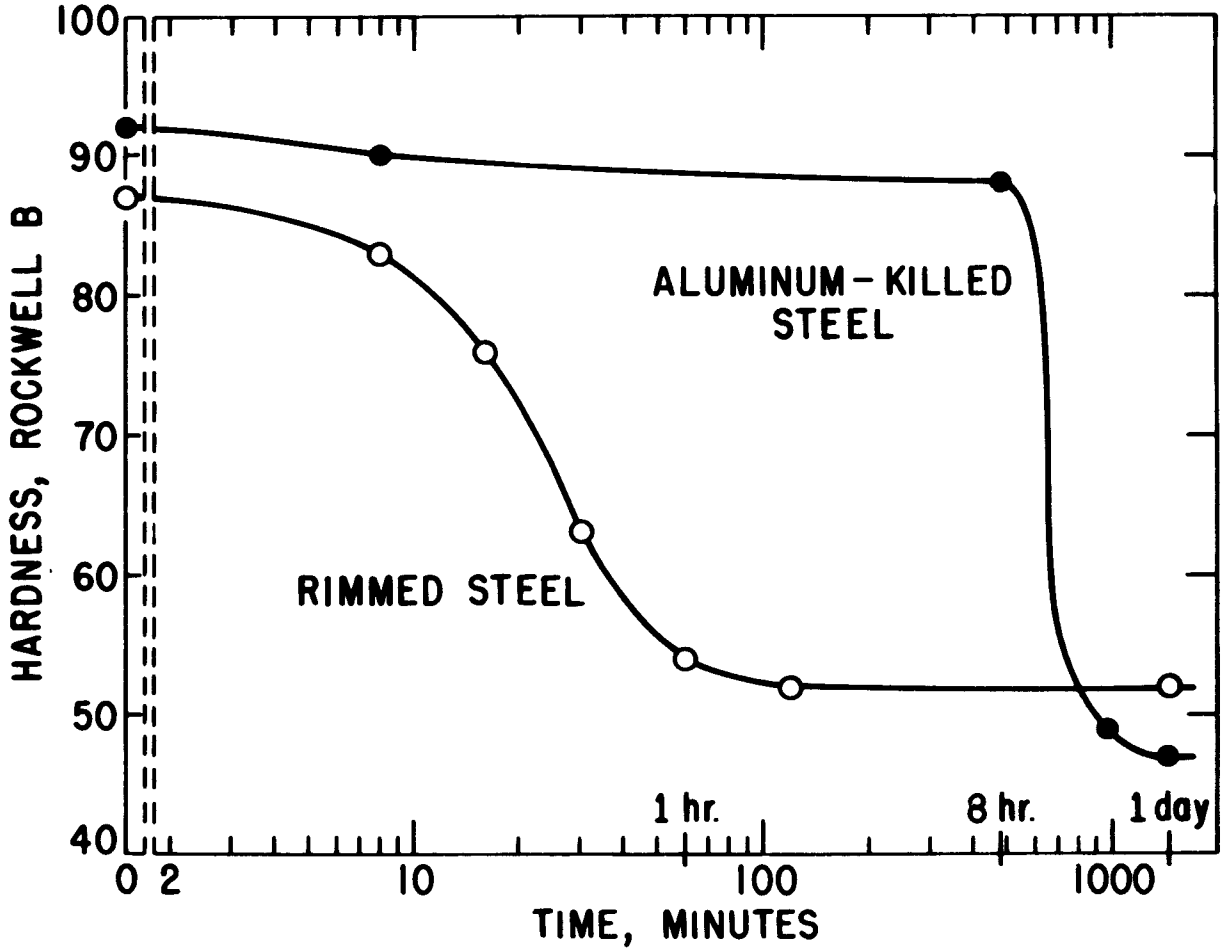

FIG. 26 -- RECRYSTALLIZATION OF LOW-CARBON SHEET STEEL AT 565°C, AFTER 40% COLD REDUCTION.

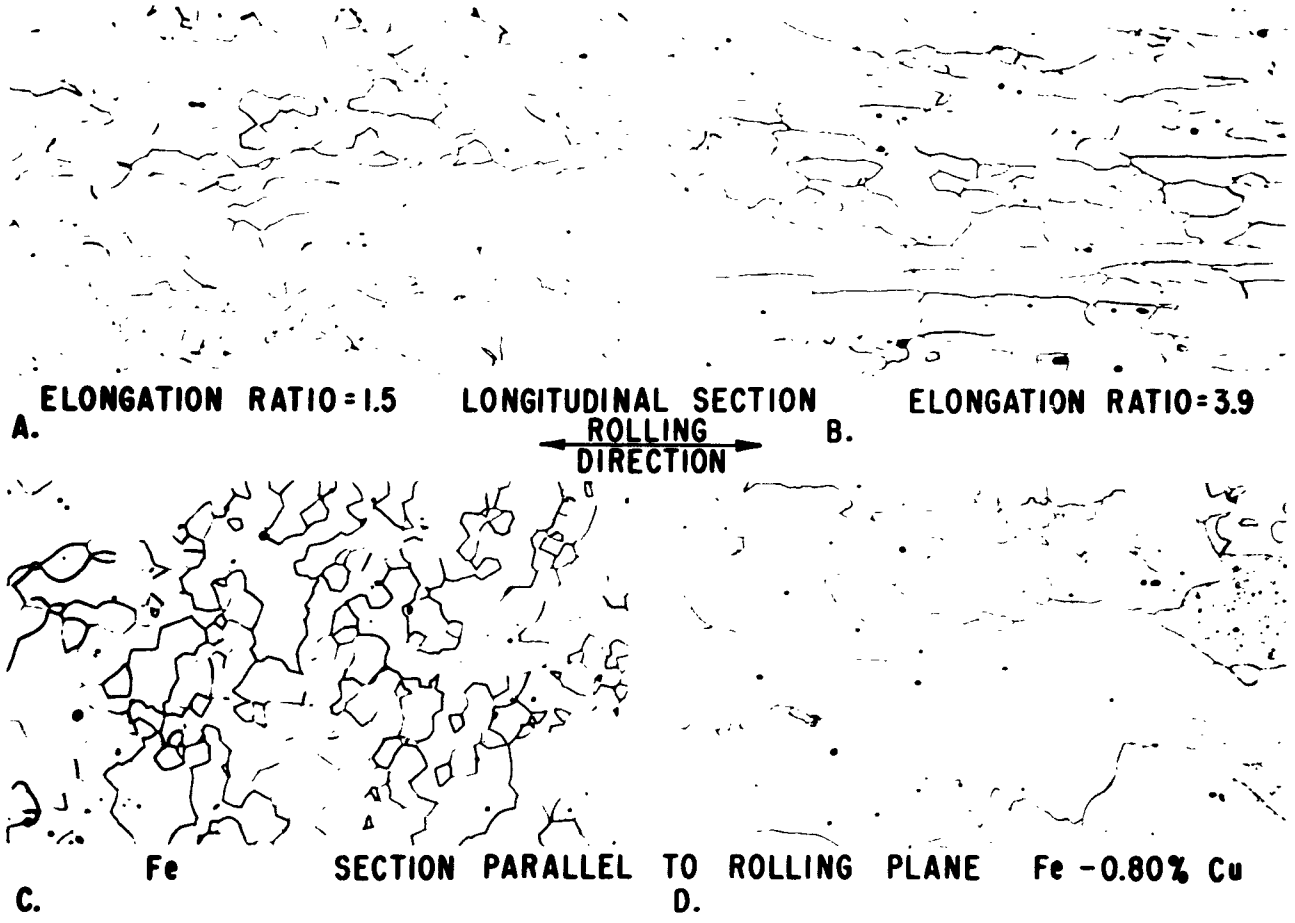

FIG. 27 -- EFFECT OF PRECIPITATION BEFORE RECRYSTALLIZATION ON FERRITE GRAIN STRUCTURE. (QUENCHED FROM 925°C, COLD ROLLED 90%, PRETREATED 3 HRS. AT 500°C, RECRYSTALLIZED AT 700°C)
200X NITAL ETCH

FIG. 28 -- COPPER PRECIPITATED IN CELL BOUNDARIES. Fe-0.8% Cu, COLD ROLLED 60%, HELD 3 HRS. AT 500°C, 10 MIN. AT 650°C.

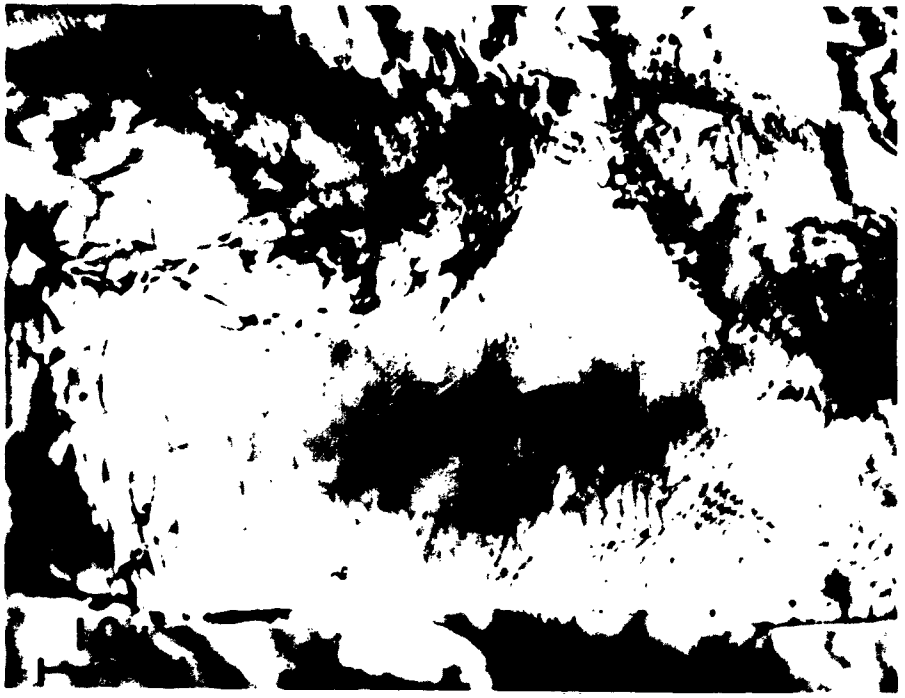

FIG. 29 -- COPPER PRECIPITATED IN GRAIN BOUNDARY DURING TREATMENT AT 500°C PRIOR TO RECRYSTALLIZATION. Fe-0.8% Cu, QUENCHED FROM 925°C, C. R. 60%, HELD 3 HRS. AT 500°C.

(a) AS QUENCHED WITHOUT ROLLING, DISLOCATION DENSITY=$10^8/cm^2$.

(b) ROLLED 40% AT 1100°C DISLOCATION DENSITY =$1x10^{10}/cm^2$.

(c) ROLLED 68% AT 1100°C DISLOCATION DENSITY =$5x10^{10}/cm^2$.

FIG. 30 -- DISLOCATION STRUCTURES IN AN Fe-1.8%P ALLOY, QUENCHED FROM 1100°C AFTER ROLLING, THEN AGED 8 HRS. AT 500°C. 500X

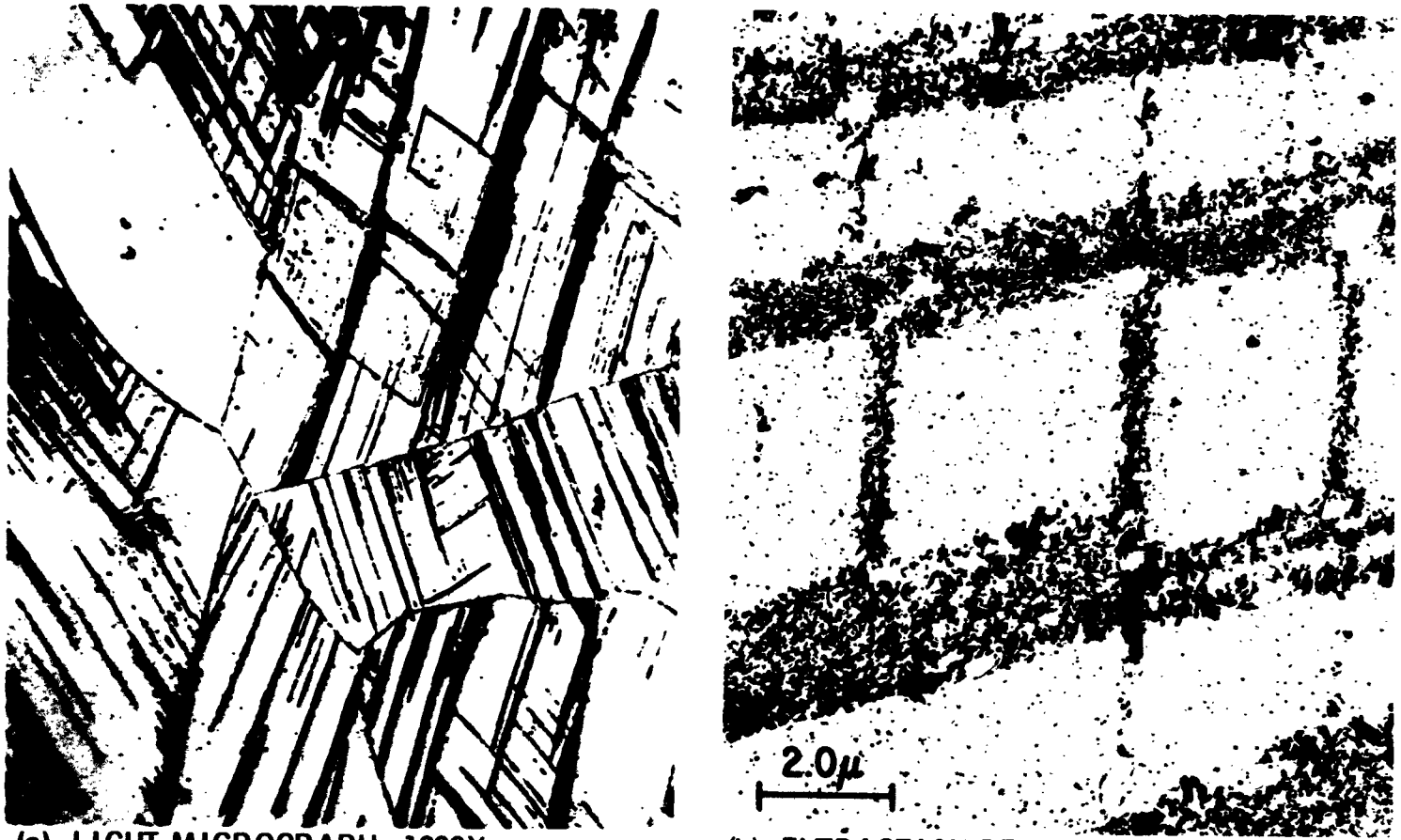

(a) LIGHT MICROGRAPH, 1000X

(b) EXTRACTION REPLICA

FIG. 31 -- STRUCTURE OF TYPE 316 STAINLESS STEEL QUENCHED FROM 1095°C STRAINED 25%, AGED AT 480°C AND AT 705°C, THEN CREEP TESTED AT 705°C.

Deformation and Annealing Sub-Structures of Niobium and their Relation to the Mechanical Properties and Precipitation Phenomena.

A. Berghezan and A. Fourdeux

Union Carbide European Research Associates, S.A.
95 Rue Gatti de Gamond, Bruxelles 18, Belgium.

Part I : Deformation Sub-Structure of Niobium and its Relation to Mechanical Properties.

Introduction

During the last decade, several deformation theories of metals have been developed, most of them based exclusively on theoretical models of the dislocation structure of deformed metals. Of particular interest are those related to the b.c.c. metals as they represent a very important class of materials such as iron, steel and refractory metals. Among these theories, that of Cottrell was received with particular enthusiasm since it appeared to be of rather general applicability.

Cottrell's theory tries mainly to explain the σ_o and k parameters of the Petch (1) empirical equations which relate the brittle fracture stress and the lower yield point to the grain diameter by the following simple equations :

$$\sigma_t = \sigma_o + k_f \cdot d^{-\frac{1}{2}}$$

$$\sigma_y = \sigma_o + k_y \cdot d^{-\frac{1}{2}}$$

Another important fact, found by Heslop and Petch (2), is the large increase in the yield stress when the deformation temperature is decreased. Fig. 1 shows graphically the important experimental factors found by Petch.

Since the σ_o and k parameters are not interpreted in the Petch relation, Cottrell (3) tried to give them a physical meaning. In his concept σ_o should be considered as the shear stress resisting the movement of dislocations along the slip planes after they have been unpinned from the impurity atmosphere, whereas k is the product of the shear stress (σ_D) needed to unpin a dislocation from its atmosphere and the distance (l) which separates the first dislocation in a pile-up against a grain boundary barrier from the source at which the dislocations of the pile-ups were nucleated. In the Cottrell notation, the Petch relation becomes

$$\sigma_y = \sigma_i + k_y \cdot d^{-\frac{1}{2}} \quad \text{where } k_y = \sigma_D \cdot l^{\frac{1}{2}}$$

This theory thus assumes a definite dislocation model (Fig. 2) of the deformation process in which three factors are given an important physical meaning : the lattice friction stresses (σ_i), the pile-up of dislocations against specific barriers (grain boundaries) and the dislocation sources situated inside the grains.

The Cottrell theory developed only for iron and steel has also been found adequate for the refractory metals both of group V (V, Nb, Ta) and VI (Cr, Mo, W) of the periodic table (4-11). It was therefore thought that this theory might be considered as valid for the deformation of all the b.c.c. metals. However, further work on refractory metals, principally by Johnson's group (12) (Johnson and Wronski (13)), questioned its extension to the refractory metals, although this doubt was not shared by all workers and the applicability to iron and steel was never called into question.

A number of further theories have been developed based on other hypothetical dislocation mechanisms, but all suffered from the fact that their exact verification was extremely difficult, if not impossible, so long as the behavior of the dislocations must be inferred from indirect measurements. With the advent of transmission electron microscopy, however, the situation changed almost overnight because at last a tool was available whereby the deformation process could directly be observed at an atomic scale. The primary purpose of the present work is to report the contributions of this technique to the experimental evaluation of the principal theories that have been proposed and to study at first hand the interaction between the dislocations and impurities remaining in the metal during the deformation and precipitation annealing. The present study, however, is in the nature of a progress report since the results are so far confined to niobium deformed only at room temperature.

Experimental Techniques.

Niobium which had been prepared by electron beam melting was used in all experiments and had the following analysis : 210 ppm carbon, 100 ppm oxygen and 90 ppm nitrogen. The ingots which were initially of 10 mm diameter were first cold rolled to a thickness of 0.1 mm and then annealed in vacuum at various temperatures and for various times to permit recrystallization and grain growth.

It was found necessary to perform two series of deformations ; one inside and the other outside the electron microscope. The final dislocation pattern observed in the latter series can frequently be understood only when the various steps in producing this pattern are seen in the microscope itself. The deformations outside the microscope started with the 0.1 mm sheets which were stretched in a Chevenard micro-tensile machine up to precisely predetermined points on the stress-strain curve and the samples so prepared were electrolytically thinned for viewing in the electron microscope ; the samples stretched in the instrument were first electrolytically thinned.

The majority of the samples used to investigate the initial, recrystallized material were treated at 1100°C for periods up to 15 hours and produced metal with grain sizes in the range between 5 and 10 μ diameter.

These samples are characterized by the complete absence of sub-boundary networks and an extremely small dislocation density within the grains ; the grain boundaries appear to have achieved at least quasi-stable

positions since the interboundary angles at intersections approximate 120° (See Fig. 3). In Fig. 4 the stress-strain curve of these samples is shown, where it is seen that the elastic limit is decidedly low but there is an extremely large elongation. The most striking feature, however, is the extraordinarily small rate of work hardening - it may in fact even be zero. In this respect niobium definitely differs from iron and the members of group VI where the work hardening rate is appreciably larger.

Examination of Samples Deformed Outside the Electron Microscope

The early stages of the deformation are characterized by a very great heterogeneity. So long as the total deformation remains below about 3.5% there is an enormous difference in the behavior of different grains ; some show large dislocation concentrations while others seem to have been totally unaffected ; a fact which is undoubtedly to be attributed to the different orientations of the grains. This is seen clearly in Figs. 5, 6, 7 and 8 which represent different fields in a sample elongated by 1.9%. Two different types of dislocation may be seen : long dislocation lines and dislocation loops. These differ considerably in aspect and distribution. The lines are sometimes straight and well-oriented but more often they are irregular ; curved with frequent cusps or straighter with numerous jogs. The loops appear to be of two different sorts : small, almost round rings and large elongated loops. It is believed that they are formed by two different mechanisms, as will be mentioned in some more detail later.

The rôle of grain boundaries in the deformation process is worthy of special note since, on occasion, they are seen to serve as preferred sources of dislocations (Fig. 9) or as acceptors of mobile dislocations and at all times they form very effective barriers, but against which the dislocations do not form pile-ups (Fig. 10). This last is of particular significance in b. c. c. metals because precipitate particles, as will be seen in a moment, cannot serve this function. When acting in their guise as acceptors, the grain boundaries readily accommodate the newly arriving dislocations thereby modifying their structure far more drastically than would correspond to the change of dislocation density within the grains.

On the portion of the stress-strain curve between about 2% and 3.5% elongation the deformation remains very heterogeneous from grain to grain but there is a considerable increase in dislocation density particularly of the two kinds of dislocation loops mentioned above. These appear to increase more rapidly than do the mobile dislocations. This may be seen in Fig. 11 which is reasonably typical of this stage although it should be emphasized again that there is a wide variation from grain to grain again probably depending on orientation.

In Fig. 12 a high angle grain boundary is seen. In the starting material these boundaries do not show normally any structure because their dislocation network is too fine to be resolved, but the fresh dislocations arriving at the boundaries during the deformation make changes in the initial uniform contrast and the new dislocations can readily be resolved and studied.

Thus it appears reasonable to assume that the dislocations seen here are new ones that have been accepted by the boundary. However, it is not yet certain whether these new arrivals lie actually in the plane of the boundary or in closely neighboring planes ; the latter is the more probable.

One other important point is illustrated by this figure (Fig. 12) : the grain boundaries are at first not "rigid" and only serve to stop the dislocations ; but they are rather "plastic" in that they accommodate the new arrivals into their structure thereby growing and producing kinks, etc. and rearranging their structures. As this process continues, however, the boundaries become more and more rigid and find it increasingly difficult to accommodate the further dislocations.

The interaction of mobile dislocations with precipitate particles is illustrated in Fig. 13 and 14. Here it should be cautioned that the apparent size of the precipitate particles is exaggerated by the low magnification used ; at higher magnification they appear as small dots along the dislocation line on which they nucleated during recrystallization annealing but perpendicularly oriented to it. It is clear from these figures that precipitates, as already mentioned, are very ineffective barriers to the movement of dislocations in these metals ; only a few dislocations and some rings have been pinned. One other frequently observed phenomenon is seen in Fig. 13 : the dislocation lines often separate regions of considerable contrast on the plate. This, as shown by some calculations of Amelinckx (14), is due to the fact that each dislocation line forms an elementary polygonization wall and the minute difference in orientation so produced is sufficient to increase the contrast as observed.

We now proceed to the next stage of the deformation process, between 4 and 5% elongation. The heterogeneity from grain to grain drops markedly, no grain being found now without fresh dislocations in it. In the grains of higher dislocation density there is a very perceptible tendency toward grouping ; the nodular tangles of dislocations are seen in Fig. 15 and 16. The onset of this grouping is probably to be explained by interaction of the mobile dislocations with more sessile prismatic loops. At any rate, in many regions, the grouping seems clearly associated with a higher loop density. Fig. 17 shows further examples of interaction with precipitate particles. Once again one is astonished at the ineffectiveness of these particles in producing pile up ; only a bit of debris and some rings are actually immobilized in this way. Other interesting interactions are seen at A, B, and C in Fig. 17 : at these points two $\frac{a}{2}$ [111] dislocations have combined to form a segment of a [100] dislocation. On annealing these fragments then increase their length and form hexagonal networks of twist boundaries ; a process favored by higher temperature (15).

On increasing the deformation to 5.5% elongation the dislocation density is found to be still on the increase but at a distinctly lower rate. The tangles which were forming earlier now transform into long skeins of tangled

dislocations which rapidly extend until they join up to produce some very confused cells (Fig. 18). Isolated tangled skeins still persist, however, up to 7-8% elongation (Fig. 19). At this stage the individual dislocations are generally still resolved.

The contours of the skeins within the crystal grains appear to be determined by the regions of higher ring or loop density as is particularly well seen in Fig. 20 where the location of the skeins appears to coincide with the presence of larger numbers of loops. Nevertheless, despite the growth of the tangled network of skeins there is a still greater increase in dislocation density within the grain boundaries. As seen in Fig. 21 the individual dislocations in these boundaries can no longer be resolved and the whole boundary begins to take on a spotty appearance. Again, the presence of precipitate particles does not seem significantly to alter the dislocation array in their immediate neighborhoods.

As the deformation is still further increased the skeins gather in more dislocations and form rather well-defined networks (Fig. 22) The grain boundaries, however, still keep ahead and now form regions of almost uniform black contrast (Fig. 23). Another significant feature now emerges : when the developing network of skeins intersects a grain boundary the angle of intersection is invariably close to 90° ; this angle is characteristic of the junctions of polygonization walls with high angle grain boundaries (16).

Continuing along the stress-strain curve as the point of rupture is approached the dislocation walls become much better defined and assume a striking geometric regularity ; the dislocation density in the contracted walls has grown to a point where the individuals can no longer be resolved. Fig. 24 and Fig. 25 show this characteristic situation before and after rupture and the highly regular cells are clearly evident. The growth of dislocation density in the walls has, of course, largely depleted the remaining crystals and increased the disorientation between adjacent cells. The length of an edge of the square cells is of the order of 0.5 μ while the longer dimension of the rectangular cells may reach 1 μ or even more. It is evident, then, that the deformation process has led to a decided subdivision of many of the original crystallites into a much smaller, geometrically regular network of square and rectangular cells of astonishingly uniform size. This agrees well with earlier observations of Wood (17), Hirsch (18) and others (19),(20) who found a similar phenomenon in iron, aluminum and aluminum alloys. Nevertheless, it must be remarked that this process of subdivision is not completely uniform throughout the structure. Some of the cells which got started late in the deformation process never catch up and, at the point of rupture, it is still possible to find crystallites - such as the one shown in Fig. 26 - which are still in a rather primitive state so far as building a cell structure is concerned.

Finally, in Fig. 27, an extremely interesting effect is seen. Particles of precipitate are here throwing out dislocation loops by a prismatic punching mechanism thereby giving rise to a very characteristic

pattern. In a sample with a considerable number of precipitate particles this could be a significant source of the relatively sessile dislocation loops (21). This may also contribute to dispersion hardening.

Discussion of Results on Samples Deformed Outside the Microscope.

We have seen that the deformation process in niobium is characterized by an initial rapid increase in the number of mobile dislocations and, what is especially significant, an even larger increase in the density of the far less mobile prismatic loops and rings. This stage is followed by a progressive grouping of the mobile dislocations into nodular tangles, then into skeins and finally into well-defined and highly regular walls. It appears that the distribution of these walls is principally determined by the arrangement of the loops, a process which may be visualized as follows : In the earliest stages of the deformation the mobile dislocations can cross-slip very easily in the b.c.c. structure and hence readily by-pass the loops. However, as the density of such loops increases the mobile dislocations find it progressively more difficult to cross-slip over their whole lengths and consequently only a portion of the dislocation can engage in this sport. The partial slipping produces jogs which reduce mobility and inaugurates the early beginnings of grouping. At the same time some climb is to be expected and this, together with the cross-slip, bring the dislocations out of their original slip plane and produce the irregular tangles in place of pile-ups. These tangles, as we have seen, are the forerunners of the well-organized walls to be formed later, but the progress toward this final state is rendered difficult by the limited climb. Consequently the rearrangement of the tangles into the regular orientation of the walls proceeds relatively slowly as compared to the development of the grain boundaries already present. Still, the fact that when finally formed the walls make the same angles (near 90°) with the high angle grain boundaries and that they produce a disorientation somewhat less sharp but of the same order as that of the polygonization walls forces us to consider even the initial tangles as incipient polygonization walls.

This view finds additional support in some recent work by Keh (22), (23) on iron at low and at high temperatures. He observed that at low temperatures there was little tendency toward grouping of the dislocations but at higher temperatures a dislocation structure was achieved which was nearly as regular as the polygonization walls. This strengthens the argument in our case that the tangled skeins are in fact the first step in polygonization.

Still further confirmation is found in recent observations by Morgand (24) on Armco and zone refined iron. The tangled dislocation structures were found to be far more regular in the purer material showing that increased purity has in some respects the same influence as raising the temperature. It appears, therefore, that in Morgand's experiments the refined metal underwent a more advanced dynamical recovery than the Armco iron ; and here again we must conclude that the tangled dislocation groups are to be considered as the primitive ancestors of sub-boundaries but with dislocation structures still far from their equilibrium positions.

A further deduction from our studies is the significant rôle played by the initial grain boundaries in the progress of the deformation process. These structures show contradictory behavior in that they not only nucleate the majority of the mobile dislocations but they also accept and, consequently, terminate the motion of, considerable numbers of these dislocations. As we have seen, however, they are at first plastic and accommodate the majority of the newcomers which reach them into their structures with considerable ease. In so doing the boundaries extend and become somewhat ragged, but as the density of accommodated dislocations increases they become more rigid and this fact seems to have a profound influence in decreasing the nucleation of new dislocations ; a process which substantially ceases in the course of the deformation process. This can be seen in the relative unavailability of new dislocations from this point on. During the rest of the deformation the walls improve their ordering and contract considerably but hardly add any new dislocations. In view of the fact that extensive pile-ups of dislocations behind barriers has not been observed in our studies and since it is generally accepted that in those metals showing pile-ups it is the back field stresses produced by these dislocation pile-ups which rob them of sufficient plasticity further to withstand rupture, it is reasonable to assume that the process just described is, at least in niobium, the one which prepares this material for the final debacle. If this were so, it would give an interpretation of the observed extremely low rate of work hardening ; a phenomenon which is probably characteristic of the influence of the extensive dislocation pile-ups ; we shall return to this point.

Observations during Stretching within the Electron Microscope.

We now pass on to the results of experiments performed within the electron microscope which nicely complement the work described thus far. Here we can actually follow the movement of the individual dislocation and, because of the tracks which are fortunately left behind, such movement can even be seen in the photographs.

The most striking observation in watching the movement of dislocations in stressed niobium is the fact that they follow extremely sinuous paths. This is even true at the very beginning of the deformation and is illustrated in Fig. 28 and 29 where the moving dislocations appear to deviate from their slip planes with no appreciable hindrance. In fact straight paths, in direct contrast to the situation in f. c. c. metals, are very rare because nearly all dislocations have more or less screw character and consequently easily change from one slip plane to another. This gives the overall impression that the dislocations do not remain on any precise slip plane. However, if the motion be carefully analysed, it will be found that each segment of the path in fact lies in a (110) slip plane and pursues precisely a [111] direction. No doubt this difference in behavior as compared to f. c. c. metals is to be explained by the greater number of available active slip planes making smaller angles with one another. In Fig. 29 we also see the first emergence of dislocation loops which only appear in regions where slip has already occurred. In Fig. 30 we see that the slip seems to be more pronounced

near the grain boundaries and in Fig. 31 we observe that it becomes more and more prolific inside the grains as the deformation progresses.

The rôle of grain boundaries in nucleating dislocations is apparent in Fig. 32 where it is seen that a single boundary can send out dislocations in both lateral directions. Here again one sees the relatively high density of dislocation loops in the region which has experienced slip while outside such regions they are completely absent. This underlines that even within a crystallite there is considerable heterogeneity from one place to another in the effects produced. In Fig. 33 we again see the grain boundaries in the guise of dislocation acceptors and we note once more the absence of pile-up. Finally, an indication of the markedly different behavior of different grains is apparent in this figure.

In Figs. 34 and 35 we are able to contrast the relatively sessile prismatic loops and rings already described with the mobile dislocations ; whereas the latter have passed completely through the photograph, the former have shown no perceptible movement. There is some reason to believe that the rings and the distended loops may be formed by separate mechanisms. In the former case, the small rings are apparently produced by condensation of vacancies since, when watching the sample being stressed in the microscope, they seem suddenly to appear with no apparent preparation for their coming. The rings are found from the very beginning of the process even in regions where cross-slip has been very limited and this suggests that the point defects may have been produced by dislocations of indeterminate axis according to the mechanism of Kuhlmann, Wilsdorf and Wilsdorf (25). This conviction is strengthened by the frequent appearance of dislocation lines with sharp cusps - seen clearly at the arrows in Fig. 36 and also in Fig. 32 - which must be expected if the Kuhlmann, Wilsdorf and Wilsdorf mechanism were operative.

For the formation of the elongated loops we have no definite suggestions beyond the possibility that they may be produced by one or both of the two mechanisms already proposed : double cross-slip followed by closing up of the dislocation dipole (26), (27), (28), (29) or by the interaction between two mixed dislocations on parallel slip planes (30).

The interaction of mobile dislocations with precipitate particles could be better followed during the studies inside the microscope. The very minor rôle played by such interaction is clearly apparent in Fig. 36 and also in Fig. 37. Here again the effectiveness of cross-slip in enabling the dislocations to escape entrapment is well revealed. Particularly instructive in this connection, however, are the next four figures (# 38-41 inclusive) which show the same field at successive instants. If attention be fixed on the precipitate particles A, B, C and D in these figures, it will immediately become apparent that not more than 3 to 6 dislocations pile up behind each particle and, although a plethora of new dislocations follow the original ones, by a cross-slip zig-zag movement reminescent of the football field, they all circumvent the traffic congestion. Nevertheless, a few

dislocations are pinned.

Fig. 42 is especially instructive because it shows that large precipitate arrays can temporarily slow down dislocation movement. Even here, however, most of the dislocations escape through cross-slip but they are largely deflected from the penumbra of the particle. It is believed that this photograph provides strong support for the cross-slip mechanism for avoiding pile-up.

Still another significant observation is shown in Fig. 43 where a Piobert-Lüders or striction band is shown the edge of which is serving as a source of dislocations - a nucleation possibility already predicted by Johnson (40) in his theory of the deformation of b. c. c. metals. In Fig. 44 the subdivision of such a Lüders band into blocks reminiscent of those already reported in aluminum is seen. It is striking here, however, that these dividing walls, in direct contradistinction to the results for aluminum (31), are not effective dislocation barriers and produce no significant pile-up.

To summarize the conclusions from studies inside the electron microscope it seems well established that the most important single feature of the deformation mechanism is the predominant importance of cross-slip which determines all the remaining characteristic features : absence of dislocation pile-ups, failure of total dislocations to separate into partials, and the weak or transitory trapping of dislocations behind precipitate particles. These facts well explain the extremely low work hardening rate * shown by the stress-strain curve as well as the extreme ductility of b. c. c. metals (when sufficiently free of interstitials) which can easily surpass that of f. c. c. metals. A further deduction from the absence of visible separation of total dislocations suggests that the appearance of large stacking faults in such metals is highly improbable and indicates that those reported in annealed samples (32), (33) are probably due to a local segregation of impurities - in all likelihood introduced through contamination during annealing. All this is further in accord with Crussard's (36) view that the Suzuki effect might produce such stacking faults in b. c. c. metals.

Summary and Conclusions.

Some observations on the impact of the results here reported on the deformation theories which have been advanced to date will now be made. We started our discussion with Cottrell's attempts to provide through a specific dislocation model a general theoretical basis for the purely empirical relations discovered by Petch. In the model chosen for this purpose, dislocation sources within the grains and large dislocation pile-ups against the grain boundaries played key rôles. Unfortunately, our electron microscope results do not support this model. In fact, neither in our work nor in the results of Keh and Morgand on iron can large dislocation pile-ups be detected at the boundaries. Although the

---

* It will be seen later that an additional reduction of the work hardening rate is expected from the dynamical recovery which operates by both cross-slip and climb.

boundaries do, in fact, accept dislocations and accommodate them into their structure, thus serving as a sort of barrier, they also act as the primary, if not the only, source of dislocations during the earlier stages of the deformation and this fact has yet to be introduced into any model used as a basis for a general theory. Furthermore, we have already seen that the boundaries during a considerable portion of the deformation are not "rigid" but rather plastic. The main effect of this fact is a continuous rearrangement in the boundary structure as new dislocations are absorbed, the gradual development of rigidity during the deformation process and the progressive drying up of these boundaries as dislocation sources. Here we see the elements of a theory of "source hardening" which increases with plastic strain and which several theoreticians - for example, N.F. Mott (35) have been seeking. Another point worth stressing is the fact that the grain boundaries, since they completely surround the grains and hence cannot be avoided by cross-slip are really the only effective barriers, but even these, because of their ready and efficient fitting of the acquired dislocations into their structures, do not cause the pile-ups of the sort visualized in the Cottrell theory and actually observed only in certain f.c.c. metals (alloys).

We are thus led to recognize the vital rôle played by grain boundaries in the deformation process and it is certainly in their ambivalent behavior as both sources and sinks of dislocations that the extremely high ductility of pure niobium is to be sought. This indicates that the ductility is dependent on grain size and further suggests that a new interpretation of the Petch parameters should be made on the basis of a more realistic model, since Cottrell formulated his before direct observations of dislocation structure became possible.

No attempt will be made here to reinterpret the Petch relations in a quantitative way - in our view such treatment must await more extensive measurements on other b.c.c. metals over a considerably wider range of temperatures than the single temperature results reported here. Furthermore, significantly more detailed studies of the effect of impurities must be carried out and such studies will at present be rendered extremely difficult by the uncertainty of the analyses in these pure materials and the ever present danger of serious contamination of initially carefully refined material during the necessary heat treatments.

During this discussion the small influence of precipitate particles - especially the smaller ones - in hindering the motion of dislocations in niobium has been pointed out several times. It follows from this fact that precipitates, at least at low concentration, should not greatly affect the mechanical properties of such metals. Actually, the principal precipitates in the niobium used here prove to be carbides and we conclude that this metal should be able to tolerate relatively large quantities of carbon before the mechanical properties begin to be impaired. It must also be recalled that the

precipitate particles themselves can, by prismatic punching during the deformation, nucleate copious quantities of dislocations and this augmented supply will increase with the concentration of precipitate. It appears reasonable, on the basis of our studies, to suggest that the lower observable limit of carbide influence on mechanical behavior of niobium might be of the order of twice the analysis of the present samples - that is, about 500 p.p.m. On the other hand oxygen behaves considerably differently, but its quantitative behavior cannot presently be predicted.

The introduction of the tangled skeins of dislocations and their development during the deformation process into well-defined cell-walls has some extremely puzzling aspects particularly with respect to the actual influence such structures have on mechanical behavior. The presence and similarity of these arrangements in two b.c.c. metals, niobium and iron, as well as in f.c.c. metals requires considerable explanation in view of the considerable difference in mechanical behavior of these two types. The mystery is deepened by the fact that the jog theory of deformation, based on the density of dislocations in the tangles proposed by Hirsch (35), (36) for f.c.c. metals, has been shown by Keh (22) to be applicable also to iron despite the fact that Li (37) has shown that the Hirsch formula cannot hold for b.c.c. metals for completely different reasons. To resolve this difficulty, Li has proposed a new theory applying some ideas concerning the repulsive forces between the mobile dislocations and those in the skeins first put forth by Friedel (38) and Saada (39). However, contrary to these authors, Li does not believe that the mobile dislocations penetrate the array of dislocations in the skeins but rather that the latter move cooperatively. These conflicting points need clarifying.

However, it seems inescapable that neither the presence of the skeins nor their subsequent development into a regular system of cell-walls achieves any detectable work-hardening. It may be that the very concentration of the new dislocations into such regular structures, thereby leaving considerable areas almost free, may serve so to change the average distribution that the mean free path of a mobile dislocation is actually increased. Such a mechanism would, therefore, counteract the opposite tendency of the gradually stiffening grain boundaries in decreasing ductility. Said another way the steady draining off of the mobile dislocations into the tangled, but rather concentrated cell-walls may be a measure of the extent of dynamic recovery which the metal experiences during deformation. This idea needs to be verified by further work but it does seem to fit all the facts known so far. In particular, the parabolic aspect of the stress-strain curve of polycrystalline materials could be explained as the progress of the dynamic recovery in counteracting the stress fields due to the increasing numbers of new dislocations. The same mechanism might apply to stage III of the work hardening curves of f.c.c. single crystals - this stage is produced by the onset of dynamic recovery. Further support is found in the observation by Keh that at low temperatures, where the yield stress is significantly higher, there is no tendency of the dislocations to group and by the observation by Morgand that this grouping, at a given temperature, is greatly favored by high purity. This induces in the stress-strain curve a steady plastic strain which thus appears to be a result of both cross-slip and climb since both should

operate during the dynamical recovery.

Finally, it is known that some extremely pure metals may begin to recrystallize during deformation at room temperature. In iron and niobium there is no question of this because of their high melting points but it does appear to us that a corresponding rôle in holding down the rate of work hardening might be assumed by the ordering inherent in the dynamical recovery and this, together with the concomitant effects of cross-slip, could perfectly well, in our view, explain the near zero work hardening rate observed in pure niobium.

Part II : Annealing Sub-Structures of Niobium and Preferential Precipitation on Dislocations.

A. Polygonization in Niobium.

The most striking feature of the structure evolution in deformed niobium is the tendency to form stable polygonization boundaries of tilt, twist and intermediate character. Figs. 45, 46 and 47 show, respectively, examples of each of these types. Actually, polygonization is seen to be a very easy process in niobium which implies the possibility of large amounts of climb and hence of high concentrations of vacancies which do not anneal out up to the polygonization temperature. The mechanism by which this concentration is maintained may be shown to be associated with the presence of dislocation rings formed in large quantities during the room temperature deformation as may be seen in Fig. 49 where the density is of the order of $5 \times 10^{14}/cm^3$. These rings, which are of 70 to 100 Å diameter and hence only resolved at high magnifications, appear to be formed by condensation of vacancies during the deformation ; a process already shown (41) to occur in zinc. In that case, however, the dislocation rings surround stacking faults which is not true in b.c.c. metals.

If the samples are annealed at 750°C following deformation the rings are seen (Fig. 50) to expand significantly to 300 to 600 Å diameter either by capture of existing free vacancies or by the disappearance of some of the smaller rings, since their density simultaneously decreases to 0.5 to $2 \times 10^{14}/cm^2$. This evolution of the rings does not appear to be accompanied by any particular rearrangement of the mobile dislocations.

If the samples are annealed at a higher temperature (~ 900°C) the dislocation rings disappear completely by contraction while the mobile dislocations rearrange themselves into polygonization walls (Fig. 51). Since these two phenomena appear simultaneously it is reasonable to assume that they are connected. Since the contraction of the rings, in turn, doubtless occurs with reemission of the vacancies, it is further reasonable to assume that in the course of this contraction the metal receives a flux of vacancies

which, as a result of the greatly facilitated climb, triggers the polygonization process. Support for this interpretation is provided by the phenomena observed at the intermediate temperature of 825°C ; here in some regions only polygonization is observed in others only expanded rings, but the two never occur together.

The high incidence of twist boundaries is an extremely interesting feature of these structures. According to the geometrical dislocation model such a boundary should possess a losange-shaped pattern with sides parallel to $[2\bar{1}1]$ and $[\bar{2}11]$. This model, however, is not stable since at points of intersection the dislocations react according to the equation

$$\frac{a}{2}[111] + \frac{a}{2}[1\bar{1}\bar{1}] \longrightarrow a[100]$$

to form a [100] segment, thereby transforming the losange into a hexagonal network. Such a reaction may be seen to happen each time a single dislocation reaches a pure tilt boundary and this produces a zig-zag pattern (see arrows) in the regular parallel array of dislocation lines in the tilt boundary (Fig.48). It follows that the interaction of two or more dislocations converts locally a tilt into a twist boundary (Fig.52) and accounts for the prevalence of twist boundaries in niobium ; this should be equally true of other b.c.c. metals.

A further interesting observation is concerned with the interaction of grain boundary junctions during annealing as seen in Fig.53 where a pure tilt boundary interacts with a pure twist boundary. It is clearly seen that, at the intersection, the dislocation concentration increases and the mesh size of the resulting network correspondingly decreases. As multiple junctions are formed this process is repeated and the structure becomes progressively more complicated (Fig.54) and more fine-meshed until it can no longer be resolved in the electron microscope. The final result is boundaries of higher angle of disorientation the structures of which are deducible from this mechanism of repeated junctions.

B. Precipitation Studies.

It is well known from many optical microscope studies (42), (43), (44) that the precipitation of a second phase takes place preferentially along dislocation lines, particularly low angle grain boundaries. This is shown in Fig.55 in an aluminum alloy (42) and transmission electron microscopy has generally confirmed this conclusion (45), (46), (47). In Fig. 56 the decoration of a single dislocation in niobium is shown while Fig.57 shows a tilt boundary where each dislocation is individually decorated. In Fig. 58 a new phenomenon of considerable interest is seen ; this is a twist boundary where only certain dislocations are decorated with precipitate. These are all parallel and have a Bürgers vector of the $\frac{a}{2}[111]$ type ; the undecorated dislocations are also parallel but differently oriented having a Bürgers vector [100]. Figs. 59 and 60 show that at small supersaturations the precipitation begins, not on the dislocations in boundary networks, but rather at isolated

dislocations. This shows that these isolated dislocations have a larger field of attraction than those which are grouped into boundaries or, said another way, the free energy per dislocation is a function of their separation and this naturally influences the nucleation rate. It may be concluded that, when the impurity content is low, precipitation on individual dislocations will be preferred. Further important conclusions are that the amount of precipitation seems to be related to the dislocation density and no precipitation is found in areas free of dislocations. Proof of these statements may be found in Figs. 61, 62, 63 and 64 the last two of which show samples first annealed at a high temperature (>1200°C) to dissolve the majority of impurities. On cooling they show no precipitation. One of these was then deformed 2%, the other 5% at room temperature and both were annealed 15 hours at 1000°C. The dislocations of both samples are now decorated but the samples 5% deformed have a higher dislocation density and, as is readily seen, a greater amount of precipitation. Since the total impurity content is the same in both samples, it is clear that the amount of precipitation is determined by the precipitation sites available.

In another experiment six identical samples were solution-treated at 1500°C and cooled to room temperature. Thereupon three of the samples were stretched to rupture and all six were reannealed in the precipitation range ; i.e. 15 hours at 1000°C. The undeformed samples showed neither dislocations nor precipitation (Fig. 63) while the ruptured samples showed copious decoration of the numerous dislocations present (Fig. 64). It is concluded that, at least at the supersaturation level of these samples, precipitation occurs only on dislocations. In the case of more contaminated samples having very high supersaturations there may be some precipitation between the dislocations (Figs. 65 and 66) but it always starts preferentially on them.

As the degree of saturation depends on the temperature, these phenomena should be influenced also by the annealing precipitation temperature.

In Fig. 67 the penetration of oxygen into a niobium sample during annealing in a poor vacuum is shown. There is apparently preferential penetration of oxygen along grain boundaries and, in some cases, along individual dislocations as shown by the precipitate laid down. The precipitate particles, which have not actually been identified, are presumed to be oxide.

In some samples, where the precipitation was carried out in a better vacuum (2×10^{-7} to 10^{-8} mm Hg) or where the samples were protected by a niobium foil, the precipitate particles have actually been identified after extraction on a carbon replica. This technique permits identification of the origin (grain boundaries or interior of the grains) of the particles. Fig. 68 shows precipitate particles from an individual dislocation line which were found, by electron diffraction, to have the hexagonal structure characteristic of Nb_2N or Nb_2C. Fig. 69 shows precipitates extracted from high angle grain boundaries which have the cubic structure of NbC or NbN. The lattice

parameters of the carbides and nitrides are so similar that positive identification is impossible although these are more probably carbides because of the high carbon content of the samples.

A curiosity extracted in these experiments are the rosettes shown in Fig. 70 where the dislocation line is at the center of the rosette. It is possible that growth in this form causes a minimum of lattice strain.

The authors are particularly grateful to Dr. R. H. Gillette, Director of our Laboratory, for the constant advice, helpful discussions and the help in the editing of the manuscript.

REFERENCES.

1. N.J. PETCH - J. Iron Steel Inst. 174 (1953) p. 25.

2. J. HESLOP and N.J. PETCH - Phil. Mag. 1 (1956) p. 866.

3. A.H. COTTRELL - Trans. A.I.M.E. - 212 (1958) p. 192.

4. M.A.ADAMS,A.C.ROBERTS and R.E.SMALLMAN, Acta Met.8 (1960)p.238.

5. A.A. JOHNSON - Acta Met. 8 (1960) p. 737.

6. A.T. CHURCHMAN - J. Inst. Metals 88 (1960) p. 221.

7. R.C. KOO - J. Less Common Metals 4 (1962) p. 138.

8. M.A. ADAMS and A. IANNUCCI - Private communication.

9. M.J. MARCINKOWSKI and H.A. LIPSITT - Acta Met. 10 (1962) p. 95.

10. H.J. BECHTOLD, Trans. ASM 46 (1954) 1449.

11. H.J. BECHTOLD and P.G. SHEWMON - Trans. ASM 46 (1954) 972.

12. A.A. JOHNSON - Phil. Mag. 5 (1960) p. 413.

13. A.S. WRONSKI and A.A. JOHNSON - Phil. Mag. 7 (1962) p. 213 ;
A. WRONSKI - Thesis 1961 (Imperial College).

14. S. AMELINCKX - Private communication.

15. A. BERGHEZAN and A. FOURDEUX - 4ème. Colloque de Métallurgie (Saclay (1960) - Propriétés des joints de grains (Presses Univ. de France, 108, Bd. St. Germain (1961) p. 127 and Compt. Rend. 252 (1961) p. 1462.

16. A. BERGHEZAN - Thesis 1952 - Pub. Scient. et Techn. Ministère de l'Air, 2, Av. de la Porte d'Issy, Paris (1953).

17. W.A. WOOD and W.A. RACHINGER, J. Inst. Met. Mars 1949, p. 371.

18. P. GAY, P.B. HIRSCH and J.H. KELLER, Acta Cryst. 7 (1954) p. 41.

19. A. BERGHEZAN and J. HERENGUEL - Comptes Rendus 240 (1955) p. 1343.

20. A. BERGHEZAN - Métaux, Corrosion, Industrie 359-360 (Juillet-Août 1955, p. 1).

21. A. FOURDEUX and A. BERGHEZAN - Comptes Rendus 252 (1961) p. 1462.

22. A.S. KEH - Proc. A.I.M.E. Symposium on "Direct Observation of Imperfections in Crystals" - Interscience (1962) p. 213.

23. A.S. KEH and S. WEISSMAN - in press "Electron Microscopy and Strength of Crystals" by Interscience.

24. P. MORGAND - Compt. Rend. 254 (1962) p. 2578.

25. D. KUHLMANN-WILSDORF and H.G.F. WILSDORF - Acta Met. 10 (1962) p. 584.

26. B.P. PRICE - Phil. Mag. 5 (1960) p. 873 and J. Appl. Phys. 32 (1961).

27. J.T. FOURIE and H.G.F. WILSDORF - J. Appl. Phys. 31 (1960) 2219.

28. J.R. LOW, Jr. and A.M. TURKALO - Acta Met. 10 (1962) p. 215.

29. R. BENSON, G. THOMAS and J. WASHBURN - Direct Observations of Imperfections in Crystals - Edited by J.B. Newkirk and J.H. Wernick - Interscience Publ. (1962) p. 375.

30. A.S. TETELMAN - Dislocation Dipole Formation in Deformed Crystals - [Report - 1962 - of the University of Paris (Physique des Solides) Boîte Postale N° 11, Orsay (S. et O.) France]

31. A. BERGHEZAN and A. FOURDEUX - J. Appl. Phys. Vol. 30 (1959) p. 1913.

32. A. FOURDEUX and A. BERGHEZAN - J. Inst. Metals 89 -(1960) p. 31.

33. A. FOURDEUX and A. BERGHEZAN - Letter Editor J. Inst. Metals - July (1961) p. 191.

34. C. CRUSSARD - Compt. Rend. 252 (1961) p. 273.

35. N.F. MOTT - Trans. A.I.M.E. 218 (1960) p. 962.

36. J.E. BAILEY and P.B. HIRSCH - Phil. Mag. 5 (1960) p. 485.

37. J.C.M. LI - Discussion on work by Keh, see Ref. 16.

38. J. FRIEDEL - Symp. Internal Stresses and Fatigue of Metals, G.M. Tech. Center Detroit (1959).

39. G. SAADA - Acta Met. 8 (1960) p. 20 ; Acta Met. 8 (1960) p. 841 and Acta Met. 9 (1961) p. 166.

40. A.A. JOHNSON - Phil. Mag. 7 (1962) p. 177.

41. A. BERGHEZAN, A. FOURDEUX and S. AMELINCKX - Acta Met. 9 (1961) p. 464.

42. P. LACOMBE and A. BERGHEZAN, C.R. Ac. Sci., Paris 226 (1948) p. 2152 ; 229 (1949) p. 365 and Alluminio 4 (1949) p. 1.

43. R. CASTAING and A. GUINIER - C.R. Ac. Sci. Paris 228 (1949) p. 2033.

44. H. WILSDORF and D. KUHLMANN-WILSDORF, Rept. Conf. Defects Crystalline Solids - Bristol (1954) p. 175.

45. D. Mc LEAN and K.F. HALE - Electron Microscopy Conference - Exeter (England) 1959.

46. G. THOMAS, Phil. Mag. 4 [41] (1959), p. 606.

47. A. BERGHEZAN and A. FOURDEUX - 4ème. Colloque de Métallurgie (June 1960 - Saclay - France) - "Propriétés des Joints de Grains" - Edition : Institut des Sciences et Techniques Nucléaires - Presses Universitaires de France, 108, Bd. Saint-Germain, Paris (1961).

Figure 1

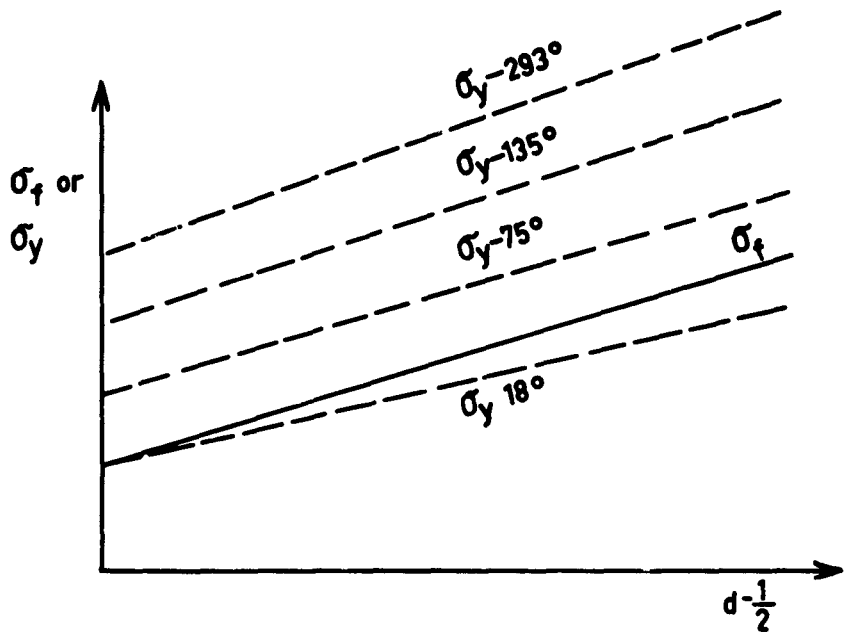

Figure 2

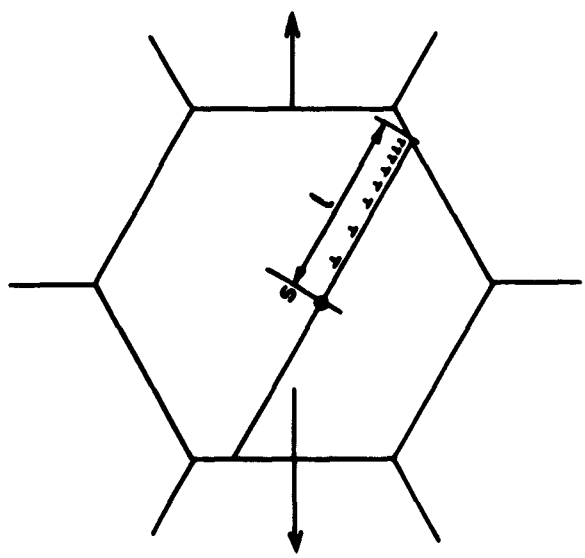

Figure 3

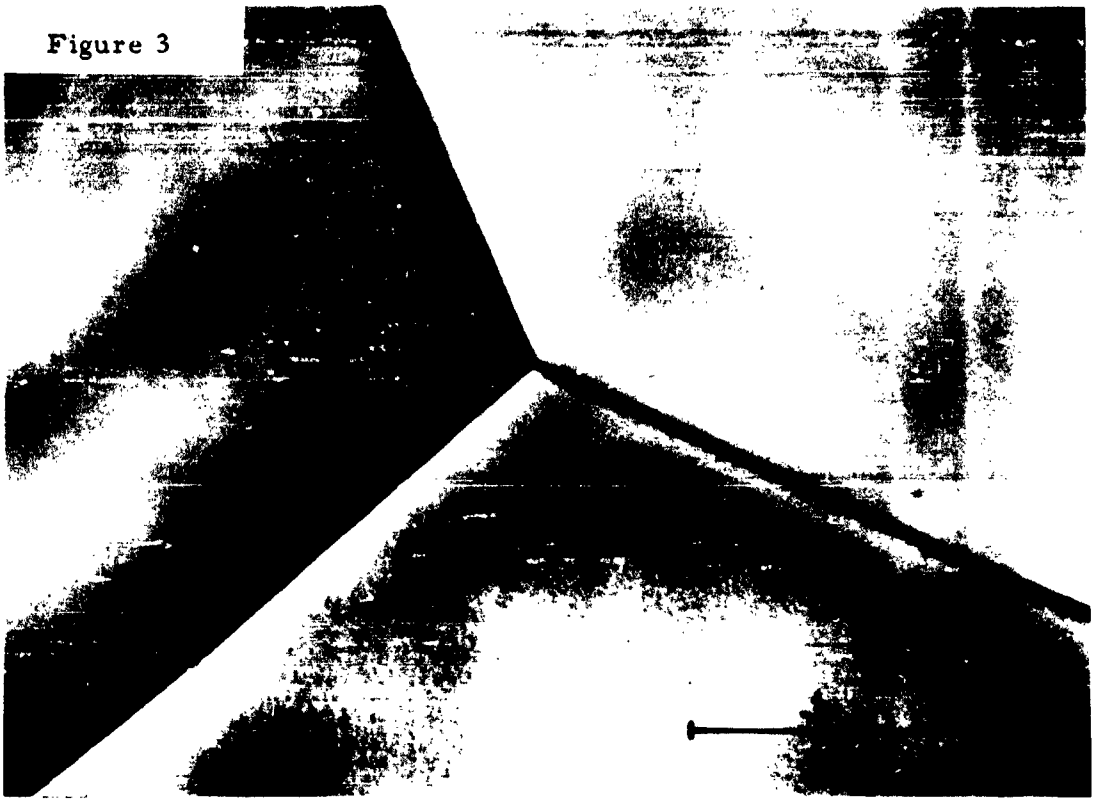

Figure 4

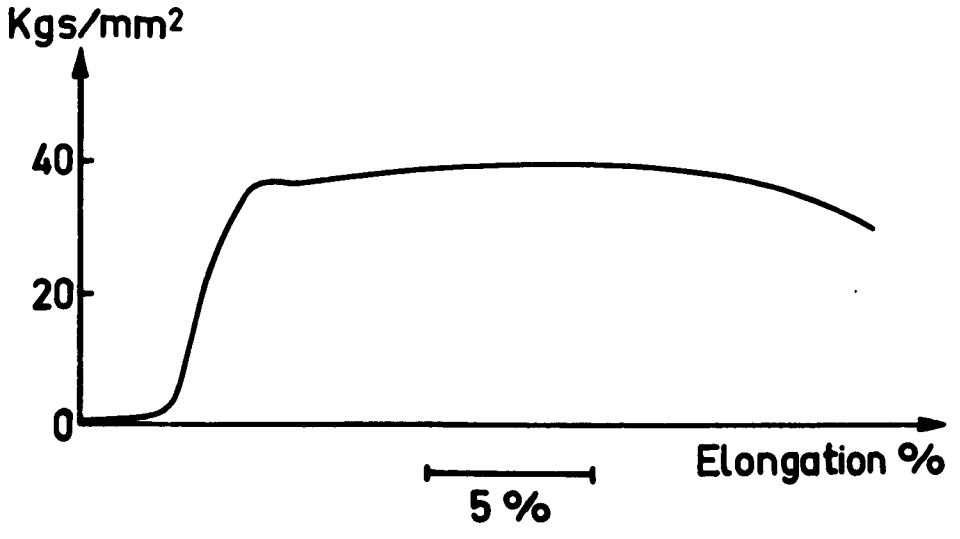

Figure 5

Figure 6

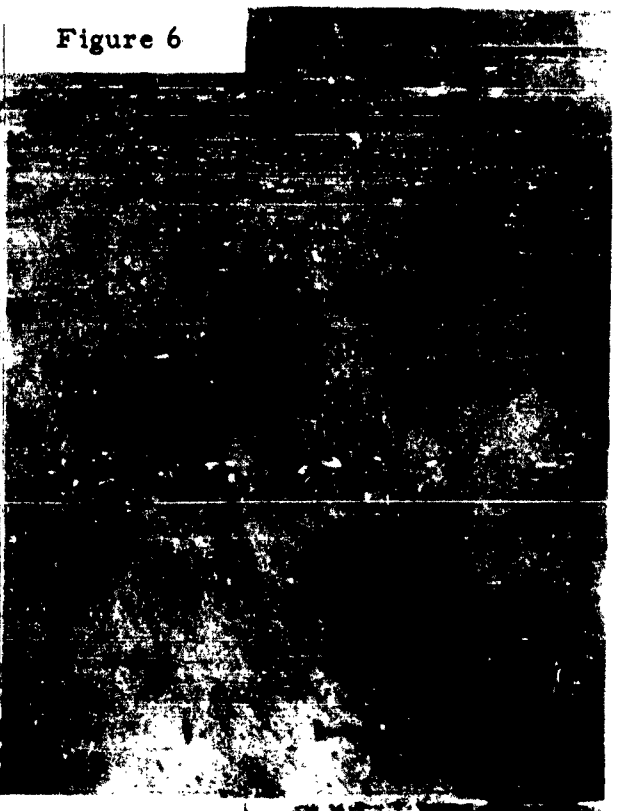

Figure 7

Figure 8

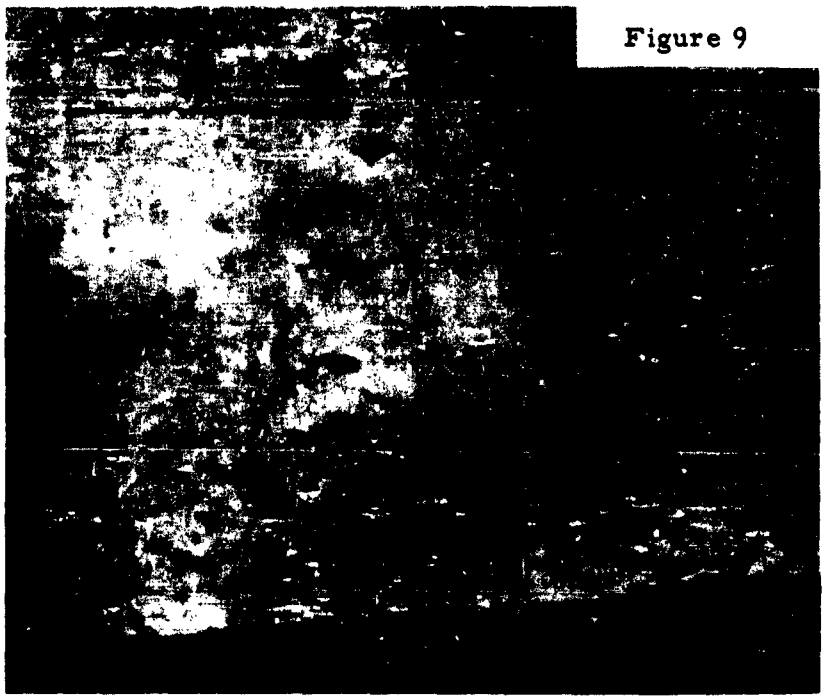

Figure 9

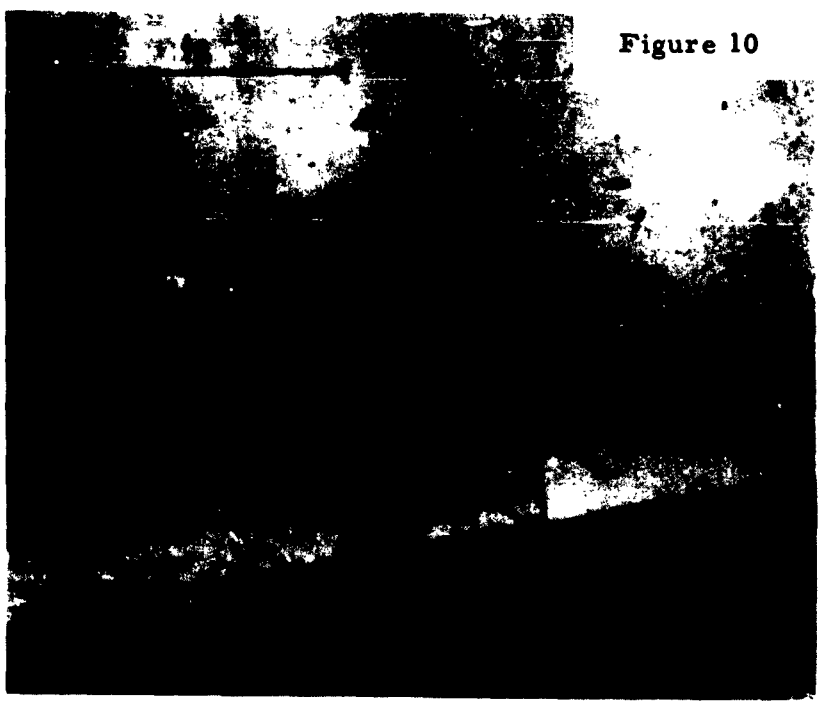

Figure 10

Figure 11

Figure 12

Figure 13

Figure 14

Figure 15

Figure 16

Figure 17

Figure 18

Figure 19

Figure 20

Figure 21

Figure 22

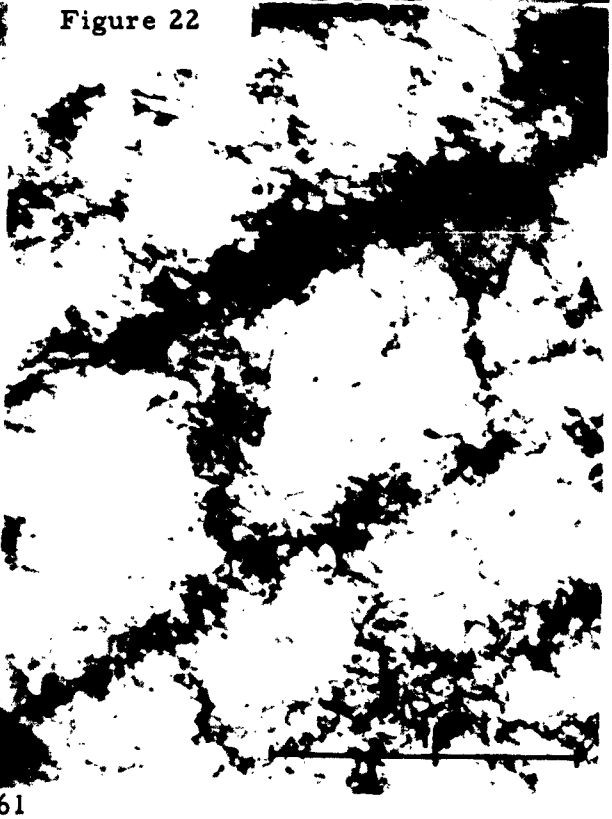

Figure 23

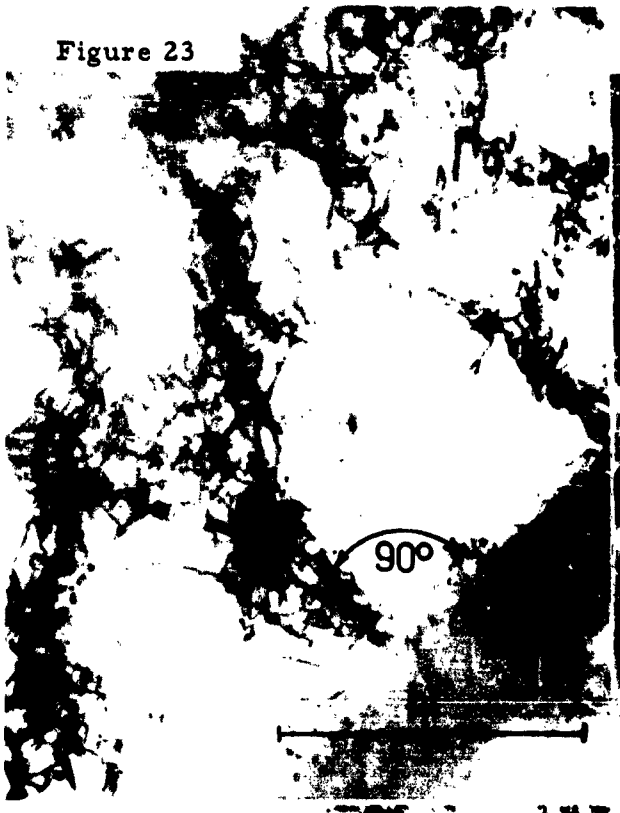

Figure 24

Figure 25

Figure 26

Figure 27

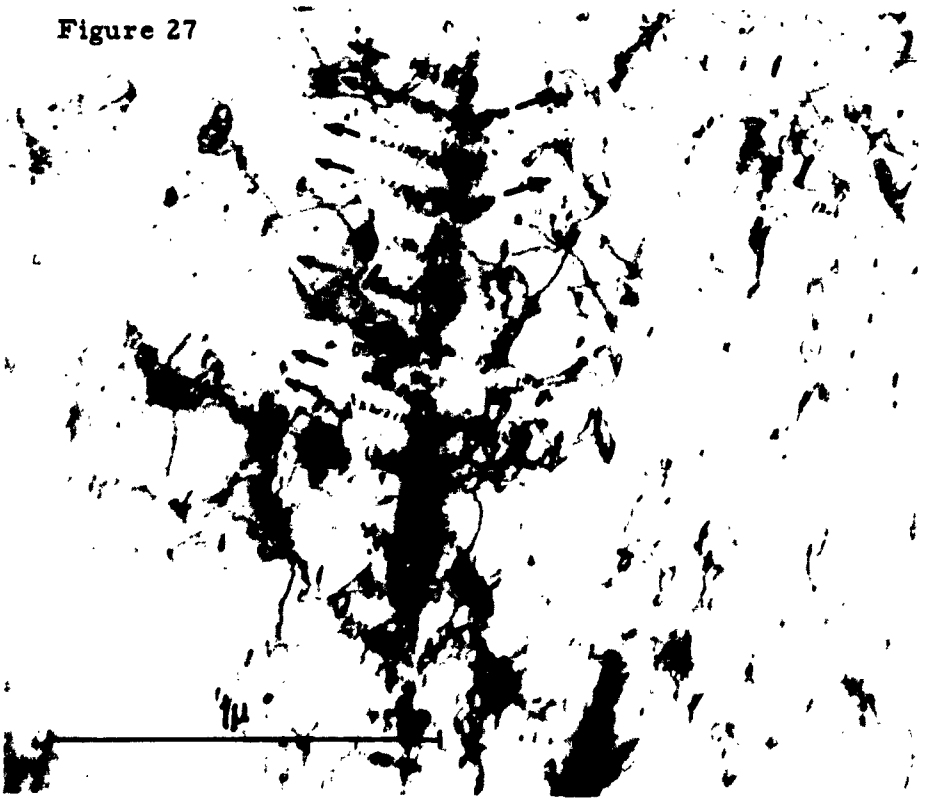

Figure 28

Figure 29

Figure 30

Figure 31

Figure 32

Figure 33

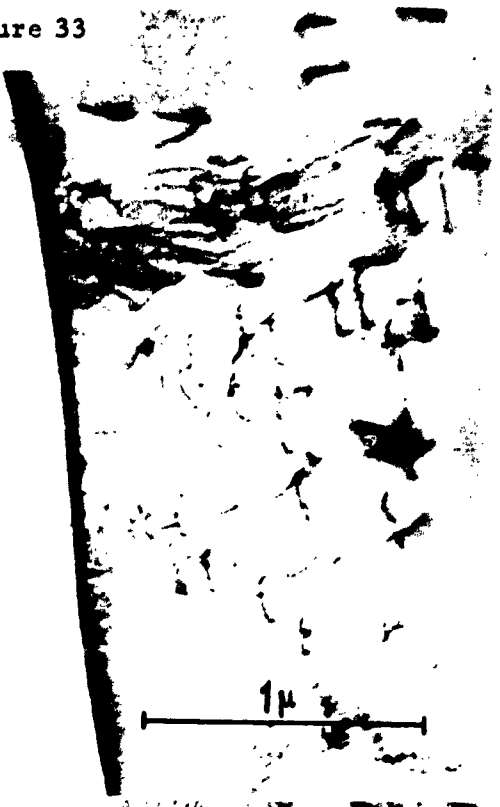

Figure 34

Figure 35

Figure 36

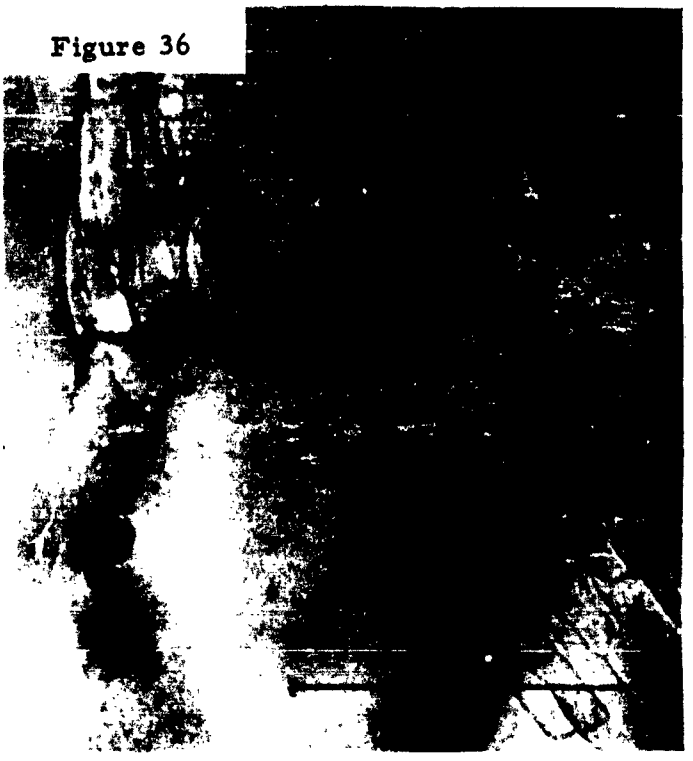

Figure 37

Figure 38

Figure 39

Figure 40

Figure 41

Figure 42

Figure 43

Figure 44

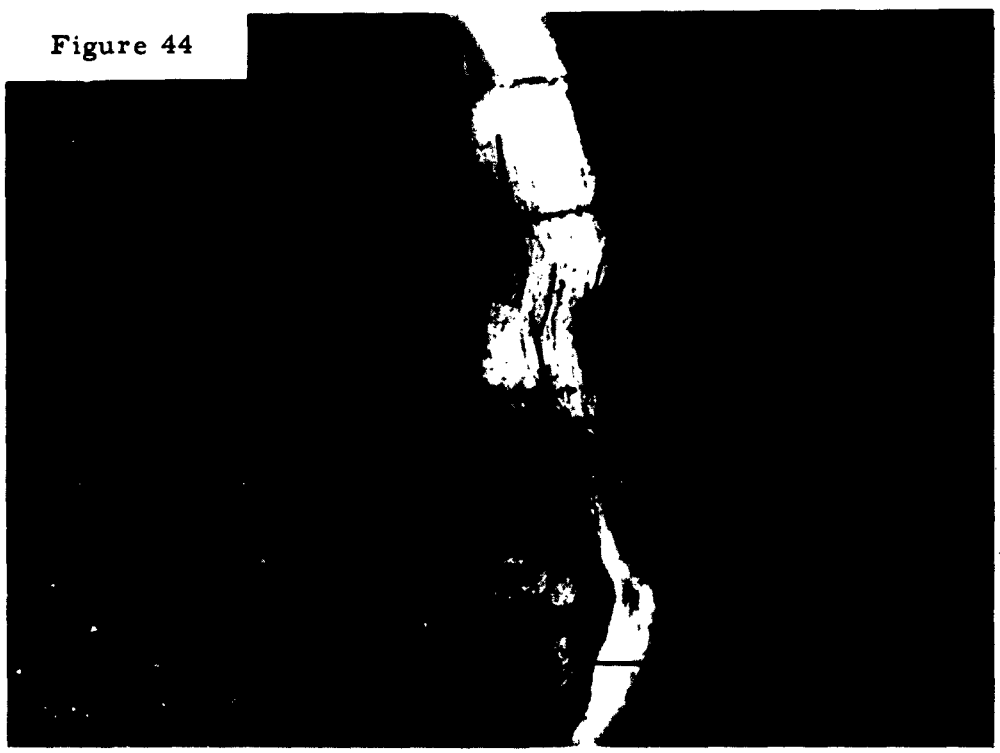

Figure 45

Figure 46

Figure 47

Figure 48

Figure 49

Figure 50

Figure 51

Figure 52

Figure 53

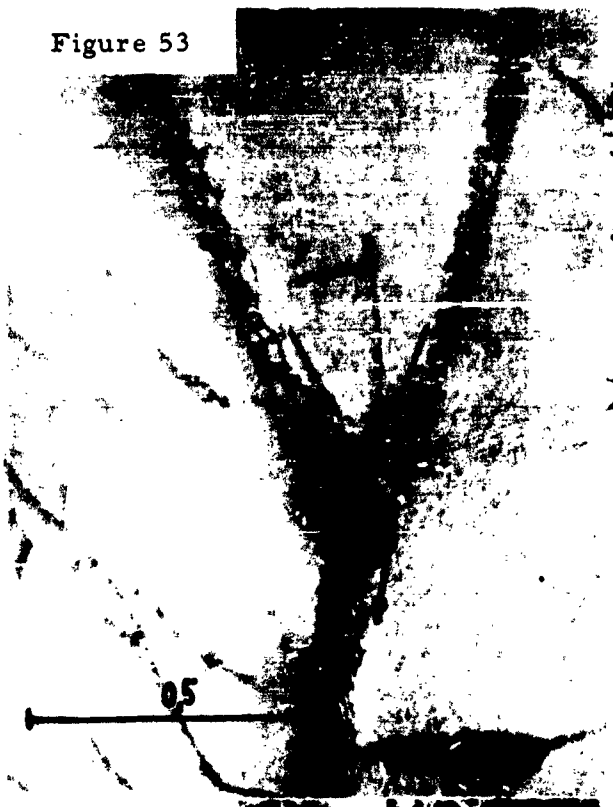

Figure 54

Figure 55

Figure 56

Figure 57

Figure 58

Figure 59

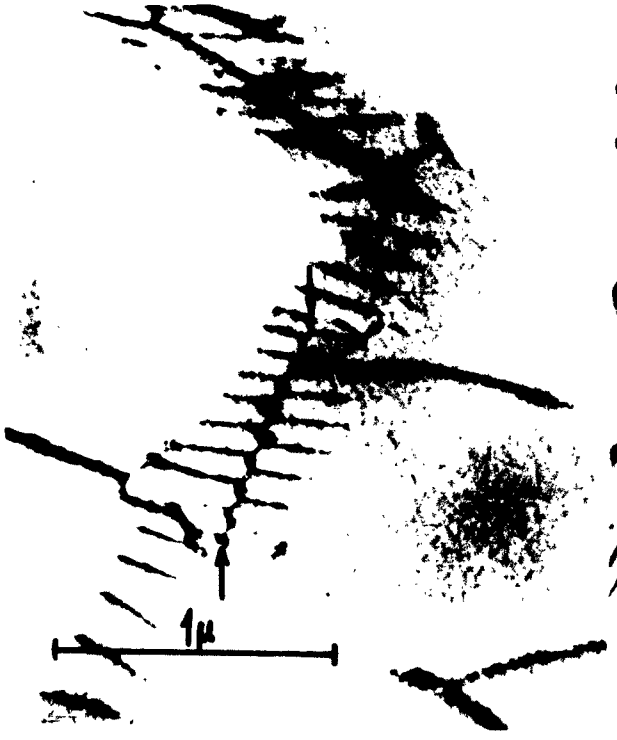

Figure 60

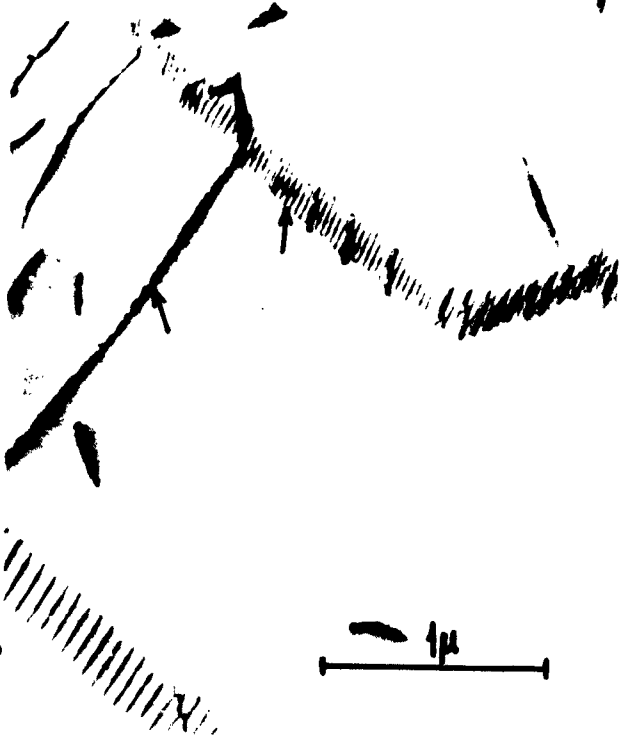

Figure 61

Figure 62

Figure 63

Figure 64

Figure 66

Figure 67

Figure 68

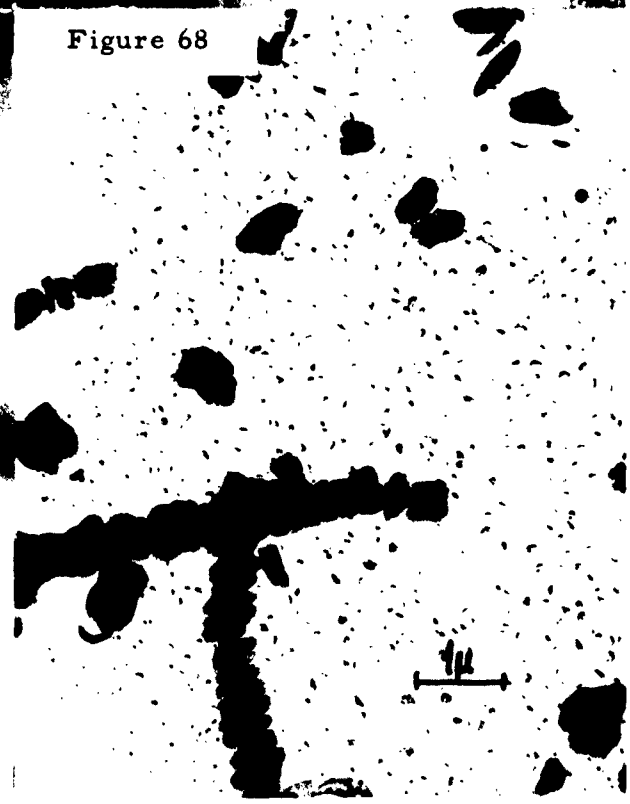

Figure 69

Figure 70

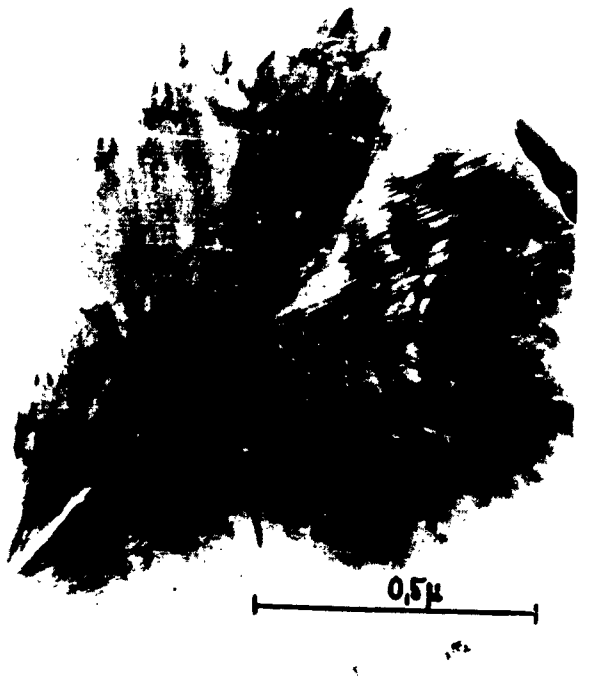

THE ROLE OF SUB-STRUCTURE IN PHASE TRANSFORMATIONS

R. M. Fisher

Edgar C. Bain Laboratory
For Fundamental Research
United States Steel Corporation

Abstract

Lattice defects, particularly dislocations, play important roles in the nucleation and propagation of phase transformations and so plastic deformation prior to or during transformation provides a possible means of controlling the kinetics and the resulting microstructure. The available experimental evidence and the present status of our understanding of these effects will be reviewed for transformations from austenite, formation of sigma phase and the development of anti-phase domain structures in ordered alloys.

Introduction

Sub-structure can play several different roles in phase transformation or precipitation processes as it can be involved in both the nucleation and propagation of the new phase and also may itself be generated by the transformation process. Because of the ambiguity of the term 'sub-structure', in this report it will be taken to mean any dislocation array and these various roles will be discussed and related to some of the previous work on the decomposition of austenite, ordering transformations and the formation of sigma phase.

Most of the conceivable roles that dislocations might play in phase transformation and precipitation are illustrated schematically in Figure 1. As shown in Fig. 1a, the nucleation sites for the formation of a second phase (β) may be at either dislocations (top sketch) or in the case of f.c.c. crystals at stacking faults. The detailed features of these processes will depend on the crystal structures of the parent and product phases as well as any lattice expansion or contraction which may be involved and in many cases nucleation will occur only

on specific dislocation configurations such as pure screw or edge segments, jogs, etc.

In body-centered cubic metals, the precipitation of carbon or nitrogen at low temperatures is usually observed to occur along dislocation lines. Figure 2 shows an example of carbon precipitation on a dislocation network in vanadium and other examples of such precipitation in iron can be found in the review paper by Keh, Leslie and Speich in this symposium.

Observations of the precipitation of carbide on stacking faults in f.c.c. stainless steels have been reported by Hatwell and Votava[2] and van Aswegen and Honeycombe[3].

Possible roles of dislocations in the propagation or growth of a phase transformation are illustrated in Fig. 1b. In the case of diffusionless or martensitic transformations, the atomic rearrangement occurs by shear processes and the interface between the parent and product phases consists of an appropriate dislocation array as indicated at the top of the β region in the figure. The transformation in this case proceeds by the movement of the dislocations in the array. If the transformation occurs by diffusion and results in a volume change, nearby dislocations can act as sources or sinks to supply or absorb vacancies required to accommodate such volume changes as illustrated at the bottom interface of the β phase in the sketch.

The inverse of the processes shown in Fig. 1a, b can also be expected to occur, i.e., the generation of dislocation sub-structure during the growth of the new phase and several different possibilities are illustrated in Fig. 1c. At the right of the β phase region is shown the case where the volume change during the transformation is negative (i.e., shrinkage). Here vacancy loops may be produced[4] which then move away from the particle by a combination of glide and climb (absorption of vacancies). An example of such vacancy loops observed by Smallman[5] in Al-3.5pctMg alloys is shown in Figure 3. A detailed analysis of such dislocation loop configurations in these alloys has been carried out by Embury[6] and Nicholson. At the left side, a positive volume change is shown

which will result in the formation of interstitial loops. These loops may move away from the particle by glide as before, but in this case they will shrink by the absorption of vacancies from the lattice. An example of such loops produced during the precipitation of chromium carbide in an 80pct Cr- 20pct Fe alloy is shown in Figure 4.

Interface dislocations as shown schematically at the top of the β region in Fig. 1c may be produced to accommodate the misfit between the two lattices when coherency is lost. This structure has been observed along the cementite-ferrite interface in pearlite[18] and after cellular precipitation of Ni_3Ti in an austenitic Fe-30 Ni-6 Ti alloy (Speich)[7].

Finally as shown at the bottom of the β region in Fig. 1c, defect structures particularly stacking or sequence faults may be generated in the growing phase itself as illustrated in the figure. These may be formed during transformation directly or they may result from the presence of sub-structure i.e., dislocation arrays in the parent phase. Examples of these effects have been observed and will be discussed further in other sections.

Formation of Sigma Phase

The pronounced effect of cold-work in accelerating the rate of formation of sigma-phase in iron-chromium alloys is very well-known. It was first observed by Cook and Jones[8] and has been used extensively since then to hasten the approach to equilibrium in alloys where sigma phase might be expected to form.

The effect of cold work is very large even for transformations within the single phase field, i.e., where no long range diffusion is required. As an example, a heavily rolled sample of 46pct Cr-Fe will transform completely to sigma in several hours at 650°C whereas annealed samples will require several hundred hours. The results of quantitative measurements of the transformation kinetics by Pomey and Bastien[9] and Williams and Paxton[10] are summarized in Figure 5. In both investigations the alloys contained approximately 46 wt.pct Cr; Pomey and Bastien cold-rolled their materials 90 pct. and determined the extent of

transformation by quantitative dilatometric measurements, whereas Williams and Paxton used filings and followed the reaction by magnetic measurements.

These data show that the transformation rate is increased by approximately a factor of 100 although whether it is the nucleation or the growth of sigma that is affected is not apparent. A detailed investigation has been initiated on this subject and some of the preliminary results will be outlined briefly in this report as well as some other aspects of the role of sub-structure in the transformation which have been observed.

The effect of cold-work on the growth rate was determined by measuring the diameter of a number of the largest particles that could be found in the sample following the procedure frequently used in studying the pearlite reaction. The results of the measurements on specimens deformed varying amounts by cold-reduction are shown in Figure 6 and it is clear that the growth rate is increased substantially. The apparent inversion between 85 and 90 pct. is puzzling; possibly it is related to the fact that 90 pct. samples were deformed using a different set of rolls and under different conditions or it may be a real effect as will be discussed further.

Measurements of the nucleation of sigma phase indicated that cold work does not have a pronounced influence. The results suggest that a particular amount of cold work introduced a fixed number of nuclei and that even for 95 pct. reduction the increase over the annealed specimens is less than a factor of five. Thin foil observations are in accord with this conclusion. Figure 7 shows a transmission electron micrograph of a specimen deformed 5 pct. and then aged for 16 hours at 650°C. Unlike the case of precipitation (Vanadium Figure 2) shown previously, there is no evidence of transformation beginning at the dislocations. Polygonization and recrystallization occurred in specimens more heavily deformed (90 pct.) and aged 30 min. at 650°C as shown in Figure 8 with no evidence for sigma nucleation in most regions.

Feng and Levesque[11] have reported sigma formation along deformation twins in rhenium - molybdenum alloys. Deformation twins were produced in

annealed samples of the 46 pct. alloy used in this study by means of hardness indentations or punch marks on previously polished surfaces. Twinned areas were photographed and then after aging in hydrogen at 650°C the identical area was located and re-examined. An optical micrograph of the specimen after etching with glyceregia (the recommended etchant for sigma) is shown in Figure 9. From a preliminary examination of such areas it appeared that as reported, the twins had transferred to sigma. However, after further aging and using different metallographic procedures it was found that such twins were not sigma. Occasionally, definite sigma particles could be identified which were associated with the twins particularly at intersections. An example of this is shown in Figure 10. Thin foil studies of deformation structures in these alloys have shown that very intense localized deformation often occurs at twin intersections as illustrated in Figure 11. The rate of growth of sigma was also found to be enhanced along some of the twins as shown in Figure 12 causing the particles to have rather irregular shapes. In heavily cold-rolled specimens, the sigma particles maintain a more spherical shape.

Thin foil observations of partially transformed specimens show that some recovery and polygonization occurs ahead of the growing sigma phase. Figs. 14a and 14b show examples after 15 min. and 30 min. at 650°C following 90 pct. cold reduction and it is clear that the subgrains are becoming more perfect as aging proceeds. The growth measurements indicated that the rate was decreasing during this period. The apparent discrepancy in growth rate between samples deformed 85 and 90 pct. may be associated with more rapid and pronounced recovery in the samples given the greater cold reduction.

It may also be noted in these figures that the sigma particles contain faults parallel to the growth direction. These have been studied in detail by Marcinkowski and Miller[12] and found to be sequence faults. A large number of different fault configurations are possible because of the complex crystal structure of sigma. Marcinkowski and Miller suggest that these faults are generated during the transformation and this idea was borne out by these observations. Figure 15 shows an example of a fault corresponding to a dislocation subboundary in the ferrite.

Discussion

These preliminary results indicate that sigma phase is nucleated at regions of very high dislocation density, possibly when recrystallization begins at these points. From a study of sigma formation in a series of austenitic stainless steels, Lena and Curry[13] also concluded that there was a correlation between the effect of cold work on sigma formation and on recrystallization. In annealed specimens sigma formation begins at certain points along the grain boundaries where specific orientation relationships exist between the grains so that the sigma nucleus can be coherent with both grains simultaneously. (These results will be reported in detail separately.) However, despite this restriction on nucleation and the apparent connection with recrystallization, it must be emphasized that cold work appears to influence growth far more than it does nucleation.

The origin of the effect of dislocation density on the rate of growth of sigma phase is not clear. In some respects the growth of sigma particles in the single phase field where no composition change occurs is similar to recrystallization and grain growth. This similarity is suggested by the micrographs in Figure 14 showing the interface between sigma and the ferrite matrix. The difference, of course, is that the recrystallized 'grain' has a different crystal structure than the deformed matrix.

The increase in growth rate in heavily deformed specimens (approx. 100X) is of the same order of magnitude as the effect of cold work on grain growth in deformed as compared to annealed specimens. An Arrhenius-type plot of the time for 50 pct. transformation at different temperatures (from the data of Ref. 9 and 10) gives the identical slope of 31,000 calories for both annealed and deformed specimens. This value is comparable to measured activation energies of recrystallization. However, its interpretation as with similar measurements of recrystallization is complicated by the possibility of recovery occurrring in the lattice ahead of the growing interface so that the driving force is decreasing with time. This effect is clearly evident from a comparison of Figs. 14a and 14b, but might not have been as pronounced in the references cited.

The stored energy of cold-work recovered when sigma is formed, even in the most heavily deformed specimens, would not be more than 200 cals/mol. If this stored energy becomes the dominant driving force for growing sigma phase then the chemical free energy involved must be unusually small. Sigma is a more dense phase than ferrite and the strain energy developed by the volume change could result in a substantial reduction in the effective driving force. Any detailed analysis of the sigma transformation will require more experimental information than is now available, but it is apparent that substructure plays important roles in the formation of sigma phase.

Decomposition of austenite

Sufficient information is not available as yet to indicate the role of substructure in the decomposition of austenite in any detail, but the results of a number of investigations suggest that a close relationship does exist. Studies have been made of the effect of applied stress on the pearlite[14, 15], bainite[15, 16], proeutectoid ferrite[16, 17] and martensite[15] transformation and in all cases above a threshold stress level, a marked acceleration of the rate of transformation was obtained. Without going into a detailed discussion of the experimental observations and their interpretation, it seems quite clear that these transformations can be nucleated by plastic deformation of austenite. There appears to be little effect of stress in the propagation or growth rate of the transformations but further study of this point is desirable.

Dislocation sub-structure is generated during transformations from the austenite. This is evident as extra-plasticity which occurs during transformation under stress[15] and in the case of the pearlite reaction, metallographic effects may also be noted[18]. Here, even in the absence of an externally applied stress, sufficient deformation of the austenite occurs to cause appreciable polygonization ahead of the transformation which results in the formation of small angle subgrains within the pearlite colony. It has also been observed[18] that the dislocations in the polygonized boundaries can block the growth of the cementite lamellae but not the ferrite. Finally it appears[18] that sub-structure in the form of closely

spaced stacking faults is generated in the cementite particles during the pearlite transformation.

Currently much interest is concentrated on microstructures produced by extensive plastic deformation during or prior to transformation, i.e., treatments usually referred to as ausforming or thermomechanical treatment. Our lack of a full understanding of the relation between dislocation sub-structure and transformation, handicaps attempts to interpret such structures. For example Figure 16 shows a carbon extraction replica of an ausformed sample of an experimental steel (composition listed below) kindly supplied by Dr. Victor Zackay[19]. This specimen was deformed 90 pct. at a temperature of about 500°C i.e., in the temperature range between the C curves for pearlite and bainite formation. From the micrograph it is clear that carbide precipitation has occurred along the deformation bands but it is impossible at the moment to choose between the several mechanisms that are conceivable. These are:

(1) carbide precipitated from the austenite on dislocations introduced by the deformation,

(2) the deformation accelerated the bainite reaction,

(3) the deformation raised the M_s temperature so that martensite formed which immediately tempered.

The first mechanism has been suggested by Grange[20] and the latter two are both consistent with observations on the effect of deformation on the bainite[14, 15] and martensite[15] transformation discussed below.

These brief remarks are intended to emphasize that dislocation substructure does appear to have an important role in transformation from the austenite and that insufficient experiments specifically designed to investigate these effects have been carried out. Such studies would be very valuable as they might shed considerable new light on the mechanisms of the transformations and also lead to more effective thermo-mechanical or ausforming processes.

Composition of ausformed steel

3 Cr 1.5Ni 0.75Mn 0.5Mo 1.5Si 0.63C

Formation of Superlattice Domain Structures

Dislocation sub-structure has an important and rather unique role in the formation of superlattice domains during ordering. The reason for this is that in many structures, the unit of slip, i.e., the Burgers vector responsible for anti-phase domain boundaries and an interaction can occur; in $AuCu_3$ for example these are both $1/2\ a_o\ \langle 110 \rangle$. That is, the extra half plane of atoms which constitutes the dislocation can eliminate the out of step boundary which otherwise would be present and terminate the anti-phase boundary at the slip plane. This effect is illustrated in the schematic drawing by Marcinkowski[21] shown in Figure 17. This figure also shows that the movement of individual slip dislocations in an ordered structure creates new anti-phase boundaries. The energy associated with this process results in strong coupling between pairs of dislocations which greatly reduces the stress necessary to drive dislocations through an ordered lattice.

The termination of anti-phase boundaries on dislocations present in the specimen prior to formation of the domain structure has been observed by Pashley[22] and Marcinkowski[21] previously. A difficulty that is encountered here is that the contrast conditions are such that only two-thirds of the boundaries are revealed[23] in any particular micrograph. Thus, most of the apparent terminal points of boundaries in micrographs are due to this reason rather than a true termination of the boundary. The point indicated in Figure 18 of a specimen of $AuCu_3$ slowly cooled from above the critical ordering temperature (approx. 385°C) corresponds to a point where termination on a dislocation has taken place. The extended boundaries running across the micrographs were produced by movement of single dislocations in the thin foil. This deformation occurred during handling of the thin foil specimen and boundaries of this sort would not normally be formed in bulk specimens.

If the dislocation density within the specimen prior to ordering is very high it can markedly influence the size of the anti-phase domains since their size will be essentially equal to the dislocation spacing. The rate of growth of the

domains will also be retarded since this will involve dislocation climb processes. Roessler, Novick and Bever[24] have recently studied the annealing of $AuCu_3$ after cold work using electrical resistivity and X-ray techniques and noted the retardation of domain growth as discussed above.

A similar study of the effect of sub-structure on domain size is currently underway in this laboratory[25] using transmission electron microscopy. It has been found that domains formed during slow cooling of heavily cold-rolled $AuCu_3$ are only 1/30 to 1/10 to size of these in annealed specimens given the same cooling treatment. Since the strength of ordered alloys only depends strongly on domain size if they are very small, means of achieving very small domains are of considerable interest.

Summary

Dislocation sub-structure can be expected to take several important roles in phase transformations and these are discussed in connection with the nucleation and propagation or growth of precipitation or phase change. In the case of precipitation from solid solution, nucleation or dislocations on stacking faults has been observed in many systems although detailed analysis has not been carried out as yet.

Observations of the effect of plastic strain on decomposition of austenite suggests that dislocations introduced by deformation of the parent austenite can serve to nucleate the pro-eutectoid ferrite, pearlite and bainite reactions, although a direct connection has been demonstrated. The importance of these effects in developing ausforming processes is pointed out.

The effect of cold work on accelerating the formation of sigma phase in approx. 50-atomic percent Fe-Cr alloys is found to be mainly due to increasing the growth rate. It is suggested that the strain energy stored in the lattice by cold-work and released by the transformation makes a very large contribution to the driving force.

The unique relation between dislocations and the domain configuration in

ordered alloys is discussed and the manner in which dislocation density controls domain size is pointed out.

The various mechanisms by which sub-structure may be generated by phase transformation are described. Examples are shown of vacancy or interstitial loops generated by volume changes during precipitation and of growth faults in the new phase due to defects in the parent lattice.

Acknowledgments

It is a pleasure to acknowledge the value of discussions with various members of the staff and management of the E. C. Bain Laboratory for Fundamental Research and the able assistance of Albert Szirmae in carrying out the experimental work described in this paper.

References

1. A. S. Keh, W. C. Leslie and G. R. Speich, this conference.
2. H. Hatwell and E. Votava, Acta Met. Vol. 9, p. 945, 1961.
3. J. S. T. van Aswegen and R. W. K. Honeycombe, Acta Met. Vol. 10, p. 262, 1962.
4. D. A. Jones and J. W. Mitchell, Phil. Mag. Vol. 8 - series 3, p. 1, 1958.
5. R. E. Smallman, The Metallurgist 1, p. 146, 1960.
6. J. D. Embury and R. B. Nicholson, Proceedings Fifth International Conference on Electron Microscopy, Academic Press, Vol. I, p. J-1.
7. G. R. Speich, to be published, Trans. AIME 19o3.
8. A. J. Cook and F. W. Jones, J. Iron and Steel Inst. 1943, Vol. 144, p. 217.
9. G. Pomey and P. Bastien, Rev. de Met. 1956, Vol. 53, p. 147.
10. R. O. Williams and H. W. Paxton, J. Iron and Steel Inst., 1957 Vol. 185, p. 358.
11. C. Feng and P. Levesque, Trans. AIME, 1961, Vol. 221, p. 1278.
12. M. J. Marcinkowski and D. S. Miller, Phil. Mag. Vol. 7, No. 78, p. 1025-1059, 1962.
13. A. J. Lena and W. E. Curry, Trans. ASM 47, 1955, p. 193-210.
14. G. L. Kehl and S. Bhattacharyya, Trans. ASM 48, p. 234-248, 1956.

15. L. F. Porter and P. C. Rosenthal, Acta Met. Vol. 7, 1959, p. 504-514.

16. S. Bhattacharyya and G. L. Kehl, Trans. ASM 47, p. 351, 1955.

17. A. H. Cottrell, J. Iron and Steel Inst. Vol. 151, p. 93, 1945.

18. L. S. Darken and R. M. Fisher, 'Decomposition of Austenite by Diffusional Processes,' Zackay-Aaronson, Interscience, 1962.

19. Victor Zackay, Private communication.

20. R. A. Grange, Private communication.

21. M. J. Marcinkowski, 'Strength of Crystals,' Thomas-Washburn, Interscience, 1962.

22. D. W. Pashley and A. E. D. Presland, J. Inst. Metals, 1958-59, Vol. 87, p. 419.

23. R. M. Fisher and M. J. Marcinkowski, Phil. Mag. Vol. 6, No. 71, 1961, p. 1385-1405.

24. B. Roessler, D. T. Novick and M. B. Bever, to be published.

25. R. M. Fisher and M. J. Marcinkowski, to be published.

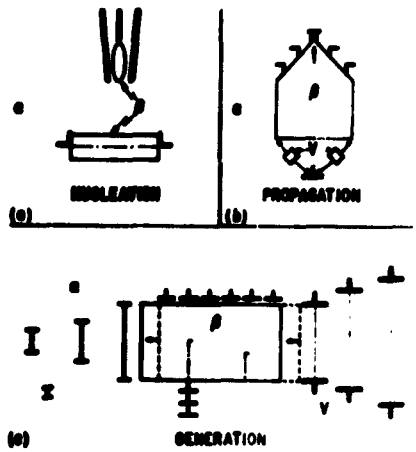

Fig. 1. Schematic Illustration of roles of dislocation sub-structure in phase transformation.
a) in nucleation b) in propagation
c) generation of sub-structure by the transformation.

Fig. 2. Carbide precipitation on dislocation network in Vanadium.

20,000X

Fig. 3. Vacancy loops formed during precipitation of Al- 3.5pct.Mg alloy (Smallman[5]).

40,000X

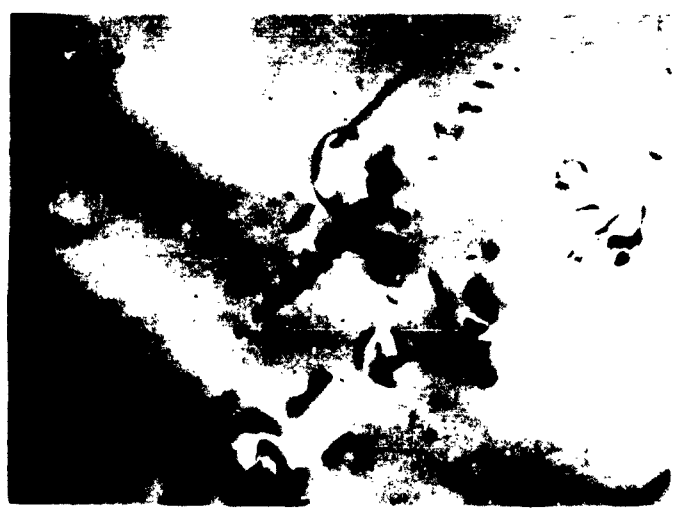

Fig. 4. Interstitial loops formed during carbide precipitation in 80 pct,Cr- Fe at 600°C.

40,000X

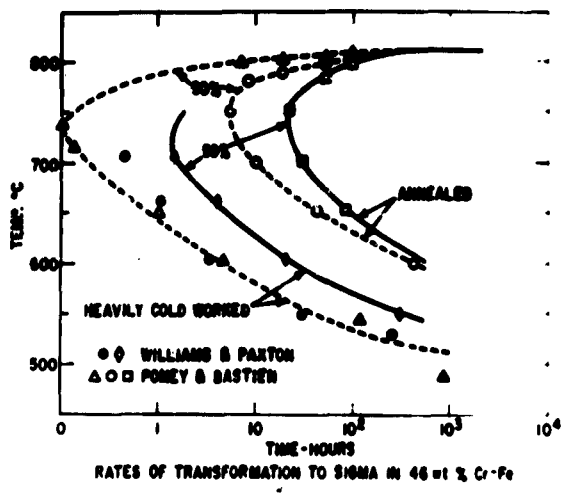

Fig. 5. Effect of cold work on formation of sigma phase.

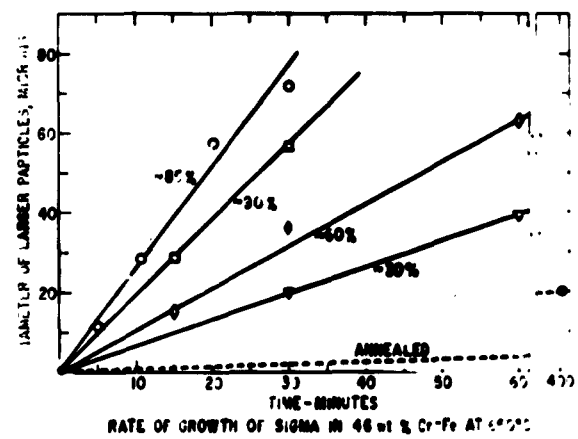

Fig. 6. Effect of cold work on growth rate of sigma phase.

Fig. 7. 46 pct. Cr- Fe cold-rolled 5 pct. and annealed 16 hours at 650°C.

20,000X

Fig. 8. 46 pct. Cr -Fe cold-rolled 90 pct. and annealed 30 min. at 650°C.

20,000X

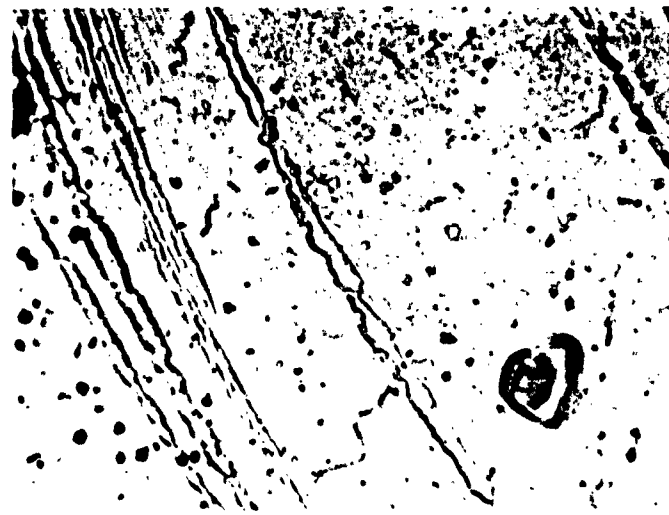

Fig. 9. 'Apparent' sigma formation along deformation twins in 46 pct. Cr - Fe during annealing at 650°C.

1000X

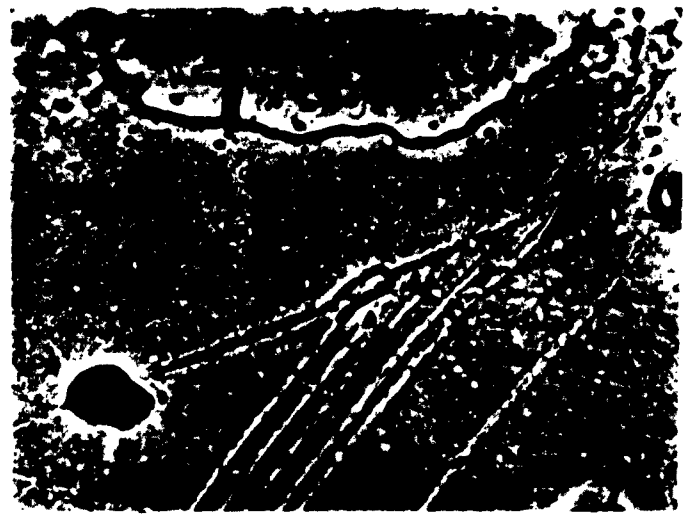

Fig.10. Sigma formation at intersection of deformation twins in 46 pct. Cr - Fe during annealing at 650°C.

1000X

Fig. 11. High dislocation density at intersection of deformation twins in 46 pct. Cr - Fe.

20,000X

Fig. 12. Rapid growth of sigma phase along deformation twins in 46 pct. Cr - Fe during annealing at 650°C.

500X

Fig. 13. Interface between sigma phase and deformed matrix in 46 pct. Cr - Fe annealed for 15 min. at 650°C.

20,000X

Fig. 14. Interface between sigma phase and deformed matrix in 46 pct. Cr - Fe annealed for 30 min. at 650°C.

20,000X

Fig. 15. Growth fault following sub-structure during growth of sigma at 650°C.

20,000X

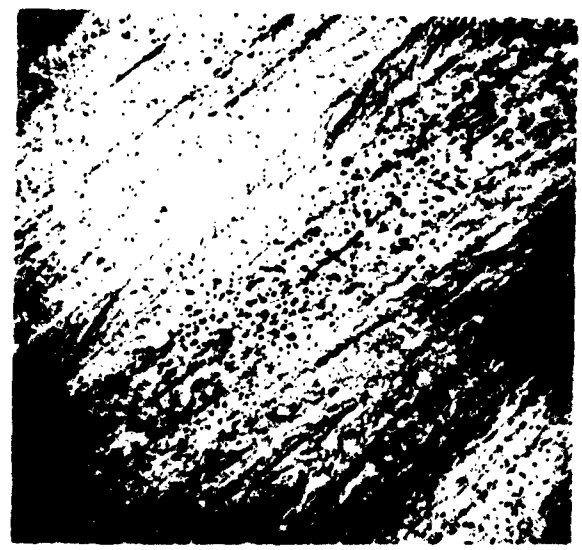

Fig. 16. Carbon extraction replica showing carbide precipitation along deformation band in ausformed steel 18.

15,000X

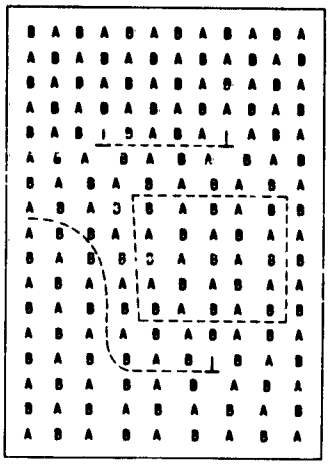

Fig. 17. Schematic illustration of relation between dislocation sub-structure and anti-phase boundaries in ordered structures[20].

Fig. 18. Termination of thermal anti-phase boundary on dislocation.

40,000X

Discussion at ASD Symposium on "The Role Of Structure in The Mechanical Behavior of Metals", (Dec. 5-7, 1962 in Orlando, Florida)

EFFECT OF SUBSTRUCTURE ON FRACTURE OF TUNGSTEN AND MOLYBDENUM

by B.S. Lement, ManLabs, Inc.

Since 1959, a comprehensive investigation[1, 2, 3] of substructure and mechanical properties of refractory metals sponsored by ASD has been carried out by ManLabs, Inc. in collaboration with M.I.T. and Rutgers in this country and with the universities of Liverpool and Cambridge in England. Some of the results obtained by Rutgers, Liverpool and M.I.T. have been presented during this Symposium. I would like to discuss some of the results obtained by ManLabs, which has the objective of elucidating the role of substructure with respect to the ductile-brittle transition in tungsten and molybdenum.

One of the main questions has been to decide whether primary grain size or subgrain size plays the more important role in fracture. Based on the Griffith-Orowan relation, the magnitude of the critical crack length was utilized as a criterion for answering this question. Calculations of critical crack length (2c) were made on the assumption that the effective surface energy for crack propagation (γ') as used in the Griffith-Orowan relation is approximately the same as in the Cottrell-Petch relation. It was also assumed that the fracture stress based on the Griffith-Orowan relation is equal to (or slightly less than) the fracture stress based on the Cottrell-Petch relation. This second assumption is at least partly justified on the basis that no evidence of the occurrence of microcracks prior to fracture of the materials studied has been found.

Under these conditions, it is believed that a crack forms when the Cottrell-Petch relation is satisfied and almost simultaneously attains the critical size required for propagation in accordance with the Griffith-Orowan relation. Propagation of this crack should involve the same γ' value as for the Cottrell-Petch relation at least until the first barrier is encountered. Even though the crack propagation energy (γ_1') associated with crossing such a barrier is presumably greater than for moving between barriers, the crack should cross the barrier provided that

$$\frac{\gamma_1'}{\gamma'} \leq \frac{c}{d} \tag{1}$$

where 2d is the distance between barriers and 2c is the critical crack length. Equation (1) presumably holds since no microcracks were observed prior to fracture of the materials studied.

Assuming that no necking occurs prior to fracture, the fracture stress (σ_F) is given in terms of the shear modulus (G) and the yield stress parameter (k_y) in the following relations:

Cottrell-Petch: $$\sigma_F = \frac{2G\gamma'}{k_y} d^{-1/2} \tag{2}$$

Griffith-Orowan: $$\sigma_F = (1.7\, G\gamma')^{1/2}\, c^{-1/2} \tag{3}$$

Rosenfield[4] has reported that the yield parameter k_y based on primary grain size is given by the following approximate relation:

$$k_y = 5 \times 10^{-5} G \tag{4}$$

Combining equations (2), (3) and (4) gives

$$\frac{c}{d} = 1.0 \times 10^{-9} \frac{G}{\gamma'} \tag{5}$$

Assuming that the ratio of subgrain size (d_s) to primary grain size (d) is approximately constant, the yield stress parameter based on subgrain size (k_{ys}) is related to k_y as follows:

$$\frac{k_{ys}}{k_y} = \left(\frac{d_s}{d}\right)^{1/2} \tag{6}$$

The corresponding equation to (5) for the ratio of critical crack length ($2c_s$) to subgrain size ($2d_s$), which involves the effective surface energy (γ_s') based on subboundaries acting as dislocation obstacles, is as follows:

$$\frac{c_s}{d_s} = 10^{-9}\left(\frac{d_s}{d}\right)\left(\frac{G}{\gamma_s'}\right) \tag{7}$$

Knowing the measured values of σ_F, d and d_s, the above equations enable calculations of γ', γ_s', c/d and c_s/d_s to be made. Such calculations are valid provided that a σ_F value is used that corresponds to a test temperature below the tensile ductility transition (T_d) at which essentially no necking occurs prior to fracture. For this situation, plastic constraint does not have to be taken into account, i.e. Cottrell's β-value = 1.

For the case of severely drawn tungsten wire (about 75 ppm total interstitial content) recovery annealed at five temperatures between 20°C and 1400°C, the increases in fiber width (d) and subgrain size (d_s) with annealing temperature were determined by microexamination using both light and electron microscopy. It was found that $d_s/d \approx 0.1$. From the measured values of σ_F corresponding to temperatures just below T_d, where fracture occurred with relatively little reduction in area, the following calculations were made:

Calculated on Basis of Primary Grain Size*	Calculated on Basis of Subgrain Size
$\gamma' = 7000$ ergs/cm^2	$\gamma_s' = 200$ ergs/cm^2
$c/d = 0.2$	$c_s/d_s = 0.01$

*Corrected for the effect of preferred orientation, i.e. slip occurs in a direction that is about 35° with respect to the fiber direction. Therefore, the effective grain size is about 1.8 times the fiber width.

The calculation based on primary grain size indicates that γ' is about 7000 ergs/cm^2, which is a more reasonable value than the value of 200 ergs based on subgrain size because surface energy measurements give values of 2000-3000 ergs. Assuming that the calculations based on primary grain size are more valid than based on subgrain size, it appears that the critical crack length is approximately equal to the subgrain size ($c \approx 0.2\ d$ and $d_s \approx 0.1d$).

Similar calculations were carried out for molybdenum strip (about 70 ppm total interstitial content) given about 5, 45 and 90% reduction by rolling starting with the recrystallized condition. In this case a correction was made for the decrease in primary grain size, due to the occurrence of appreciable reduction in area (about 15%) prior to fracture. In addition, the flow stress parameter (k_f) was substituted for k_y, and k_f was taken as approximately equal to $0.3\ k_y$[2].

Calculated on Basis of Primary Grain Size*	Calculated on Basis of Subgrain Size**
$\gamma' \approx 3000$ ergs/cm^2	$\gamma'_s \approx 100$ ergs/cm^2
$c/d \approx 0.04$	$c_s/d_s \approx 0.04$

*Corrected for preferred orientation and reduction in area: The correction factor $\approx 1.8\ d\ (\frac{1-\Delta A}{2A})$ where $\frac{\Delta A}{A}$ is the fractional reduction in area.

**Corrected for reduction in area only. *By measurement, d_s was found $\cong 0.04d$.

The calculated value of γ' based on primary grain size agrees with accepted surface energy values (2000 - 3000 ergs/cm^2) and is at the low end of the range (3000 to 12,000 ergs/cm^2) previously reported by other investigators[5, 6, 7]; but the subgrain value of 100 ergs/cm^2 appears too low. Again it is found that the critical crack length based on primary grain size is approximately equal to the subgrain size ($c \approx 0.04\ d$ and $d_s \approx 0.04\ d$).

To summarize the results for the tungsten and molybdenum materials studied, the primary grain boundaries appear to constitute the main barriers to crack propagation since the calculated values of effective surface energy obtained on this basis are more reasonable than on the basis of subboundary obstacles. On the other hand, the fact that the calculated critical crack size was found to be approximately equal to the subgrain size suggests that subboundaries may also influence fracture behavior.

For the moderately worked molybdenum strip (about 45% reduction in area), the tensile ductility transition temperature (T_d) does not appear to change appreciably on annealing in the recovery range. However, annealing at 1000°C results in a significant increase in T_d of about 30°C. This correlates with the onset of recrystallization as manifest by the formationof substructure-free regions. These appear to be considerably larger than the polygonized subgrains representing the unrecrystallized matrix, but definitely smaller than the primary grain size. Since no appreciable change in either the polygonized subgrain size or the primary grain size was found to occur as a result of the 1000°C anneal, the increase in transition temperature is ascribed to the formation of the recrystallized regions. Within these substructure-free regions, larger cracks can presumably form as compared to the polygonized subgrains. Therefore, a decrease in fracture stress and a corresponding increase in T_d would be expected.

References

(1) Lement, B.S., Thomas, D.A., Weissmann, S., Owen, W.S., and Hirsch, P.B., "Substructure and Mechanical Properties of Refractory Metals", WADD Technical Report 61-181, Part I (Aug. 1961).

(2) Lement, B.S., Thomas, D.A., Weissmann, S., Owen, W.S., and Hirsch, P.B., "Substructure and Mechanical Properties of Refractory Metals", WADD Technical Report 61-181, Part II (June 1962).

(3) Lement, B.S., Thomas, D.A., Weissmann, S., Owen, W.S., and Hirsch, P.B., "Substructure and Mechanical Properties of Refractory Metals", Contract No. AF33(657)-8424, Progress Report No. 1 (Aug. 15, 1962).

(4) Rosenfield, A.R., referred to in Owen, W.S. and Hull, D., "The Fracture Transitions in Refractory Metals", AIME Symposium in Chicago (April 1962).

(5) Ault, R.T. and Spretnak, J.W., "Initial Yielding and Fracture in Notched Sheet Molybdenum", ASD-TDT-62-223 (April 1962).

(6) Cottrell, A.H., "Theory of Brittle Fracture in Steel and Similar Metals", Trans. AIME, 212 (1958) 192-202.

(7) Johnson, A.A., "The Effect of Grain Size on the Tensile Properties of High-Purity Molybdenum at Room Temperature", Phil. Mag. 4 (1960) 1944-199.

Aeronautical Systems Division, Dir/Materials and Processes, Metals and Ceramics Lab, Wright-Patterson AFB, Ohio.
Rpt No. ASD-TDR-63-324. SYMPOSIUM ON THE ROLE OF SUBSTRUCTURE IN THE MECHANICAL BEHAVIOR OF METALS. Final report, Apr 63, 504pp. incl illus., tables, 572 refs.
Unclassified Report

The papers contained in this technical documentary report were presented at a symposium which dealt with the subject of substructure and its effect on the mechanical properties of metals. The symposium was held in Orlando, Florida on 5-7 December 1962. Both review papers and reports of

(over)

current research are included. The following general subject areas are covered: experimental techniques for observing and measuring substructure; development of substructure by deformation, recovery, and recrystallization; the role of substructure in yielding, twinning, and fracture; and the role of substructure in transformation and precipitation.

1. Mechanical behavior of metals
2. Substructure
3. Dislocation
4. Plastic deformation
5. Fracture
I. AFSC Project 7351, Task 735101
II. Not aval fr OTS
III. In ASTIA collection

Aeronautical Systems Division, Dir/Materials and Processes, Metals and Ceramics Lab, Wright-Patterson AFB, Ohio.
Rpt No. ASD-TDR-63-324. SYMPOSIUM ON THE ROLE OF SUBSTRUCTURE IN THE MECHANICAL BEHAVIOR OF METALS. Final report, Apr 63, 504pp. incl illus., tables, 572 refs.
Unclassified Report

The papers contained in this technical documentary report were presented at a symposium which dealt with the subject of substructure and its effect on the mechanical properties of metals. The symposium was held in Orlando, Florida on 5-7 December 1962. Both review papers and reports of

(over)

current research are included. The following general subject areas are covered: experimental techniques for observing and measuring substructure; development of substructure by deformation, recovery, and recrystallization; the role of substructure in yielding, twinning, and fracture; and the role of substructure in transformation and precipitation.

1. Mechanical behavior of metals
2. Substructure
3. Dislocation
4. Plastic deformation
5. Fracture
I. AFSC Project 7351, Task 735101
II. Not aval fr OTS
III. In ASTIA collection